Late Cretaceous to Early Miocene Magmatic and Tectonic Evolution of Central Panama

Jian Wang (王建)

School of Earth and Environmental Sciences

Cardiff University

Submitted in partial fulfilment of the requirements for the degree of

Doctor of Philosophy (PhD)

December 2020

ACKNOWLEDGEMENTS

This four years' PhD is the biggest adventure so far in my life. I met so many wonderful people during this journey. My PhD is only possible with their help.

Firstly, I want to thank my supervisors David Buchs and Andrew Kerr. David provides such a wonderful project in Panama which makes it possible for me to study subduction zone magmatism. His expertise in field geology and working in tropical area is impressive. I feel very lucky to have this opportunity to go to the field with him. Andrew always supported me with useful advices and decent suggestion of related papers. Taking his undergraduate lectures and thin section practicals helped me build a solid foundation for petrology. All these helped me grow confidence in being a geologist for the future career.

I want to thank China Scholarship Council, Cardiff University, and Authority of Panama Canal. Without their financial support, I cannot make it here and cannot finish my PhD.

I want to thank Roberto, Rodrigo and Romi from Authority of Panama Canal, Henry from Cardiff University, Xenia, Celso and Mario from Dirección General de Recursos Minerales, Eric and Johany from Panama University for their help in the field. I want to thank Tony for the wonderful thin sections, Iain for whole rock geochemistry, Duncan for SEM, and Marc for Sr-Nd-Pb isotopes. Without all the lab work in Cardiff University, my PhD is not possible. I also thank my master supervisor Guanghai Shi from China University of Geosciences (Beijing) who supported me with zircon selecting and Andy from Birkbeck College who analysed zircon dating.

I want to thank my PhD colleagues at Cardiff University. You are the most wonderful person I have ever met! Talking with you let me know different cultures. It is always enjoyable to talk with you about rocks and things unrelated to rocks, Jamie and Joanna. Many thanks go to Will and Emma for all the discussion and revision for my thesis. My thesis is highly improved with your help.

I want to thank Dr Lam. Life is really amazing to let you be my landlord. Talking about medicine and different religions let me know different cultures.

I want to thank professors at Cardiff University. You let me know what science is and how to do science.

Cardiff is such a beautiful city and I feel so luck to study here. No matter what kind of pressure I am under, I felt relieved whenever I went to Bute Park.

Last, I want to thank my family for all the support during and before my PhD. My grandpa always encouraged me to do what I like. This thesis is for you. I know you are somewhere watching me and encouraging me.

ABSTRACT

Panama Volcanic Arc (PVA) has a long magmatic history lasting from subduction initiation to the present. Different magmatic phases, e.g. pre-Oligocene arc and Cordillera arc, show different compositions which associate different tectonic settings. To better understand the magmatic and tectonic evolution of PVA, detailed work was conducted in central Panama (from El Valle to the west of Cerro Azul).

Whole rock geochemistry shows that the pre-Oligocene Chagres Complex range from basaltic to andesitic while the post-Eocene rocks range from basaltic to rhyolitic. The Chagres complex have similar major elements as those of the post-Eocene mafic rocks but have smaller content of the most incompatible elements, as the former are similar to the oceanic arc basalt and the latter similar to the continental arc basalt. Las Cascadas Formation crystallized from a magma mush similar to the one for the Panama Formation and mineral/glass chemistry further indicate the Las Cascadas Formation magma extracted from the magma mush with or without trapping crystal framework of the mush.

Whole rock Sr-Nd-Pb isotopes show that the ambient mantle is the Caribbean Large Igneous Province mantle with HIMU component. Trace element and isotope modelling show that the Chagres Complex have the highest sediment melt and partial melting degree while these parameters are smaller for the Panama Formation. The Cabra/Pedro Miguel Formation have the highest AOC melt and the lowest sediment melt.

As the crust thickened through time, the mantle wedge became colder and the melting field in the mantle wedge moved downward and away from the trench, which resulted in the pre-Oligocene arc migrating away from the trench to the post-Eocene arc. The corresponding location of slab fluid/melt releasing also moved downward to a higher pressure due to which slab input decrease from the Chagres Complex to the Panama Formation. The decreasing slab input, probably along with the downward isotherms gave rise to the decreasing partial melting degree. When the Cocos-Nazca spreading centre subducted beneath central Panama, a slab window formed which facilitated AOC melting. Partial melting of ambient mantle metasomatized by this AOC melt formed the Cabra/Pedro Miguel Formation. The olivine basalts have the lowest partial melting degrees which mark the cessation of magmatism in central Panama.

TABLE OF CONTENTS

1 INTRODUCTION

1.1 Volcanic Arc Magmatism

The volcanic arc sits on Earth's convergent margins, in which oceanic lithosphere subducts beneath another oceanic lithosphere (i.e. island arc) or continental lithosphere (continental arc). The difference between arc magmatism and intraplate magmatisms such as the formation of the middle ocean ridge basalt (MORB) and oceanic island basalt (OIB) is the role water plays in the arc magmatism generation. Magmatism on Earth is controlled by three factors: temperature, pressure, and water content. Decreasing pressure and increasing temperature, which is responsible for the formation of MORB and OIB respectively, can both give rise to mantle melting. When the oceanic lithosphere subducts at convergence margins, it dehydrates as it undergoes metamorphism to eclogite (Gill, 1981; Peacock, 1993) to release aqueous fluids, which trigger flux melting at the water-saturated solidus (Grove et al., 2006). Another possibility is these fluids metasomatize the overlying mantle to form hydrous minerals. The solidus of this metasomatized mantle is reduced and this mantle wedge can go through partial melting under appropriate condition (Plank and Langmuir, 1988; Davies and Stevenson, 1992, Zheng, 2019).

When the mantle melting occurs, elements from the subducting slab along with the ambient mantle (the mantle prior to slab fluid metasomatism; Tuner and Langmuir, 2015) go to the Earth's surface through arc magmatism. The residue of the slab will go deep into the upper mantle-lower mantle boundary (Zhao et al., 2009; Garel et al., 2015) or core-mantle boundary (Pradhan et al., 2015) to join deep Earth processes. Therefore, subduction zone processes play an important role in chemical recycling on Earth (Martin and Hermann, 2018) and studying the arc magmatism can help understand the chemical recycling.

1.1.1 Geochemical Heterogeneity of Arc Magmatism

When melting occurs in the mantle wedge, trace elements display a preference either for the melt or the solid phase. Trace elements which tend to go into the solid phase, i.e. minerals are described as compatible elements while those tend to go into the melt are described as incompatible elements. For the incompatible elements, it could be further divided into several subgroups based on the ratios of charge to element radius. Elements with high charge to radius ratio are known as high field strength elements (HFSE) which include Nb, Ta, Ti, Zr, Hf, and sometimes also Th, U. Elements with large radius and small charge are known as large ion lithophile elements (LILE) which are primarily the alkali and alkali earth elements (e.g. K, Rb, Cs, Sr, Ba). Arc rocks are enriched in LILE, Pb, U, Th, and light rare earth elements (LREE) while depleted in HFSE in primitive mantle or N-MORB normalised multi-element diagram (Fig. 1.1). Therefore, LILE, Pb, U, Th, and LREE are usually called 'fluid mobile' elements as they can be mobilised during slab devolatilization (Spandler and Pirard, 2013; Zheng, 2019). HFSE are called 'fluid immobile' elements as they are considered to stay in the

slab residue during slab dehydration. They are classified as nonconservative and conservative elements respectively by Pearce and Peat (1995). However, studies show these immobile elements can also be mobilised in slab melts or supercritical fluids (Pearce and Peat, 1995; Pearce et al., 2005; Kessel, 2005; Plank, 2014; Turner et al., 2015).

Apart from the different slab addition, varying composition of primitive arc magma can also be caused by the ambient mantle as the sub-arc ambient mantle may be heterogeneous before being metasomatized by slab material (e.g. Hochstaedter et al., 2000; Churikova et al., 2001; Caulfield et al., 2008; Turner et al., 2017). Apart from the above two factors, the melting degree of the mantle source also plays an important role in controlling the arc magma geochemistry (Woodhead and Johnson, 1993; Pearce and Peate, 1995; Tollstrup et al., 2010; Shuto et al., 2015).

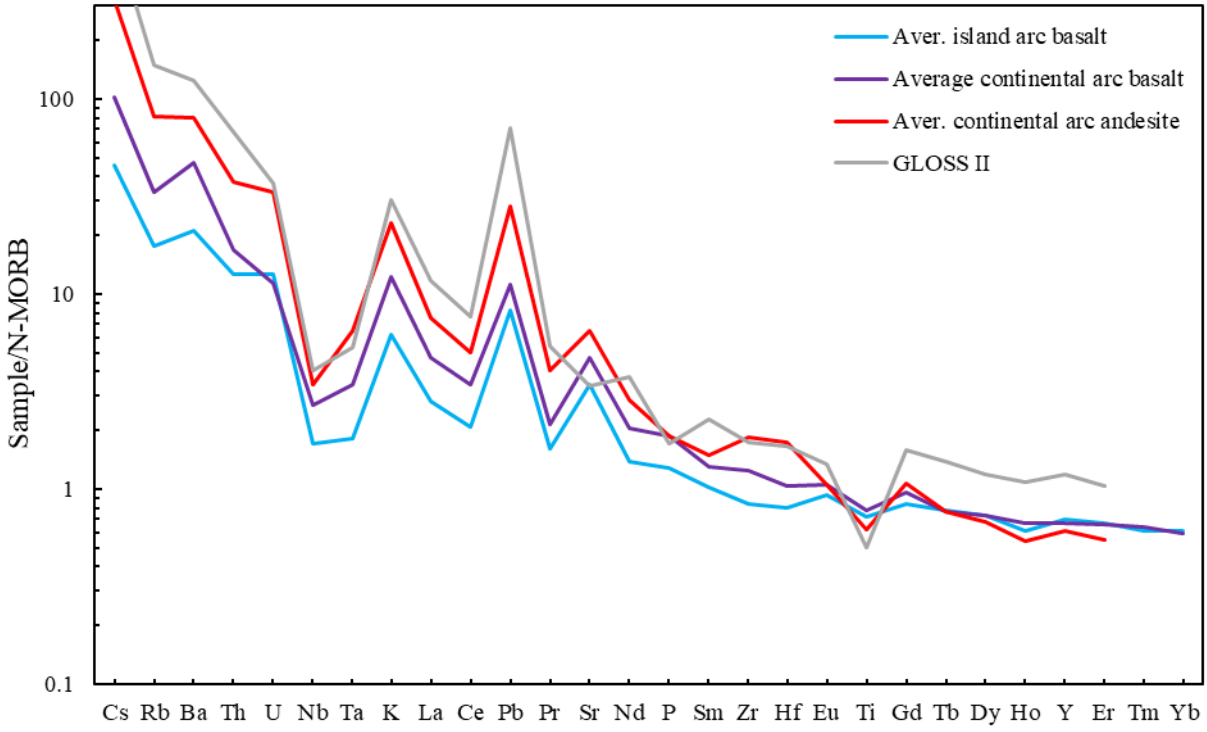

Fig. 1.1 N-MORB normalised multi-element diagram. Average compositions of arc rocks are from Kelemen et al. (2013) and GLOSS II is from Plank (2013).

1.1.1.1 Slab dehydration and melting

The subducting slab is an oceanic lithosphere formed in the middle ocean ridge, which includes the oceanic crust and lithospheric mantle. An oceanic crust is composed of a thin sedimentary cover layer (including pelites, carbonates, cherts, and volcanoclastic sediments) whose composition varies largely from place to place, a basaltic layer built of pillow lavas and sheeted dikes, and a gabbroic layer with an upper part chemically similar to MORB but a lower part mostly composed of cumulates including differentiated high-Mg gabbros, Fe-Ti gabbros, troctolites, and norites (Nicolas, 1989). The crust is underlain by the lithospheric mantle (mainly harzburgitic peridotite) which is partly serpentinized (Snow and Dick, 1995).

In subducting zones, cold slabs descend into the warm mantle, resulting in cooling of the mantle wedge and warming of the slab surface. The slab thermal parameter Φ (= A*V*sin θ; A is slab age, V is convergence velocity, and θ is the slab dip) is usually used to describe how cold a subduction zone is (Kirby et al., 1991). It is large for fast subduction of old lithosphere with big slab dip, e.g. Tonga arc and small for slow subduction of young lithosphere with small slab dip, e.g. Cascadia arc. However, slab thermal structure is complex and it is also affected by other factors such as slab sinking mode, i.e. downdip sinking vs rollback sinking (Kincaid and Griffiths, 2004) and mantle wedge temperature (Hall, 2012). The subducting slab undergoes metamorphic dehydration and partial melting during subducting processes which release aqueous fluids, hydrous melts or supercritical fluids to metasomatize the overlying mantle wedge. Slab thermal structure decides which fluid can be released (Peacock et al., 1994) and how much the fluid can be released (van Keken et al., 2011).

Dehydration in the forearc depth:

When the slab subducts to a shallow fore-arc level (<15 km; Bebout, 2014), the uppermost sediment and AOC layer experience large amounts of compaction, resulting in a mechanical expulsion of pore waters (Moore and Volijk, 1992). Extraction of pore waters barely change the trace element contents of the sediment (Morris et al., 2002). Apart from pore water expulsion, clay minerals in the sediment layer such as smectite-illite dehydrate at this shallow level to be low-grade metamorphic micas, releasing large amounts of mineral-bound, low chloride water (Brown et al., 2001; Kastner et al., 1991; Moore et al., 2001). LILE can be dissolved in these aqueous fluids (Bebout, 2014). The transformation of opal-A to quartz can also occur in this early stage subduction during which water can also be released (Moore and Volijk, 1992).

Beyond this depth of ~15 km, the AOC enters into the blueschist facies, in which the major hydrous minerals are chlorite, Na-rich, Ca-poor amphiboles (glaucophane to barroisite), phengite, lawsonite or zoisite, and paragonite (e.g., Sorensen, 1986). These hydrous minerals can dehydrate significantly to release large volume of aqueous fluids, through various continuous and discontinuous reaction

(Schmidt and Poli, 2014). Most of the fluid released from slab in the forearc depth will either serpentinize the cold corner of the mantle wedge, or eventually pass through to the ocean floor in the forearc region (e.g., Mariana arc, Fryer et al., 1999). Geophysical modelling (gravity, seismics, electrical conductivity, and magnetics) of fore-arc regions convincingly demonstrate that shallow slab devolatilisation leads to extensive hydration and cooling of the fore-arc mantle wedge (Bostock et al., 2002; Hyndman and Peacock, 2003).

Dehydration in the sub-arc depth:

Beyond ~2.4 GPa, the pressure-sensitive mineral amphibole breaks down (Fig. 1.2). A maximum of 1.5 wt% H_2O remains in hydrous phases of the igneous oceanic crust, e.g. lawsonite, zoisite, chloritoid, talc, and phengite (Fig. 1.2; Schmidt and Poli, 2014) which can go further down and bring water to a deeper zone. Besides, continuous reactions dominate over discontinuous reactions above ~2.4 GPa, and most reactions are subparallel to typical subduction P-T paths. Therefore, rocks in the subducting slab undergo most reactions over wide depth intervals, which gives rise to a low dehydration rates with the 1.5 wt% H_2O being lost over a wide depth range. The P-T range that defines this ‘low dehydration rate’ regime corresponds to the sub-arc depth (Schmidt and Poli, 2014).

At the pressure of 2.5-3.0 GPa, the most important hydrous minerals in metapelite are potassic micas, phengite, and biotite, with other minerals such as talc, chloritoid, and chlorite (Poli and Schmidt, 2002). The stability of these hydrous minerals and the bulk water content of metapelite are highly controlled by the composition of the metapelite.

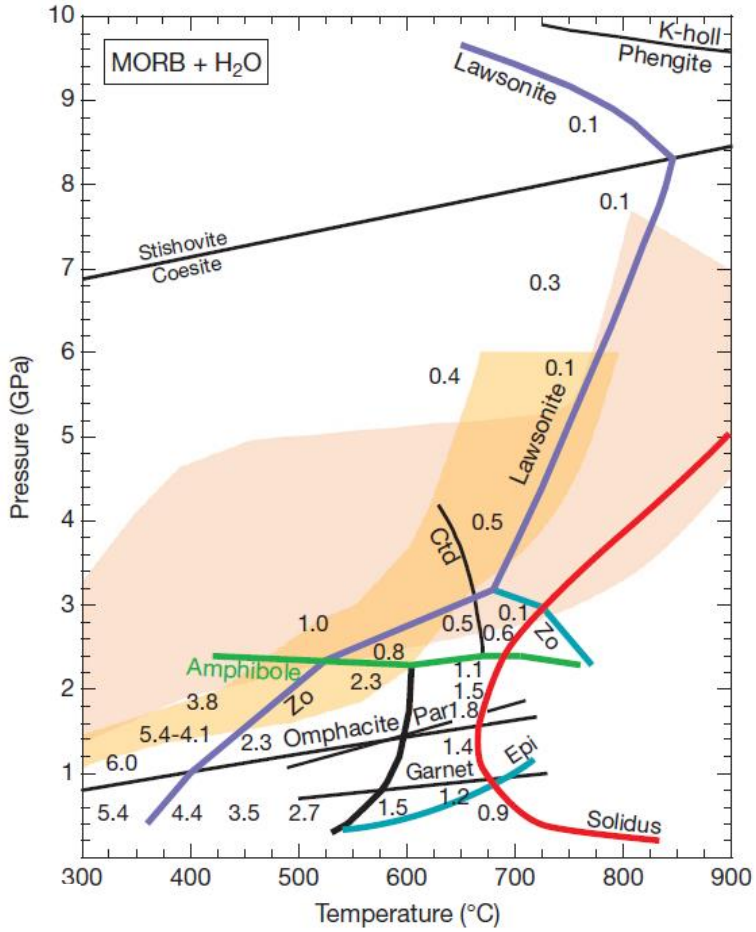

Fig. 1.2 Major phase stability boundaries in H_2O-saturated MORB and H_2O contents (numbers, in wt%) stored in hydrous phases (from Schmidt and Poli, 2014).

Slab melting:

Slab melting can be divided into two types based on whether the free fluids are present or not. Fluid-saturated melting of K-bearing basaltic crust begins at temperatures of 650 ℃ at 1.5 GPa, increases to 750 ℃ at 3 GPa (Lambert and Wyllie, 1972; Schmidt et al., 2004; wet solidus in Fig. 1.3 a). Although a small quantity of free fluid (<0.1 vol%) formed by dehydration would not be sufficient to produce a significant melt portion, fluid-saturated melting could be achieved at relatively low temperatures favored by addition of aqueous fluid from dehydrating serpentinized peridotite below oceanic crust (Poli and Schmidt, 2002; Grove et al., 2006; Klimm et al., 2008; Schmidt and Poli, 2014). Similarly, important sediment melt fractions could result from flushing with fluids from underlying altered oceanic crust or serpentinized peridotite (Skora and Blundy, 2010).

Fluid-absent melting is defined as the production of a silicate melt with low water contents derived from partial melting of hydrous (or carbonate) minerals (amphibole and epidote/zoisite in oceanic crusts and phengite and biotite in pelites; Fig. 1.3; Schmidt and Poli, 2014). Evidence for fluid-absent

melting of the oceanic crust is seen in adakites (Defant and Drummond, 1990; Drummond et al., 1996; Castillo, 2012). This is supported by experiments of dehydration melting of amphibolite (Rapp et al., 1991; Sen and Dunn, 1994; Wolf and Wyllie, 1994). In addition, adakitic glass inclusions in sub-arc mantle xenoliths from Philippine arc lavas (Schiano et al., 1995) provide direct evidences that subducting oceanic crust can undergo partial melting. The subducted sediments which are in direct contact with the hot mantle wedge are typically at higher temperatures than the underlying igneous oceanic crust. Besides, the meting temperature for the sediments is lower than the oceanic crust (Fig. 1.3). Thus, if the amphibolite can melt, the overlying sediments must also melt through phengite-dominated melting (Poli and Schmidt, 2004). However, other studies suggest sediment melting occurs in the form of fluid-saturated melting as sediment (e.g. radiolarian clay) cannot melt in fluid-absent experiments (~1 wt% H_2O) even at temperatures higher than 900 ℃ (Skora and Blundy, 2010).

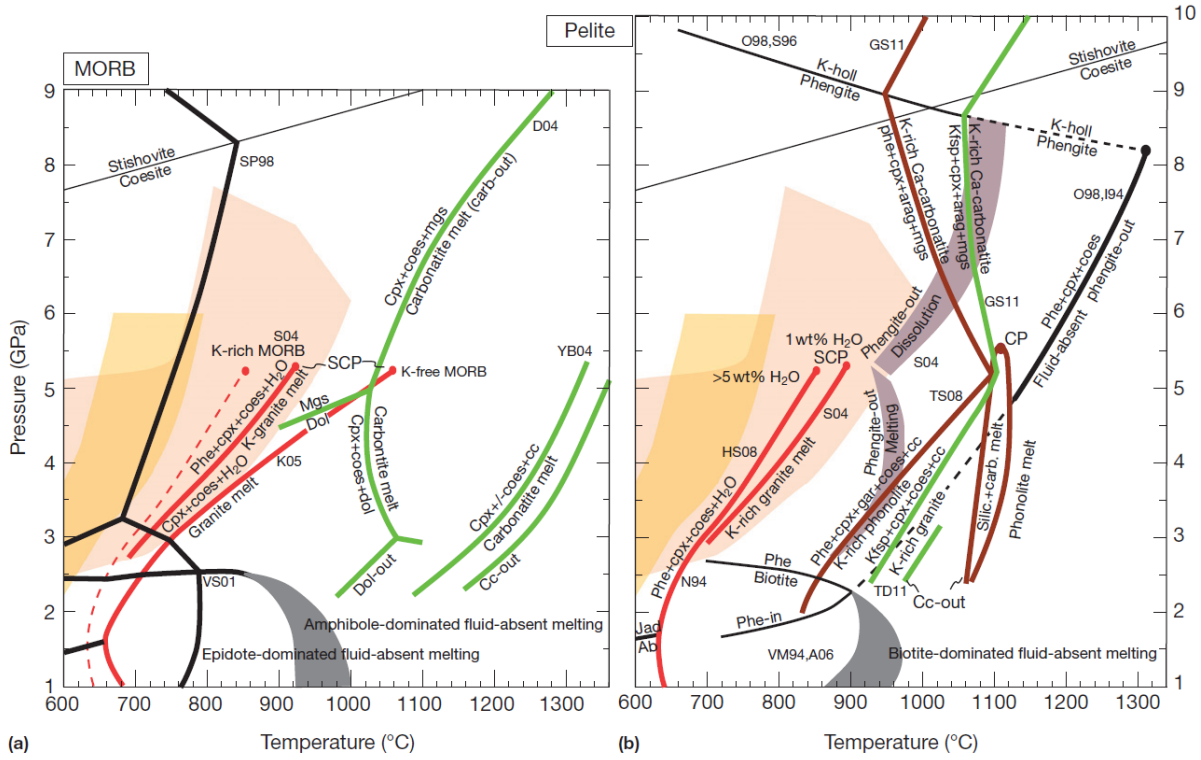

Fig. 1.3 Compilation of melting reactions in (a) MORB and (b) pelite. Diagrams are from Schmidt and Poli (2014).

1.1.1.2 Slab contributions to arc magmatism: sediment component vs AOC component

All dehydration reactions in oceanic lithosphere take place at temperatures that diffusion rates in most minerals are insignificant in terms of the time span of fluid production (Schmidt and Poli, 2014). This suggests that elements released into fluids are controlled by the reactive volume of their host minerals.

In other words, element compatibility is controlled by the stability of their main host minerals. Below is a brief description of mineral behaviour, i.e. incompatibility, mainly based on experiment studies. Trace elements are divided into five groups which is modified from Schmidt and Poli (2014):

- Highly soluble elements (Rb, Ba, Pb are soluble in aqueous fluids; Johnson and Plank, 1999; Kessel, 2005; Hermann and Rubatto, 2009; Fig. 1.4) where the aqueous fluid/mineral >>1. They partition strongly into aqueous fluids. Sr is fluid mobile and is not retained to any solid residue at any temperature (Hermann and Rubatto, 2009). The concentration of such elements may continuously decrease in the fluid as dehydration increases with increasing depth. Therefore concentrations might already be very low in fluids produced at the sub-arc depth due to the effective removal from the subducting crust at shallow levels.
- Elements with partition coefficients close to 1 (e.g., Be; Marschall et al., 2007). In this case, the concentration in the fluid does not change as subduction progresses (Fig. 1.4). The original concentration before dehydration plays a dominant role in this case.
- Elements that partition strongly into a particular hydrous phase (e.g., La, Ce, Sr into lawsonite or epidote, the latter also hosting most of the Th) and have only moderate to low cpx/fluid and gar/fluid partition coefficients. These elements will quantitatively enter into the fluid when their host minerals break down. These discontinuous reactions cause a pulse in their concentrations that is not proportional to the fluid volume. However, recent studies show that LREE and Th are highly controlled by accessory minerals such as allanite/monazite (Klimm et al., 2008; Hermann and Rubatto, 2009; Skora and Blundy, 2010). A relative cool temperature (cool subduction zone) at the sub-arc depth could promote minerals (e.g. antigorite) in the underlying crust breaking down to release aqueous fluids, which facilitates sufficient partial melting of sediment. This melting could consume monazite and dissolve the entire LREE+Th of sediment (Skora and Blundy, 2010).
- Elements that partition strongly into mica (e.g., Rb and Ba are highly fluid mobile but can be partly held back by phengite; Hermann, 2002; Hermann and Rubatto, 2009). As mica dissolves with increasing depth and temperature, these elements enter into the fluid only at a greater depth, its flux at low temperature and pressure being small.
- Elements that strongly partition into anhydrous mineral cpx or garnet (HREE) or into accessory minerals that are stable during devolatilization, such as rutile (Nb-Ta-Ti; Brenan et al., 1995b; Hermann and Rubatto, 2009; Rustioni et al., 2021), zircon (Zr, Hf; Hermann and Rubatto, 2009), and monazite (LREE and Th; Klimm et al., 2008; Hermann and Rubatto, 2009; Skora and Blundy, 2010). Such elements could be returned to replenish the deep mantle trace element reservoir. However, accessory minerals (rutile, zircon, and monazite) have strongly increasing $D_{melt/solid}$ with increasing temperature. When these mineral exhausted,

LREE+Th from monazite and Nb-Ta-Ti from rutile can be totally exsolved (Skora and Blundy, 2010).

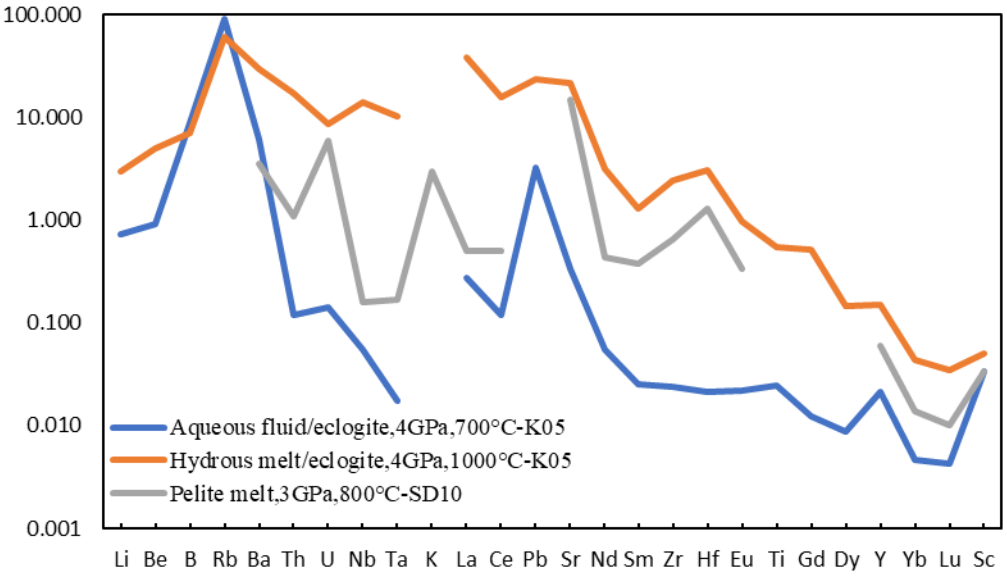

Fig. 1.4 Liquid/solid residue partition coefficients for aqueous fluid/eclogite (Kessel et al.,2005-K05), hydrous melt/eclogite (Kessel et al.,2005-K05), and pelite melt (Skora and Blundy, 2010-SB10). Rutile is an accessory mineral in all three cases.

Element contents in fluids are not only controlled by partition coefficient, but also the composition of the whole rocks. Besides, element behaviour from high pressure experiments only makes sense when it explains the chemical characteristics found in natural arc rocks.

For LILE and Pb, they are usually interpreted to come from aqueous fluid (Pearce and Peate, 1995; Pearce et al., 2005), such as AOC aqueous fluids (Elliott et al.,1997; Elliott et al.,2003). HP aqueous fluids are relatively dilute solutions (Si, Al, and alkali), with solute loads of ~5 to 15 wt.% (Hermann and Rubatto, 2009; Hermann and Spandler, 2008; Manning, 2004; Spandler et al., 2007). LILE contents are elevated in aqueous fluids compared to REE and HFSE, but overall trace element contents are low (*Fig.* 1.4). The presence of halogens is likely to increase the content of some trace elements in the fluid as demonstrated by experiments (e.g., Keppler, 1996; Rustioni et al., 2021). However, the halogen content of HP slab fluids is expected to be low (< 5 wt.% NaCl equivalent), as a large fraction of the halogen inventory is lost from the slab at fore-arc depths (Manning, 2004; Scambelluri et al., 2004). It remains questionable that aqueous fluids are capable of transferring other required trace elements such as LREE and Th apart from LILE (Hermann and Rubatto, 2009; Spandler et al., 2007).

In this regard, slab melts, in addition to aqueous fluids are introduced to explain the ‘arc signature’. There is a general consensus that the enrichment of LREE and Th in arc rocks is caused by sediment

melts (Elliott et al.,1997; Elliott et al.,2003; Pearce and Peate, 1995). This idea has been supported by certain tracers:

- Th is extremely high in sediment and also arc rocks (Fig. 1.1). However, Th, along with Be cannot be transferred from the slab through aqueous fluids but sediment melts as they are only incompatible above the solidus (Johnson and Plank, 1999; *Fig.* 1.4). The element Nb is low in arc rocks due to its compatibility in rutile during devolatilization. Besides, Th and Nb has similar partition coefficient during mantle melting. Therefore, Th/Nb ratio rules out the effect of partial melting degree and is an indices for sediment melts (Elliott, 2003; Turner et al., 2015). Similarly Ba/Na can also display the amount of sediment melt in the mantle source (Plank and Langmuir, 1993).
- The rare earth elements generally behave as a coherent group of REE^{3+} cations with gradually decreasing ionic radii. Under oxidising conditions Ce forms Ce^{4+} ions which shows anomalous behaviour relative to other 3+ cations. As a consequence, some deep sea sediments show anomalously low Ce concentrations relative to the other REE (i.e. negative Ce anomalies; Othman et al, 1989; Toyoda et al, 1990; and Plank and Langmuir, 1998).
- ^{10}Be is a cosmogenic isotope with a short half-lift of 1.39 Ma. This suggests no ^{10}Be in the Earth's interior but it can be found in sediment. ^{10}Be in arc rocks originates from sediment subducted to the magma formation zone (Tera et al., 1986). Other isotope such as Pb could also be used to determine the sediment component (Woodhead, 1989).

The existence of AOC melts in the mantle source can be revealed not only by the formation of adakite as discussed above, but also by the formation of OIB-like rocks above subduction zones (Zheng, 2019; Zheng et al., 2020). As discussed above, Nb-Ta are compatible in rutile which is considered to be stable during slab dehydration processes. That is why there is a Nb-Ta depletion in the normalized multi-element diagram (Fig. 1.1). However, under high pressure and temperature, rutile can be melted out during slab melting (Spandler et al., 2008) and Nb becomes incompatible and will be enriched in the melt. This Nb-enriched slab melt can metasomatize the mantle wedge whose melting forms the OIB-like rocks (Zheng et al., 2019; Zheng et al., 2020).

1.1.1.3 Heterogeneous ambient mantle and variable partial melting degree

The ambient mantle beneath volcanic arcs is considered as the convecting asthenospheric mantle. However, studies on South American Andes volcanics argue for an enriched sub-continental lithospheric mantle (SCLM) as the source of arc magmas (Rogers and Hawkesworth, 1989; Kay and Abbruzzi, 1996; Turner et al., 2017). This is consistent with the Pearce (1983) which suggests relatively enriched ambient mantle sources in continental arcs on the basis of trace element abundances, and proposed the enriched melts are partially derived from the SCLM. Apart from the

continental arcs, the Ryukyu island arc is also characterized by EM1-type enrichments (Hoang and Uto, 2006). Although it is not underlain by SCLM, the Ryukyu arc lie close to the Sini-Korean cratonic region. Based on the fact that all the arcs which show SCLM component are adjacent to old continental cratons, Turner et al. (2017) propose that the SCLM material is delivered from the bases of continental lithospheric blocks into the ambient mantle wedges of arcs by corner flow. Several studies (Ewart and Hawkesworth, 1987; Woodhead et al., 1993; Pearce and Peat, 1995; Langmuir et al., 2006) have demonstrated that island arcs with back-arcs tend to be derived from depleted ambient mantle sources. The depletion could be attributed to mantle depletion caused by melt extraction beneath the back-arc spreading center (Turner et al., 2017).

Apart from the different enrichment or depletion between continental arcs and island arcs, the ambient mantle wedge varies from place to place. For example, the ambient mantle for the SW Pacific arc varies in their isotope compositions, with a clear distinction between “Indian” and “Pacific” domains (Turner et al., 1999; Pearce et al., 2007). Feigenson et al. (2004) proposes that the ambient mantle beneath the Central America arc is CLIP mantle due to the high Pb isotopic ratios in eastern Nicaragua and Costa Rican back-arc lavas. Therefore, the ambient mantle beneath different arcs is not homogeneous which could give rise to the heterogeneity of arc rock chemistry.

Apart from different volume of slab input and heterogeneous ambient mantle, the chemical variation can also be attributed to partial melting degree (Woodhead and Johnson, 1993; Pearce and Peate, 1995; Tollstrup et al., 2010; Shuto et al., 2015). As mantle melting decreases, the most incompatible elements (elements on the left side of Fig. 1.1) increase. However, the controlling factors for mantle melting is complex, which includes mantle thermal structure (Plank and Langmuir, 1998; Turner and Langmuir, 2015) and slab fluids (Cooper et al., 2020).

Therefore, the chemical composition of arc rocks is controlled by slab material, ambient mantle, and partial melting degrees.

1.1.2 Magmatic shutdown or magmatic lull in volcanic arcs

Mantle wedge goes through partial melting which is facilitated by the presence of water released from the underlying slab (Grove et al., 2006; Davies and Stevenson, 1992; Zheng, 2019; Cooper et al., 2020). Arc magmatism shutdown is widely observed in collision zone such as the Himalaya-Alps orogenic belt. As the subduction terminate, no fluids can be released from the slab to facilitate mantle wedge melting.

Apart from subduction termination, volcanic shutdown or lull is also observed above the subduction zone which possesses a slab. For example, it has been reported in Panama that oblique subduction can also cause volcanic shutdown (Buchs et al., 2019a). When the Farallon Plate break up into Cocos Plate and Nazca Plate, the Nazca Plate subducted eastward parallel to the central America trench. No

slab is renewed during this oblique subduction which means no fluids can be released to facilitate the mantle wedge melting (Buchs et al., 2019a).

The third possibility is flat subduction. Subduction with shallow dip is widely observed in Andes such as in central Chile, Peru, and Colombia. Flat subduction in these area correlates with volcanic gap based on which some suggest flat subduction might give rise to the cessation of arc magmatism (Gutscher et al., 2000a; O'Driscoll et al., 2012; Zhang et al., 2019). The possible reasons for flat subduction were listed in Gutscher et al. (2000b), such as interplate hydrostatic suction (Jischke, 1975, O'Driscoll et al., 2009) and subduction of young, buoyant lithosphere or thickened lithosphere (Pennington, 1984). However, how the flat subduction affects arc magmatism is not well studied. Gutscher et al. (2000b) suggest at the early stage of flat subduction, the slab is being heated to melt during which adakite can be formed. At the latter stage of a prolonged flat subduction, both overriding lithosphere and underlying lithosphere cool down and the asthenospheric wedge disappear. This gives rise to the cessation of arc magmatism. This evolution pattern is observed in central Chile and probably also Costa Rica (Gutscher et al., 2000b). Therefore, flat subduction could result in a magmatic shutdown.

Although subduction of spreading ridge and the formation of a slab window do not give rise to a total magmatism shutdown, but it will give rise to magmatic cessation of normal arc rocks and form peculiar rock types. As described above, mantle wedge melting is favoured by the water released from the underlying slab. When a slab window forms, the asthenosphere above the slab window will not be dehydrated as no slab releasing fluids. In this way, reduced hydration above a slab window causes normal arc volcanism to wane or cease (Thorkelson et al., 1996). Meanwhile, ‘slab window magmatism’ with tholeiitic rocks or alkaline rocks (Hole et al., 1991; Johnston and Thorkelson, 1997; Abratis and Worner et al., 2001) can form as the hot sub-slab asthenosphere upwells to heat up the mantle wedge to melt, or the sub-slab asthenospheric mantle go through decompression melting (Thorkelson et al., 1996; Schuth et al., 2004). More rarely, picrite is also found above slab windows such as in Solomon arc. The slab window, which is formed by the Woodlark spreading ridge subduction, can generate an area in the mantle that high temperature and rapid adiabatic decompression melting occurs to form high degrees of mantle melting. This high degrees of melting along with the extensional environment facilitate the disaggregation of mantle peridotite and enhance its incorporation into the primitive melts to form picrite during ascent (Schuth et al., 2004; Rohrbach et al., 2005).

1.1.3 Formation of the felsic rocks in arc settings

Felsic rocks (SiO_2 >63 wt.%) are usually explained by two end-member mechanisms: (1) partial melting of crustal material; (2) fractional crystallization of mafic magma (Fig. 1.5). The first mechanism is commonly used to interpret felsic rocks found in areas with continental crust (including continental arcs) (Cobbing and Pitcher, 1983; White and Chappell, 1983; Vielzeuf and Holloway, 1988) but can also occur in oceanic arc settings (Shukuno et al., 2006). The second mechanism is explained by melt extraction from highly crystallized magma mush (Bachmann and Bergantz, 2004; Hildreth, 2004; Bachmann and Bergantz, 2008; Barker et al., 2013).

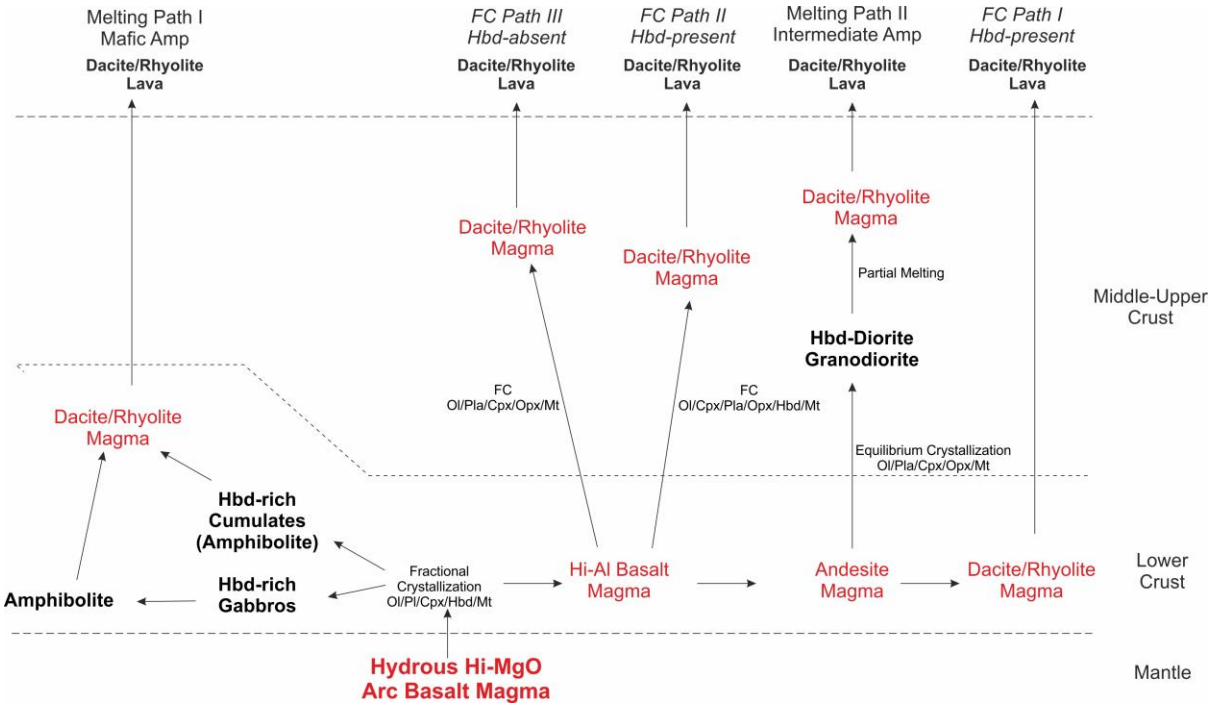

Fig. 1.5 Five possible ways to form a felsic magma (taken from Brophy, 2008)

In intra-oceanic arcs the lithologies of the lower crustal are mainly mafic/ultramafic cumulates, gabbros and possibly amphibolite. After the primitive magma generates from its mantle source, it ascends upward due to buoyancy and stalls in the lower crust level (Fig. 1.5). It cools down and crystallize to form the main body of the lower crust. However, this same primitive magma can also eventually form felsic rocks through crystallization. Felsic rocks formed by this crystallization processes and those formed by partial melting of lower crustal rocks can possesses similar chemical and isotopic characteristics (Debari and Sleep, 1991; Greene et al., 2006; Brophy, 2008; Kelemen, 2013), which makes discrimination of fractional crystallization versus crustal melting models difficult. This could give rise to contrasting views even studying the same volcanic arc such as the South Sandwich arc (Pearce et al., 1995; Leat et al., 2003) and Kermadec arc (Smith et al., 2003a, 2003b; Barker et al., 2013).

Based on the study of partition coefficient between different melts and different minerals, Brophy (2008) demonstrated that partial melting of amphibole-bearing crustal rocks should yield a REE pattern that can be distinguished from rocks formed by crystallization. Their study suggests REE patterns indicative of amphibolite melting are relatively rare in global examples of oceanic arc volcanoes. A bimodal distribution of the volcanic composition is widely found in island arcs, e.g. Izu-Bonin arc (Tamura and Tatsumi, 2002) and South Sandwich arc (Leat et al., 2003). Smith et al. (2003a, 2003b) proposed that the bimodal distribution, along with large volumes of erupted silicic magmas and their aphyric nature in the northern Kermadec arc required an amphibolite melting model to produce such patterns of magmatism. However, Barker et al. (2013) suggests the bimodal distribution in the Kermadec arc can be explained by fractional crystallization of a basaltic parental magma based on petrological, geochemical and isotopic data and element modelling. The felsic magma is extracted from a highly crystallized mush zone.

1.2 Rationale and Objectives

The PVA formed in response to the subduction of the Farallon Plate beneath the Caribbean Plate at ca. 75 Ma (Buchs et al., 2010). This event formed the pre-Oligocene Sona-Azuero Arc in western Panama and Chagres Arc in central and eastern Panama and followed by the post-Eocene Cordillera Arc (Lissinna, 2005; Wegner et al., 2011). Several studies have been conducted on these arcs but the composition of the ambient mantle and slab input are still controversial (Abratis and Worner, 2001; Feigenson et al. 2004; Lissinna, 2005; Wegner et al., 2011; Gazel et al., 2009; 2011; 2015). Gazel et al. (2009, 2011) interpreted the ambient mantle beneath PVA as a N-MORB mantle (Gazel et al., 2009; Gazel et al., 2011) while Feigenson et al. (2004) suggests it is a CLIP (Caribbean Large Igneous Province) mantle with high radiogenic Pb isotopes. In addition, the Cordillera arc is more enriched in the most incompatible elements than the Chagres Arc (and Sona-Azuero arc) which was interpreted by mantle enrichment (Wegner et al., 2011). However, other factors such as partial melting (Tollstrup et al., 2010; Guo et al., 2013; Shuto et al., 2015) and slab additions (Zheng, 2019; Zheng et al., 2020) is not considered but it plays an important role on rock geochemistry.

In the Canal area of the Central Panama, studies on magmatic variations, which are classified as hydrous magma and dry magma were recently conducted (Farris et al., 2011; Rooney et al., 2011; Farris et al., 2017; Buchs et al., 2019a). The ‘dry magma’ is the youngest magmatism in central Panama and was interpreted as a sign of magmatic cessation (Buchs et al., 2019a). But the evolution of source composition and the contemporary tectonic event remain unclear. In addition, the mechanism of the formation for the felsic rocks from the Las Cascadas Formation is not well studied (Farris et al., 2017; Buchs et al., 2019a).

Therefore, the present study in central Panama can help better understand mantle (ambient mantle and slab material) compositional evolution and associated tectonic events as volcanic arc matures. In addition, it can help understand the formation of the felsic rocks in volcanic arc settings.

The main aims of this study are to utilise the field observation, whole rock geochemistry, whole rock Sr-Nd-Pb isotopes, and mineral chemistry to:

1. Produce a coherent and comprehensive dataset for each of the igneous formations in central Panama.
2. Work out if the felsic magma formed in magma mush by crystallisation of mafic magma and other magmatic processes in magma chamber such as magma mixing.
3. Determine how the mantle source (ambient mantle and slab input such as sediment and AOC component) and degrees of partial melting evolve through time.
4. Build a model of magmatic and tectonic evolution of central Panama.

1.3 Thesis Structure

To achieve the objectives, the comparison between the Chagres Complex and the Panama Formation can provide a better understanding for the tectonomagmatic evolution as arc mature. The Caraba Formation can be used to interpret magmatic cessation in central Panama. The Las Cascadas and Panama Formation can provide information about how felsic rocks form.

Chapter 2 is the geological background of the PVA and surrounding regions. It includes magmatic evolution of the PVA and tectonic events of the PVA and surrounding regions. Chapter 3 is the detailed field observation and petrography. Chapter 4 is the whole rock geochemistry including Sr-Nd-Pb isotopes. Chapter 5 is the mineral chemistry which comprise clinopyroxene, orthopyroxene, plagioclase, and olivine. Chapter 6 is the detailed discussion chapter to interpret the results in Chapter 2-5. In this chapter, source composition, partial melting and their evolution through time, along with crystallization and magma mixing will be addressed. Finally, Chapter 7 gives a brief conclusion about this study.

2 GEOLOGICAL BACKGROUND

2.1 Tectonic Setting of the Panama Volcanic Arc

The Panama Volcanic Arc (PVA) lies on the Panama Microplate (also referred to as Chorotega and Choco Blocks) between Costa Rica and northern Colombia (Fig. 2.1). It is bordered to the southeast by the South America Plate along the Uramita Fault Zone (Duque-Caro et al., 1990; Trencamp et al., 2002). In the northwest, the Panama Microplate is bordered by the continental Chortis Block, along a poorly-defined crustal boundary associated with the serpentinitic mélange of the Mesquito Composite Oceanic Terrane (Baumgartner et al., 2008). Both of these sutures are believed to represent tectonic boundaries that developed in response to eastward migration of the Caribbean Plate relative to surrounding continents and continental microblocks (e.g., Pindell et al., 2009). In the north, the

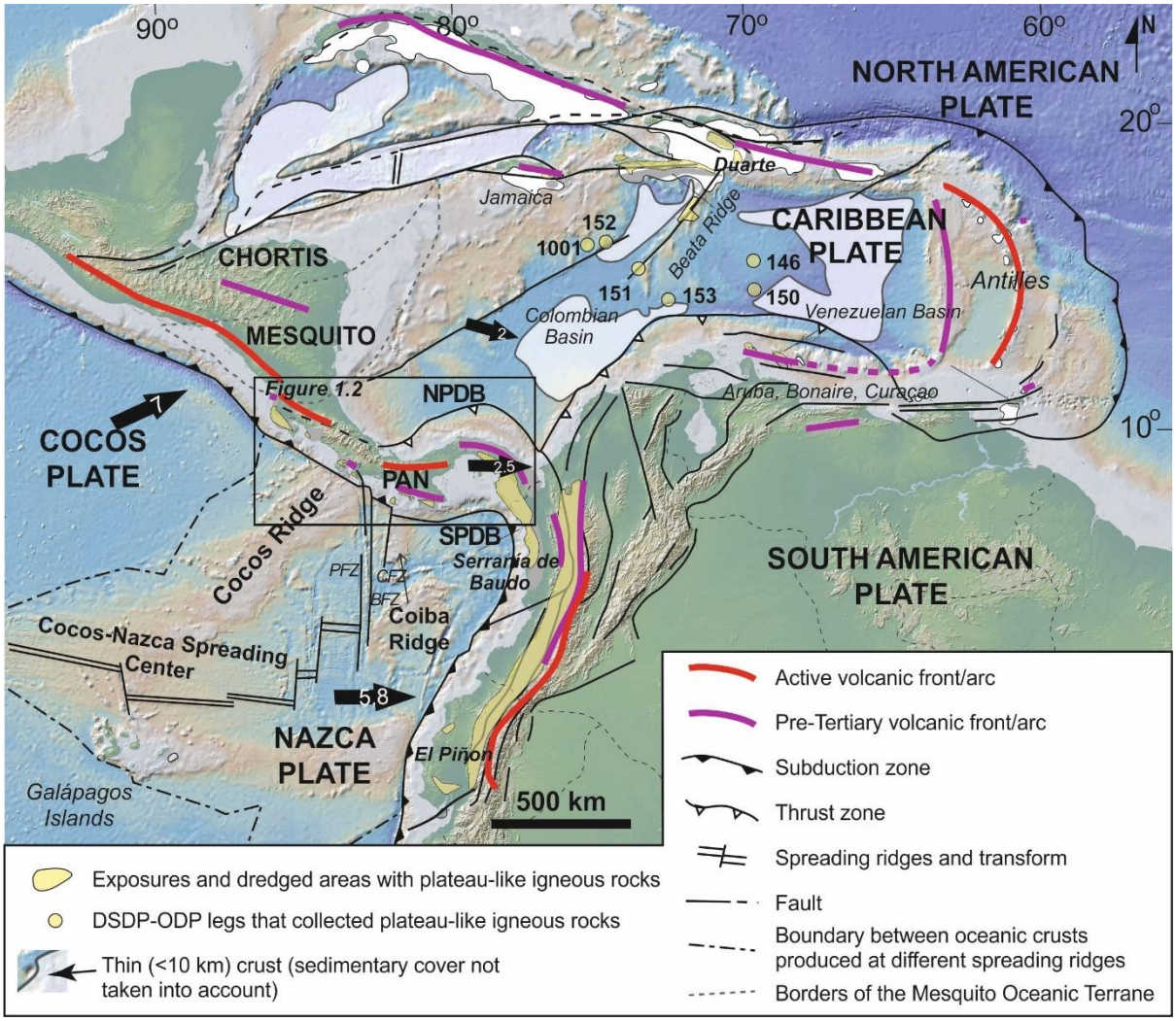

Fig. 2.1 Tectonic setting of the Panama Microplate (PAN) after Buchs et al., (2010). Black arrows show present day GPS relative velocities (cm/year) of major tectonic plates and blocks relative to stable South America (Trencamp et al., 2002)

Panama Microplate is juxtaposed with the Caribbean Plate along the North Panama Deformed Belt (NPDB) which represents a thrust belt (Adamek et al., 1988; Silver et al., 1995; Kellog et al., 1995) or an incipient subduction zone (Camacho et al., 2010) along the northern side of the PVA. The nature of the boundary is highly debated. Offshore seismic profiles collected across the belt suggest that the oblique convergence between the Caribbean Plate and the Panama Block has not formed a Wadati–Benioff (subduction) zone, but has merely led to an amagmatic overthrusting of the Caribbean Plate by the Panama Microplate (Adamek et al., 1988; Silver et al., 1990). However, a more recent study using local and regional seismicity combined with teleseismic observations suggests that the NPDB could be an active, albeit incipient, subduction zone (Camacho et al., 2010). The exact reason(s) for the formation of the NPDB remains unclear, but most studies suggest that this structure developed during collision of the PVA with the South America Plate in the Neogene (Silver et al., 1990; 1995; Farris et al., 2011; Barat et al., 2014). In the south, the Panama Microplate is bordered by the subducting Cocos and Nazca plates along the Middle American Trench and South Panama Deformed Belt (SPDB) (Mann and Corrigan, 1990; Mann and Kolarsky, 1995). In a seismic study of western Panama, Cowan et al. (1995) documented a decrease in seismicity to the east, reflecting a lateral change in stress associated with the geometry of the subducting Nazca Plate beneath the region. Deep seismicity events (~70-115 km) between the Gulf of Chiriquí and the Central Cordillera define a NE-dipping zone providing evidence for lithosphere subducting beneath Panama. High heat flow along the PVA (comparable with the Galápagos hotspot track) are four times higher than the Caribbean) (de Boer et al., 1991). Recent volcanism at Barú and the La Yeguada volcanoes (Fig. 2.2) support Holocene subduction to the NE beneath western Panama (Defant et al., 1991; Wegner et al., 2011). The boundary between the Cocos and Nazca plates along southern Costa Rica and western Panama is a 70-km-wide right-lateral transform boundary associated with three seismically active N-S-trending, right-lateral strike-slip fracture zones, the Panama, Balboa, and Coiba fracture zones, which intersect the SPDB in western Panama (Adamek et al., 1988; Kolarsky and Mann, 1995). The Panama Microplate is currently moving north-eastward at a rate of ~2.5 cm/year relative to the South American Plate (Fig. 2.1) and is colliding with northern South America (Trencamp et al., 2002). Meanwhile, the Caribbean Plate is moving south-eastward at a rate of ~ 2 cm/year and underthrusting beneath northern South America (Trencamp et al., 2002). The Cocos Plate is subducting north-eastward beneath the Panama Microplate at a rate of ~7 cm/year while the Nazca Plate is subducting approximately eastward beneath northern South America at a rate of ~5.8 cm/year (Trencamp et al., 2002). With regard to the magmatic and volcanic evolution of the PVA, no convergence occurs between the Nazca Plate and Panama Microplate along the eastern termination of the Middle American Trench (Trencamp et al., 2002). This tectonic setting has most likely led to a magmatic gap in eastern and central Panama since the Miocene (Buchs et al., 2019a), with only limited volcanic activity in western Panama in the Pliocene (e.g., Defant et al., 1991; 1992; Wegner et al., 2011).

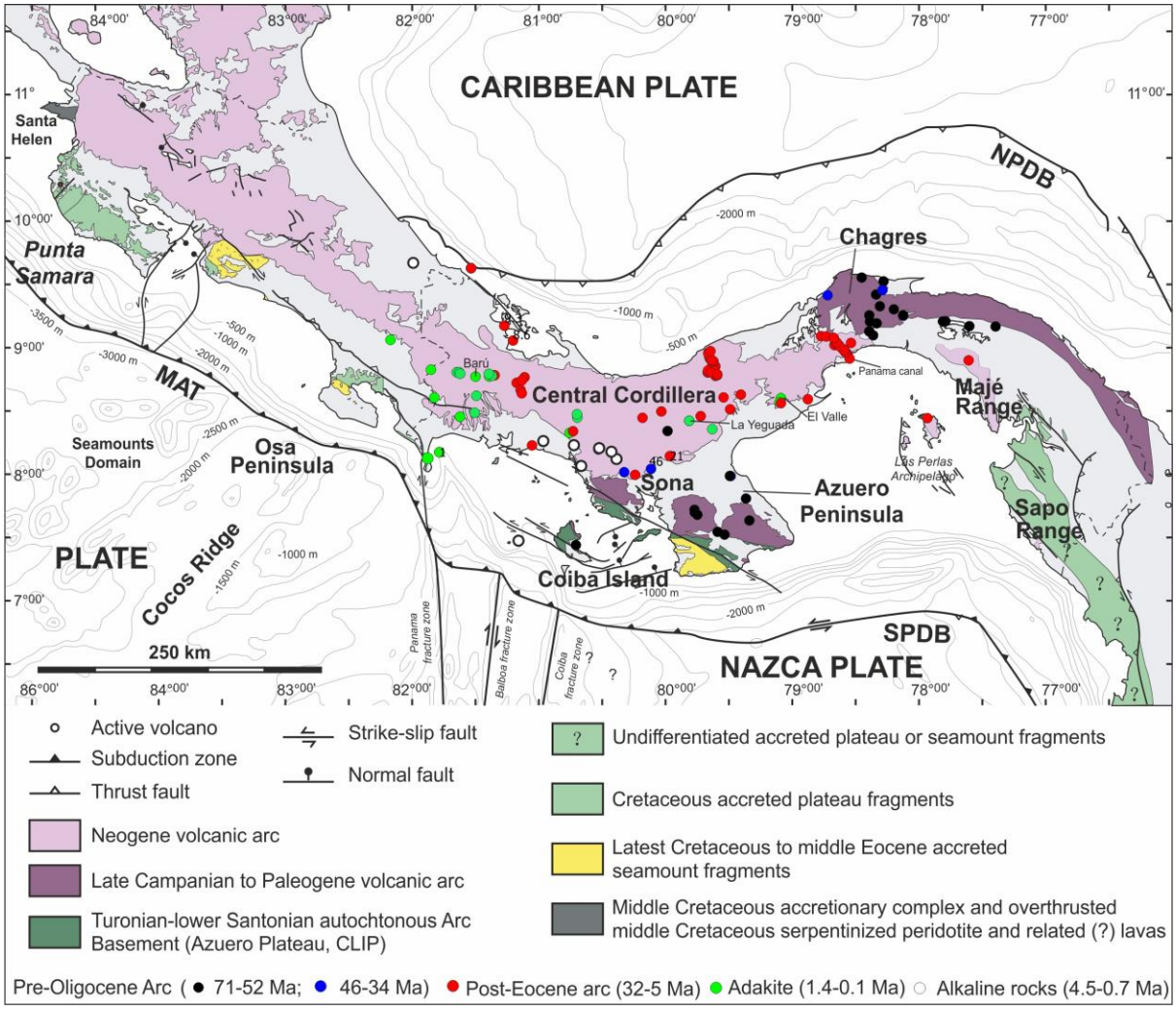

Fig. 2.2 Simplified geological map of Panama Volcanic Arc with dated samples (modified after Buchs et al., 2010).

2.2 Tectonic Evolution of the Caribbean Large Igneous Province (CLIP)

The formation and evolution of the PVA is closely associated with the tectonic evolution of the Caribbean Plate and associated Caribbean Large Igneous Province (CLIP). The CLIP is an oceanic plateau encompassing most of the modern Caribbean Plate, which is considered by several authors to have formed above the starting plume head of the palaeo-Galapagos hotspot in the Pacific, before migrating to the east in its current inter-American position (Duncan and Hargraves, 1984; Sinton et al., 1998; Hauff et al., 2000a). Crystallisation ages of igneous rocks by Ar-Ar dating from the CLIP in Central America (Nicoya, Herradura, Golfito Peninsulas in Costa Rica and Sona Peninsula in Panama), the Caribbean, northwestern Colombia, Ecuador, Curaçao, and the Greater Antilles range from 139 to 69 Ma (Hauff et al., 1997, 2000a, 2000b; Sinton et al., 1997, 1998; Kerr et al., 1997, 2002; Révillon et al., 2000; Lapierre et al., 2000; Hoernle et al., 2004). It has been inferred that a pulsing Galápagos hotspot may have formed multiple intraplate igneous plateaus since ~ 139 Ma (Hoernle et al., 2004). After the formation of the multiple volcanic structures over the Galapagos

hotspot, the plateaus drifted north-eastward during the Cretaceous and reached the Greater Antilles subduction zone located between the Americas (Duncan and Hargraves, 1984; Hauff et al., 2000a; Hoernle et al., 2002, 2004). The older (~139-133 Ma and ~118-111 Ma) plateaus were accreted along the western margin of the Greater Antilles subduction zone and then the largest plateau (~83-95 Ma) jammed to trigger a polarity reversal of subduction beneath the Greater Antilles at ~70-75 Ma (Hoernle et al., 2002).

2.3 Tectonic Evolution of the PVA

The tectonic evolution of PVA started with subduction initiation of the Farallon Plate beneath the Caribbean Plate and follows several tectonic events, such as the offset of pre-Oligocene volcanic front, bending of PVA, break-up of the Farallon Plate and subduction of the hotspot track.

2.3.1 Subduction Initiation

Previous studies have categorised subduction initiation into spontaneous and induced initiation (e.g., Stern, 2004; Stern & Gerya, 2018). With regard to spontaneous subduction initiation, large lateral density contrasts occur across profound lithospheric weaknesses of various origin without pre-existing plate motion. There are three possible types: transform collapse, passive margin collapse, and plume head margin collapse (i.e., plume-induced subduction initiation). In contrast, induced subduction initiation is triggered by continued plate convergence following collision, i.e., an oceanic plateau with a subduction zone. There are two types: a new subduction zone of similar dip to the original subduction zone can initiate behind the collision (transference) or in front of the collision (polarity reversal).

The age of subduction initiation in Panama is constrained by the oldest supra-subduction rocks in the area, which are dated by geochronological and biostratigraphical methods as Campanian (ca. 75-70 Ma) (Lissinna, 2005; Buchs et al., 2010; Wegner et al., 2011; Corral et al., 2013). These Campanian igneous rocks include proto-arc lava flows and dykes that are locally found overlying or cross-cutting oceanic plateau sequences believed to belong to the CLIP (Buchs et al., 2010; Montes et al., 2012). Several studies suggest the existence of a ~10 myr magmatic gap between the end of CLIP magmatism (ca. 85 Ma in Panama) and the formation of the proto-arc (Buchs et al., 2010; Corral et al., 2013). This is supported by the regional occurrence of pelagic limestone of Campanian age between the plateau and proto-arc (Buchs et al., 2010; Corral et al., 2013). Based on a re-interpretation of a selection of previous regional data, Whattam and Stern (2015) suggest that there is no magmatic gap between the formation of the CLIP and Panama proto-arc, and subduction initiation was induced by a plume head. Rock units younger than 100 Ma exposed along the southern margin of the Caribbean Plate and NW South America which were interpreted as CLIP, record subduction signatures (Ba/Th, Th/Nb and Ba/Nb) which increased with time beginning at 100 Ma (Whattam and

Stern, 2015). These rocks were termed as ‘plume- and arc-related’ (PAR) units which suggests subduction along southern and western margins of CLIP initiated as early as 100 Ma (Whattam and Stern, 2015). Particularly, in Sona-Azuero, according to the chemotemporal and/or chemostratigraphic vertical progression, the 89-85 Ma ‘oceanic plateau’ along with overlying proto-arc and arc rocks exhibits a chemotemporal sequence and therefore, subduction initiation in this area was estimated to occur by ~89 Ma (Whattam et al., 2020). However, this chemotemporal progression is based on their plume-induced SI model and no direct evidence proves the plateau-like rocks at the bottom representing subduction initiation.

2.3.2 Offset of the Pre-Oligocene Volcanic Front and Orocline Bending of the PVA

After the initiation of subduction for the PVA along the southern margin of the CLIP, a first phase of magmatic activity of the PVA occurred between the Late Cretaceous to Oligocene, which formed a pre-Oligocene volcanic front preserved today as the Sona-Azuero and Chagres-Bayano Arc (Lissinna, 2005; Wegner et al., 2011; Montes et al., 2012a; Montes et al., 2012b) (Fig. 2.2, Fig. 2.3). Palaeomagnetic and regional geological data suggest that these arcs, which correspond today to some of the most prominent topography in Panama, were most likely forming a continuous volcanic front in the Late Cretaceous to Eocene. This volcanic front was rotated and offset by left lateral strike-slip motion between 38 and 28 Ma (Montes et al., 2012b). The western part of this volcanic front (i.e., Chorotega Block and Sona-Azuero Arc) rotated counterclockwise by 20°, while the eastern part (i.e., the western Chocó Block and Chagres-Bayano Arc) rotated clockwise by only 0° to 5°. Soon after, between 28 and 25 Ma, the eastern part suddenly increased its clockwise rotation, to ~25°, which led to the northward displacement of the volcanic arc and to the south-shaped bending of the eastern Panama Isthmus (Mann and Corrigan, 1990; Montes et al., 2012b; Silver et al., 1990; Wadge et al., 1983). In this scenario, orocline bending occurred ca. 25 Ma, which might represent the early stages of collision with South America (Farris et al., 2011; Montes et al. 2012a). Other tectonic interpretations suggest dismemberment of the early volcanic front of the PVA and formation of tectonic blocks already in the Eocene (ca. 40 Ma) (Barat et al., 2014; Buchs et al., 2019a) (Fig. 2.3). In addition, the timing of collision of the PVA with South America is still poorly constrained, with incipient collision suggested to have started as early as the late Cretaceous in some regional tectonic reconstructions (Kennan and Pindell, 2009). However, it is generally agreed that at least some degree of causal relationship exists between the collision of the PVA with South America and the volcanic/magmatic evolution of Panama (Farris et al., 2011; Farris et al., 2017). Moreover, based on the magmatic change from hydrous arc magmatism to localized dry extensional arc magmatism, the collision between the PVA and South America ca. 25 Ma was developed by Farris et al. (2011). Aside from orocline bending and block rotation, several areas of the PVA were marked by local subsidence and formation of sedimentary basins in the Oligocene, such as the so-called “Canal Basin” in the

study area (Coates et al., 2004; Farris et la., 2011). These extensional basins may develop in response to the collision (Farris et al., 2011).

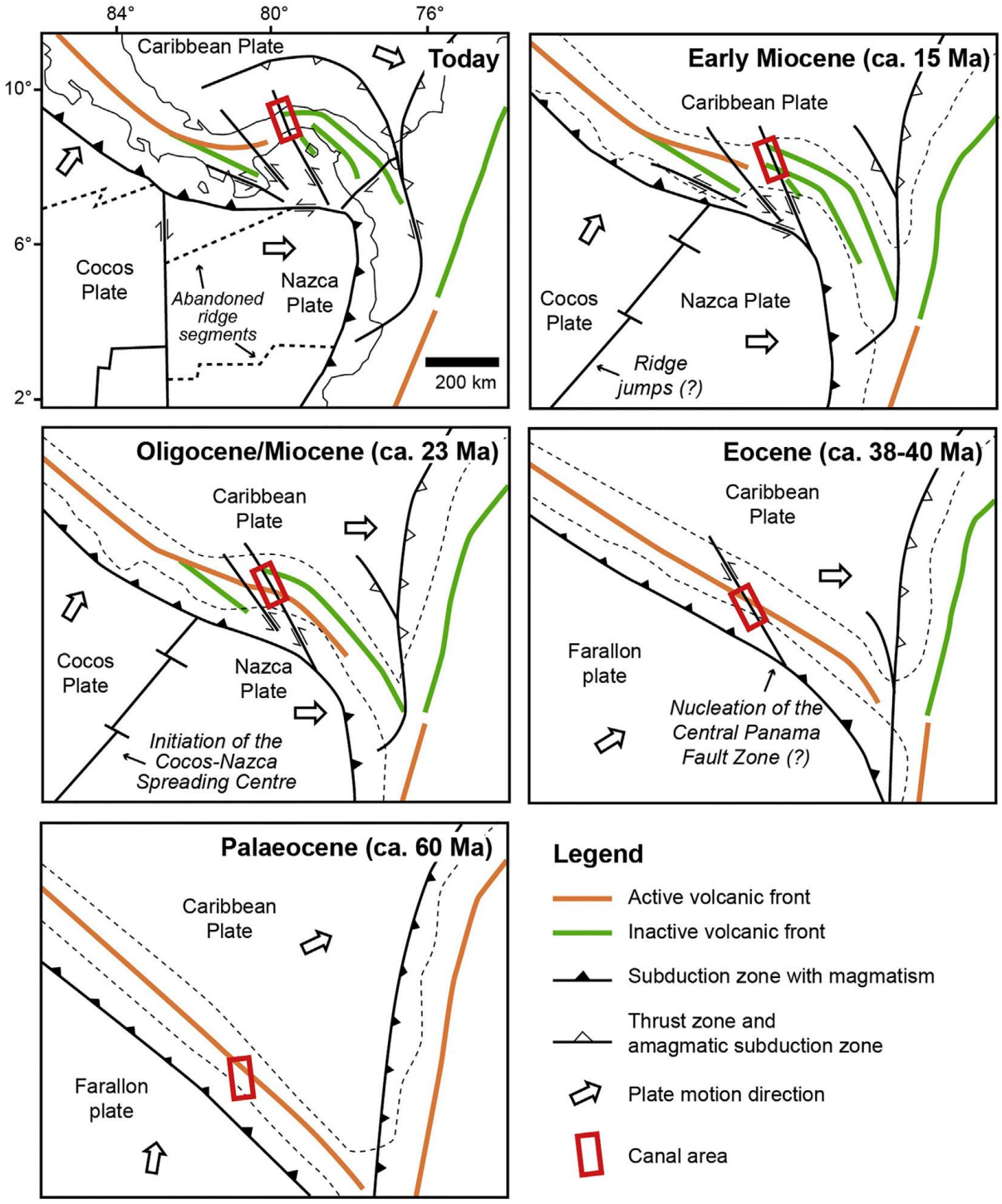

Fig. 2.3 Tectono-magmatic evolution of the Panama Volcanic Arc since the Palaeocene from Buchs et al. (2019a).

2.3.3 Breakup of the Farallon Plate and Oblique Subduction in the PVA

Another Oligocene tectonic event that most likely contributed to significant magmatic changes during the evolution of the PVA is the break-up of the Farallon Plate into the Cocos and Nazca plates at ~23

Ma, based on magnetic studies of oceanic crust (Lonsdale, 2005; Barckhausen et al., 2008). The break-up started at a location of focused crustal extension caused by overlapping spreading centres that had evolved in response to a slight reorientation of a Pacific-Farallon ridge segment and migrated toward the region of weak lithosphere created by the Galapagos hotspot. By 19.5 Ma, plate splitting from the spreading centre to the trench was complete, allowing the fully detached Cocos and Nazca plates to move independently (Barckhausen et al., 2008). The plate reorganisation following break-up of the Farallon Plate gave rise to oblique subduction in PVA, which might have triggered magmatic changes in central and eastern Panama (Buchs et al., 2019a). However, the starting time of the oblique subduction is not well constrained. The development of the Panama Triple Junction occurred no earlier than ~8.5 Ma by plate reconstruction (Morell, 2015). This tectonic rearrangement was ~15 Ma later than the break-up of the Farallon Plate into the Cocos and Nazca plates. Prior to 8.5 Ma, near-orthogonal smooth Cocos Plate subduction was occurring from north-central Costa Rica to eastern Panama. At ~8.5 Ma, the Panama Triple Junction initiated offshore northern Costa Rica and the subduction zone in Costa Rica and Panama suddenly began to experience oblique subduction (Morell, 2015). This oblique subduction is supported by shutdown of calc-alkaline volcanism of the Central Cordillera Arc in Panama (discussed below), by causing a decrease in the flux of water and/or volatiles required to produce mantle-wedge volcanism (Morell et al., 2012), and the magmatic change from calc-alkaline rocks to adakites (Rooney et al., 2011). However, an earlier age for oblique subduction was suggested by Buchs et al. (2019a). A geochemical change from calc-alkaline to tholeiitic in the Canal area between ca. 25 Ma and 16 Ma and magmatic extinction ca. 16 Ma was interpreted as suppression of water in the subduction zone, which was caused by oblique subduction. In this study, similar age (~25 Ma) with the break-up of the Farallon plate (~23 Ma) suggests oblique subduction commenced ca. 25 Ma and subduction became more oblique after Farallon plate breakup. The limited orthogonal convergence between the Nazca Plate and Panama Microplate likely led to volcanic quiescence in this segment of the PVA since the Miocene (Buchs et al., 2019a) (Fig. 2.3).

2.3.4 Galapagos Hotspot Track Subduction

Cocos Ridge, an aseismic ridge, or chain of submarine oceanic islands, is a Galapagos hotspot track which formed above the Galapagos hotspot and travelled with the Cocos Plate towards the Costa Rican subduction zone. Cocos Ridge subduction has significant impacts on tectonic events such as exhumation of Cordillera de Talamanca – about 2 km of rock uplift and exhumation within the past 1-3 Ma (Grafe et al., 2002; Morell et al., 2012) and trench embayment and increased sedimentation in the outermost fore-arc (Sak et al., 2009; Gardner et al., 2013; Vannucchi et al., 2013). The impact of Cocos Ridge subduction on magmatism in the PVA is highly debated. Abratis and Worner (2001) suggest a slab window was formed in the Miocene due to collision between Cocos Ridge and PVA. Slab melting and upwelling of Galapagos-type mantle formed adakite and alkaline rocks respectively. Few researchers have proposed that the cessation of mantle-wedge-derived volcanism in the

Cordillera de Talamanca was induced by Cocos Ridge subduction (e.g., McGeary et al., 1985; de Boer et al., 1995; Kolarsky et al., 1995). However, Morell (2015) highlights that this late Miocene arc extinction is not only found in the Cordillera de Talamanca but also in the Central Cordillera Arc and magmatic cessation is attributed to oblique subduction of Nazca Plate. Another debate is the initial subduction/collision of the Cocos Ridge with the PVA, with proposed ages ranging from 8 Ma to 1 Ma (1 Ma by Londsdale and Klitgord, 1978; 2-3 Ma by MacMillan et al., 2004; 3.5 Ma by Collins et al., 1995 and Gans et al., 2003; 5 Ma by de Boer et al., 1995 and Hoernle et al., 2002; 8 Ma by Abratis and Wörner, 2001 and Gazel et al., 2009). A recent study on plate reconstruction suggests Cocos Ridge subduction began at a time earlier than 2.5 Ma (Morell, 2015).

Apart from Cocos Ridge, subduction of Galapagos hotspot track might have commenced in Eocene (~ 50 Ma) as recovered by magmatic rocks, which are believed to comprise a Galapagos hotspot component to explain high radiogenic Pb isotope (e.g. >18.8 for $^{206}Pb/^{204}Pb$; Gazel et la., 2015). This hotspot track subduction ended in ~ 40 Ma and recurred ~ 8 Ma up until the present. Moreover, as revealed by accreted pieces of the hotspot track along the western Panamanian Pacific coast and inshore islands, Galapagos hotspot track subduction beneath PVA can date back to 66 Ma (Lissinna, 2005).

2.4 Magmatic Evolution of the PVA

As mentioned above, the PVA formed as a response of subduction of the Farallon Plate in the Cretaceous-Oligocene, and Cocos and Nazca plates thereafter, below the Caribbean Plate that hosts the CLIP. Five main magmatic phases can been identified during the evolution of the PVA, which likely correlates to significant tectonic changes in the region: (1) a proto-arc phase in the Late Cretaceous (Campanian-Maastrichtian), which is associated with incipient subduction and primitive island arc magmatism; (2) a pre-Oligocene calc-alkaline to tholeiitic phase; (3) a post-Eocene calc-alkaline to tholeiitic phase; (4) a late Oligocene to early Miocene calc-alkaline to tholeiitic phase in the Canal area, associated with a decrease of fluid supply from the slab and magmatic cessation in central and, possibly, eastern Panama; and (5) Pliocene to recent alkaline to adakite magmatism in western Panama. Key chemical characteristics of these phases and their possible link to tectonic changes are summarised below.

2.4.1 Proto-arc Magmatic Phase (Late Cretaceous)

The initiation of subduction along the SW edge of the Caribbean Plate is believed to have occurred ca. 75 Ma, corresponding to the emplacement of the oldest supra-subduction igneous rocks, or proto-arc, in Panama (Buchs et al., 2010). The proto-arc rocks occur as (i) mafic-intermediate lavas that are commonly associated in the field with pelagic limestone that includes Late Campanian foraminifera, and (ii) dykes that cross-cut Coniacian-Santonian (and possibly older) plateau sequences. Although some models suggest an older age of subduction initiation in southern Central America (Whattam and

Stern, 2015; Whattam et al., 2020), volcanic arc sequences dated by Ar-Ar and zircon dating so far are no older than ca. 75 Ma (e.g., Lissinna, 2005; Buchs et al., 2010; Wegner et al., 2011; Corral et al., 2011). Texture and mineralogy of these proto-arc rocks exhibit large variability, displaying subophitic, intersertal, and porphyritic textures. The rocks can contain clinopyroxene, plagioclase, an opaque mineral, orthopyroxene, amphibole, alkali-feldspar and glass (Buchs et al., 2010). The proto-arc igneous rocks are predominantly composed of basalt with subordinate basaltic andesite and andesite. Significantly for the recognition of proto-arc sequences, these rocks have unique geochemical characteristics that are intermediate between those of igneous rocks from oceanic plateau and volcanic arc settings (Buchs et al., 2010; Wegner et al., 2011). In contrast to plateau, proto-arc rocks have Nb-Ta-Ti depletion in trace element pattern even though the depletion degree is smaller than arc rocks. Chondrite-normalised rare earth element (REE) profiles are relatively flat, with slight positive La/Sm_{CN} (~1.0-2.1) values than plateau rocks (Fig. 2.4). In N-MORB normalised trace element patterns, unlike the enrichment in arc rocks, Th in proto-arc has low content comparing with other HFSE and HREE which is similar to plateau rocks (Buchs et al., 2010). Th/Nb (0.08-0.5) is slightly higher than the value in the plateau. A detailed geochemical and temporal study of the proto-arc, including characterisation of the Nd isotopic composition of its source, is being finalised at Cardiff University by Joanna Brims. To date, most igneous rocks with proto-arc characteristics have been found in the Golfito Complex in south Costa Rica and the Azuero Marginal Complex in the Azuero and Sona Peninsulas in western Panama (Buchs et al., 2010) (Fig. 2.2). Although proto-arc sequences are expected to extend to central Panama, there are so far only rare possible candidates in the lowermost igneous sequences of the eastern side of the San Blas Range (Montes et al., 2012).

2.4.2 Pre-Oligocene Magmatic Phase

The pre-Oligocene arc rocks (late Cretaceous to Eocene) are mainly preserved in the Azuero and Sona Peninsulas in western Panama and San Blas Cordillera in eastern Panama, where they are referred to as Sona-Azuero Arc and Chagres Arc, respectively. In the Chagres Arc, rocks are mainly mafic to felsic lavas and intrusions spanning from 68 to 39 Ma (Fig. 2.6 A) (Lissinna, 2005; Worner et al., 2009; Wegner et al., 2011; Maury et al., 1995; Montes et al., 2012a). This arc exposes a deeply eroded section of submarine lavas to volcanic breccias cross-cut by subvolcanic intrusive rocks and dyke swarms, with locally tuffaceous, hemipelagic sediments (Wörner et al., 2009). Large intrusive complexes of gabbro, granodiorite, tonalite, and granite are common. Mafic to intermediate lavas in this area can be further subdivided into high Mg# (>60) and low Mg# (<60) rocks (Wegner et al., 2011; Buchs et al., 2019a). Rocks in this arc are mainly tholeiitic, with some calc-alkaline samples and a broad temporal change in magma compositions from tholeiitic to (low-K) calc-alkaline (Wegner et al., 2011; Montes et al., 2012a). Rare earth elements range from LREE slightly depleted to slightly enriched in the spider diagram with La/Sm ranging from 0.6 to 5.2 (Fig. 2.4). All rocks show typical arc characteristics, e.g., relative Nb-Ta-Ti depletion in PM (primitive mantle) or N-MORB normalised

multi-element diagrams and trace element ratios, especially Th/Nb (0.08-1.8) is significantly higher than plateau and proto-arc rocks (Fig. 2.4). Variable geochemical characteristics propose that the source might be heterogeneous which is also supported by relatively large range of Nd-Pb isotopes ($^{143}Nd/^{144}Nd(i)$=0.51283-0.51294, $^{206}Pb/^{204}Pb(i)$ =18.75-19.07; Wegner et al., 2011).

Rocks from the Sona-Azuero Arc are mostly basalt and andesite, with minor diorite intrusions ranging from 71 to 40 Ma in age (Lissinna, 2005; Wegner et al., 2011). These rocks are similar to that of the Chagres Arc, in that rocks are primarily tholeiitic with subordinate calc-alkaline rocks. These rocks are relatively homogeneous with slight LREE-enrichment in spider diagrams (La/Sm=2.0-4.3). Trace element ratios, such as Th/Nb (0.4-1.0), are similar to those from rocks of the Chagres Arc. Rocks from Sona-Azuero have distinctly lower radiogenic Nd and Pb isotopes ($^{143}Nd/^{144}Nd(i)$=0.512864-0.512866, $^{206}Pb/^{204}Pb(i)$=8.53-18.65) than the Chagres Arc which are interpreted as higher sediment component (Wegner et al., 2011). Apart from rocks in Sona-Azuero, pre-Oligocene rocks are also found in central Cordillera with ages from 34 to 46 Ma (Lissinna, 2005). These rocks are different from rocks in Sona-Azuero as they are more enriched in the most incompatible elements which makes them look similar to the younger arc magmatism discussed below.

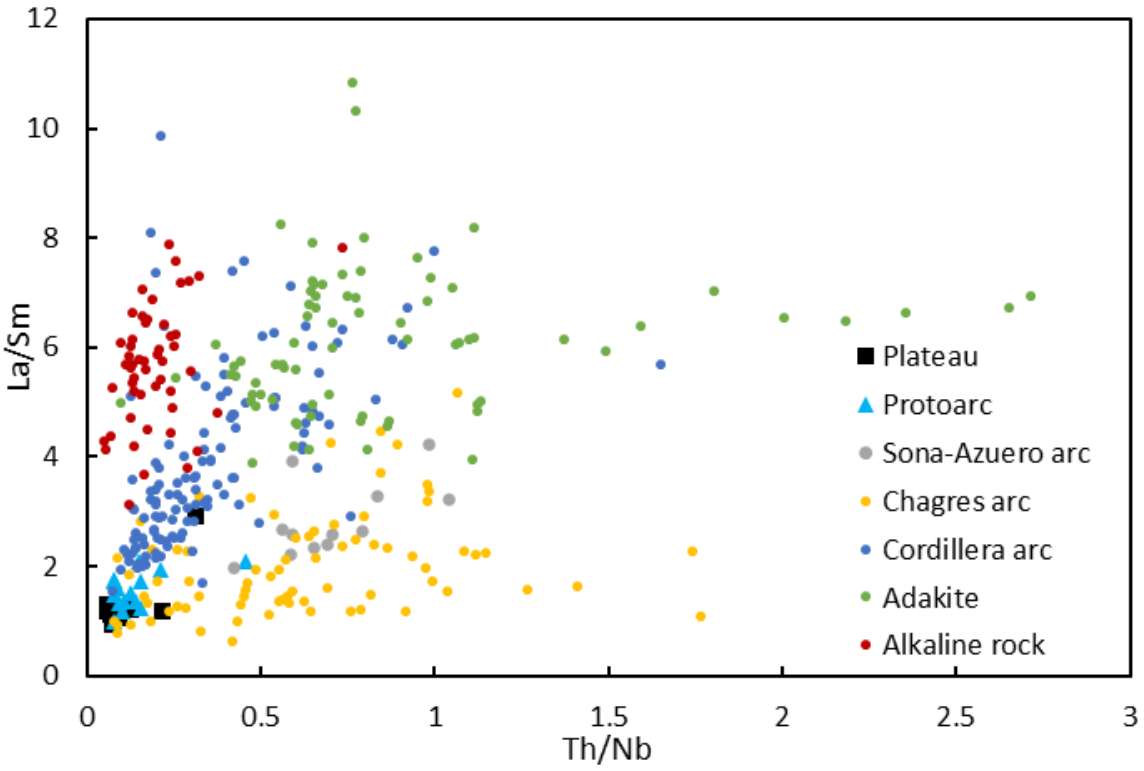

Fig. 2.4 Representative trace element ratios for rocks in PVA (data are from Lissinna, 2005; Buchs et al., 2010; Wegner et al., 2011)

2.4.3 Post-Eocene Magmatic Phase

Post-Eocene magmatism of the PVA is well constrained in western Panama where it forms the Central Cordillera Arc ('Cordilleran Arc' of Wegner et al., 2011) that was dated between 34 and 5 Ma (Lissinna, 2005; Wegner et al., 2011; Baker et al., 2016) (Fig. 2.6). Rocks are mafic to felsic with lavas of basalt to rhyolite and intrusions of diorite to granite (Lissinna, 2005; Wegner et al., 2011). These rocks differ compositionally from those of the pre-Oligocene Arc, in that they comprise higher La/Sm (1.5-9.9; Fig. 2.4) and Th/Nb (0.07-1.7) values. High La/Sm may indicate their derivation from a less-depleted mantle source (Wegner et al., 2011). However, isotopic analysis of these rocks has revealed high radiogenic Nd and Pb ($^{143}Nd/^{144}Nd(i)$=0.51292-0.51302, $^{206}Pb/^{204}Pb(i)$=18.79-19.12), which is typically interpreted as a depleted mantle source. In eastern Panama, only rare occurrences of post-Eocene volcanic arc rocks have been reported, e.g., in the Majé Range (ca. 18.9± 0.4 Ma; Whattam et al., 2012), Bahia Piña (ca. 21.7± 0.3 Ma Ma; Lissinna, 2005) and the Pearl Islands (18.4-21.9 Ma; Lissinna, 2005).

2.4.4 Magmatism in the Canal Area (Late Oligocene-Early Miocene)

In central Panama, the PVA can be subdivided into a pre-Oligocene (66 to 39 Ma) volcanic front in the north and east, which is part of Chagres-Bayano Arc (Fig. 2.2) as discussed in section 2.4.2, and Oligocene to Early Miocene (25-16 Ma) arc sequences in the south and west. The oldest volcanic rock is the clast from Bas Obispo Formation (25-26 Ma; Buchs et al., 2019b) and amphibole-bearing andesite in Cerro Patacon (25 Ma; Rooney et al., 2011). The andesitic clasts in Bas Obispo Formation are slightly enriched in the most incompatible elements which is similar to the pre-Oligocene Arc (Fig. 2.5). Cerro Patacon andesite is a hypabyssal intrusion, that is more enriched in the most incompatible elements which is similar to the post-Eocene Arc (Central Cordillera Arc) (Fig. 2.5). The youngest magmatic phase, Pedro Miguel Group (16-18 Ma) has a similar trace element pattern with Central Cordillera Arc and it has the less enrichment of large ion lithophile elements (LILEs) comparing with pre-Oligocene Arc and Bas Obispo Formation (Farris et al., 2011; 2017; Buchs et al., 2019a). The hydrous magmatism changed to be less hydrous magmatism ca. 25 Ma and finally terminated ca. 16 Ma in Canal area. This cessation occurred shortly after the break-up of the Farallon Plate at ca. 23 Ma (Lonsdale, 2005), suggesting a potential link between volcanic shutdown and transition from orthogonal to oblique subduction along Central and Eastern Panama as oblique subduction contributed less slab input (Buchs et al., 2019a). Conversely, Farris et al. (2017) suggest that this anhydrous magmatism formed in an extensional setting, e.g. canal basin which is triggered by collision between PVA and South American Plate. In addition to mafic-intermediate rocks, felsic rocks in this area are grouped into Las Cascadas Formation (Farris et al., 2011,2017; Buchs et al., 2019b). This formation are enriched in incompatible elements but has similar trace element ratios such as Nb/Yb with the Cordilleran arc. It is interpreted to be formed by assimilation-fractional crystallisation (AFC) of mafic magmas by Farris et al. (2017).

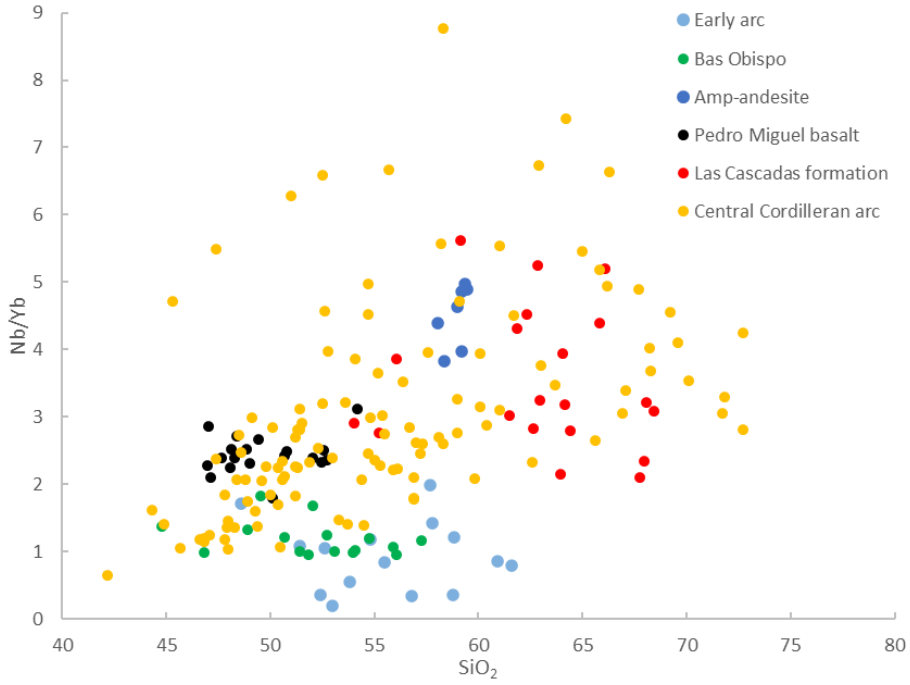

Fig. 2.5 Rocks in central Panama (data from Rooney et al., 2011; Farris et al., 2017; Wegner et al., 2011; Buchs et al., 2019a,2019b)

2.4.5 Alkaline and Adakite Magmatism (Pliocene to Recent)

The most recent magmatism in the PVA was associated with the emplacement of alkaline basalts and adakites with age ranges of 4.5-0.7 Ma and 1.4-0.1 Ma, respectively (Lissinna, 2005; Wegner et al., 2011; Gazel et al., 2011). These rocks occur over most of western Panama and are associated with dormant volcanic centres (Abratis and Wörner, 2001; Defant et al., 1992; Gazel et al., 2011) (Fig. 2.2). 'Adakite' was originally proposed as a genetic term to define intermediate to high-silica, high Sr/Y (>~20) and La/Yb (>~20) volcanic and plutonic rocks derived from melting of the basaltic portion of oceanic crust (young and hot) subducted beneath volcanic arcs (Defant and Drummond, 1990; Castillo, 2012). Some petrologists (e.g., Martin et al., 2005) extended the original definition and the new definition includes high-SiO_2 adakites (SiO_2 >60 wt.%) and low-SiO_2 adakites (SiO_2 <60 wt.%), corresponding to pristine slab melts and melts derived from metasomatised peridotite, respectively. However, adakites in the PVA were recently interpreted to be the product of arc basalt crystallisation. To avoid this concept confusion, rocks with adakite characteristics, e.g., high Sr/Y (> ~20) and La/Yb (>~20), are termed as adakite in this study, regardless of the forming mechanism. As can be expected, adakites in PVA have steep chondrite normalised REE patterns (La/Sm=3.9-10.9) and high Th/Nb values (0.1-2.7; Fig. 2.4). Alkaline basalts also have steep chondrite normalised REE pattern (La/Sm=3.1-8.9) with comparatively lower Th/Nb values (0.05-0.7) (Fig. 2.4). The alkaline basalts were interpreted to derive from partial melting of upwelling asthenosphere with minor

contributions from subduction components (Abratis and Wörner, 2001; Gazel et al., 2011). The mechanism of adakite formation in the PVA remains controversial. They are mainly interpreted to reflect slab melting in response to the collision of the Cocos Ridge, subduction of the Cocos-Nazca plate boundary and/or formation of a slab window in Western Panama (Abratis and Wörner, 2001; Lissinna, 2005). Radiogenic isotope data support well this hypothesis in westernmost Panama, where Pb isotopes in adakites and alkaline basalts plot on a mixing trend between depleted mantle and Galapagos hotspot track compositions, hence suggesting contribution from partial melts of the Cocos Ridge (Abratis and Wörner, 2001; Gazel et al., 2011). Other studies argue that deep crustal garnet and/or amphibole crystallisation also played a significant role in the formation of adakites in El Valle volcano (above the Nazca Plate close to central Panama) (Hidalgo et al., 2011) and Barú volcano above the Cocos-Nazca-Panama triple junction (Hidalgo and Rooney, 2014). Rocks with adakite signatures (high Sr/Y and high La/Yb) but formed by fractionation is termed as ‘adakite-like’, ‘adakitic’ rocks (Hidalgo et al., 2011; Hidalgo and Rooney, 2014) or ‘adakitic-like’ rocks (Maje Range, Cerro Patacon, Pataquilla in Central Panama by Whattam et al. (2012).

2.4.6 Volcanic Gap(s) or Continuous Magmatism of the PVA?

Ar-Ar and zircon U-Pb dating of the volcanic arc in western Panama suggests continuous magmatic activity since the late Cretaceous (Fig. 2.6A). This activity was nonetheless associated with northward migration of the volcanic front in the Eocene ca. 34-40 Ma (Lissinna, 2005; Wegner et al., 2011), most likely during transition from the pre-Oligocene to post-Eocene magmatic phases (Buchs et al., 2019a) (Fig. 2.3). On the contrary, geochronological data suggests the existence of a magmatic gap between 26 and 39 in central and eastern Panama (Fig. 2.6 A). However, detrital zircon grains collected from alluvial deposits in eastern Panama and sandstones from the Lower Miocene Culebra and Cucaracha formations and the Eocene Gatuncillo Formation in Central Panama (Montes et al., 2012a; Ramirez et al., 2016) suggest no magmatic gap in central and eastern Panama (Fig. 2.6 B). Therefore, although it has been suggested by some studies that a magmatic gap might occur in central and eastern Panama in the Eocene (Montes et al.2012a), the combination of dating of igneous rocks and detrital zircon grains suggests that, similarly to western Panama, magmatic activity was probably continuous between the late Cretaceous and early Miocene in central and eastern Panama.

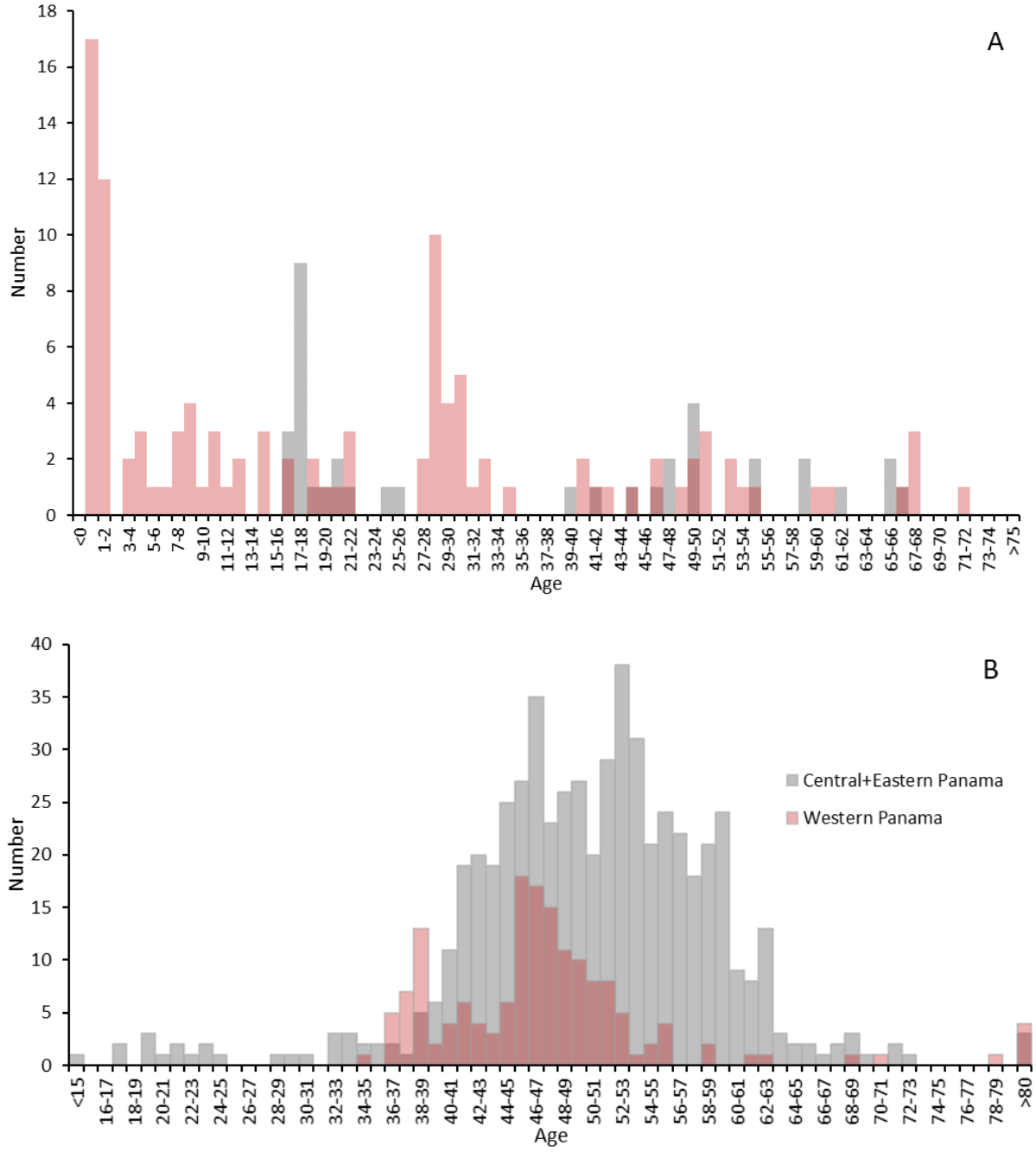

Fig. 2.6 Age histogram for PVA. (A) Ar-Ar ages and zircon U-Pb age of magmatic rocks (data compiled from Lissinna (2005), Gazel et al. (2011), Hidalgo et al. (2011), Wegner et al. (2011), Montes et al. (2012a), Whattam et al. (2012), Baker et al. (2016), Buchs et al. (2019a), Buchs et al. (2019b)). (B) Detrital zircon ages (data compiled from Montes et al. (2012a), Ramirez et al. (2016))

2.5 Geology of Central Panama

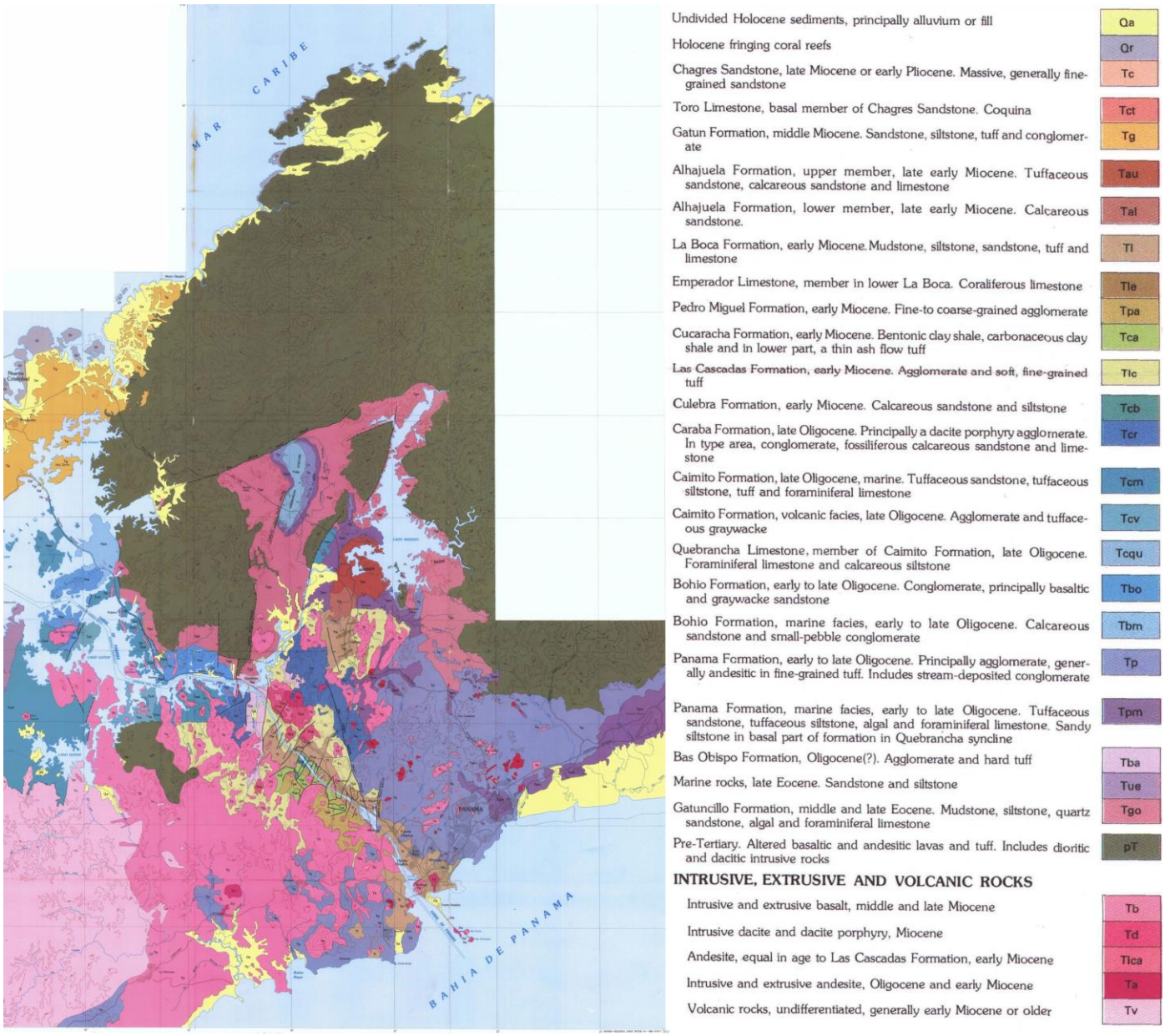

Fig. 2.7 Steward map for central Panama (Steward and Steward, 1980) (the black square represents the study area).

Central Panama in this study is defined here as the area that surrounds the Panama Canal, from the El Valle in the west to the Cerro Azul in the east. It includes a lowland area bordered to the east by an ancient (inactive) volcanic cordillera and the pre-Oligocene Charges-Bayano Arc in the north (Fig. 2.7). A Panama Canal Basin occur in the lowland area, which hosts several hundred of meters of sedimentary deposits (e.g., Kirby et al., 2008). A deep-shear zone trending northwest- southeast, approximately parallel to the Panama Canal was discovered with geophysical methods (Case,1974; Lowrie et al., 1982) which might have led to the formation of the basin. the Panama Canal Basin

exists in a structurally complex area, as indicated by a large amount of faults trending northeast-southwest such as Rio Pedro Miguel Fault (Fig. 2.7) and Rio Gatun Fault (Stewart et al., 1980).

Excavation work conducted along the Panama Canal since the 19th century has greatly facilitated geological studies along a 5-10 km wide transect across the isthmus. Several geologic surveys were conducted during the initial and subsequent excavations of the Panama Canal (MacDonald, 1915; Woodring, 1957; Stewart et al., 1980). This means that the stratigraphy and geological evolution of this area is relatively well constrained and understood. Stewart et al. (1980) is the most detailed geological map published to date in central Panama (Fig. 2.7). More recently, the study of volcanic units along the canal was conducted by several studies that benefited from a new phase of expansion of the Canal between 2008 and 2016 (Kirby et al., 2008; Farris et al., 2011; 2017; Rooney et al., 2011; 2015; Buchs et al., 2019a; 2019b). In contrast, only explorative studies have been carried out in the rugged, highly vegetated terrain associated with the Chagres-Bayano Arc (e.g., Wörner et al., 2005; Montes et al., 2012b) and surrounding vegetated lowlands. These areas remain poorly understood compared to the geology exposed and drilled along the Canal.

2.5.1 Pre-Oligocene Basement Complex

The lowest exposed stratigraphic levels, or "basement", of central Panama includes an Upper Cretaceous to Eocene (65-39 Ma) magmatic complex. This complex is exposed in the Charges-Bayano Arc in the east, with only minor possible occurrences in the lowland arc of central Panama. No outcrop is found in central Panama. This pre-Oligocene magmatic basement was termed as 'pre-tertiary group' ('Pre-T') on the Steward map, which is not accurate based on the ages.

The Chagres-Bayano Arc complex can be subdivided into two main units that consist of volcaniclastic sequences and cross-cutting intrusive igneous rocks (Worner et al., 2009; Montes et al., 2012b). This complex represents a deeply eroded section of a submarine lava flow–dyke complex, associated with overlying and intercalated volcanic breccias and subvolcanic intrusive rocks, dyke swarms, and large intrusive complexes (Worner et al., 2009). The volcaniclastic sequences in the southern side of the eastern termination of the Charges-Bayano Arc were further divided into three units based on lithostratigraphic criteria by Montes et al. (2012b). The volcanic rocks in the upper unit are predominantly dark-grey diabase, massive basalt, and amygdaloidal pillow basalt. There are rare, lenticular volcanic breccia layers interbedded with the pillow basalt. Discontinuous layers of stratiform chert, tuffaceous siltstone, and micritic pelagic/hemipelagic limestone form lenses within the basalt. Very fine-grained basaltic and andesitic dikes crosscut the volcanic and marine sediments. The dikes are composed of clinopyroxene crystals and lath- shaped, randomly oriented plagioclase crystals. Overlying the lower volcaniclastic unit, the middle volcaniclastic unit consists of massive basalt-andesite, pillow basalt, and diabase sills and dikes. Chert beds and tuffaceous siltstone that are

up to 2 m thick and continuous for > 1 km are interbedded with the volcanic layers. Fine-grained basaltic and rare medium-grained dioritic dikes cross-cut the sequence of volcaniclastics and marine sediments. The basalts and the andesite mostly have plagioclase, clinopyroxene, and rare orthopyroxene phenocrysts while some of the basalts contain only plagioclase phenocrysts. The upper unit consists of lavas and volcanic breccia. The lavas are stratiform, massive andesitic lavas with centimetre-scale layering interbedded by andesitic breccias which probably represent a lava top or lava base. The plutonic rocks are two-pyroxene gabbro to diorite, clinopyroxene quartz diorite and granodiorite. All these plutons are massive, with only local and poorly defined magmatic foliation (Montes et al., 2012b).

2.5.2 Gatuncillo Formation

The basement complex is unconformably overlain by the Middle to Upper Eocene Gatuncillo Formation, which occurs west to the Alajuela Lake (Fig. 2.7, Table 2.1). This unit is characterised by mudstone, siltstone, quartz sandstone, and foraminiferal (shallow-marine) limestone (Stewart et al., 1980; Montes et al., 2012b). The Gatuncillo Formation was described as a mostly muddy unit in the Quebrancha syncline (Fig. 2.7), and more sandy and conglomeratic in the rest of central Panama (Woodring, 1957).

2.5.3 Bohio Formation

The Oligocene Bohio Formation is mainly distributed around Gatun Lake. This unit is characterised by a coarse, boulder conglomerate defined by basaltic clasts and matrix, with occasional marine facies of calcareous sandstone and small pebble conglomerate (Woodring, 1957; Steward et al., 1980).

2.5.4 Camito Formation

The overlying late Oligocene Caimito Formation contains tuffaceous sandstone and siltstone, tuff, agglomerates, and limestones (Steward et al., 1980).

2.5.5 Bas Obispo Formation

Bas Obispo Formation is an Oligocene formation mainly found in central Panama. Even though this formation was described as an agglomerate by early studies (e.g., Woodring et al., 1957; Steward et al., 1980), well-rounded imbricated pebbles and cobbles in new exposures unambiguously record the occurrence of bedload fluvial sediments and therefore, was considered as a conglomerate deposit by Buchs et al. (2019b) (Fig. 2.8). The clasts in the sandy matrix are composed of porphyritic andesite with multiply-zoned plagioclase and clinopyroxene. The Ar-Ar ages of ~ 25 Ma for these clasts in their study suggest the deposition of this formation is younger than ~25 Ma.

2.5.6 Panama Formation

Panama Formation is characterised by agglomerate, tuffaceous sandstone, tuffaceous siltstone and limestone (Steward et al., 1980). The sedimentary member (tuffaceous sandstone, tuffaceous siltstone and limestone) is termed as Panama marine member.

Table 2.1 Stratigraphy of the study area

<table>
<tr><th>Epoch</th><th>Age</th><th colspan="5">Formation</th></tr>
<tr><td colspan="7">Quanternary</td></tr>
<tr><td>Pliocene</td><td></td><td colspan="5">No deposition</td></tr>
<tr><td rowspan="5">Miocene</td><td>Late</td><td colspan="5">No deposition</td></tr>
<tr><td>Middle</td><td colspan="5">Gatun</td></tr>
<tr><td rowspan="3">Early</td><td colspan="3">Pedro Miguel (17-18 Ma)[2]</td><td rowspan="3">Culebra</td><td rowspan="3">Alhajuela</td></tr>
<tr><td rowspan="2">Cucaracha (18-19 Ma)[1,3]</td><td>La Boca (18 Ma)[1]</td></tr>
<tr><td></td></tr>
<tr><td colspan="3">Las Cacadas (19-21 Ma)[2,4]</td></tr>
<tr><td rowspan="3">Oligocene</td><td>Late</td><td rowspan="3">Panama</td><td rowspan="3">Bohio</td><td>Bas Obispo (25 Ma)[1]</td><td>Caraba</td><td>Caimito</td></tr>
<tr><td>Middle</td><td colspan="3"></td></tr>
<tr><td>Early</td><td colspan="3"></td></tr>
<tr><td rowspan="3">Eocene</td><td>Late</td><td colspan="5" rowspan="2">Gatuncillo</td></tr>
<tr><td>Middle</td></tr>
<tr><td>Early</td><td colspan="5">No deposition</td></tr>
<tr><td colspan="7">Pre-Tertiary Basement Complex</td></tr>
</table>

*[1]Buchs et al. (2019b); [2]Buchs et al. (2019a); [3]MacFadden et al. (2014); [4]Montes et al. (2012b)

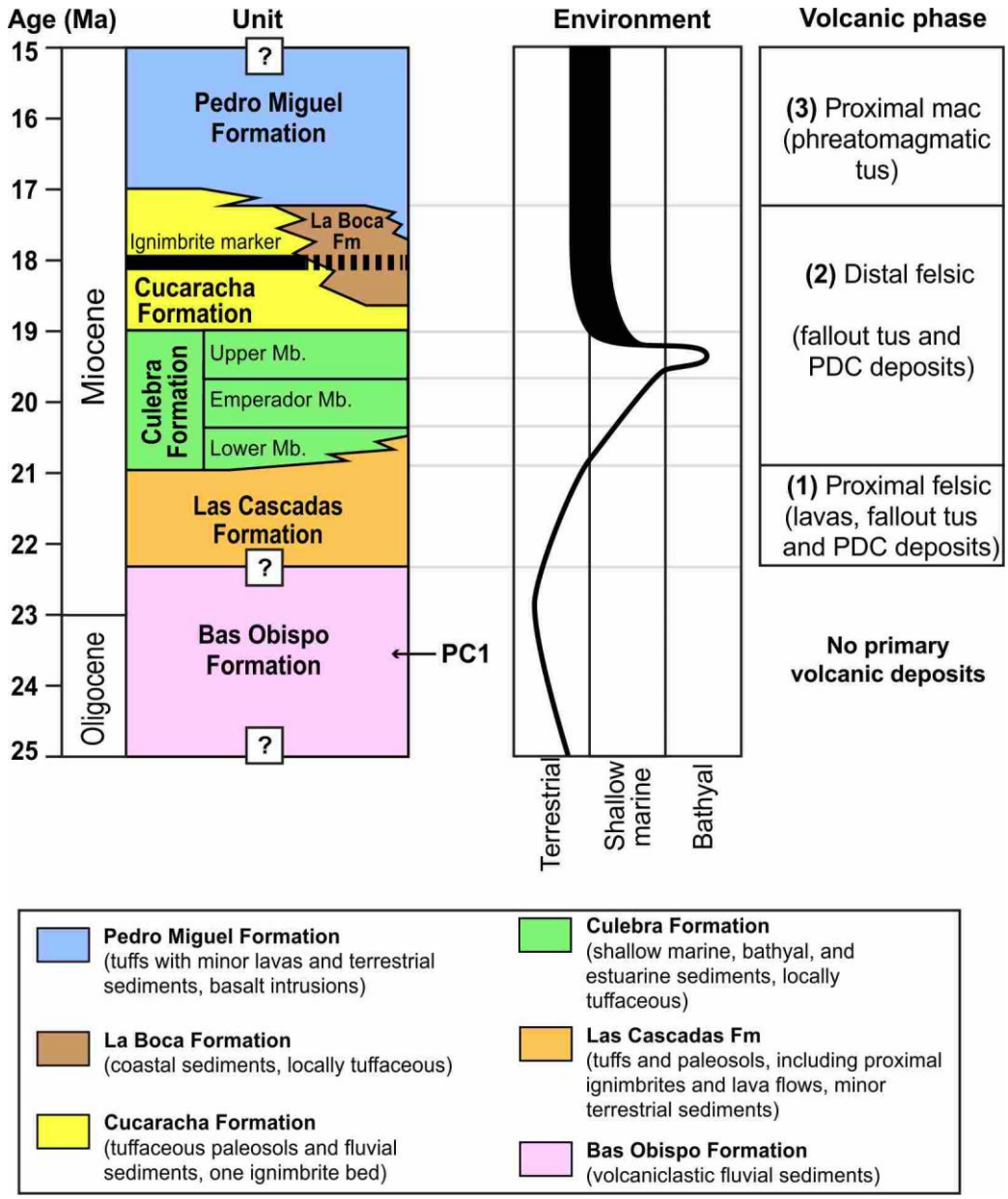

Fig. 2.8 Stratigraphy along the Panama Canal from Buchs et al. (2019a)

2.5.7 Caraba Formation

Another Oligocene formation is Caraba Formation which is described as ‘late Oligocene dacite porphyry agglomerate and in type area conglomerate, fossilferous calcareous sandstone and limestone by Steward et al. (1980).

2.5.8 Las Cascadas Formation

The early Miocene Formation is well studied recently along the canal. For Las Cascadas Formation, it is described as ‘agglomerate and fine-grained tuff’ by Steward et al. (1980). In the new studies along the Canal, it is defined as silicic tuff (including pyroclastic density flow or ignimbrite) and dacitic-andesitic lava flows (Farris et al., 2017; Buchs et al., 2019a). Ignimbrites in this formation typically include high abundance of large lithics (e.g., flow-banded dacite) and/or flattened pumices (>40

vol%), with only minor (<10% volume) pyroxene and plagioclase phenocrysts embedded in an eutaxitic matrix and locally include carbonised plant fragments. These ignimbrites are commonly interbedded with fallout fine tuff to coarse lapilli-tuff, with locally large cm-sized accretionary lapilli and intermediate-felsic lithics. These deposits are associated with red to white tuffaceous paleosols (Buchs et al., 2019b). All these indicates a terrestrial environment. Tuffs in this formation can be interbedded with silicic lava flows or crosscut by lavas/dykes (Farris et al., 2017; Buchs et al., 2019b). The Ar-Ar ages of plagioclase from a dacite and a tuff are 21.1 Ma and 20.9 Ma, respectively (Buchs et al., 2019a).

2.5.9 Culebra Formation

The Culebra Formation is mainly calcareous sandstone and siltstone (Steward et al., 1980). However, pervasive occurrence of altered fine to coarse tuffs of intermediate-felsic composition, locally with remnants of lithics, plagioclase and pyroxene suggests part of this formation is sourced by volcanic products (Buchs et al., 2019b). The Culebra Formation marks a marine transgression on top of the subaerial Las Cascadas Formation, with transition from lagoon to reef and bathyal environments in the Lower, Emperador and lower Upper Members of the Culebra Formation (van den Bold, 1972; Johnstone and Kirby, 2006; Kirby et al., 2008). Marine sedimentation along the Gaillard Cut was followed by a transition to a delta system in the uppermost Culebra Formation (Kirby et al., 2008). Recent U-Pb zircon geochronology has determined an age of 19 Ma for the tuffs of the Upper Member (Montes et al., 2012b).

2.5.10 Cucaracha Formation

Cucaracha Formation is mainly composed of clay shale, and ash tuff (Steward et al., 1980; Kirby et al., 2008). Green to red (more rarely white) clayey paleosols in this formation locally preserve an original tuff fabric with flattened ghosts of cm-sized pumices (Buchs et al., 2019b). In addition, the Cucaracha Formation includes a distinctive ignimbrite (5–8 m thick), that is locally found on top of fallout tuff and/or charcoaled tree stumps which indicates a range of terrestrial environments (i.e., mangroves, coastal swamps, rivers and flood plains) (Buchs et al., 2019b). Five new Ar-Ar analyses plagioclase by Buchs et al. (2019b) from ignimbrite define a constrained 17.9 to 18.0 Ma age of crystallisation.

2.5.11 La Boca Formation

Above it is La Boca Formation which is mudstone, siltstone, sandstone, tuff and limestone (Steward et al., 1980). An Ar-Ar age of 17.90 ± 0.08 Ma for plagioclase in a brown intermediate (?) tuff indicates this formation is at least partly contemporaneous deposition with the Cucaracha Formation (Buchs et al., 2019b). Together, the La Boca and Cucaracha formations record sedimentation along a palaeo-shoreline during the early Miocene (ca. 18 Ma), under the influence of continued distal volcanic activity (Buchs et al., 2019b).

2.5.12 Pedro Miguel Formation

This formation is defined differently by different people (Steward et al., 1980; Farris et al., 2017; Buchs et al., 2019a). The original Steward map defined Pedro Miguel Formation as ‘fine- to coarse-grained agglomerate’ (Steward et al., 1980). However, the most recent study by Buchs et al. (2019a) define this formation as being predominantly composed of basalt to basaltic andesitic tuffs and large mafic intrusions with olivine ± pyroxenes ± plagioclase phenocrysts. It was revealed in this study that this formation is mostly composed of tuff cones and large mafic intrusions, with only limited evidence for diatremes. Basalt in their definition corresponds to ‘Late Basalt Formation’ in Farris et al. (2017) and is part of ‘Tb’ in the west of Canal on the Steward map. Ar-Ar dating for basalt yield an age range of 17-18 Ma (Buchs et al., 2019a), as discussed in section 2.4.4.

2.5.13 Alhajuela Formation

The least studied late Miocene formation is Alhajuela Formation which consists of two members on the Steward map. The lower member is mainly calcareous sandstone and the upper member is tuffaceous sandstone, calcareous sandstone and limestone. This formation is only mapped near Alhajuela Lake. The youngest formation in the study area is Gatun Formation, which comprises sandstone, siltstone, tuff and conglomerate on the Steward map. This formation around the Gatun Lake is described in detail by Rooney et al. (2015).

2.5.14 Poorly Studied Volcanic Bodies

On the Steward map, there are Miocene igneous rocks termed as basalt (Tb), dacite (Td), andesite (Tlca and Ta) and undifferentiated volcanic rocks (Tv) distributed in the formations discussed above. Among these rocks, some andesite (Ta) was studied by Rooney et al. (2011). Some basalt (Tb) along the canal was included into Pedro Miguel Formation (Buchs et al., 2019a) or termed as Late Basalt Formation (Farris et al., 2011; 2017). The transition and termination of magmatism in central Panama were addressed by these studies. The tectonic controls on magmatic change and termination are controversial. Buchs et al. (2019a) consider oblique subduction as the factor while Farris et al. (2011; 2017) prefer PVA extension caused by collision between PVA and the South America Plate. In addition, the formation of felsic rocks in settings of oceanic arcs is highly debated.

3 FIELD OBSERVATIONS AND PETROGRAPHY

Thirteen weeks of fieldwork was carried out in central Panama during two field campaigns in 2017 and 2018. 235 samples were collected at 228 localities along a transect across the Isthmus of Panama. The description of samples can be found in Appendix E1. Although the geological map of Stewart et al., (1980; Fig. 1.7) is by far the most detailed map for central Panama, it can be improved in several areas based on new field observations from this study.

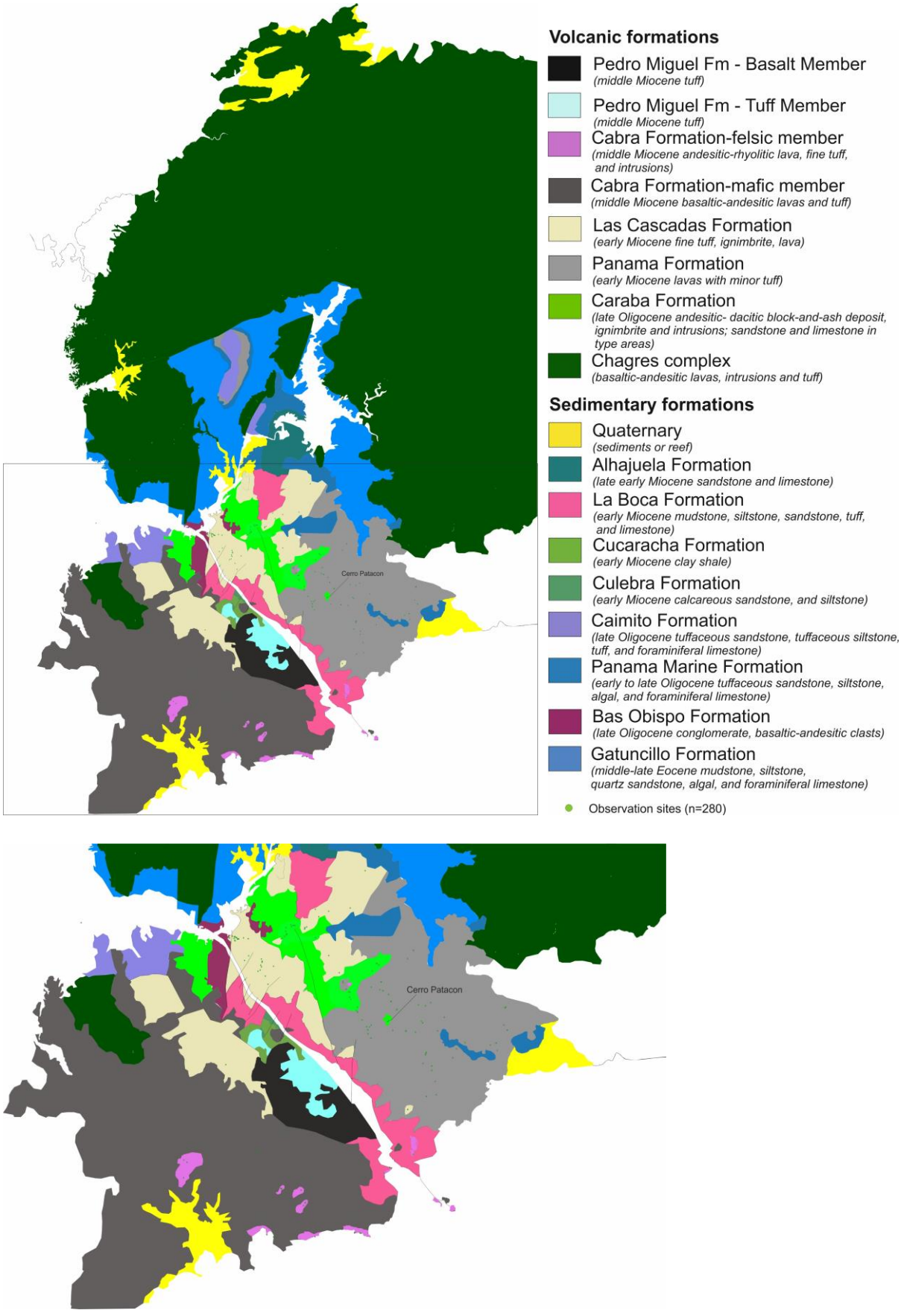

Fig. 3.1 Geological map of central Panama after Steward et al. (1980). (The area in the black rectangle is the Panama Canal area).

3.1 Chagres Complex (Pre-Oligocene: Late Cretaceous to Late Eocene)

The Late Cretaceous to Late Eocene Chagres Complex is located to the north and northeast of the Canal area, where it corresponds to the western termination of the pre-Oligocene volcanic front of the Chagres Arc found in eastern Panama. The majority of mapping and rock sampling was completed at road-side cuttings or at exposed river banks due to dense vegetation in the study area.

In the Rio Guanche area, an andesitic hypabyssal intrusion was found (Fig. 3.2 A). Plagioclase and pyroxene crystals (<2 mm in length) can be seen from hand specimen. Approximately 50 m away to the south from this intrusion, a porphyritic basaltic lava or hypabyssal intrusion comprising large clinopyroxene phenocrysts (<5 mm in length) was found. In one locality upstream, this clinopyroxene-bearing basalt host fine-grained andesitic xenoliths (Fig. 3.2 B).

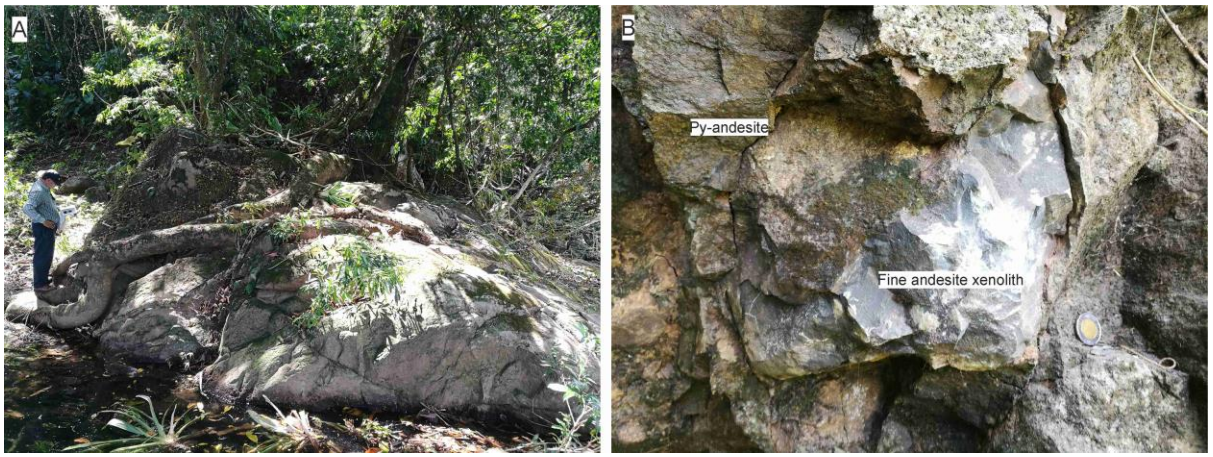

Fig. 3.2 Pictures of the Chagres Complex in Rio Guanche area. (A) Andesitic hypabyssal intrusion (sample J18-090). (B) fine andesite xenolith (sample J18-096) in pyroxene-andesite (sample J18-097).

Along the motorway in the Rio Rita area, ash tuffs are crosscut by lava flows or hypabyssal intrusions (Fig. 3.3 A). The lava flows are porphyritic with pyroxene (1-3 mm in diameter) and plagioclase as phenocrysts (1-3 mm in length). The lava represents a massive body (Fig. 3.3 A) or layered flows (Fig. 3.3 B). The tuff can be divided into loose, reddish upper part and white lower part and both are layered (Fig. 3.3 A).

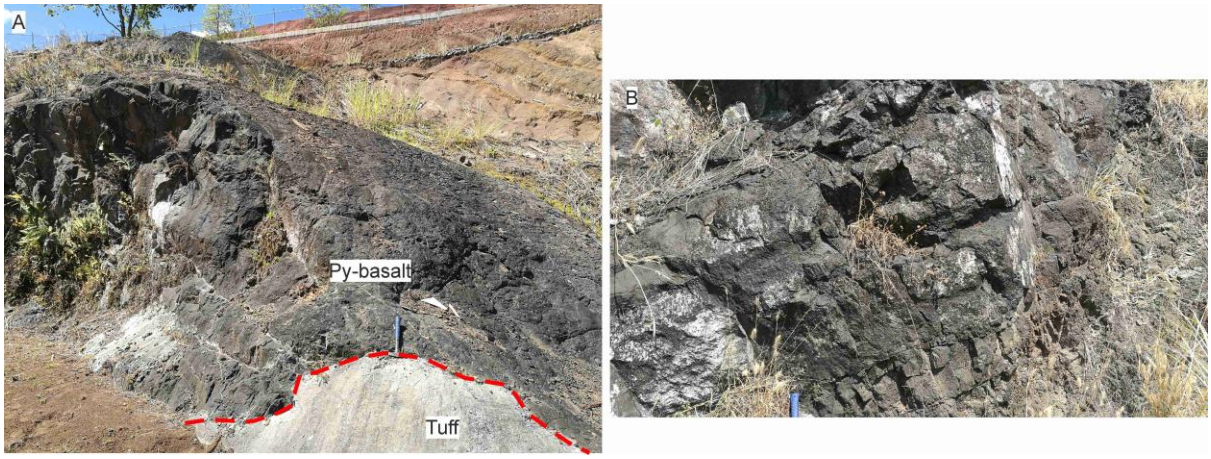

Fig. 3.3 Pictures of the Chagres Complex in Rio Rita area. (A) Fine grain tuffs crosscut by pyroxene-basalt lava flows (sample J18-088). (B) Lava flows (J18-095).

In the Rio Chagres area, a basaltic dyke was found intruding into a brecciated lava flow (Fig. 3.4 A). This basaltic dyke is fine-grained and altered. The felsic lava is highly brecciated with self-wrapped blocks up to 30 cm in diameter (Fig. 3.4 B).

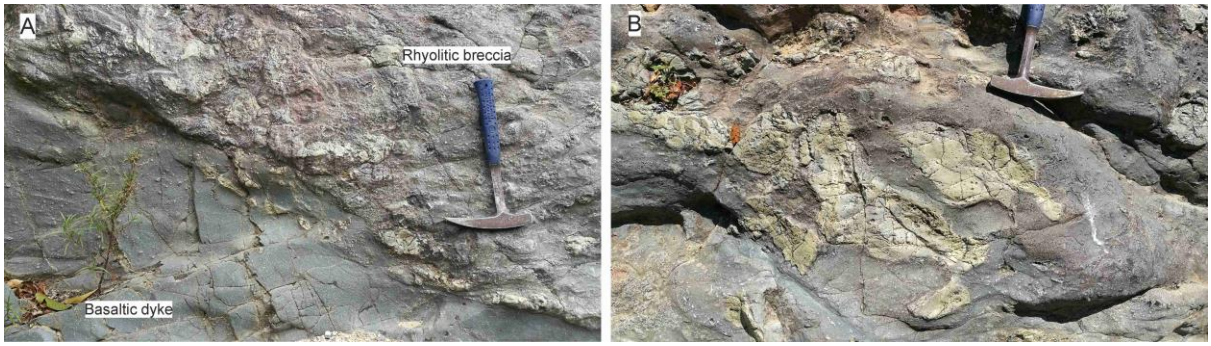

Fig. 3.4 Pictures of the Chagres Complex in Rio Chagres area. (A) Basaltic dyke (sample J18-069) intruding into rhyolitic brecciated lava flow (J18-068). (B) Detailed picture for the brecciated lava.

In the Gamboa area, both intrusions and lava flows were found. At one locality, a porphyritic andesite (sample J17-132) intruded into a fine-grained lava flow (J17-131) (Fig. 3.5 A). Columnar jointing was formed in the intrusion along the boundary. The porphyritic intrusion has amphibole (up to 3 mm) as phenocrysts. Apart from andesitic intrusions, a mafic intrusion and a gabbro were also discovered in this study (Fig. 3.5 B).

Fig. 3.5 Pictures of the Chagres Complex in Gamboa area. (A) Amphibole-andesite hypabyssal intrusion (sample J17-132) (B) Gabbro (sample J18-058).

In the Cerro Azul area, only a tonalite and diorite intrusion were found. The tonalite intrusion is composed of plagioclase, quartz, and biotite. It is a massive body with jointing structure (Fig. 3.6 A). The diorite intrusion (Fig. 3.6 B) is composed of amphibole and plagioclase and has been studied by Montes et al. (2012a).

Fig. 3.6 Pictures of the Chagres Complex in Cerro Azul area. (A) Tonalite intrusion (B) Diorite intrusion.

Rocks in this complex can be divided into two lithological subgroups based on mineral compositions. One subgroup has pyroxene (Fig. 3.7 A, B, C, D) and the other has amphibole (Fig. 3.7 E, F) as the phenocrystic phase. Phenocryst plagioclase and accessory magnetite can be found in both subgroups. The clinopyroxene-bearing rocks can be porphyritic or fine-grained with a sub-ophitic texture. For porphyritic basalt-andesite, clinopyroxene (1-3 mm; 35%), plagioclase (1-3 mm; 30%) and magnetite (0.2-0.5 mm; 5%) are phenocrysts. Clinopyroxene phenocrysts display hour-glass texture (Fig. 3.7 A) or zonation, occasionally with a rounded core (Fig. 3.7 B) or rim (Fig. 3.7 C). Plagioclase crystals are also zoned, usually displaying sieve texture (Fig. 3.7 C). The groundmass is composed of small elongated plagioclase crystals and glass. In the sub-ophitic basalt sample, clinopyroxene are

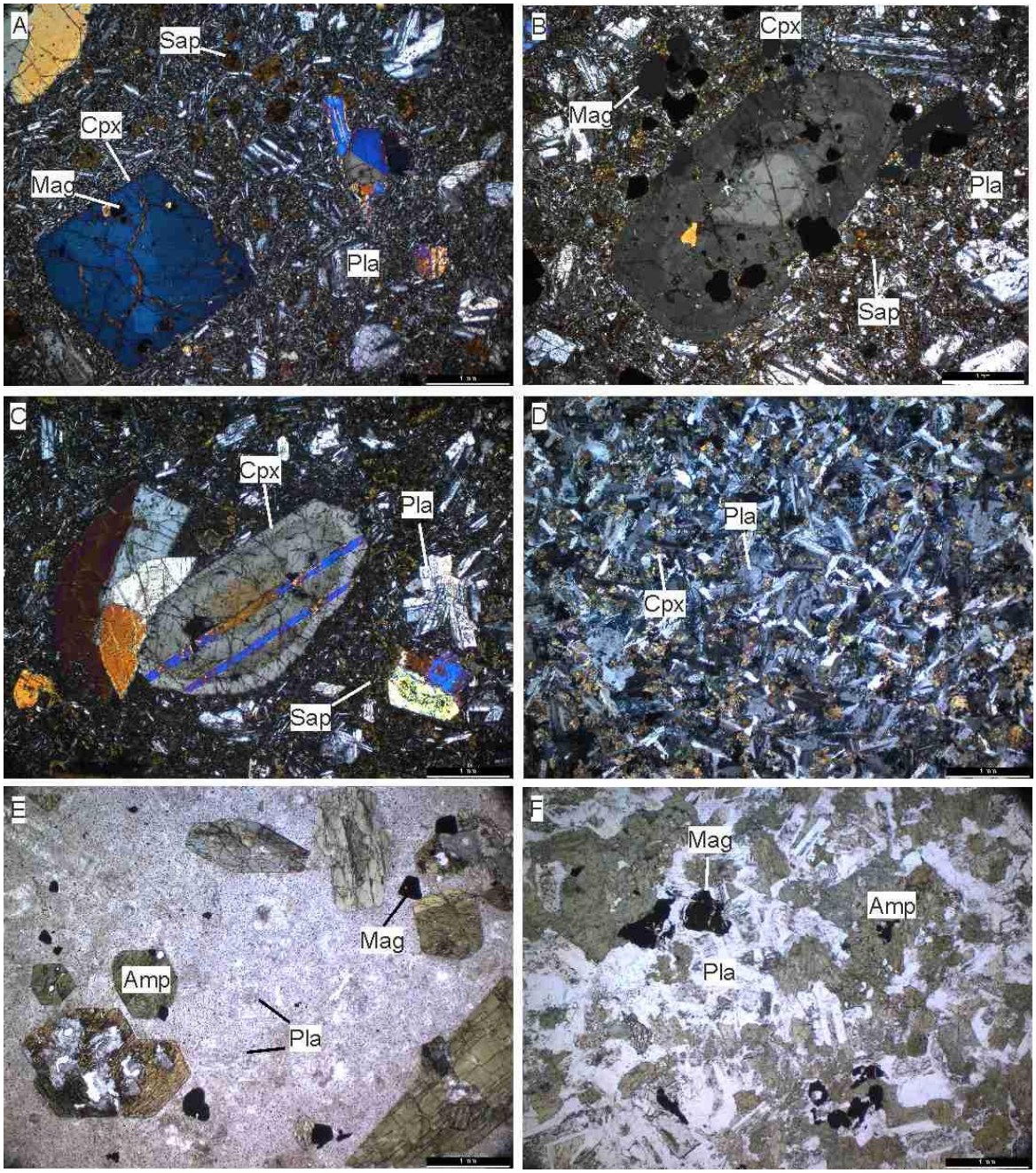

Fig. 3.7 Photomicrographs of igneous rocks in the Chagres Complex. (A) XPL view of basalt J18-097 in Rio Guanche area with clinopyroxene showing hour-glass texture (B) XPL view of basalt J18-091 in Rio Guanche area with zoned Cpx. (C) XPL view of basalt J18-088 in Rio Rita area with zoned Cpx and sieved Pla (D) Fine grained basalt J17-133 in Gamboa area (E) PPL view of amphibole-bearing andesite J17-132 in Gamoba area with Amp, Pla and Mag as phenocrysts (Pla altered to be clay minerals) (F) Amphibole bearing diorite with Amp and Pla. (Abbreviation: Cpx- clinopyroxene; Pla- plagioclase; Mag- magnetite; Amp- amphibole; Sap- saponite).

interstitial to plagioclase crystals (Fig. 3.7 D). For the amphibole bearing rocks, amphibole crystals display green-yellowish pleochroism (Fig. 3.7 E, F). In the porphyritic rocks, amphibole (0.5-3 mm, 20 vol. %), plagioclase (0.3-0.8 mm, 35 vol.%), and magnetite (0.1-0.4 mm, 8 vol.%) occur as

phenocrysts (Fig. 3.7 E). Amphibole crystals are euhedral, while plagioclase crystals are partially altered to clay minerals. In the diorite sample, plagioclase crystals are normally-zoned.

3.2 Caraba Formation (Late Oligocene)

3.2.1 Description

The Caraba Formation occurs mainly in the Soberania National Park and Camino de Cruces National Park and is the oldest volcanic formation in the Canal area. This formation is andesite-dacite and is composed of block-and-ash deposit, lapilli tuff (ignimbrite), and intrusions. A unique feature of this formation is that all the rock types are amphibole-bearing. The size of the clasts in the block-and-ash deposits varies from 2 to 30 cm. The block-and-ash deposit can be clast-contact (Fig. 3.8 A) with matrix tuff filling the interstitial space, or matrix-contact with clasts sparsely distributed in the matrix. Ignimbrite is composed of pumice clasts, crystals (plagioclase, amphibole ± biotite), and lithics (Fig. 3.8 C). It is loose in texture and not highly welded. Ignimbrite is interbedded by a thin layer (10-20 cm) of accretionary lapilli tuff (Fig. 3.8 D). In one outcrop in the Soberania National Park, block-and-ash deposit grades upward to the ignimbrite and the block-and-ash deposit is underlain by hypabyssal intrusions (Fig. 3.8 E). The amphibole-andesite intrusion was only found in the Eco Roca quarry near Cerro Patacon and it has been studied by Rooney et al. (2011).

Fig. 3.8 Photographs of outcrops of the Caraba Formation.(A) Block contacted block-and-ash deposit (B) Ash contacted block-and-ash deposit (C) Ignimbrite with pumice, lithic (Lt), plagioclase (Pla) and biotite (Bt) crystals (D) A thin lapilli tuff layer (10-20 cm) interbedded with ignimbrite (E) Dacite intrusion (F) Andesite intrusion.

Clasts in block-and-ash deposit and the underlying intrusion are amphibole bearing dacite. The amphibole bearing rock is porphyritic with phenocrysts of amphibole (1-3 mm; 20%), plagioclase (1-3 mm; 30%), and quartz (0.5-2.5 mm; 15%) (Fig. 3.9 A). Amphibole and plagioclase grains do not display zonation or resorption. Quartz crystals are usually embayed or rounded. In the amphibole-

andesite, amphibole and plagioclase are zoned and resorbed cores occur in plagioclase crystals (Fig. 3.9 B). Quartz is absent in andesite samples.

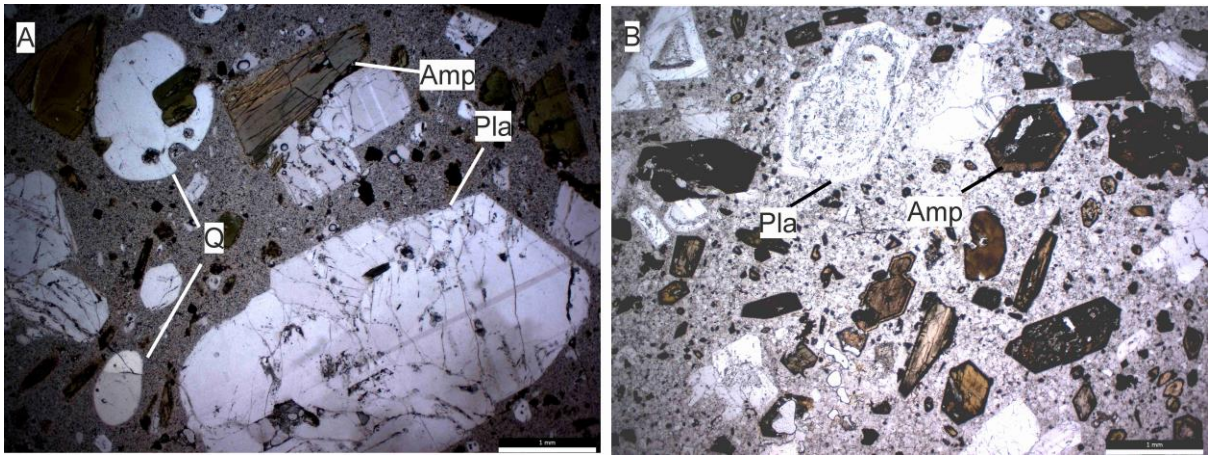

Fig. 3.9 Photomicrographs of amphibole-dacite (A) and amphibole-andesite (B) in the Caraba Formation (Abbreviation: Pla- plagioclase; Amp- amphibole; Q- quartz).

3.2.2 Interpretation

Block-and-ash deposits sit on the dacite intrusion and grade upward into ignimbrite layers (Fig. 3.8 A, B, C, E). The hypabyssal intrusion might be a lava dome. When the volcanic eruption occurred, this dome fragmented into blocks of various sizes and accumulated near to the dome to form the block-and-ash deposit. The fine grain ignimbrite (comparing with block-and-ash deposit) accumulated later and further away from the dome. An accretionary lapilli tuff layer within the ignimbrite suggests it formed in response to volcanic erupted in a subaerial environment. Under the microscope, homogeneous amphibole and plagioclase crystals in amphibole dacite suggest no magma mixing. The zoned and resorbed amphibole in the amphibole andesite were interpreted as magma mixing by Rooney et al. (2011). Of importance is the Caraba Formation was described as ‘late Oligocene dacite porphyry agglomerate, conglomerate, fossiliferous calcareous sandstone and limestone’ on the map of Stewart et al. (1980). But this is not accurate according to the description in this study.

3.3 Panama Formation (Late Oligocene to Early Miocene)

3.3.1 Description

The Panama Formation is exposed in parts of Panama City and San Migueito, where it consists mainly of lavas, hypabyssal intrusions, and seldom tuffaceous units. Lava flows can be thin (Fig. 3.10 A) and thick layer (Fig. 3.10 B) but basal and top breccias were developed which form A’a lava. The more common lava flow in the Panama Formation is the massive brecciated lavas (Fig. 3.10 C). The brecciated clasts range from 5 to 40 cm in diameter. Feeder dykes can also be found crosscutting the massive lava bodies. Volcanic bombs are common in the study area and are normally found in the more evolved, andesitic rocks (Fig. 3.10 D). These volcanic bombs are up to 2 m in diameter and are

also fragmented. Columnar texture can also be found in the field in lava flows or hypabyssal intrusions. The columnar texture is usually irregular and the hexagonal shape, which is common in columnar basalt is rare in the Panama Formation (Fig. 3.10 E). Tuffs in this formation are only found in one locality in the Panama City area, where they occur as ~3 m thick units with no obvious layering.

Fig. 3.10 Photographs of outcrops of the Panama Formation. (A) A'a lava with basal and top breccia. (B) Lava flows over a brecciated lava flow. (C) Brecciated lava flow. (D) Volcanic bombs with brecciation. (E) Irregular columnar basalt (F) Massive tuff.

Clinopyroxene, plagioclase, magnetite, and minor orthopyroxene show as phenocrysts, while glass and fine grained plagioclase crystals as groundmass. Magmatic rocks in this formation can be divided into two sub-groups based on petrographic characteristics. The first sub-group (Pam1) is characterised by large clinopyroxene phenocrysts (1-3mm, up to 6mm; 10-20 vol.%; Fig. 3.11 A, B, C). These clinopyroxene grains are all zoned (Fig. 3.11 C) or show overgrowth (Fig. 3.11 B). In addition, smaller clinopyroxene grains (0.5-1.5 mm; 10-25 vol.%) can also be found in this sub-group and they are homogeneous crystals without zonation or overgrowth (Fig. 3.11 C). Plagioclase grains (0.5-1.5 mm; 20-35 vol.%) are elongated phenocrysts, which display zoning and sieve texture (Fig. 3.11 B, C). Magnetite grains are small phenocrysts and account for a small proportion of the rock unit (0.1-0.4 mm, 5 vol.%). They are usually present in the groundmass or coexist with groundmass clinopyroxene rather than phenocrystic clinopyroxene (Fig. 3.11 C). Yellow saponites, the alteration (probably hydrothermal) mineral of glass and clinopyroxene (Fig. 3.11 A, residual clinopyroxene core can still be seen) fill the holes of sieved texture of plagioclase and clinopyroxene. Saponite veins can go through fractures of clinopyroxene crystals. In the second sub-group (Pam2), euhedral clinopyroxene grains (0.5-1 mm in diameter; ~25 vol.%) are smaller in comparison with those in the first sub-group, yet display no obvious zonation (Fig. 3.11 D). Plagioclase phenocrysts are also homogeneous crystals without zonation or sieve texture. Plagioclase grains display a continuous range of length from ~ 1 mm for phenocryst plagioclases to 0.1 mm for groundmass plagioclases. Moreover, orthopyroxene grains are more common in this sub-group (Fig. 3.11 D). They are usually euhedral and small in size (0.5-1 mm; ~8 vol.%). Magnetite (0.1-0.3 mm; ~5 vol.%) occurs with clinopyroxene or orthopyroxene.

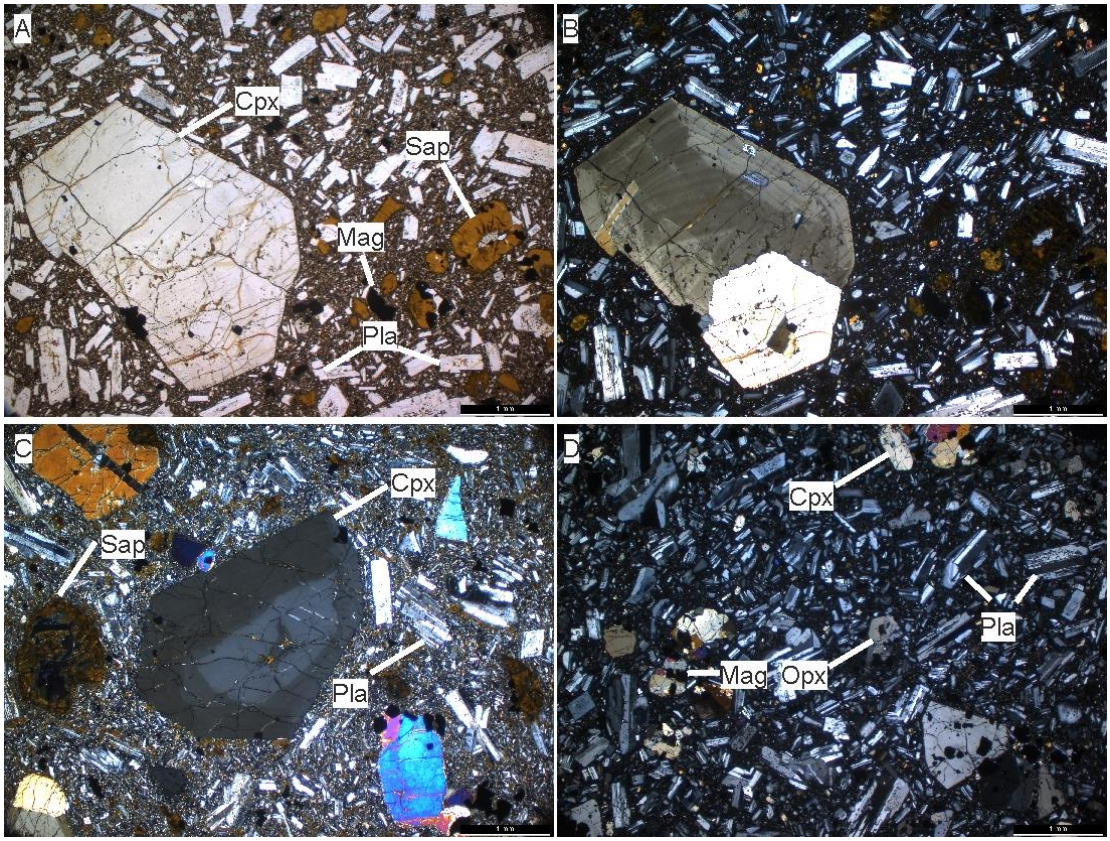

Fig. 3.11 Photomicrographs for magmatic rocks in the Panama Formation. (A) PPL view and (B) XPL view of porphyritic basaltic andesite (sample J18-059-2) with big overgrown Cpx phenocrysts and sieved Pla. Some Cpx altered to be saponite (C) XPL view of basaltic andesite (J17-059-2) with big, zoned Cpx and relatively small, homogeneous Cpx. (D) XPL view of andesite (J17-036-1) with Cpx, Pla, and Opx phenocrysts. (Abbreviation: Cpx- clinopyroxene; Pla- plagioclase; Opx- orthopyroxene; Mag- magnetite; Sap- saponite).

3.3.2 Relationship between the Panama Formation and Caraba Formation

The Panama Formation usually occurs with the Cabra Formation, especially the Cabra tuff member in Camino de Cruces National Park. Intrusions of the Panama Formation (Fig. 3.12 A) intrude tuffs (Fig. 3.12 B) of the Caraba Formation. In addition, brecciated lava flows and volcanic bombs (Fig. 3.10 D) in the Panama Formation overlie the Caraba tuff member. These field relations suggest that the Panama Formation was emplaced later than Caraba tuff member. Magma mingling between pyroxene-bearing rocks of the Panama Formation and amphibole-bearing rocks of the Caraba Formation was discovered in Panama City. Fig. 3.12 D shows the mixing boundary between amphibole-andesite (left side, Fig. 3.12 C) and pyroxene-andesite (right side). The striation structure (Fig. 3.12 E) in the boundary indicates magma mixing between these two rock types. This field relation indicates the eruption of Panama Formation can be as early as Caraba Formation.

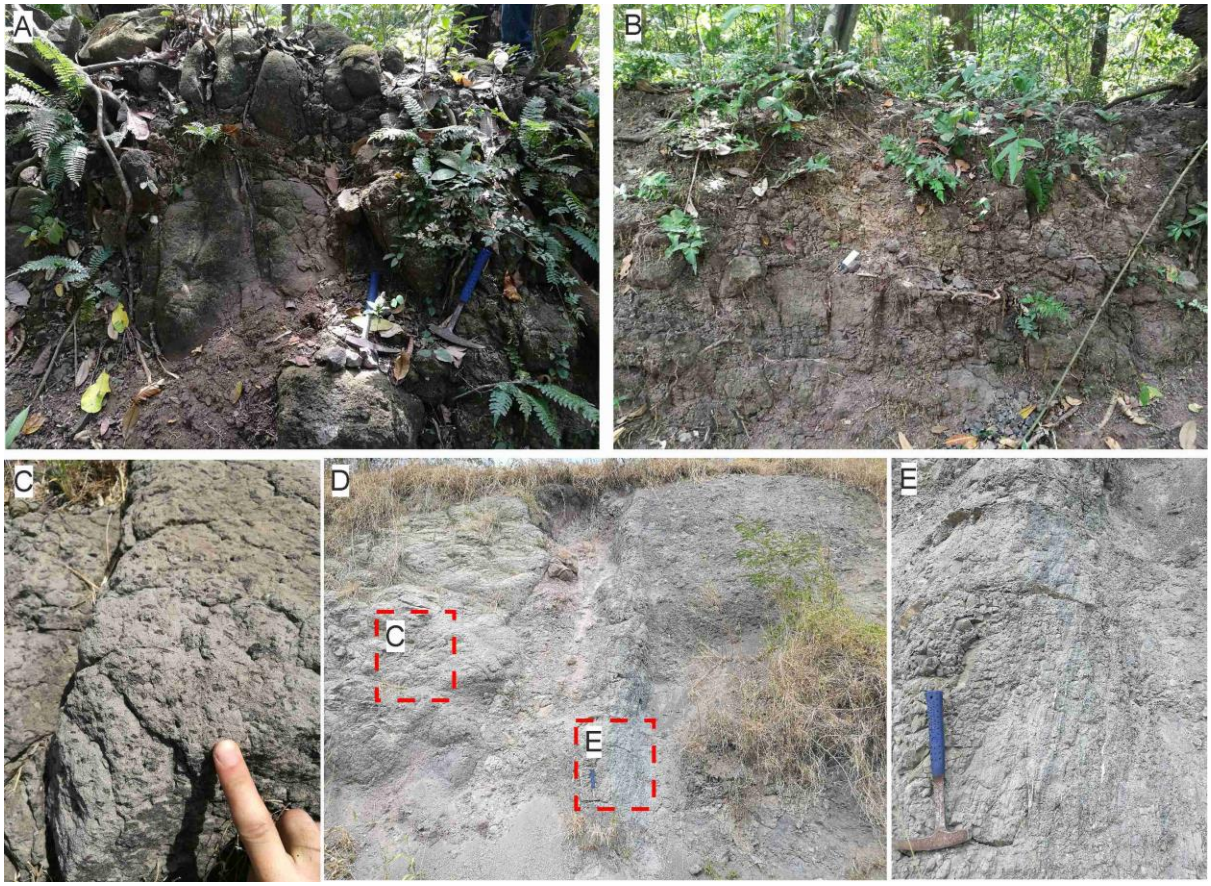

Fig. 3.12 Photographs of outcrops of the relation between the Caraba Formatin and Panama Formation. (A) Irregular columnar basalt from the Panama Formation intruding into (B) Amphibole bearing ignimbrite from the Caraba Formation. (C) Amphibole bearing rocks from the Caraba Formation. (D) Boundary of magma mingling between amphibole bearing rocks from the Caraba Formation and pyroxene bearing rocks from the Panama Formation. (E) Inset photo to show magma mingling.

Both clinopyroxene and amphibole are found as phenocrysts (Fig. 3.13). For clinopyroxene, a thin reaction rim can be found around the euhedral phenocryst (Fig. 3.13 A, B), or the phenocrysts are embayed or rounded due to resorption (Fig. 3.13 C, D). For amphibole, a clear reaction rim is also found and moreover, amphiboles are usually rounded (Fig. 3.13).

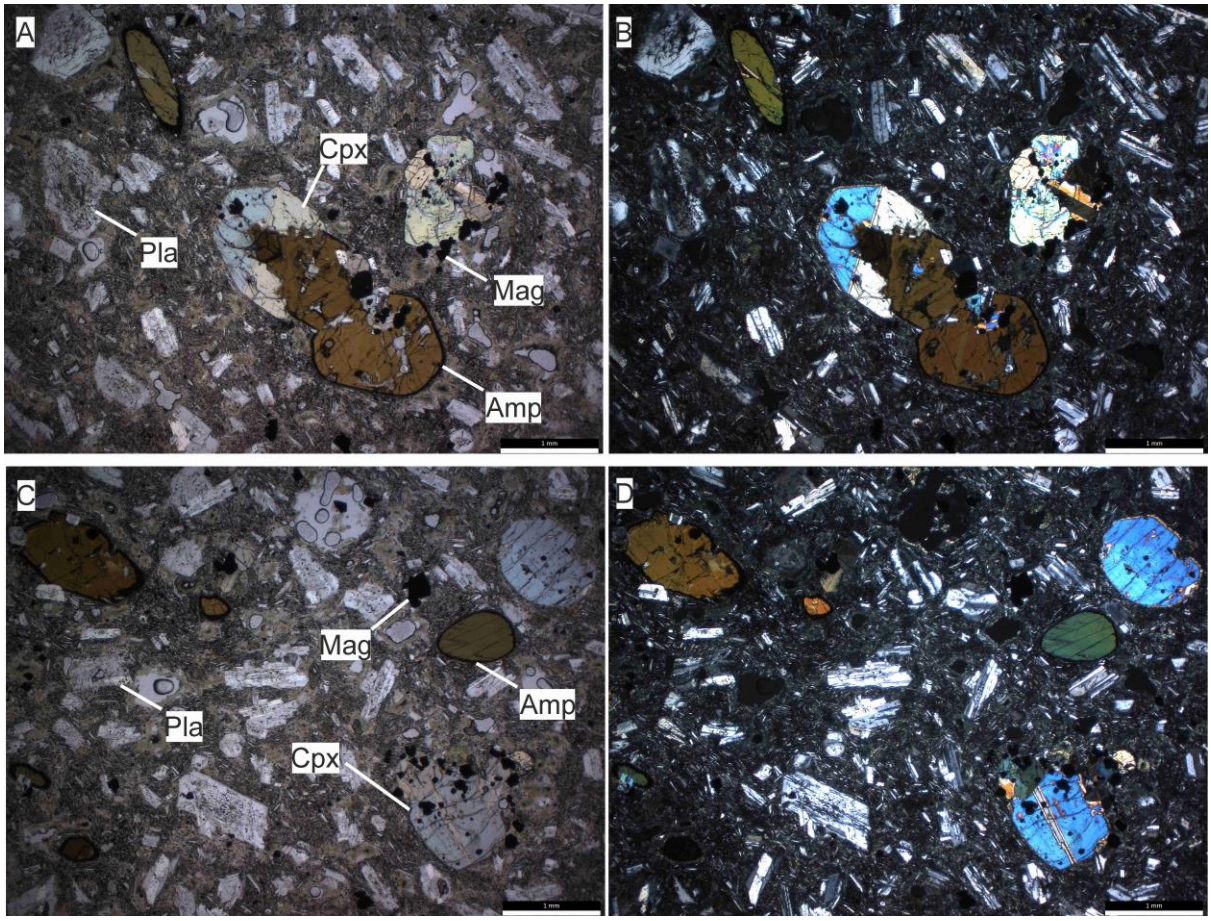

Fig. 3.13 Photomicrographs for the mixing rock (sample J18-009) between the Panama Formation and the Caraba Formation. (A) PPL view and (B) XPL view of the mixing rock with both Cpx and Amp as phenocrysts. The Cpx in the centre has a thin reaction rim and the Amp crystals are rounded with dark rims. (C) PPL view and (D) XPL view of the mixing rock. The Cpx in the right corner is embayed and the Amp next to it is rounded with dark rim. (Abbreviation: Cpx- clinopyroxene; Pla- plagioclase; Amp- amphibole; Mag- magnetite).

3.3.3 Interpretation

A'a lava flows (Fig. 3.10 A) and volcanic bombs (Fig. 3.10 D) suggest that eruption in the Panama Formation happened in a subaerial environment. This is further supported by the absence of hyaloclastite in lava flows. Jigsaw structure (Fig. 3.10 C) is usually interpreted as a result of cooling contraction in the subaerial environment (Leandro D'Elia, 2012). Clinopyroxene phenocrysts (1-3 mm, up to 6 mm in diameter) in the first sub-group are all zoned and plagioclase grains show sieve texture (Fig. 3.11 C). These disequilibrium textures are most likely attributed to magma mixing so that the clinopyroxene crystals can regrow to a relatively larger size in the recharged magmas.

Dykes in the Panama Formation that have intruded ignimbrites from the Caraba Formation suggest that the Panama Formation was emplaced after the Caraba Formation. In another locality, lava flows

of the Panama Formation mix with lava flows of the Caraba Formation, suggesting contemporaneous eruption.

The Panama Formation was previously described as a unit predominantly composed of agglomerate (Steward et al., 1980). This study suggests that this unit is mainly composed of brecciated lavas locally crosscut by dykes. Basalt and andesite bodies mapped as Tb and Ta in the map of Stewart et al. (1980) could not be distinguished from the Panama Formation based on new field and geochemical results (Chapter 3) and are therefore considered part of this unit in this study.

3.4 Las Cascadas Formation (Early Miocene)

3.4.1 Description

This formation is distributed in Soberania National Park and Chilibre (Fig. 3.1) and has been previously described by Farris et al. (2017) and Buchs et al. (2019a). From this study, the Las Cascadas Formation occurs mainly as andesitic to rhyolitic lava flows and tuffs. Lava flows mainly show irregular columnar structure (Fig. 3.14 A) or brecciation (Fig. 3.14 A, B). In a lava body in Soberania National Park, columnar jointed rocks occur in the core (Fig. 3.14 C), while flow-banded lavas (Fig. 3.14 D) constitute the inner part and brecciated lavas constitute the outer part (Fig. 3.14 E). This field relationship presents a complete sequence of dacitic or rhyolitic lava flow (Cas and Wright, 2012). In addition to the lava flows, tuff is also an important member in this formation and is found interbedded with brecciated lava flows (Fig. 3.14 F). Tuffs range in size from ash tuff to lapilli tuff in this study.

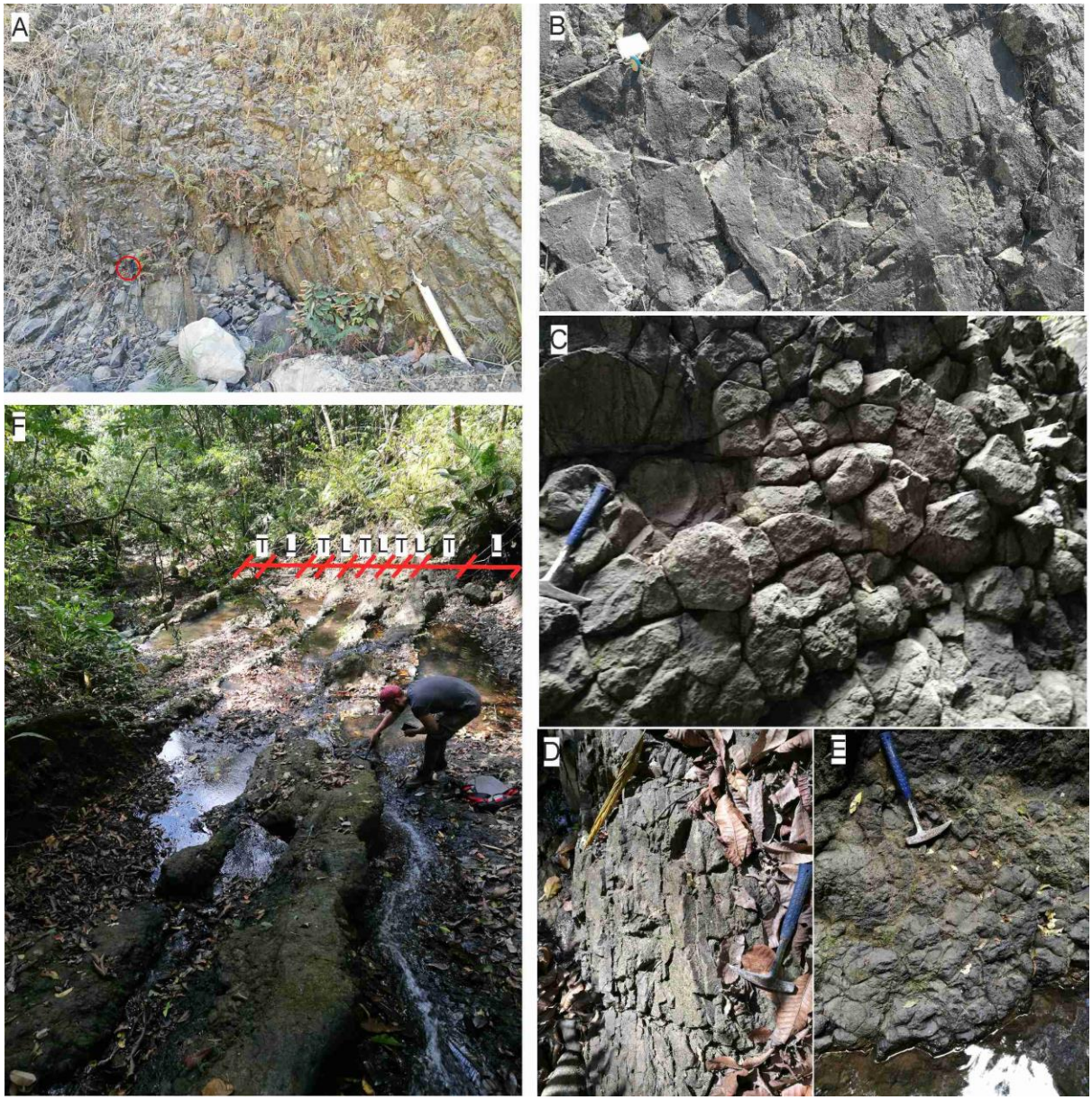

Fig. 3.14 Photographs of outcrops of the Las Cascadas Formation. (A) Columnar jointed andesitic lavas and brecciated andesitic lavas. (B) Brecciated lava flows with jigsaw structure. (C) Inner part of an andesitic-dacitic lava with irregular columnar jointing structure. (D) Out part of an andesitic-dacitic lava with flow banding structure. (E) The brecciated rim of the andesitic-dacitic lava. (F) Lapilli tuff layers interbed with brecciated lava flow.

Lava flows in this formation have glass-rich groundmass and a variable phenocryst mode ranging from 0 to ~ 45 vol.%. Rocks showing columnar jointing have the highest phenocryst content (45%), whereas flow-banded rocks have little-to-no phenocrysts (< 5 vol.%). Brecciated lava flows vary between these two and can show porphyritic and aphanitic texture. For the porphyritic rocks, glomerocrysts are common, which are composed of plagioclase, clinopyroxene, orthopyroxene, and magnetite (Fig. 3.15 A, B). Glomerocrysts in this formation are a unique feature, which have not been observed in other formations. Plagioclase accounts for the largest volume (0.5-2mm, 20-30 vol.%)

and normally resorbed to show fine to coarse sieve texture (Fig. 3.15 B, C). Clinopyroxene grains are relatively small (0.03-1 mm; 10-15 vol.%) relative to plagioclase. They are euhedral or rounded due to resorption (Fig. 3.15 B). Orthopyroxene grains are consistently smaller than clinopyroxene grains and account for smaller proportion (0.2-0.5 mm; 5 vol.%). They usually occur in glomerocrysts (Fig. 3.15 A, B). Magnetite grains are also small crystals and account for small proportion of the rock unit (0.2-0. 3mm; 5 vol.%). In addition, orthopyroxene grains are more common in Las Cascadas Formation than the Panama Formation, particularly in the less evolved rocks of the Panama Formation. For both porphyritic rocks and aphanitic rocks, glass is the main phase in groundmass (Fig. 3.15 C) and in the glomerocryst interstices. Jigsaw structure of lava flows, accretionary lapilli tuff and no hyaloclastite indicate this formation is subaerial. Rhyolite in this formation overlies andesitic tuff of the Panama Formation, indicating an eruption later than that of the Panama Formation.

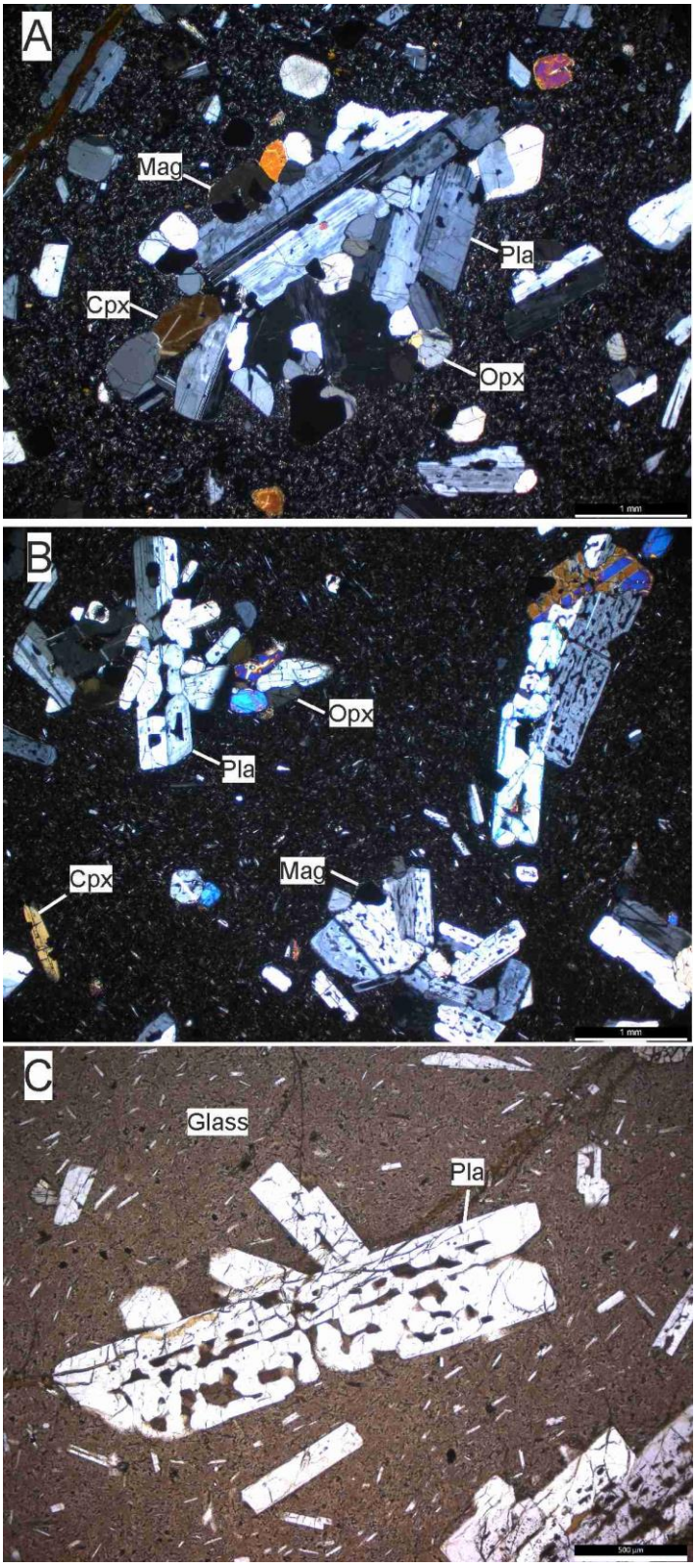

Fig. 3.15 Photomicrographs for porphyritic rocks in the Las Cascadas Formation. (A) XPL view of J17-006 to show a glomerocryst in the centre composed of Cpx, Pla, Opx, Mag. (B) XPL view of J18-057 to show a glomerocryst (up left coner), resorbed Cpx (down left corner), and Pla (up right corner) with fine sieve texture. (C) PPL view of J17-121 to show a Pla with coarse sieve texture and glass in groundmass. (Abbreviation: Cpx- clinopyroxene; Pla- plagioclase; Opx- orthopyroxene; Mag- magnetite).

3.4.2 Relationship between the Las Cascadas and Panama Formations

At one locality in the Panama City area, rhyolite of the Las Cascadas Formation is overlain by a tuff of the Panama Formation (Fig. 3.16 A). The rhyolite shows flowing rhyolitic structure (Fig. 3.16 B), while the tuff is a massive body, which has been described (see Fig. 3.10 F).

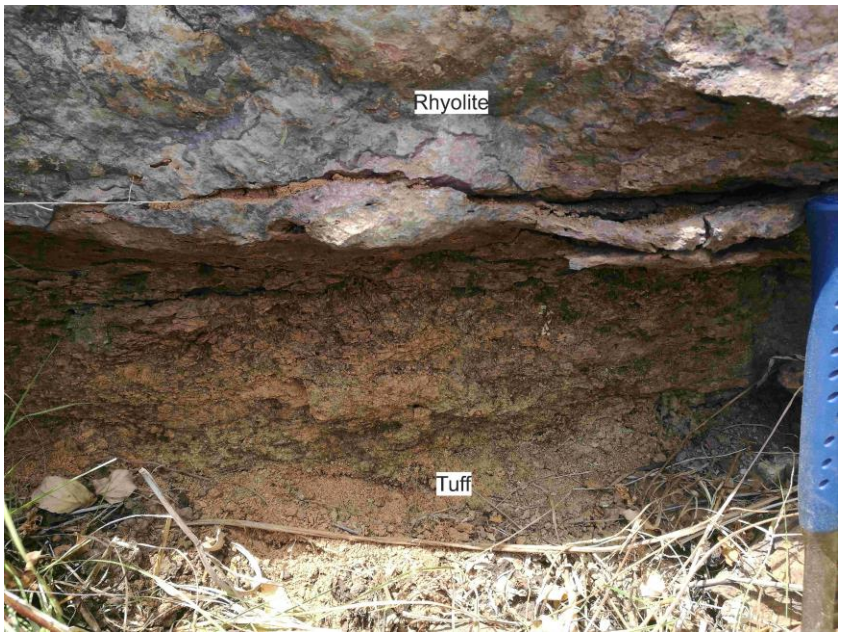

Fig. 3.16 Filed relation between Las Cascadas lava and the Panama Formation tuff

3.4.3 Interpretation

The absence of pillowed rocks and hyaloclastite suggests that lavas of the Las Cascadas Formation erupted in a subaerial environment. Lapilli tuff layers became interbedded with lava flows (Fig. 3.14 F), indicating that the volcanic eruption occurred for several cycles. Under the microscope, glomerocrysts are common in the porphyritic samples from this formation. This suggests that the magma derives from a, evolved crystal-rich magma chamber or magma mush and the glomerocrysts are the segments of the magma mush.

Rhyolite in the Las Cascadas Formation erupted above a tuff in the Panama Formation (Fig. 3.16). which suggests that at least locally, the Las Cascadas Formation was emplaced later than the Panama Formation. On the map of Steward et al. (1980), the Las Cascadas Formation is mainly composed of tuff and ‘Tlca’ is an informal name for lava flows which has a similar age with the Las Cascadas tuff. In this study, the ‘Tlca’ is incorporated into the Las Cascadas Formation. Along the Canal, the Las Cascadas Formation also includes dacitic tuffs (fallout and PDC deposits) and lavas (Stewart et al., 1980; Farris et al., 2017; Buchs et al., 2019a), which were subdivided into Dacite and Tuff members by Buchs et al. (2019a) adopted in this study to replace ‘Tlca’ to describe lava flows. Las Cascadas Formation is used to describe tuff that is similar to the original definition of the Steward map.

3.5 Cabra Formation (Early Miocene)

3.5.1 Description

This formation is distributed to the west of the Canal, extending westward to Los Aguas. This formation consists of a mafic and felsic member.

The mafic member comprises basaltic-andesitic lava flows, hypabyssal intrusions, and tuffs. Massive lava flows display hexagonal columnar structure (Fig. 3.17 A, B). These massive lavas are topographic highs and are excavated as quarries. Mafic intrusions are relatively rare and the outcrops are small (~ 10 m in diameter; Fig. 3.17 C) compared to that of lava flows. Aside from massive lava flows, thin (0.3-1 m) layered lava flows can also be found, especially in Cerro Cabra area (Fig. 3.17 D). These thin lava layers are usually interbedded with thin tuff layers (0.3-1 m). A red tuff layer interbedded in massive lava flows in Cerro Cabra area (Fig. 3.17 E, F) can be treated as a marker layer for this area.

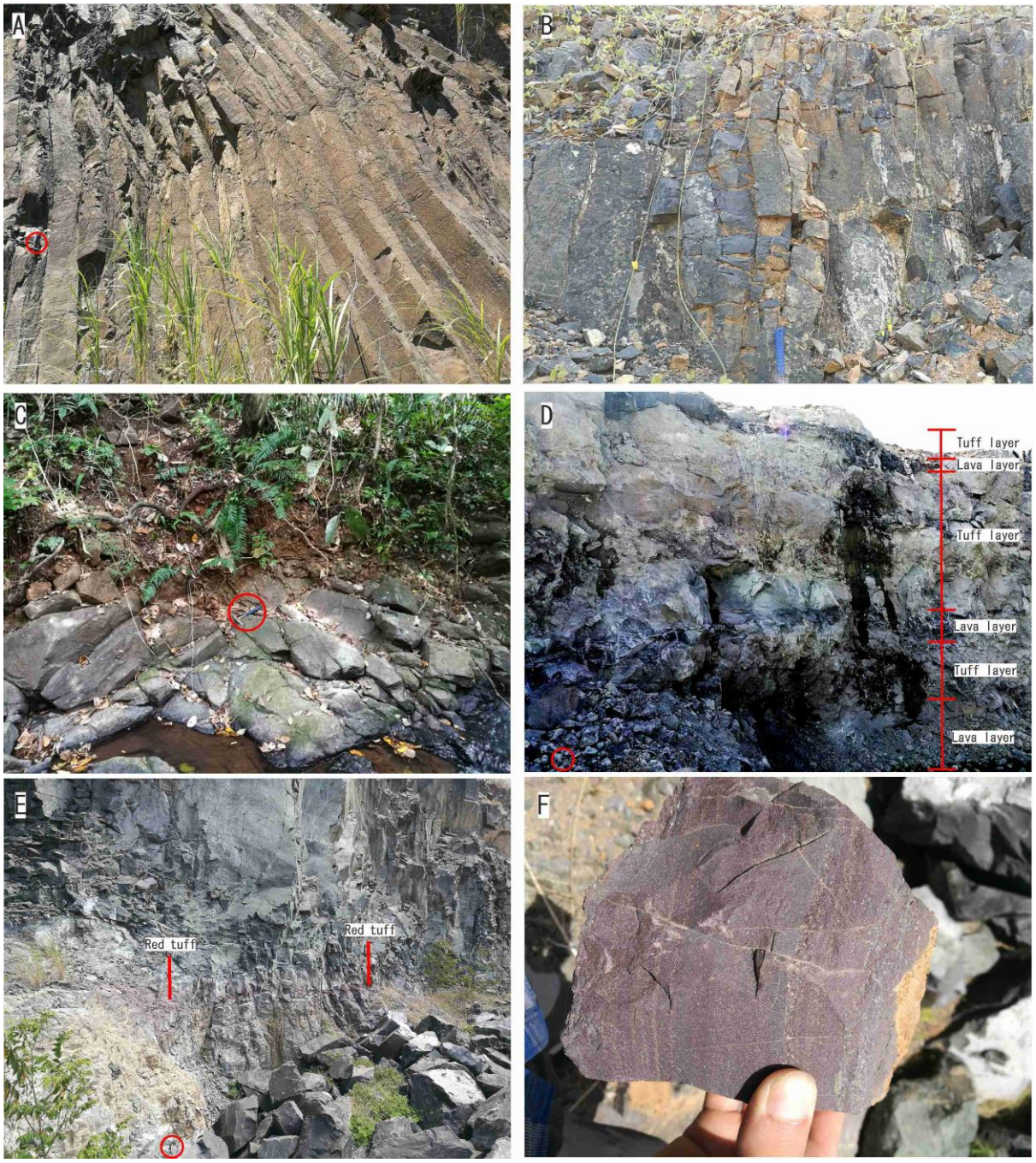

Fig. 3.17 Photographs of outcrops of the Cabra mafic member. (A) Basalt with irregular columnar jointing of J18-099. (B) Basalt with irregular columnar jointing of J18-052. (C) Massive basaltic intrusion of J17-034. (D) Tuff layers interbed with basaltic lava layers (J18-033-2). (E) A red tuff layer interbed with massive basaltic lava. (F) hand specimen from the red tuff layer. (A hammer in the red circle as scale).

The felsic rocks are mainly dacitic-rhyolitic lavas. A diorite intrusion and a lapilli tuff were also discovered in this study. Lava flows are well distributed along the coast in Cerro Cabra area (Fig. 3.1). Lava flows can be stoney with minor flow banding (Fig. 3.18 A), or black obsidian layers (partly perlitised) interbedded with white, porous pumice-like layers (Fig. 3.18 B). All these lava flows have a brecciated crust composed of pumiceous lava blocks, which can often be wrapped by obsidian flows

(Fig. 3.18 C). Apart from lava flows, felsic tuffs were also found. Tuffs in this study are composed of pumice and glass and welded (Fig. 3.18 D).

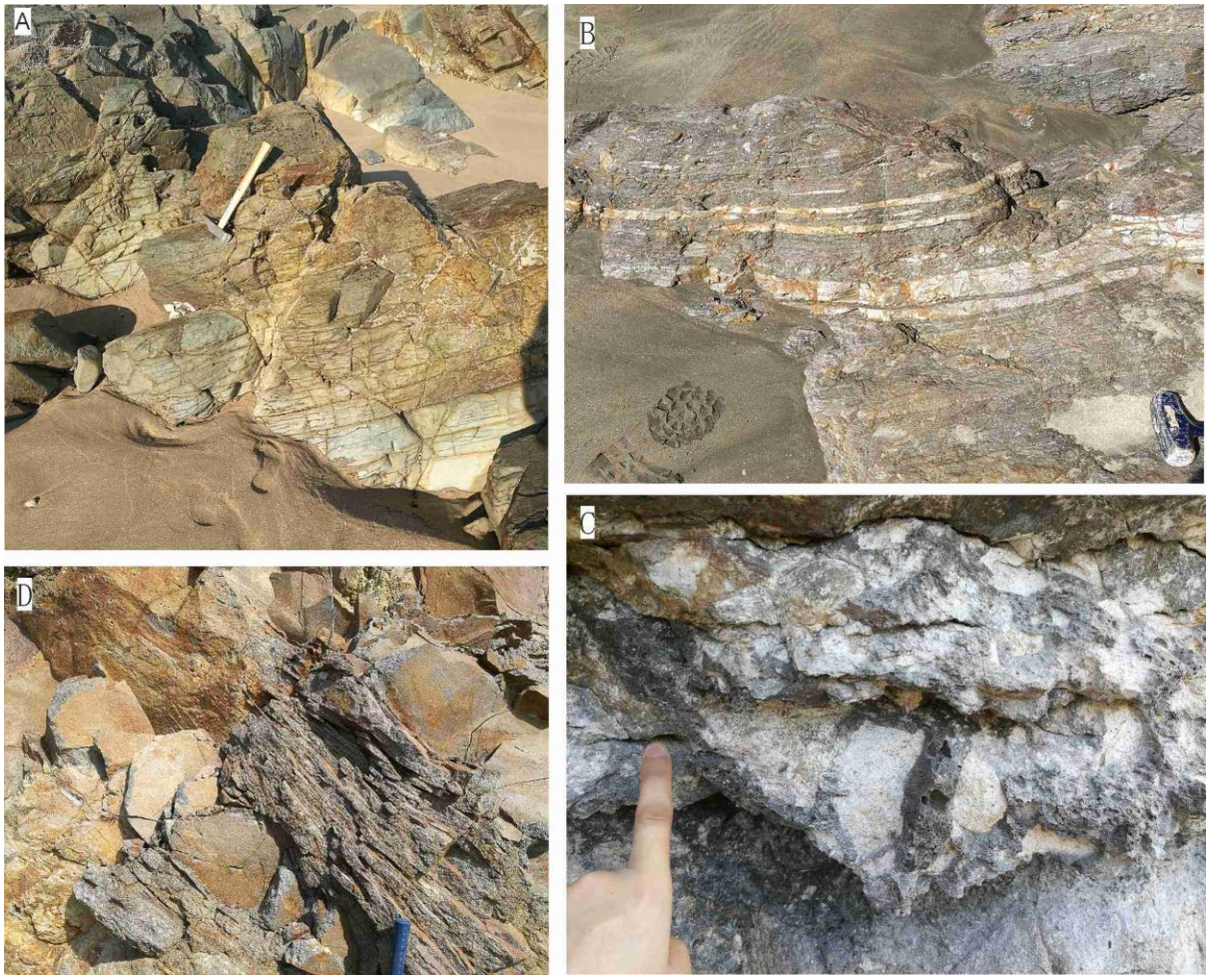

Fig. 3.18 Photographs of outcrops of the Cabra felsic member. (A) Stony dacitc-rhyolitic lava flow with slightly flow banding (J17-030-1). (B) Pumiceous layers interbed with obsidian layers. (C) Pumiceous blocks wrapped up by obsidian lavas (J18-028) (D) Layered lapilli tuff (sample J18-047).

Mingling textures between mafic and felsic rocks are frequently observed in this formation, especially within quarries in the Cerro Cabra area. Diorite was fragmented into blocks with basaltic lava filling the interstitial space (Fig. 3.19 A). In addition, basaltic rocks can host dioritic xenoliths. In a larger scale (Fig. 3.19 B), basaltic intrusions can be seen penetrating through diorite. Meanwhile, dioritic dykes penetrate through basalt intrusions (Fig. 3.19 C). Black basaltic xenoliths (<0.5 m in diameter) can also be found in the diorite dyke. The same phenomenon can be found at a smaller scale (Fig. 3.19 D) as dioritic magmas squeeze though basaltic intrusions and basaltic xenoliths were wrapped into the dioritic magma.

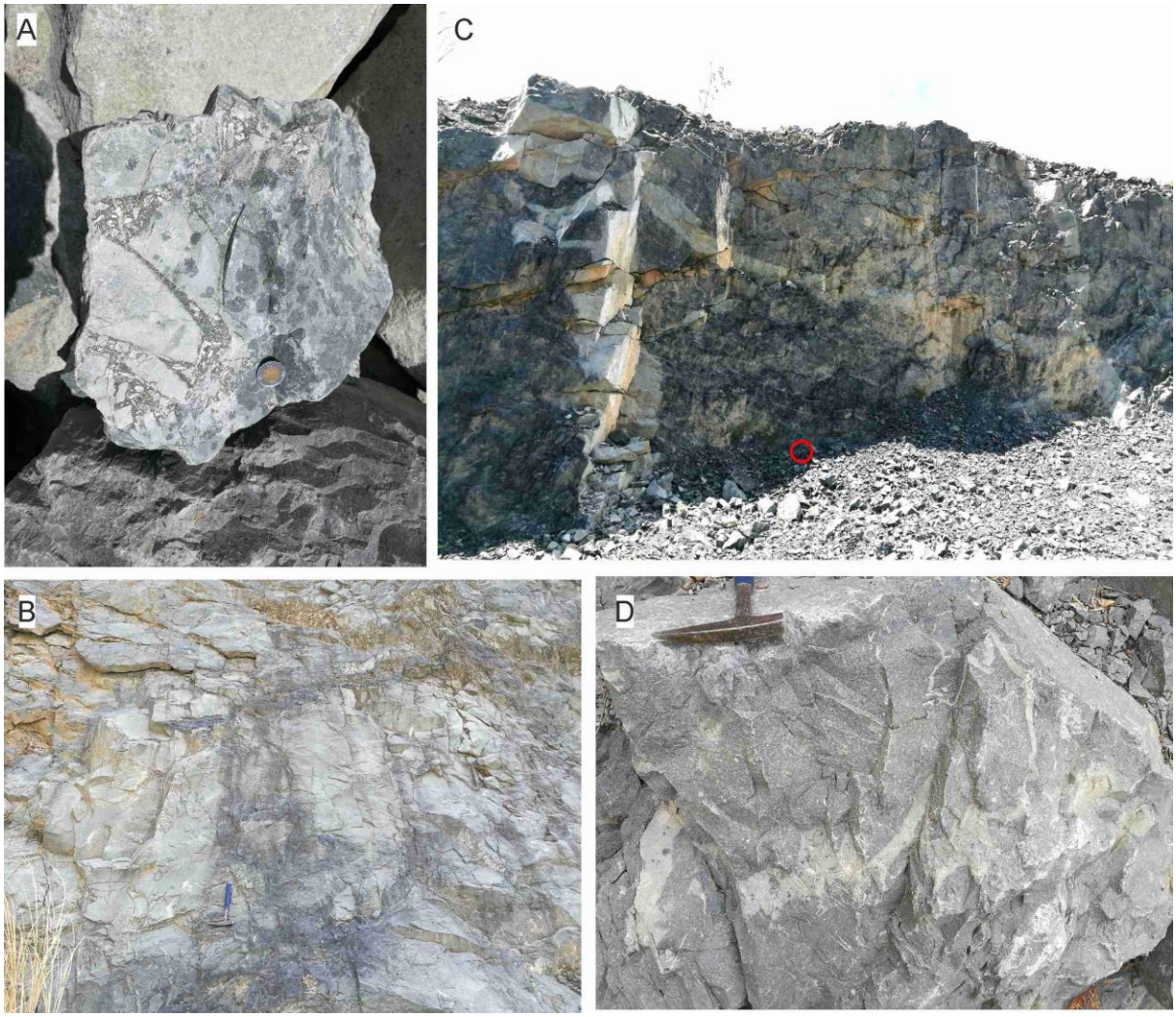

Fig. 3.19 Photographs of mingling rocks of the Cabra Formation in Cerro Cabra. (light-coloured rocks are diorite and dark-coloured rocks are basalt; red circle is a hammer for scale).

Phenocrysts in the mafic member are mainly plagioclase (0.5-1 mm), which can be homogeneous, zoned and/or sieve-textured (Fig. 3.20 A). The groundmass is composed of fine, elongated plagioclase grains, which normally show fluidal texture. Small clinopyroxene crystals occur in the interstitial space between fine-grains plagioclase grains (Fig. 3.20 A). Two olivine-bearing basalts (J18-045 and J18-052) also show similar trachytic texture except the phenocrysts are olivine grains instead plagioclase grains (Fig. 3.20 B). Euhedral olivine grains normally display skeletal texture. Trachytic texture is also common in the fine-grained lavas except that no phenocrysts occur.

Lava flow in the felsic member is usually aphanitic and feldspar is the only phenocryst if present. Intrusions, e.g. the diorite in Cerro Cabra, usually show subophitic texture with pyroxene as interstitial minerals in between elongate feldspar. Clinopyroxene grains are seldomly preserved and

most are partially to completely altered to chlorite (?). Plagioclase crystals are zoned and usually have a more rounded core in this intrusion. Quartz is also found as interstitial mineral.

Magma mixing between mafic and felsic member are also presented in thin sections. In andesite J18-034-4, olivine xenocrysts and basaltic xenoliths are found (Fig. 3.20 D). Olivine grains are embayed and altered at the rims. Elongated plagioclase in basaltic xenoliths are fluidal, which is similar to the trachytic texture in the mafic member. Glass patches can also be found in this sample while plagioclase and clinopyroxene grains occur as phenocrysts. Some of the plagioclase grains are completely altered to sericite and some clinopyroxene grains are partially altered to clay minerals.

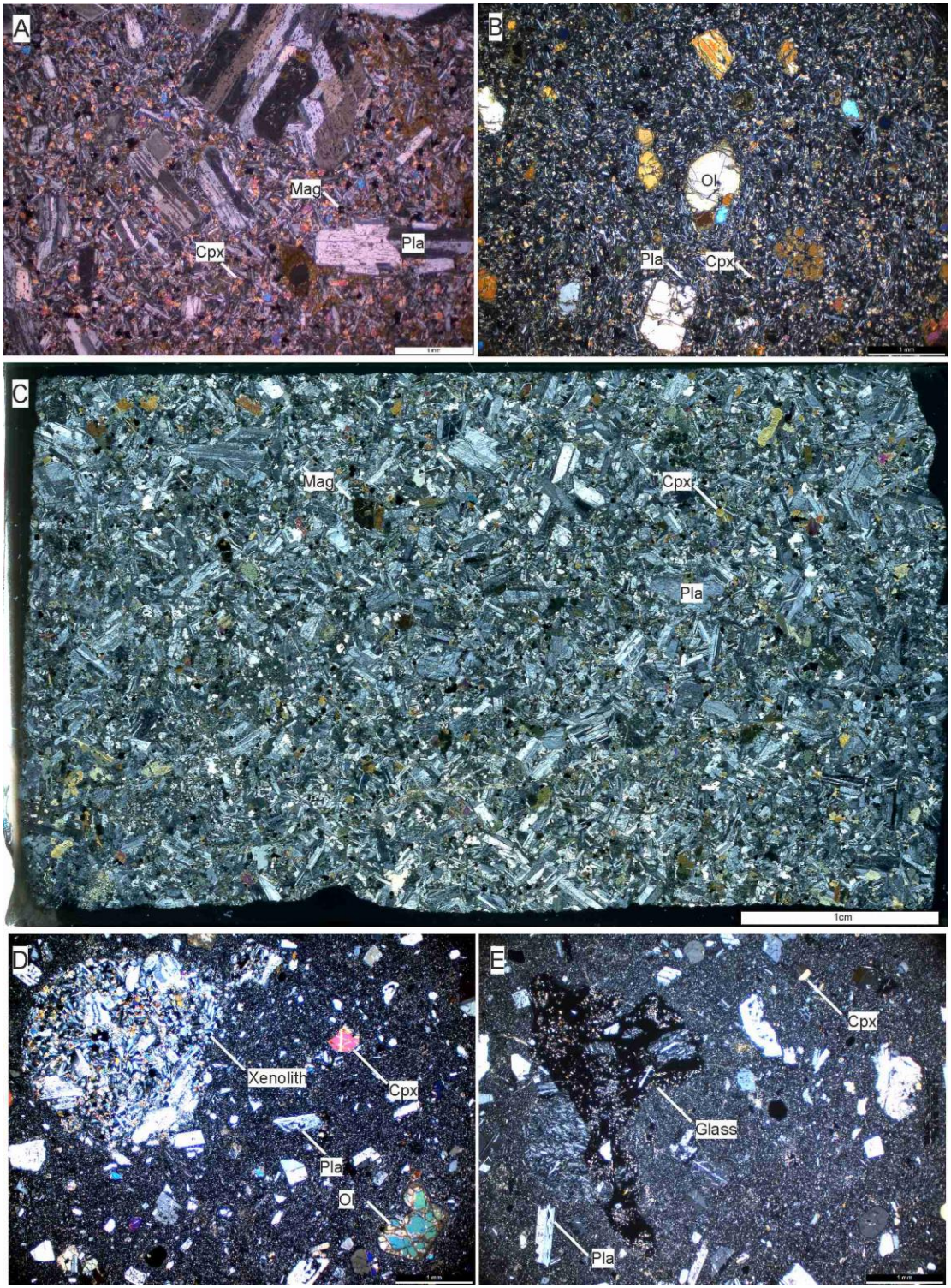

Fig. 3.20 Photomicrographs of Cabra Formation. (A) XPL view of basalt with sieved Pla phenocrysts and tiny Pla and Cpx in groundmass (sample J17-034). (B) XPL view of olivine bearing basalt with olivine phenocrysts and tiny Pla and Cpx in the trachytic groundmass (J18-052). (C) XPL view of diorite with altered Cpx in the interstitial space between Pla crystals. (D) XPL view of mixing rock J18-034-4 with basaltic xenoliths, embayed olivine phenocrysts, Cpx phenocrysts and Pla phenocrysts. (D) XPL view of J18-034-4 with galss patch as xenoliths. (Abbreviation: Cpx- clinopyroxene; Pla- plagioclase; Opx- orthopyroxene; Mag- magnetite; Ol- olivine).

3.5.2 Interpretation

Lapilli tuff layers interbedded with basaltic lava flows (Fig. 3.7 D) suggest the eruption event in the Cabra mafic member went through several cycles. The reddish tuff layer interbedded in the basalt lava might indicate an oxidised eruption environment, which infers a subaerial eruption. Plagioclase crystals are phenocrysts in the porphyritic rocks, or they otherwise occur as elongate crystals in groundmass. Clinopyroxene crystals formed in the interstitial space between plagioclase crystals in the groundmass. This suggests that plagioclase in this formation crystallised before clinopyroxene, which is distinct from the rest of formation in central Panama. This unique lithological characteristic can help recognise this formation, where such a feature has been previously observed in the Pedro Miguel Formation (Buchs et al., 2019a). This suggests a cogenetic and contemporary relationship between these two formations. The Pedro Miguel Formation overlies the Las Cascadas Formation along the Panama Canal, where it has been dated to 18-16 Ma by Ar-Ar dating and corresponds, so far, to the youngest record of local volcanism in central Panama (Buchs et al., 2019a). This unit consists of tuffs and basaltic bodies, which have been subdivided into a Tuff and Basalt members in Buchs et al. (2019a). Their subdivision is justified by the cogenetic character of these lithologies and their close association in the field. This stratigraphic subdivision corresponds to the original mapping used by Stewart et al. (1980), where the tuffs and basalts are designated as Pedro Miguel Formation and Tb (Fig. 1.7). It also chiefly corresponds to the nomenclature in Farris et al. (2017), e.g. the Pedro Miguel and Late Basalt Formation. Tb in Steward et al. (1980) or the Late Basalt Formation in Farris et al. (2017) to the west of the Canal is included into the Cabra Formation in this study.

In the outcrop in Cerro Cabra where magma mingling occurred, basalt and diorite found among each other suggests both of these two members were molten when mingling occurred. Diorite blocks with regular shape (Fig. 3.19 A) indicate brittle feature, which suggests diorite was highly crystallised when basaltic magma intruded into the magma chamber. This can also be supported by basaltic magma intruding the dioritic body (Fig. 3.19 B). However, a diorite dyke in the basalt (Fig. 3.19 C, D) indicates the crystal-rich dioritic magma can be remobilised locally to intrude the basaltic magma. Magma mingling between these two members are also found near America Bridge Abutment and Panama Bay island. It has also been described by Buchs et al., (2019a) and Farris et al., (2017). These rocks are termed as ‘Panama City Formation’ by Farris et al. (2017), but are included in ‘Cabra Formation’ in this study. An Ar-Ar age of ~ 16 Ma for a felsic rock near the America Bridge Abutment was conducted by Buchs et al. (2019a). The Cabra Formation might have the similar age.

3.6 Summary

Rocks in the pre-Oligocene Chagres Complex are mainly hypabyssal intrusions such as gabbro, diorite, tonalite, and porphyritic basalt. Lava flows can also be seen in the field, which are typically porphyritic. Tuffs are rare in this complex. Both clinopyroxene- and amphibole-bearing rocks are found in this complex.

The post-Eocene rocks are mainly distributed in the Canal area and are mainly composed of lava flows, tuffs, and hypabyssal intrusions. The oldest volcanic formation is the Caraba Formation, which are amphibole-bearing rocks. It is mainly block-and-ash deposit and ignimbrite with rare hypabyssal intrusions. The erupting environment for the tuffs was subaerial as revealed by the accretionary lapilli tuff. This formation was intruded by dykes or overlain by lava flows of the Panama Formation, which indicates a slightly older emplacement age than the Panama Formation. The Panama Formation is mainly composed of pyroxene-bearing lava flows, dykes, and rare tuffs. The sub-group with big clinopyroxene phenocrysts in the Panama Formation might be formed by magma mixing as revealed by zoned clinopyroxene and sieved plagioclase crystals. Magma mingling between Panama and Caraba Formations suggests that at least locally, these two formations were emplaced contemporaneously. The Las Cascadas Formation is mainly composed of andesitic-dacitic lava flows and tuffs. Lavas in this formation can be porphyritic or aphanitic. Glomerocrysts composed of plagioclase, clinopyroxene, orthopyroxene, and magnetite are common in the porphyritic rocks and plagioclase phenocrysts are sieved, while clinopyroxene phenocrysts are rounded. Rhyolite in the Las Cascadas Formation overlies the tuff in the Panama Formation, suggesting the Las Cascadas Formation lavas erupted later than the Panama Formation, at least locally. For the Cabra Formation, no clinopyroxene phenocrysts is a unique characteristic and can be considered a lithological sign to recognise this formation. Magma mingling and mixing is common in this formation and it is the youngest magmatism in the study area.

4 WHOLE ROCK GEOCHEMISTRY

In this chapter, whole rock geochemistry results are presented. The full dataset can be found in Appendix E2.

Total iron was measured as Fe_2O_3 and are presented throughout this study as $Fe_2O_{3(T)}$. To convert to total $FeO_{(T)}$, a conversion factor is applied:

$$FeO(T) = Fe_2O_3(T) \times 0.8998. \quad \text{Equation 4.1}$$

Molar magnesium number (Mg#) is calculated from wt.% values using the following equation:

$$Mg\# = (MgO/40.3)/ (MgO/40.3+2*Fe_2O_{3(T)}/159.69). \quad \text{Equation 4.2}$$

La/Sm_{CN} is the ratio of chondrite normalised La to chondrite normalised Sm. $Gd/Yb_{(N)}$ has the similar definition, e.g., the ratio of chondrite normalised Gd to chondrite normalised Yb. The chondrite values are from Sun and McDonough (1989). Europium anomalies displayed on chondrite-normalised rare earth element (REE) diagrams were calculated using:

$$Eu / Eu^* = 2*Eu_N / (Gd_N + Sm_N) \text{ (chondrite normalised).} \quad \text{Equation 4.3}$$

For element anomaly on N-MORB normalised trace element diagrams (N-MORB from Sun and McDonough, 1989), the follow equations are adopted:

$$Nb / Nb^* = 2*Nb_N/(Th_N+La_N) \text{ (N-MORB normalised),} \quad \text{Equation 4.4}$$

$$Sr / Sr^* = 2*Sr_N / (Pr_N + Nd_N) \text{ (N-MORB normalised),} \quad \text{Equation 4.5}$$

$$Ti / Ti^* = 2*Ti_N / (Sm_N + Gd_N) \text{ (N-MORB normalised),} \quad \text{Equation 4.6}$$

$$Zr / Zr^* = 2*Zr_N / (Sm_N+Gd_N) \text{ (N-MORB normalised),} \quad \text{Equation 4.7}$$

$$Sr / Sr^* = 2*Sr_N / (Pr_N + Nd_N) \text{ (N-MORB normalised),} \quad \text{Equation 4.8}$$

$$P / P^* = 2*P_N / (Nd_N + Sm_N) \text{ (N-MORB normalised).} \quad \text{Equation 4.9}$$

The quality of the data is discussed in detail which can be found in Appendix A. Here I would like to provide a brief explanation for the trace element data before showing them in the Result and interpret them in the Discussion.

Whole rock geochemistry data was analysed by ICP-OES for the major elements and ICP-MS for the trace elements. Two different batches were analysed two different methods in different years. As can

be seen from Figure A3(A), trace elements with content between 1 and 10 ppm correlate well with each other. However, one element Pb is slightly off the trend which suggests one of the analytical method might yield the Pb value with higher error. Figure A3(B) shows the analytical error for the standard JB1a by Method 1 and 2. Apart from the large error of element Sn, the Method 1 also yield a large error (>5%) for Pb. However, the error for Pb in Method 2 is highly reduced (<2.5%). This suggests the poor correlation of Pb between these two methods is caused by the analytical problem in Method 1 while the Method 2 gives a good value. Besides, although the error caused by Method 1 exists in this database, the error is low which suggests the interpretation by Pb, such as isotope modelling in the Discussion can still provide reasonable clues for people to better understand magmatic-tectonic evolution of PVA.

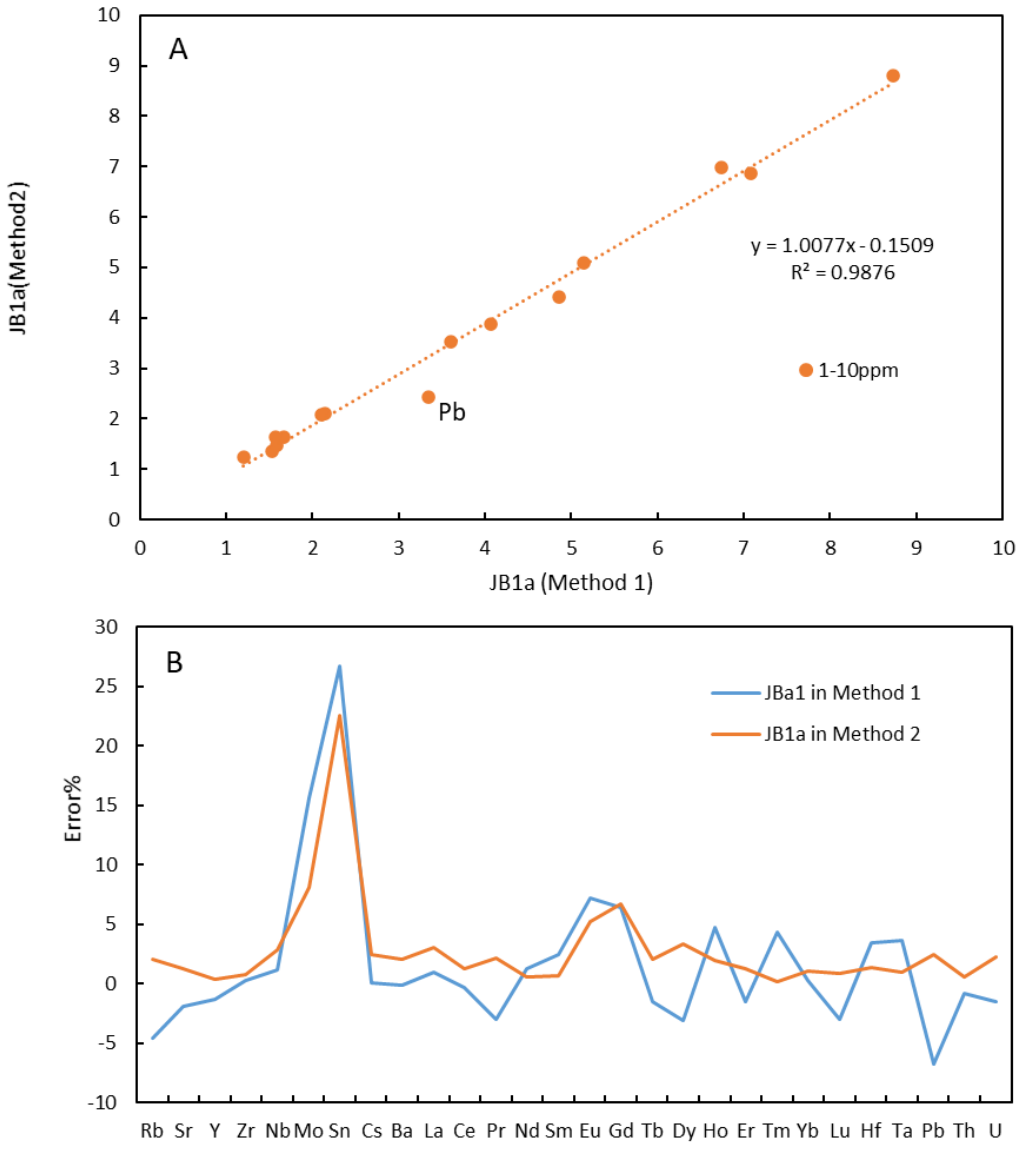

Figure A3 from Appendix A. (A) Comparison of trace elements in JB1a analysed by ICP-MS between Method 1 and Method 2 (B) Errors for trace elements analysed by Method 1 and 2 for the standard JB1a.

4.1 Alteration and Element Mobility

Prior to interpretation, geochemical data must be assessed in terms of secondary alteration and element mobility. Sub-solidus element mobility is driven by weathering, diagenesis, metamorphism, or through interactions with hydrothermal fluids, each of which can consequently alter the composition of a rock (Pearce, 1996). Without being properly constrained, the modifications caused by secondary alteration and element remobilisation can potentially lead to incorrect petrogenetic interpretations.

The ability of an element to be remobilised during secondary alteration is related to its ionic potential (charge/radius). Elements of low ionic potential (< 0.03 pm^{-1}) tend to enter solution as hydrated cations, while elements with high ionic potential (> 0.10 pm^{-1}) are removed in solution as hydrated oxyanions (Pearce 1996; Hastie et al. 2007). In general, the most mobile elements are Cs, Rb, K, Sr, Pb, Ba which are known as large ion lithophile elements (LILE) (Rollinson, 1993). Conversely, the most immobile elements are those with intermediate ionic potentials (0.03 - 0.10 pm^{-1}), which tend to remain in the solid product during alteration (Pearce, 1996). Such elements include REEs (excluding Eu^{2+} and La), Zr, Hf, Nb, Ta, Y, Ti, Cr, Th, Al, Sc and Ga (Pearce, 1996; Hastie et al., 2007). And the incompatible elements of them which has high charge to ion size (Zr, Hf, Nb, Ta, Ti) are usually called high field strength element (HFSE). Pearce (1996) suggested that the immobile behaviour exhibited by elements with intermediate ionic potential reduces as metamorphic conditions approach upper amphibolite-granulite facies.

To assess element mobility, each element is plotted against Zr following the method used by Cann (1970). Zirconium is incompatible during fractionation of basaltic magma and is considered to be relatively immobile at low degrees of metamorphism (Pearce 1996). Therefore, when other incompatible elements are plotted against Zr, there should be a positive linear correlation. In contrast, if secondary remobilisation has affected the elements in question, a large degree of scatter will be observed. However, below low-grade metamorphism, secondary alteration is not likely to be responsible for poor positive correlation between incompatible and immobile elements. It is most likely to be due to different degrees of contamination or a heterogeneous mantle source. In this study, $R^2 > 0.7$ represents a good correlation, R^2 of 0.4 – 0.7 represents a moderate correlation, and $R^2 < 0.4$ represents a poor correlation. However, narrow range of elements, such as Y in the Panama Formation (Fig. 4.3) can results in a clustering effect and give rise to low R^2 value. Therefore, alteration in this chapter should not only be considered by R^2 in elements vs Zr diagrams but also petrographic observation.

4.1.1 Chagres Complex

Rocks in Central Panama are relatively fresh, even for the most altered rocks of the Chagres complex. The highest metamorphic grade observed in the Chagres complex is albite-epidote hornfels facies,

which was found in one sample in Gamboa. This volcanic rock was intruded by porphyritic andesite. The loss on ignition (LOI, see Appendix A) of the Chagres complex ranges from 0.4 to 4.4 wt.% with one anomalous sample with 6.1 wt.%. In the elements versus Zr diagrams (Fig. 4.1), all elements except for La, Sm, and Y show poor to moderate correlation with Zr. Poor correlation between Nb and Zr and cannot be caused by alteration as Nb is not mobile to alteration.

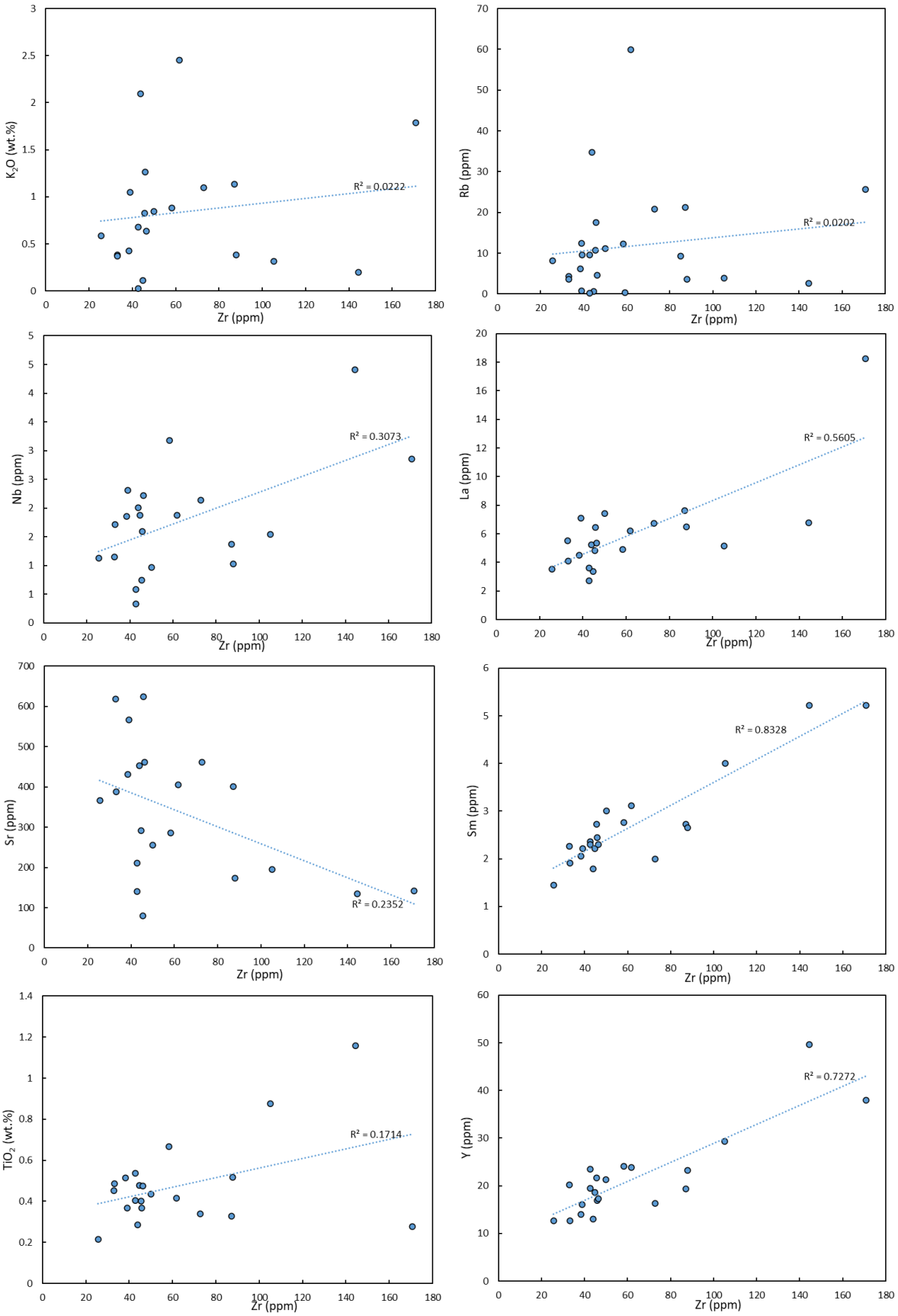

Fig. 4.1 Representative elements plotted against Zr for the Chagres complex

4.1.2 Caraba Formation

The LOI of amphibole-bearing rocks of the Caraba Formation ranges from 0.6 to 1.8 wt.%. Phenocrysts in dacites, e.g. amphibole, plagioclase and quartz are fresh. In Fig. 4.2, Nb and Sm have a moderate correlation with Zr while the rest have a poor correlation with Zr.

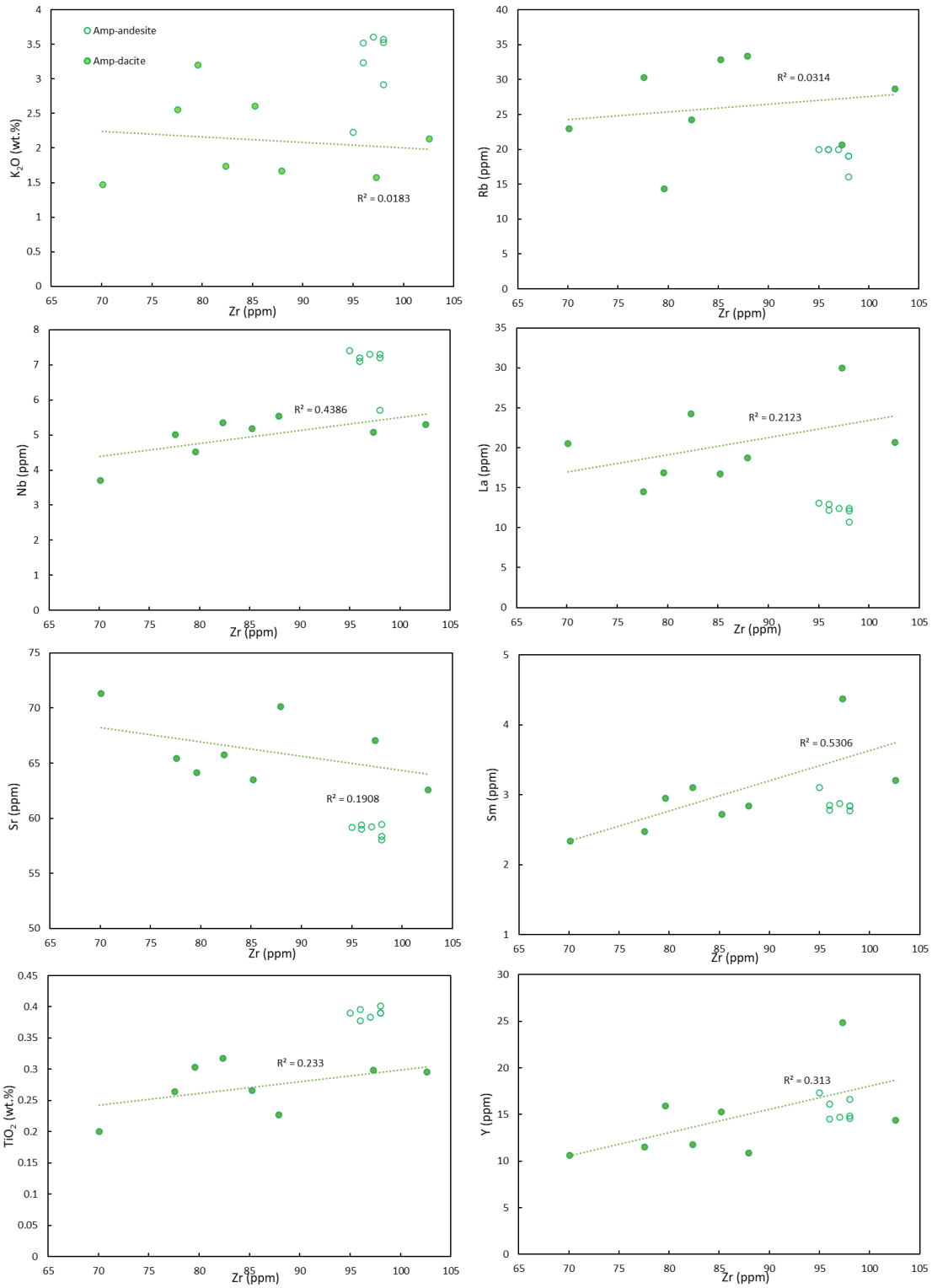

Fig. 4.2 Representative elements plotted against Zr for the Caraba Formation. (amphibole-bearing andesites are from Rooney et al., 2011)

4.1.3 Panama and Las Cascadas Formation

The LOI of rocks of the Panama Formation ranges from -0.02 to 2.9 wt.% with two high LOI exceptions of 4.4 wt.% and 5.8 wt.%. Clinopyroxene and plagioclase phenocrysts are generally fresh, with minor saponite (a trioctahedral mineral of smectite group). In Fig. 4.3, Sr and Rb have a moderate correlation with Zr while La has a strong correlation with Zr. The poor correlation between Zr and K_2O, Nb, Sm, TiO_2, and Y may be due to the narrow ranges of these elements.

Aphyric and porphyritic rocks of the Las Cascadas Formation are typically fresh. Rocks in the Las Cascadas Formation possesses an LOI range of 0.2 to 3.8 wt.%. However, the element concentrations in rocks of this formation are more scattered than those of the Panama Formation (Fig. 4.3). Strontium has a moderate correlation with Zr while the rest show poor correlation. The poor correlation is not caused by alteration, but rather other geological processes, such as magma mixing or narrow ranges of element contents.

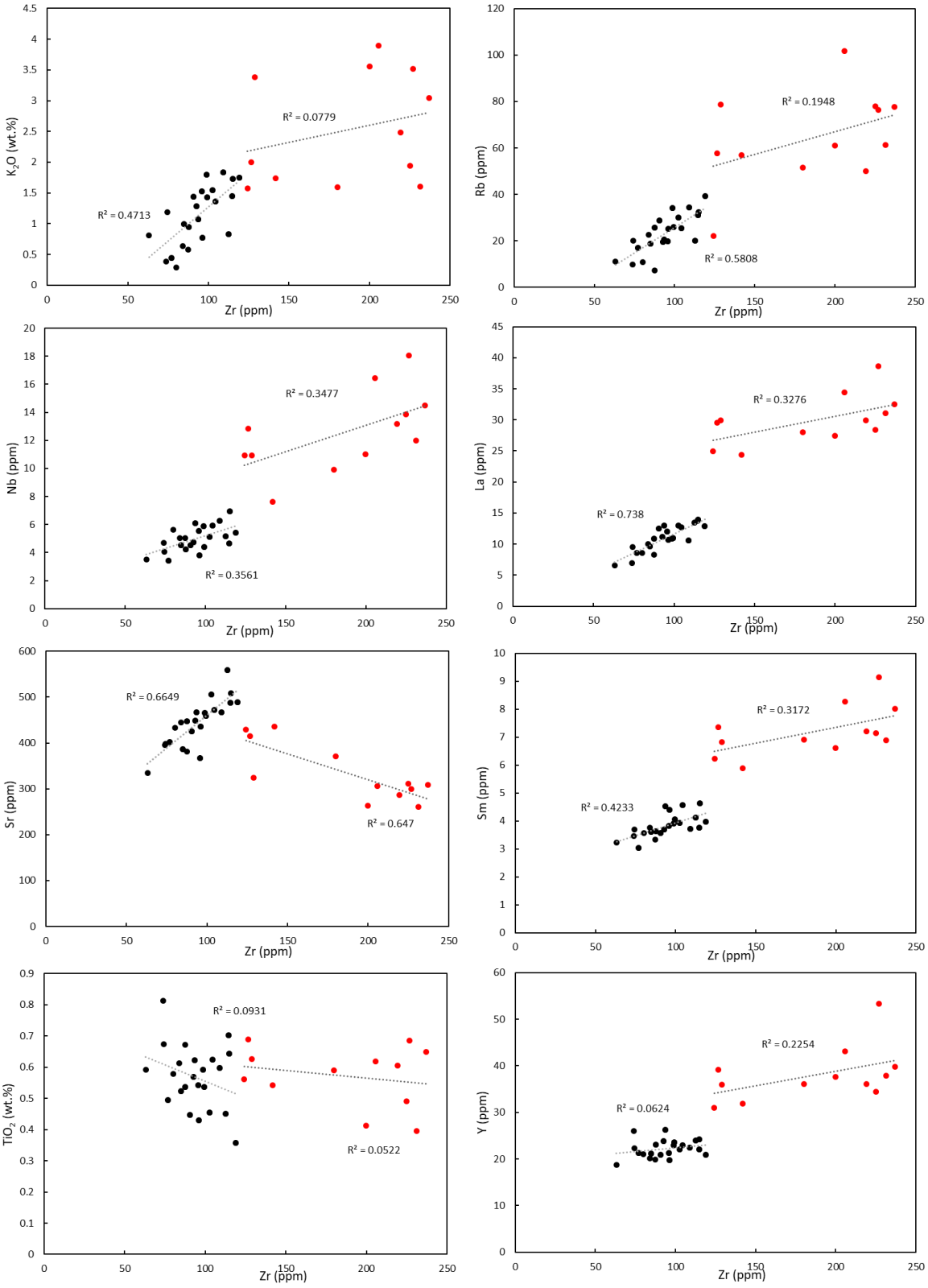

Fig. 4.3 Representative elements plotted against Zr for the Panama (black) and Las Cascadas Formation (red, including the Las Cascadas Formation 1 and 2).

4.1.4 Cabra Formation

Rocks in the Cabra mafic member are fresh. The altered rocks are normally found in Cerro Cabra hill where magma mingling occurred. Plagioclase phenocrysts in these rocks were altered to be sericite. The LOI of the Cabra mafic member ranges from -0.02 to 1.6% with one exception of 6.6 wt.%. The two fresh olivine-bearing basalts were excluded when calculating R^2 in the bivariant diagrams (Fig. 4.4) due to their extremely high MgO, LREE, and Nb concentrations. All elements show poor correlation, which might be due to narrow range of element content, where Zr content ranges from 56-141 ppm and Sm content ranges from 13-21 ppm.

The felsic member of the Cabra Formation comprises an LOI range of 0.4 to 3.1 wt.%. In addition, two highly altered rhyolite samples possess an LOI content of 5.2 (sample J18-028) and 5.3 wt.% (J18-029). A good correlation was found in the La vs Zr diagram while the rest show poor correlation (Fig. 4.4). Two samples with extremely low Sr content (10.9 ppm and 10.0 ppm respectively) are from altered samples J18-028 and J18-029. Therefore, caution should be taken when deriving interpretations from these two samples. Sample J17-104 (dacite) has an extremely low Rb (1.5 ppm) but also low LOI (1.83 wt.%) content, which indicate low Rb might not be caused by alteration.

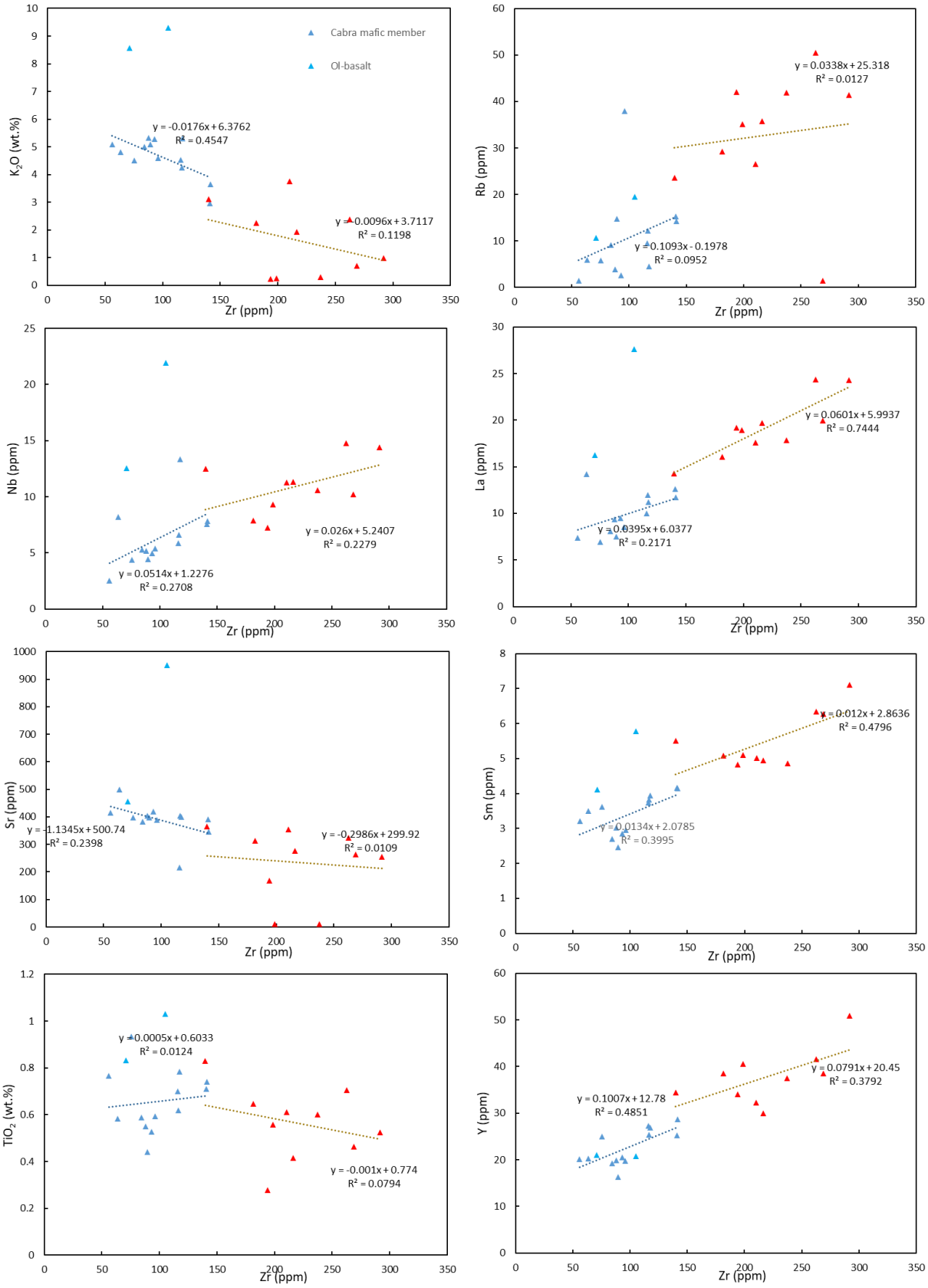

Fig. 4.4 Representative elements plotted against Zr for the Cabra Formation

4.2 Rock Classification

4.2.1 Chagres Complex

As can be seen from the total alkali versus SiO_2 (TAS) diagram (Fig. 4.5 A), the Chagres Complex samples are sub-alkaline and range mainly from basalt to andesite. One sample (J17-015) with a SiO_2 concentration of 38.6 wt.% and a LOI content of 14.8 wt.% is amygdaloidal, as marked by calcite-filled amygdales. One sample has extremely low alkalis (Na_2O+K_2O = 0.06 wt.%) which is caused by alteration. In the Th vs Co diagram (Fig. 4.5 B), rocks range from basalt to andesite. Samples in this group are mainly basaltic andesite and the discrimination in both diagrams are consistent with each other.

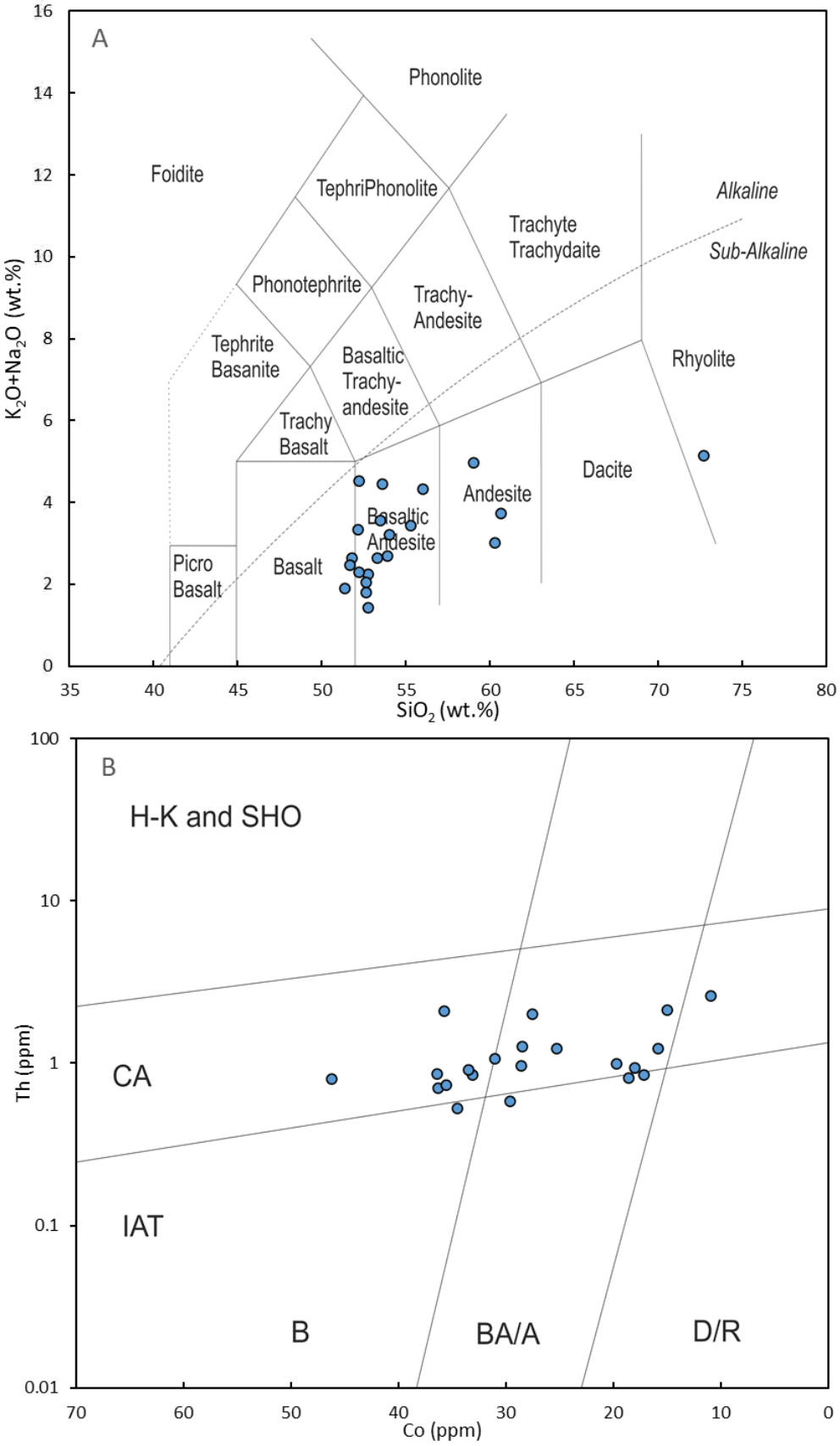

Fig. 4.5 (A) Total alkali vs. SiO_2 (TAS) diagram (redrawn from Le Maitre et al., 1989) and (B) Th vs Co classification diagram (Hastie et al., 2007) for the Chagres complex.

4.2.2 Caraba Formation

As can be seen from TAS diagram (Fig. 4.6 A), the Caraba Formation samples are sub-alkaline and range mainly from andesite to dacite. In the Th vs Co diagram (Fig. 4.6 B), rocks in this study plot in the andesite and dacite field which is overall consistent with the result in TAS. Rocks from Rooney et al. (2011) do not have Co values.

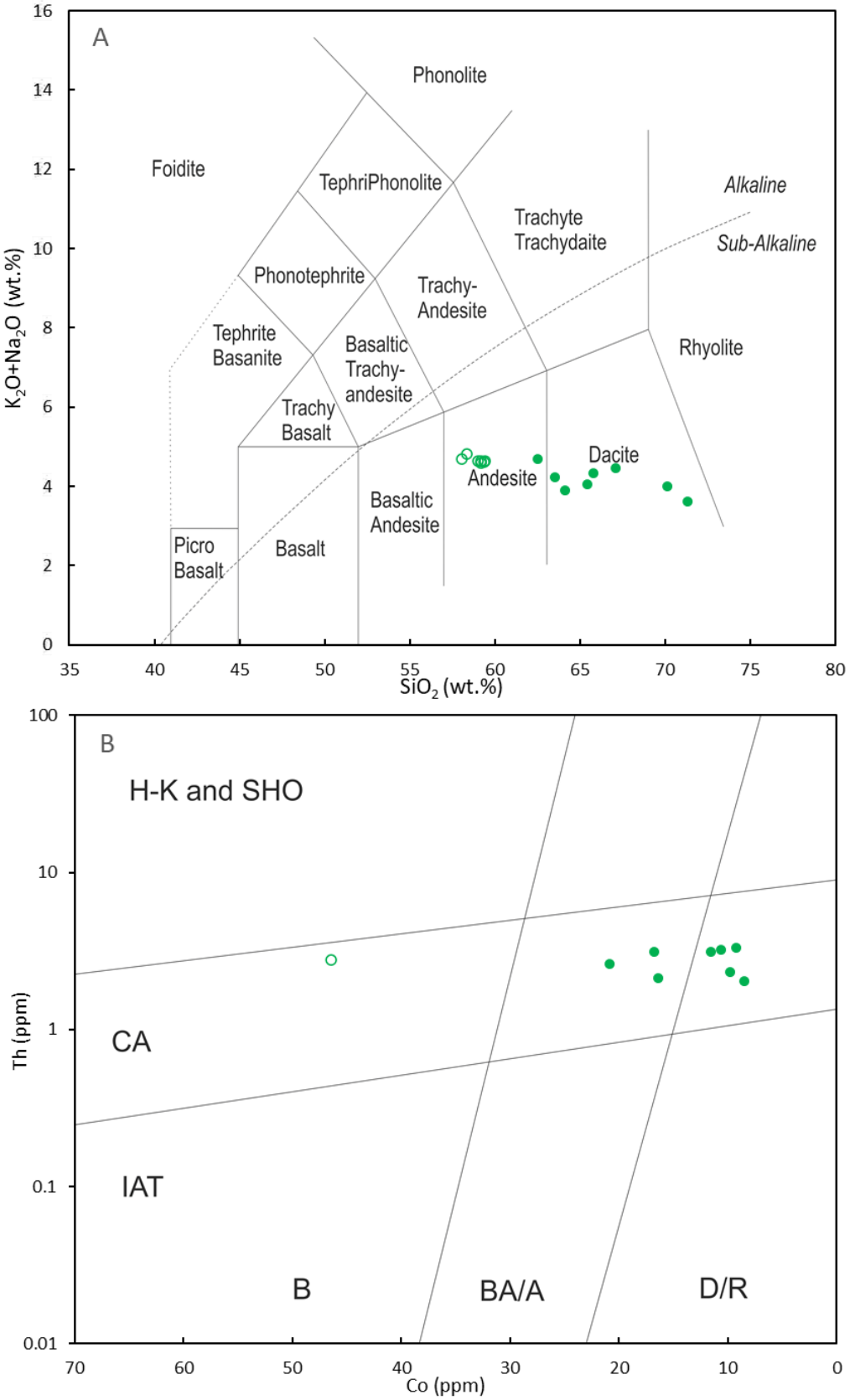

Fig. 4.6 (A) Total alkali vs. SiO_2 (TAS) diagram (redrawn from Le Maitre et al., 1989) and (B) Th vs Co classification diagram (Hastie et al., 2007) for the Caraba Formation.

4.2.3 Panama and Las Cascadas Formation

As can be seen from TAS diagram, samples from the Panama Formation range from basalt to andesite, while those from the Las Cascadas Formation range from andesite to dacite with the aphyric samples (Las Cascadas Formation2) in the dacite filed while the porphyritic samples (Las Cascadas Formation 1) in the andesite field (Fig. 4.7 A). Both formations comprise sub-alkaline rocks. In the Th vs Co diagram (Fig. 4.7 B), rocks of the Panama Formation extend from the basalt field to the basaltic andesite/andesite field, while rocks of the Las Cascadas Formation 1 are mainly basaltic andesite to andesite and the Las Cascadas Formation 2 are dacite to rhyolite.

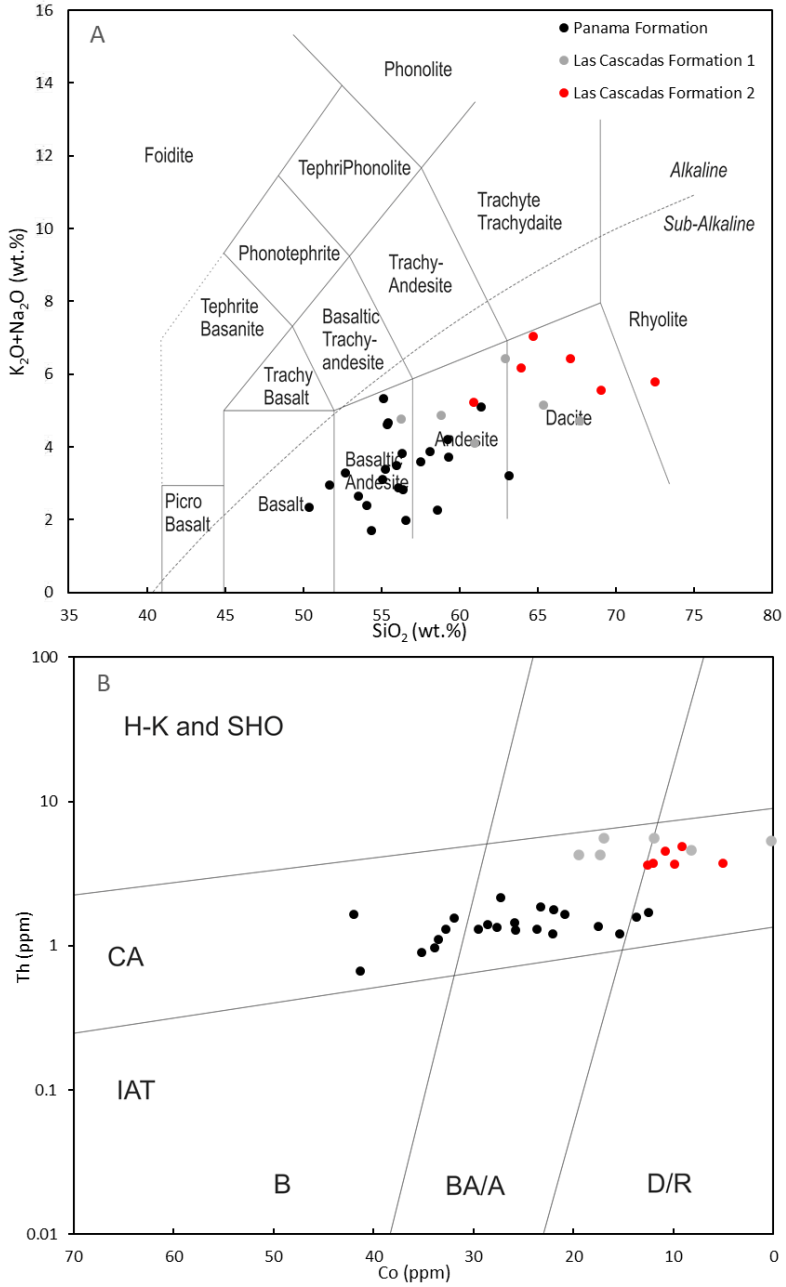

Fig. 4.7 (A) Total alkali vs. SiO_2 (TAS) diagram (redrawn from Le Maitre et al., 1989) and (B) Th vs Co classification diagram (Hastie et al., 2007) for the Panama Formation and Las Cascadas Formation.

4.2.4 Cabra Formation

As can be seen from TAS diagram, the Cabra mafic member ranges from basalt to andesite, while the Cabra felsic member range from andesite to dacite (Fig. 4.8 A). Two olivine-bearing basalts (blue triangles) possess the lowest silica content (48.5 wt.% for J18-045 and 50.8 wt.% for J18-052). Both members are sub-alkalic. Samples J18-028 and J18-029 possess low total alkali concentrations (1.8 wt.% and 2.3 wt.% respectively) which are caused by alteration. Aside from these samples, samples from the Cabra Formation form the linear trend in the TAS diagram. In the Th vs Co diagram (Fig. 4.8 B), all except for the two olivine-bearing basalt samples from the Cabra mafic member are mainly basaltic andesite or andesite, while samples from the Cabra felsic member are mainly dacite or rhyolite. For the two olivine-bearing basalts, both are basalt in both diagrams.

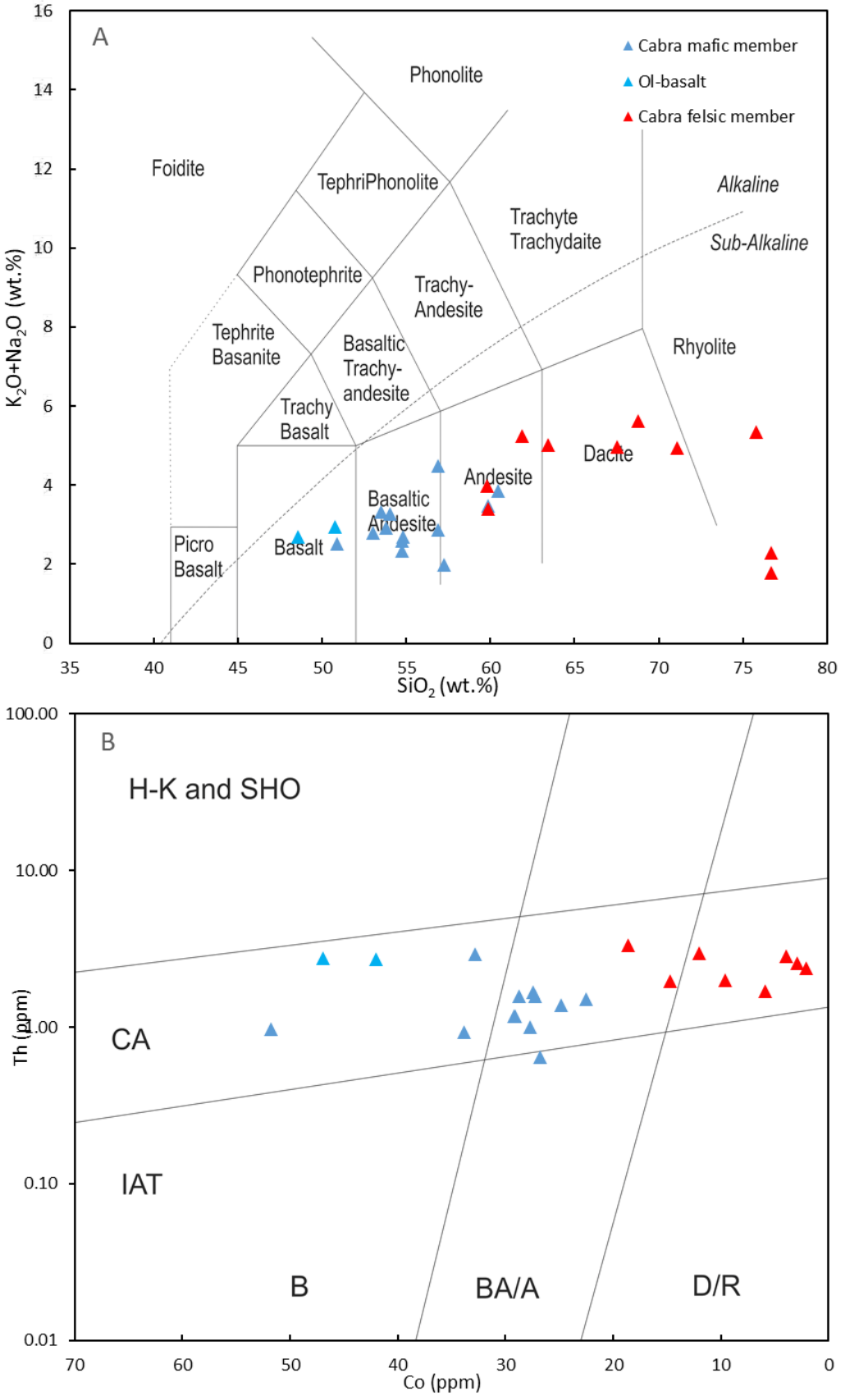

Fig. 4.8 (A) Total alkali vs. SiO_2 (TAS) diagram (redrawn from Le Maitre et al., 1989) and (B) Th vs Co classification diagram (Hastie et al., 2007) for the Cabra Formation

4.3 Major Elements

4.3.1 Chagres Complex

Samples from the Chagres Complex broadly range in SiO_2 content from 49.2 to 60.6 wt.% with one sample of 72.7 wt.% (Fig. 4.9). The TiO_2 content has a large range from 0.36 to 1.93 wt.%. A negative correlation was found in MgO vs SiO_2, CaO vs SiO_2 and Fe_2O_3 vs SiO_2 (Fig. 4.9). The K_2O content displays a positive correlation with SiO_2.

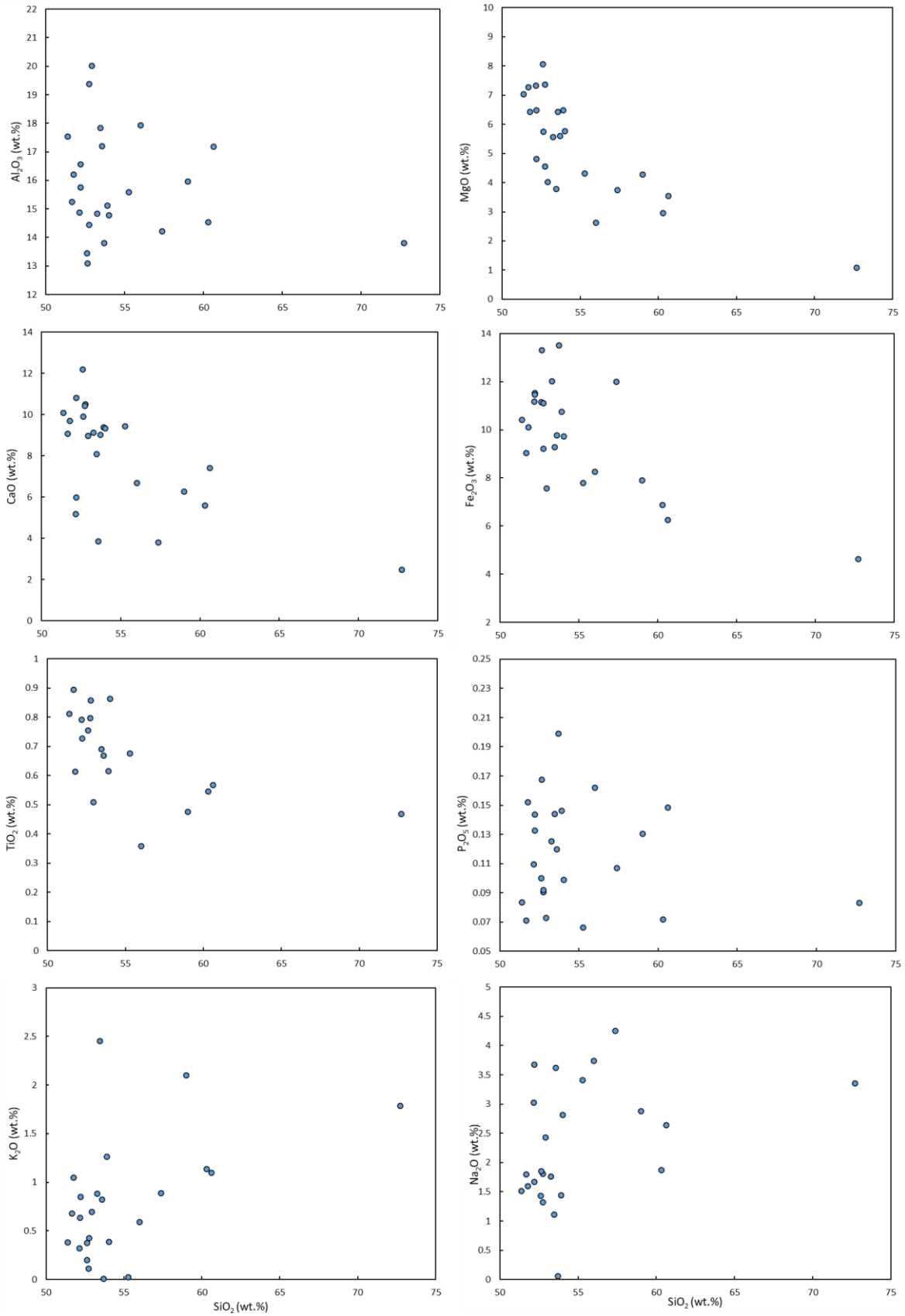

Fig. 4.9 Representative major elements plotted against SiO_2 (Harker diagrams) for rocks of the Chagres Complex.

4.3.2 Caraba Formation

Samples from the Caraba Formation range in SiO_2 content from 62.5 to 71.3 wt.% (Fig. 4.10). Al_2O_3, MgO, CaO, Fe_2O_3, TiO_2 decrease with decreasing SiO_2. Furthermore, dacites form a continuous trend with amphibole-bearing andesite in these diagrams (Fig. 4.10).

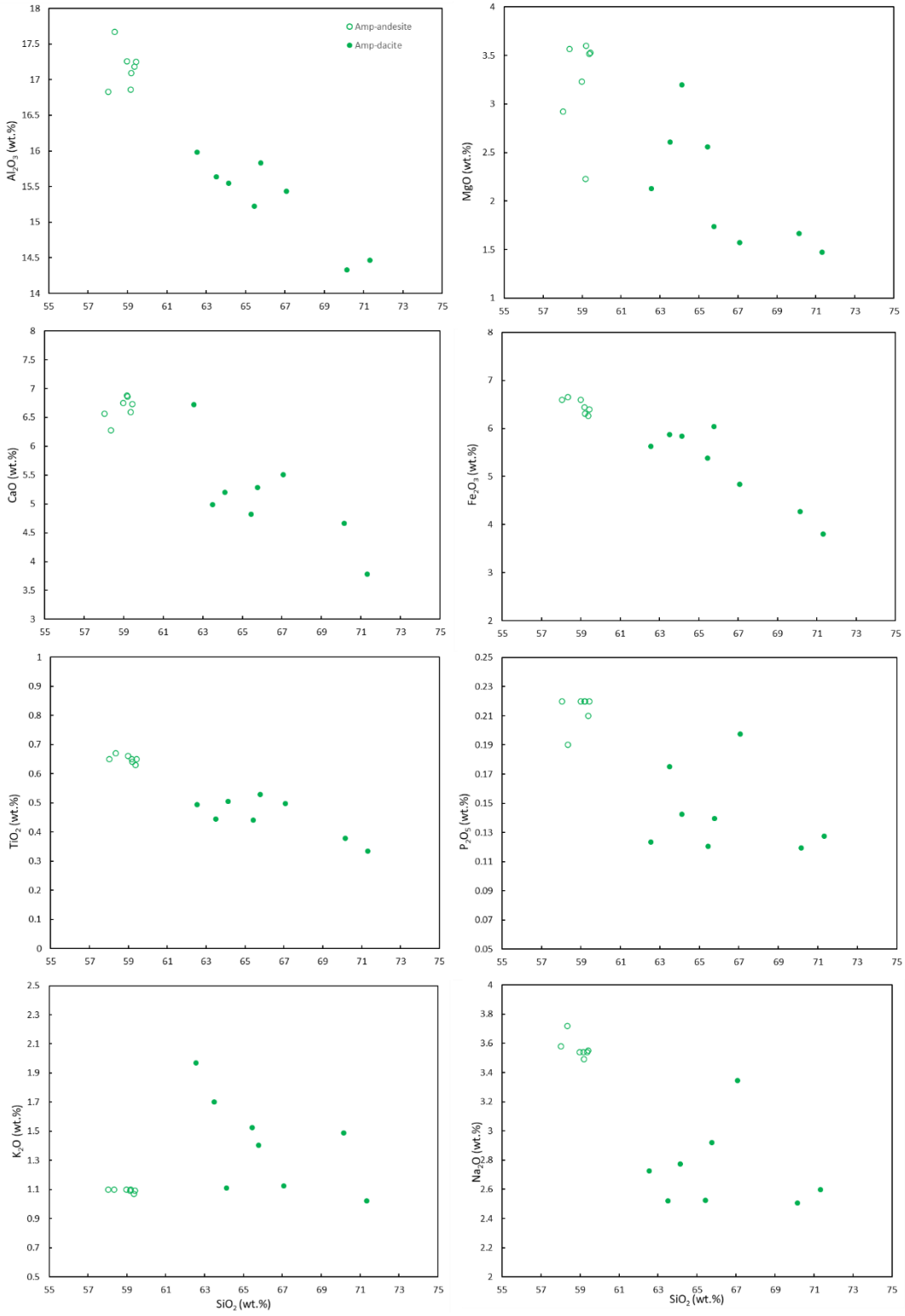

Fig. 4.10 Representative major elements plotted against SiO2 (Harker diagrams) for rocks of the Caraba Formation

4.3.3 Panama and Las Cascadas Formation

Samples from the Panama Formation range in SiO_2 content from 50.35 to 63.18 wt.% for Panama Formation while those from the Las Cascadas Formation range from 56.26 to 72.50 wt.%.(Fig. 4.11). Rocks from the Las Cascadas Formation has overall higher SiO_2 content than Panama Formation, but the values overlap between the Panama Formation and Las Cascadas Formation 1. This overlap is also found in MgO which is 1.26-6.58 wt.% for rocks from the Panama Formation and 0.42-3.12 wt.% for Las Cascadas Formation. MgO ranges from 1.1 to 3.1 wt.% for the Las Cascadas Formation 1 and 0.4 to 0.6 wt.% for the Las Cascadas Formation 2 with one exception of 1.8 wt.% (J17-011). The TiO_2 content ranges from 0.60 to 1.36 wt.% for Panama Formation and it has a similar range from 0.66 to 1.15 wt.% for Las Cascadas Formation.

All diagrams except for TiO_2 versus SiO_2 display a linear trend for both Panama Formation and Las Cascadas Formation (Fig. 4.11) and the trend continues from the Panama Formation to the Las Cascadas Formation. In rocks of the Panama and Las Cascadas formations, MgO, CaO, Fe_2O_3 decrease with increasing SiO_2, whereas Na_2O, K_2O, and P_2O_5 increase with increasing SiO_2 (Fig. 4.11). Moreover, Al_2O_3 content increases with increasing SiO_2 in rocks of the Panama Formation, however, a negative correlation of these elements is observed in rocks of the Las Cascadas Formation. An inflection point regarding Al_2O_3 versus SiO_2 is observed at 57-59 wt.% (Fig. 4.11).

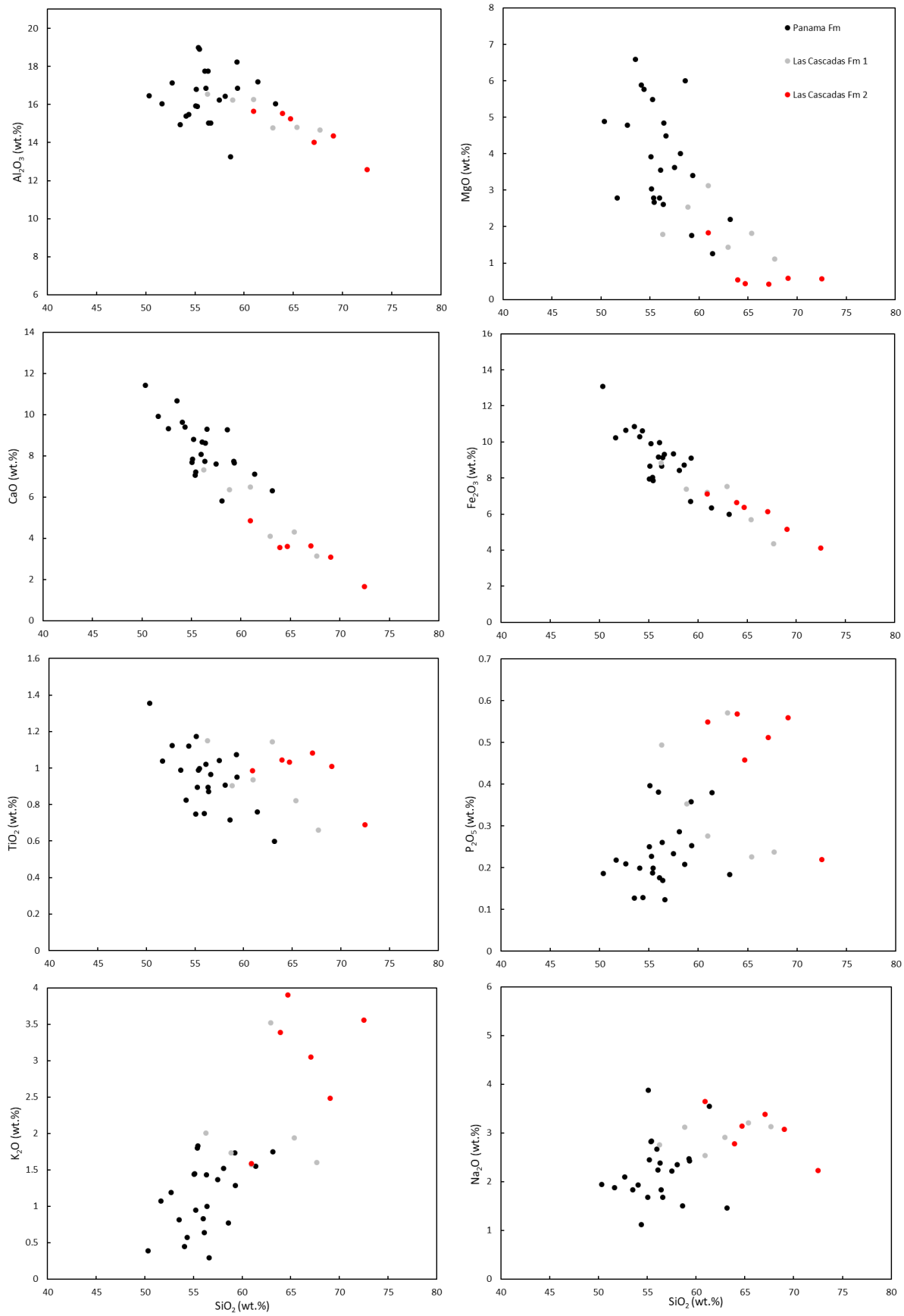

Fig. 4.11 Representative major elements plotted against SiO_2 (Harker diagrams) for Panama and Las Cascadas Formations (data compiled from Buchs et al., 2019a and Farris et al., 2017)*

4.3.4 Cabra Formation

The SiO_2 content of the Carbra mafic member ranges from 48.54 to 60.46 wt.% while MgO content ranges from 2.97 to 9.3 wt.% (Fig. 4.12). The large range of MgO is caused by two olivine-bearing basalts which have a high MgO content of 8.57 wt.% and 9.30 wt.%. TiO_2 has a large range from 0.73 to 1.72 wt.% for the mafic member with the highest found in one olivine bearing basalt and it ranges from 0.47 to 1.39 wt.% for the felsic member.

Harker diagrams show good positive correlations for rocks of the Cabra Formation (Fig. 4.12). MgO, CaO and Fe_2O_3 decrease with increasing SiO_2. This negative correlation is observed in TiO_2 vs SiO_2 and P_2O_5 vs SiO_2 with a less correlated trend. K_2O and Na_2O increase as SiO_2 increases and the scattered samples, especially the ones with extremely low K_2O or Na_2O are highly altered. A negative correlation is also found in Al_2O_3 vs SiO_2 diagram when the olivine bearing basalts are excluded. The Cabra mafic member and felsic member are overlapped based on major elements and form a continuous trend (Fig. 4.12). The criteria to divide them is based on trace element Yb which is discussed below.

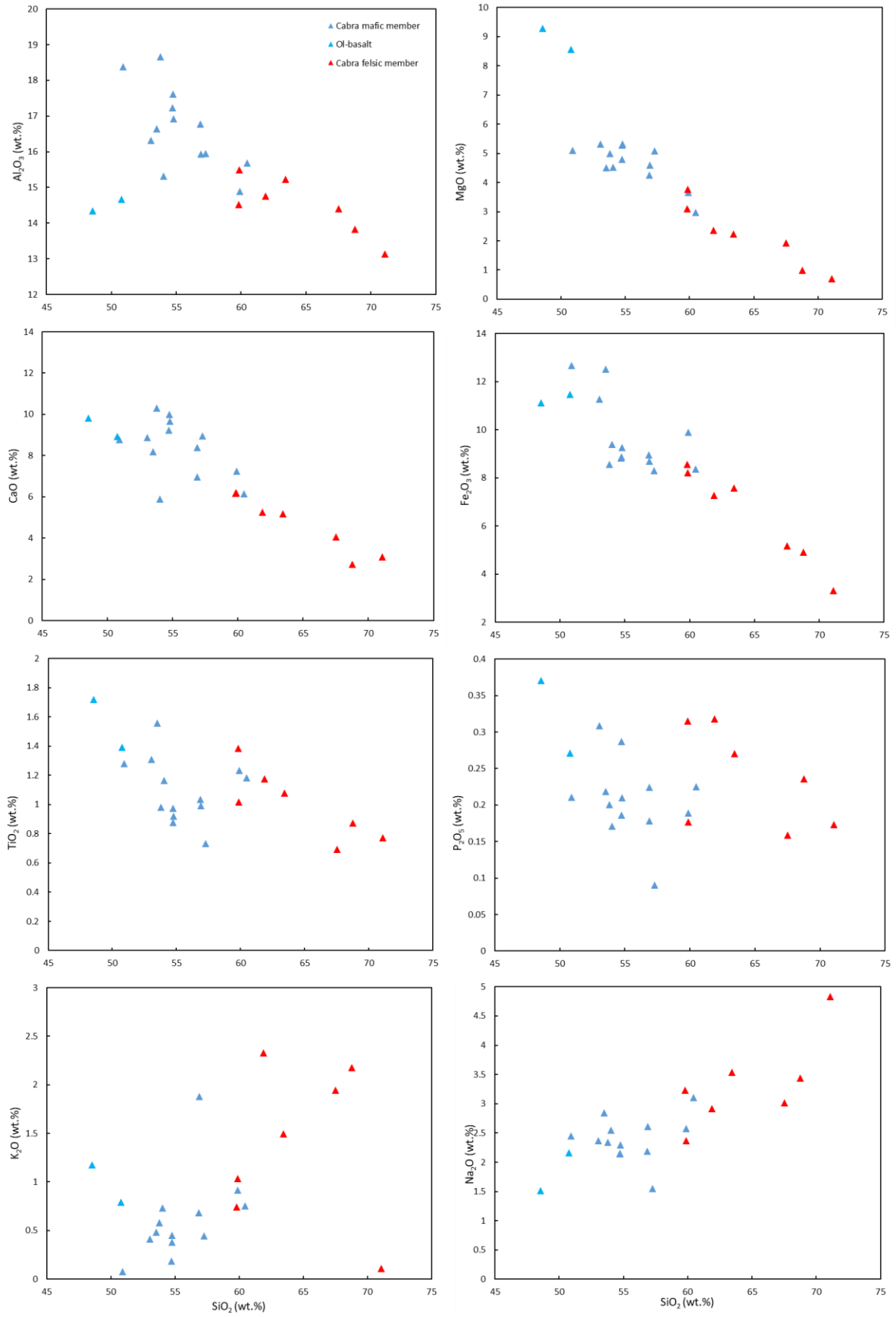

Fig. 4.12 Representative major elements plotted against SiO_2 (Harker diagrams) for Cabra Formation

4.4 Trace Elements

4.4.1 Chagres Complex

As can be seen from Fig. 4.13, compatible element Ni varies from 2.2 to 89.5 ppm. It is scattered in Ni versus MgO but a slight positive correlation can still be observed. Scandium has a range of 13.0 to 62.7 ppm and V has a range of 57.4 to 450.4 ppm. Both Sc and V share a positive correlation with MgO. Incompatible elements (e.g., Rb, Sr, Nb, La, and Yb) do not show clear patterns when plotted against MgO. The extreme high value for La (18.25 ppm) is from a granite sample.

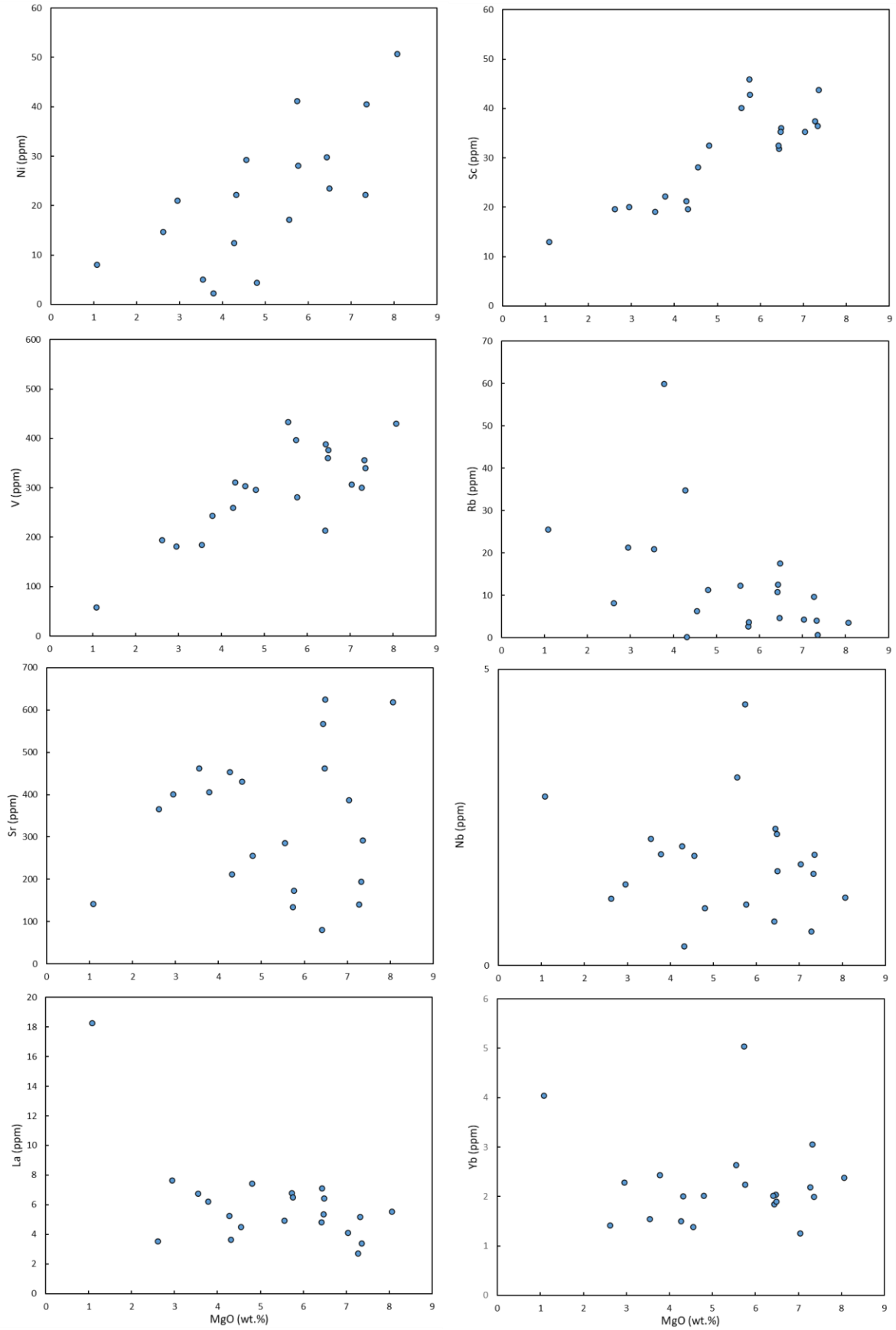

Fig. 4.13 Representative trace elements plotted against MgO for the Chagres Complex

On a chondrite-normalised REE plot (Fig. 4.14 A), LREE in samples from the Chagres Complex range from slightly depleted to slightly enriched. $La/Sm_{(CN)}$ ranges from 0.74 to 2.19. A granite sample (J17-057-2) with the highest $La_{(CN)}$ (58.85) has a similar $La/Sm_{(CN)}$ (2.19) to other samples in this group. $Gd/Yb_{(CN)}$ ranges from 0.85 to 1.30 displaying relatively flat HREE patterns. Rocks from the Chagres complex display an Eu/Eu* range of slightly negative (~ 0.62) to slightly positive (~ 1.41) anomalies. N-MORB-normalised trace element patterns (Fig. 4.14 B) show that Nb-Ta-Ti are remarkably depleted in comparison with adjacent elements. Nb/Nb* ranges from 0.03 to 0.41 and Ti/Ti* ranges from 0.21 to 1.00. The fluid mobile elements, such as Cs, Ba, and U are generally enriched relative to Nb, Ta, Zr, Hf and HREE. It should be cautious to interpreted fluid mobile elements in this group due to alteration. It is worth mentioning that one fresh sample, J18-004 with low LOI (0.95 wt.%), show negative Pb and Sr anomalies.

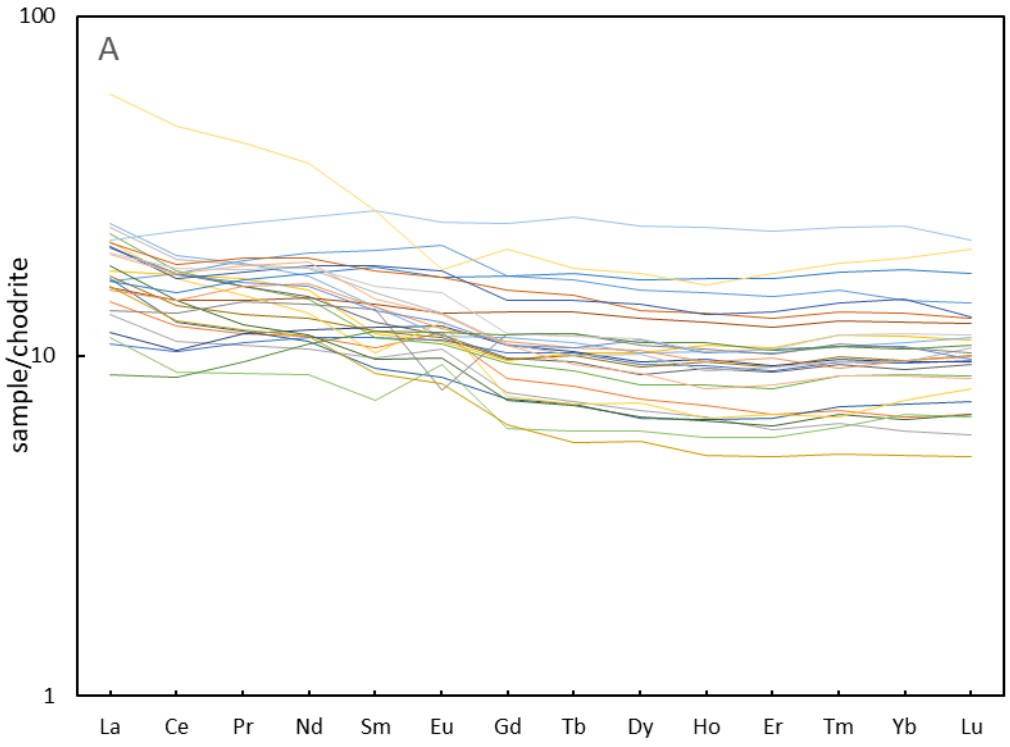

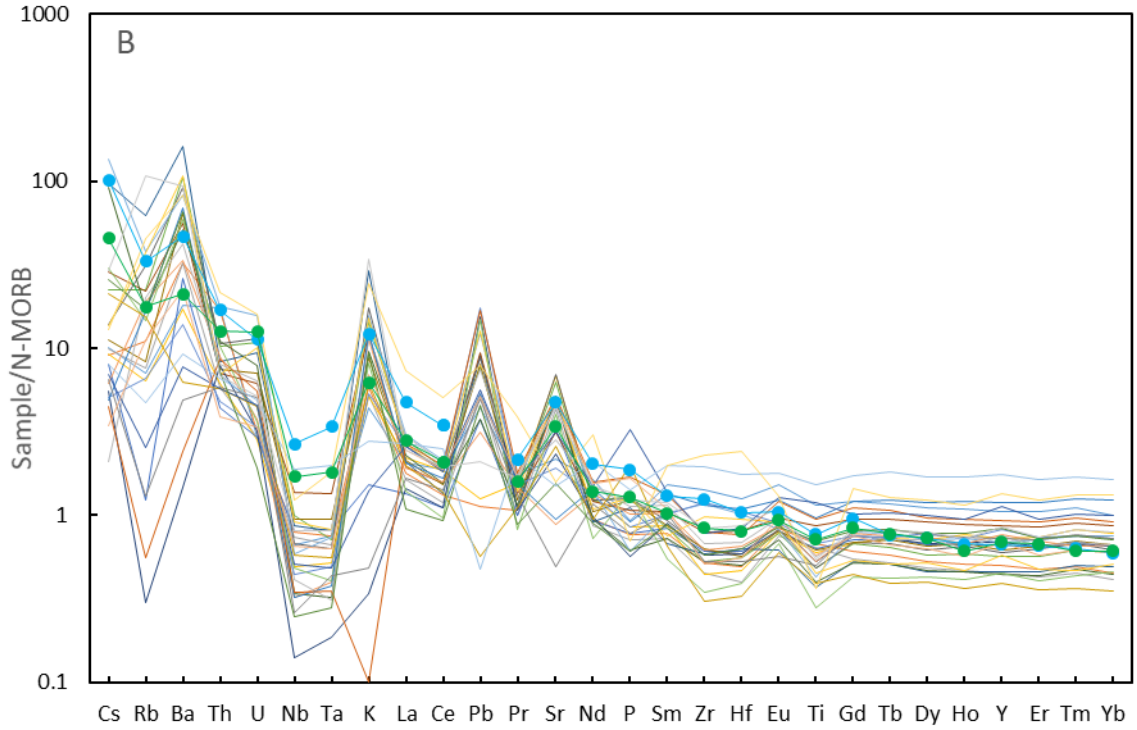

Fig. 4.14 Chondrite-normalised REE diagram (A) and N-MORB normalised trace element diagram (B) for Chagres complex (the blue line is the average continental arc basalt and the green line is the average island arc basalt from Kelemen, 2003; chondrite and N-MORB values are form Sun and McDonough, 1989).

The diagrams in Fig. 4.15 are used to constrain the tectonic setting from which rocks were erupted or emplaced. On the V versus Ti diagram (Fig. 4.15 A), rocks are mainly plotted in the arc tholeiitic field with basaltic sample J17-058 and J18-004 in MORB/BABB (middle ocean ridge basalt/back arc basin basalt) field. On the Th/Yb vs Nb/Yb diagram (Fig. 4.15 B), rocks are all in the volcanic arc field.

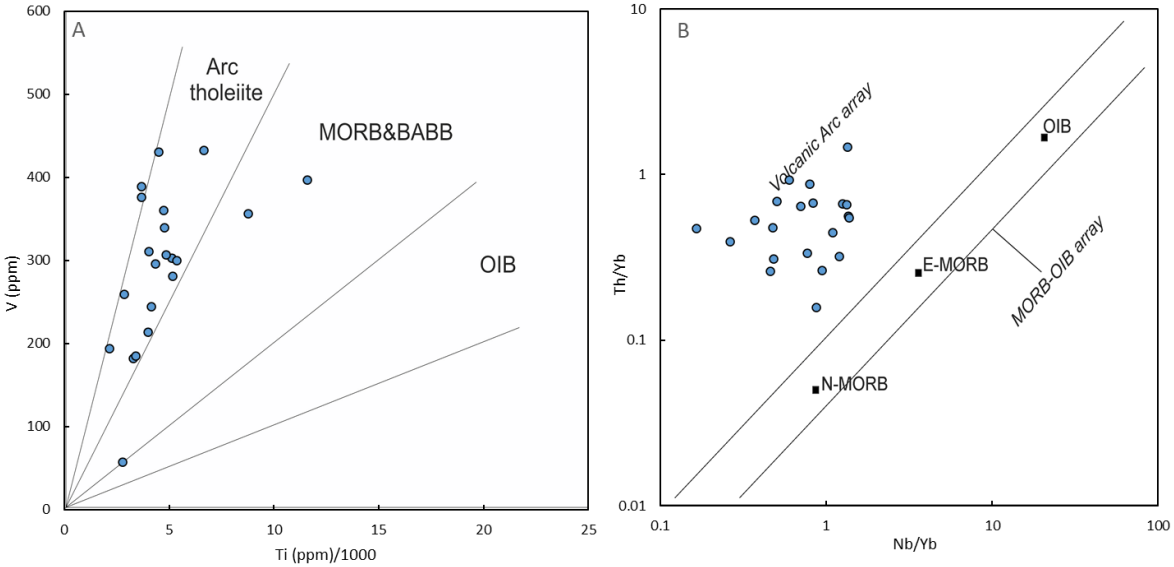

Fig. 4.15 (A) V vs Ti (Shervais, 1982) and (B) Th/Yb vs Nb/Yb (Pearce, 1995) for Chagres.

4.4.2 Caraba Formation

For amphibole-bearing dacite in this study, compatible element Ni varies from 10.5 to 34.3 ppm for the dacites (Fig. 4.16). It is scattered in Ni versus MgO. Scandium has a range of 8.9 to 18.6 ppm and V has a range of 110.1 to 175.6 ppm. Both Sc and V share a positive correlation with MgO. Incompatible elements Sr and La display negative correlation with MgO. Rb and Yb display positive correlation with MgO. Andesite data from Rooney et al. (2011) generally forms a continuous trend especially in V, Sr, La, Yb versus MgO diagrams.

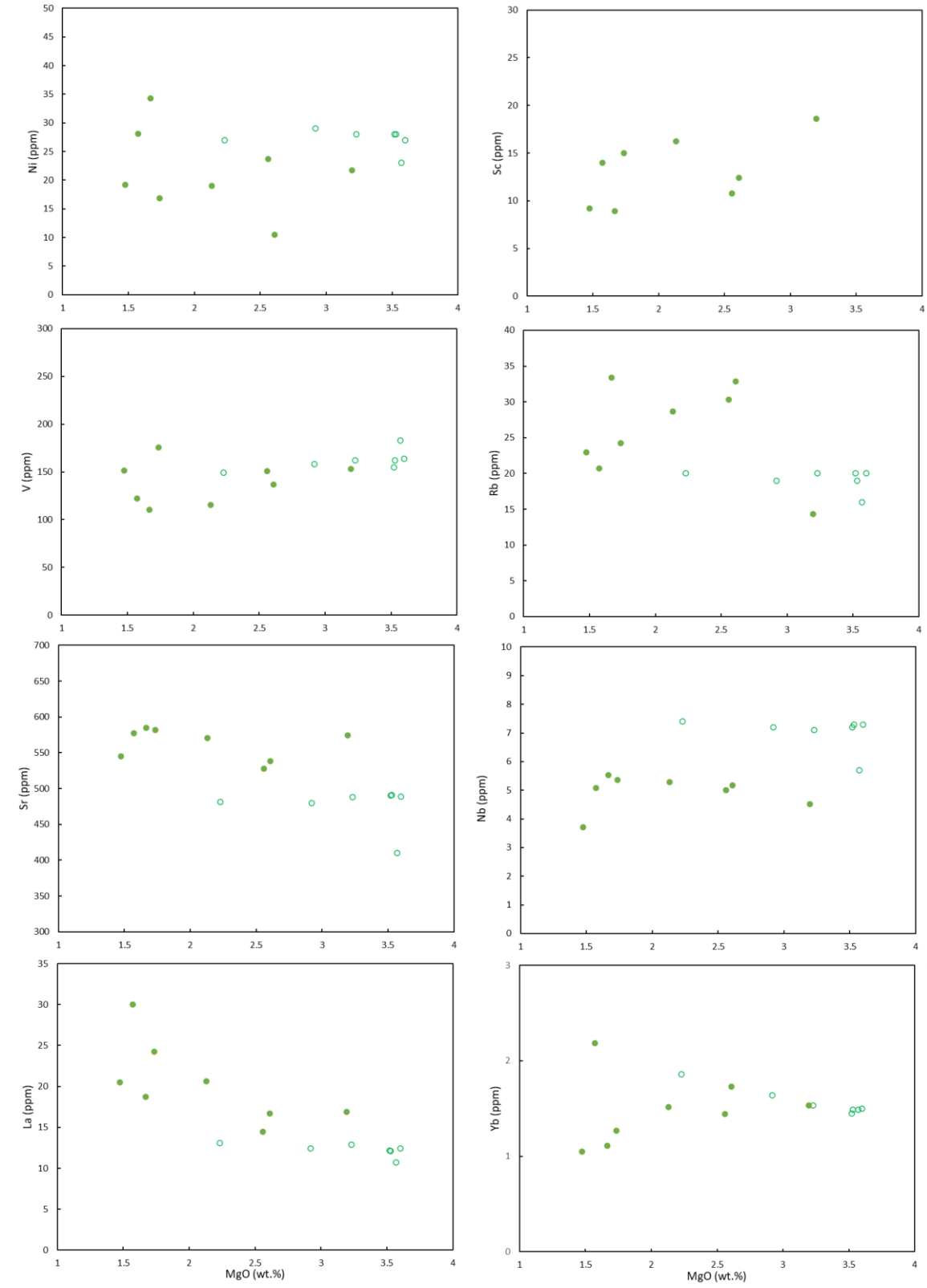

Fig. 4.16 Representative trace elements plotted against MgO for the Caraba Formation

On a chondrite-normalised REE plot (Fig. 4.17 A), LREE in the Caraba Formation are enriched. $La/Sm_{(CN)}$ ranges from 3.6 to 5.5 for the dacite and 2.4 to 2.8 for the andesite. $Gd/Yb_{(CN)}$ ranges from 1.27 to 1.79 for the dacites and 1.29 to 1.48 for the andesites, which display slightly enriched HREE.

Rocks generally display positive Eu/Eu* anomalies (0.97-1.34) for the dacites and the andesites (1.02-1.06). N-MORB-normalised trace element diagram (Fig. 4.17 B) shows that Nb-Ta-Ti are markedly depleted compared to adjacent elements. Nb/Nb* ranges from 0.13 to 0.16 and Ti/Ti* ranges from 0.28 to 0.45 for the dacites while Nb/Nb* ranges from 0.29 to 0.32 and Ti/Ti* ranges from 0.52 to 0.58 for the andesites. The more incompatible elements on the left are more enriched than less incompatible elements on the right (Fig. 4.17 B). The fluid mobile elements such as Cs, Rb, Ba, U, K and Pb are overall enriched relative to Nb, Ta, Zr, Hf and HREE. A positive Sr anomaly is observed for the Caraba Formation. The N-MORB normalised multi-element patterns of rocks from the Caraba Formation are broadly similar to the average continental arc basalt from Kelemen (2003) apart from the lower HREE.

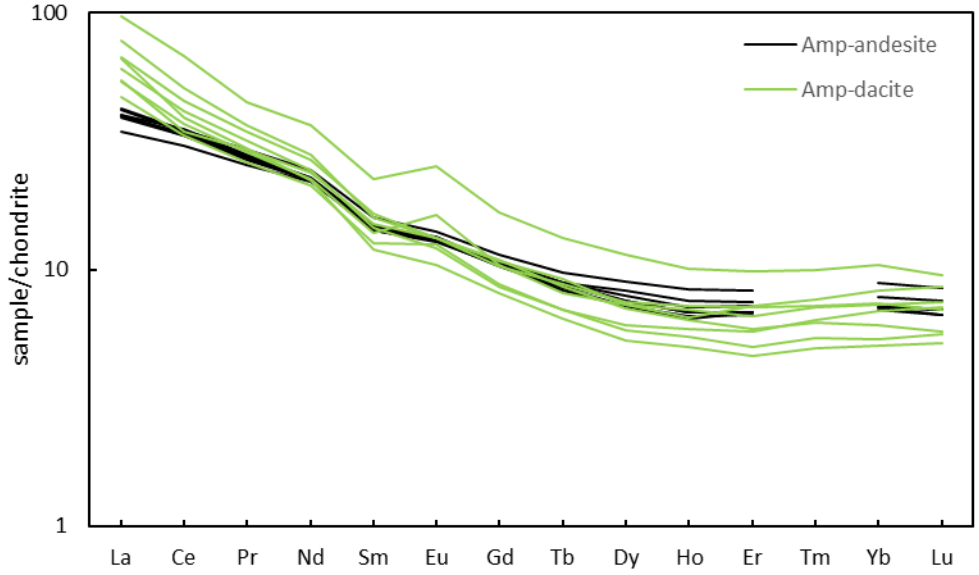

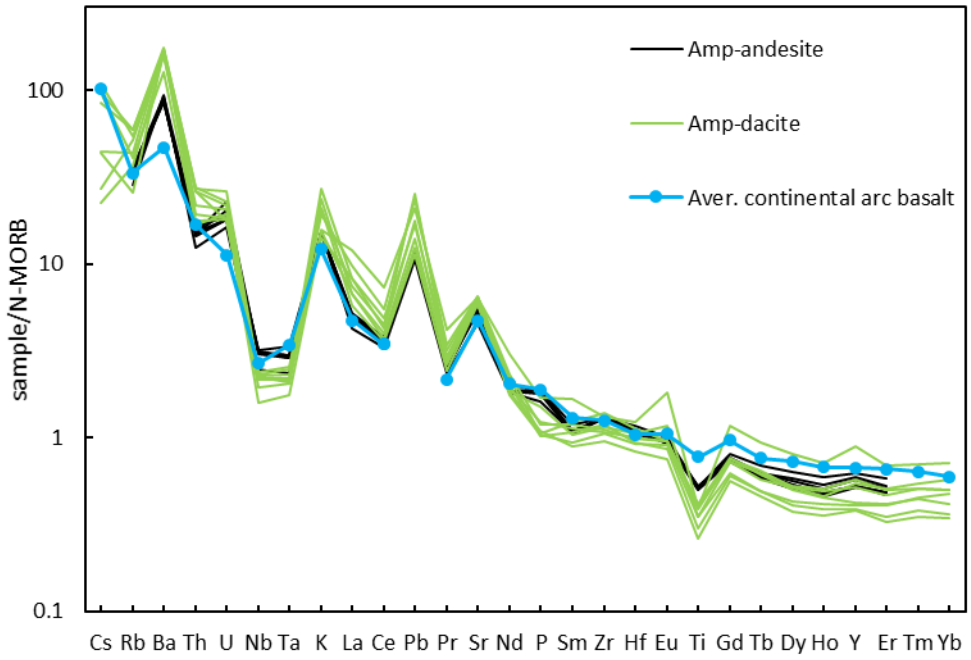

Fig. 4.17 Chondrite-normalised REE diagram (A) and N-MORB normalised trace element diagram (B) for the Caraba Formation (chondrite and N-MORB values are form Sun and McDonough, 1989).

In Th/Yb vs Nb/Yb diagram, rocks of the Caraba Formation are in the volcanic arc field (Fig. 4.18).

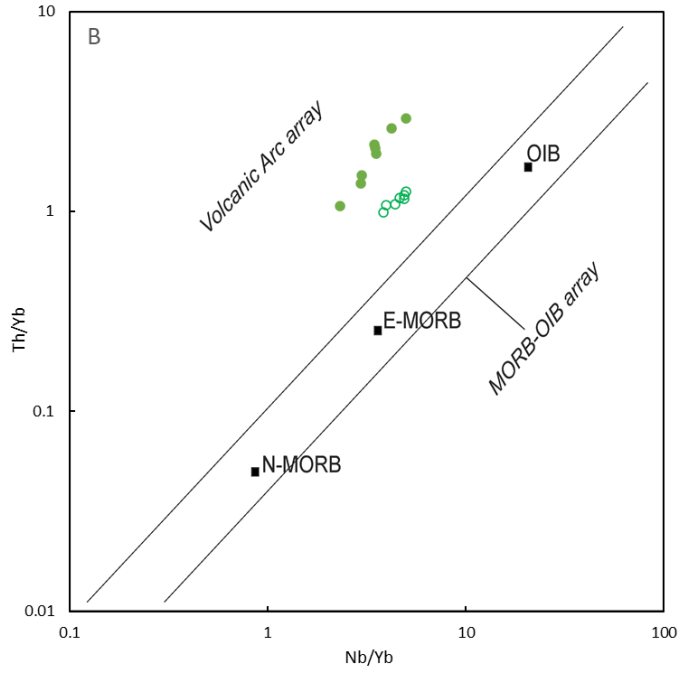

Fig. 4.18 Th/Yb vs Nb/Yb (Pearce, 1995) for the Caraba Formation.

4.4.3 Panama and Las Cascadas Formation

As can be seen from Fig. 4.19, compatible element Ni varies from 1.9 to 50.2 ppm with two exceptions of 542.97 ppm (J17-084) and 239.49 ppm (J18-024). Nickel is scattered in Ni versus MgO for rocks of the Las Cascadas Formation, but displays a positive correlation trend can still be observed for Panama Formation when excluding the two exceptions. Both Sc and V have a positive correlation with MgO and the trend is continuous between Panama Formation and Las Cascadas Formation. Incompatible elements (*e.g.*, Rb, Nb, La, and Nb) show strong negative correlations when plotted against MgO. As MgO decreases, these elements increase exponentially. A gap between Panama and Las Cascadas Formation is shown in these diagrams, especially for La versus MgO and Yb versus MgO. In Sr vs MgO diagram, Sr increases with decreasing MgO in the Panama Formation and decreases with decreasing MgO in the Las Cascadas Formation. Comparing with the less incompatible element (e.g., Yb), the more incompatible elements (e.g., Rb, Nb and La) increase more rapidly. Even though rocks of the Las Cascadas Formation 1 have higher MgO content than the Las Cascadas Formation 2, they have similar range of the trace element contents.

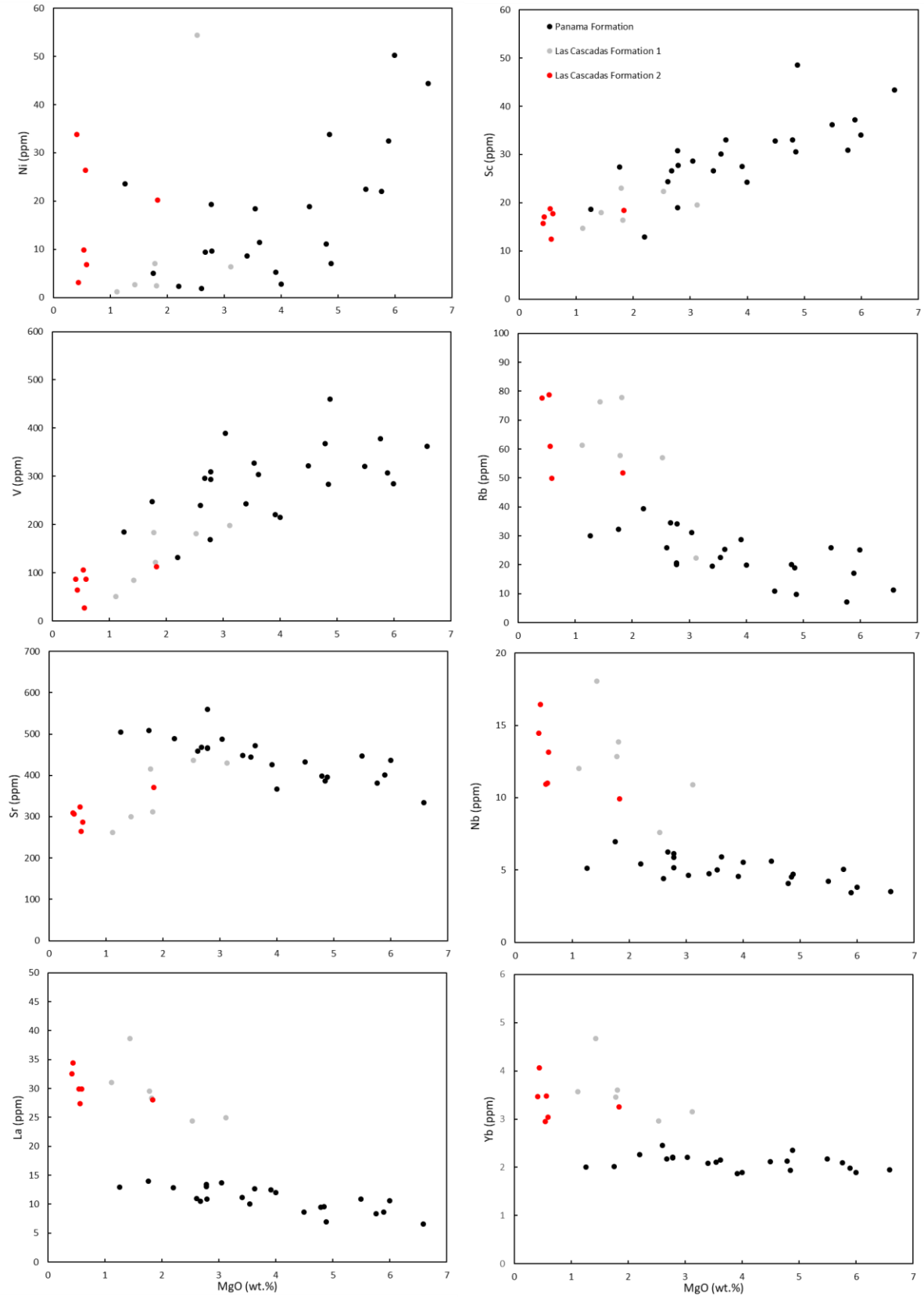

Fig. 4.19 Representative trace elements plotted against MgO for Panama and Las Cascadas group

On a chondrite-normalised REE diagram (Fig. 4.20 A), LREE in the Panama Formation and Las Cascadas Formation are enriched. $La/Sm_{(N)}$ ranges from 1.27 to 2.30 for Panama Formation and 2.50

to 2.83 for Las Cascadas Formation. $Gd/Yb_{(N)}$ ranges from 1.21 to 1.79 for Panama Formation and 1.38 to 1.76 for Las Cascadas Formation, which display slightly enriched HREE. Rocks of the Panama Formation display an Eu/Eu* range from negative (~0.93) to positive (~1.21) anomalies while rocks in the Las Cascadas Formation display negative anomalies (0.76-0.99). N-MORB-normalised trace element diagram (Fig. 4.20 B) show that Nb-Ta-Ti are markedly depleted compared to adjacent elements. Nb/Nb* ranges from 0.15 to 0.48 and Ti/Ti* ranges from 0.37 to 0.94 for the Panama Formation while Nb/Nb* ranges from 0.12 to 0.26 and Ti/Ti* ranges from 0.24 to 0.39 for the Las Cascadas Formation. The more incompatible elements on the left are more enriched than less incompatible elements on the right (Fig. 4.20 B). The fluid mobile elements such as Cs, Rb, Ba, U, K and Pb are overall enriched relative to Nb, Ta, Zr, Hf and HREE. A positive Sr anomaly is observed for the Panama Formation, while a negative Sr anomaly is observed for the Las Cascadas Formation. The N-MORB normalised multi-element patterns of rocks from the Panama Formation are broadly similar to the average continental arc basalt from Kelemen (2003). These two formations share similar patterns on the trace element diagram with Las Cascadas Formation having overall higher element contents.

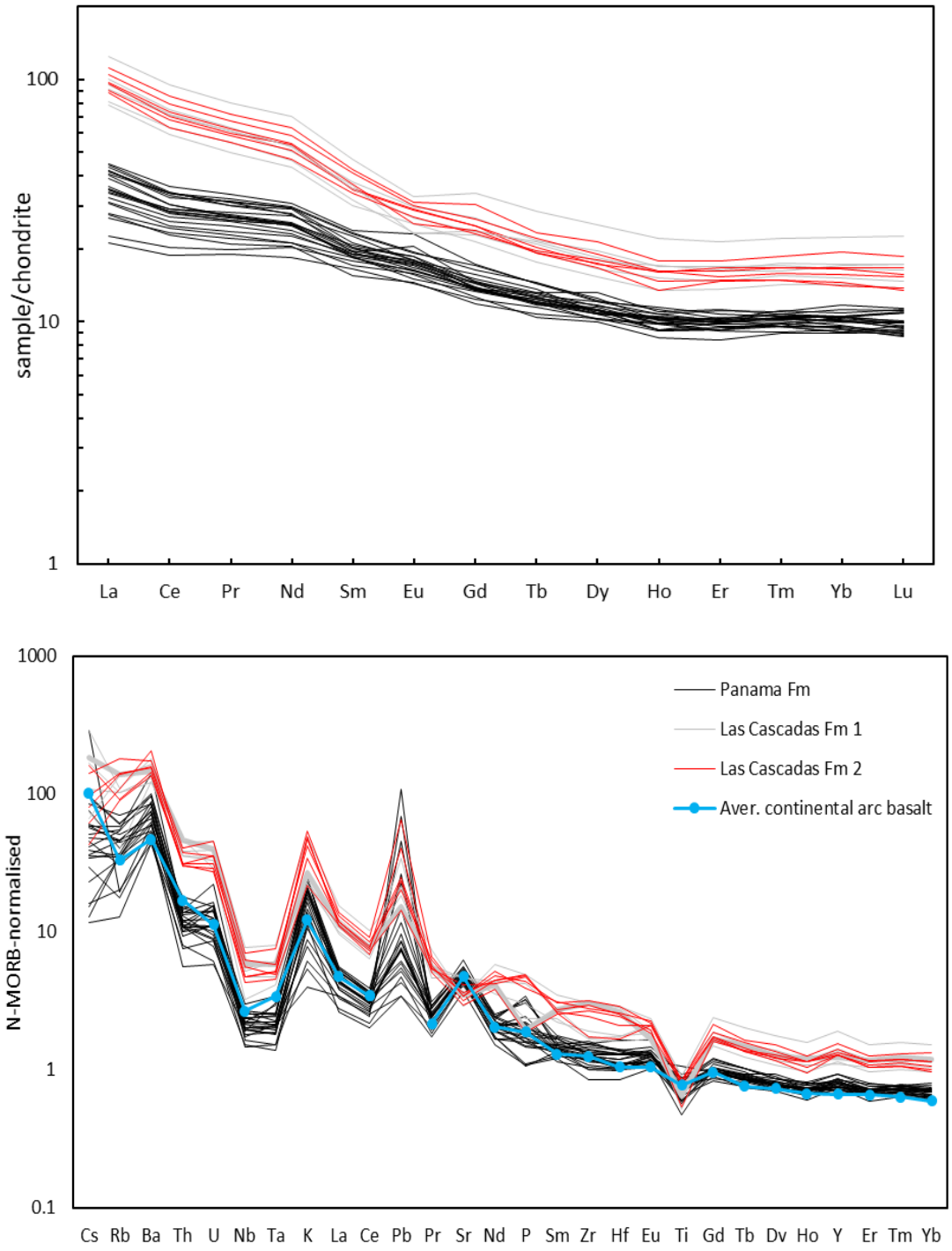

Fig. 4.20 Chondrite-normalised REE diagram (A) and N-MORB normalised trace element diagram (B) for Panama and Las Cascadas group (chondrite and N-MORB values are form Sun and McDonough, 1989; average continental arc basalt is from Kelemen et al., 2003)

Rocks of the Las Cascadas Formation are also plotted in the V versus Ti diagram for comparison even though it is only suitable for mafic rocks. Rocks in the Panama Formation plot in arc tholeiite field but evolve to the MORB/BABB field (Fig. 4.21 A). Rocks in the Panama Formation and Las Cascadas Formation form a continuous trend and rocks in the Las Cascadas Formation 2 are more evolved in V

vs Ti/1000 diagram. In Th/Yb vs Nb/Yb diagram, all the Panama Formation and Las Cascadas Formation are in the volcanic arc field (Fig. 4.21 B).

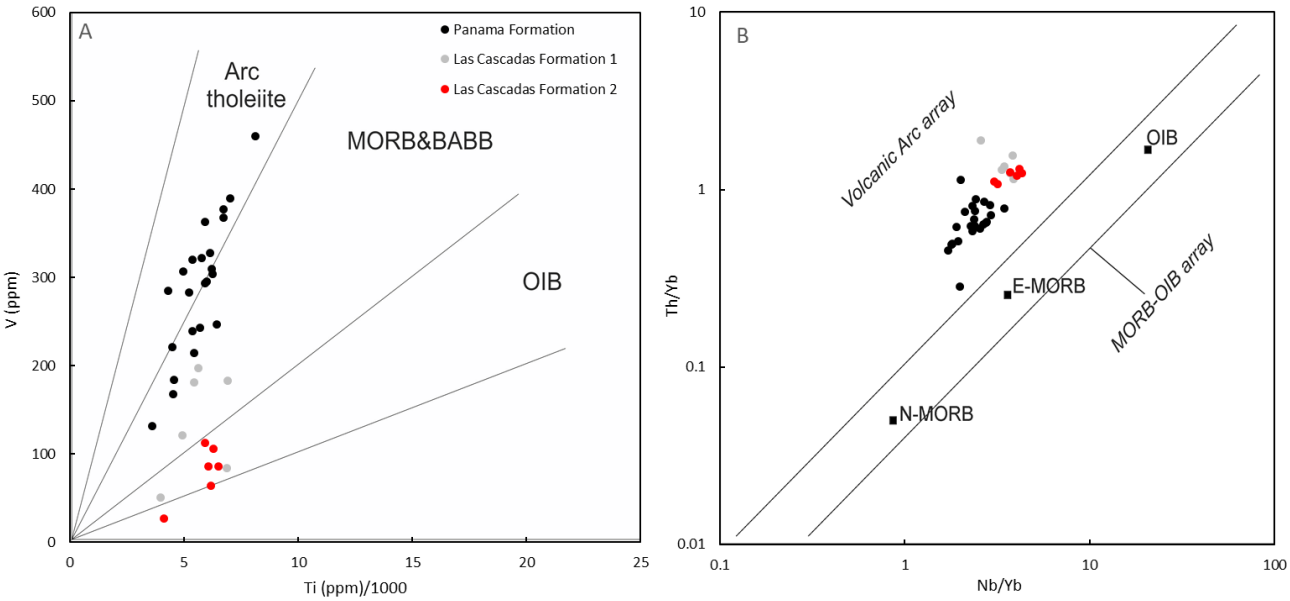

Fig. 4.21 (A) V vs Ti (Shervais, 1982) and (B) Th/Yb vs Nb/Yb (Pearce, 1995) for the Panama Formation and Las Cascadas Formation

4.4.4 Cabra Formation

As can be seen from Fig. 4.22, except for J17-031 which has an extremely high Ni (1292.4 ppm; MgO = 53.0 wt.%), Cabra mafic member shows a positive correlation in the Ni vs MgO diagram. Two olivine-bearing basalts (J18-045 and J18-052) have high MgO and Ni contents. Similar positive correlation is observed for the Cabra felsic member except for one sample, J18-034-4 which has high Ni content (274.4 ppm). Scandium has a positive correlation with MgO for the felsic member, but no obvious trend is observed in the mafic member, even after excluding the olivine-bearing basalt. Similarly, V shares a positive correlation with MgO in the felsic member. Overall, incompatible elements Rb, Nb, La, Yb increase with decreasing MgO when the olivine bearing basalts are excluded. One extremely low Rb value (1.46 ppm in J17-104) in Rb vs MgO can be caused by alteration which also has extremely low Ba content (48.76 ppm, not shown here). Two extremely low Sr contents (10.93 ppm in J18-028 and 9.95 ppm in J18-029) in Sr vs MgO diagram are from two highly altered vesicular lava samples on a beach. All diagrams except for Yb vs MgO display a continuous trend between the mafic member and the felsic member which is consistent with the major elements. In Yb vs MgO diagram, a gap is found between these two members (1.67-2.78 ppm for the mafic member and 3.27-4.51 ppm for the felsic member) and Yb content is the criteria to divide Cabra Formation into the Cabra mafic member and Cabra felsic member.

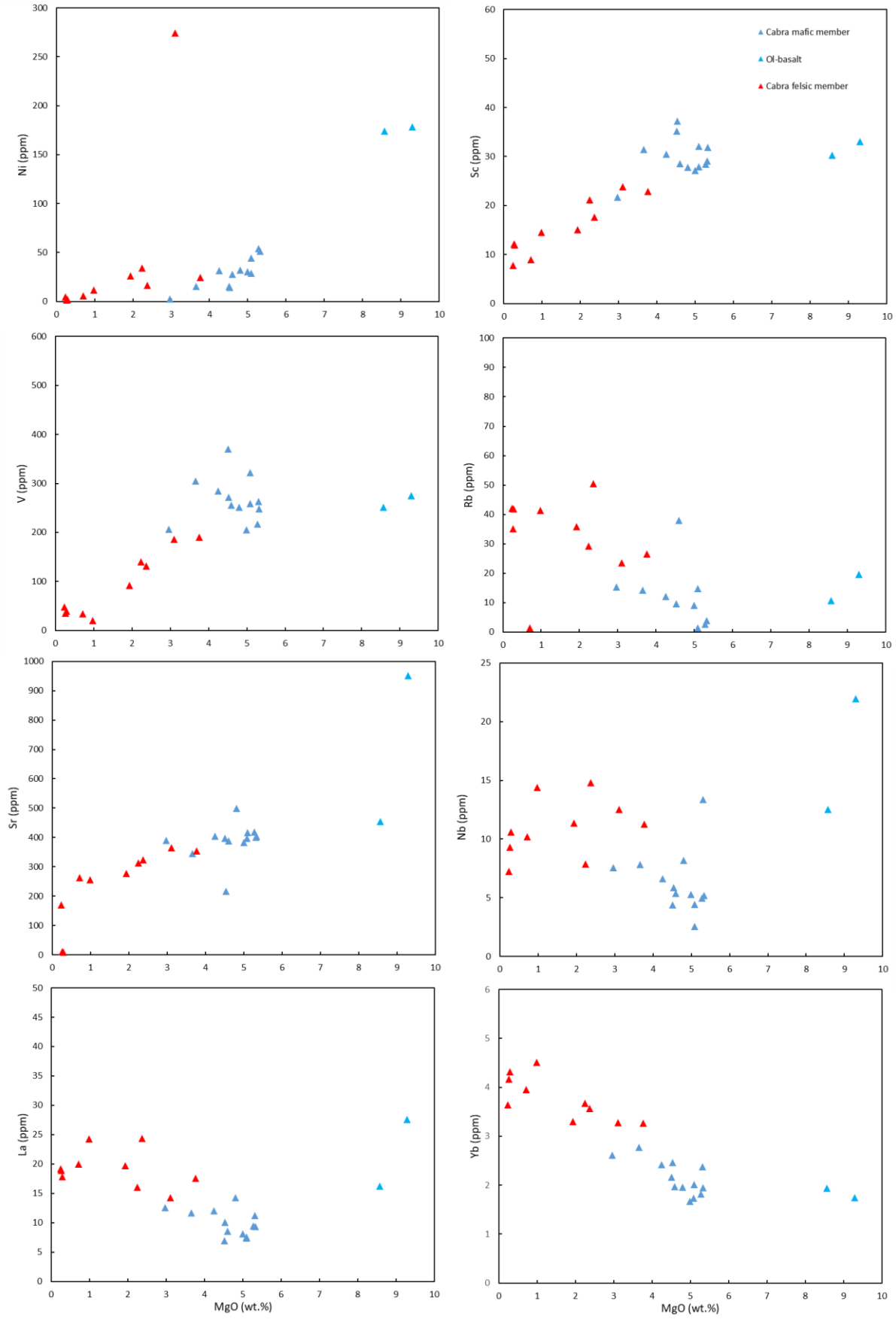

Fig. 4.22 Representative trace elements plotted against MgO for Cabra formation

On the chondrite-normalised REE diagram (Fig. 4.23 A), Cabra Formation is enriched in LREE with $La/Sm_{(CN)}$ range from 1.21 to 3.0 (1.21-2.56 without olivine basalts) for the mafic member and 1.63 to 2.51 for the felsic member. This formation is also enriched in MREE comparing to HREE. $Gd/Yb_{(CN)}$ ranges from 1.22 to 2.32 (1.22-1.41 without olivine basalts) for the mafic member. The felsic member ranges from 1.00 to 1.36 with an exception of 0.86 (J18-029). In the mafic group, Eu displays slight positive anomaly (Eu/Eu* =0.97-1.20) and in the felsic group it displays a slightly negative anomaly (Eu*/Eu=0.61-1.07) (Fig. 4.23 A). On the N-MORB-normalised multi-element diagram (Fig. 4.23 B), the Cabra mafic member displays negative Nb-Ta-Ti anomaly. The negative Nb anomaly spans a large range from Nb/Nb*= 0.16 to 0.91. Ti/Ti* ranges from 0.65 to 1.02. For the felsic member, Nb/Nb* ranges from 0.20 to 0.52 while Ti/Ti* ranges from 0.23 to 0.61. The more incompatible elements on the left are more enriched than less incompatible elements on the right (Fig. 4.23 B). The fluid mobile elements such as Cs, Rb, Ba, U and Pb are overall enriched relative to Nb, Ta, Zr, Hf and HREE. Positive Ba and Sr anomalies are observed for the mafic member and Pb generally shows a positive anomaly, except for the two olivine bearing basalts which display negative anomaly. The same pattern is observed for K, which displays positive anomaly in most of the mafic member rocks, but samples without a positive anomaly are also found (Fig. 4.23 B). For the felsic member, Ba and Pb display positive anomalies and Sr displays a negative anomaly. Potassium displays positive anomaly for all the samples except one, J17-104 which also has an extremely low Rb concentration (Fig. 4.22). Zirconium and hafnium display remarkedly positive anomaly for the felsic member while this anomaly is absent in the mafic member.

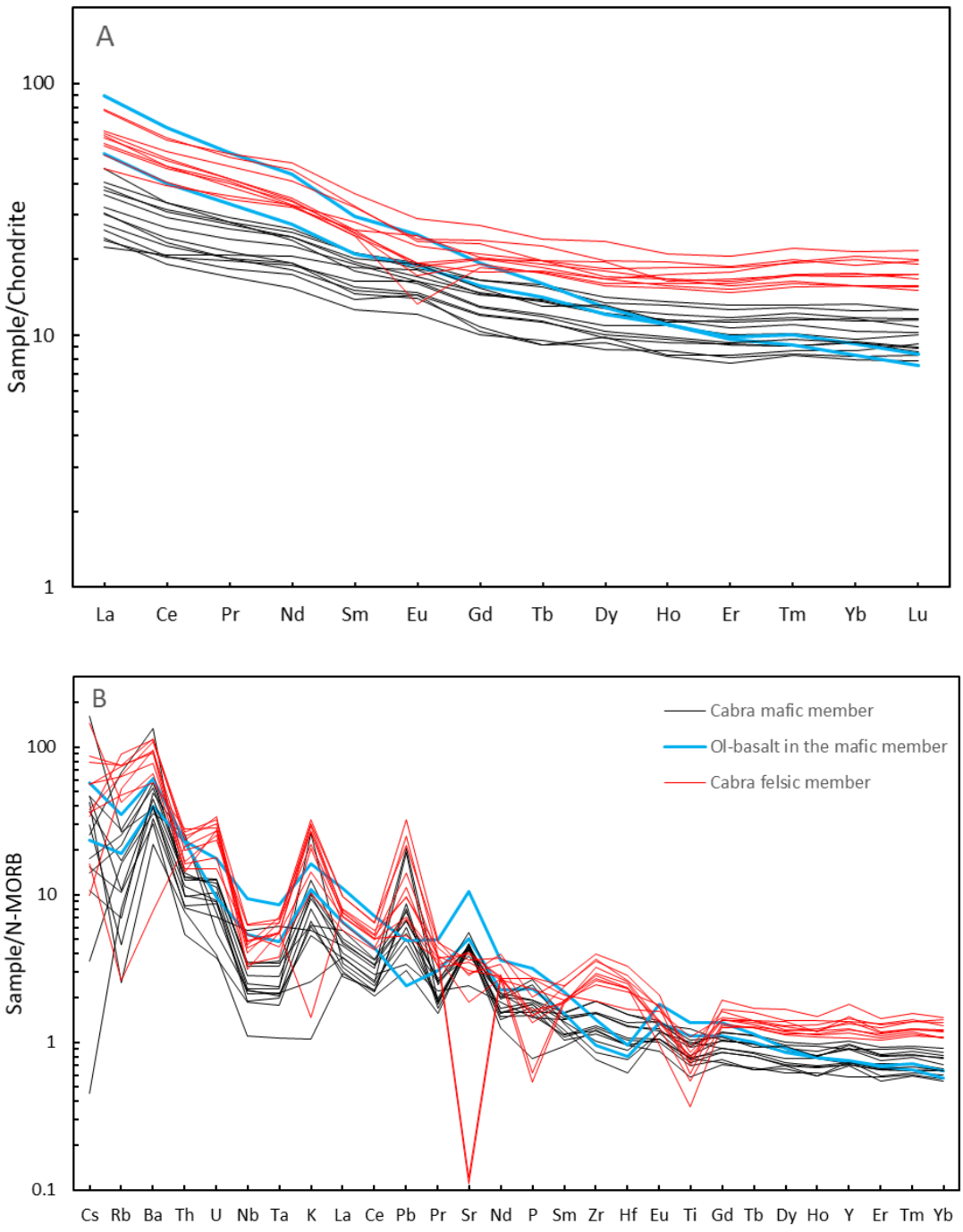

Fig. 4.23 Chondrite-normalised REE diagram (A) and N-MORB normalised trace element diagram (B) for Cabra formation (chondrite and N-MORB values are form Sun and McDonough, 1989).

As can be seen from V versus Ti diagram (Fig. 4.24 A), Cabra mafic member except for one sample J18-043 are plotted in the MORB/BABB field. On the Th/Yb vs Nb/Yb diagram (Fig. 4.24 B), most of the samples are in the volcanic arc field. However, J17-031 are on the MORB-OIB array close to E-MORB. One olivine-bearing basalt, J18-045 is also on the MORB-OIB array close to the OIB.

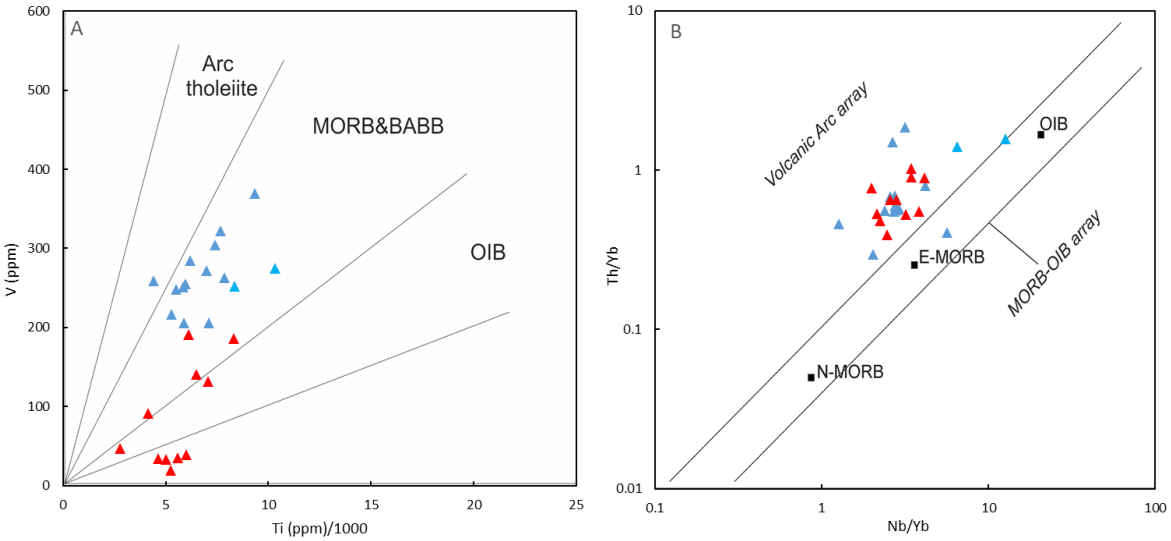

Fig. 4.24 (A) V vs Ti (Shervais, 1982) and (B) Th/Yb vs Nb/Yb (Pearce, 1995) for Cabra Formation (Cabra felsic member are also plotted in the diagrams for comparison).

4.5 Sr-Nd-Pb isotopes

22 samples were analysed for Sr-Nd-Pb isotopes. 3 from the Chagres complex, 2 from the Bas Obispo Formation, 1 from the Caraba Formation (amphibole andesite in Cerro Patacon), 7 from the Panama formation, 2 from the Las Cascadas Formation, 7 from the Cabra Formation and 1 from the Pedro Miguel Formation were selected for analysis. The analytical method can be found in Appendix C and the full dataset can be found in Appendix E4. Age corrected values (initial values) were calculated based on ages from different sources. Chagres Complex has long magmatic history and is not well constrained by ages. The time span for this group is 68 to 40 Ma (Lissinna, 2005; Wegner et al., 2011) and therefore 50 Ma was chosen for this group for age correction. The age of Bas Obispo group is revealed as 25 Ma by Buchs et al., (2019b). Amphibole bearing andesite from Cerro Patacon was dated as 25 Ma by Ar-Ar dating (Rooney et al., 2011) so 25 Ma was chosen for age correction for the Caraba Formation. Two samples from the Panama Formation were selected and sent for Ar-Ar dating but the data has not been collected. Based on stratigraphy, 21 Ma is chosen for this Formation. Sample J17-006 from the Las Cascadas Formation has been dated by Ar-Ar method as 16 Ma (unpublished data from supervisor Dr. David Buchs). Zircon dating was conducted for J18-094-5 with the result of 16 Ma so 16 Ma was chosen for the Cabra Formation. The Pedro Miguel Formation have been well studied by Buchs et al. (2019a) which gives the age of 18-16 Ma and therefore 16 Ma was used for age correction for this formation. The age correction equations are shown below:

$$\frac{143_{Nd}}{144_{Nd}}(i) = \frac{143_{Nd}}{144_{Nd}}(m) - \frac{147_{Sm}}{144_{Nd}}(m) \times \left(e^{\lambda t} - 1\right) \quad (\lambda = 6.54E-12) \quad Equation\ 4.10$$

$$\frac{87_{Sr}}{86_{Sr}}(i) = \frac{87_{Sr}}{86_{Sr}}(m) - \frac{87_{Rb}}{86_{Sr}}(m) \times \left(e^{\lambda t} - 1\right) \quad (\lambda = 1.42E-11) \quad Equation\ 4.11$$

$$\frac{206_{Pb}}{204_{Pb}}(i) = \frac{206_{Pb}}{204_{Pb}}(m) - \frac{238_{U}}{204_{Pb}}(m) \times \left(e^{\lambda t} - 1\right) \quad (\lambda = 1.55E-10) \quad Equation\ 4.12$$

$$\frac{207_{Pb}}{204_{Pb}}(i) = \frac{207_{Pb}}{204_{Pb}}(m) - \frac{235_{U}}{204_{Pb}}(m) \times \left(e^{\lambda t} - 1\right) \quad (\lambda = 9.85E-10) \quad Equation\ 4.13$$

$$\frac{208_{Pb}}{204_{Pb}}(i) = \frac{208_{Pb}}{204_{Pb}}(m) - \frac{232_{Th}}{204_{Pb}}(m) \times \left(e^{\lambda t} - 1\right) \quad (\lambda = 4.95E-11) \quad Equation\ 4.14$$

where (i) indicates the initial value while (m) indicates the measured value, t is the age of the rock.

An alterative way of expressing isotope ratios is the epsilon notation (DePaolo and Wasserburg, 1976). Isotope ratios are only strictly comparable if the samples plotted are of the same age. The epsilon value is a measure of the deviation of a sample from the expected value in a uniform reservoir (chondrite or CHUR in this study) and may be used as a normalising parameter for sample of different age. It is normally calculated for Nd, which is affected the most by age comparing with Sr and Pb. The definition of epsilon Nd can be seen in Equation 5.6.

$$\varepsilon Nd = \left(\frac{\frac{143Nd}{144Nd}(i)}{\frac{143Nd}{144Nd}(CHUR,t)} - 1\right) \times 10000 \qquad \text{Equation 4.15}$$

$\frac{143_{Nd}}{144_{Nd}}$(CHUR,t) can be calculated as:

$$\frac{143_{Nd}}{144_{Nd}}(CHUR,t) = \frac{143_{Nd}}{144_{Nd}}(CHUR,today) - \frac{147_{Sm}}{144_{Nd}}CHUR,today) \times \left(e^{\lambda t} - 1\right) \qquad \text{Equation 4.16}$$

Where $\frac{143_{Nd}}{144_{Nd}}$(CHUR,today) is 0.512638, $\frac{147_{Sm}}{144_{Nd}}$CHUR,today) is 0.1967, and λ is the same to the one in Equation 4.10. εNd can be calculated by putting the values from Equation 4.10 and Equation 4.16 into Equation 4.15.

4.5.1 Sr isotope

The $^{87}Sr/^{86}Sr(i)$ for the Chagres Complex ranges from 0.70337 to 0.70368 (Fig. 4.25). It is 0.70373 - 0.70377 for the Bas Obispo Formation. The Panama Formation has $^{87}Sr/^{86}Sr(i)$ of 0.70362 - 0.70403. The range of 0.703660 – 0.703663 is collected for two samples from the Las Cascadas Formation. One value of 0.70365 is obtained for an amphibole bearing andesite from the Caraba Formation. The Cabra felsic group has the range of 0.70339 - 0.70350 and it is 0.70336 - 0.70348 for the Cabra mafic group. One value of 0.70331 was collected for the Pedro Miguel Formation (Fig. 4.25).

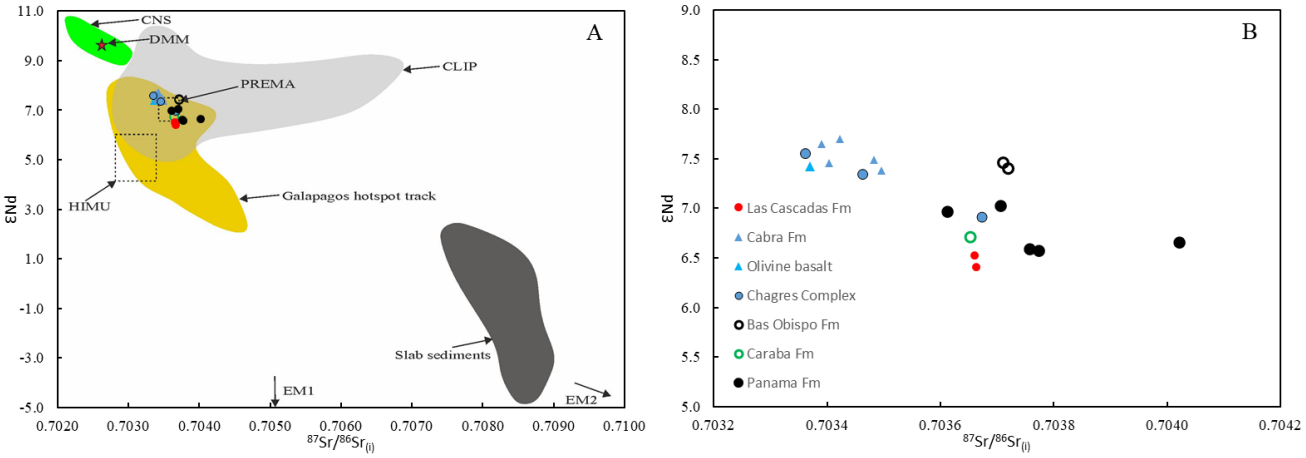

Fig. 4.25 εNd vs initial values of Sr in this study. Also plotted are average DMM (depleted MORB mantle, from Workman and Hart (2005) but originally from Sun an Langmuir (2003)); CNS (Cocos-Nazca spreading ridge from Werner et al. (2003)); Galapagos hotspot track from Werner et al., 2003 and Hoernle et al., 2000; slab sediments on the Cocos Plate from Sadofsky et al. (2009), Feigenson et al.(2004), and Plank and Languir (1998); CLIP (Caribbean Large Igneous Province) from Kerr et al. (1997a) and Hauff et al. (2000a, 2000b).

4.5.2 Nd isotope

The $^{143}Nd/^{144}Nd(i)$ for the Chagres Complex ranges from 0.51292 to 0.51296 (Fig. 4.25). It is 0.512985 - 0.512988 for the Bas Obispo group. The Panama Formation has the values of 0.51292 - 0.51297. The range of 0.512915 – 0.512946 was collected for the Las Cascadas Formation. One

amphibole andesite from the Caraba Formation has a value of 0.51295. 0.51300- 0.51301 are obtained for the Cabra felsic group and 0.51300 - 0.51301 are obtained for the Cabra mafic group. The value of 0.51302 was collected for one sample from the Pedro Miguel Formation.

The εNd for the Chagres Complex ranges from 6.92 to 7.55 (Fig. 4.25). It is 7.41 – 7.46 for the Bas Obispo group. The Panama Formation has the values of 6.55-7.01. The range of 6.41-6.52 was collected for the Las Cascadas Formation. One amphibole andesite from the Caraba Formation has a value of 6.72. 7.38 – 7.65 are obtained for the Cabra felsic group and 7.43 – 7.7 are obtained for the Cabra mafic group. The value of 7.83 was collected for one sample from the Pedro Miguel Formation (Fig. 4.25).

4.5.3 Pb isotope

The $^{206}Pb/^{204}Pb(i)$ for the Chagres Complex ranges from 18.798 to 18.878 (Fig. 4.26 A). It is 19.037 – 19.044 for the Bas Obispo group. The Panama Formation has the values of 18.898 – 18.989. The range of 18.973 – 18.988 are collected for the Las Cascadas Formation. One amphibole andesite from the Caraba Formation has a value of 18.903. 18.852- 18.885 are obtained for Cabra felsic group and 18.829 – 18.908 are obtained for Cabra mafic group. The value of 18.794 was collected for one sample from the Pedro Miguel Formation.

The $^{207}Pb/^{204}Pb(i)$ for the Chagres Complex ranges from 15.585 to 15.597 (Fig. 4.26 A). It is 15.604 – 15.606 for the Bas Obispo group. The Panama Formation has the values of 15.597 – 15.602. The range of 15.600 – 15.601 are collected for the Las Cascadas Formation. One amphibole andesite from the Caraba Formation has a value of 15.602. 15.586- 15.588 are obtained for the Cabra felsic group and 15.577 – 15.591 are obtained for the Cabra mafic group. The value of 15.574 was collected for one sample from the Pedro Miguel Formation.

The $^{208}Pb/^{204}Pb(i)$ for the Chagres Complex ranges from 38.417 to 38.504 (Fig. 4.26 B). It is 38.725 – 38.736 for the Bas Obispo group. The Panama Formation has the values of 38.600 – 38.678. The range of 38.664 – 38.689 are collected for the Las Cascadas Formation. One amphibole andesite from the Caraba Formation has a value of 38.589. 38.577- 38.584 are obtained for the Cabra felsic group and 38.448 – 38.614 are obtained for the Cabra mafic group. The value of 38.474 was collected for one sample from the Pedro Miguel Formation.

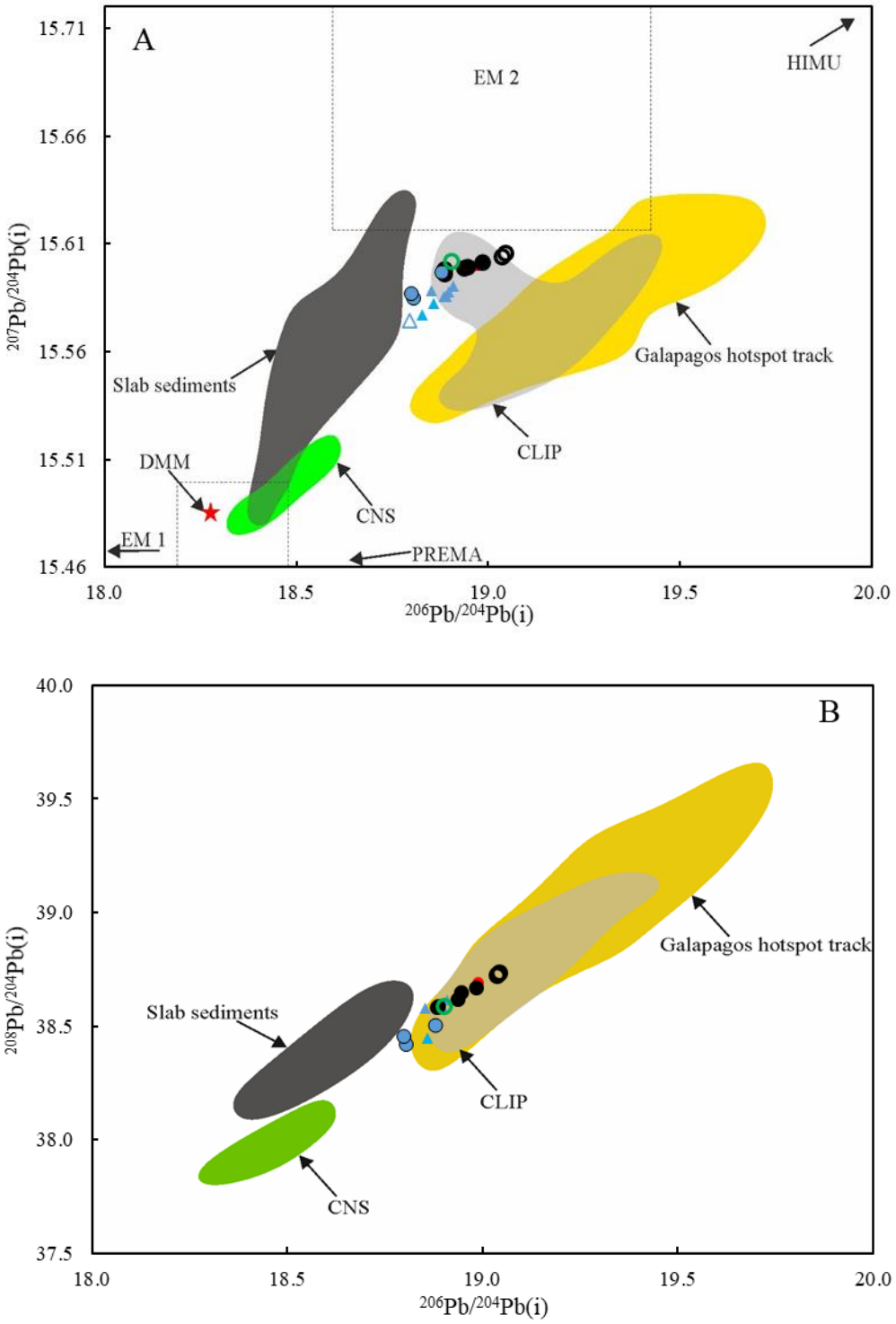

Fig. 4.26 (A) $^{206}Pb/^{204}Pb(i)$ vs $^{207}Pb/^{204}Pb(i)$ and (B) $^{208}Pb/^{204}Pb(i)$ vs $^{207}Pb/^{204}Pb(i)$ in this study. Also plotted are average DMM (depleted MORB mantle, from Workman and Hart (2005) but originally from Sun an Langmuir (2003)); CNS (Cocos-Nazca spreading ridge from Werner et al. (2003)); Galapagos hotspot track from Werner et al., 2003 and Hoernle et al., 2000; slab sediments on the Cocos Plate from Sadofsky et al. (2009), Feigenson et al.(2004), and Plank and Languir (1998); CLIP (Caribbean Large Igneous Province) from Kerr et al. (1997a) and Hauff et al. (2000a, 2000b).

4.6 Summary

Chagres Complex has the highest LOI in this study which indicates the highest alteration. This is also consistent with the oldest age in this complex. The rest of rocks generally have low value of LOI. Rocks in the Chagres complex and Cabra Formation range from basalt to rhyolite. Rocks in the Panama Formation are basalt to andesite while rocks in the Las Cascadas Formation are andesite to rhyolite. Rocks in the Caraba Formation range from andesite to dacite. Rocks in the Panama Formation, Las Cascadas Formation, and Cabra Formation are in between calc-alkaline and tholeiitic trend with several exceptions from the Las Cascadas Formation and Cabra felsic member which plot in the tholeiitic field. Rocks in the Caraba Formation show calc-alkaline trend (Fig. 4.27 A). It is consistent with $FeO_{(T)}/MgO$ vs SiO_2 diagram in which rocks in the Panama Formation, Las Cascadas Formation, and Cabra Formation are on the boundary of calc-alkaline and tholeiitic field with several exceptions from the Las Cascadas Formation and Cabra felsic member which plot in the tholeiitic field (Fig. 4.27 B). Rocks in the Caraba Formation plot in the low-Fe calc-alkaline field.

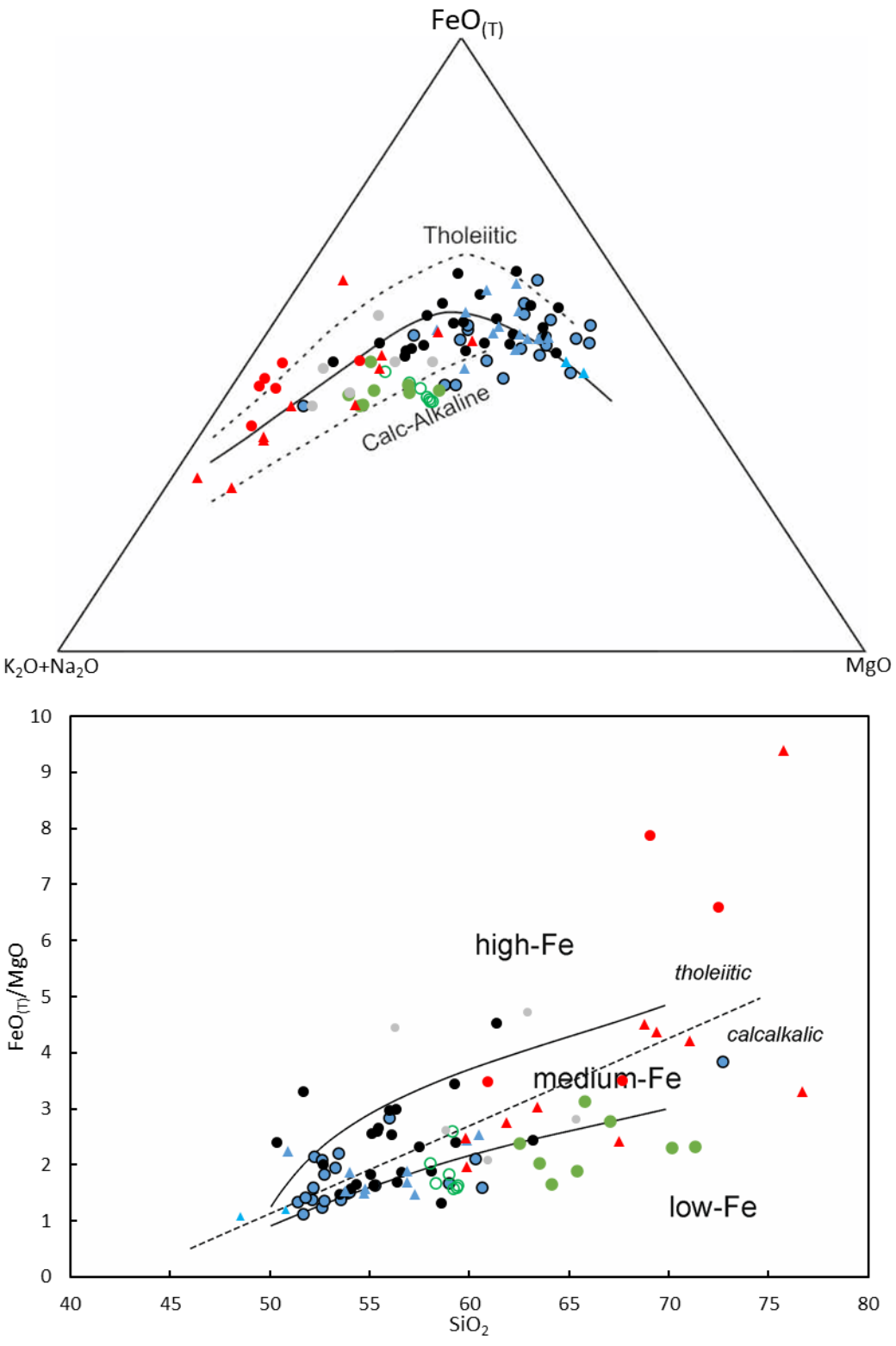

Fig. 4.27 (A) AFM and (B) $FeO_{(T)}/MgO$ vs SiO_2 diagram (revised from Arculus, 2003; The discriminant boundary (dashed line) between tholeiitic and calcalkalic suites is from Miyashiro (1974)).

From the trace elements, all rocks show significant arc signature, e.g. Nb-Ta-Ti depletion on N-MORB normalised multi-element diagram. The amphibole-bearing rocks in the Caraba Formation have lower HREE contents than the pyroxene-bearing rocks in the other formations. In the Dy/Dy* vs Dy/Yb diagram, rocks in the Caraba Formation has the lowest Dy/Dy* and Dy/Yb showing amphibole crystallization while rocks in the rest of formations have relatively high Dy/Dy* (Fig. 4.28).

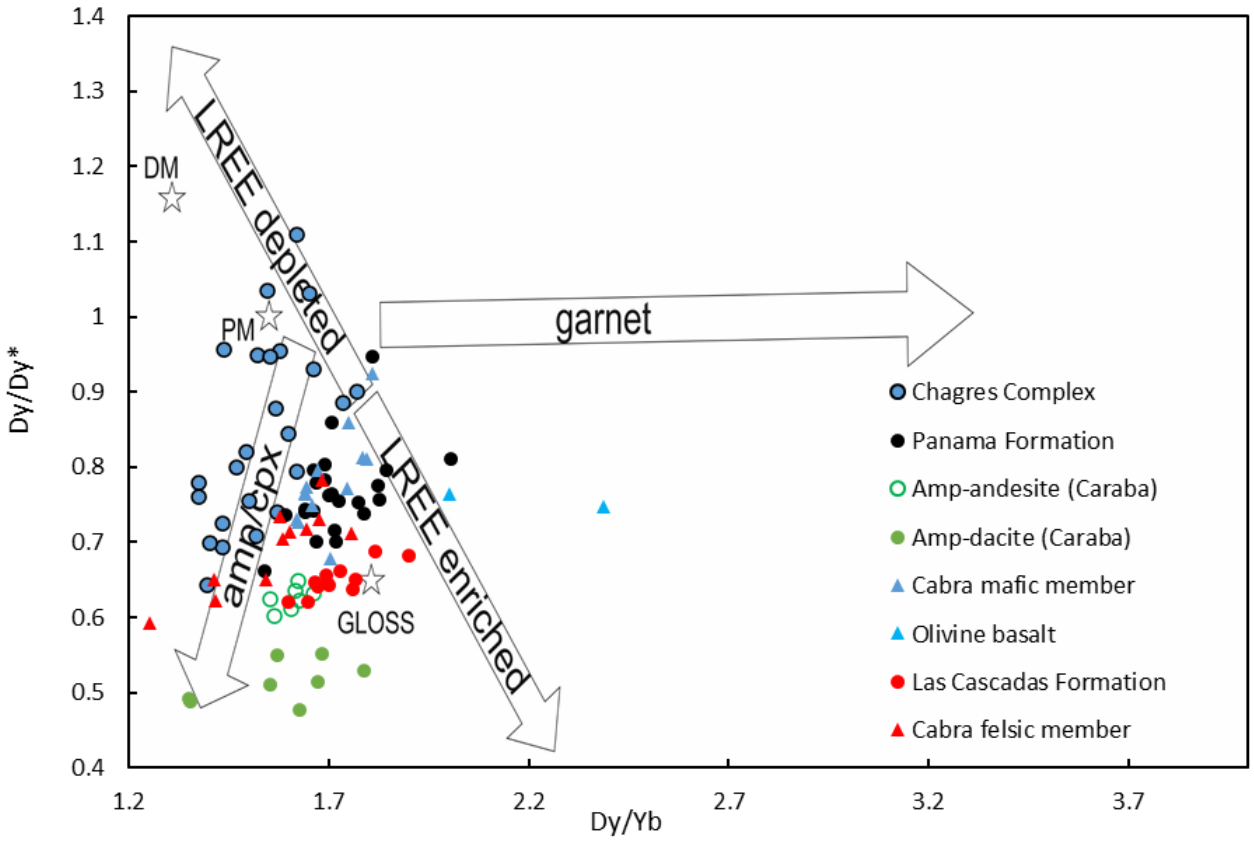

Fig. 4.28 Dy/Dy vs Dy/Yb diagram from Davidson et al. (2013).*

The Cabra Formation/Pedro Miguel Formation have the highest εNd values while the rest of samples such as the Panama, Las Cascadas, and Caraba Formation have lower values (Fig. 4.25). The Chagres Complex spans a large range. The Panama/Las Cascadas/Caraba Formation also have lower $^{87}Sr/^{86}Sr(i)$ values than the Cabra/Pedro Miguel Formation. The Chagres Complex has the similar range with the Cabra/Pedro Miguel Formation.

In the $^{206}Pb/^{204}Pb(i)$ vs $^{207}Pb/^{204}Pb(i)$ diagram, the Panama Formation, Las Cascadas Formation, Caraba Formation, and Bas Obispo Formation show a linear trend while Cabra Formation and Pedro

Miguel Formation form another linear trend (Fig. 4.26 A). The Chagres Complex are between these two trends. This regularity can also be seen in the $^{208}Pb/^{204}Pb(i)$ vs $^{207}Pb/^{204}Pb(i)$ (Fig. 4.26 B).

5 MINERAL CHEMISTRY

This section discusses mineral compositions in this study. The composition of minerals such as clinopyroxene can provide insight into the conditions under which it crystallised, such as the pressure and temperature (Nimis, 1995; Putirka, 2008). It can also reflect the tectonic setting in which the rock emplaced (Le Bas et al., 1962; Nisbet and Pearce, 1977; Leterrier et al., 1982; Loucks, 1990). Moreover, the composition of olivine may provide information regarding the source rock (i.e., peridotite or pyroxenite; Sobolev et al. 2005).

Clinopyroxene, plagioclase, orthopyroxene, and olivine crystals as well as glass/matrix were identified for quantitative analysis using SEM-EDS spot analysis at Cardiff University. The reader is referred to Appendix B for the analytical method and Appendix E3 for the data.

The Mg# of clinopyroxene was calculated using the method of Putirka (2008). In this method, the wt.% of the oxides is used to derive their molecular proportion, then their atomic proportion, which is subsequently used to calculate the ionic proportion of the elements. These ionic proportions were then used to calculate the Mg# of pyroxene and olivine (Equation 5.1) and end members of the analysed pyroxene (Equation 5.2, Equation 5.3, Equation 5.4) and feldspar (Equation 5.5, Equation 5.6, Equation 5.7).

The Mg# of pyroxene and olivine and endmembers of pyroxenes were determined using the following equations:

Equation 5.1 $Mg\# = Mg^{2+}/(Mg^{2+}+Fe^{2+})*100$

Equation 5.2 $En = Mg^{2+}/(Ca^{2+}+Mg^{2+}+Fe^{2+})*100$

Equation 5.3 $Fs = Fe^{2+}/(Ca^{2+}+Mg^{2+}+Fe^{2+})*100$

Equation 5.4 $Wo = Ca^{2+}/(Ca^{2+}+Mg^{2+}+Fe^{2+})*100$

The endmembers of feldspar in feldspar classification diagrams (An-Ab-Or) were determined using the following equations:

Equation 5.5 $An = Ca^{2+}/(Ca^{2+}+Na^{+}+K^{+})*100$

Equation 5.6 $Ab = Na^{+}/(Ca^{2+}+Na^{+}+K^{+})*100$

Equation 5.7 $Or = K^{+}/(Ca^{2+}+Na^{+}+K^{+})*100$

Anorthite number (An) in plagioclase was determined with the following equation:

Equation 5.8 $An = Ca^{2+}/(Ca^{2+}+Na^{+})*100$

5.1 Chagres Complex

Phenocryst clinopyroxene and plagioclase were analysed by SEM-EDS for this group. No orthopyroxene was found in samples from this location.

5.1.1 Clinopyroxene

Clinopyroxene in this group is mainly augite with subordinate diopside (Fig. 5.1). It exhibits the following compositional ranges: Mg# = 67-88, Wo = 35-48, En = 39-50, Fs =7-22. On bivariant diagrams (Fig. 5.2), TiO_2 (0.08-0.77 wt.%) and FeO (4.2-13.1 wt.%) increase with decreasing Mg#. CaO (16.9-23.0 wt.%) and SiO_2 (48.6-54.1 wt.%) decreases with decreasing Mg# and the trend is less pronounced in an SiO_2 versus Mg# diagram. As Mg# decreases, Al_2O_3 (1.6-6.3 wt.%) shows different trends for different samples. The Al_2O_3 content decreases with decreasing Mg# in J18-091 and increases in other samples. The MnO content (0.04-0.54 wt.%) increases with decreasing Mg# but shows a higher slope gradient at lower Mg# (< 75) especially for J17-132.

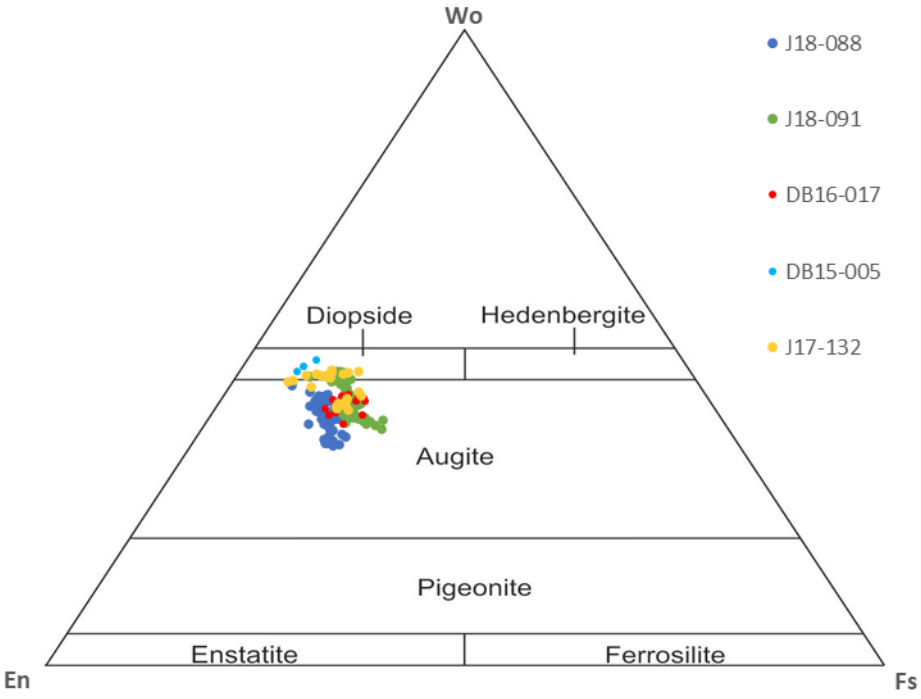

Fig. 5.1 Clinopyroxene classification for Chagres complex (classification diagram from Morimoto et al., 1988).

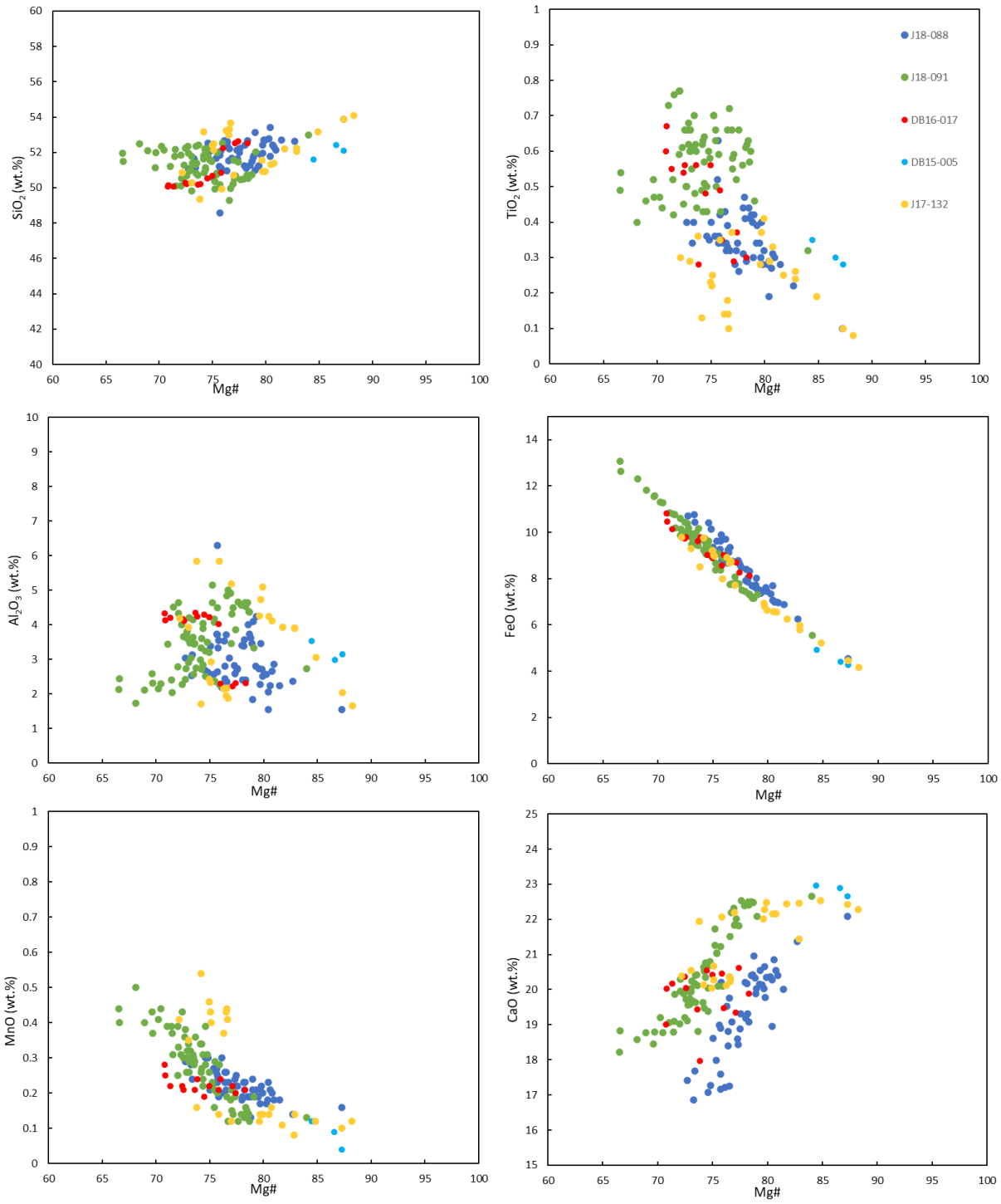

Fig. 5.2 Representative oxides plotted against Mg# for clinopyroxene of Chagres complex.

Clinopyroxene from individual samples in this complex are relatively homogeneous. In a Rhodes diagram (Fig. 5.3 A), J18-088, J18-091 and DB16-017A are overall in equilibrium with their whole rock composition while J17-132 and DB15-005 plot above the equilibrium zone. All samples have clinopyroxene with concentrated Mg# which forms a unimodal distribution (Fig. 5.3 B,C,D,E,F). Samples J18-088, J18-091 and J17-132 contain several high-Mg# clinopyroxene grains which plot away from their peak composition. All clinopyroxene grains from this complex, plot in the supra-subduction or orogenic field in the diagram of Leterrier (1982) and all except J18-091 plot in the tholeiitic arc field (Fig. 5.3 G). Clinopyroxene in J18-091 plots along the boundary between calc-alkaline arc and tholeiitic arc. The ratio of Ti/Al increases as Mg# decreases with the steepest slope in J18-091 and the shallowest slope in J17-132 (Fig. 5.3 H).

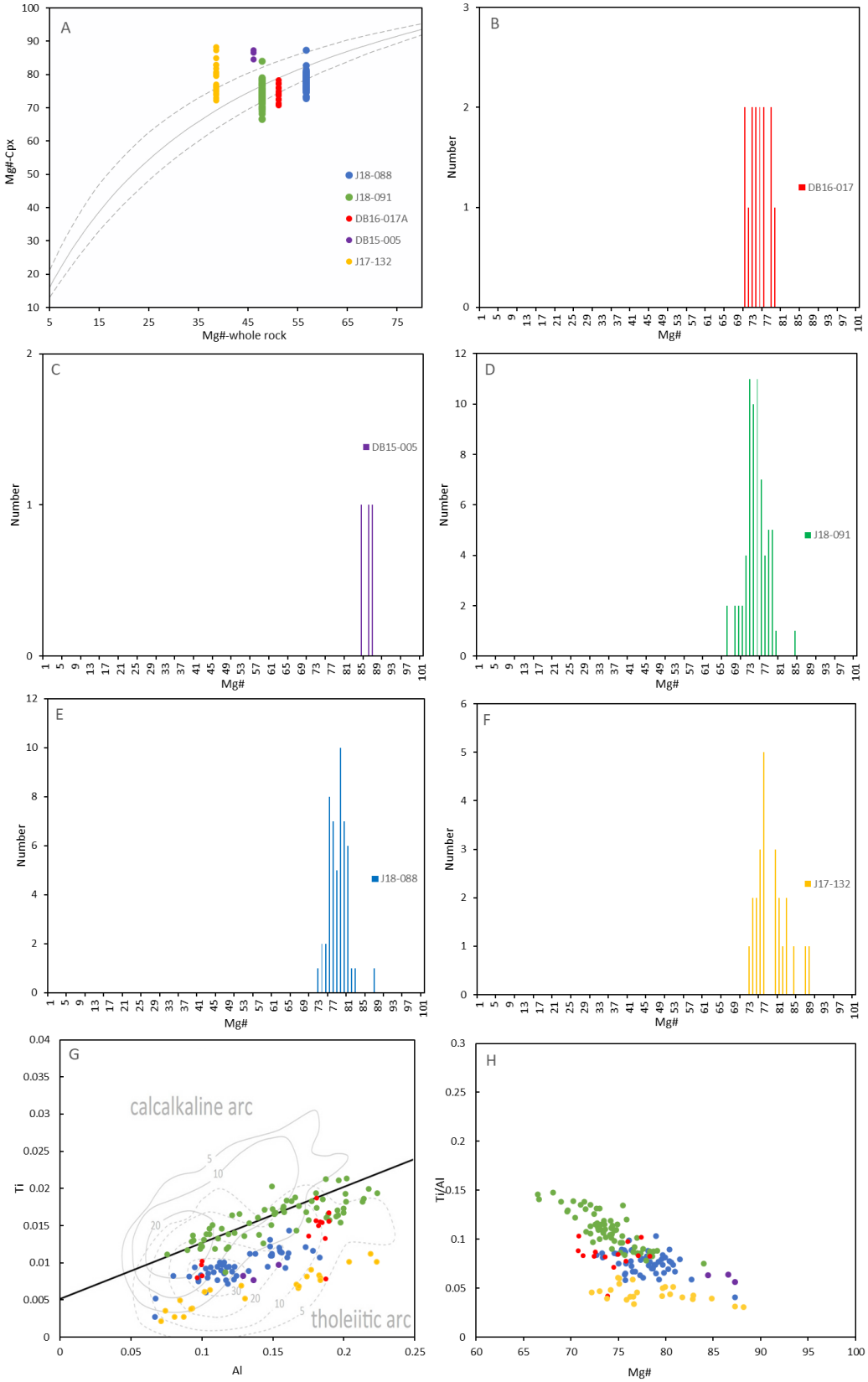

Fig. 5.3 Rhodes diagram, Mg# distribution diagram and bivariant diagrams for clinopyroxene in Chagres complex. (A) Rhodes diagram (Kd=0.28±0.08 from Putirka (2008)). (B) (C) (D) (E) (F) Mg# distribution diagram (G) Ti vs Al (boundary from Leterrier (1982) and Al, Ti are calculated based on 4 cations). (H) Ti/Al vs Mg#.

Clinopyroxene in this complex can be homogeneous or zoned. For zoned clinopyroxene, both normal and reversed compositional zonation is observed (Fig. 5.4). An example of a clinopyroxene phenocryst with normal compositional zonation usually has a high Mg# (~ 87) core and a low Mg# (~ 79) rim (Fig. 5.4 A), whereas grains showing reversed compositional zonation have a low Mg# (~ 75) core and a high Mg# (~ 81) rim (Fig. 5.4 B).

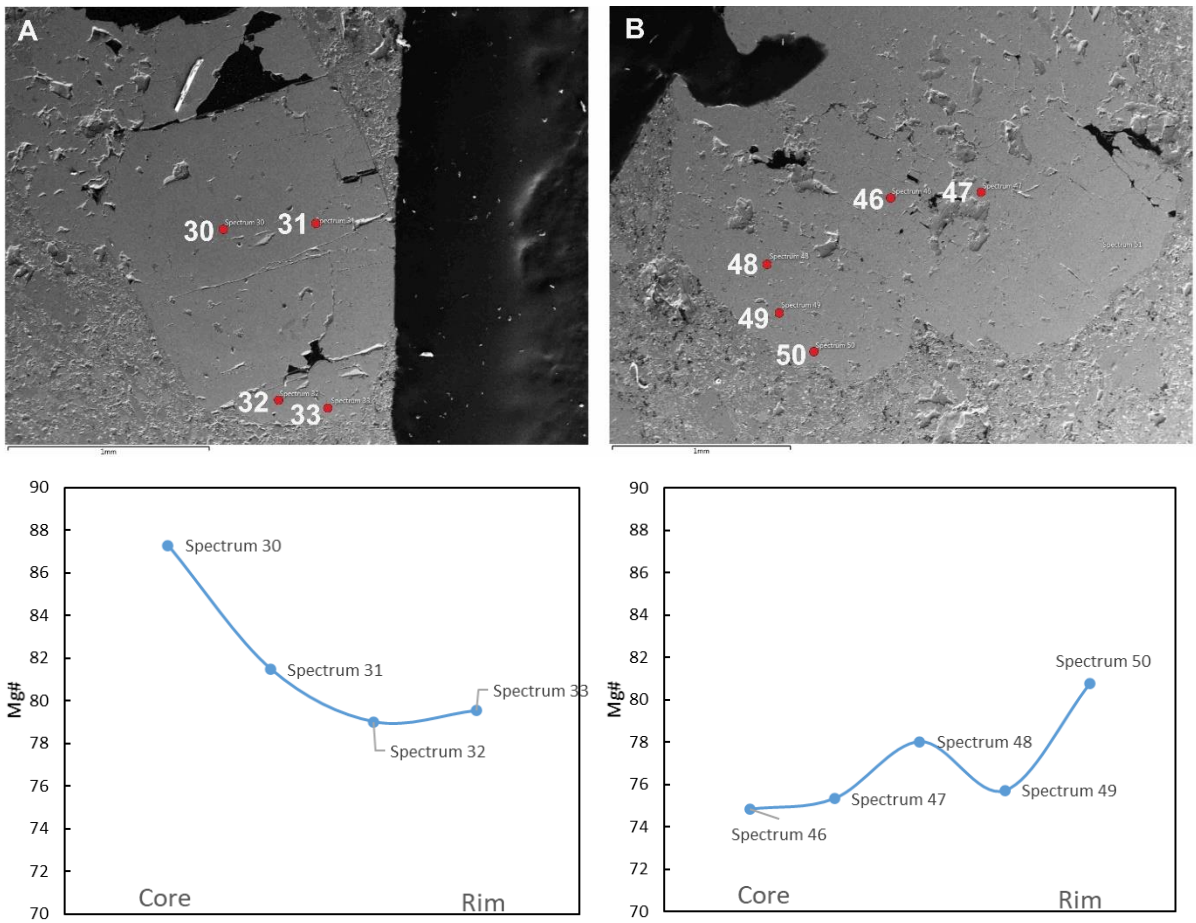

Fig. 5.4 Normal zonation (A) and reversed zonation (B) of clinopyroxene in J18-088.

5.1.2 Plagioclase

Plagioclase crystals display a variable composition ranging from anorthite to oligoclase (Fig. 5.5). The An value ranges from 59-86 for sample J18-088, 59-86 for sample J18-091 and 26-87 for sample J17-132 (only nine analyses and the distribution diagram is not shown) (Fig. 5.6).

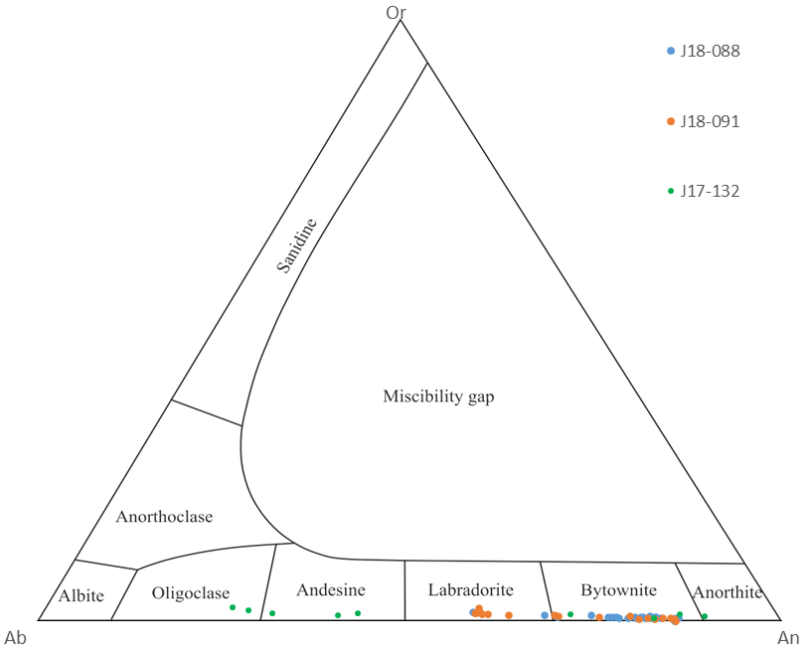

Fig. 5.5 Feldspar classification for Chagres complex (classification diagram from Smith and Brown, 1988).

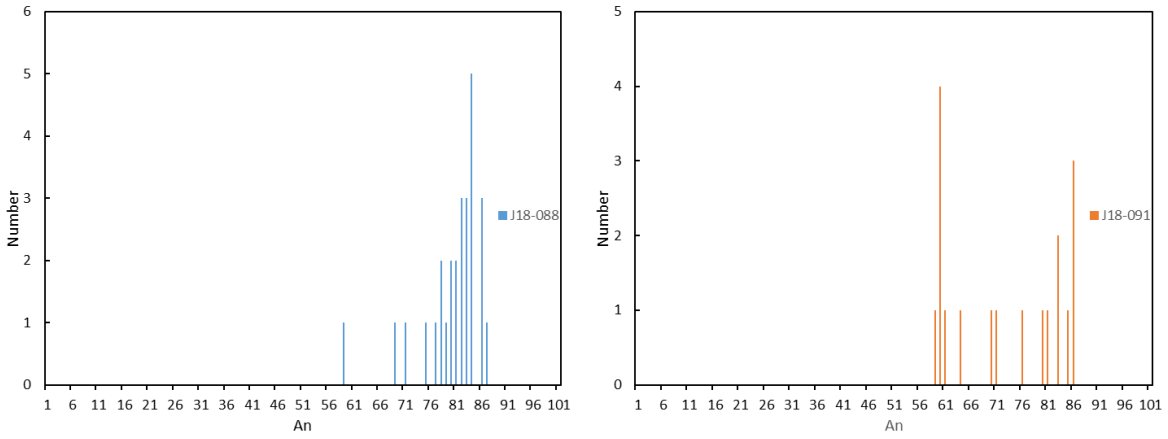

Fig. 5.6 An distribution for plagioclase in Chagres Complex.

Normal compositional zonation is common, while reversed compositional zonation is less common (Fig. 5.7). In examples displaying normal zonation, An number of the core can be up to ~ 85 and the rim, as low as ~ 77 (Fig. 5.7 A). In reversed zonation, An number of the core is as low as ~ 68 and the rim, up to ~80 (Fig. 5.7 B).

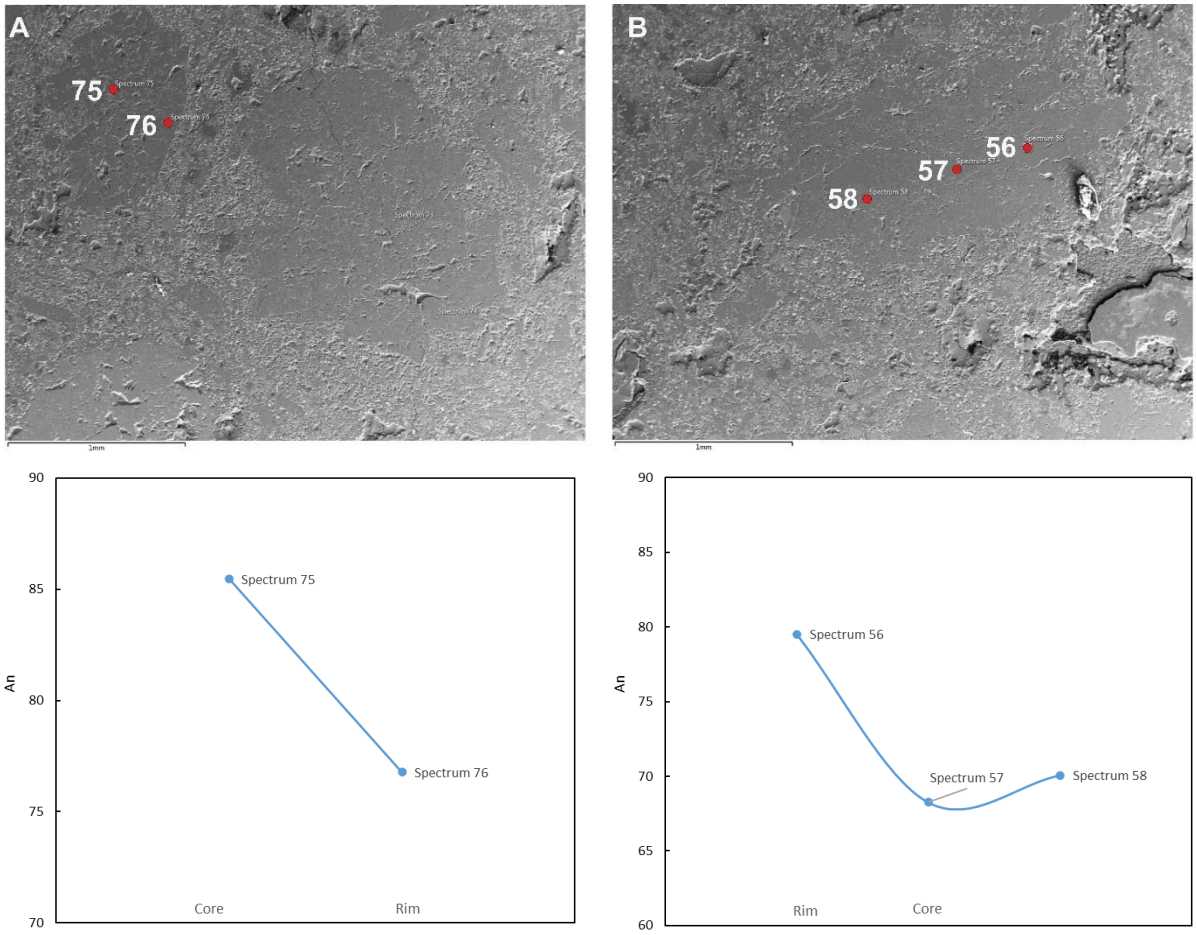

Fig. 5.7 Normal zonation (A) and reversed zonation (B) of plagioclase in J18-088.

5.2 Bas Obispo Formation

5.2.1 Clinopyroxene

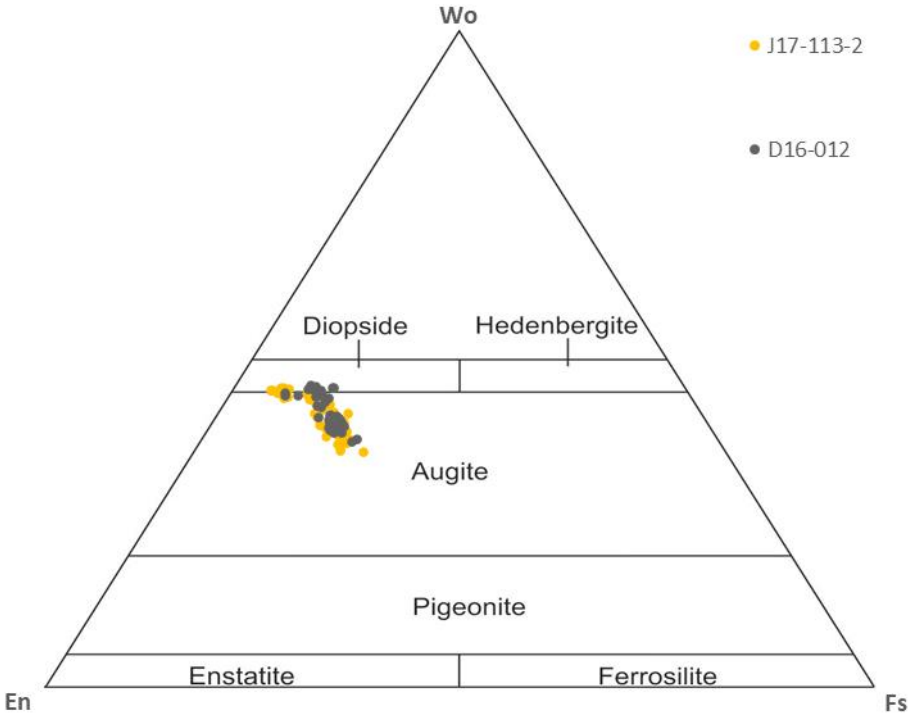

Fig. 5.8 Clinopyroxene classification for Bas Obispo Formation (classification diagram from Morimoto et al., 1988).

Clinopyroxene in this group is mainly augite with subordinate diopside (Fig. 5.8). The grains exhibit the following composition ranges: Mg# = 69-92, Wo = 36-46, En = 42-50, and Fs =5-20. On bivariant diagrams (Fig. 5.9), TiO_2 (0.14-0.75 wt.%) and FeO (2.9-12.2 wt.%) increase with decreasing Mg#. On the contrary, CaO (17.2-22.9 wt.%) decreases with decreasing Mg# and SiO_2 (50.1-54.9 wt.%) show the similar trend. As Mg# decreases, Al_2O_3 (1.3-4.8 wt.%) increases first and then decreases in these two samples. MnO (0.08-0.47 wt.%) increases with decreasing Mg# but shows a steeper slope at lower Mg#. Clinopyroxene in J17-113-2 spans a large range in composition and high Mg# (>84) clinopyroxene is in disequilibrium with the whole rock composition (Fig. 5.10). In Mg# distribution diagrams, clinopyroxene has a bimodal distribution. In bivariant diagrams, clinopyroxene plot as three groups: low Mg# (<79) group plot in the calc-alkaline arc field while the high Mg# (>79) groups plot in the tholeiitic arc field in Al-Ti diagram (Fig. 5.10). In Mg#-Ti/Al diagram, Ti/Al increase with decreasing Mg# and the slope is steeper at low Mg#. For sample D16-012, high Mg# (>79) clinopyroxene is not in equilibrium with the whole rock composition while low Mg# (<79) clinopyroxene is in equilibrium. No bimodal Mg# distribution is observed in this sample but several high Mg# away from the peak composition are found. High Mg# (>79) are in the tholeiitic arc field while low Mg# (<79) plot on the boundary in Al-Ti diagram and Ti/Al increases more rapidly at the low Mg# (Fig. 5.11).

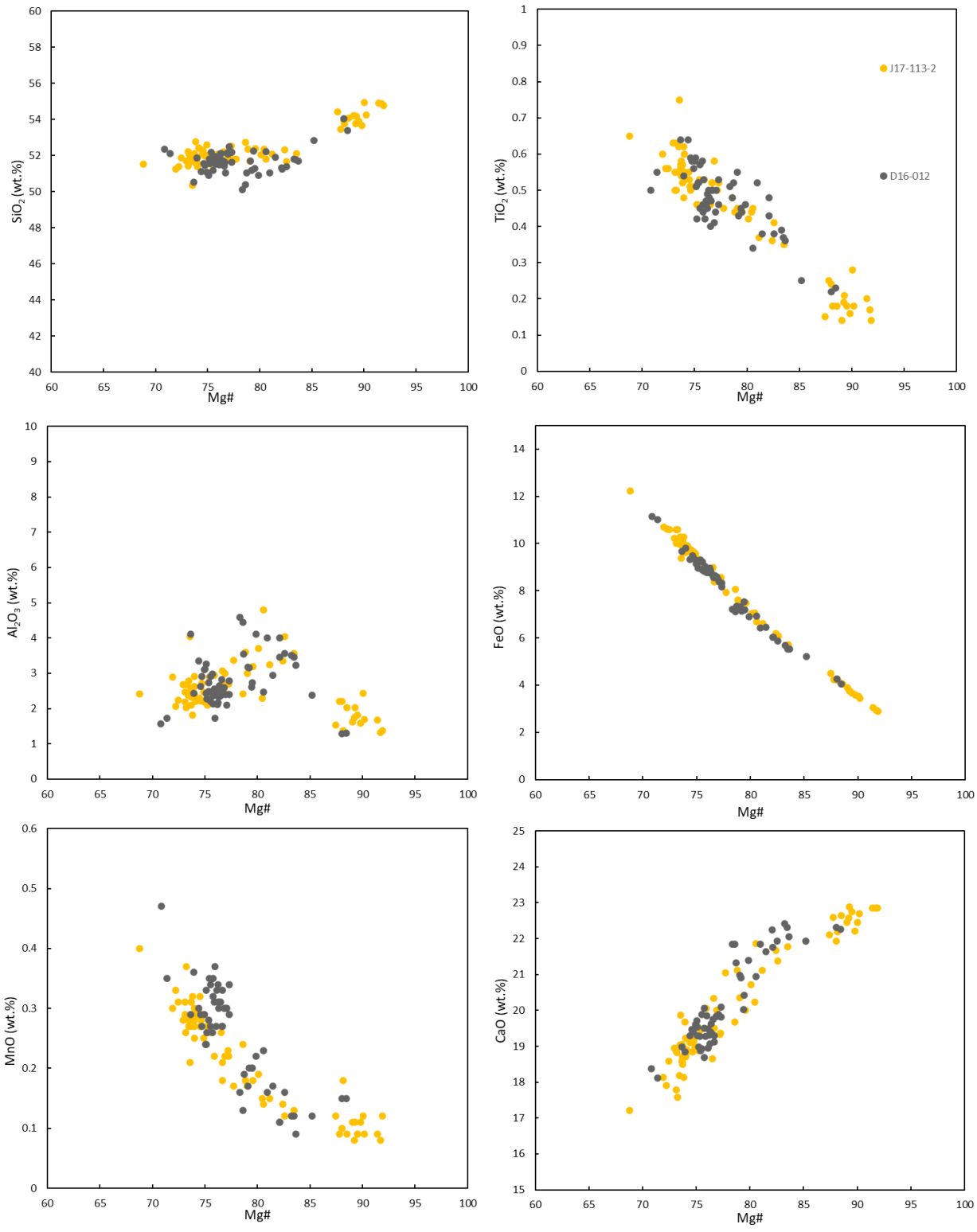

Fig. 5.9 Representative elements plotted against Mg# for clinopyroxene of Bas Obispo Formation.

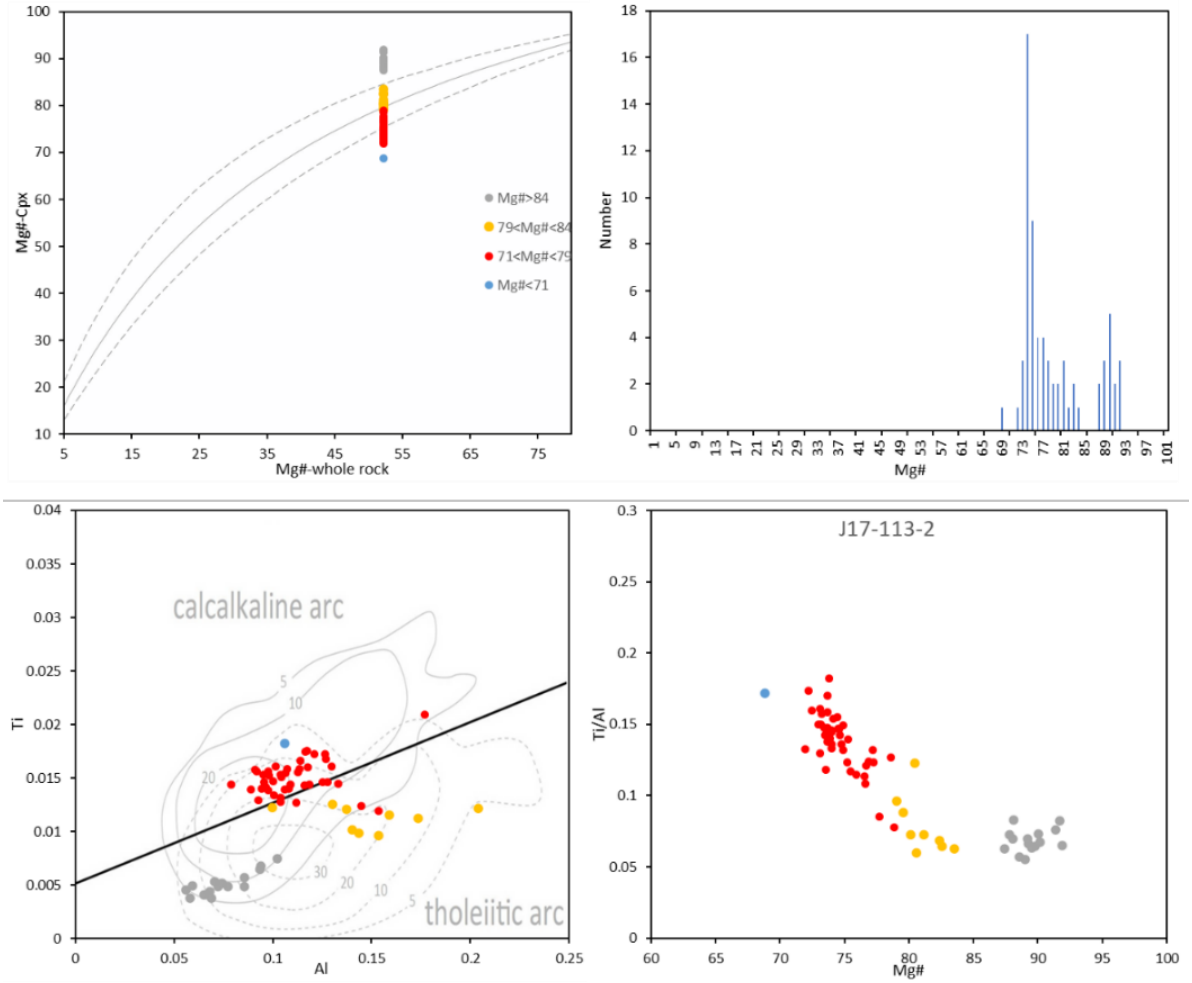

Fig. 5.10 Rhodes diagram, Mg# distribution diagram, Ti vs Al and Ti/Al vs Mg# for clinopyroxene in J17-113-2 (In Rhodes diagram, Kd=0.28±0.08 from Putirka (2008); boundary in Ti vs Al is from Leterrier (1982) and Al, Ti are calculated based on 4 cations).

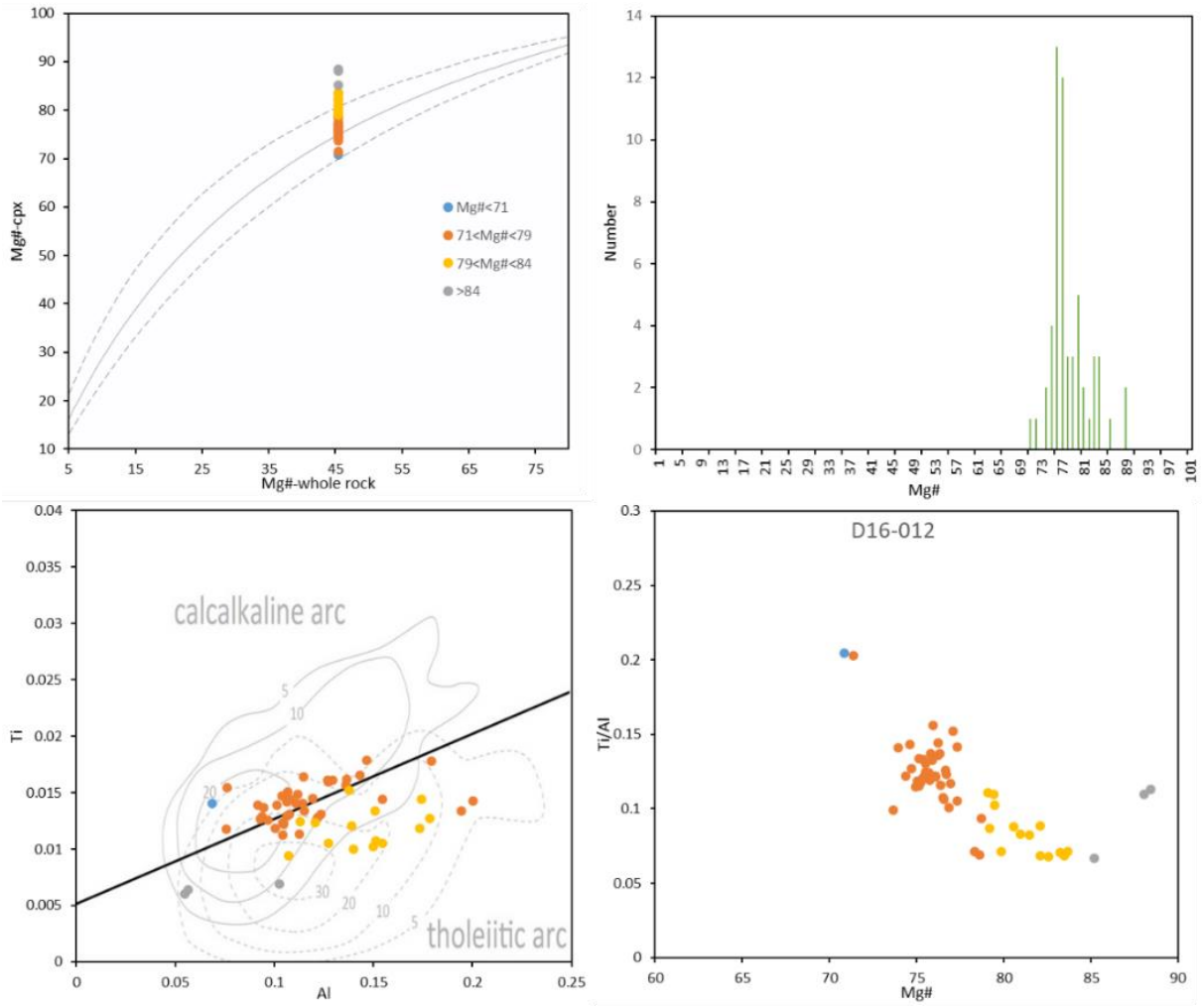

Fig. 5.11 Rhodes diagram, Mg# distribution diagram, Ti vs Al and Ti/Al vs Mg# for clinopyroxene in D16-012 (In Rhodes diagram, Kd=0.28±0.08 from Putirka (2008); boundary in Ti vs Al is from Leterrier (1982) and Al, Ti are calculated based on 4 cations).

Zonation is common in this group. In normal zonation, high Mg# (up to 90) occurs in the core and low Mg# (<75) in the rim (Fig. 5.12). Only a few cases of reverse zonation have been found.

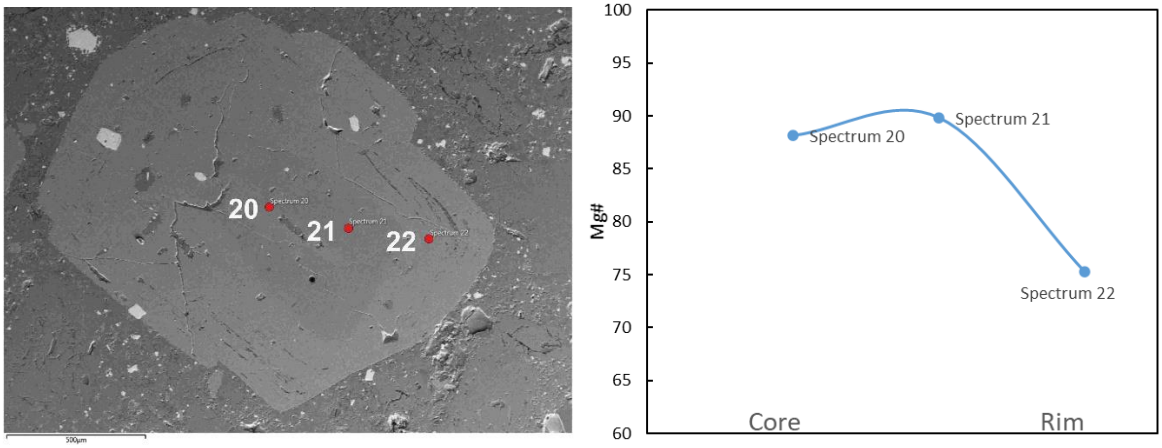

Fig. 5.12 Normal zonation of clinopyroxene in J17-113-2.

5.2.2 Plagioclase

Feldspar in this group range in composition from albite to bytownite. The An value ranges from 1 to 80 in D16-012 and from 55 to 87 in J17-113-2 (limited analysis in J17-113-2). Both normal zonation and reversed zonation are common in this group (Fig. 5.15, Fig. 5.16). In normal zonation, the An-number of the core can be >85 and the rim can be <60 (Fig. 5.15). It is worth mentioning that albite is usually found as the core in reversed zonation with An<5 for the core and An>60 for the rim (Fig. 5.16).

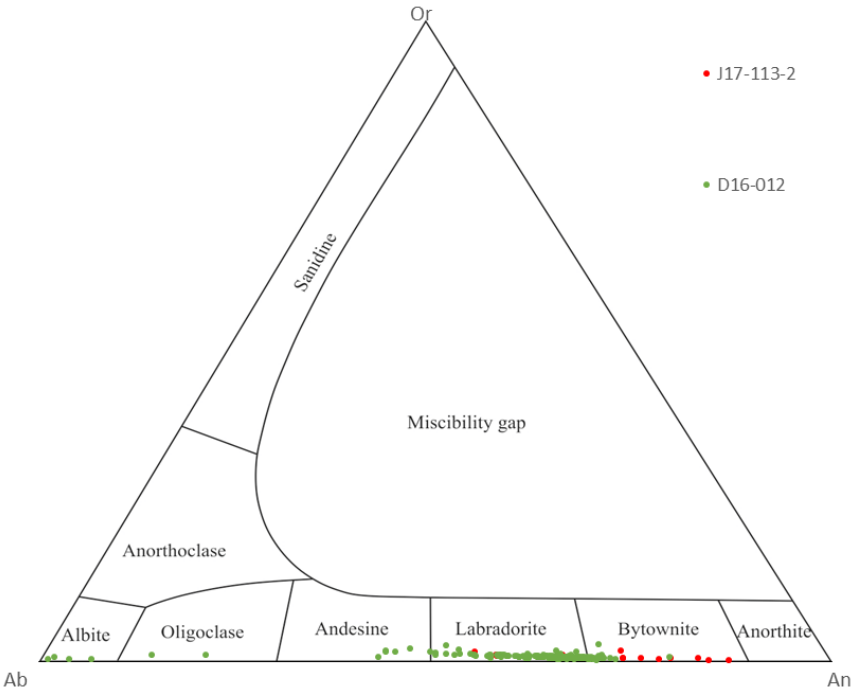

Fig. 5.13 Feldspar classification for Bas Obispo Formation (classification diagram from Smith and Brown (1988)).

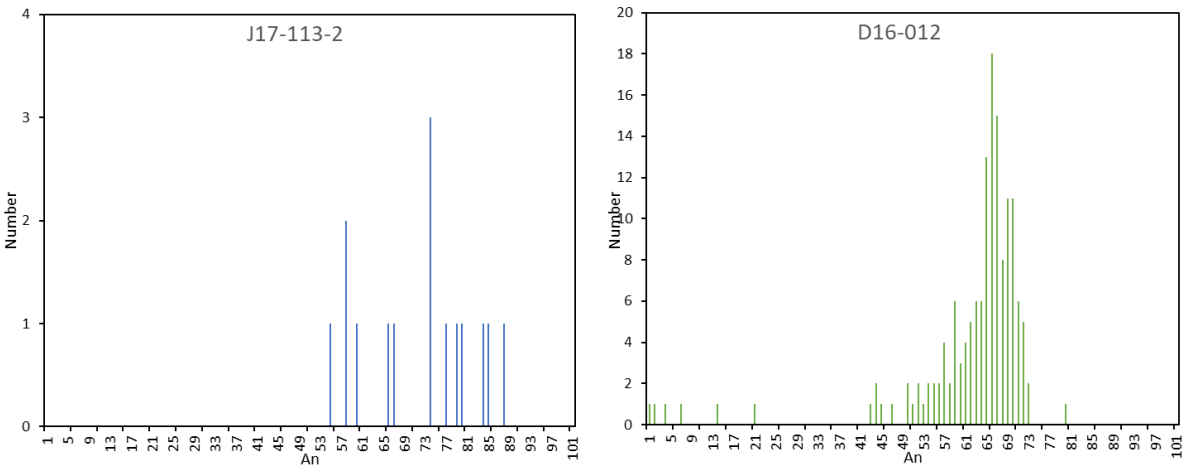

Fig. 5.14 An-number distribution for plagioclase in the Bas Obispo Formation.

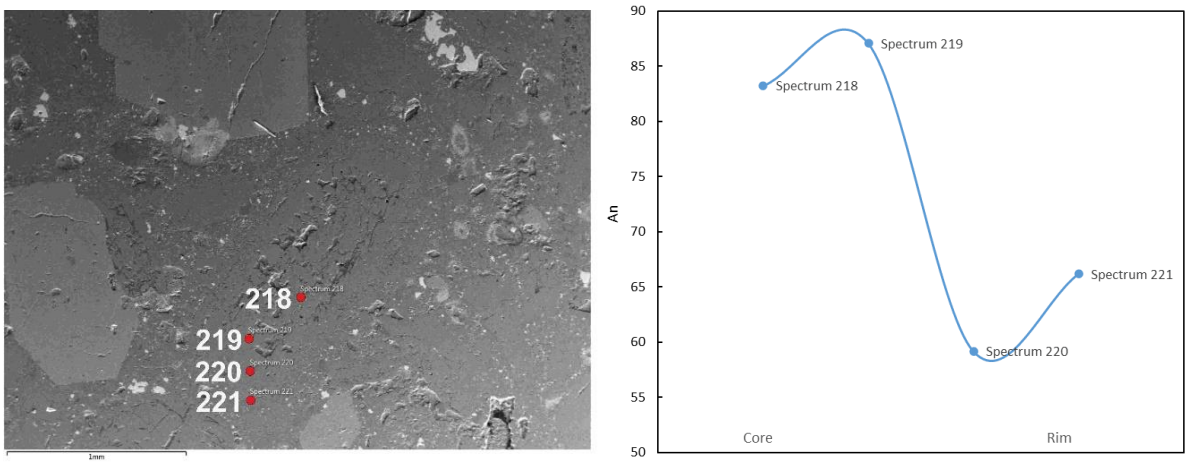

Fig. 5.15 Normal zonation of plagioclase in J17-113-2.

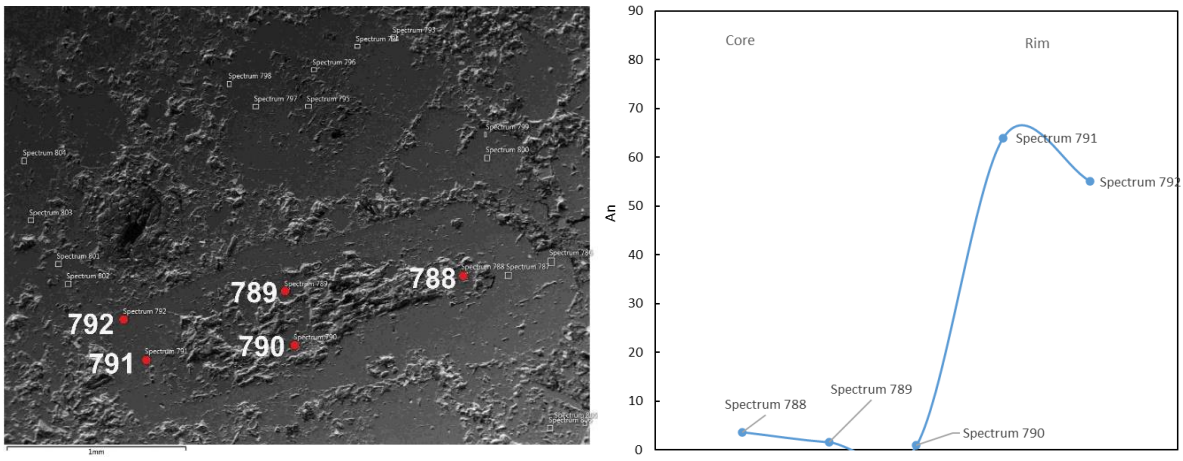

Fig. 5.16 Reversed zonation of plagioclase in D16-012.

5.3 Panama Formation

Clinopyroxene, plagioclase, orthopyroxene, saponite, glass, and matrix from the Panama Formation have been analysed by SEM-EDS.

5.3.1 Clinopyroxene

Clinopyroxene in this group are mainly augite with subordinate diopside (Fig. 5.17). Pigeonite is rare and one has been found in J17-001. They (pigeonite not included) exhibit the following compositional ranges: Mg#= 66-90, Wo= 32-46, En= 41-51, Fs=6-23. On bivariant diagrams (Fig. 5.18), TiO_2 (0.07-0.87 wt.%) and FeO (3.6-13.7 wt.%) increase with decreasing Mg#. CaO (13.9-22.7 wt.%) and SiO_2 (48.9-54.9 wt.%) decreases as Mg# decreases and the slope is steeper at lower Mg# in CaO vs Mg# diagram. As Mg# decreases, Al_2O_3 (0.46-9.8 wt.%) increases first and then decreases. MnO (0.08-0.54 wt.%) increases with decreasing Mg# but shows steeper slope at lower Mg#.

Clinopyroxene from individual samples in this group have variable Mg# and Ti/Al (Fig. 5.24; Fig. 5.20; Fig. 5.21; Fig. 5.22; Fig. 5.23; Fig. 5.24), and rocks can be divided into two sub-groups

according to clinopyroxene composition. One sub-group (Pam1) has a large range and bimodal or 3-peak distribution of Mg# and shows disequilibrium in Rhodes diagrams (Fig. 5.24; Fig. 5.20; Fig. 5.21; Fig. 5.22) (including sample J18-059-2, J17-059-2, J17-102 and J17-001). The other sub-group (Pam2) has relatively homogeneous clinopyroxene which appears to be in equilibrium and has a unimodal distribution (Fig. 5.23; Fig. 5.24). Samples J17-053, J17-082, J17-084 and especially J17-036-1 and J18-100 are the typical samples in this group. For clinopyroxene in Pam1, as Mg# decreases, Ti/Al increases more rapidly at lower Mg# than at higher Mg#. The clinopyroxene compositions of the Panama Formation and Las Cascadas Formation (discussed below), can be divided into 3 groups: CPX1, CPX2, CPX3. CPX1 have high Mg# (> 77), low Al and low Ti/Al (< 0.15), and plot in tholeiitic arc field on a Ti vs Al diagram. CPX2 have low Mg# (< 77) and low Ti/Al (< 0.15), and plot below or along the boundary in the Ti vs Al diagram, whereas CPX3 have low Mg# (< 77) and high Ti/Al (> 0.15), and plot in the calc-alkaline arc field.

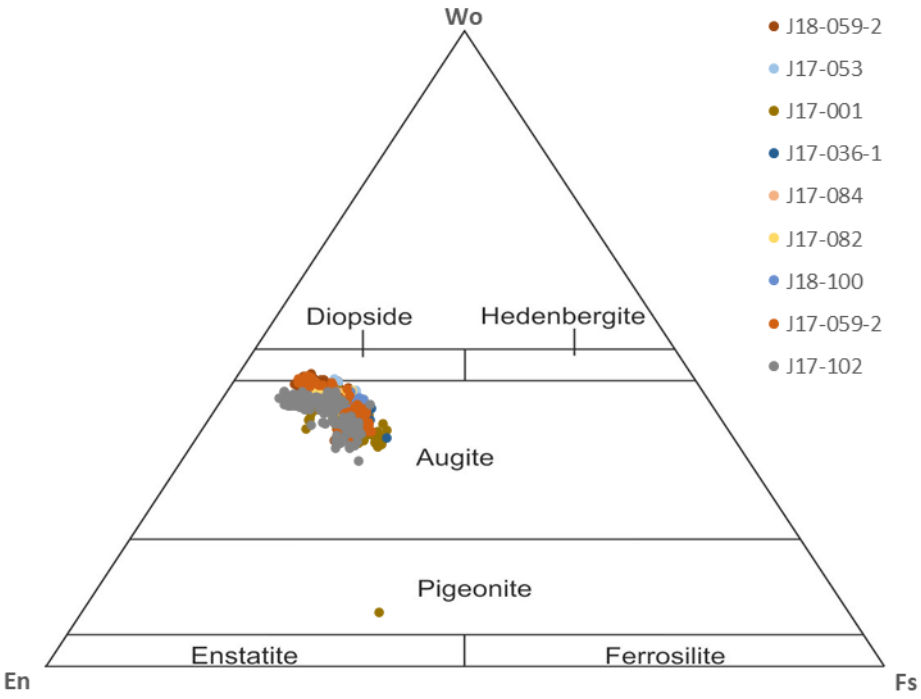

Fig. 5.17 Clinopyroxene classification for Panama Formation (classification diagram from Morimoto et al., 1988).

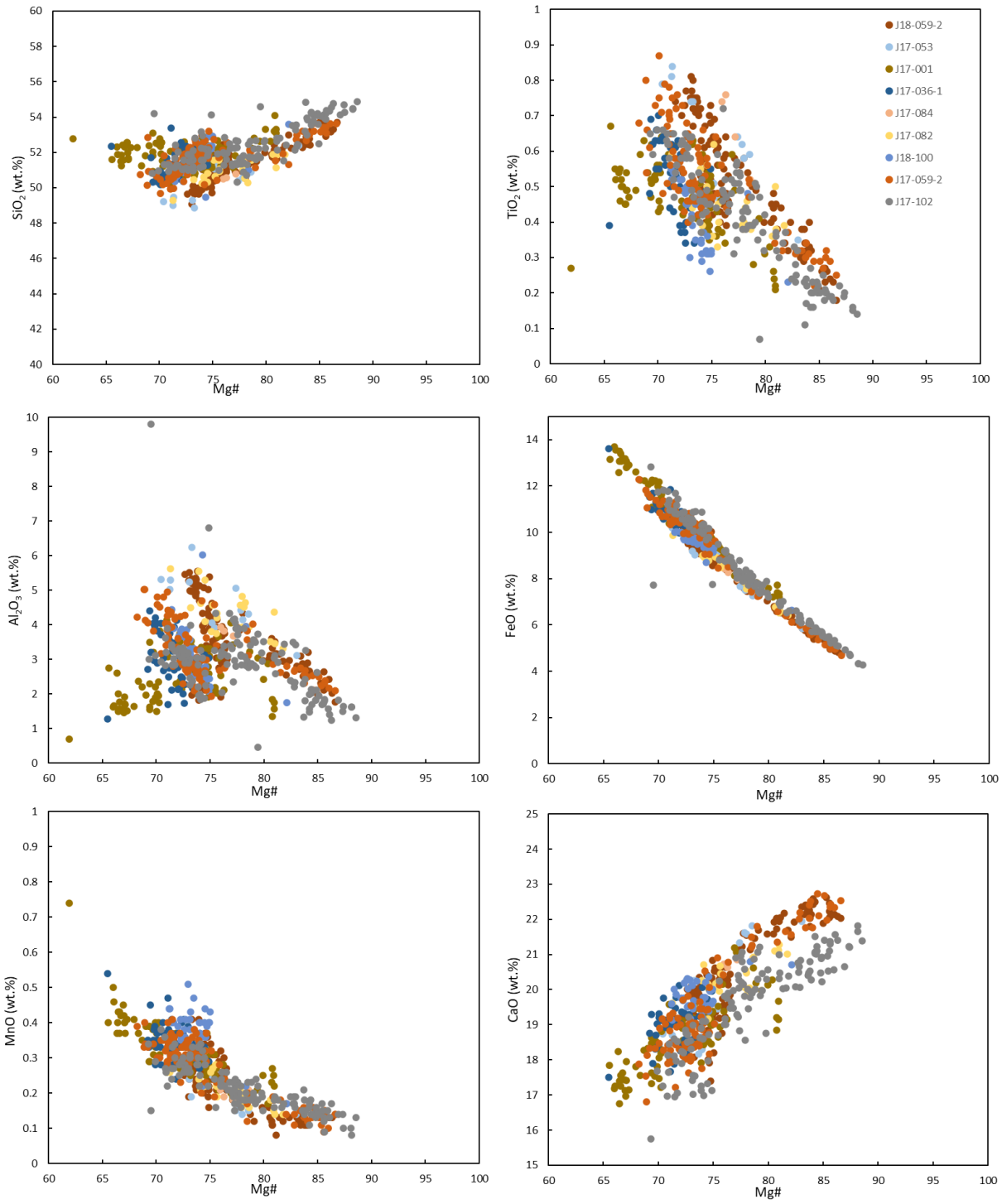

Fig. 5.18 Representative elements plotted against Mg# for clinopyroxene of Panama Formation.

For sample J18-059-2, only CPX1 and CPX2 are found. Mg# ranges from 72 to 87 and CPX2 are in equilibrium while CPX1 are above the equilibrium in Rhodes diagram (Fig. 5.19). Clinopyroxene crystals show bimodal distribution in the Mg# distribution diagram. CPX1 plot in the tholeiitic arc field while CPX2 plot along the boundary in Ti vs Al diagram. Ti/Al increases with decreasing Mg# but CPX2 show steeper slope than CPX1.

Similar to J18-059-2, only CPX1 and CPX2 are found in J17-059-2; Mg# ranges from 68 to 87 and parts of both CPX1 and CPX2 are not in equilibrium in Rhodes diagram (Fig. 5.20). In Mg# distribution diagram, it shows a bimodal distribution. CPX1 plot in the tholeiitic arc field while CPX2 plot along the boundary in Ti vs Al diagram. Ti/Al increases with decreasing Mg# but CPX2 seem to have steeper slope than CPX1.

For sample J17-102, only CPX1 and CPX2 are found and Mg# ranges from 69 to 89. CPX1, further divided into Mg#> 81and 75<Mg<81, are overall in equilibrium with the whole rock composition while CPX2 are below the equilibrium zone in Rhodes diagram (Fig. 5.21). In Mg# distribution diagram, it shows a three-peak distribution. CPX1 (Mg#> 75) plot in the tholeiitic arc field while CPX2 plot along the boundary in Ti vs Al diagram. Ti/Al increases with decreasing Mg# but CPX2 have steeper slope than CPX1.

In sample J17-001, CPX1, CPX2 and CPX3 are all found and Mg# ranges from 62 to 81. CPX1 and CPX2 are in equilibrium with the whole rock while CPX3 are below the equilibrium zone in the Rhodes diagram (Fig. 5.22).). In Mg# distribution diagram, it shows three-peak (or four-peak?) distribution. In Ti vs Al diagram, CPX1 plot in the tholeiitic arc field, CPX2 plot along the boundary, and CPX3 plot in calc-alkaline arc field. Ti/Al increases with decreasing Mg#.

Clinopyroxene in Pam2 are quite homogeneous and mainly belong to group CPX2 in these two samples but two CPX3 crystals are found in J17-036-1 and two CPX1 crystals are found in J18-100 (Fig. 5.23; Fig. 5.24). Overall, clinopyroxene in Pam2 is in equilibrium with its whole rock compositions with only several exceptions below (Fig. 5.23) or above (Fig. 5.24) the equilibrium zone. Mg# is clustered to form unimodal distribution when excluding the exceptions. In the Ti vs Al diagram, clinopyroxene in J17-036-1 plot along the boundary while clinopyroxene in J18-100 plot below the boundary. The rest of the samples in Pam2, e.g., J17-053, J17-084 and J17-082 have a relatively low content of phenocrysts, especially for J17-084 for which only four analyses were collected. Clinopyroxene in these three samples is in equilibrium with their whole rock compositions and Mg# is clustered to form unimodal distribution (Fig. 5.25). In the Ti vs Al diagram, clinopyroxene plots below the boundary (J17-053 and J17-082) or along the boundary (J17-084). No obvious trend was found in Ti/Al vs Mg# diagram and most of the clinopyroxene in these three samples are in group CPX2 (Fig. 5.25).

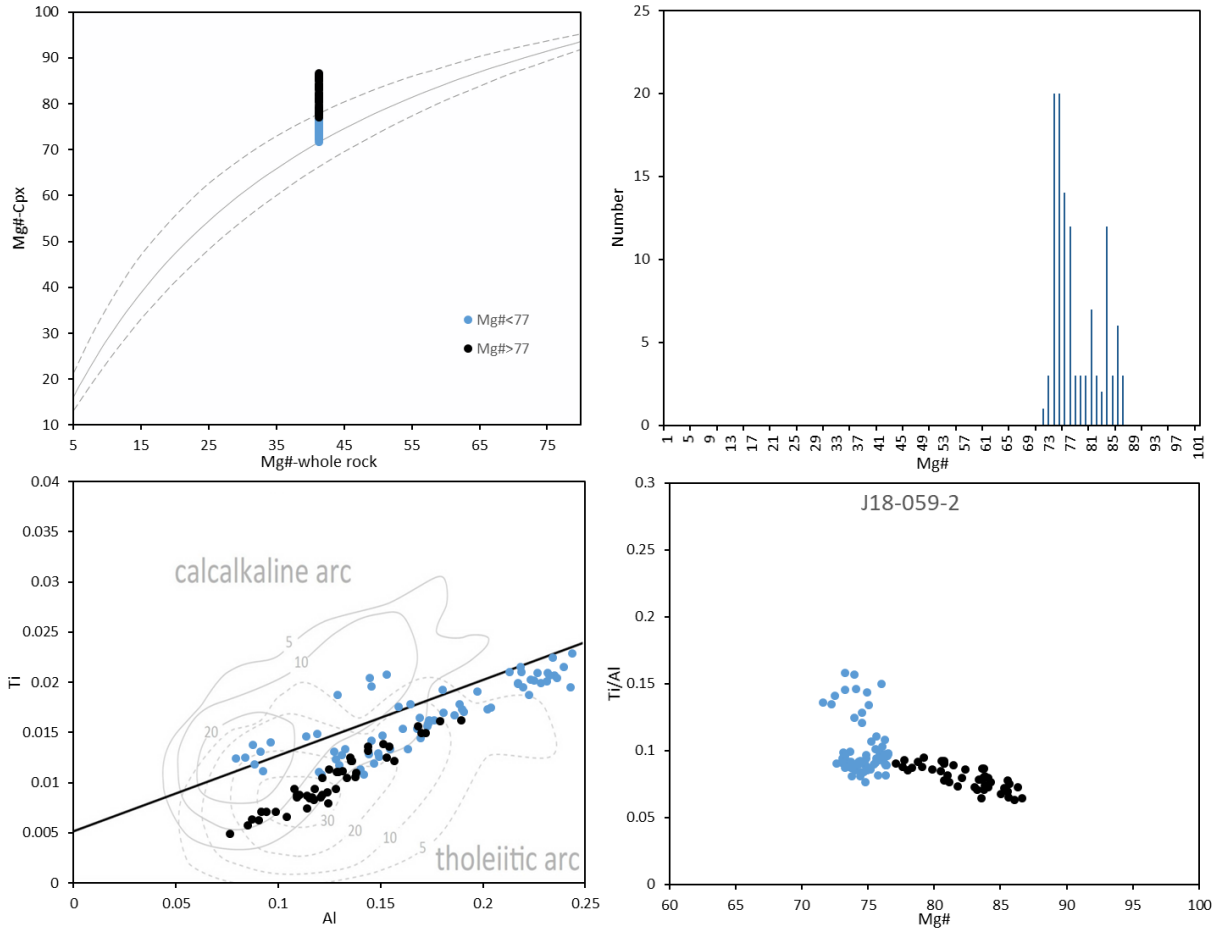

Fig. 5.19 Rhodes diagram (Kd=0.28±0.08 from Putirka (2008)), distribution diagram, Ti vs Al (boundary is from Leterrier (1982) and Al, Ti are calculated based on 4 cations) and Ti/Al vs Mg# for clinopyroxene in J18-059-2.

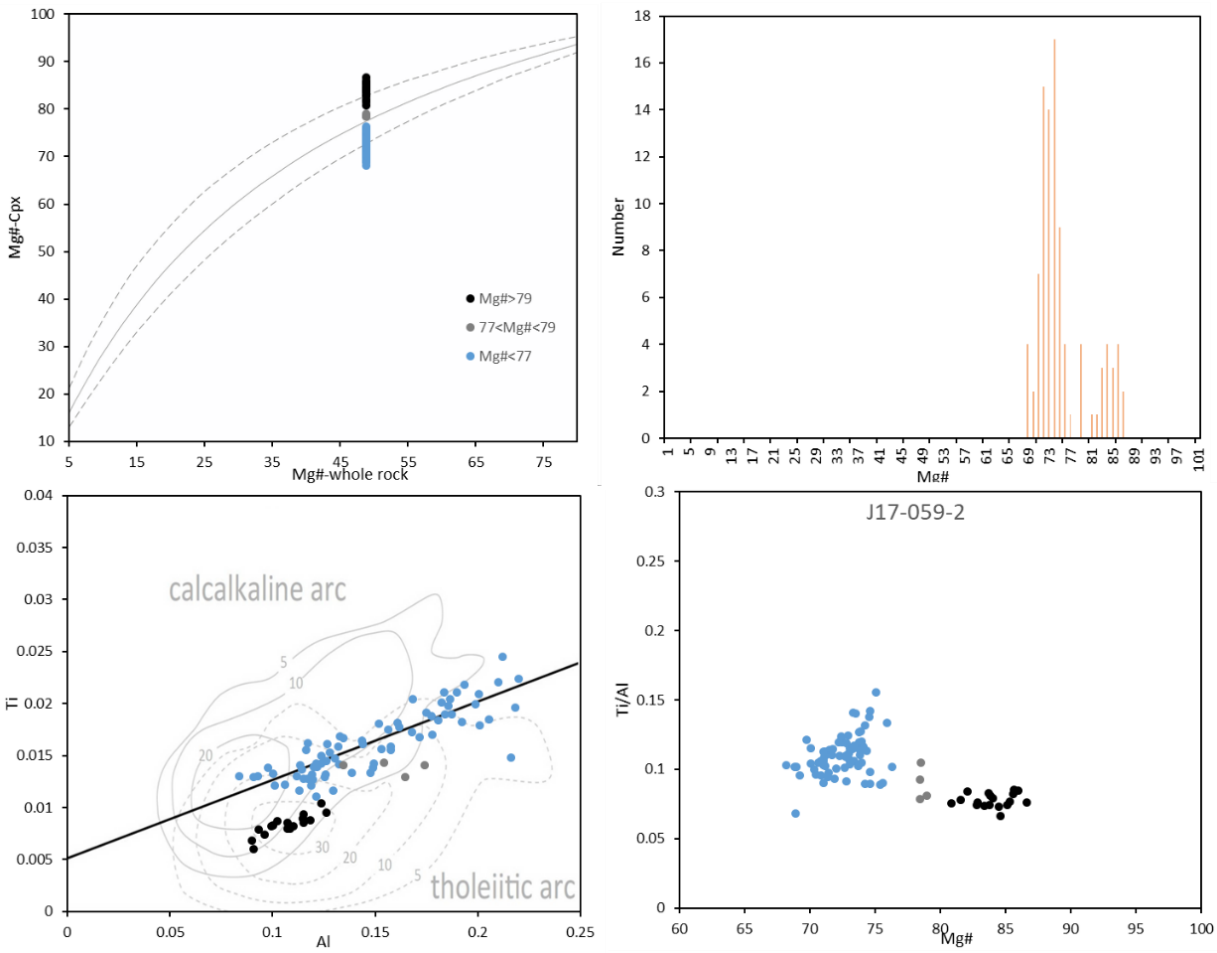

Fig. 5.20 Rhodes diagram (Kd=0.28±0.08 from Putirka (2008)), distribution diagram, Ti vs Al (boundary is from Leterrier (1982) and Al, Ti are calculated based on 4 cations) and Ti/Al vs Mg# for clinopyroxene in J17-059-2.

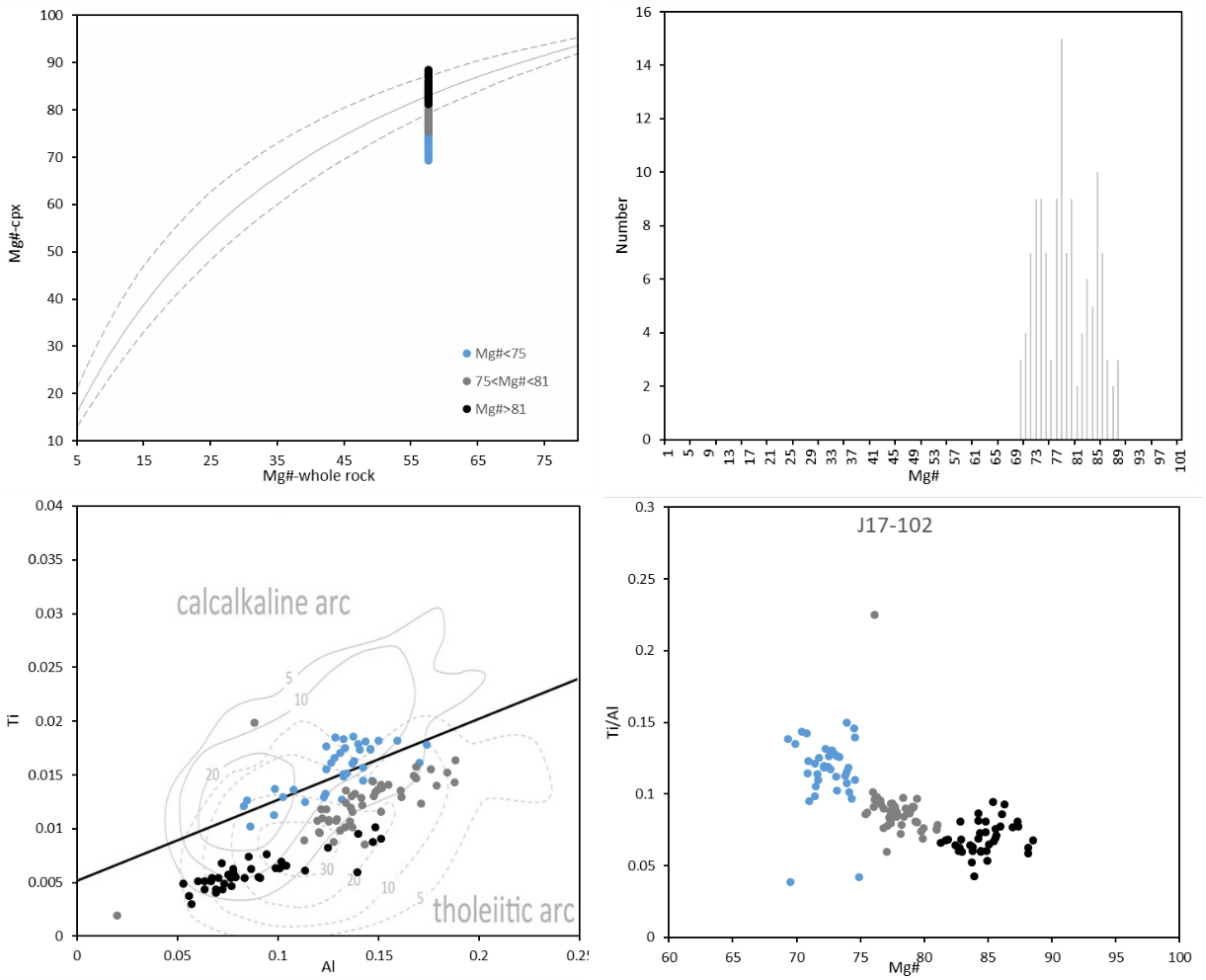

Fig. 5.21 Rhodes diagram (Kd=0.28±0.08 from Putirka (2008)), distribution diagram, Ti vs Al (boundary is from Leterrier (1982) and Al, Ti are calculated based on 4 cations) and Ti/Al vs Mg# for clinopyroxene in J17-102.

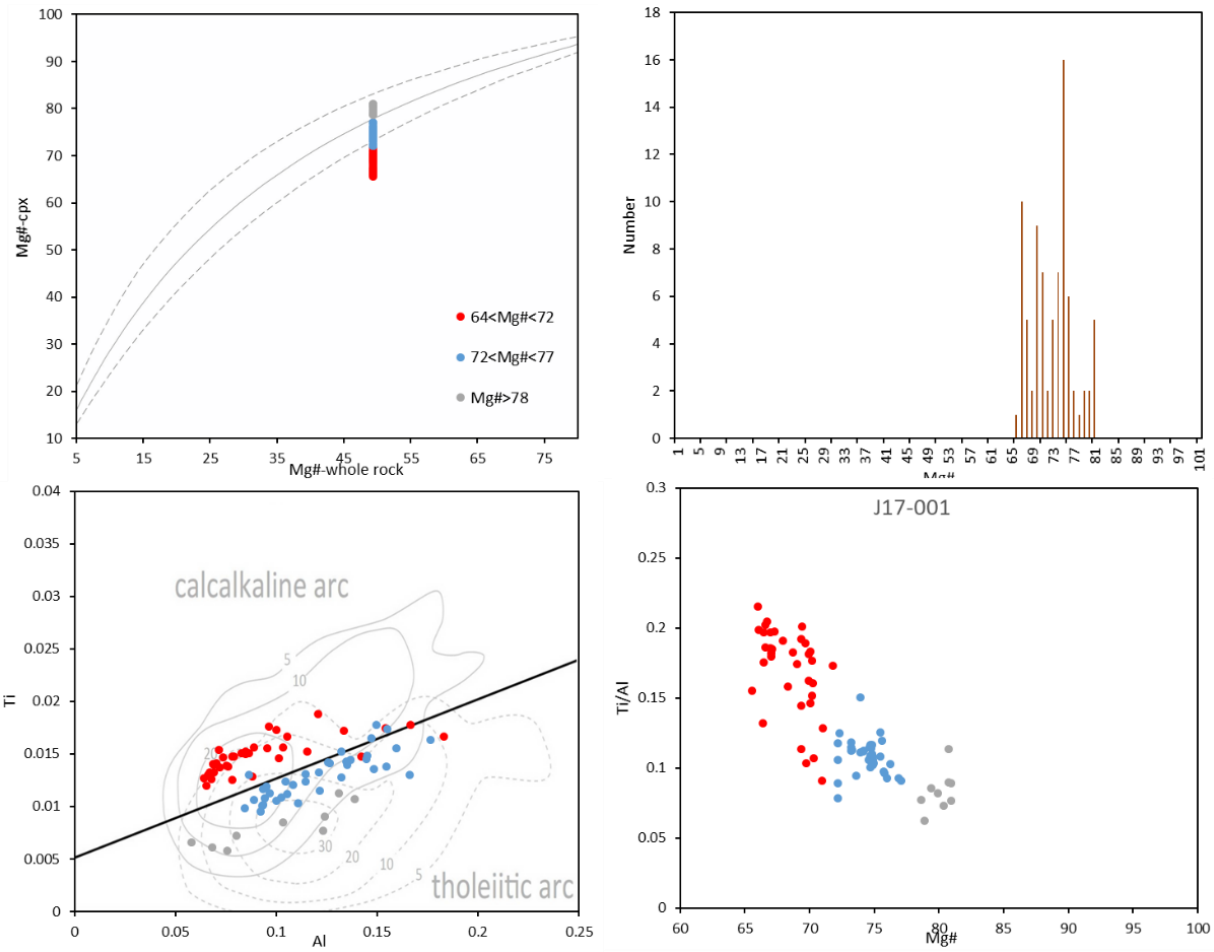

Fig. 5.22 Rhodes diagram (Kd=0.28±0.08 from Putirka (2008)), distribution diagram, Ti vs Al (boundary is from Leterrier (1982) and Al, Ti are calculated based on 4 cations) and Ti/Al vs Mg# for clinopyroxene in J17-001 (these diagrams are only based on Mg#, some CPX2 are included into CPX3 as red filled circles).

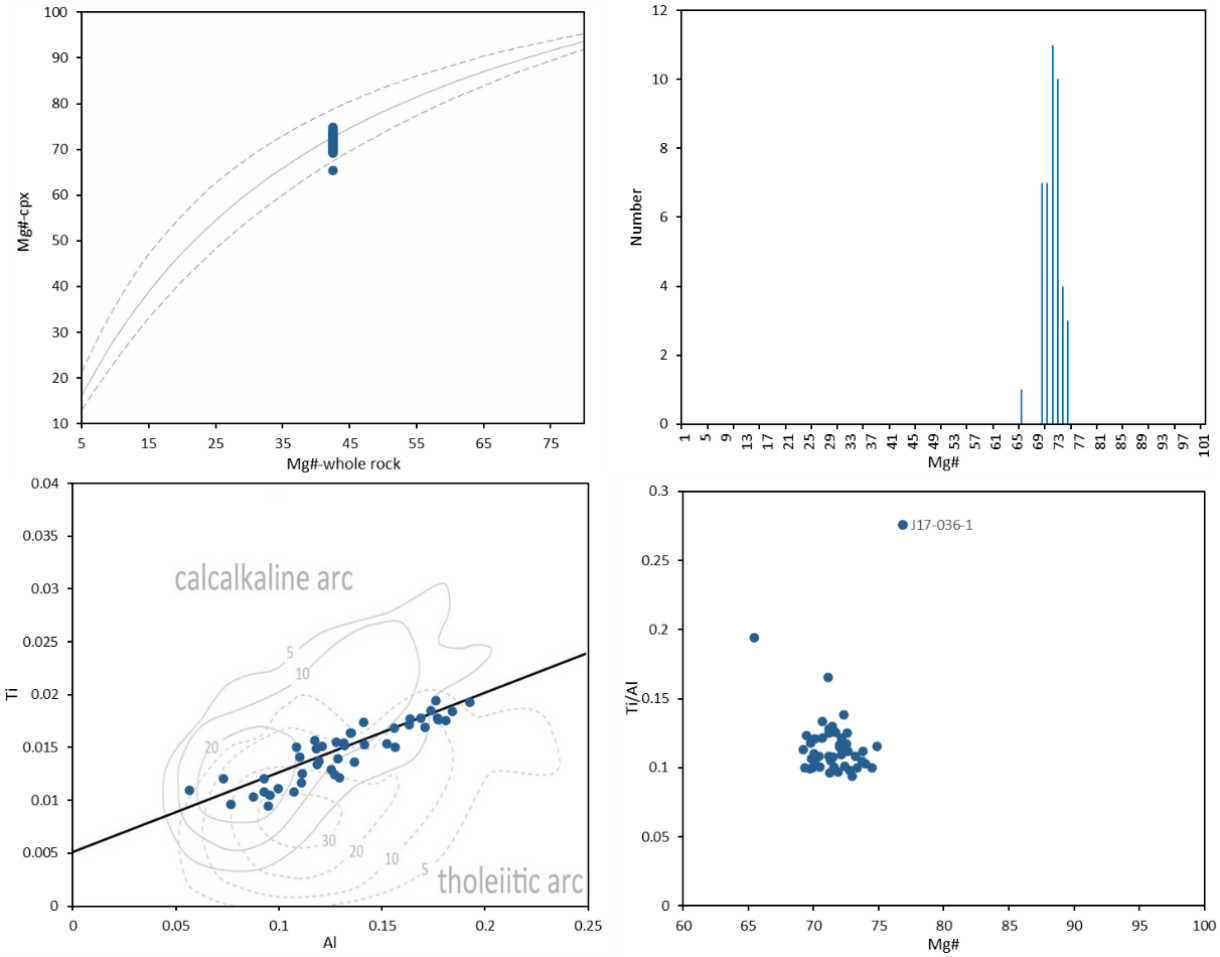

Fig. 5.23 Rhodes diagram (Kd=0.28±0.08 from Putirka (2008)), distribution diagram, Ti vs Al (boundary is from Leterrier (1982) and Al, Ti are calculated based on 4 cations) and Ti/Al vs Mg# for clinopyroxene in J17-036-1.

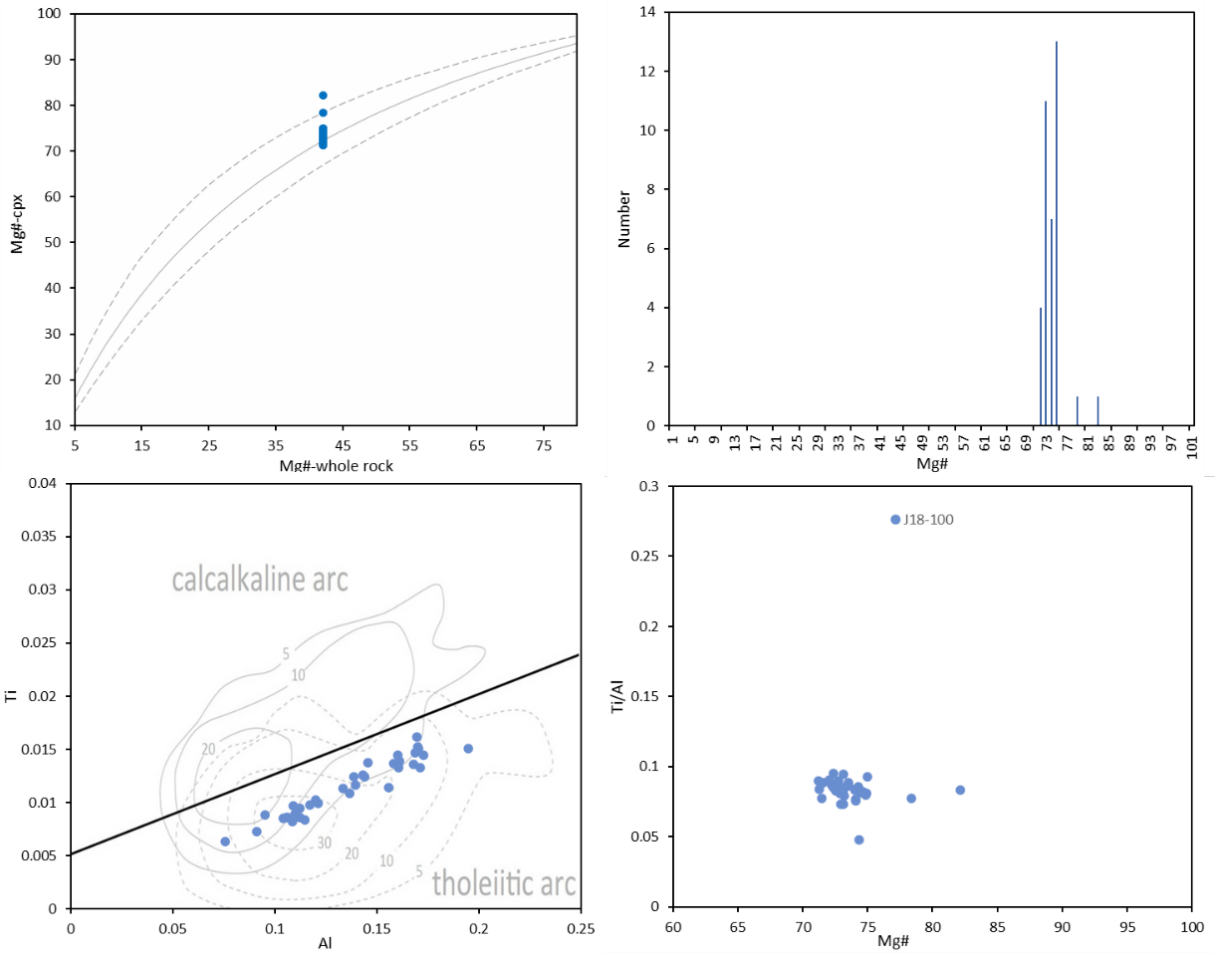

Fig. 5.24 Rhodes diagram (Kd=0.28±0.08 from Putirka (2008)), distribution diagram, Ti vs Al (boundary is from Leterrier (1982) and Al, Ti are calculated based on 4 cations) and Ti/Al vs Mg# for clinopyroxene in J18-100.

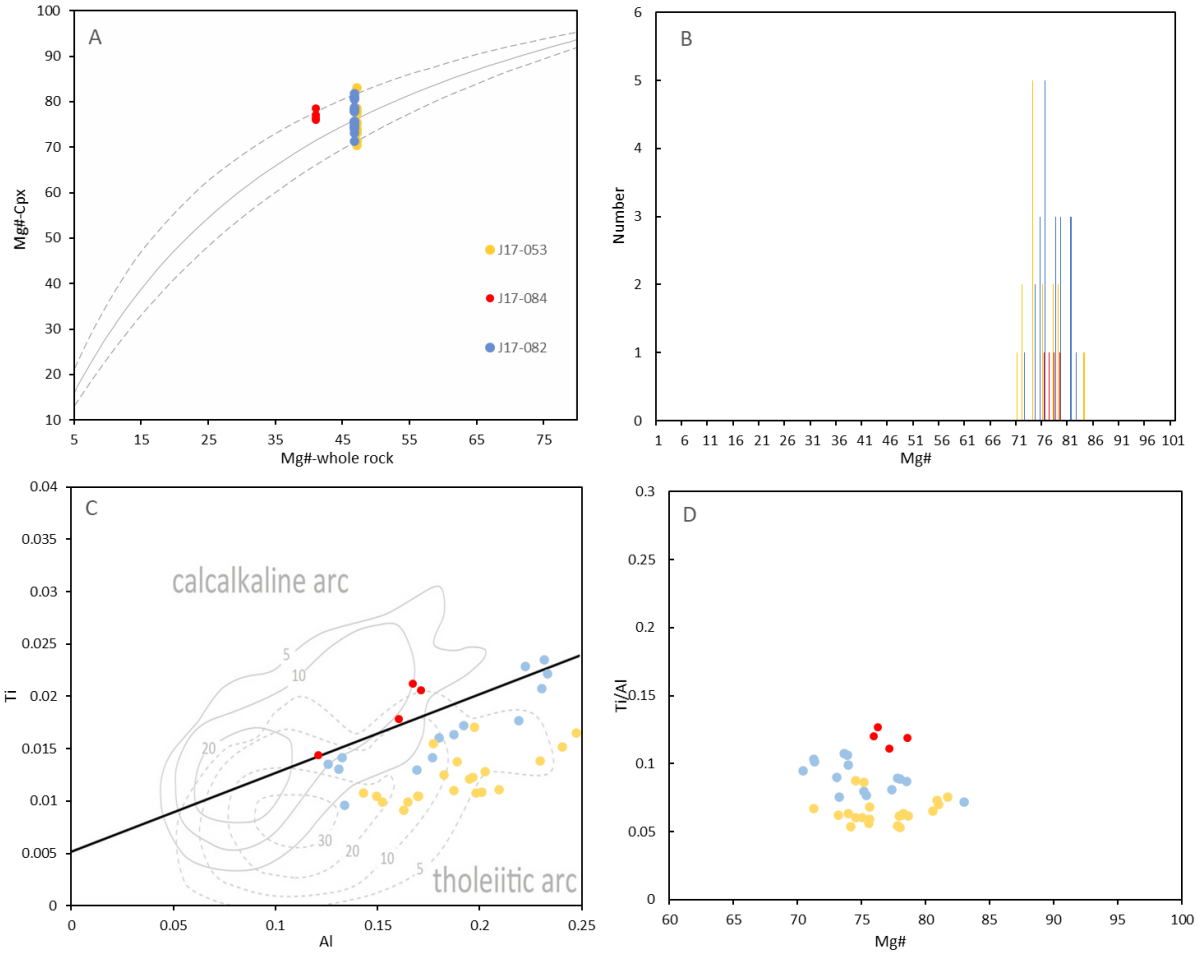

Fig. 5.25 Rhodes diagram (Kd=0.28±0.08 from Putirka (2008)), distribution diagram, Ti vs Al (boundary is from Leterrier (1982) and Al, Ti are calculated based on 4 cations) and Ti/Al vs Mg# for clinopyroxene in J17-053, J17-084 and J17-082.

In sample J18-059-2, CPX1 composition does not occur as single crystals and is only found as the core with CPX2 as the rim (Fig. 5.26 A). For phenocrysts with only CPX2 composition, Mg# spans a small range from 73 to 76 and both normal zonation and reversed zonation (Fig. 5.26 B) are common.

In sample J17-059-2, both reversed zonation (Fig. 5.27) and normal zonation is common for phenocrysts with only CPX2 composition. When phenocrysts are zoned with high Mg# (CPX1) and low Mg# (CPX2), CPX1 are only found as cores and CPX2 as mantle/rim. For phenocrysts with only CPX1 composition, they usually occur as reverse zoned crystals.

In sample J17-102, clinopyroxene phenocrysts are normally zoned. For normal zonation (Fig. 5.28), the core and mantle are CPX1 and the rim is CPX2. However, the CPX1 core can be slightly reversed, e.g., Mg# increases first from core to mantle before decreasing to rim. For reversed zonation in phenocrysts with only CPX1 composition, the clinopyroxene has a low Mg# core and high Mg# mantle/rim (Fig. 5.29). For reversed zonation in phenocrysts with only CPX2 composition, CPX2 can be found in the core with CPX2 as mantle/rim. Apart from these clinopyroxenes with simple zonation,

complex oscillatory zonation is also common in this sample. In Fig. 5.30, the phenocryst can be as long as ~5 mm with remarkedly zonation in crossed-polarised light and the BSE image. Taking spectrum 1426 and 1429 as the core (1427 and 1428 are orthopyroxene inclusions), Mg# increases and then decreases and this occurs at least three times which form three peaks from spectrum 1429 to 1434. This also demonstrates that clinopyroxene phenocrysts in this sample can be reversely zoned with CPX2 as the core while CPX1 as the rim, which was not found in J18-059-2 and J17-059-2.

J17-001 comprises CPX1, CPX2 and CPX3. Due to small size of phenocrysts, J17-001 does not show complex zonation and Mg# spans a small range in individual phenocrysts. Normal zonation is the dominant zonation type in this sample. CPX1 only account for a small amount in the dataset of this study and they are only found as the core, with CPX2 or CPX3 as the mantle/rim. CPX2 and CPX3 can also be found together in one phenocryst and these phenocrysts show normal zonation with CPX2 gradually evolving to be CPX3 (Fig. 5.31).

Clinopyroxene phenocrysts in J17-036-1 and J18-100 are relatively small (0.5-1 mm in diameter) comparing with Pam1 and are normally euhedral. The composition spans a small range in individual crystals and the maximum difference of Mg# in single phenocrysts is 6 (Fig. 5.32 A). Both normal zonation (Fig. 5.32 B) and reversed zonation (Fig. 5.32 A) can be found but normal zonation is the dominant type.

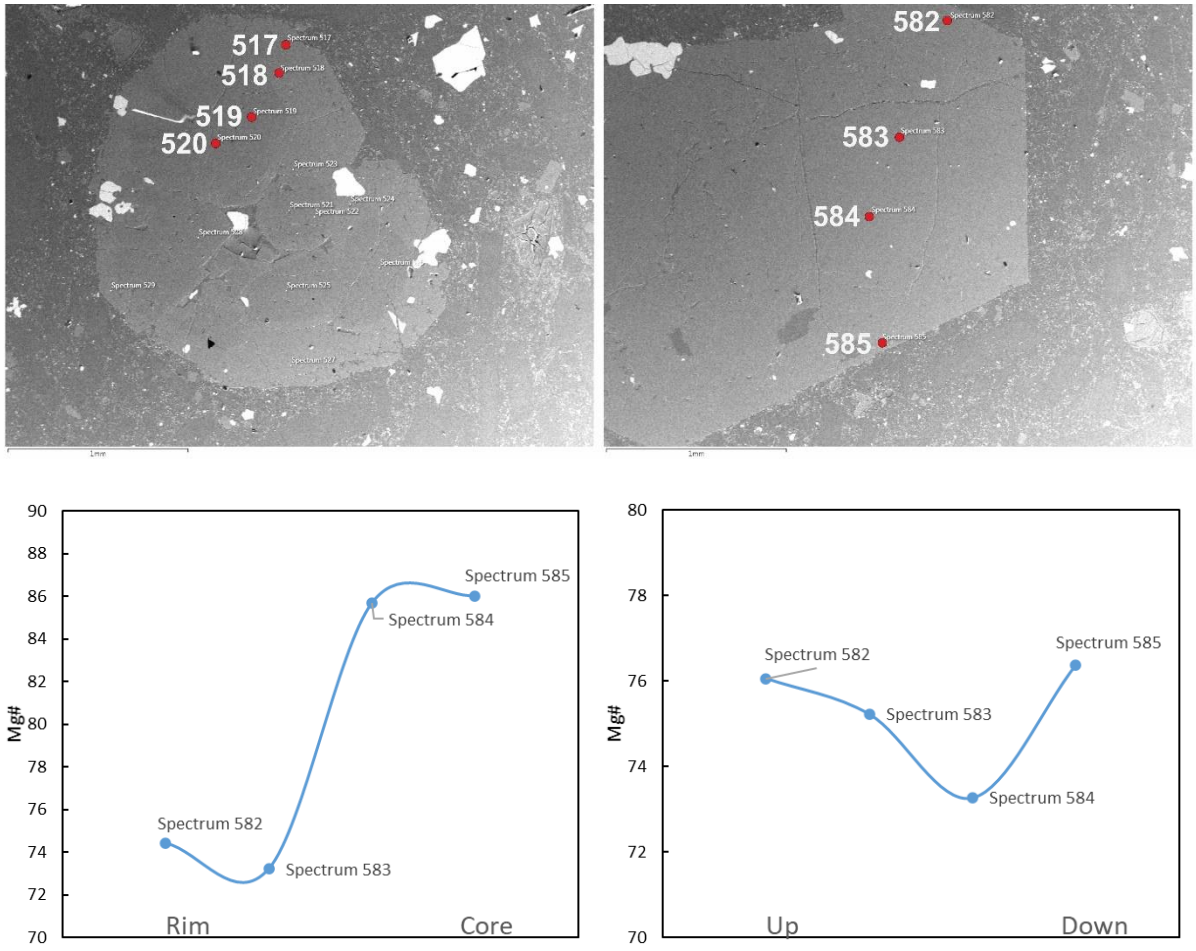

Fig. 5.26 Normal zonation (A) and reversed zonation (B) in J18-059-2.

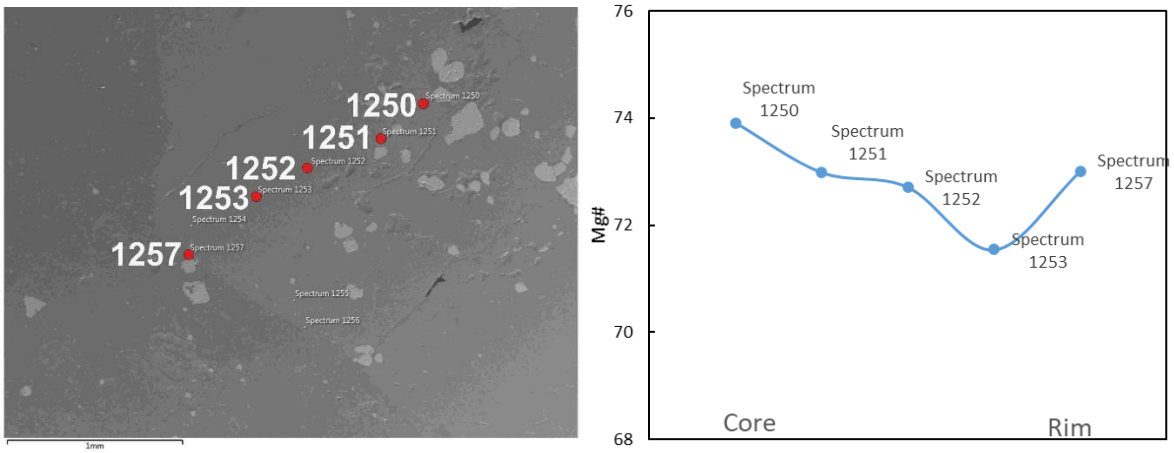

Fig. 5.27 Reversed zonation of sample J17-059-2.

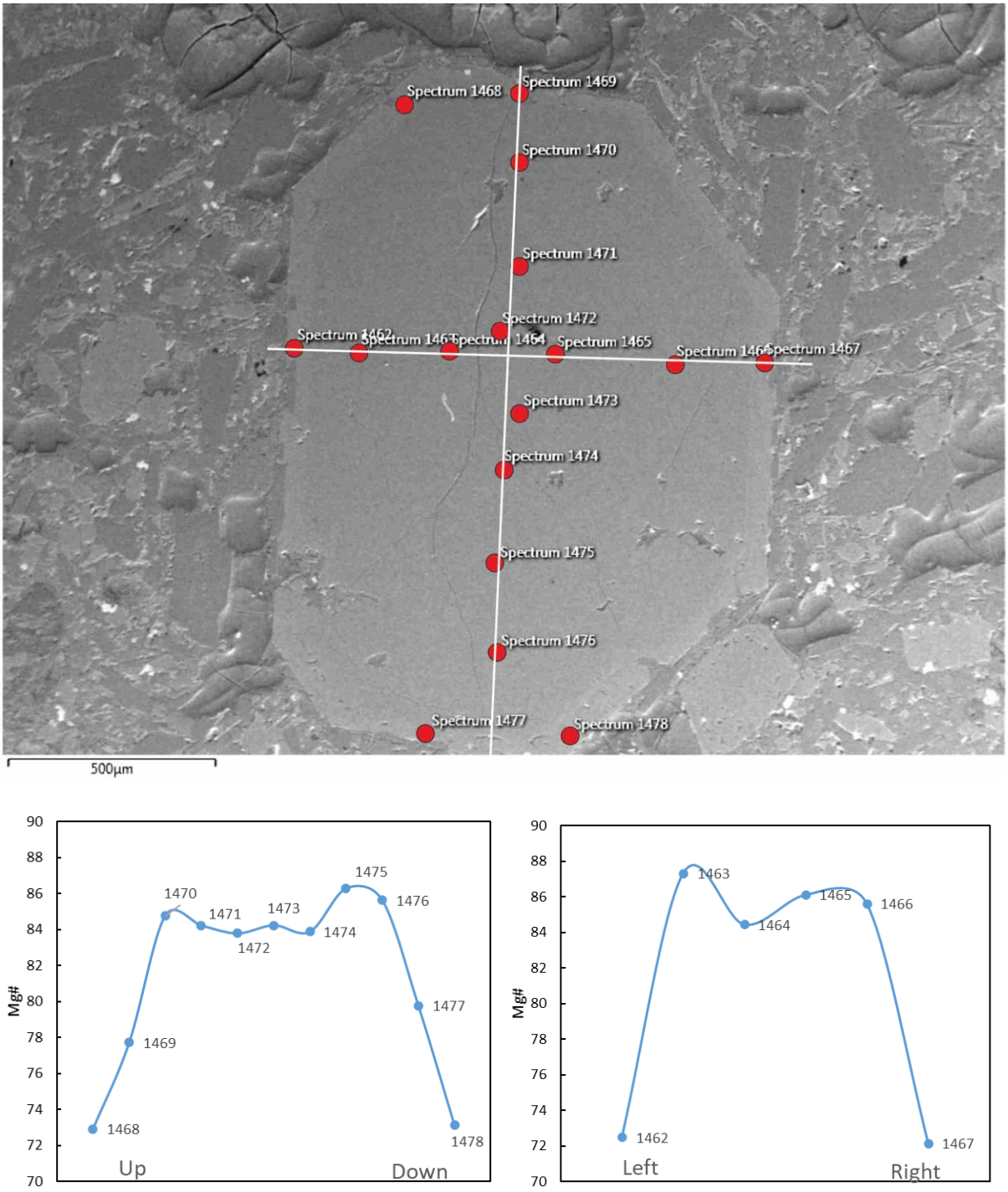

Fig. 5.28 Normal zonation for J17-102.

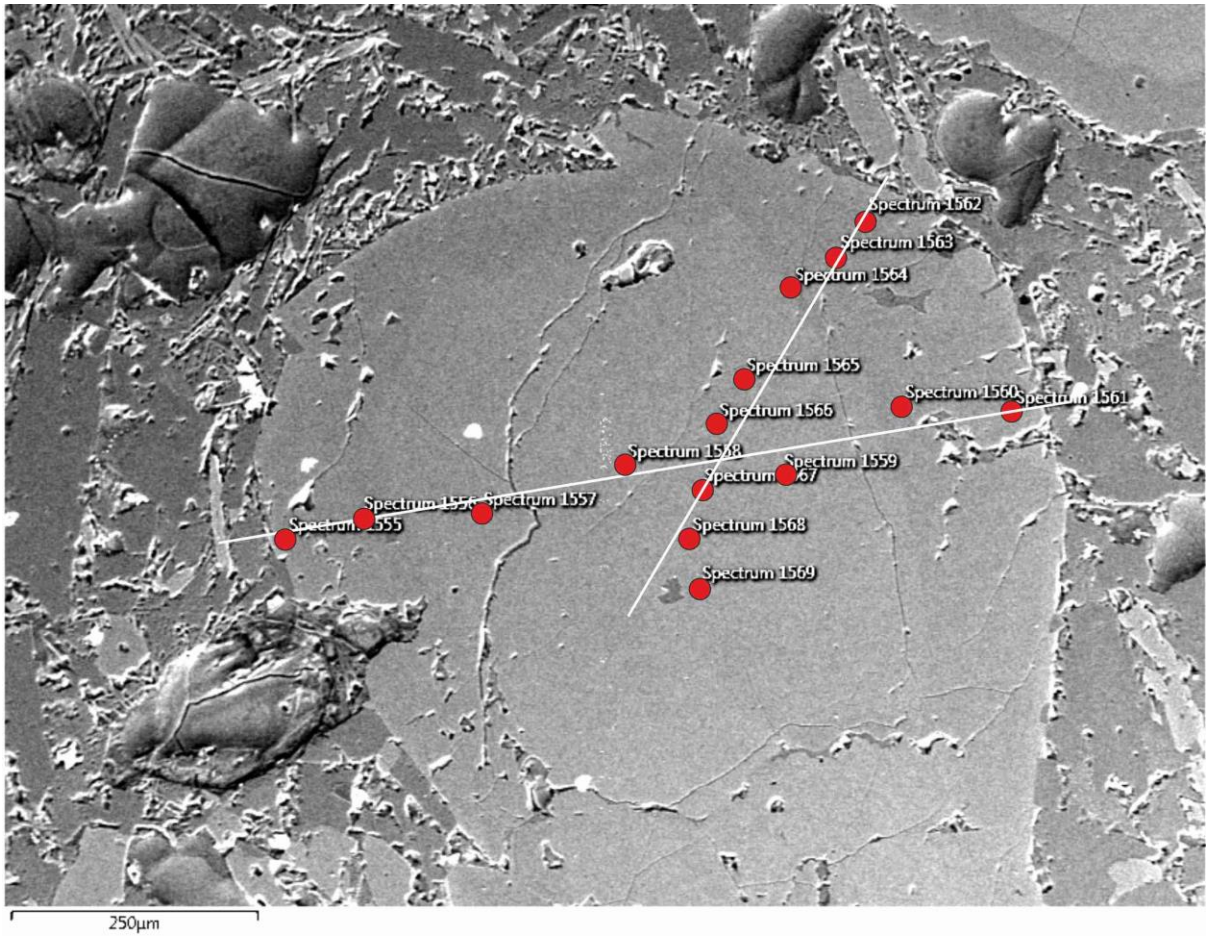

Fig. 5.29 Reverse zonation in J17-102.

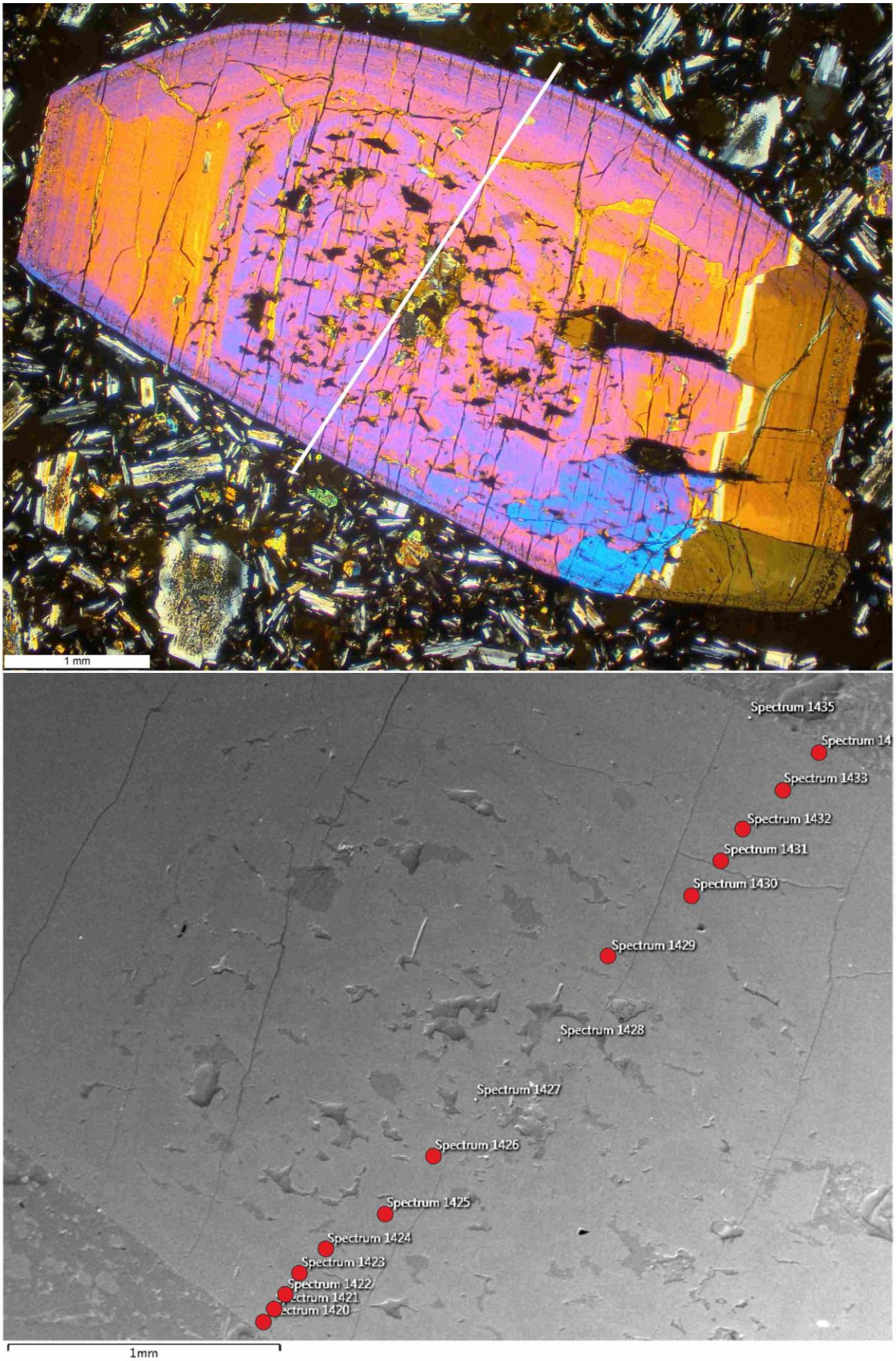
1 mm
Spectrum 1435
Spectrum 14
Spectrum 1433
Spectrum 1432
Spectrum 1431
Spectrum 1430
Spectrum 1429
Spectrum 1428
Spectrum 1427
Spectrum 1426
Spectrum 1425
Spectrum 1424
Spectrum 1423
Spectrum 1422
ectrum 1421
ectrum 1420
1mm

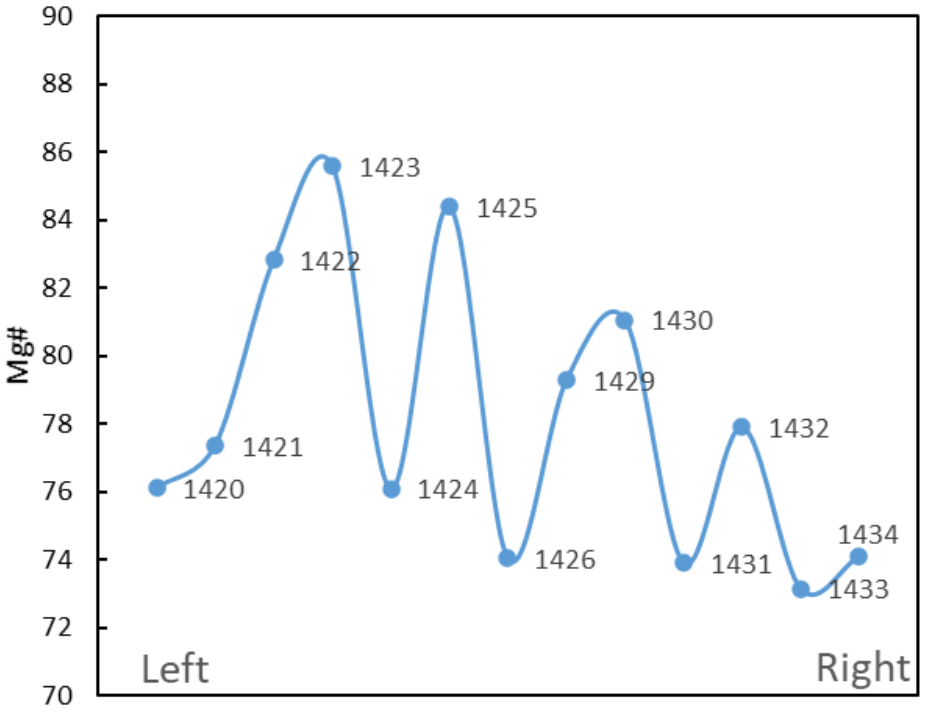

Fig. 5.30 Oscillatory zonation of clinopyroxene in J17-102 (spectrum 1427, 1428 are orthopyroxene).

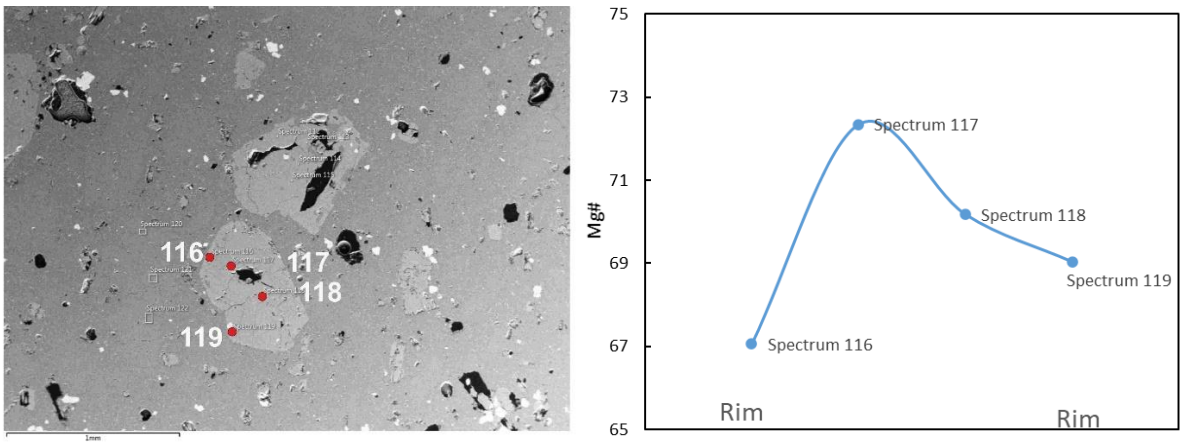

Fig. 5.31 Normal zonation in J17-001 (Spectrum 117 is CPX2 and the rest are CPX3).

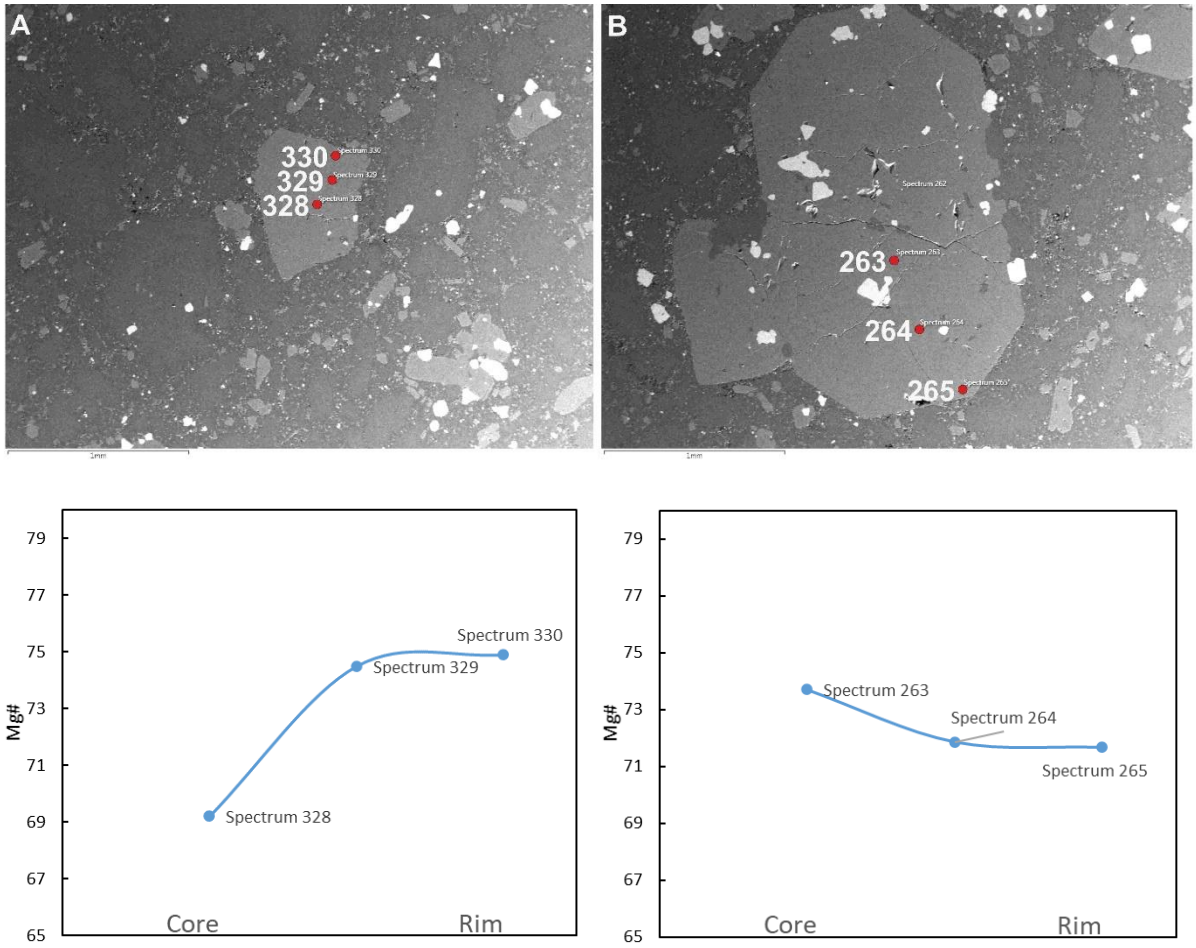

Fig. 5.32 Reversed zonation (A) and normal zonation (B) in J17-036-1.

5.3.2 Plagioclase

Plagioclase feldspar in the Panama Formation has composition ranging from labradorite to bytownite (Fig. 5.40). Three analyses plot in the miscibility gap area which are excluded from the diagram.

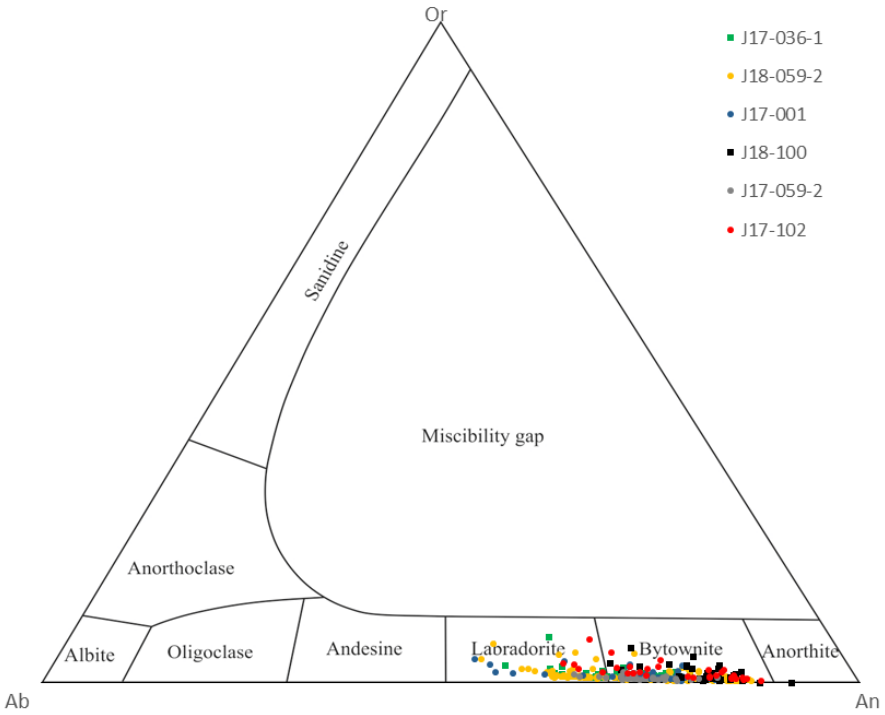

Fig. 5.33 Feldspar classification for Panama Formation (classification diagram from Smith and Brown., 1988).

As can be seen from the An distribution diagram (Fig. 5.34), plagioclase in Pam1 shows large range (An=53-88). A bimodal (or 3-peak) distribution in J18-059-2 is consistent with the clinopyroxene distribution. Plagioclase data in J17-059-2 was only analysed in one crystal. It is the same to J17-102 in which plagioclase data were only from two phenocrysts. In J17-001, plagioclase crystals are clustered in the range of An= 73-80, with several exceptions. In Pam2, An-number of plagioclase grains are clustered, but with several scattered high and low An plagioclase crystals. This is also consistent with clinopyroxene distribution in Pam2. Plagioclase in J18-100 overall has a very high An value (70-92).

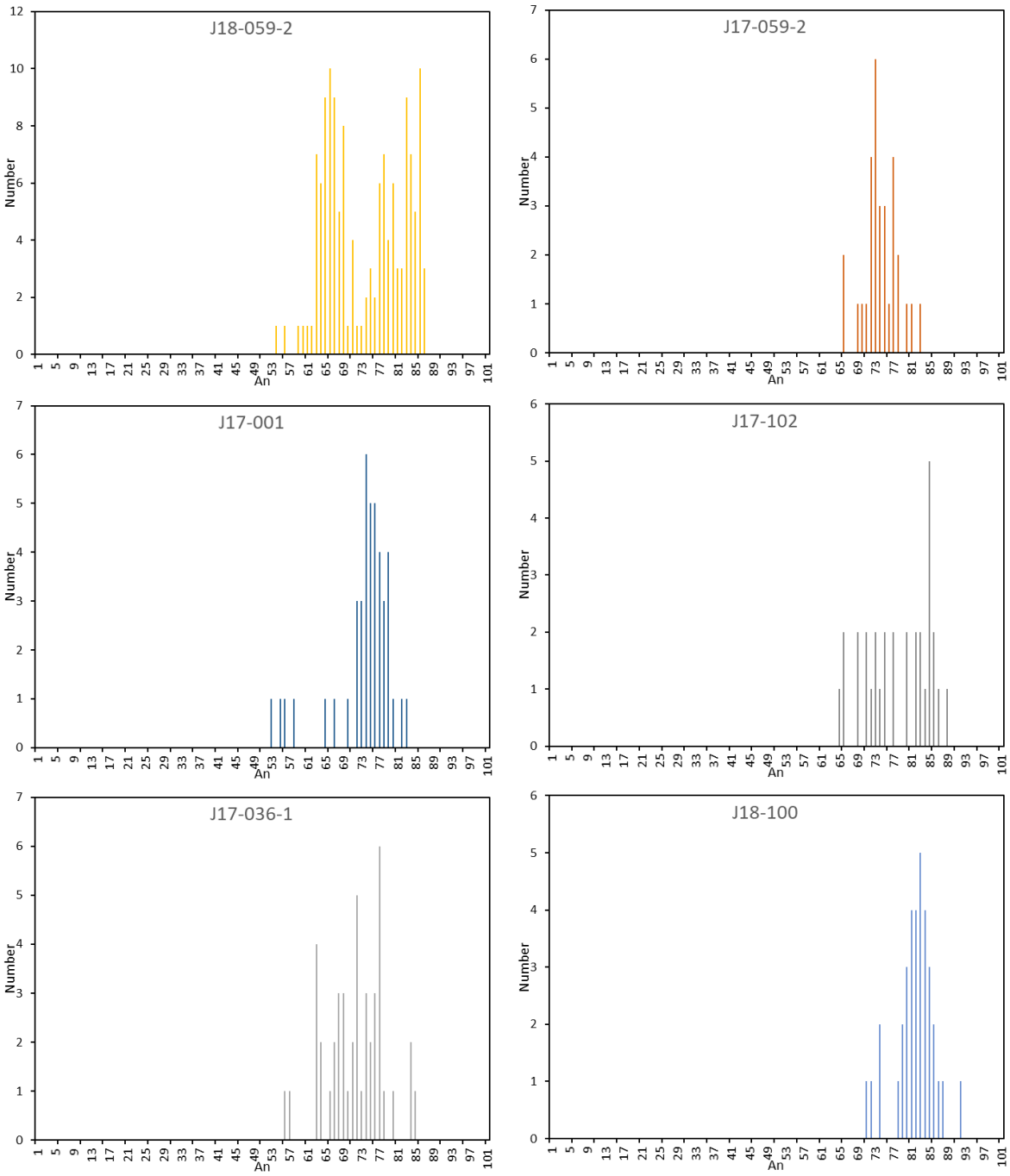

Fig. 5.34 An-based plagioclase distribution for Panama Formation.

Both normal zonation and reversed zonation of plagioclase are common in the Panama Formation. For Pam1 samples such as J18-059-2, normal zonation is the dominant type but reversed zonation can also be found. If plagioclase composition in J18-059-2 is divided into high An-number (>77) and low An-number (<77), both normal zonation and reversed zonation can be seen in high An-number plagioclase (Fig. 5.35). Both reversed and normal zonation can also be found in plagioclase with low An-number. When a plagioclase has high An and low An composition, high An is only found in the core with the crystal showing normal zonation (Fig. 5.36). This is consistent with clinopyroxene phenocrysts in which CPX1 rim with CPX2 core are not found. In this plagioclase crystal, the An difference between the core and the rim is up to 18. In sample J17-001, normal zonation is the main zonation type with occasionally reversed zonation (Fig. 5.37).

Both normal and reversed zonation are found in Pam2 (Fig. 5.38). An-number in J17-036-1 are overall lower than that in J18-100. The three analyses of high An-number in J17-036-1 as shown in the distribution diagram (Fig. 5.34) are the core of a plagioclase phenocryst which shows normal zonation. One extremely high An analysis (An= 92) in J18-100 is the mantle of a crystal showing reversed zonation. Plagioclase also occur in glomerocrysts coexisting with orthopyroxene or clinopyroxene. In these glomerocrysts, plagioclase has low An values (<82) if with orthopyroxene (Fig. 5.39 A) and the An values are high (>82) if with clinopyroxene (Fig. 5.39 B).

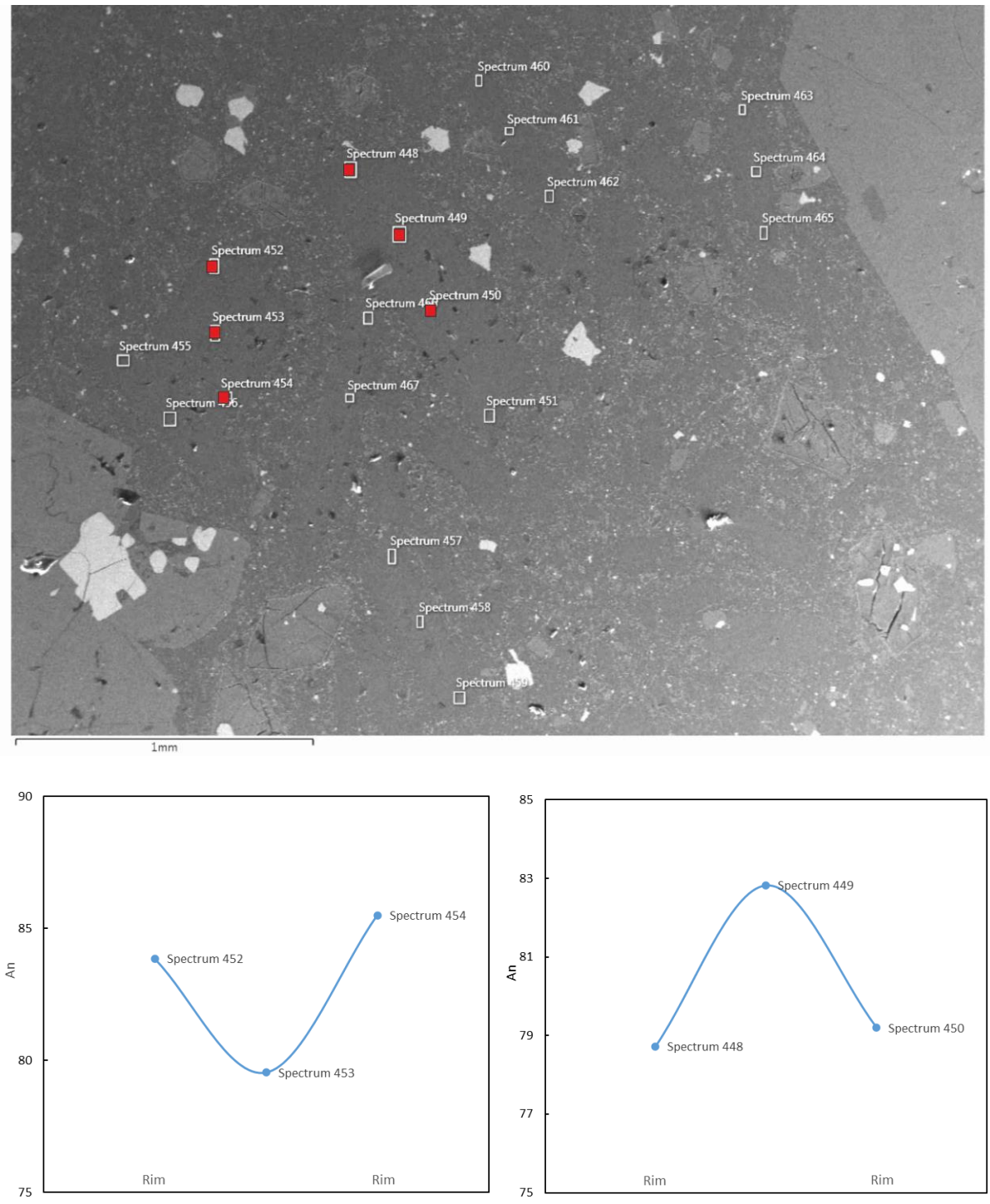

Fig. 5.35 Reversed zonation and normal zonation of plagioclase in J18-059-2.

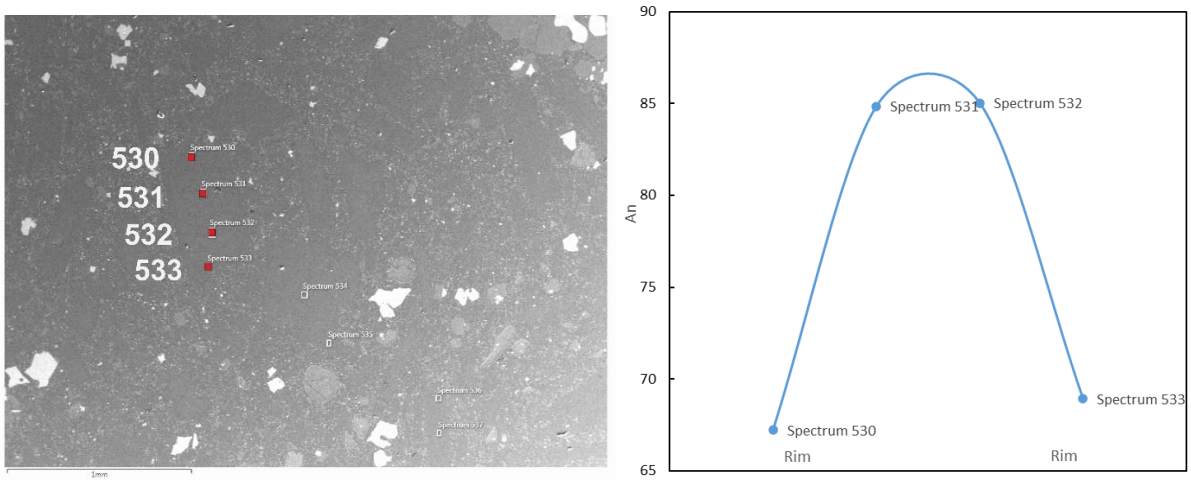

Fig. 5.36 Normal zonation of plagioclase in J18-059-2.

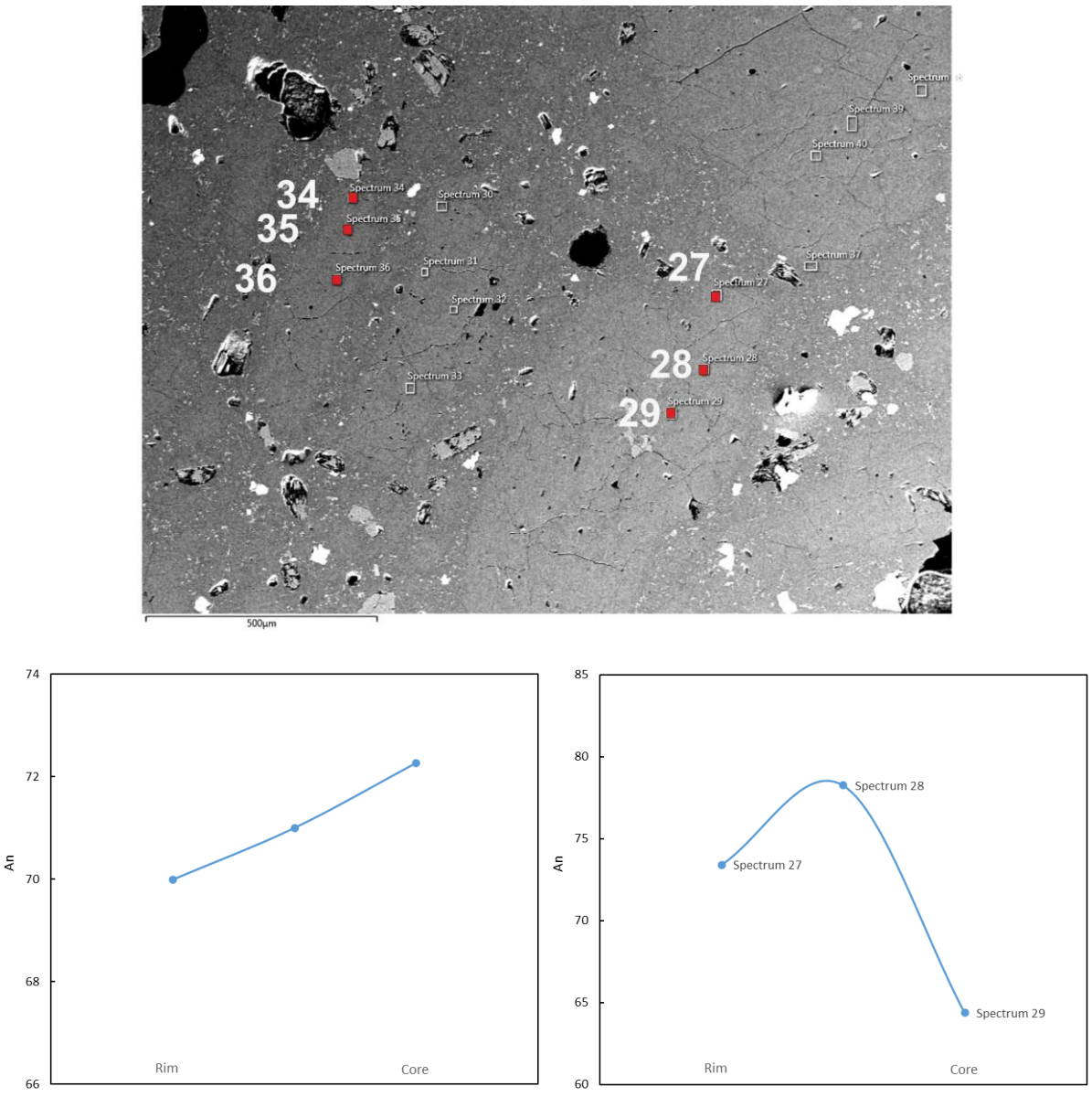

Fig. 5.37 Normal zonation reversed zonation for plagioclase in J17-001.

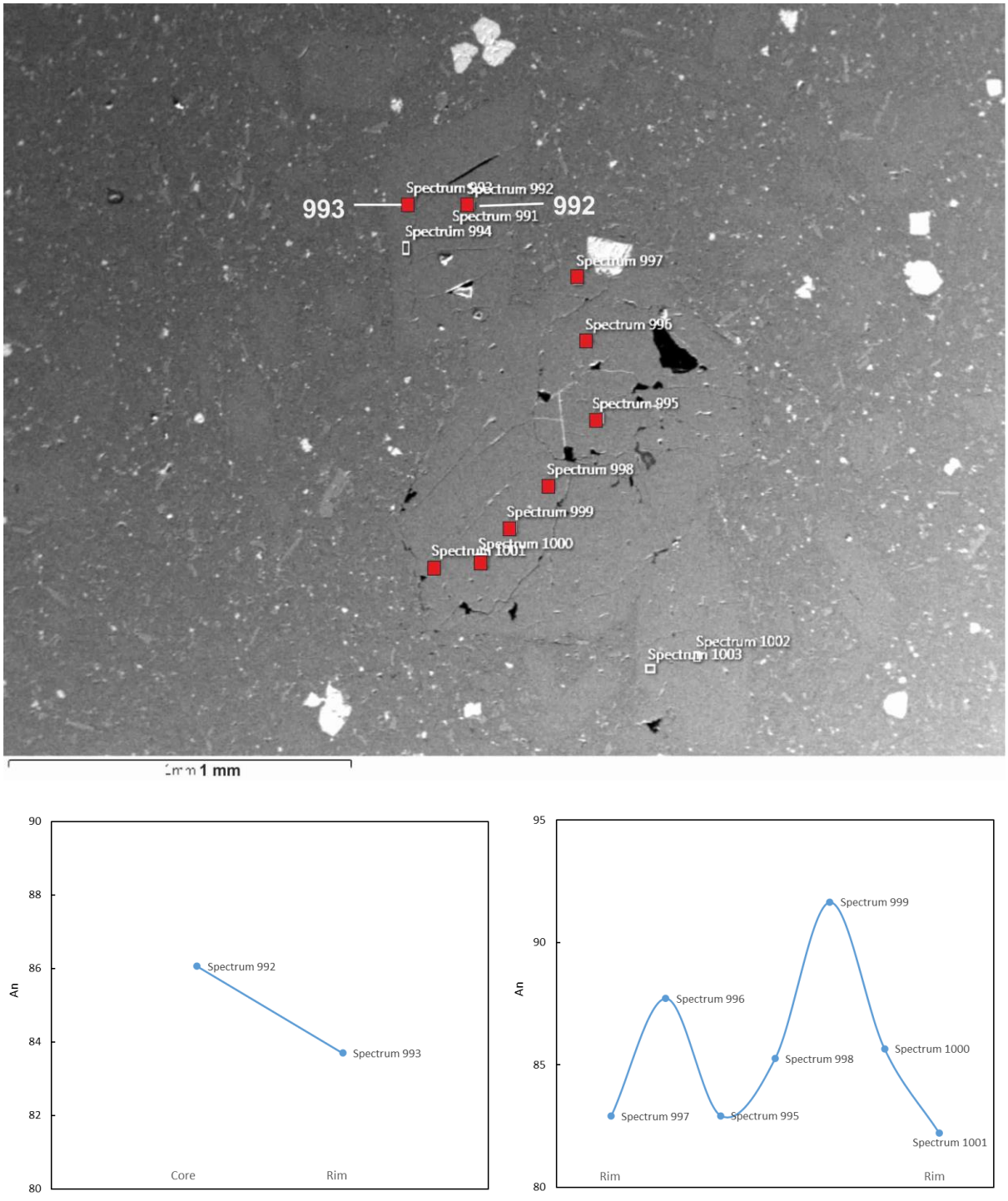

Fig. 5.38 Normal and reversed zonation of plagioclase in J18-100.

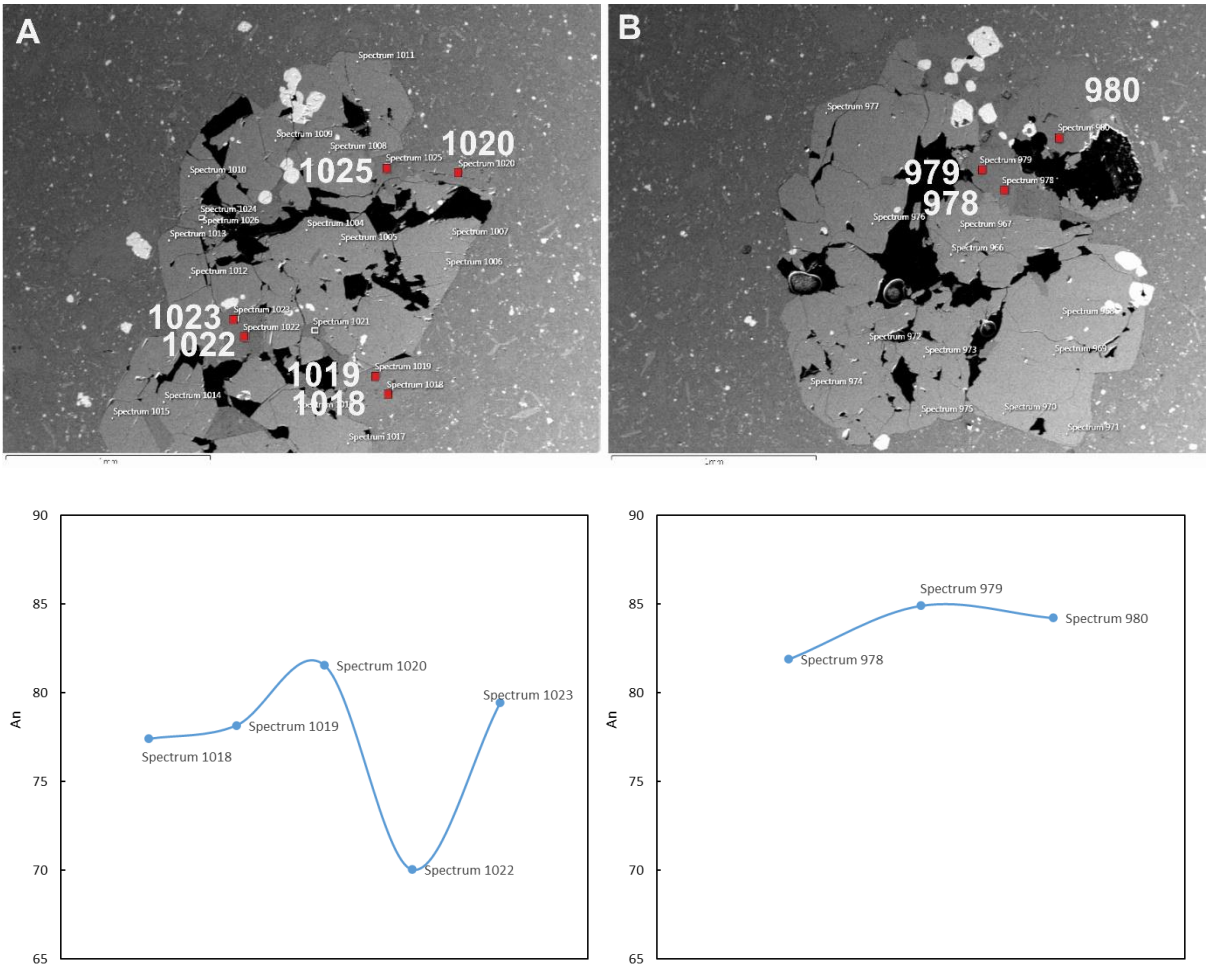

Fig. 5.39 Plagioclase in glomerocryst in J18-100. (A) Low An plagioclase coexists with orthopyroxene (B) High An plagioclase coexist with clinopyroxene.

5.3.3 Orthopyroxene

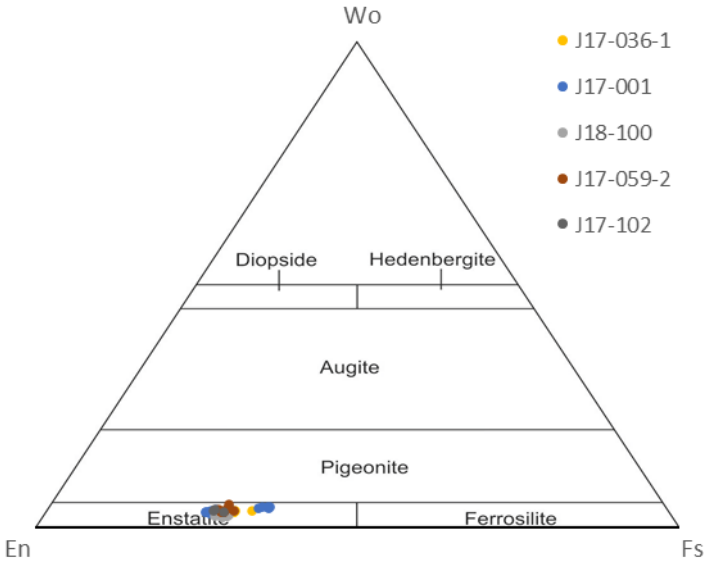

Fig. 5.40 Orthopyroxene classification for Panama Formation (classification diagram from Morimoto et al., 1988).

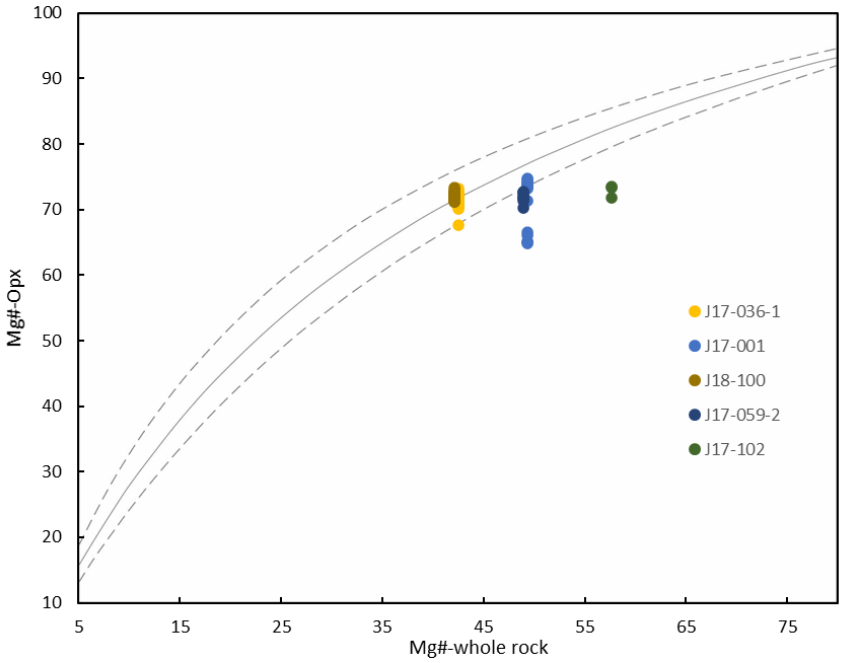

Fig. 5.41 Rhodes diagram for orthopyroxene in Panama Formation (Kd=0.29±0.06 from Putirka, 2008).

Orthopyroxene in the Panama Formation is enstatite (Fig. 5.40), and is rare compared to clinopyroxene and plagioclase. Orthopyroxene is more common in Pam2 (J17-036-1 and J18-100) than Pam1, where it is not found in all Pam1 samples. Orthopyroxene is not in equilibrium with the whole-rock composition in Pam1 samples while it is in equilibrium in Pam2 samples (Fig. 5.41). In J18-100, orthopyroxene is normally found in glomerocrysts (Fig. 5.39 A). In J17-036-1, orthopyroxene occurs as single crystals or these grains coexist with clinopyroxene to form

orthopyroxene-clinopyroxene couples, which will be used as a thermobarometer (discussed in section 6.1.1).

5.4 Las Cascadas Formation

For this group, clinopyroxene, plagioclase, and orthopyroxene grains have been analysed using ASEM.

5.4.1 Clinopyroxene

Clinopyroxene in rocks of the Las Cascadas Formation is quite homogeneous and is augitic in composition (Fig. 5.42). It exhibits the following compositional range: Mg# = 68-78, Wo = 36-43, En = 40-46, and Fs =13-21. Clinopyroxene shows a small variation in composition: Mg#= 68-73 for J17-121, Mg#= 70-78 for J17-006 and Mg#= 69-74 for J17-009. The FeO (8.0-12.3 wt.%), MnO (0.22-0.75 wt.%) and TiO_2 (0.35-0.81 wt.%) content increases with decreasing Mg#. The range of SiO_2 (49.6-53.2 wt.%), Al_2O_3 (1.1-4.3 wt.%), and CaO (17.5-20.9 wt.%) content is quite narrow, whereby Al_2O_3 and CaO contents show slight positive correlations with Mg# (Fig. 5.43).

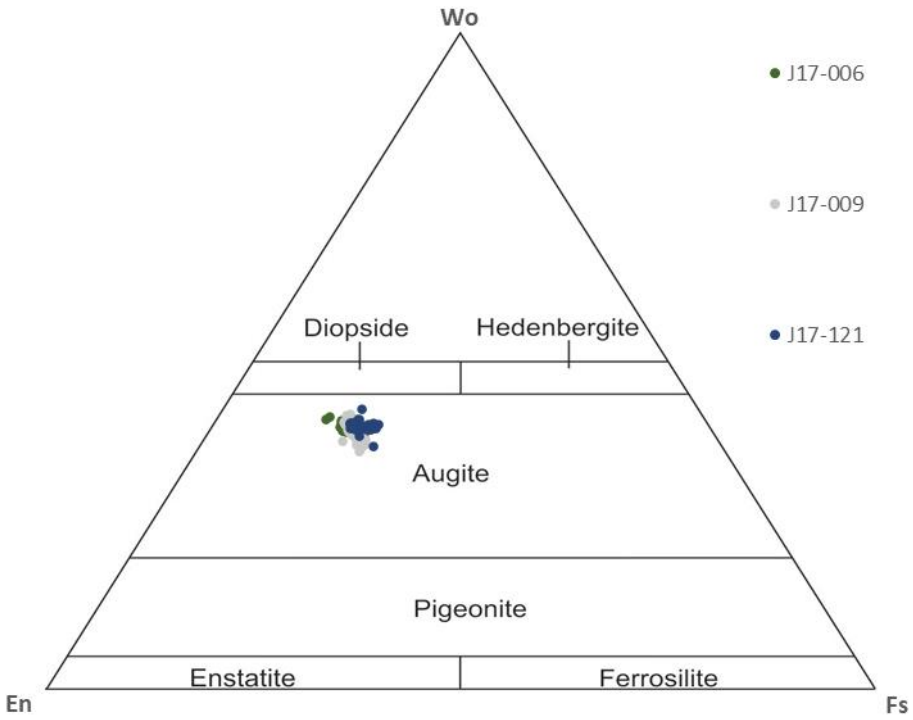

Fig. 5.42 Clinopyroxene classification in rocks of the Las Cascadas Formation (classification diagram from Morimoto et al., 1988).

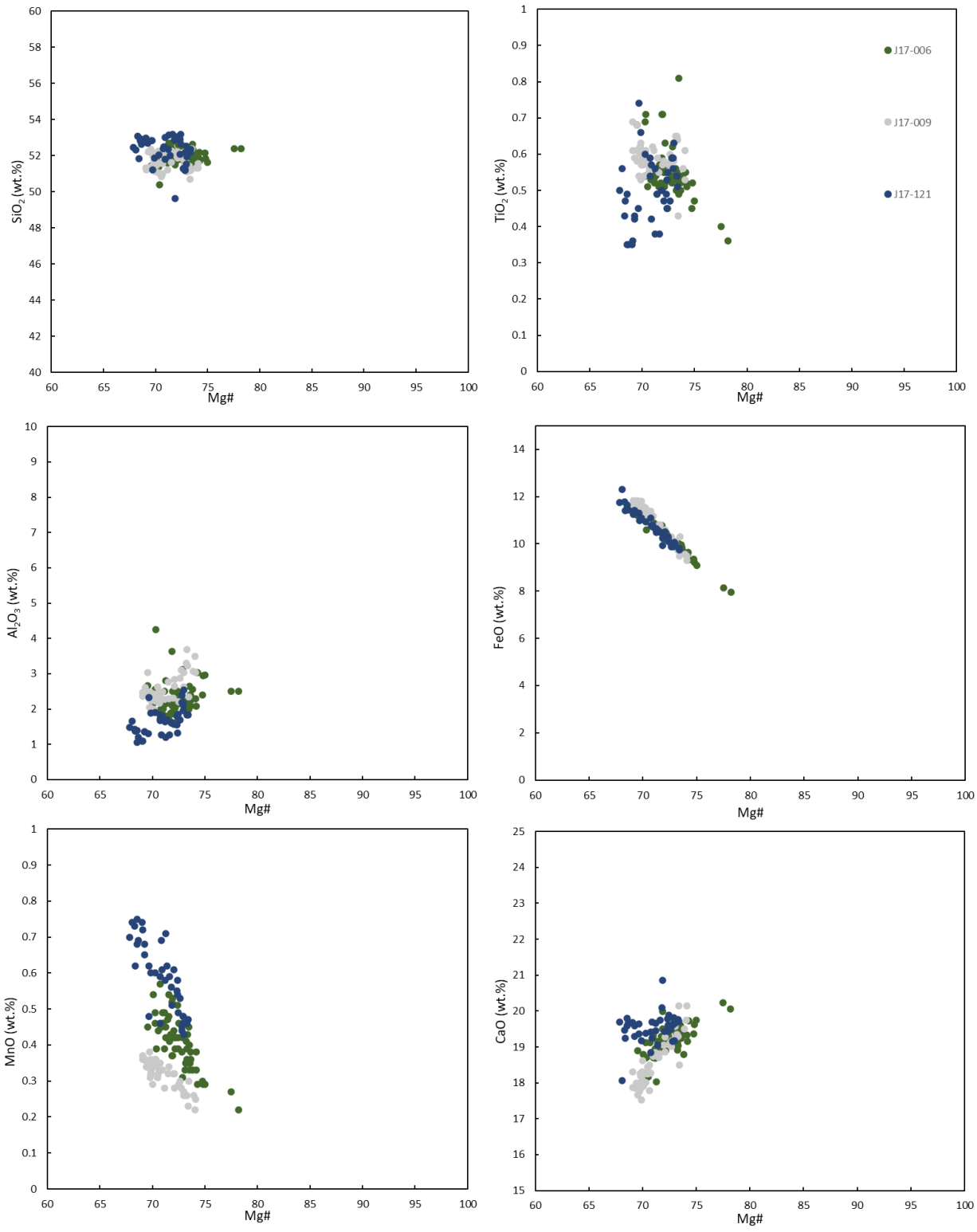

Fig. 5.43 Representative elements plotted against Mg# for clinopyroxene of Las Cascadas Formation.

Clinopyroxene in all three samples (J17-006, J17-009, and J17-121) plot above the equilibrium line in the Rhodes diagram (Fig. 5.44, Fig. 5.45, Fig. 5.46). J17-121 and J17-006 are within the equilibrium zone while J17-009 is above the equilibrium zone. The clinopyroxene in this group have a unimodal distribution and plot above the boundary in the Ti vs Al diagram. For J17-121, Ti/Al higher than 0.15 means that this clinopyroxene classifies as CPX3 (Fig. 5.44). In J17-006 and J17-009, the clinopyroxene is mainly CPX3 but CPX2 are also found and there is a clear transition from CPX2 to CPX3 (Fig. 5.45, Fig. 5.46).

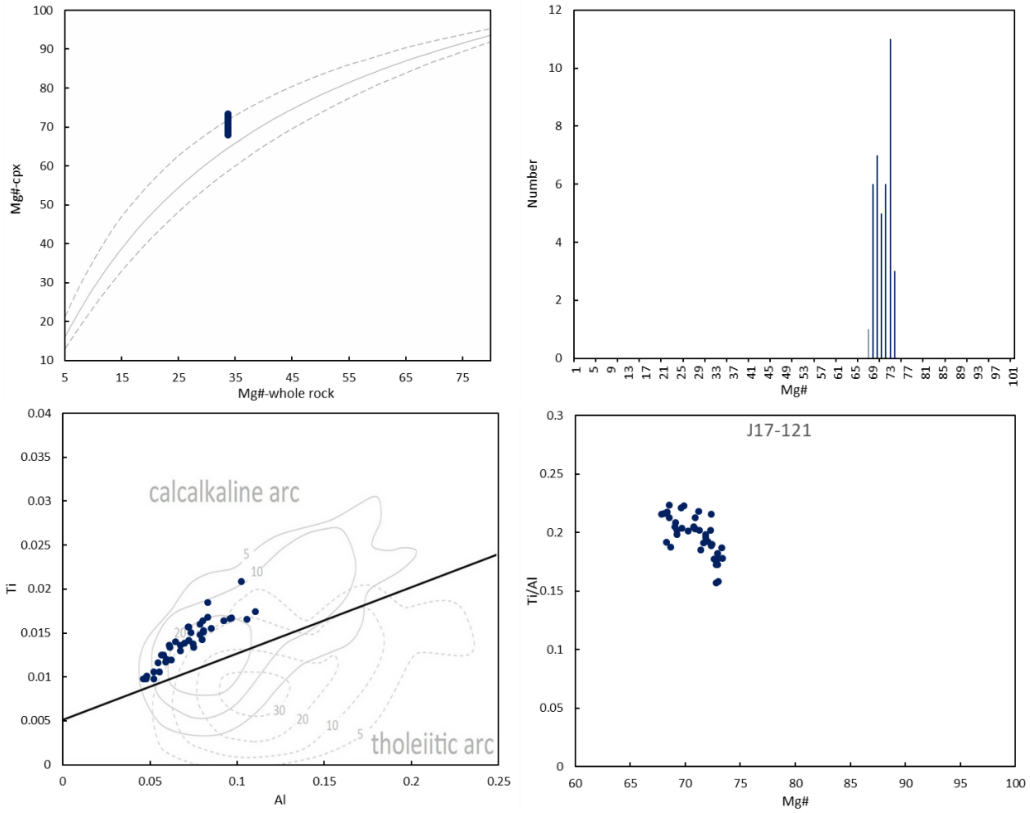

Fig. 5.44 Rhodes diagram (Kd=0.28 ± 0.08 from Putirka, 2008), distribution diagram, Ti vs Al (boundary is from Leterrier, 1982 and Al, Ti are calculated based on 4 cations) and Ti/Al vs Mg# for clinopyroxene in J17-121.

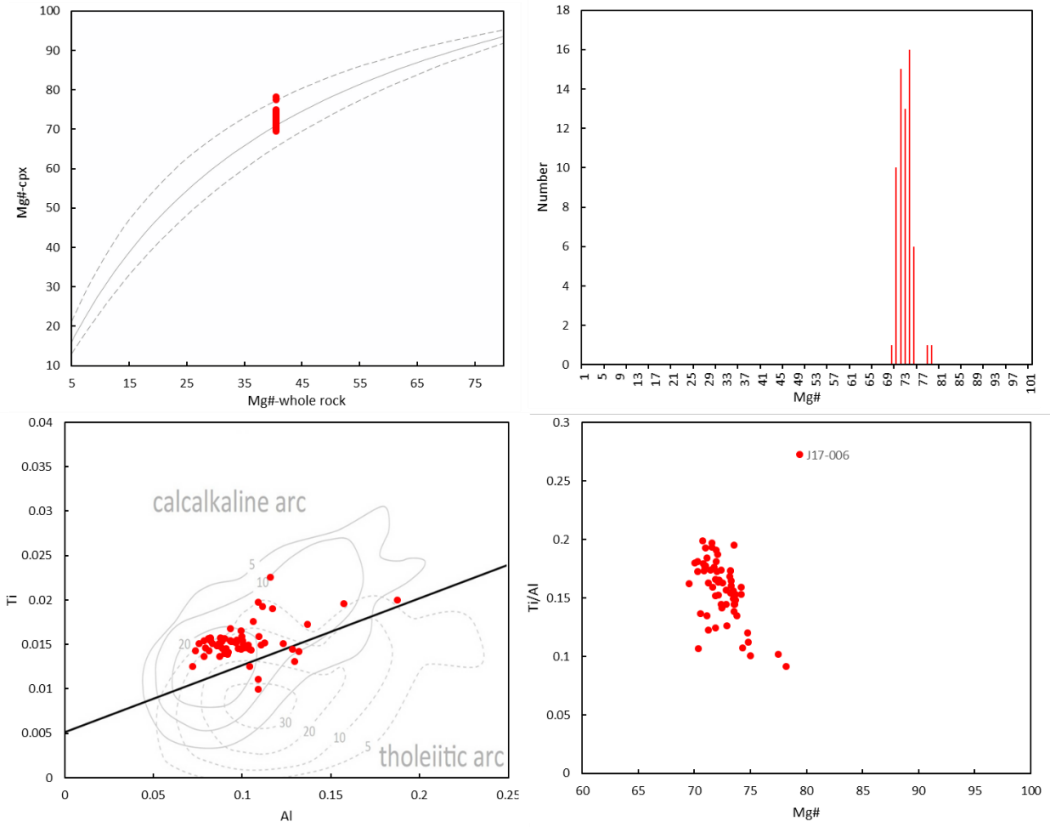

Fig. 5.45 Rhodes diagram (Kd=0.28 ± 0.08 from Putirka, 2008), distribution diagram, Ti vs Al (boundary is from Leterrier, 1982 and Al, Ti are calculated based on 4 cations) and Ti/Al vs Mg# for clinopyroxene in J17-006.

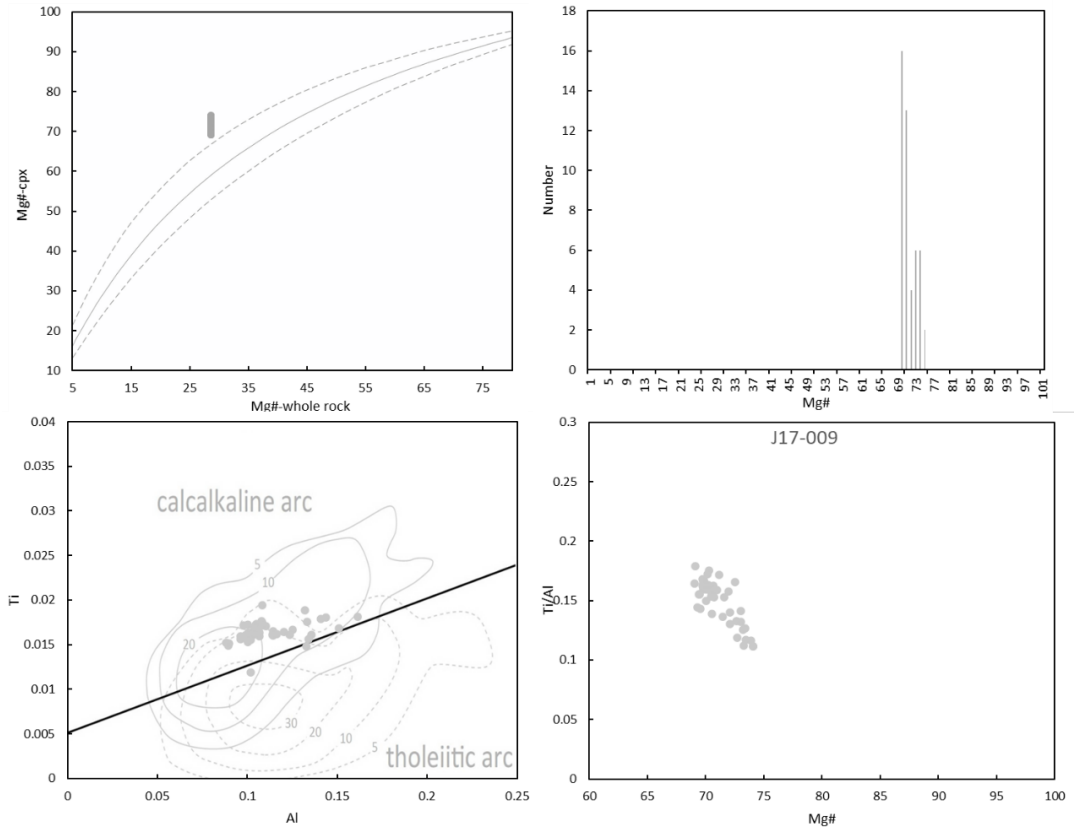

Fig. 5.46 Rhodes diagram (Kd=0.28±0.08 from Putirka, 2008), distribution diagram, Ti vs Al (boundary is from Leterrier, 1982 and Al, Ti are calculated based on 4 cations) and Ti/Al vs Mg# for clinopyroxene in J17-009.

Both normal and reversed zonation are common, but the Mg# range is smaller compared with Pam1 (Fig. 5.47, Fig. 5.48).

Even though clinopyroxene in this study is divided into CPX1, CPX2 and CPX3, they are not separate groups. Instead, clinopyroxene forms a continuous composition from CPX1 to CPX2 to CPX3. In a phenocryst as shown in Fig. 5.49, from spectrum 71 (right) to spectrum 70 (left), the composition evolves gradually from CPX2 to CPX3. This is consistent with the gradual transition as shown in Ti/Al vs Mg# diagram (Fig. 5.45, Fig. 5.46).

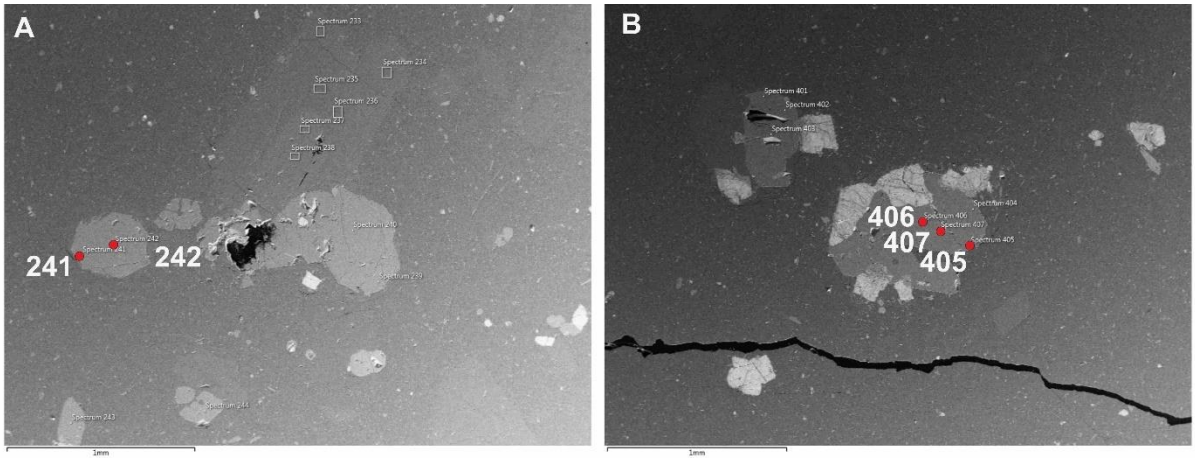

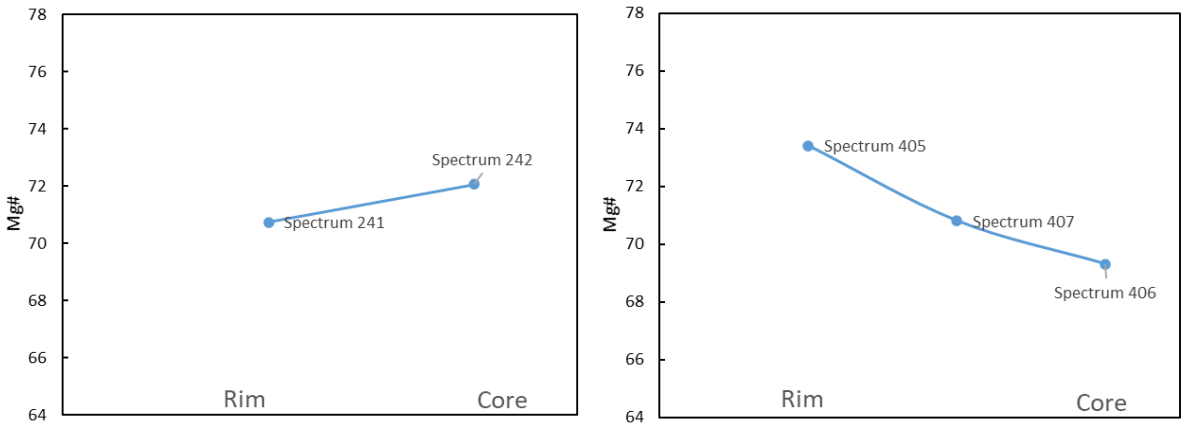

Fig. 5.47 Normal and reversed zonation of clinopyroxene in J17-121.

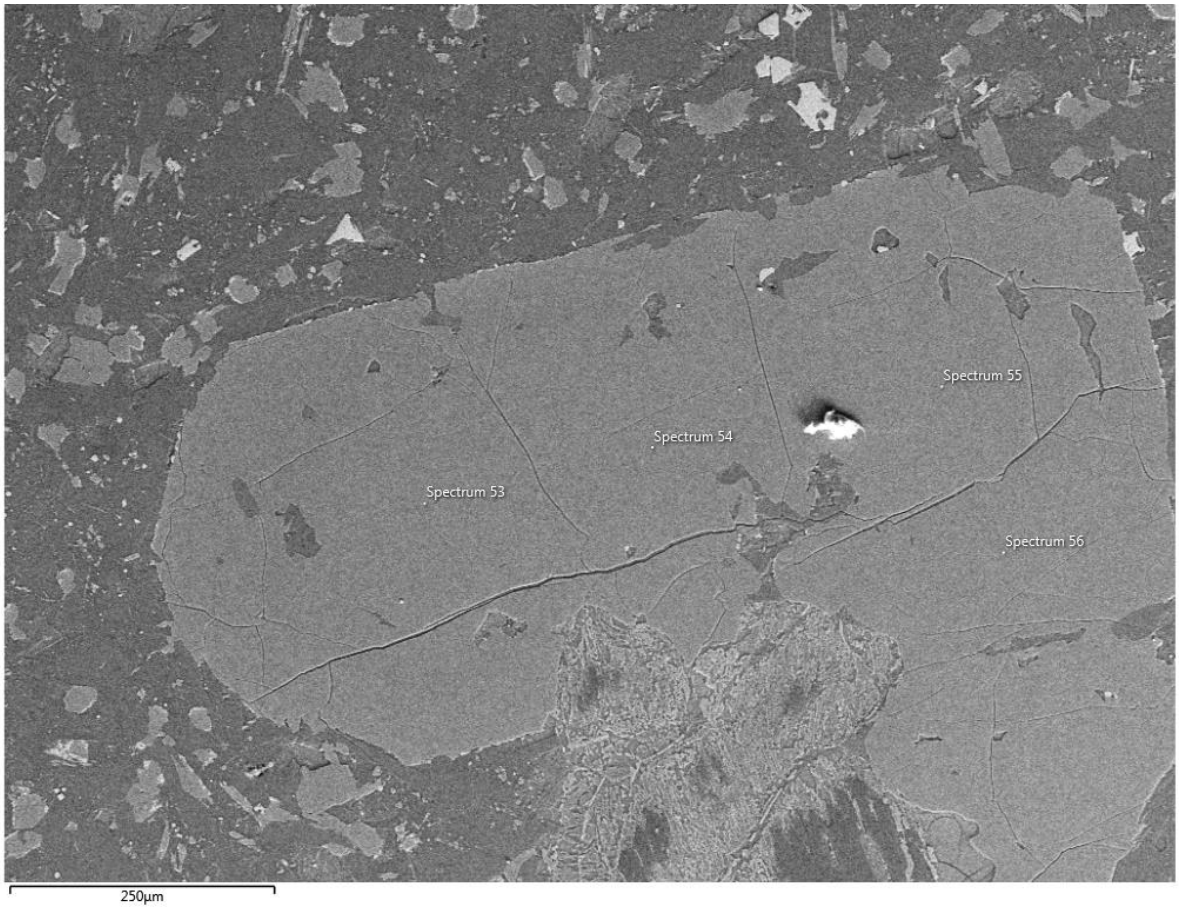

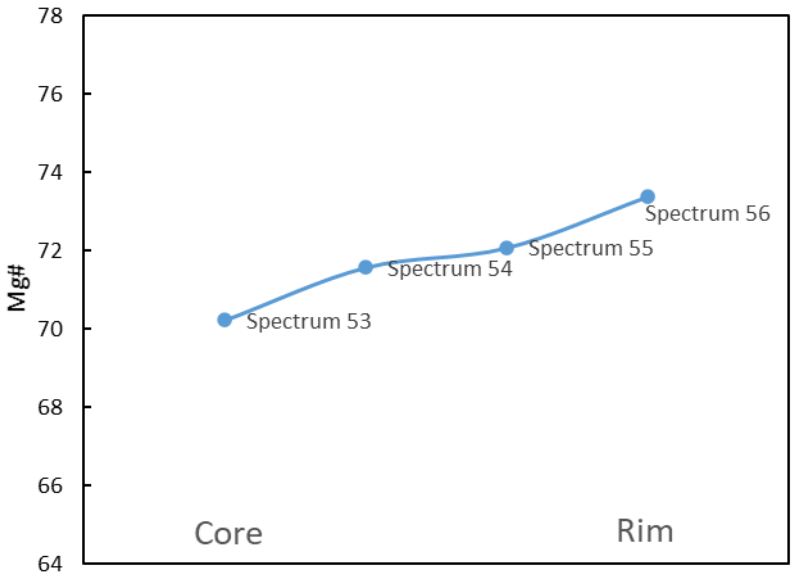

Fig. 5.48 Reversed zonation and sieved texture of clinopyroxene in J17-009.

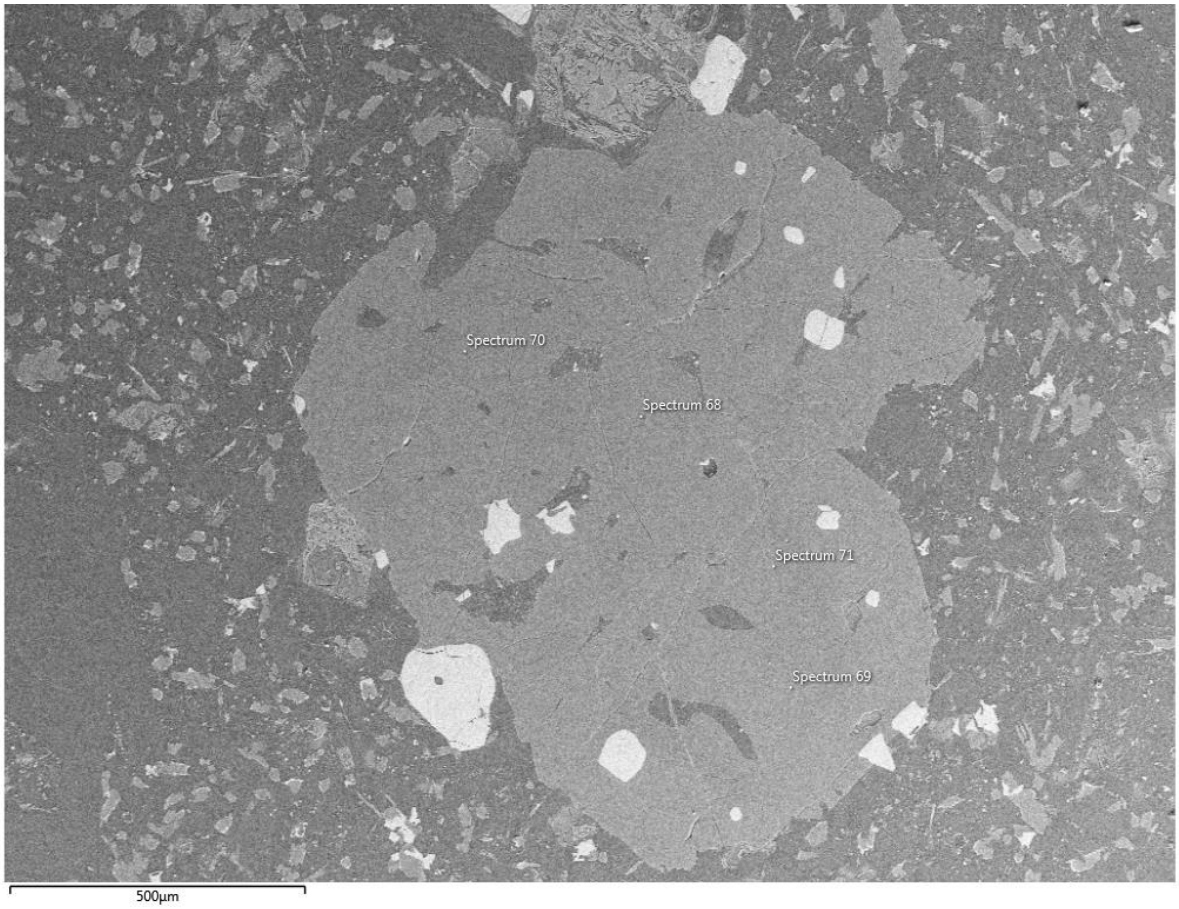

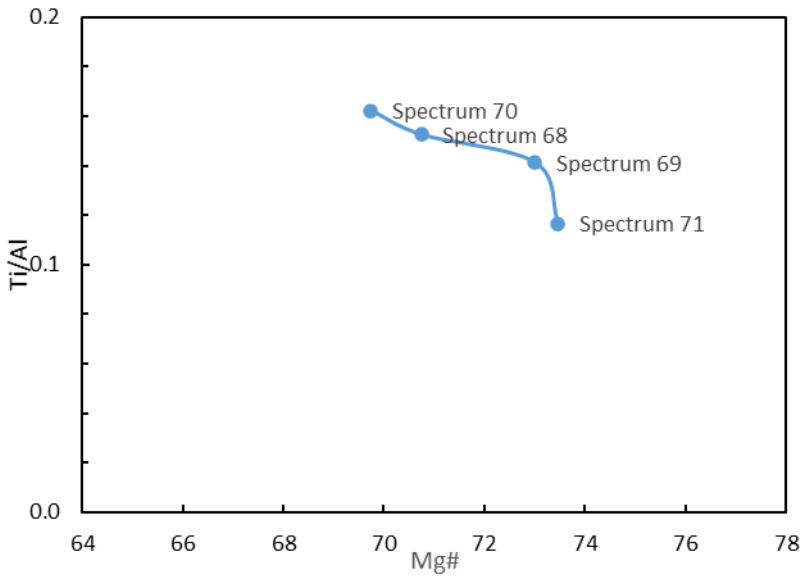

Fig. 5.49 Gradual transition from CPX2 to CPX3 in J17-009 (Spectrum 69, 71 are CPX2 and 68, 70 are CPX3).

5.4.2 Plagioclase

Plagioclase crystals display composition spanning a wide range from andesine to bytownite (Fig. 5.50) (An= 30-78 for J17-121 and An= 41-80 for J17-006). The overall An value has a unimodal distribution (Fig. 5.51).

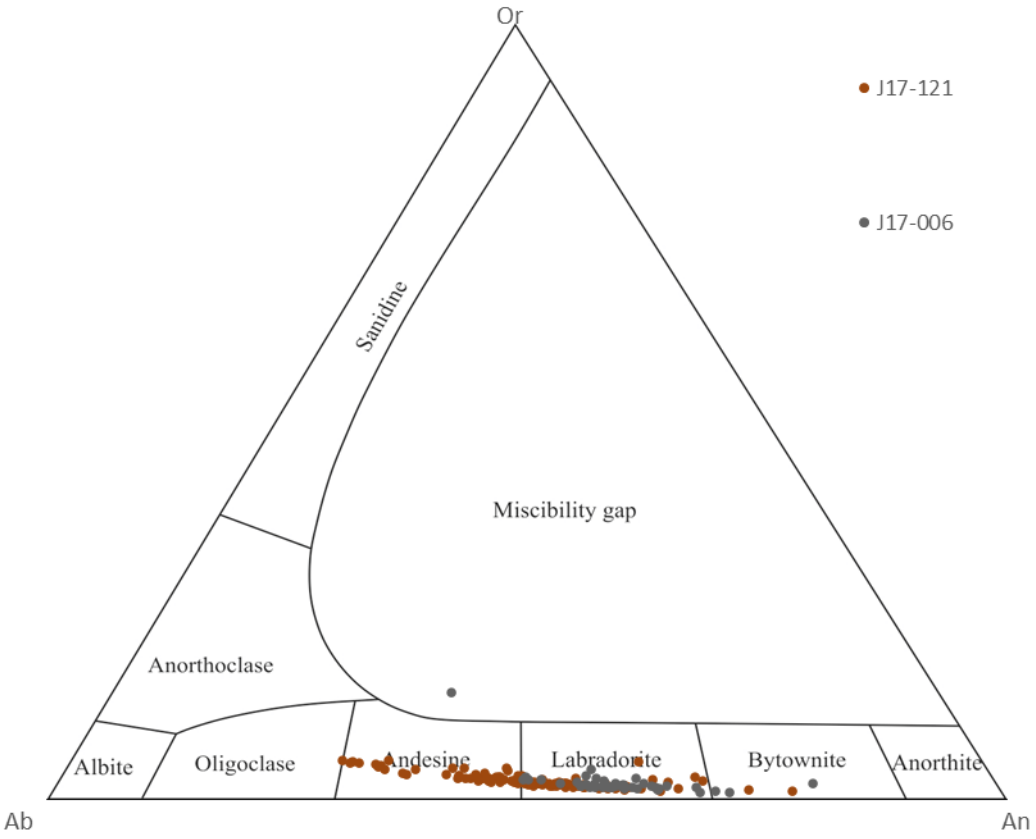

Fig. 5.50 Feldspar classication for Las Cascadas Formation (classification diagram from Smith and Brown., 1988).

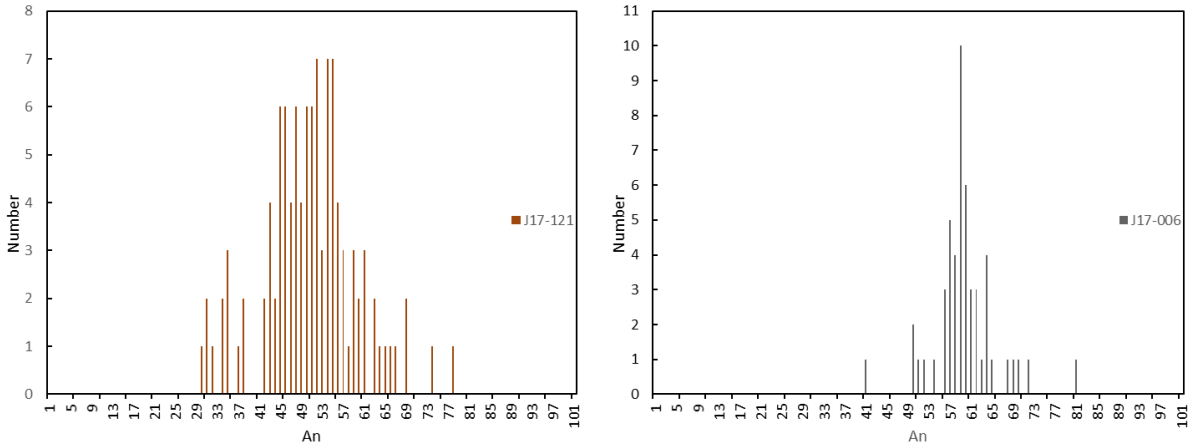

Fig. 5.51 Histograms (bins = 100) of An number of plagioclase from the Las Cascadas Formation.

Both normal zonation and reversed zonation can be found in the Las Cascadas Formation (Fig. 5.52). Sieve texture plagioclase is common in this formation.

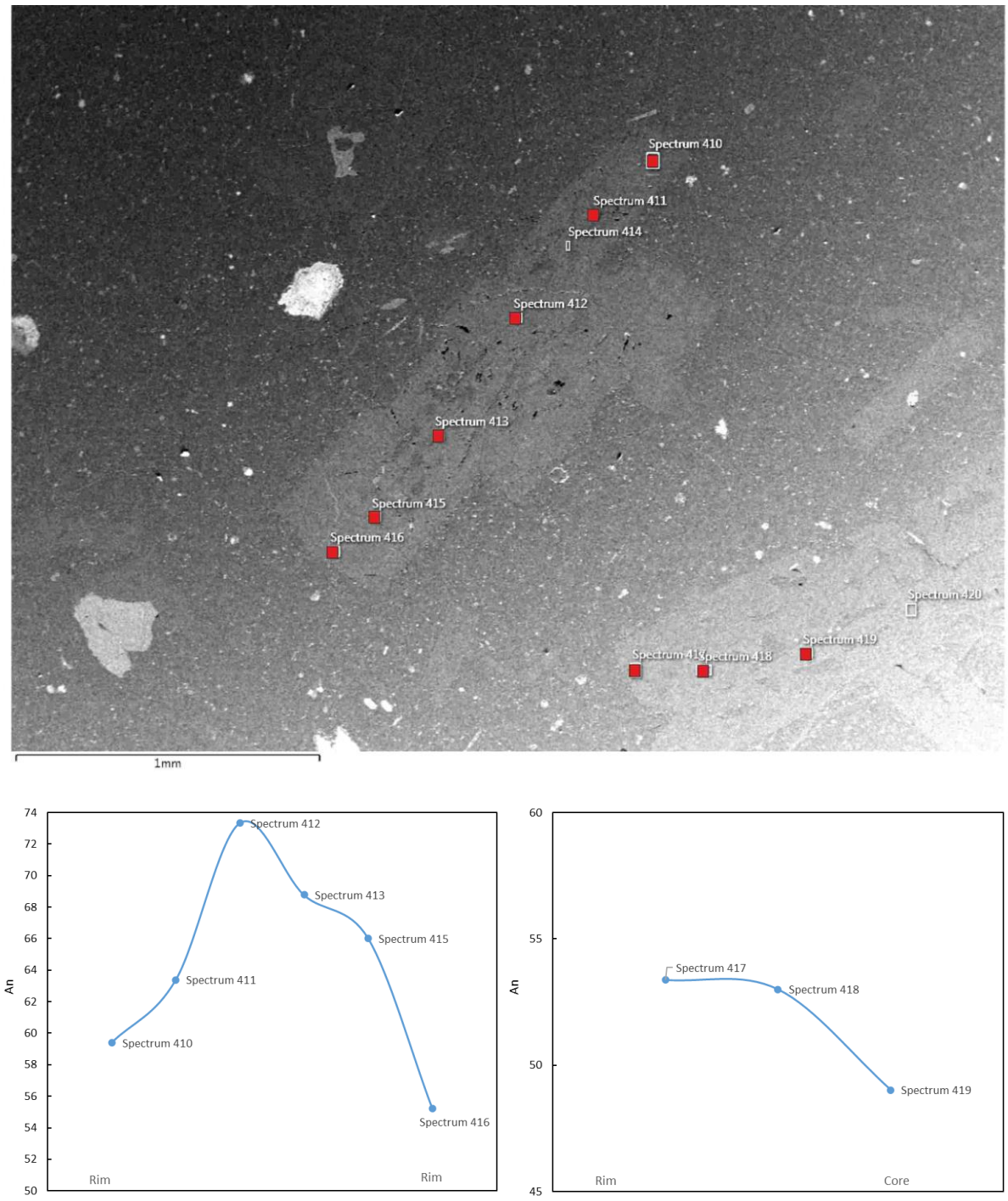

Fig. 5.52 Normal and reversed zonation of plagioclase in J17-121.

5.4.3 Orthopyroxene

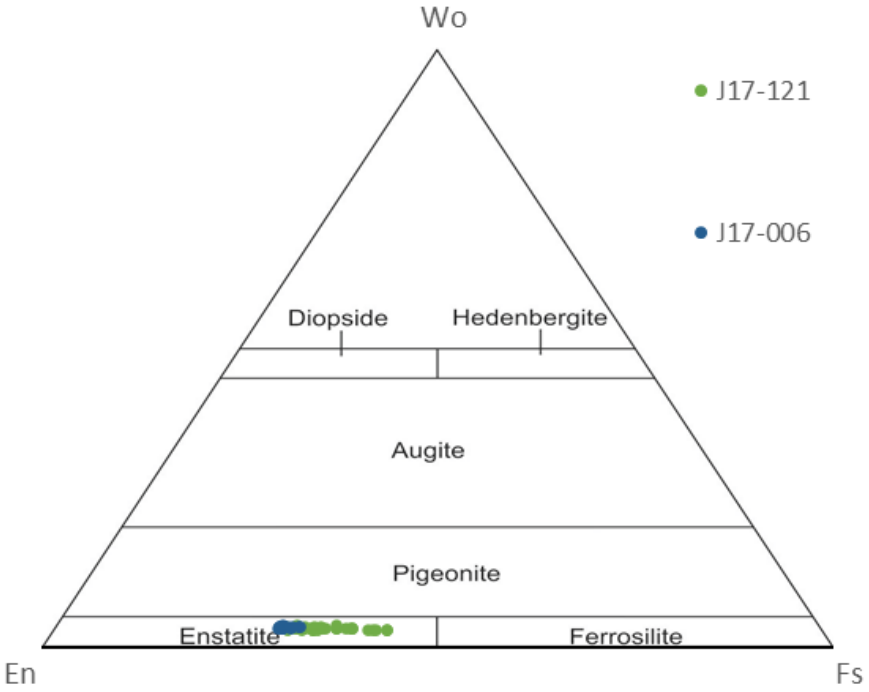

Fig. 5.53 Orthopyroxene classification (classification diagram from Morimoto et al. (1988)).

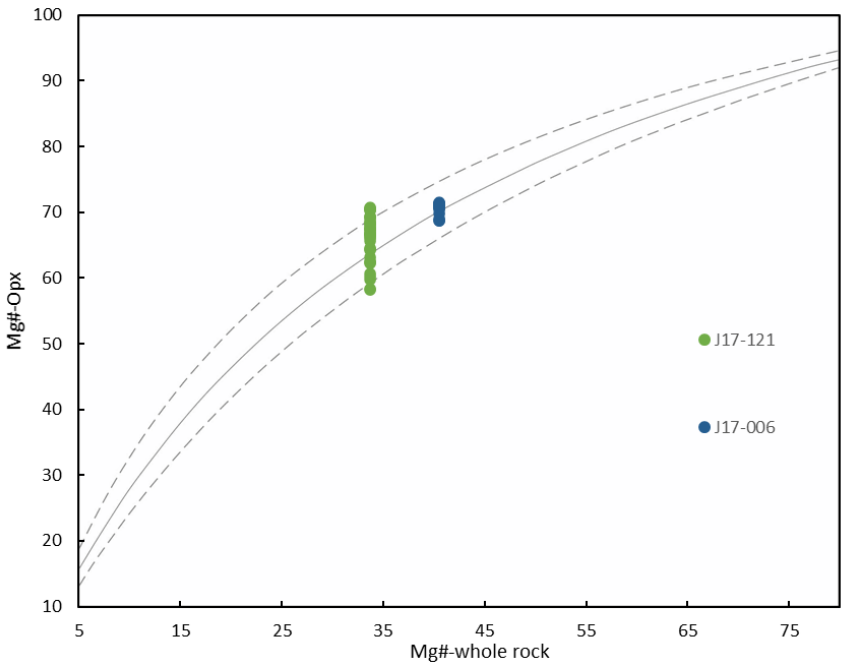

Fig. 5.54 Rhodes diagram for orthopyroxene in Las Cascadas Formation (Kd=0.29±0.06 from Putirka (2008)).

Orthopyroxene is seldom observed compared to clinopyroxene and plagioclase in rocks of this formation. They are more common in this formation than in Panama Formation. All the orthopyroxene plots in the enstatite field with a compositional range of En = 55-68, Fs = 29-42, and

Wo =3-4 for J17-121 and En = 66-67, Fs = 28-31, and Wo =3-4 for J17-006. In the Rhodes diagram (Fig. 5.54), orthopyroxene in these two samples is in equilibrium with their whole rock compositions.

5.5 Cabra Formation

In this formation, clinopyroxene, plagioclase, olivine, and orthopyroxene were analysed by ASEM. For analysed samples, J18-045 and J18-052 are two olivine-bearing basalts of the Cabra mafic member. J17-034 is an olivine-free basaltic andesite found in the Cabra mafic member. J18-034-4 and J19-094-5 are andesite and diorite, respectively, in the Cabra felsic member.

5.5.1 Clinopyroxene

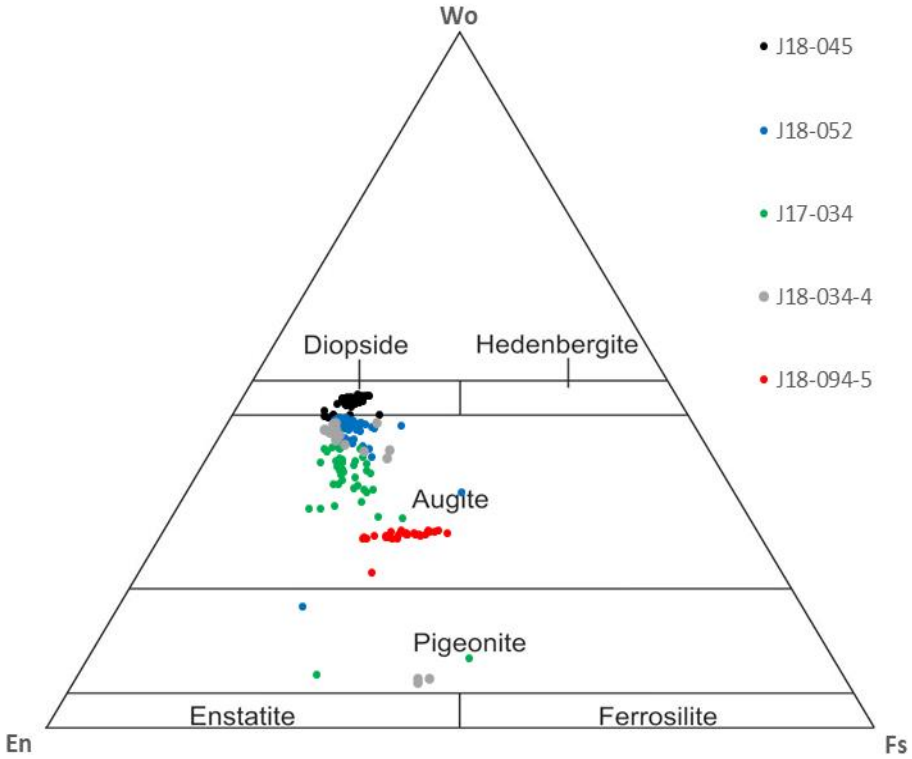

Fig. 5.55 Clinopyroxene classification for Cabra formation (classification diagram from Morimoto et al. (1988)).

Clinopyroxene in this formation is mainly augite with subordinate diopside found mainly in J18-045 (Fig. 5.55). Pigeonite is also found in this formation. In basalt, the clinopyroxene (excluding pigeonite) exhibit the following compositional ranges: Mg# = 51-80, Wo = 30-50 (34-48 for Ol-basalts), En = 33-52 (33-45 for Ol-basalt), and Fs =11-33. Clinopyroxene in the andesite (e.g., J18-034-4) exhibits the following compositional ranges: Mg# = 65-79, Wo = 39-44, En = 38-45, and Fs =12-22 and clinopyroxene in the diorite (e.g., J18-094-5) exhibits the following compositional ranges: Mg# = 53-67, Wo = 22-28, En = 38-49, and Fs =25-34. Clinopyroxene in this formation is a later stage mineral than plagioclase (with the exception of J18-034-4) and they all form fine-grained crystals in the groundmass. Overall, TiO_2 (0.43-3.98 wt.% for the mafic member and 0.08-1.49 wt.%

for the felsic member), FeO (6.5-19.2 wt.% for the mafic member and 7.5-18.6 wt.% for the felsic member) and MnO (0.09-0.47 wt.% for the mafic member and 0.14-0.59 for the felsic member) content increase with decreasing Mg# (Fig. 5.56). The TiO_2 content increases with decreasing Mg# even though different samples have different slopes. The SiO_2 (42.3-53.7 wt.% for the mafic member and 48.7-54.4 wt.% for the felsic member) and CaO (14.5-22.3 wt.% for the mafic member and 10.9-21.0 wt.% for the felsic member) content have a slightly positive correlation with Mg#. Al_2O_3 (1.3-8.5 for the mafic member and 1.2-6.2 for the felsic member) does not show a clear correlation with Mg#.

The clinopyroxene is in disequilibrium with co-existing whole-rock composition even though the distribution is unimodal (Fig. 5.57). This could be attributed to that clinopyroxene is not phenocryst but a groundmass phase.

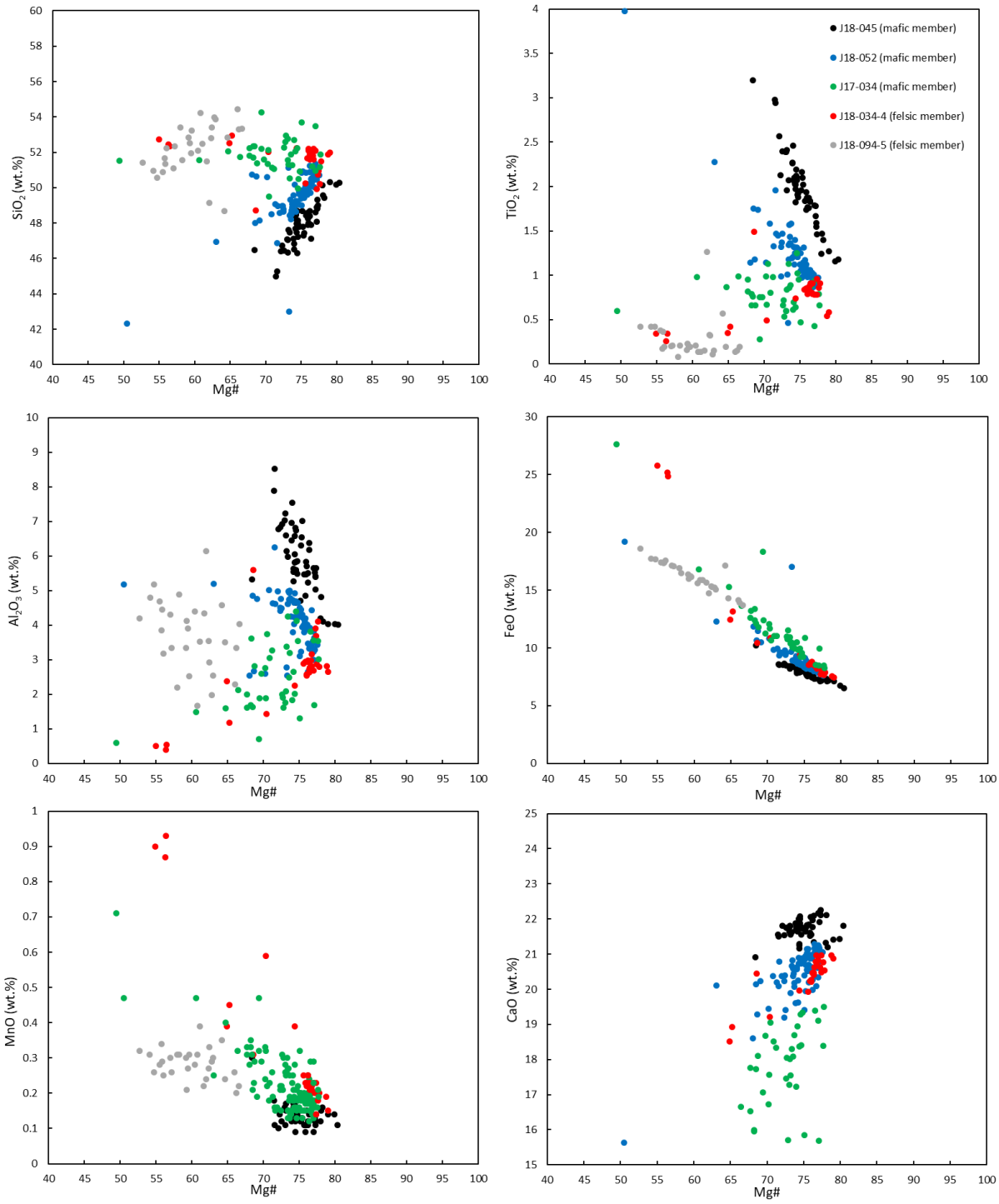

Fig. 5.56 Representative elements plotted against Mg# for clinopyroxene of Cabra Formation.

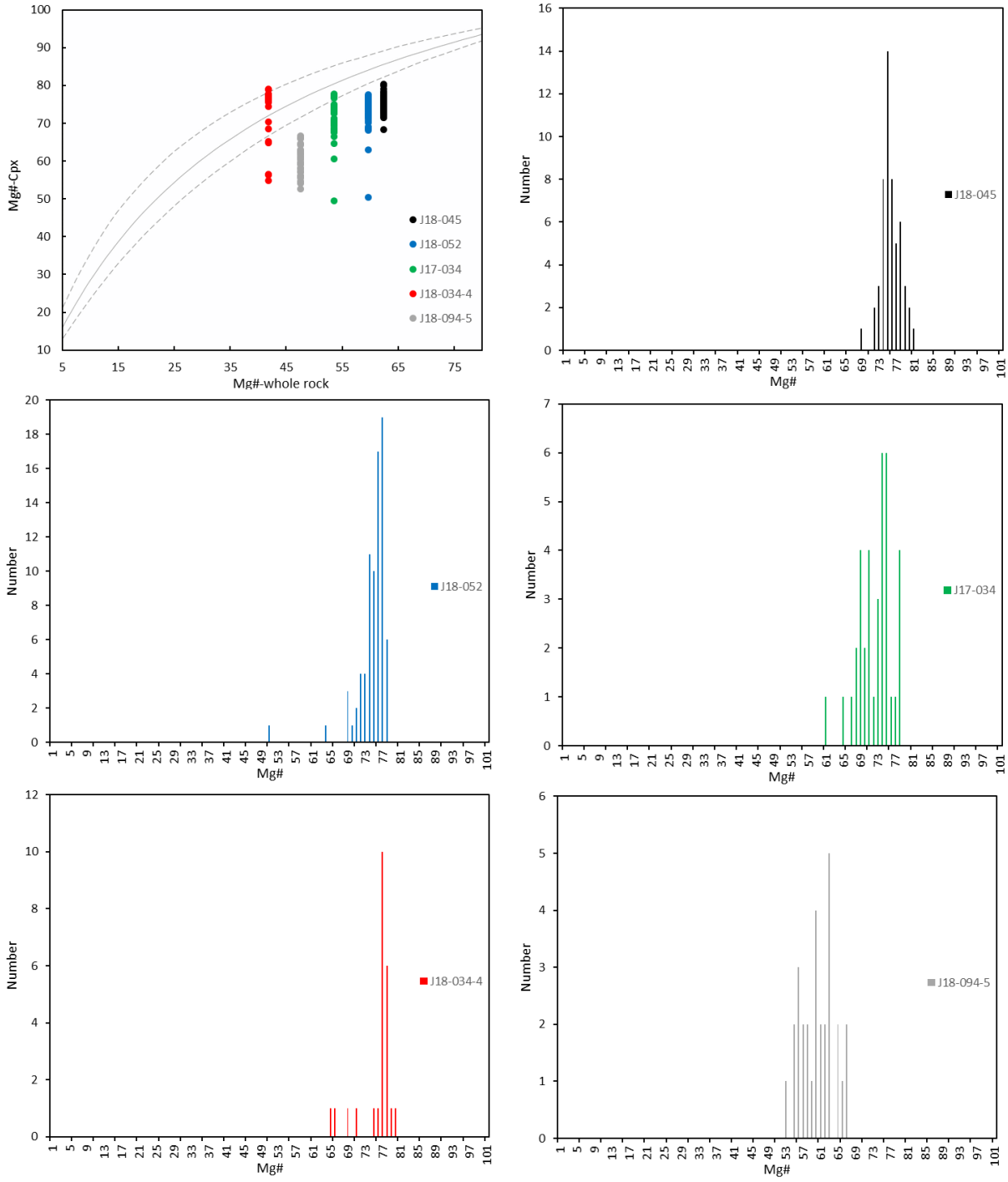

Fig. 5.57 Rhodes diagram and distribution diagram for Cabra formation (In Rhodes diagram, Kd=0.28±0.08 from Putirka (2008)).

High Ca clinopyroxene, e.g., diopside and augite, are plotted in discrimination diagrams (Fig. 5.58). Clinopyroxene in J18-094-5, which has Mg# < 65 and show evidence for Ti fractionation due to coeval ilmenite crystallization (Buchs et al., 2019a) are excluded from these diagrams. Clinopyroxene in J18-045 plots in the alkaline field while clinopyroxene in J18-052 straddles the boundary between the alkaline and sub-alkaline fields in the Ca-Na-Ti diagram (Fig. 5.58A). Clinopyroxene in J17-034 and J18-034-4 plots in sub-alkaline field, except for several clinopyroxene crystals in J18-034-4

which plot as ‘MORB-like’ in Ca-Ti+Cr diagram (Fig. 5.58B). In the TiO_2-Na_2O-CaO diagram (Fig. 5.58C), clinopyroxene in samples J18-045 and J18-052 plots in the ‘within plate field’ and they, along with J17-034, plot in the MORB field in TiO_2-SiO_2/100-Na_2O field (Fig. 5.58D). Clinopyroxene in J17-036-1 are the reference in these diagrams and some clinopyroxene in J18-034-4 is similar to these reference clinopyroxene grains, which plot in the supra-subduction or volcanic arc field (Fig. 5.58 B,C,D).

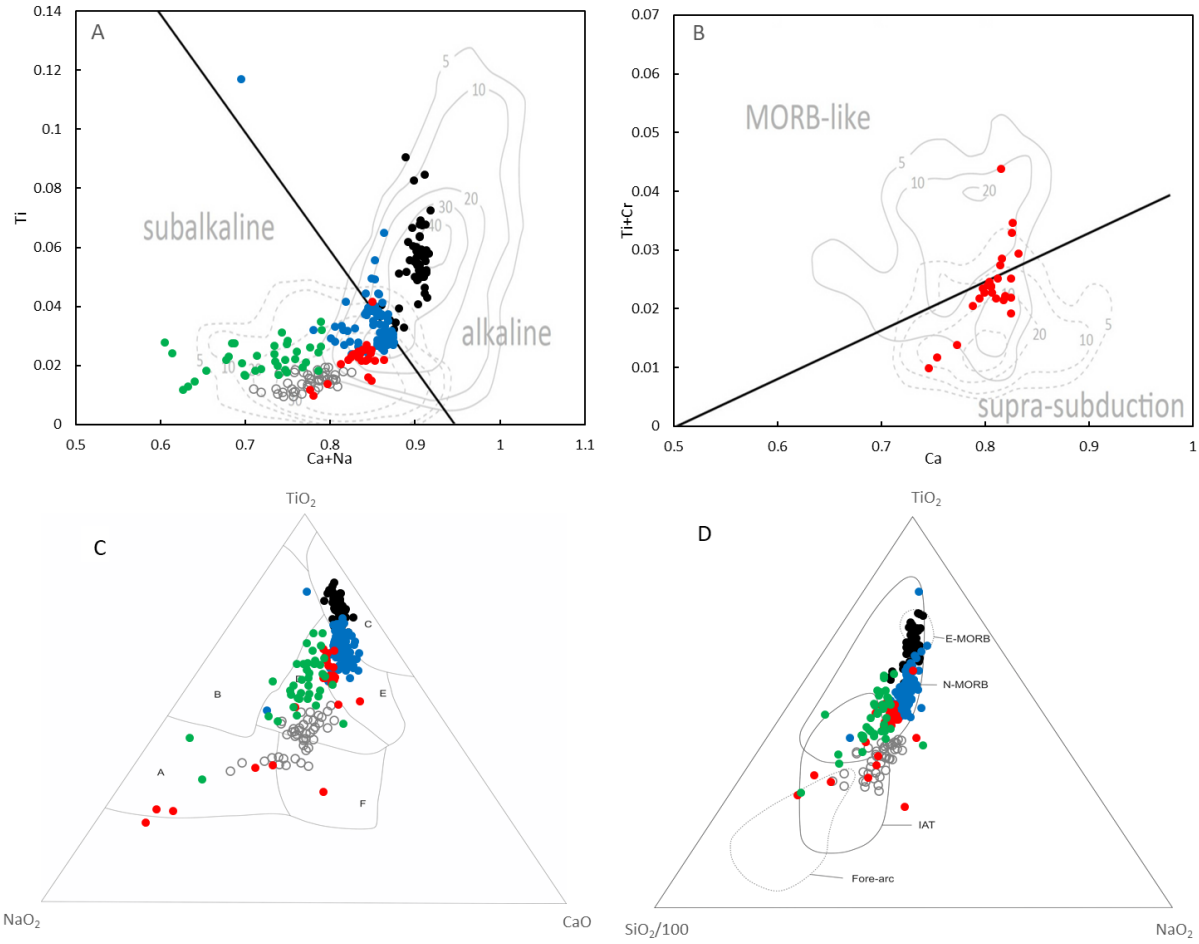

Fig. 5.58 Discrimination diagrams for clinopyroxene in Cabra formation (A,B from Leterrier (1982) and cations are calculated based on 4 cations; C from Nisbet and Pearce (1977) (A: VAB; B: OFB; C:WPA; D:all; E: VAB+WPT+WPA; F: VAB+WPA; G: WPA); D from Beccaluva et al., 1989; circle is J17-036-1 from Pam2 as reference).

Clinopyroxene in the mafic member are all very fine-grained in groundmass (Fig. 5.59). In the felsic member, reversed zonation is common in diorite J18-094-5 (Fig. 5.60). In andesite J18-034-4, clinopyroxene is euhedral and is relatively homogeneous in composition (Fig. 5.61).

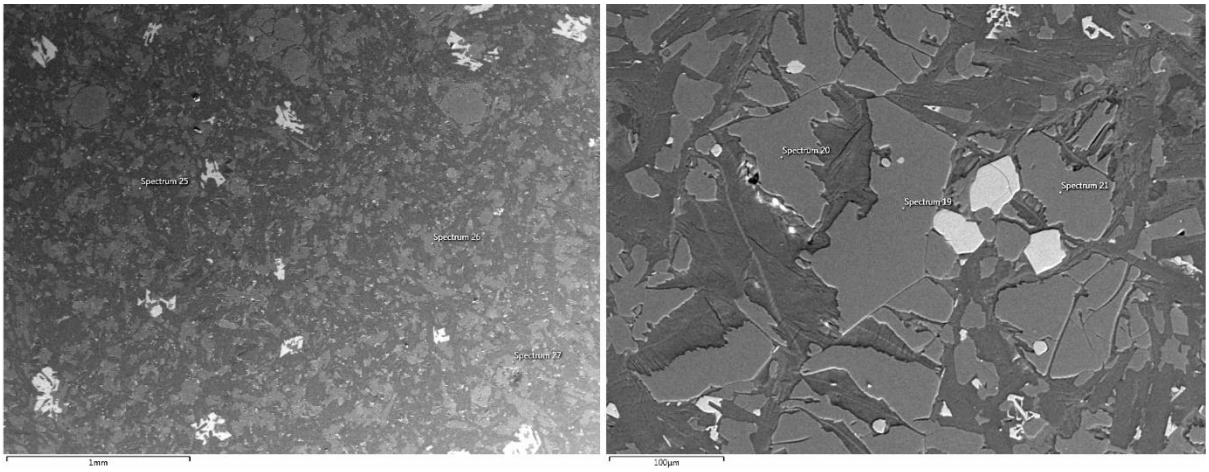

Fig. 5.59 Very fine-grained clinopyroxene in the groundmass of rocks in the Cabra mafic member.

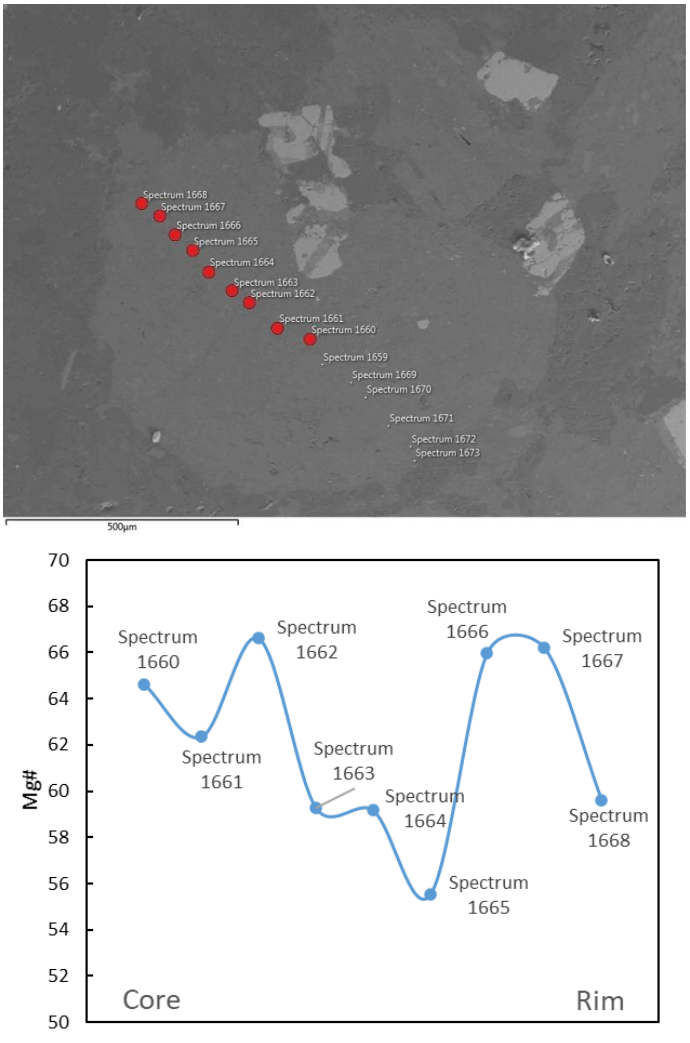

Fig. 5.60 Reversed zonation of clinopyroxene in J18-094-5.

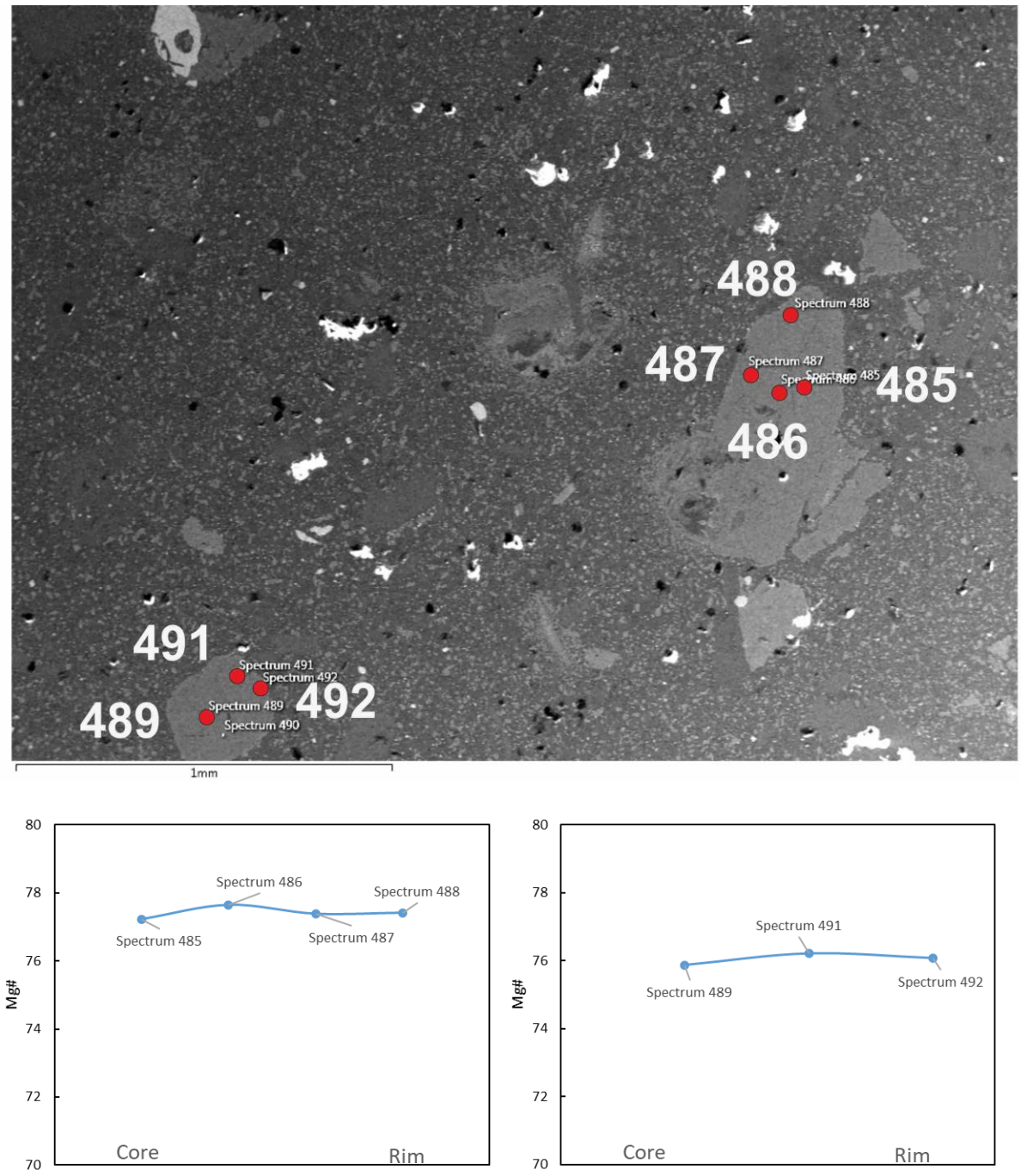

Fig. 5.61 Relatively homogeneous composition of clinopyroxene in J18-034-4.

5.5.2 Plagioclase

Feldspar in the Cabra Formation is plagioclase with a composition ranging from oligoclase to bytownite (Fig. 5.62). Three analyses plot in the miscibility gap area which might be due to analytical problems.

Plagioclase in J18-045 and J18-052 is fine-grained mass of crystals in the groundmass. An-number ranges from 64 to 73 for J18-045 with one exception of An =26 and it ranges from 51 to 69 for J18-

052 (Fig. 5.63). Plagioclase in J17-034 are phenocrysts and show a large range of composition from 47 to 86. A large compositional range of is also found in J18-034-4 with An = 37-79. Plagioclase in J18-094-5 has a low An value from 23 to 62.

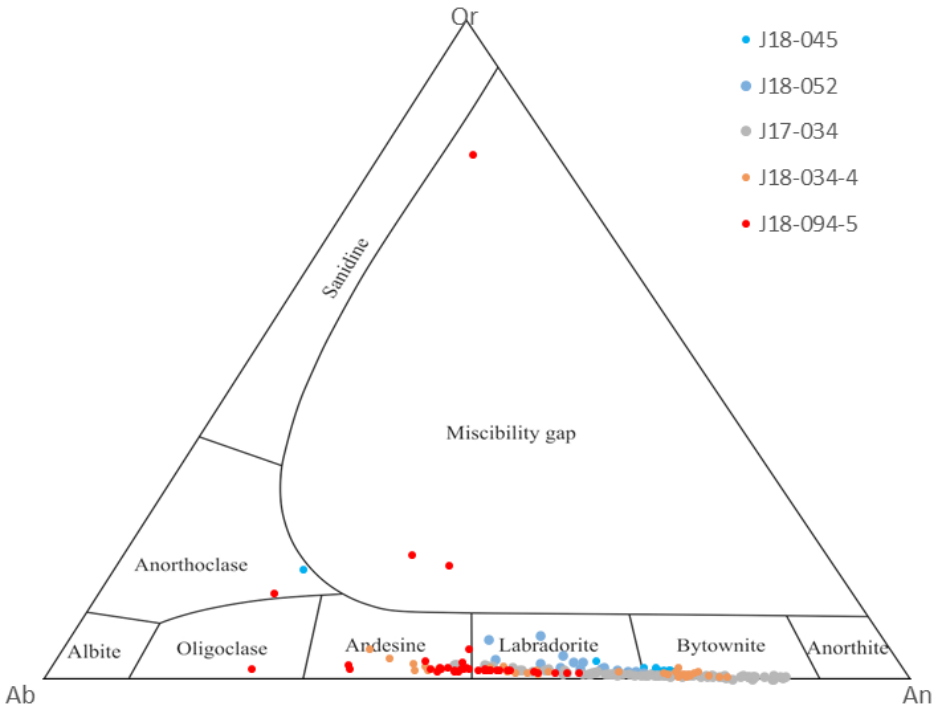

Fig. 5.62 Plagioclase classification for Cabra Formation (classification diagram from Smith and Brown., 1988).

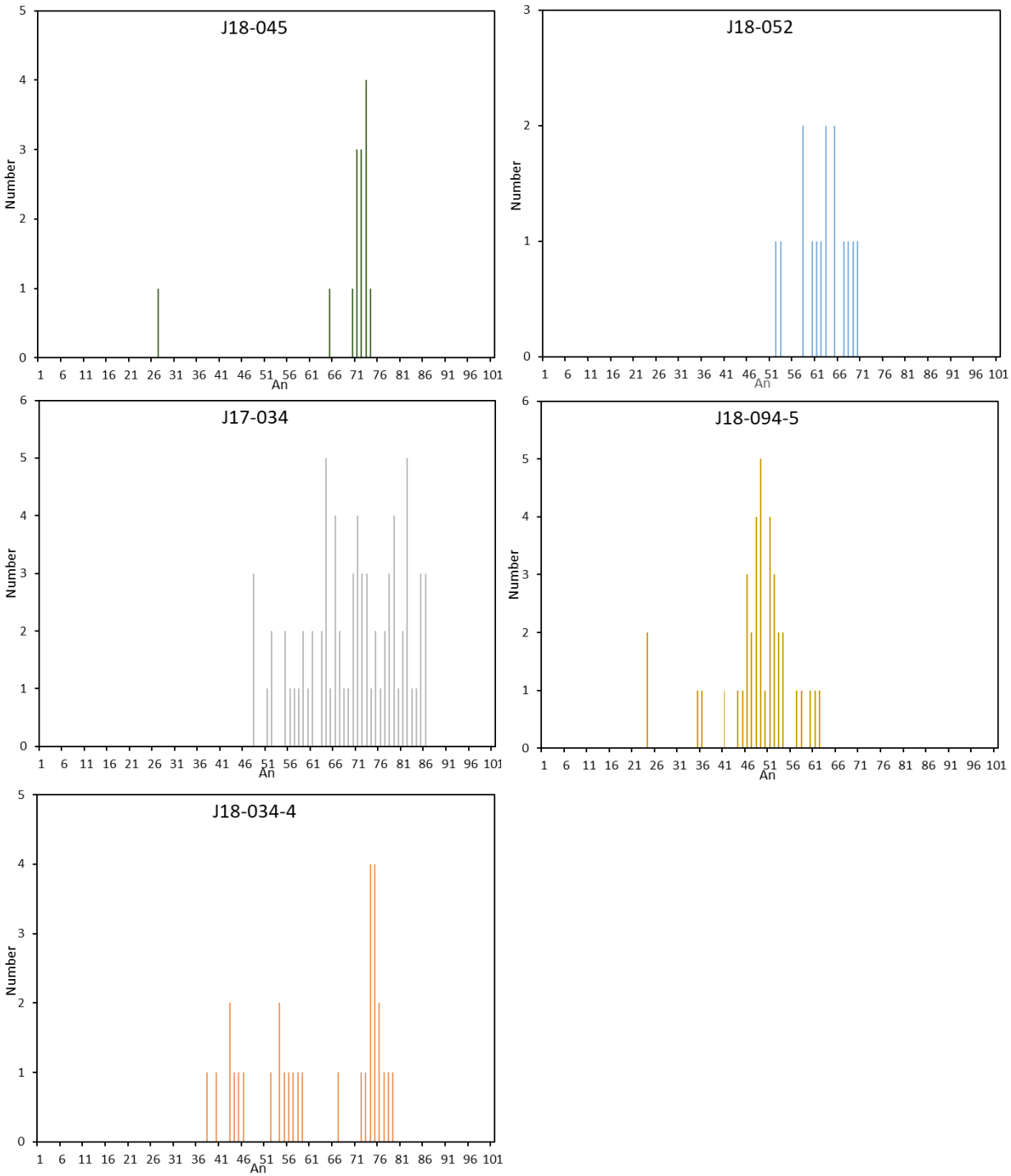

Fig. 5.63 An number distribution for Cabra Formation.

Plagioclase phenocrysts in J17-034 show mainly reversed zonation with a large compositional range in single crystals (Fig. 5.64). High An content, up to 86, are always found in the cores while the rim has An contents as low as 58 (Fig. 5.64). It is similar for J18-094-5 only with lower An and a smaller range of composition (Fig. 5.65). Plagioclase phenocrysts in J18-034-4 are relatively homogeneous in individual crystals without obvious zonation. This is consistent with the composition of clinopyroxene in these samples (Fig. 5.61). However, different crystals have variable composition with An = 45 for

some crystals and An = 75 for other crystals (Fig. 5.66). Plagioclase in a xenolith in J18-034-4 have a relatively low An-number from ~35 to 60 (Fig. 5.67) and belong to the low value endmember based on the An distribution (Fig. 5.63).

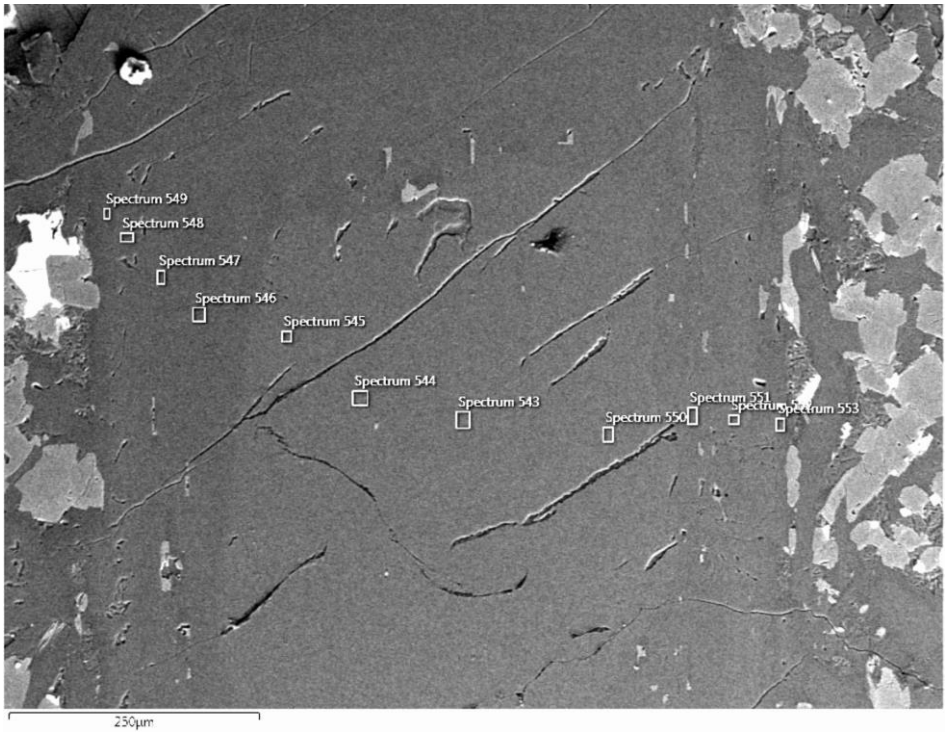

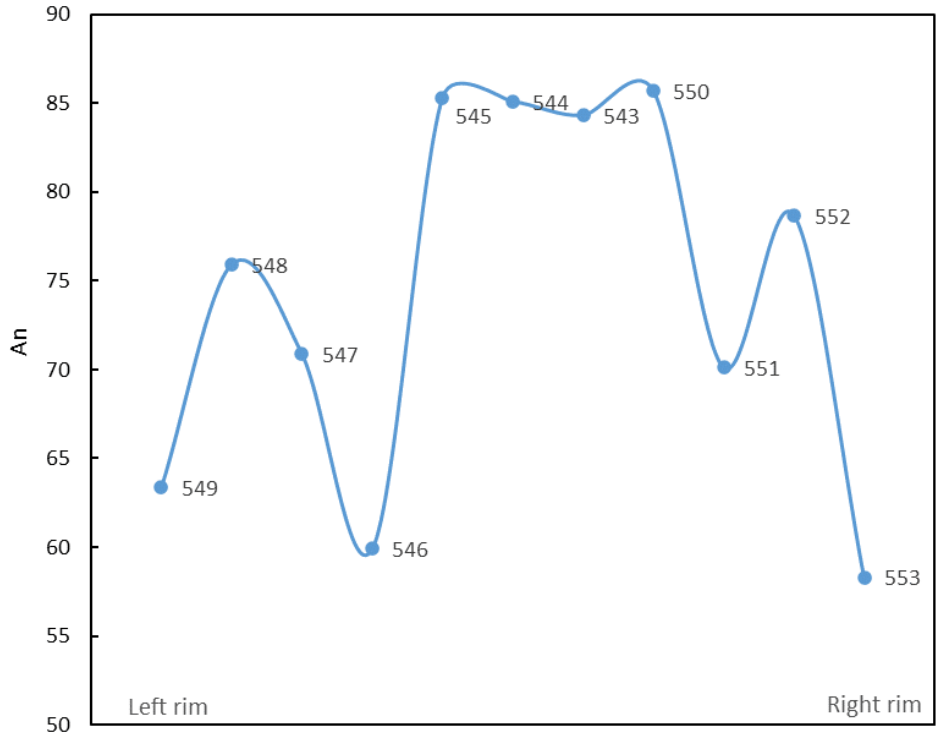

Fig. 5.64 Reversed zonation in J17-034.

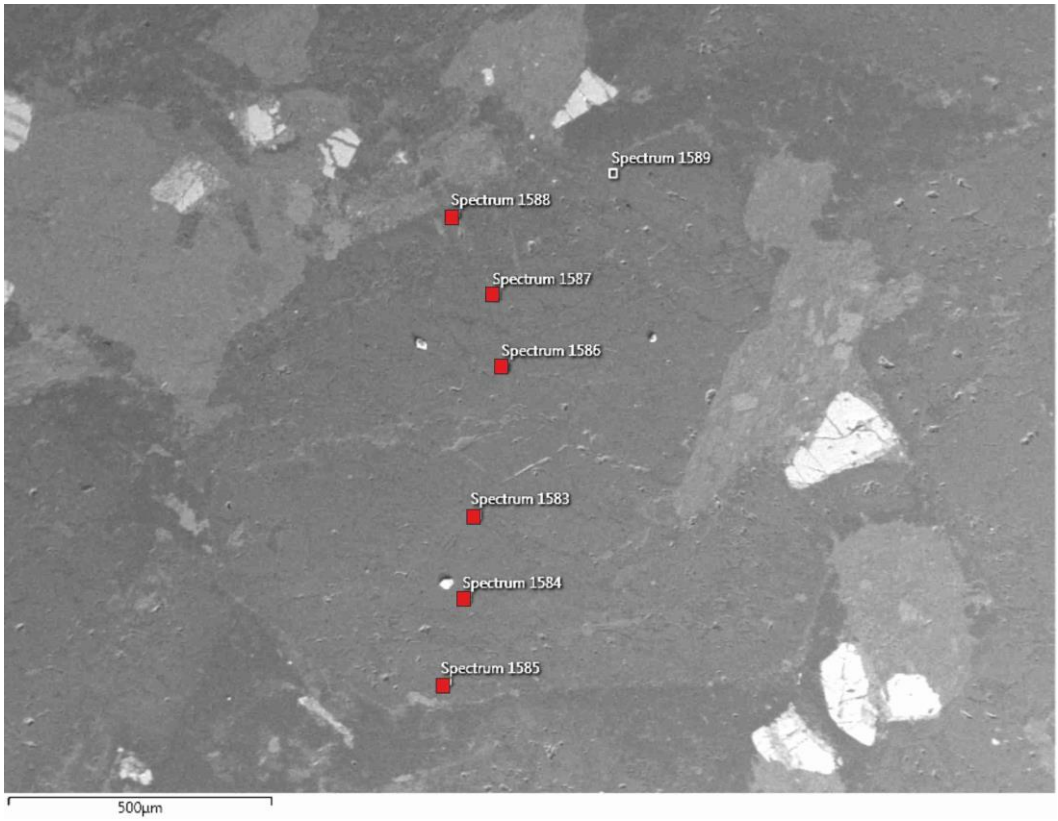

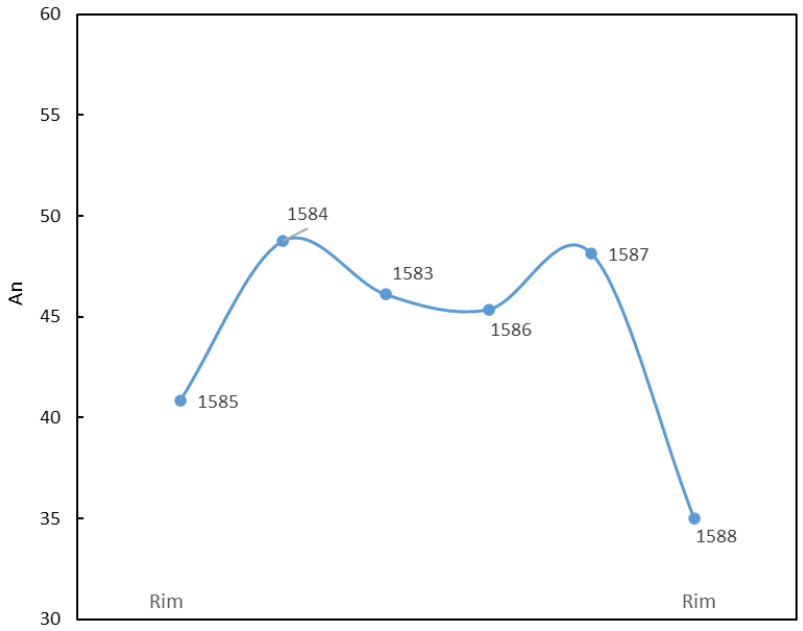

Fig. 5.65 Reversed zonation of plagioclase in J18-095-4.

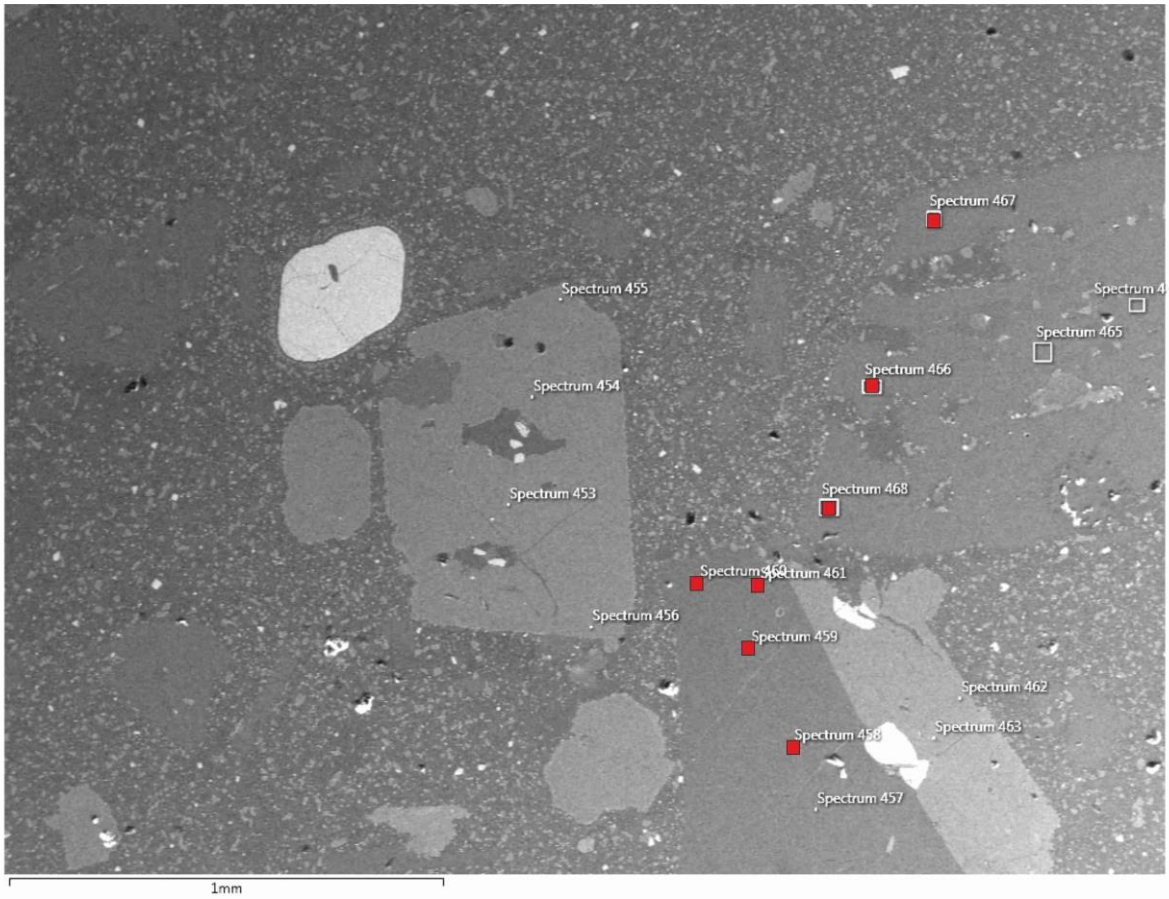

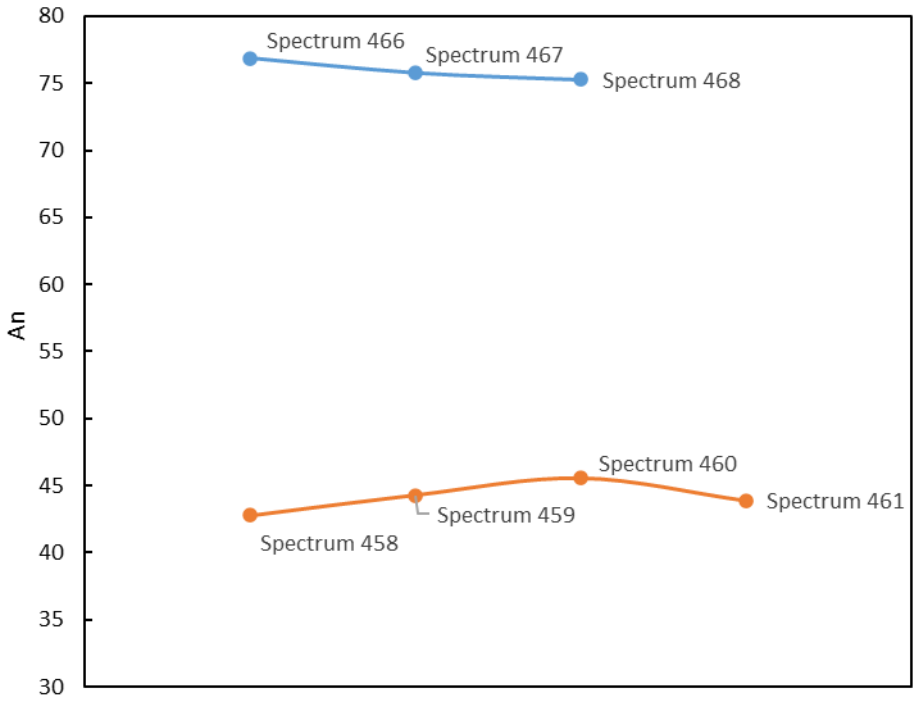

Fig. 5.66 Variable composition of different plagioclase crystals in J18-034-4.

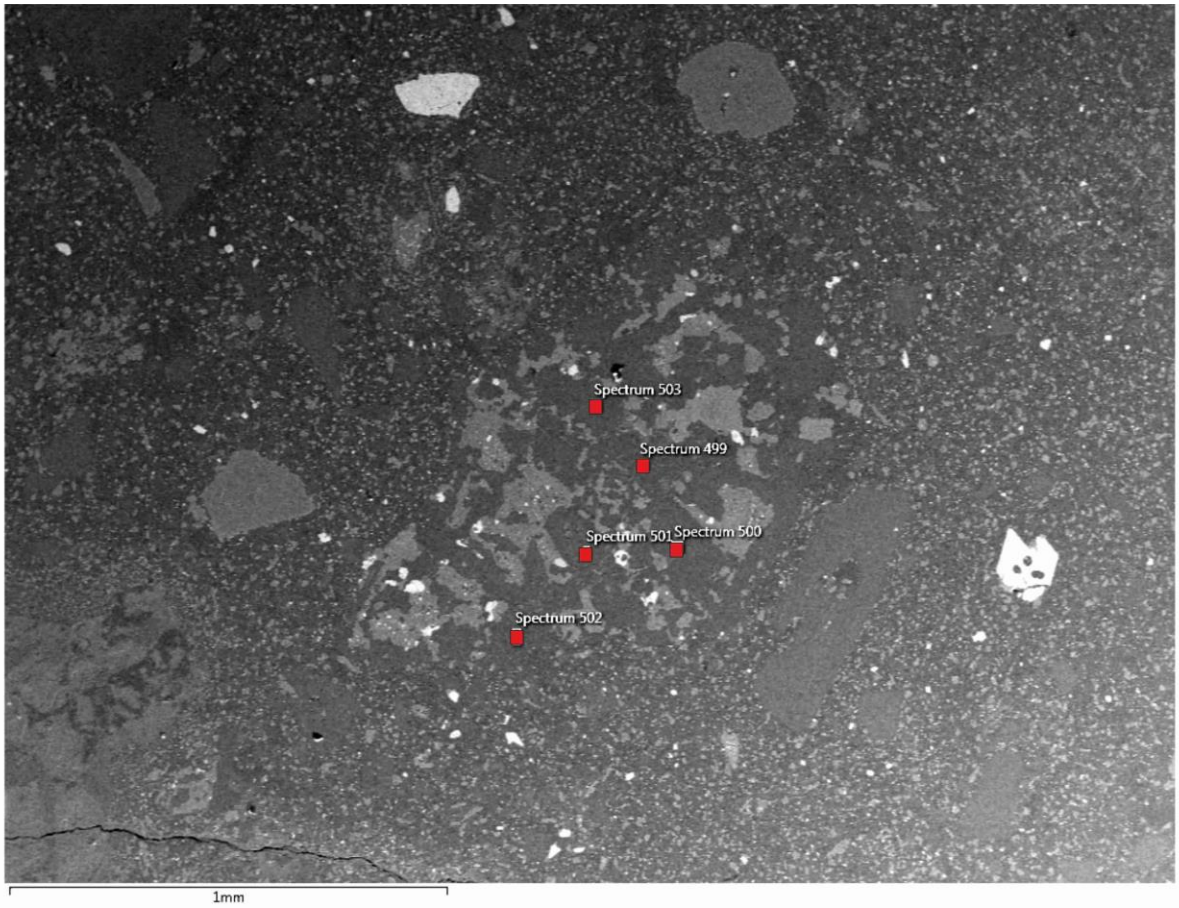

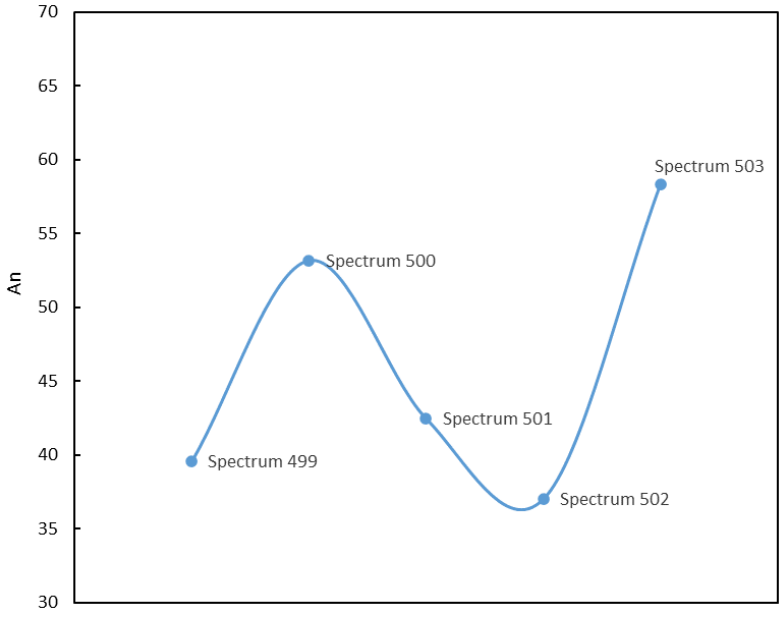

Fig. 5.67 Composition of plagioclase in xenoliths in J18-034-4.

5.5.3 Orthopyroxene

Orthopyroxene is only found in J18-034-4 and these are enstatite with a compositional range of En = 58-70, Fs = 27-38, and Wo =3-4 (Fig. 5.68). Orthopyroxene can be found in the core, while pigeonite comprises the rim (Fig. 5.69).

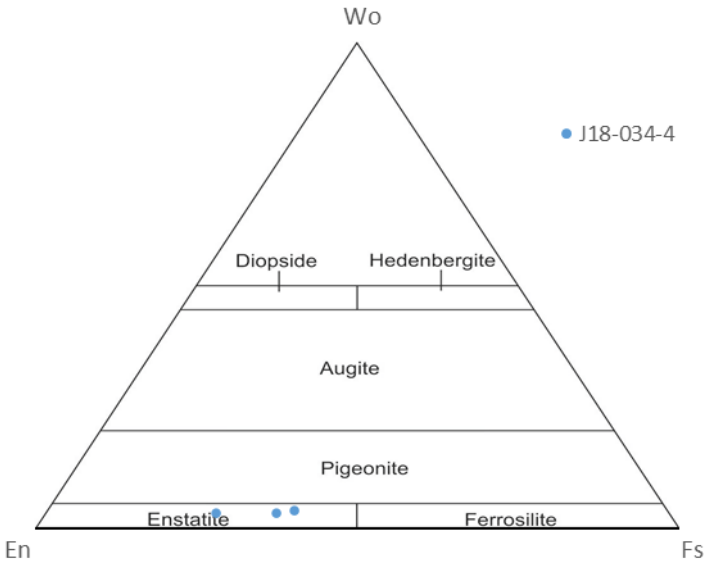

Fig. 5.68 Orthopyroxene classification for J18-034-4 (classification diagram from Morimoto et al., 1988).

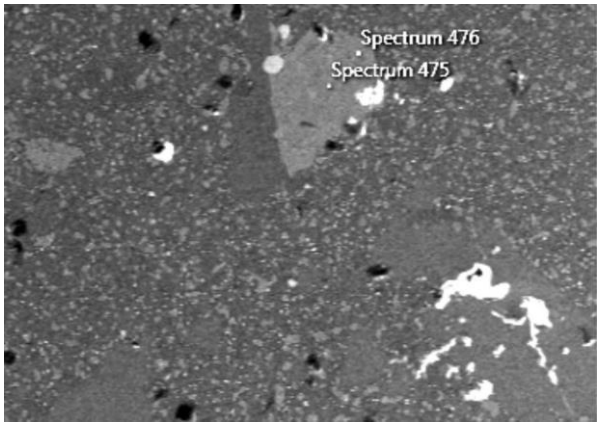

Fig. 5.69 Orthopyroxene in J18-034-4 (Spectrum 475 is orthopyroxene and 476 is pigeonite).

5.5.4 Olivine

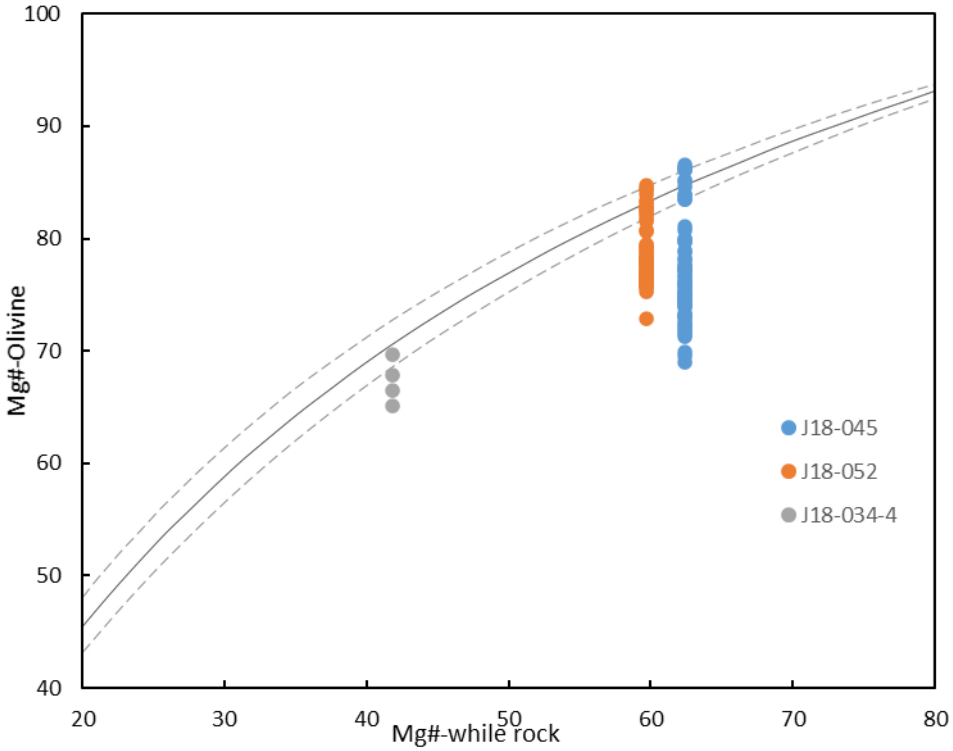

Fig. 5.70 Rhodes diagram for olivine in Cabra formation (Kd= 0.30±0.03 from Putirka, 2008).

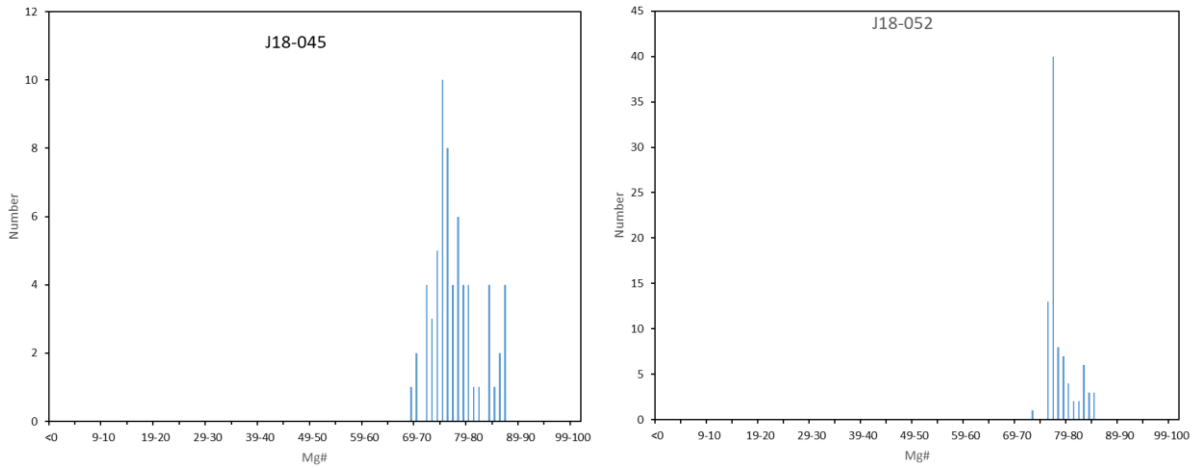

Fig. 5.71 Mg# distribution diagram for Olivine in Cabra Formation.

Olivine is found in J18-045, J18-052 and J18-034-4. Mg# ranges from 69 to 87, 73-85 and 65-70 for J18-045, J18-052 and J18-034-4, respectively. The large range of composition mean that most of crystals are not in equilibrium with their host rock (Fig. 5.70) which might be due to olivine accumulation. In the Mg# distribution diagram (Fig. 5.71), bimodal distribution, especially in J18-052 is observed. Olivine in this group shows normal zonation or no zonation (Fig. 5.72, Fig. 5.73). With normal zonation, Fo can be up to ~ 86 in the core and ~ 75 in the rim.

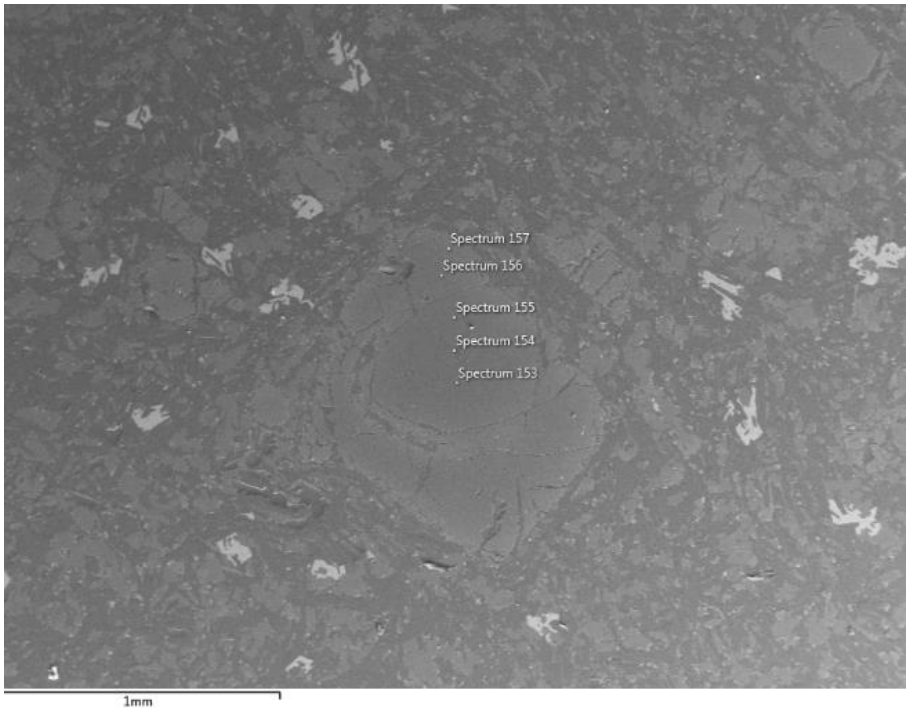

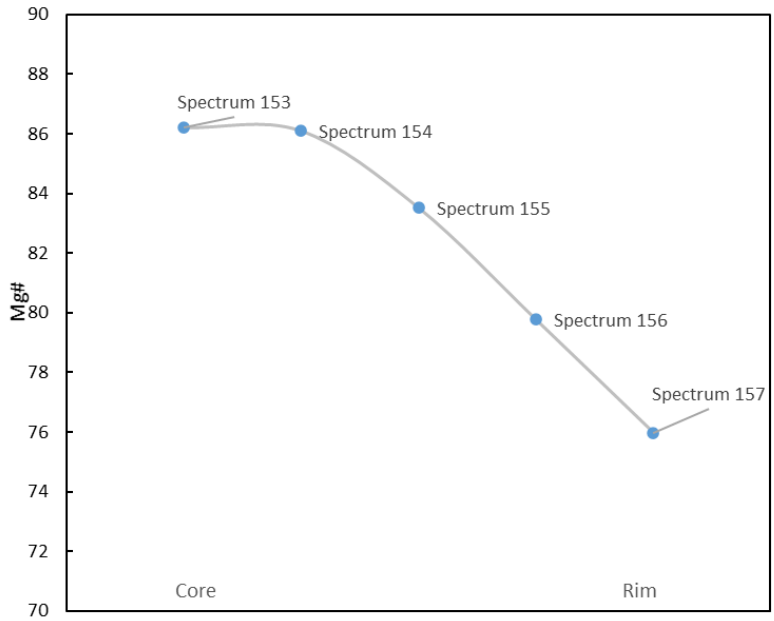

Fig. 5.72 Normal zonation of olivine in J18-045.

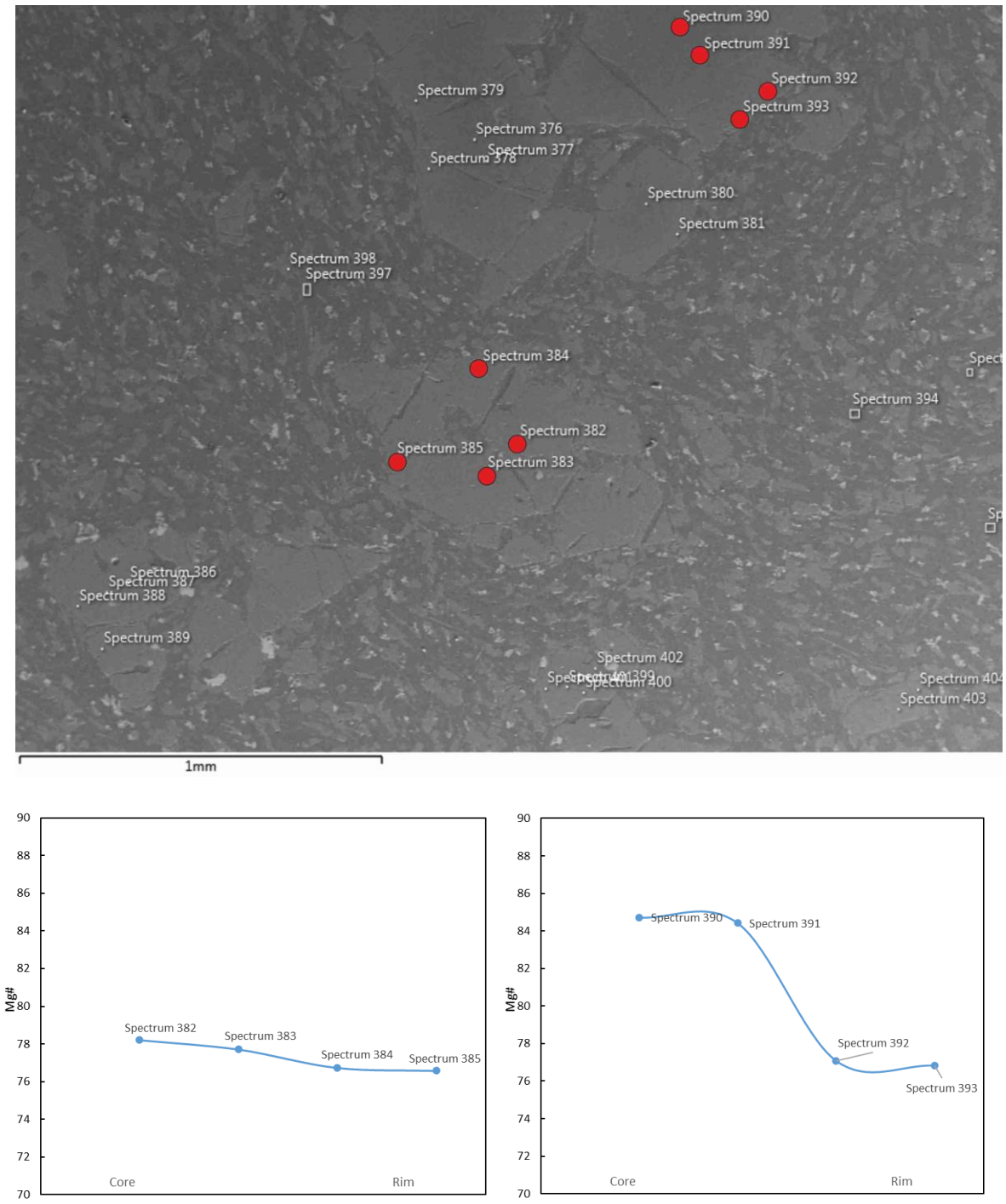

Fig. 5.73 Homogeneous olivine and normally zoned olivine in J18-052.

5.6 Relationship between Clinopyroxene and Whole Rock Composition

The composition of clinopyroxene is controlled by the composition of its host magma (Kushiro, 1960; Le Bas, 1962; Nisbet and Pearce, 1977; Leterrier et al., 1982; Loucks, 1990) and pressure and temperature of the magma (Nimis, 1995; Putirka, 2008). To check the relationship between clinopyroxene composition and host magma composition, the composition of clinopyroxene grains have been plotted against their respective whole-rock compositions. To rule out the effect of different sources, only samples from the Panama and Las Cascadas Formations have been selected, since these two formations are cogenetic due to similar isotopes. To rule out the effect of magma mixing, only samples without significant evidence magma mixing are selected, e.g., samples in which clinopyroxene phenocrysts show unimodal Mg# distribution and are in equilibrium in the Rhodes diagram and plagioclase phenocrysts show a unimodal An-number distribution. The clinopyroxene composition for each sample is represented by the average composition of clinopyroxene phenocrysts in the sample.

Firstly, the relationship between elemental compositions and Mg# of clinopyroxene and SiO_2 of the whole-rock was plotted. As can be seen from the diagrams (Fig. 5.74), SiO_2, and MnO of clinopyroxene shows a good positive correlation with SiO_2 of the whole-rock while Al_2O_3 and Mg# show a negative correlation with the whole-rock. The CaO, Na_2O, and TiO_2 content shows a slightly weaker negative correlation with SiO_2 of the whole rock. However, TiO_2 of clinopyroxene correlates well with TiO_2 of the whole rock.

Secondly, the relationship between elemental compositions of clinopyroxene and Mg# of the whole rock was plotted. As can be seen from Fig. 5.75, SiO_2, and MnO of clinopyroxene show a good negative correlation with Mg# of the whole rock while Al_2O_3 and Mg# show a positive correlation with Mg# of the whole rock. CaO, Na_2O, TiO_2 show weak positive correlation with Mg# of the whole rock. Fig. 5.75 show trends that are in contrast to the trends in Fig. 5.74 but the R squared values in Fig. 5.74 are higher than that in Fig. 5.75. This indicates elements in clinopyroxenes are controlled by the composition of the magma. SiO_2 of the whole rock has a better correlation with clinopyroxene composition than Mg#.

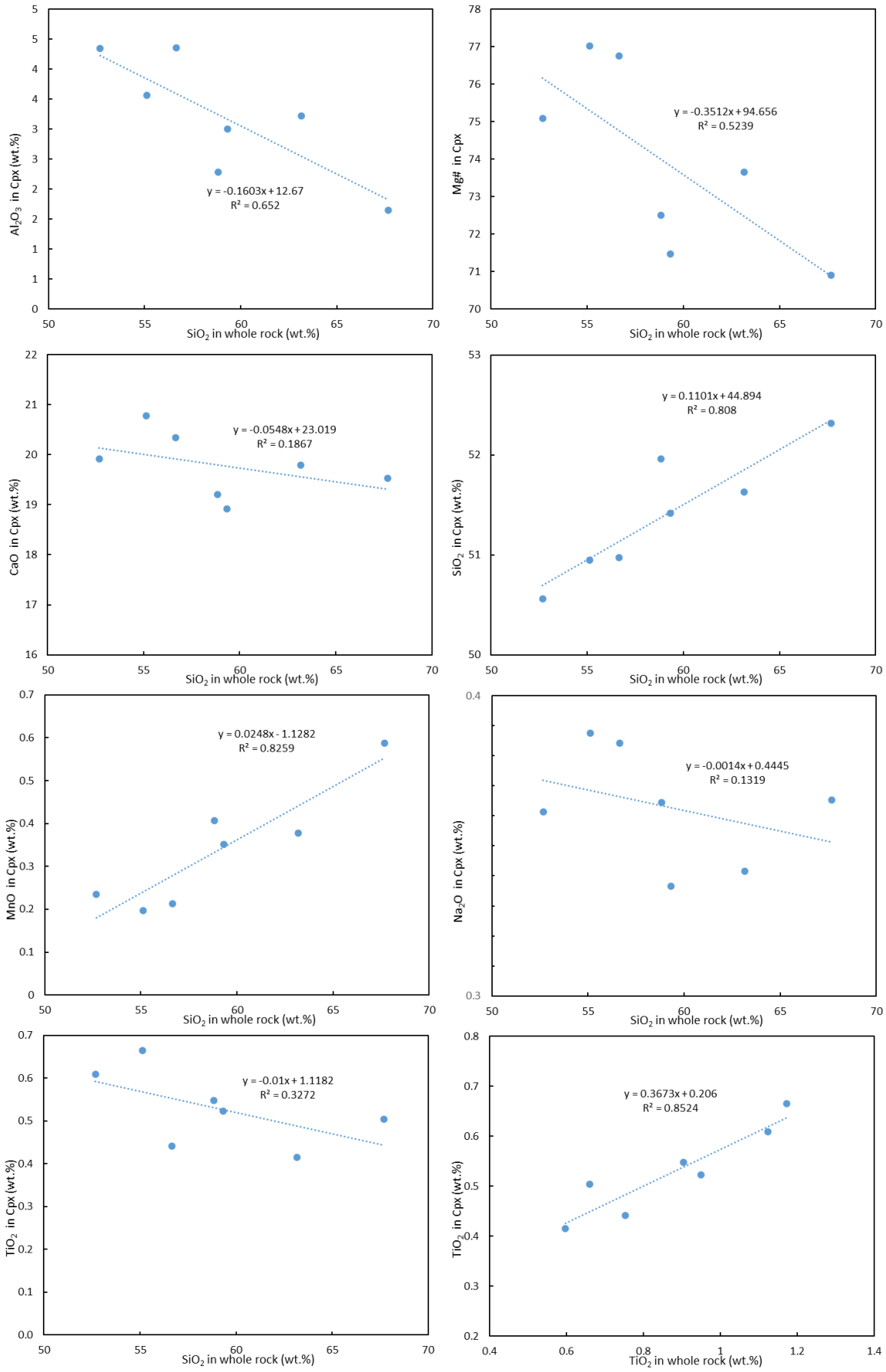

Fig. 5.74 Representative elements of clinopyroxene plotted against SiO_2 of whole rocks.

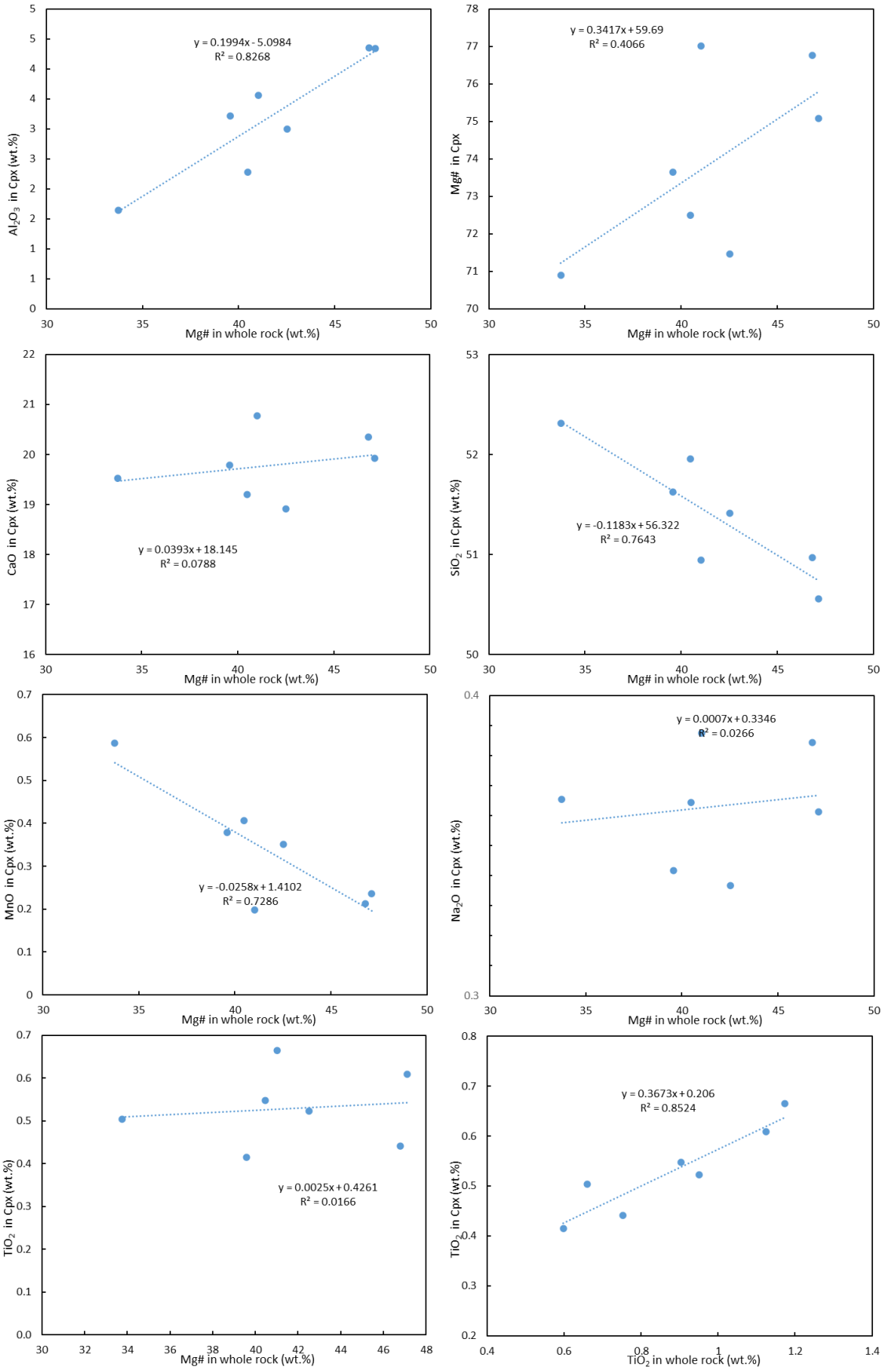

Fig. 5.75 Representative elements of clinopyroxene plotted against MgO of whole rocks.

5.7 Summary

Fig. 5.76 summarises the composition of all clinopyroxene grains analysed in central Panama. The composition of clinopyroxene grains from different groups overlap. The majority of clinopyroxene analyses plot in the augite field with some of the Chagres Complex and Cabra Formation in the diopside field. A few of the Cabra Formation are pigeonite. Therefore, there generally appears to be one major clinopyroxene population for rocks in central Panama.

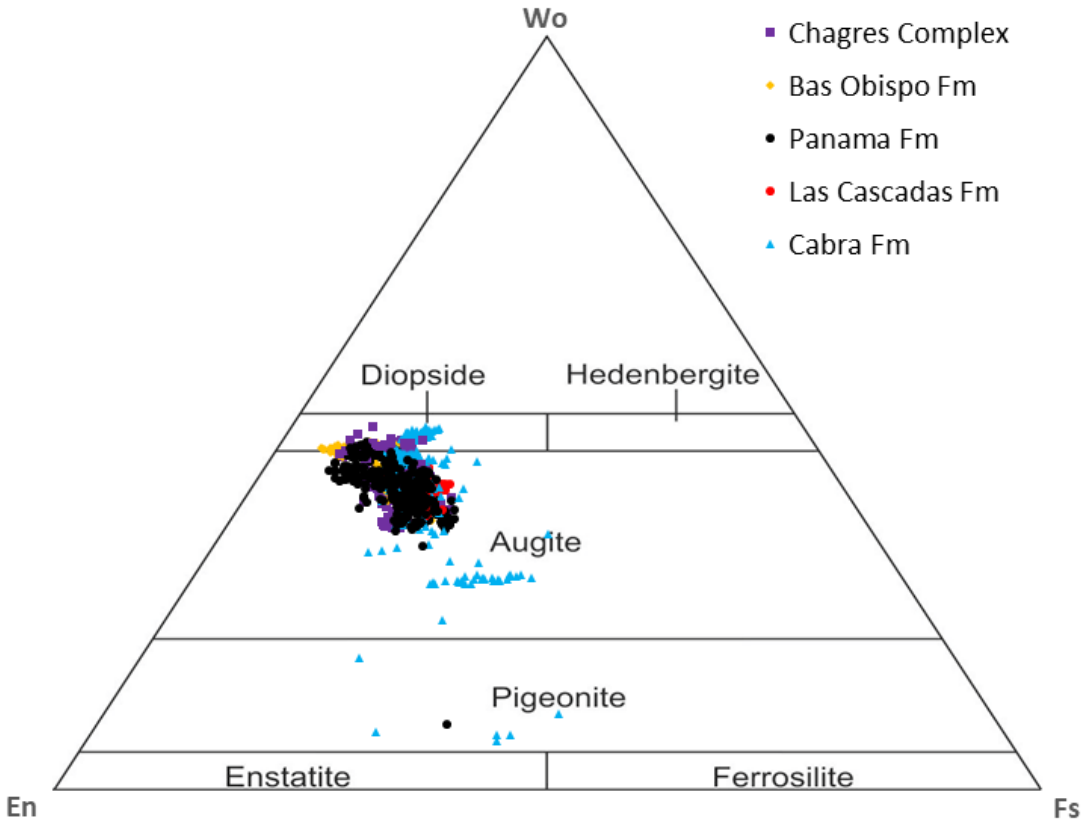

Fig. 5.76 Clinopyroxene classification for all clinopyroxene grains in this study (classification diagram from Morimoto et al. (1988)).

As can be seen from Rhodes diagram (Fig. 5.77), all the clinopyroxene grains do not display equilibrium with their host rocks. Clinopyroxene grains of the Las Cascadas Formation are overall above the equilibrium line while those of the Cabra Formation are overall below the equilibrium line. The Chagres Complex, Bas Obispo Formation, and Panama Formation possess clinopyroxenes having large range of composition from above to below the equilibrium line. They normally show bimodal or even three-peak distribution in terms of Mg#. This large compositional variation can also occur in single crystals showing significant zonation, e.g. normal, reversed, or oscillatory zonation.

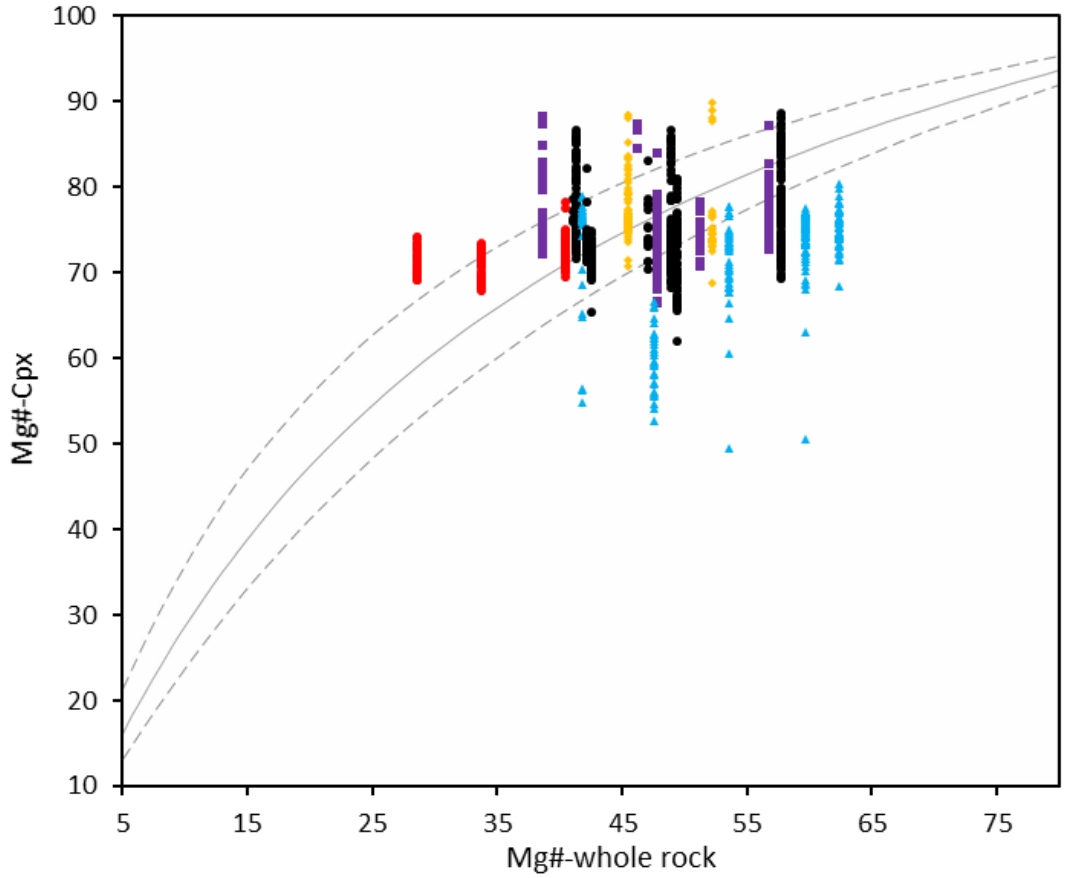

Fig. 5.77 Rhodes diagram for all clinopyroxene grains in central Panama (Kd=0.28±0.08 from Putirka (2008); symbols are the same to those in Fig. 5.76).

Fig. 5.78 highlights the plagioclase composition of rocks in central Panama. nearly all grains plot along the albite-anorthite solid state solution line with a few exceptions from J18-094-5 in the Cabra Formation. Overall, plagioclase of the Chagres Complex and Panama Formation are similar ranging from bytownite to labradorite. Plagioclase of the Las Cascadas Formation range from labradorite to andesine, which is consistent with their more evolved composition than that of the Chagres Complex and Panama Formation. The Bas Obispo Formation possesses plagioclase grains of large range of composition, ranging from bytownite to albite. The Cabra Formation also have a large range of plagioclase grains compositionally which is consistent with their large range of whole rock composition. Plagioclase grains of the mafic rocks in this formation are bytownite to labradorite while plagioclase grains of the felsic rocks are labradorite to andesine. Large compositional variation of plagioclase of the Chagres Complex, Panama Formation, and the Cabra Formation can be found in single crystals which show normal or reversed zonation. This is also consistent with the characteristics of clinopyroxenes.

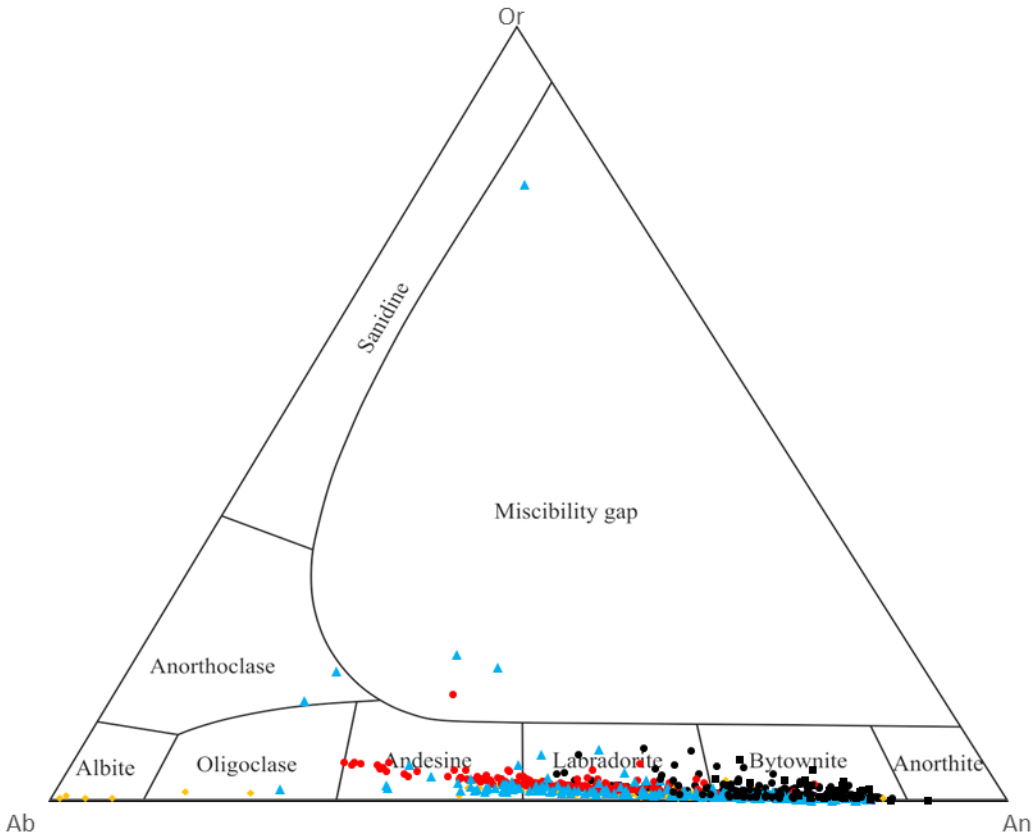

Fig. 5.78 Plagioclase classification for all plagioclase grains in central Panama (classification diagram from Smith and Brown., 1988; symbols are the same to those in Fig. 5.76).

6 DISCUSSION

The following chapter will discuss and evaluate the whole rock geochemical and mineral chemical data presented in the previous chapters and their implication for the origin and evolution of the rocks in Central Panama. The discussion will begin by examining the magmatic differentiation, such as fractional crystallisation and magma mixing, which have affected the chemistry of the rocks. This will be achieved through utilising both the whole rock major and trace element data and the mineral chemistry major element data. The rhyolite-MELTS program (Gualda et al., 2012; Ghiorso and Gualda, 2015) will be utilised to constrain the petrogenesis and crustal processes of the Panama, Las Cascadas, and Cabra Formation magmas. Chagres Complex have a large range of ages (Lissinna, 2005; Wegner et al., 2011) which is meaningless to do modelling in rhyolite-MELTS v.1.1.x since they are most likely not related. Application to wet intermediate magma compositions is limited by the lack of appropriate thermodynamic models for hydrous minerals, particularly amphibole and biotite (Gualda et al., 2012). Therefore, the amphibole bearing formation of the Caraba Formation was not modelled by rhyolite-MELTS or MELTS.

Mantle source components will be characterised by Sr-Nd-Pb isotopes. The relative proportions for them will be achieved by trace element modelling and isotope modelling. Parameters derived from these models including proportions of mantle components and partial melting degree will be applied to a large range of elements on N-MORB normalised multi-element pattern of the primary melts. The primary melts can be obtained from PRIMACALC2 (Kimura and Ariskin, 2014) which is designed to calculate the primary melt for arc rocks. Finally, geochemical interpretations and modelling results will be utilised to discuss the magmatic and tectonic evolution of central Panama, such as evolution of the source, degrees of partial melting, and associated tectonic events.

6.1 Crystallisation and Magma Mixing

The following sections examine the nature of fractional crystallisation during the evolution of the magmas and resulting trends observed between the Panama Formation and Las Cascadas Formation, the mafic member and the felsic member in the Cabra Formation. The magmatic processes in the plumbing system such as magma mixing, melt extraction for these formations are also evaluated based on whole rock geochemistry and mineral chemistry.

With regard to the whole rock major elements, fractional crystallisation has been modelled using the rhyolite-MELTS computer software programme (Gualda et al., 2012; Ghiorso and Gualda, 2015). The thermodynamic modeling software rhyolite-MELTS, similar to the previous version MELTS (Ghiorso and Sack, 1995; Asimow and Ghiorso, 1998), allows users to understand the chemical and phase assemblage evolution of magmatic systems over a range of pressures (0-2 GPa) and temperatures (500 – 2000 °C). MELTS has been extensively applied to understand the evolution of relatively dry mafic–

intermediate magmas (e.g. Ghiorso, 1997; Gaetani et al., 1998). The number of relevant experiments on silicic systems were limited at the time of calibration of MELTS, therefore the modified calibration for rhyolite-MELTS is optimised for fluid-bearing silicic systems and should be used in place of MELTS for modelling phase relations in hydrous silicic systems (Gualda et al., 2012).

Rhyolite-MELTS has three versions: rhyolite-MELTS v.1.0.x for fluid-absent systems, rhyolite-MELTS v.1.1.x for fluid-present systems which are also quartz saturated (e.g. magmas that terminally crystallise at the quartz-, two-feldspar-, fluid-saturated ternary minimum), and rhyolite-MELTS v.1.1.x for fluid-present systems which are not quartz saturated. Apart from small amount of quartz formed in the diorite J18-094-5 from the Cabra Formation, no quartz are found in the Panama, Las Cascadas, and Cabra Formation samples. Therefore, the version of rhyolite-MELTS v.1.1.x was utilised for modelling. The resulting models help to assess and constrain the conditions and extent of fractional crystallisation observed in rocks in Panama Canal area. Conditions of pressure should be set in the MELTS to constrain the depth at which the magmas crystallise and the liquidus will then be calculated automatically. To set a reasonable value, pressure was calculated for the Panama Formation by mineral thermobarometers prior to MELTS modelling.

6.1.1 Panama Formation and Las Cascadas Formation

6.1.1.1 P-T estimates

As discussed in Chapter 5, samples in the Panama and Las Cascadas formation have gone through variable degrees of magma mixing. Therefore, samples with only minor magma mixing were chosen for the estimation of P-T conditions. Results from clinopyroxene-orthopyroxene couples are considered to yield the more reliable results than other thermobarometers, such as clinopyroxene-only, clinopyroxene-liquid and orthopyroxene-liquid thermobarometers which are also calculated for comparison. It is easier to reach an equilibrium between clinopyroxene and orthopyroxene than between minerals and the melt.

Andesitic sample J17-036-1 and J18-100 of Pam2 (note: Pam2 is the subgroup of the Panama Formation in which clinopyroxenes are all small and homogeneous while Pam1 is the subgroup that big and zoned clinopyroxenes are presented; these two subgroups have been described in Chapter 3) and andesitic J17-006 and dacitic J17-121 from the Las Cascadas Formation were chosen for clinopyroxene and orthopyroxene analysis. Only clinopyroxene and orthopyroxene in contact (Fig. 6.1) are selected for clinopyroxene-orthopyroxene P-T calculation (cases such as orthopyroxene overgrows around clinopyroxene crystals, e.g., in J17-036-1 are ruled out). All clinopyroxene-orthopyroxene couples are in equilibrium in Rhodes diagram (Fig. 6.2). When doing clinopyroxene-liquid and clinopyroxene only P-T calculations, exceptions such as one low Mg# clinopyroxene and one low Mg# orthopyroxene in J17-036-1, two high Mg# clinopyroxene in J18-100 and two high Mg# clinopyroxene in J17-006 have been ruled out since they should be xenocrysts or antecrysts. As can be

seen from Table 6.1 and Fig. 6.3, the lower limit, upper limit, and the mean value for J17-036-1 are 2.9, 5.4, and 4.1 kbars respectively. They are 3.6, 5.2, and 4.3 kbars respectively for J18-100. The values are lower for the Las Cascadas Formation samples. The lower limit, upper limit, and the mean value are 2.9, 4.0 , and 3.6 kbars respectively for J17-006 while they are 2.5, 2.9, and 2.7 kbars for J17-121. The values of pressure as revealed by clinopyroxene-orthopyroxene couples span a large range from 2.5 to 5.4 kbars. Therefore, 2.5 kbars, 5.4 kbars, and the mean value of J17-036-1, e.g. 4.1 kbars were chosen for rhyolite-MELTS modelling.

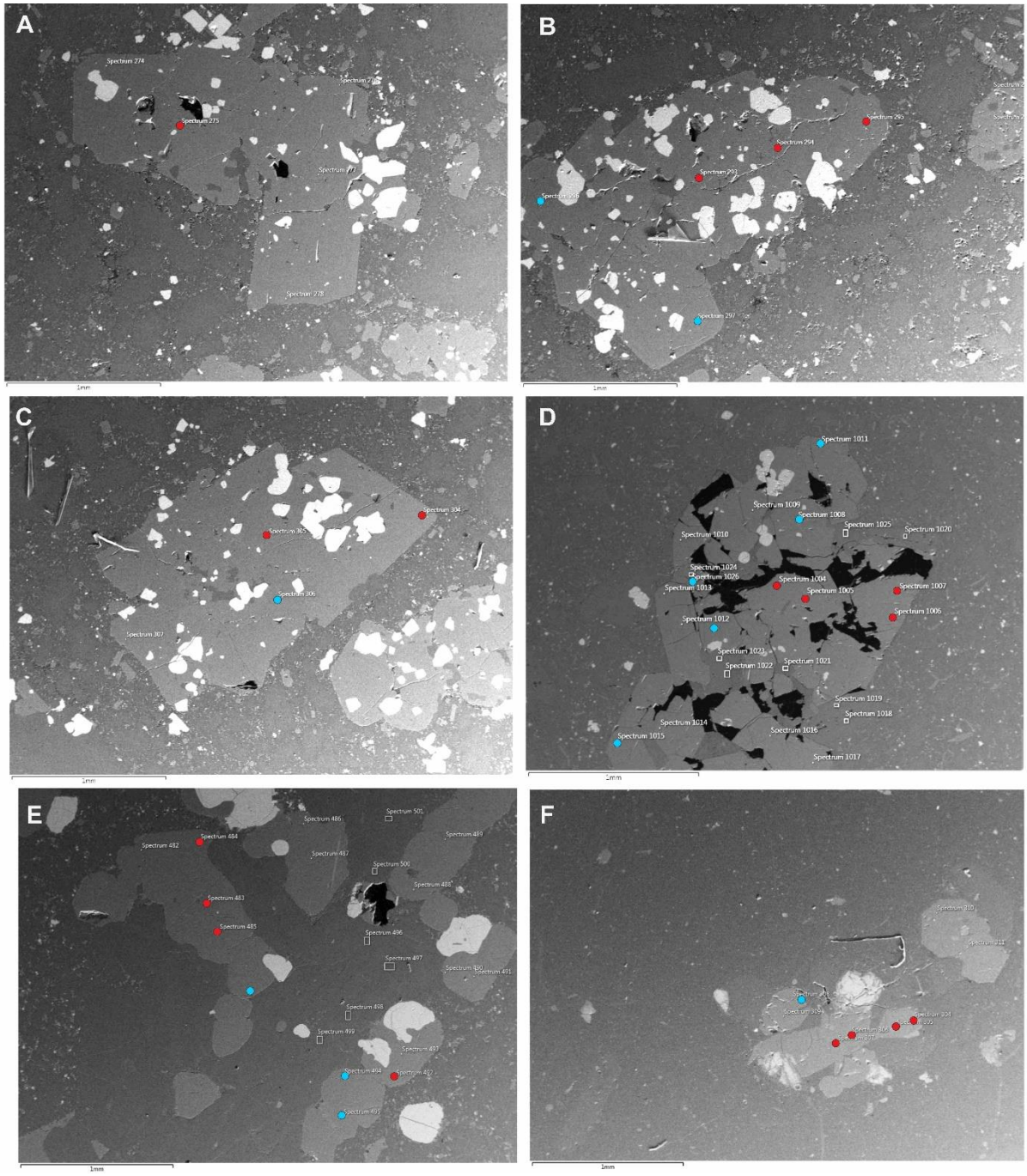

Fig. 6.1 Orthopyroxene-clinopyroxene couples for P-T caculations in the Panama and the Las Cascadas Formation (red filled circles are Cpx and blue filled circles are Opx). (A) (B) (C) Cpx-Opx in J17-036-1 from

the Panama Formation. (D) Cpx-Opx in J18-100 from the Panama Formation. (E) Cpx-Opx in J17-006 from the Las Cascadas Formation. (F) Cpx-Opx in J17-121 from the Las Cascadas Formation.

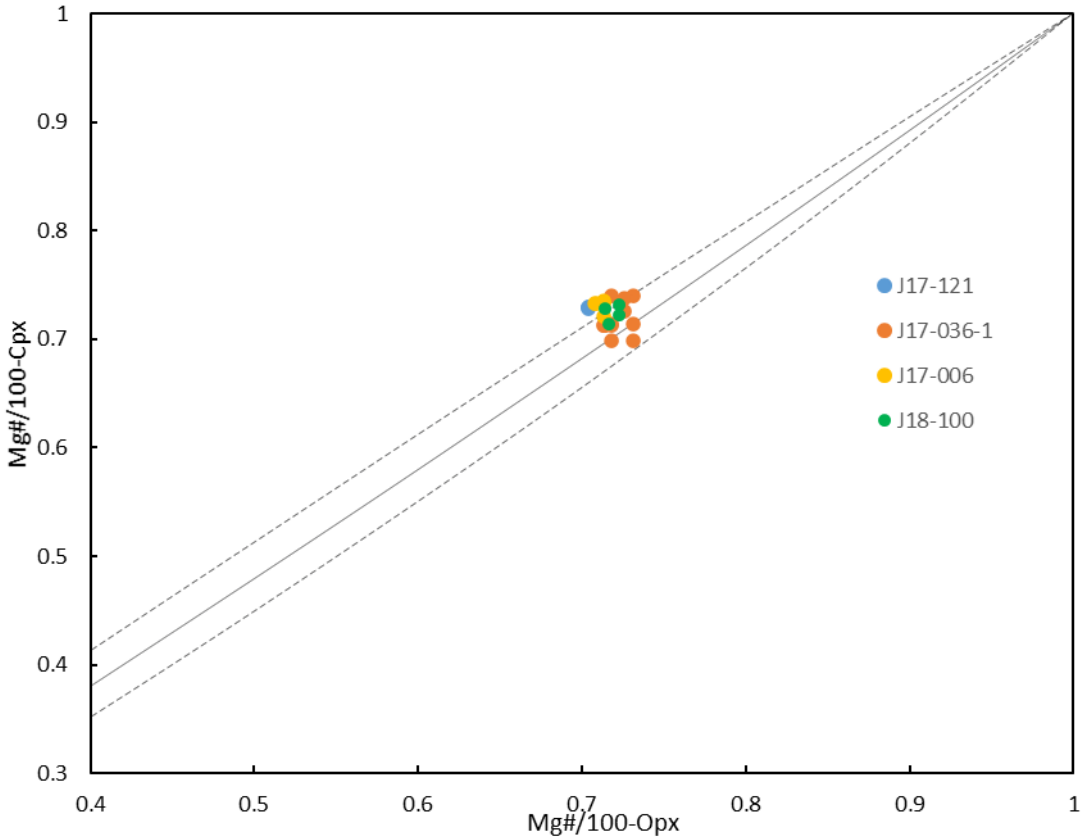

Fig. 6.2 Rhodes diagram for Clinopyroxene-Orthopyroxene couples (K_d (Fe-Mg)$^{cpx\text{-}opx}$ = 1.09±0.14 from Putirka, 2008).

Table 6.1 P-T calculations for the Panama and Las Cascadas Formation

		Opx-Cpx	Opx-liq	Cpx only	Cpx-liq	Cpx-liq	**Opx-Cpx**		Cpx only (for comparison)	
		Putirka (2008)			Putirka (2008)	Putirka et al (2003)	Putirka (2008) (Mg#>75)		Putirka (2008)	
		Eqn 36	Eqn. 28a	Eqn. 32d	Eqn. 33 (hydrous)		Eqn 39		Eqn 32b	
		T(°C)	T(°C)	T(°C)	T(°C)	T(°C)	P(kbar)	Depth(km)	P(kbar)	Depth(km)
J17-036-1	Max	1041	1219	1168	1113	1141	5.4	20	5.6	21
	Min	981	1090	1132	1064	1107	2.9	11	1.3	5
	Mean	1001	1129	1158	1094	1128	**4.1 (n=8)**	**15**	4.0	14
	sd	17	38	7	11	7	0.7	2.6	1.0	3.7
J18-100	Max	971	1056	1181	1054	1122	5.2	19	6.9	25

	Min	959	1044	1144	1006	1089	3.6	13	3.2	12
	Mean	964	1048	1169	1033	1108	**4.3 (n=4)**	**16**	5.2	19
	sd	5	3	7	9	6	0.6	2.2	0.8	2.8
J17-006	Max	994	1059	1173	1110	1139	4.0	14	5.9	22
	Min	962	1042	1143	1077	1117	2.9	11	2.1	8
	Mean	982	1053	1162	1093	1127	**3.6 (n=6)**	**13**	3.4	13
	sd	10	5	6	7	5	0.4	1.5	0.7	2.5
J17-121	Max	953	975	1126	912	1001	2.9	11	4.0	14
	Min	946	922	1093	891	984	2.5	9	1.2	4
	Mean	949	955	1113	903	994	**2.7 (n=4)**	**10**	3.0	11
	sd	3	15	9	6	5	0.2	0.7	0.6	2.2

**depth (km), based on crustal density (2.8 g/cm3). ρgh=P -> (2.8*1000kg/m^3)*(9.8N/kg)*h=n*10^8 N/m^2 (kbar=10^8N/m^2) -> h=n*100/2.8/9.8*

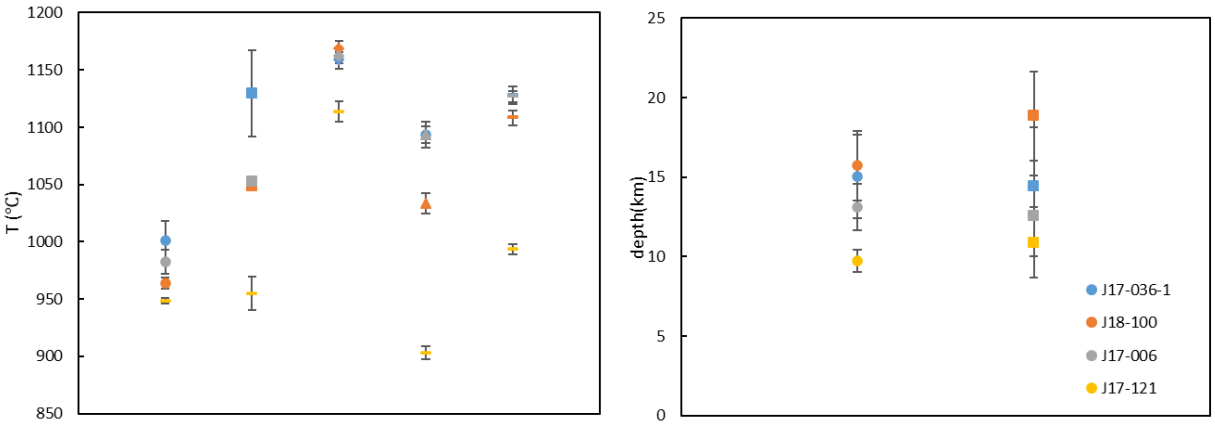

Fig. 6.3 Comparison of P-T between Panama Formation (J17-036-1 and J18-100) and the Las Cascadas Formation (J17-006 and J7-121).

6.1.1.2 Crystallisation Revealed by Whole Rock Geochemistry

Prior to doing rhyolite-MELTS modelling, the effect of magma mixing should be considered first. Magma mixing is substantial in the Pam1 of the Panama Formation as revealed by oscillatory zonation of clinopyroxenes in Chapter 5 and in the discussion below while magma mixing is minor in some samples of the Panama Formation (e.g. Pam2). Pam2 samples are basaltic andesite to andesite while Pam1 samples are basalt to basaltic andesite. In the major element vs SiO_2 plot (Fig. 3.11), an inflection point forms in the Al_2O_3 vs SiO_2 diagram at 57-59 wt.% of SiO_2 and Pam1 occur to the left of this point while Pam2 occur near and slightly to the right of the point. As Pam1 have both CPX1

(Mg#>77 but mainly >80) and CPX2 (Mg#<77 but mainly ~73) while Pam2 mainly have CPX2 (Chapter 5), Pam1 can be considered as mixture of Pam2 magma and less evolved magma. No mixing between low SiO_2 magmas on the left of the inflection point and high SiO_2 magmas on the right were formed. Therefore, the less evolved magma can still be treated as the parental magma for modelling despite the effect of magma mixing.

J18-059-1, which has the highest MgO content (6.6 wt.%) and lowest La (6.6 ppm) and Zr (63.2 ppm) in the Panama Formation was selected as the starting composition for rhyolite-MELTS modelling. The highest pressure (5400 bars) in J17-036-1, the lowest pressure (2500 bars) in J17-121, and the mean value (4100 bars) in J17-036-1 calculated by clinopyroxene-orthopyroxene barometer were chosen for the pressure in the modelling. Three different water contents (1%, 2%, and 4%) are chosen for each pressure. Oxygen fugacity buffer of NNO were applied to this rock in the modelling due to the arc setting (Fig. 6.4). Therefore, there are 9 fractional crystallisation schemes in the rhyolite-MELTS modelling. Model 1: 1 wt.% water and 2500 bars of pressure; Model 2: 1 wt.% water and 4100 bars of pressure; Model 3: 1 wt.% water and 5400 bars of pressure; Model 4: 2 wt.% water and 2500 bars of pressure; Model 5: 2 wt.% water and 4100 bars of pressure; Model 6: 2 wt.% water and 5400 bars of pressure; Model 7: 4 wt.% water and 2500 bars of pressure; Model 8: 4 wt.% water and 4100 bars of pressure; Model 9: 4 wt.% water and 5400 bars of pressure. All models were ran 80% crystallisation.

Overall as can be seen from Fig. 6.4 -6.6, lower pressure models are off the liquid line of descent in Al_2O_3 vs SiO_2 diagram no matter what the water content is. High water (4%) models do not fit the crystallisation trend in Fe_2O_3 vs SiO_2 and TiO_2 vs SiO_2 diagrams regardless of pressure (Fig. 6.6). The low water content (1%) models normally do not fit the trend well within the Panama Formation in the Al_2O_3 vs SiO_2 diagram but they work better in Fe_2O_3, TiO_2 vs SiO_2 diagrams (Fig. 6.4). The model of 4100 bar + 2 wt.% water yield good results in every bivariant diagrams and therefore it is considered as the best fit model.

In the 4100 bar+2 wt.% model, crystallisation begins at 1161 °C with clinopyroxene before being joined by magnetite at 1111 °C (~18% crystallisation) (Fig. 6.7). Plagioclase then joins the crystallising assemblage at 1086 °C after 25 % crystallization. Then orthopyroxene crystallises at 1076 °C slightly later than plagioclase. The lowest MgO in the Panama Formation is 1.26 wt.% (J17-089) which corresponds to around 60 % crystallisation while the lowest MgO in the Las Cascadas Formation is 0.42 wt.% (DJ17-016) which corresponds to around 72% crystallisation. Crystallisation in the Panama Formation and Las Cascadas Formation ends before the occurrence of quartz which first saturates at around 77% crystallisation (Fig. 6.7).

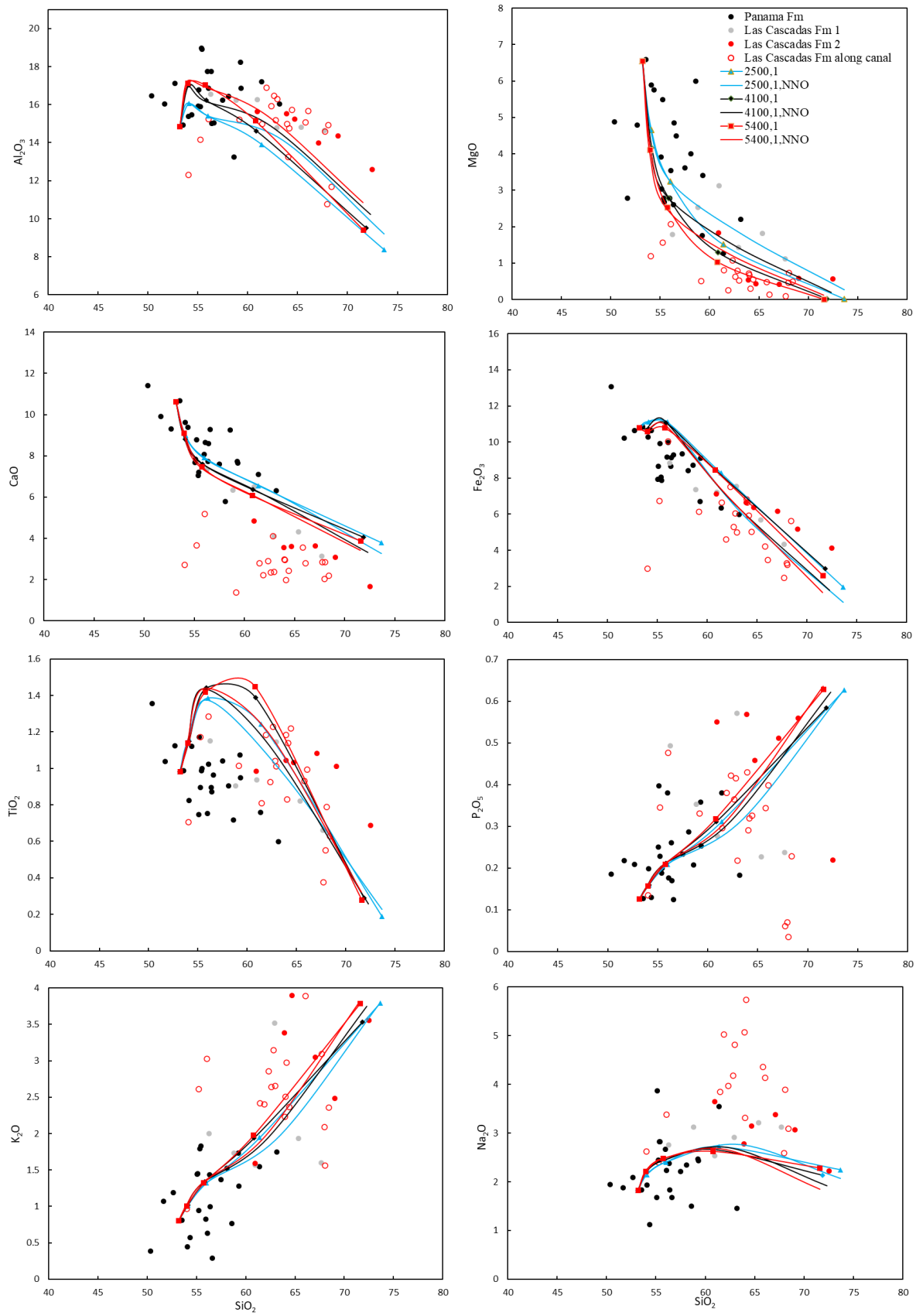

Fig. 6.4 Rhyolite-MELTS modelling for the case of 1 wt.% water. Three pressures of 2500 bars, 4100bars, and 5400 bars with fO_2 of NNO constraint at 20% crystallisation intervals from 0-80% crystallisation are shown in the diagram. The ones without fO_2 constraint are also shown for comparison.

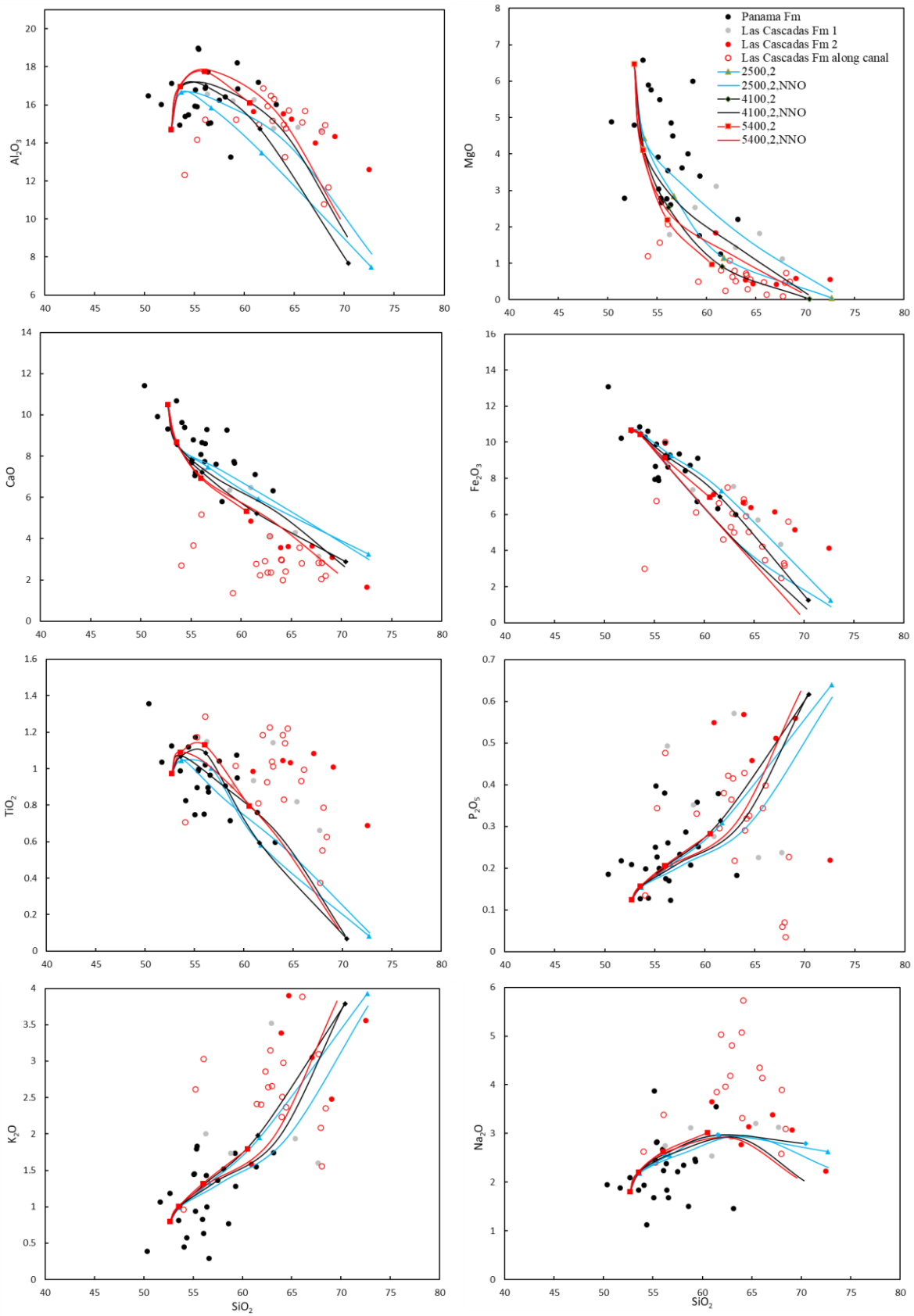

Fig. 6.5 Rhyolite-MELTS modelling for the case of 2 wt.% water. Three pressures of 2500 bars, 4100bars, and 5400 bars with fO_2 of NNO constraint at 20% crystallisation intervals from 0-80% crystallisation are shown in the diagram. The ones without fO2 constraint are also shown for comparison.

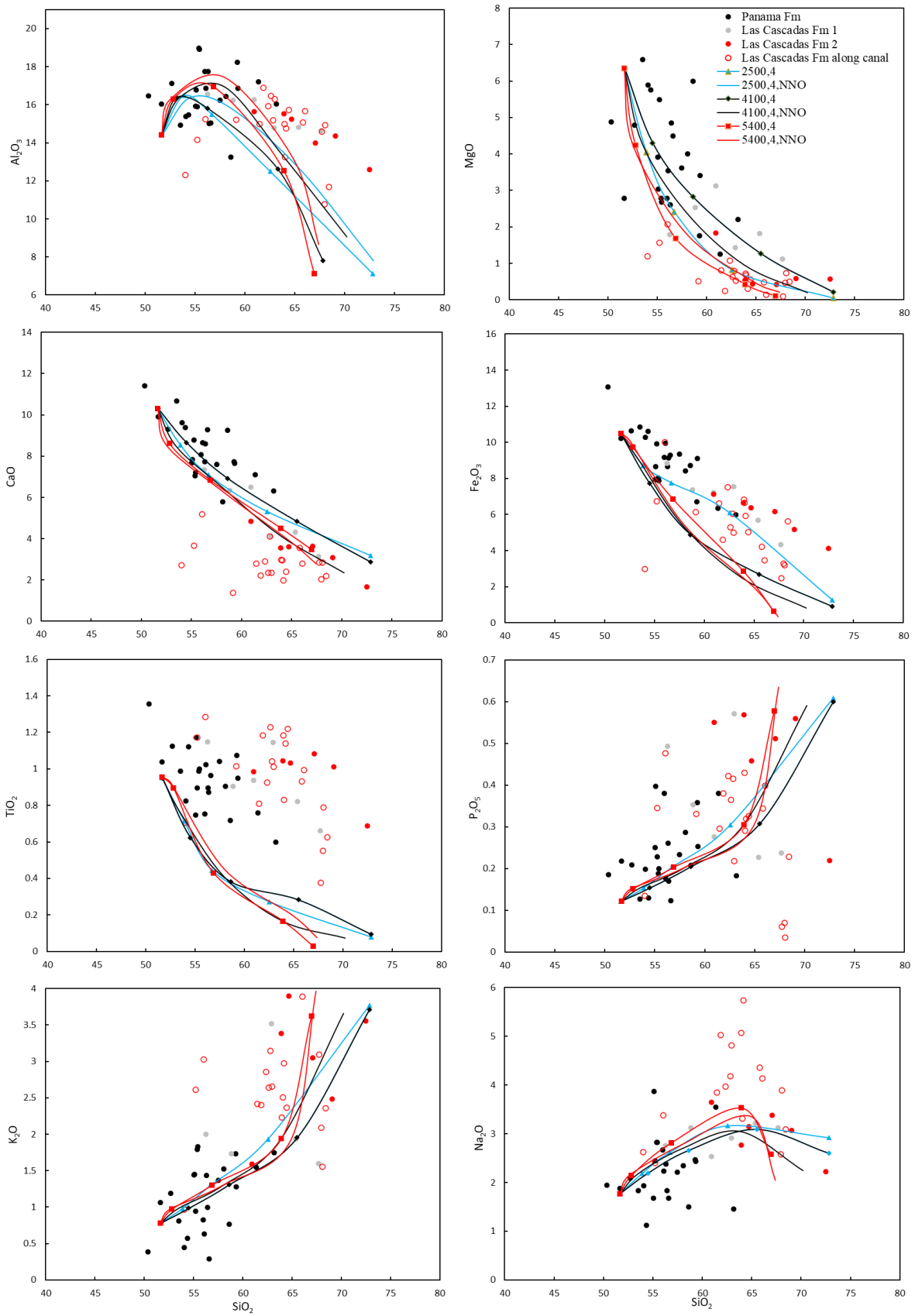

Fig. 6.6 Rhyolite-MELTS modelling for the case of 4 wt.% water. Three pressures of 2500 bars, 4100bars, and 5400 bars with fO_2 of NNO constraint at 20% crystallisation intervals from 0-80% crystallisation are shown in the diagram. The ones without fO_2 constraint are also shown for comparison.

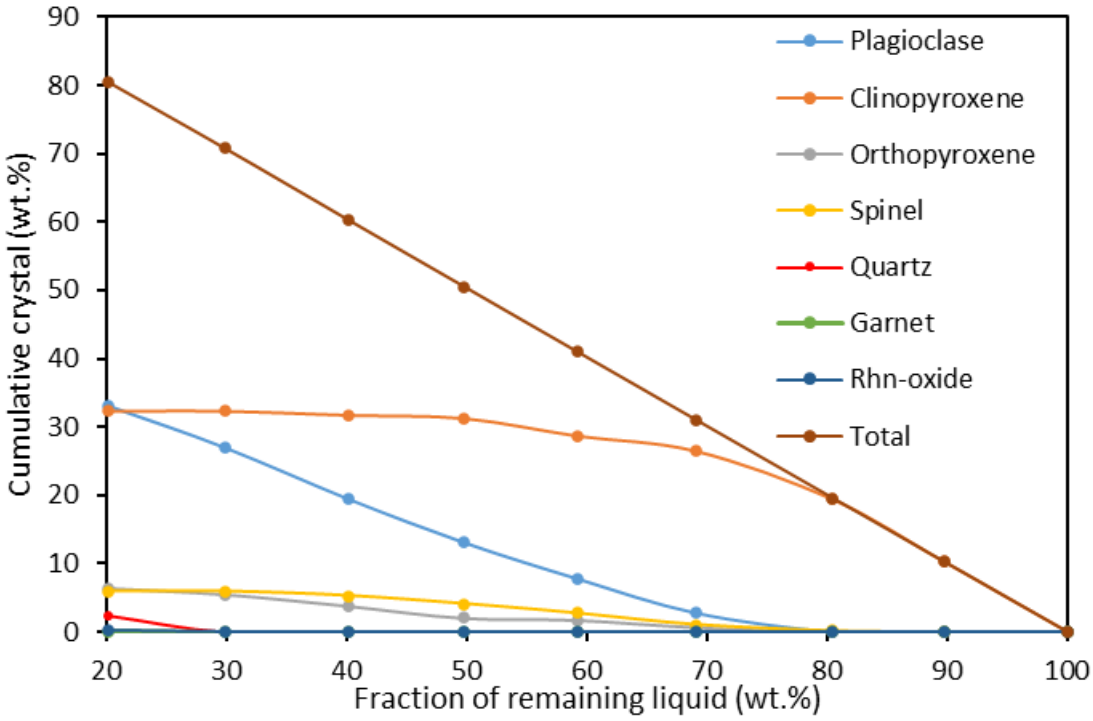

Fig. 6.7 Proportion of minerals formed during fractional crystallisation of J18-059-1 at 4100 bar+2 wt.% water at 10% intervals of crystallisation by rhyolite-MELTS.

In the AFM diagram (Fig. 6.8 A), 4100 bars + 2 wt.% +NNO model is off the trend while the 4100 bars + 1 wt.% + NNO model works better. This also can be seen in Fig. 6.8 B. When fO_2 is not constrained, they work exactly along the crystallisation trend (Fig. 6.8 A, B).

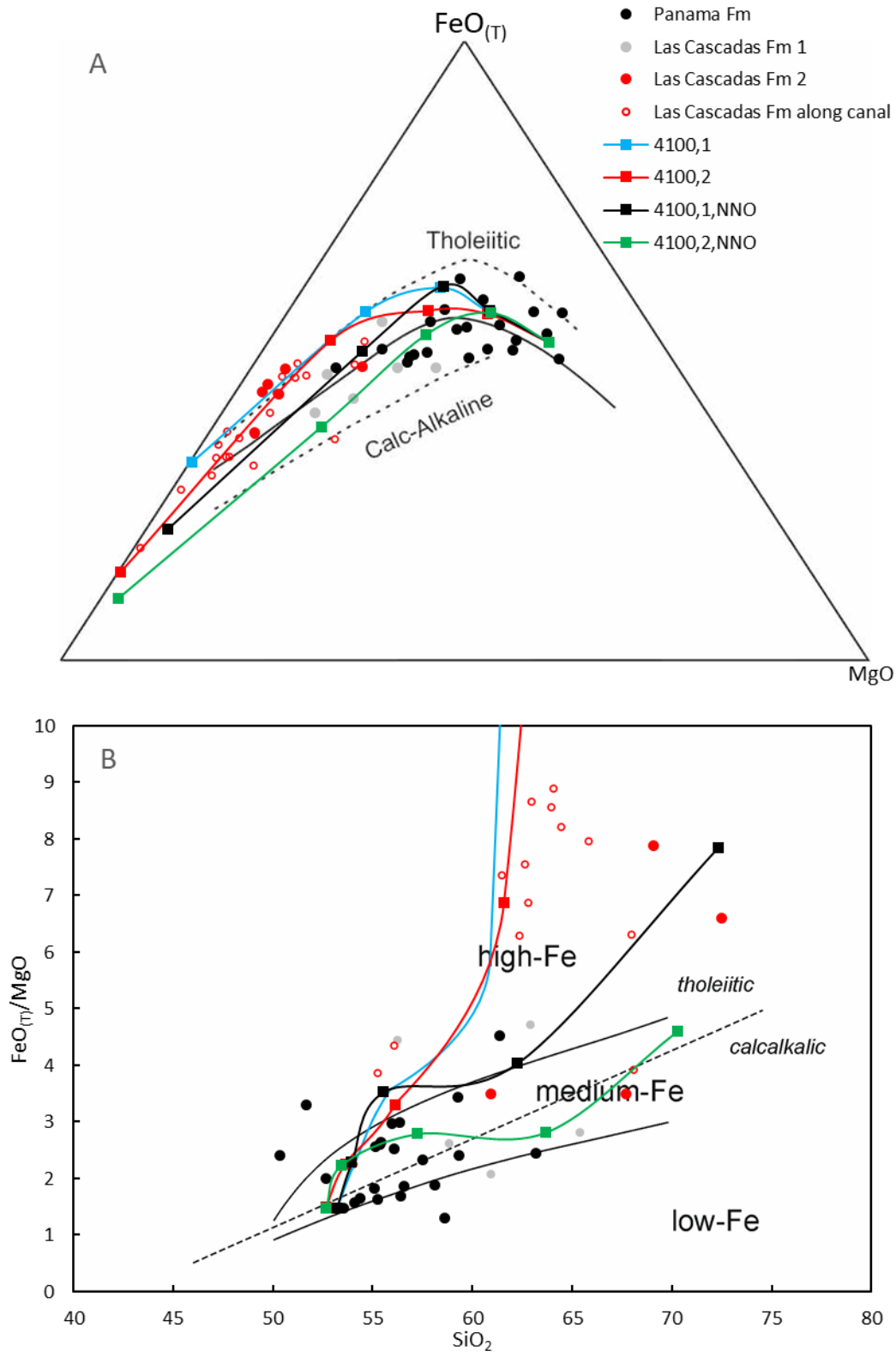

Fig. 6.8 (A)AFM and (B) FeO(T)/MgO vs SiO_2 diagram.

Crystallisation can also be investigated by trace element patterns on the chondrite-normalised REE diagrams (Eu/Eu*) or N-MROB normalised multi-element diagrams (for Sr/Sr*, Ti/Ti*, and P/P*).

Sr/Sr* decreases slightly with decreasing MgO within the Panama Formation while decreases significantly within the Las Cascadas Formation (Fig. 6.9). This is consistent with later stage plagioclase crystallisation. Eu/Eu* does not decrease as MgO decreases which indicates Eu is the Eu^{3+} and shows the same behaviour as the rest of the REE. This also suggests magmas of the Panama Formation and Las Cascadas Formation are oxidised. Ti/Ti* decreases with decreasing MgO is consistent with Fe-Ti oxide crystallisation at the early stage. P/P* increases as MgO decreases within the Panama Formation and decreases significantly with decreasing MgO within the Las Cascadas Formation which suggest no apatite crystallisation in the Panama Formation but apatite crystallisation in the Las Cascadas Formation.

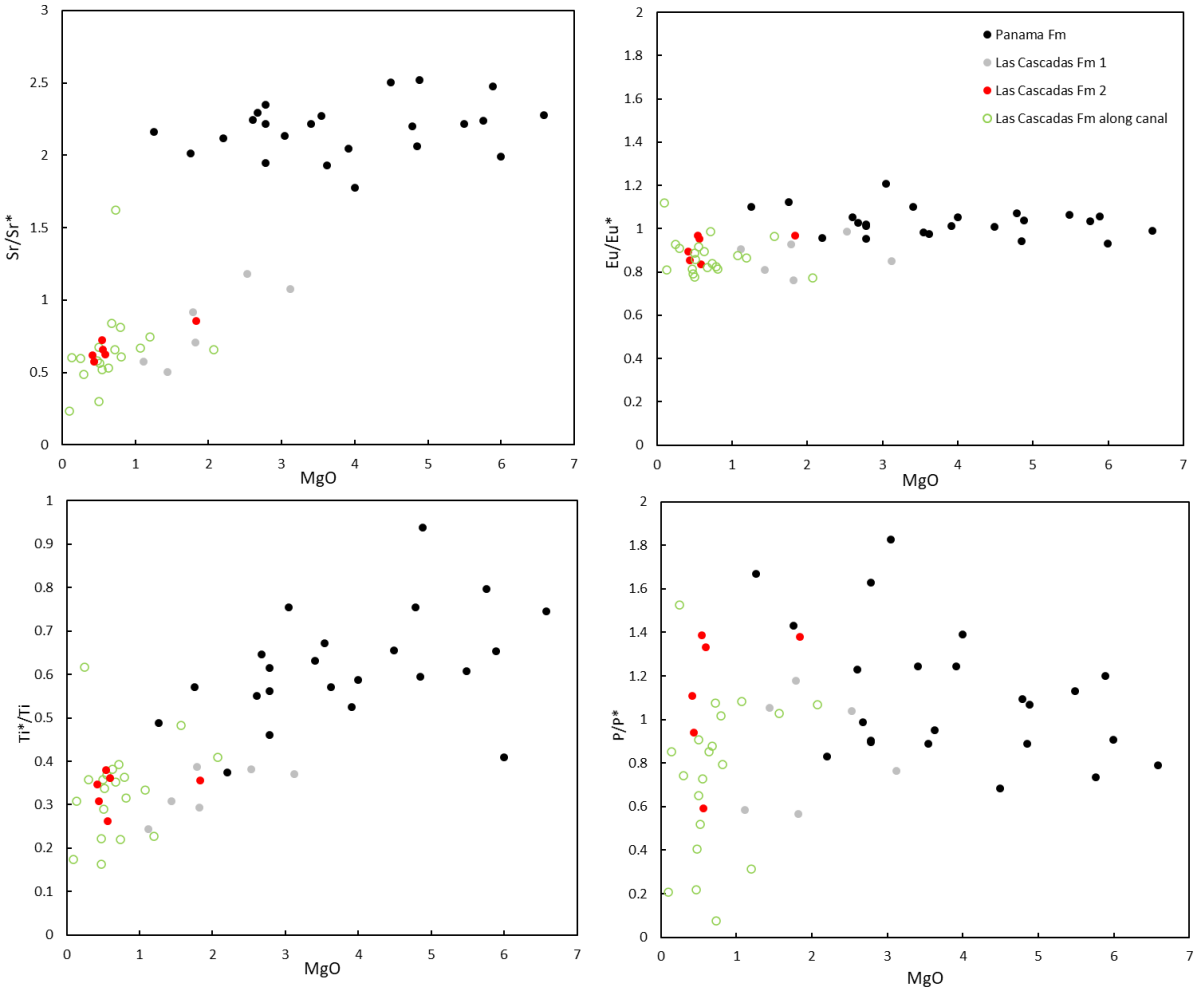

Fig. 6.9 Trace element anomaly vs MgO

Sample J18-059-1 is also considered as the starting composition in the trace element modelling. As mineral proportions change with increasing crystallisation degrees, the bulk partition coefficient also changes. In the model, the mineral assemblage at different degrees of crystallisation derived from rhyolite-MELTS modelling (4100 bar+2 wt.% water+NNO) was used to calculate the bulk partition

coefficient (Table 6.2). Partition coefficients between minerals and intermediate melts were chosen for modelling (Table 6.3). Fractional crystallisation is applied to the crystallisation modelling and the equation is below:

$$C = C_0 \times F^{(D-1)} \qquad \text{Equation 6.1}$$

where C_0 is the trace element concentration of parental melt, F is the fraction of remaining melt and D is the bulk partition coefficient.

Table 6.2 Mineral proportions at each 10% crystallisation interval derived from rhyolite-MELTS for trace element modelling of fractional crystallisation.

Mineral	% at 10%	% at 20%	% at 30%	% at 40%	% at 50%	% at 60%	% at 70%	% at 80%
pla	0.0	0.0	8.8	18.9	25.8	32.2	38.0	41.1
cpx	100.0	99.2	85.5	70.1	62.0	52.7	45.7	40.2
opx	0.0	0.0	2.3	4.3	4.1	6.3	7.8	7.9
mag	0	0.8	3.4	6.7	8.2	8.8	8.4	7.4

Table 6.3 Partition coefficients in trace elements modelling (U, Sr and Zr are the average value of mafic melts and felsic melts from Rollinson, 1993, Eu in plagioclase is Eu^{3+} from Drake and Weill, 1975; Ti from Pearce and Norry, 1979. The rest are for intermediate melts from Borg and Clynne (1998)).

	Pla	Cpx	Opx	Mag
Rb	0.02	0.0019	0.001	0.01
Ba	0.23	0.0007	0.0005	0.01
U	0.0515	0.125	0.145	0.01
Nb	0.01	0.005	0.15	0.01
K	0.263	0.0022	0.0011	0.01
La	0.13	0.12	0.016	0.01
Ce	0.09	0.18	0.019	0.01
Sr	2.335	0.288	0.0245	0.01
Nd	0.063	0.4	0.03	0.01
Sm	0.045	0.7	0.042	0.01
Zr	0.0915	0.35	0.19	0.01
Eu	0.079	0.69	0.052	0.01
Ti	0.05	0.4	0.25	9

Gd	0.037	0.88	0.066	0.01
Tb	0.03	0.92	0.08	0.01
Dy	0.029	1.1	0.12	0.01
Ho	0.026	1.1	0.16	0.01
Er	0.025	1	0.2	0.01
Tm	0.024	0.95	0.25	0.01
Yb	0.023	0.9	0.36	0.01
Lu	0.022	0.85	0.45	0.01

For the highest trace element content of the Panama Formation, 50% crystallisation works well for HREE (Gd-Yb) in these two models (Fig. 6.10). For the more incompatible elements, from Rb to La on the multi-elements diagram, it requires 60% crystallisation. 50-60% is consistent with the crystallisation degree derived from the MELTS modelling. For the Las Cascadas Formation, only low MgO (<1 wt.%) samples are used to draw the upper and lower boundary since they are not affected by mineral accumulation in magma mush (discussed below). 70% crystallisation works well for the HREE. For the more incompatible elements, it requires ~80% crystallisation (Fig. 6.10). 70-80% crystallisation is consistent with the crystallisation degree derived from the major element modelled by rhyolite-MELTS.

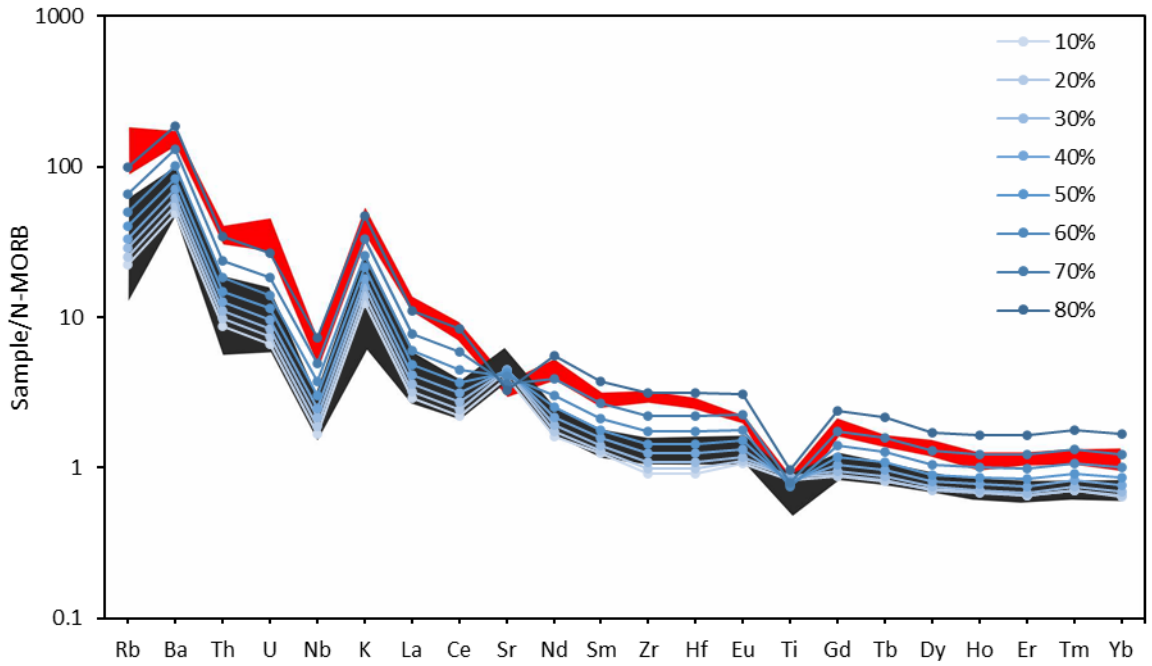

Fig. 6.10 Trace element modelling of fractional crystallisation from the parent magma J18-059-1 for the Panama Formation and Las Cascadas Formation. Modelling with changing bulk partition coefficient based on rhyolite-MELTS modelling (Compositional lines from the modelling indicate intervals of 10% crystallisation. The black range is the Panama Formation and the red range is the Las Cascadas Formation).

6.1.1.3 Crystallisation Revealed by Clinopyroxene

Mineral composition is mainly controlled by the host magma as shown in Fig. 4.74 and Fig. 4.75. As magma evolves from mafic to felsic composition, the minerals also evolve correspondingly. A continuous trend of clinopyroxenes in the Panama Formation and Las Cascadas Formation (Fig. 4.18 and Fig. 4.43) suggests clinopyroxenes in these two formations are from a continuous crystallisation process.

As can be seen from the Al_2O_3 vs Mg# diagram of clinopyroxene crystals in the Panama Formation and Las Cascadas Formation (Fig. 6.11 A), Al_2O_3 increases firstly with decreasing Mg# (from CPX1 to CPX2) and then decreases with decreasing Mg# (from CPX2 to CPX3) due to plagioclase crystallisation which decreases the Al_2O_3 content in the host magma. This transition is corresponding to the inflection in whole rock SiO_2-Al_2O_3 diagram (Fig.3.8).

TiO_2 in clinopyroxene increases as Mg# decreases and then keep constant with decreasing Mg# (Fig. 6.11 B). It is consistent with whole rock Ti content which remains the same during Fe-Ti oxide crystallisation. Ti in magma is incompatible element at the early stage of crystallisation and becomes compatible as Ti bearing oxides such as magnetite crystallise at a later stage. This can be revealed by petrography as magnetite coexist with CPX2 and CPX3 rather than CPX1. This is also supported by rhyolite-MELTS modelling in which Fe-Ti oxide starts to crystallise at ~12% crystallisation at step 7 (Fig. 6.7).

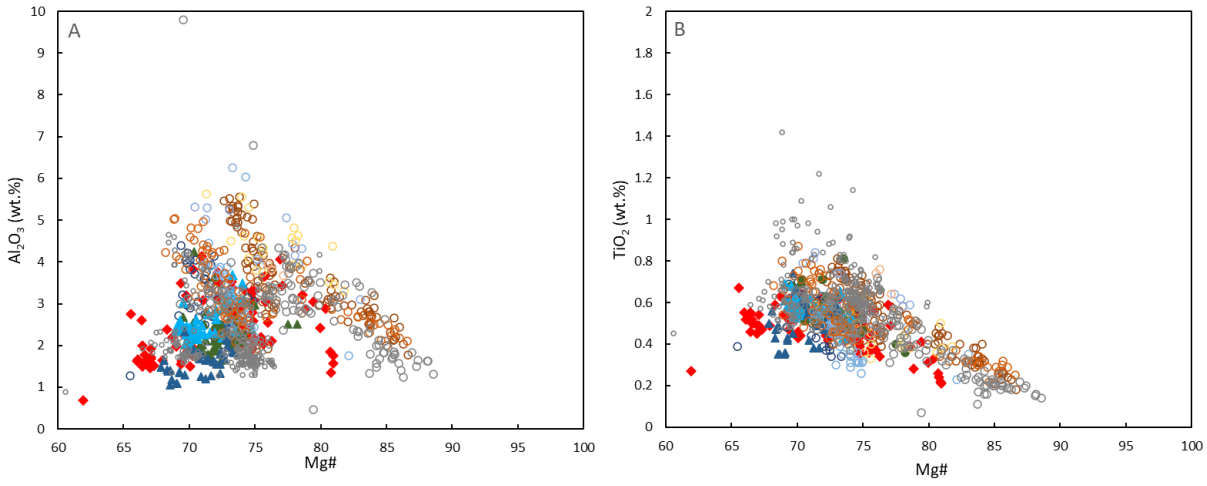

Fig. 6.11 (A) Al_2O_3 vs Mg# and (B) TiO_2 vs Mg# for clinopyroxene in the Panama and Las Cascadas Formation (filled triangles are the Las Cascadas Formation; filled circles are the Panama Formation; filled diamonds are J17-001; small grey circles are Las Cascadas Formation along canal from Buchs et al. (2019a)).

To make it clearer, Ti/Al vs Mg# diagram is created to illustrate crystallisation from the perspective of clinopyroxene composition (Fig. 6.12). From CPX1 to CPX2, Ti/Al increase as Mg# decreases, which is attributed to larger magnitude of increase of Al_2O_3 comparing with TiO_2. From CPX2 to CPX3, Al_2O_3 decreases rapidly due to plagioclase crystallisation and TiO_2 remains constant due to Ti bearing

oxide crystallisation and this gives rise to rapid increase of Ti/Al. The inflection point where CPX2 locates is consistent with the inflection point where J17-036-1 locates in whole rock SiO_2-Al_2O_3 diagram (Fig. 3.11). Less evolved rocks (before the inflection point in whole rock SiO_2-Al_2O_3 diagram) possess CPX1 and CPX2 while the more evolved rocks possess CPX2 or CPX3. The inflection point on the Ti/Al vs Mg# diagram is corresponding to 20 - 30% crystallisation which is consistent with the initiation of plagioclase crystallisation at ~25 crystallisation (Fig. 6.12 and Fig. 6.7).

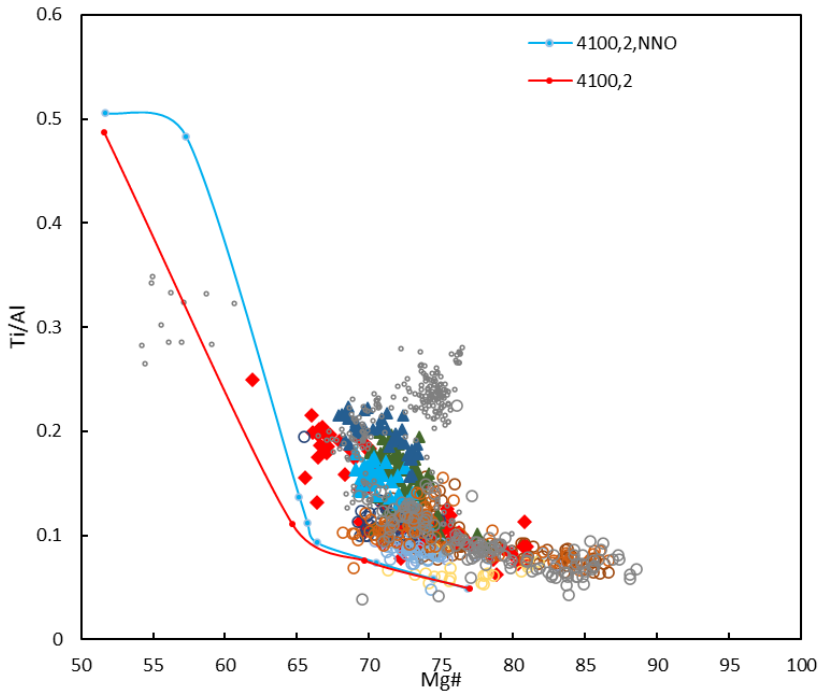

Fig. 6.12 Mg#-Ti/Al diagram for clinopyroxene in Panama and Las Cascadas Formation (filled triangles are the Las Cascadas Formation; circles are the Panama Formation; filled diamonds are J17-001; small grey circles are Las Cascadas Formation along canal from Buchs et al. (2019a). Two rhyolite-MELTS models are 4100 bars+ 2 wt.% water with fO_2 of NNO and 4100 bars+2 wt.% without fO_2 constraint respectively).

The only problem in rhyolite-MELTS modelling is low Ca clinopyroxene forms with high Ca clinopyroxene. As revealed by ASEM, only minor pigeonite are found in the Panama Formation but 5-10 vol.% of orthopyroxene are found in the evolved rocks of the Panama Formation and Las Cascadas Formation. This might be explained by low pressure crystallisation which reduce the formation of low Ca clinopyroxene but facilitates orthopyroxene crystallisation.

6.1.1.4 Magma Mixing in the Panama Formation Revealed by Clinopyroxene

Clinopyroxene can be well preserved and not affected by alteration or metamorphism (Letterier, 1982). The composition of clinopyroxene is closely related to the composition of its equilibrated melts, pressure and temperature, which can reflect the origins of the clinopyroxene (Mollo et al.,

2016). The clinopyroxene composition can reflect the original magma which is easy to be obscured by later processes such as magma mixing.

In sample J17-102 (Pam1), big clinopyroxene phenocrysts show obvious oscillatory zones with compositions of CPX1, CPX2, and CPX3 (Fig. 4.30) indicating that the phenocrysts crystallised in an open magma system (Streck, 2008; Tomiya and Takahashi, 2005). The core is CPX2 which is surrounded by high Mg# CPX1. It is then surrounded by evolved melts to form CPX2. Later, it is entrained by more primitive melts and forms CPX1. This process repeats several times. The factors leading to oscillatory zoned pyroxene phenocrysts, which have been described in numerous igneous systems, include intrinsic and extrinsic mechanisms (Shore and Fowler, 1996). The intrinsic models are typically based on crystallisation kinetics and the interplay between the rate of crystallisation and the diffusion rates of cations in the melt. The extrinsic models that produce oscillatory zoning result from the changes in liquid compositions due to external forcing including the magma chamber replenishment events (Elardo and Shearer, 2014; Simonetti et al., 1996), the convection in magma chambers where the phenocrysts move back and forth due to the local difference in the pressure, temperature and/or magma compositions, and the changes in temperatures and compositions of equilibrium melts due to the cyclical changes in water pressure (e.g., Turner and Verhoogen, 1960). The intrinsic mechanism usually results in short-scale, low-amplitude fine banding. Local depletion of a boundary layer is considered to prevent the growth of coarse bands of approximately >15 μm (Elardo and Shearer, 2014). The production of compositions of oscillatory zoned phenocrysts by extrinsic models is not considered to be responsible for diffusion rates or local nonlinear crystal growth but, rather, to depend on the magma compositions in which the phenocryst is growing. In this study, the oscillatory zoning pattern observed in clinopyroxenes in J17-102 is approximately 50–250 μm in width (Fig. 4.30), which is difficult to produce by intrinsic mechanisms. In addition, the mechanisms of phenocryst convection and cyclical changes in water pressure can hardly change the clinopyroxene elemental compositions. Besides, porphyritic texture of the Panama Formation samples indicates they derived from magma mush which further argues against convection (Sinton and Detrick, 1992). Therefore, based on the data in this study, the oscillatory zoning in clinopyroxene in the Panama Formation likely reflects magma mixing with large-scale compositional variations in the magma rather than the effects of crystallisation kinetics.

Wide compositional distribution and reversed zonation of clinopyroxenes are signs for magma mixing (Nakagawa et al., 1999). Bimodal or 3-peak distribution of Mg# with large range of values in the Panama Formation, no matter the clinopyroxene is normal zoned, reversed zoned or oscillatory zoned, suggests clinopyroxene growth is affected by composition change rather than intrinsic factors. CPX1 in some samples (e.g., J17-059-2 and J18-059-2) only show as core while CPX2 show as mantle/rim or as single crystals. This suggests CPX1 in these samples are most likely antecrysts trapped in evolved magma which grows CPX2 around CPX1. Therefore, before erupting, magma chamber can

be recharged several times by primitive and evolved magma in turn (J17-102) or can be recharged once (J17-059-2 and J18-059-2).

Recharge mixing can occur between different batches of co-genetic magmas, including cooled magma mush and recharged magma (e.g., Cashman et al., 2017; Spera and Bohrson, 2018), or mixing between magmas of different origins, such as mantle-derived and crust derived magma, (e.g., Liang et al., 2018). In this study, clinopyroxene in the Panama Formation forms an evolution trend as shown in Fig. 6.11 and Fig. 6.12 suggests co-genetic magma mixing. This is consistent with evolution trend revealed by Harker diagrams.

6.1.1.5 Las Cascadas Formation: Interstitial Melt Extracted from Magma Mush

The Las Cascadas Formation, especially the aphyric group (SiO_2 = 61-73 wt.%), along with the Cabra felsic member in 6.1.2, are the most felsic rocks in central Panama. Felsic rocks (SiO_2 >63 wt.%) are usually explained by two end-member mechanisms: (1) partial melting of crustal material; (2) fractional crystallisation of mafic magma. The first mechanism is commonly found in areas with continental crust (including continental arcs) (Cobbing and Pitcher, 1983; White and Chappell, 1983; Vielzeuf and Holloway, 1988) but can also occur in oceanic arc settings (Shukuno et al., 2006). The second mechanism is explained by melt extraction from highly crystallised magma mush (Bachmann and Bergantz, 2004; Hildreth, 2004; Bachmann and Bergantz, 2008; Barker et al., 2013). The Las Cascadas and Panama Formation have the same range in terms of Sr-Nd-Pb isotopes (Chapter 4). Besides, both major element and trace elements of the Las Cascadas Formation can be well achieved by high degree of fractional crystallisation of the Panama Formation, as discussed above. Therefore, the Las Cascadas Formation is likely formed in a magma mush by the first mechanism rather than partial melting of lower crust.

Magma chambers have traditionally been considered to be magma-filled reservoirs, where melt evolution is controlled by the removal of crystals through crystal settling. The crystal setting can be caused by gravity in which case heavy minerals settle to the bottom after formation or by heat loss in which case crystals settle along the margin of the chamber (Langmuir, 1989). After crystal settling, the margin of the magma chamber is covered by crystals while away from the margin, the magma chamber is still magma-filled reservoir. However, the increasing evidence shows that magma chambers are predominantly filled by crystal mush regardless of tectonic settings such as volcanic arc and middle ocean ridge (Bachmann and Bergantz, 2004; Cashman et al., 2017; Cooper, 2017; Johan et al., 2019; Bennett et al., 2019). This is also supported by geophysical observations that no melt-filled chambers, but crystal mushes were found in middle ocean ridge (Sinton and Detrick, 1992). In a magma mush, melts are predicted to migrate by porous flow (McKenzie, 1984) while in a magma-filled chamber, melt transport can readily occur by dyking (Johan et al., 2019).

As shown in Fig.3.14 and Fig. 6.10, there is a gap between the Panama Formation and Las Cascadas Formation in the chondrite normalised REE diagram and the N-MORB normalised diagram. The highest trace element content in the Panama Formation can be achieved by 50-60% crystallisation of J18-059-1 while the lowest trace element content in the Las Cascadas Formation can be achieved by ~70% crystallisation. From major elements, the Panama Formation and Las Cascadas Formation form a continuous trend in the Harker diagram with the Panama Formation ranging from basalt to andesite and the Las Cascadas Formation ranging from basaltic andesite to rhyolite.

The presence of the gap in trace elements and the absence of gap in major elements can be seen from Fig. 6.13. Incompatible elements such as La and Yb become concentrated exponentially with decreasing fractionation index MgO (or SiO_2). Las Cascadas 2 on the crystallisation trend are all aphyric with MgO <1 wt.%. This suggests the aphyric samples are the crystallisation product the Panama Formation or a similar parent magma to the Panama Formation. When this parent magma crystallised to a relatively small degree, e.g. < 45 vol% as represented by the phenocrysts in the Panama Formation, magma in this magma chamber can erupt. When it reaches higher crystallinity, e.g. > 50 vol % (Bachmann and Bergantz, 2004), this magma is 'lock-up' and convection is hampered. At this stage, two-phase (crystal-liquid) flow occurs which eventually causes melt segregation from magma mush (Bachmann and Bergantz, 2004). The compositional gap in both major elements and trace elements between this interstitial melt and the bulk composition of the magma mush corresponds to the gap between the Las Cascadas 2 and the Panama Formation. However, samples of the Las Cascadas Formation 1 (porphyritic group) plot away from the crystallisation trend and have relatively high MgO content, but similar trace element content comparing with other Las Cascadas samples. These 'off-trend' samples of the Las Cascadas 1 are on the mixing line between an evolved sample of the Las Cascadas Formation 2 (aphyric) and crystal assemblage (clinopyroxene and plagioclase) or one mafic sample of the Panama Formation. The Las Cascadas 1 except J17-011 are porphyritic and a large amount of the phenocrysts are glomerocrysts (Fig. 2.15). Glomerocrysts are usually considered as the indicator of the pieces of framework of magma mush (Cashman et al., 2017; Bennett et al., 2019). Therefore, the Las Cascadas 1 is a mixture of crystal assemblage from the framework of magma mush and the interstitial melt that is similar to the bulk composition of the Las Cascadas 2. Through this 'crystal entrainment', the gap in major elements is obscured as major elements such as MgO in the Las Cascadas Formation increases (> 1wt. %) to reach the similar value to the evolved samples of the Panama Formation. Meanwhile, the trace element gap is preserved due to the extremely high trace elements in the end-member of the interstitial melt. Al these evidences indicate the silicic rocks of the Las Cascadas Formation are the interstitial melts extracted from a magma mush and glomerocrysts in the Las Cascadas 1 are the mush framework entrained during melt extracting or erupting.

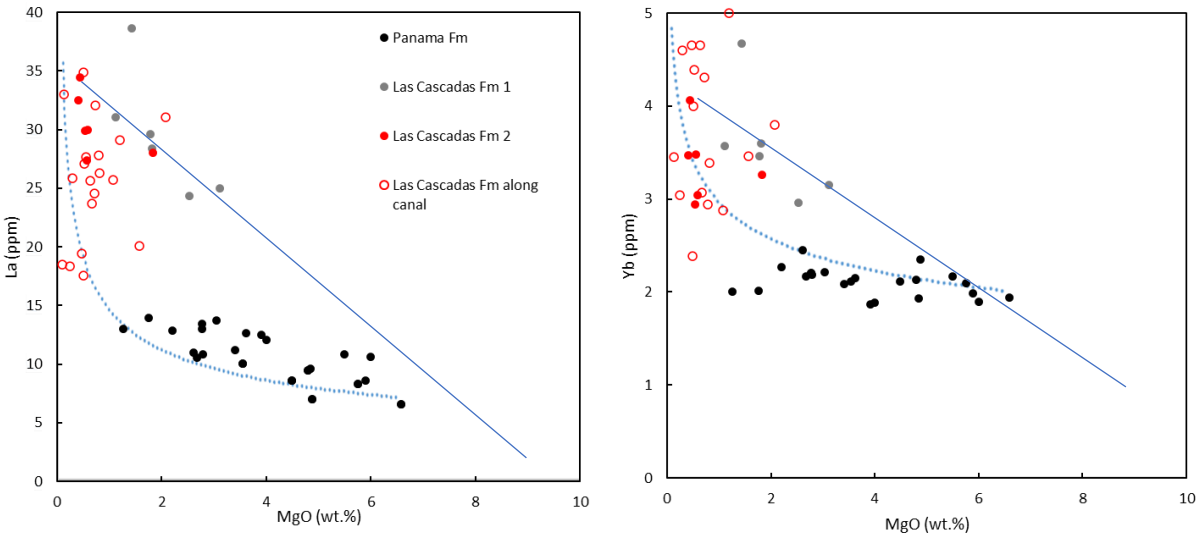

Fig. 6.13 Crystal entrainment between Las Cascadas Formation 2 magma and clinopyroxene+plagioclase assemblage revealed by trace elements-MgO (blue dashed line is based on rhyolite-MELTS modelling with J18-059-1 as the starting composition discussed above).

To further test the Las Cascadas 2 are the extracted melt from magma mush, interstitial melt in the glomerocrysts from the porphyritic Las Cascadas Formation 1 and from the Panama Formation, matrix glass in the Las Cascadas 1, and whole rock composition of the Las Cascadas 2 are compared. As can be seen from Fig. 6.14, matrix in samples from the Las Cascadas 1, especially matrix glass in J17-121, has a very similar composition with the bulk composition of the Las Cascadas 2 especially in terms of SiO_2, Al_2O_3, MgO, CaO, and Fe_2O_3. The glass analyses in J17-121 have a low MgO content (0.18-0.52 wt.%) which is consistent with the whole rock MgO content of the aphyric samples in the Las Cascadas Formation 2 (MgO= 0.42-0.6 wt.%). It is the same for the interstitial melt composition in J18-100 in which MgO spans from 0.34 to 0.41 wt.%. This suggests the Las Cascadas 2 and the matrix glass of the Las Cascadas 1 come from the similar source. The composition similarity between the matrix glass and the interstitial melt in glomerocrysts in J17-121 indicates the Las Cascadas 2 and the matrix glass of the Las Cascadas 1 could be the interstitial melt of a magma mush. The glomerocrysts are the framework of the magma mush and were entrapped in the erupting magma of the Las Cascadas Formation. The similarity between these interstitial melts and the interstitial melt in glomerocrysts of J18-100 (MgO=2.2 wt.%) and matrix of J17-036-1 (MgO=3.4 wt.%) from the Panama Formation suggests the magma mush for the Las Cascadas Formation is similar to the one for the Panama Formation. It is worth mentioning that even rhyolite-MELTS modelling does not match well in SiO_2-TiO_2 diagram, the interstitial glass and matrix from these two samples are among the Las Cascadas Formation.

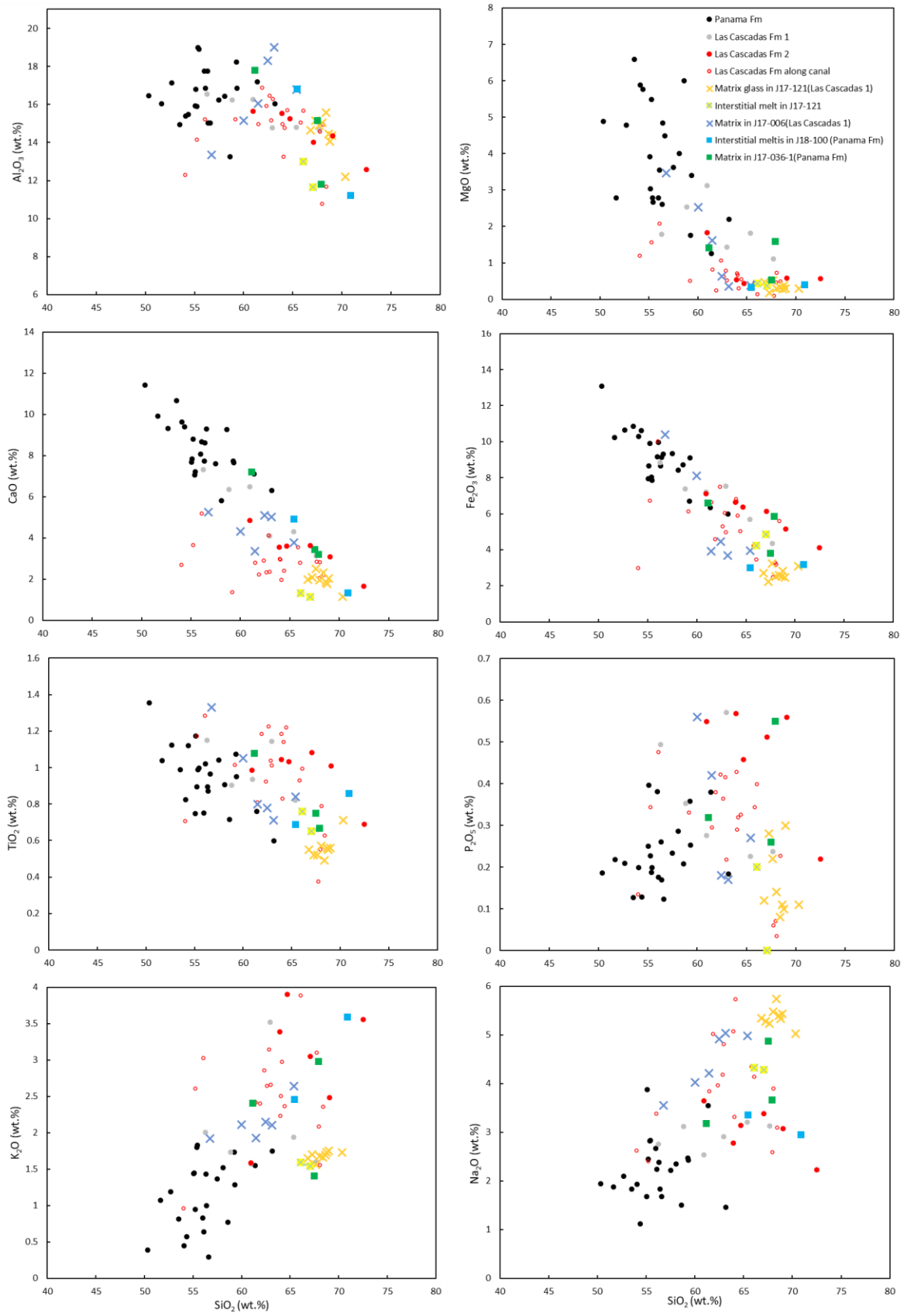

Fig. 6.14 Bivariate diagram of major elements showing the relationship between the interstitial melts in glomercrysts of the Las Cascadas 1 and Panama Formation, matrix glass in the Las Cascadas 1, and bulk composition of the Las Cascadas 2, Las Cascadas 1, and Panama Formation.

The magma mush for the Las Cascadas Formation is at a more evolved stage than the one for the Panama Formation which can be recognised by the mineral composition. Clinopyroxenes from the Las Cascadas 1 are on a continuous evolving trend with clinopyroxenes from the Panama Formation, with some overlapped (Fig. 5.76 in Chapter 5). This can also be clearly recognised in Fig. 6.12. All these suggest the magma mush for the Las Cascadas Formation are at a more evolved stage than the magma mush for the Panama Formation if they are from the same plumbing system. When the crystallinity of the magma mush is below the locking point (Bachmann and Bergantz, 2004), magma can erupt to form the Panama Formation. When the magma mush continues to evolve and the crystallinity reaches above the locking point, magma is not eruptive and volcanic rocks cannot be collected in the field for this range of composition. But interstitial melts can be segregated apart from the crystals to form the aphyric Las Cascadas 2. This is the reason why there is a gap in terms of major and trace elements between the Panama Formation and Las Cascadas 2. When the interstitial melts extract from the highly crystallised magma mush, or when the interstitial melts accumulate somewhere in the plumbing system and then erupt, framework of the magma mush, e.g. glomerocrysts and phenocrysts in the Las Cascadas 1 (and some rocks of the Panama Formation), are inevitably picked up. Interstitial melts with entrapped glomerocrysts and phenocryst forms the porphyritic samples of the Las Cascadas 1. This small volume of entrapped mineral assemblage, e.g. <30 vol.%, increased major elements such as MgO more significantly than the trace elements for the Las Cascadas Formation which obscured the gap of major elements but preserved the gap of trace elements between the Las Cascadas Formation and Panama Formation (Fig. 6.13).

Melt extraction and crystal entrainment can also be seen in the Rhodes diagram (*Fig. 6.15*). Clinopyroxene analyses for the Las Cascadas 1 are quite homogeneous based on major element content and Mg# (~70). However, the whole rock composition of J17-121, J17-006 and J17-009 spans a large range. Clinopyroxene crystals in all these three samples are above the equilibrium line (solid curve in *Fig. 6.15*) in the Rhodes diagram. Clinopyroxenes in rocks of the Las Cascadas Formation along the canal are also above the equilibrium zone (*Fig. 6.15*; Buchs et al., 2019a). All these indicate clinopyroxenes in the Las Cascadas 1 were picked up from the framework of the magma mush.

To show Las Cascadas Formation 1 can be formed by picking up crystal assemblage of mush framework during interstitial melt extracting and accumulating, a simplified model with two endmembers is made as can be seen from Fig. 6.15. Aphyric sample J17-040 from the Las Cascadas Formation 2 is selected as the interstitial melt. To keep it simple and achievable in Rhodes diagram, the endmember of crystal assemblage is represented by clinopyroxene spectrum 506 from J17-006 without other minerals such as plagioclase which is another main phase in glomerocrysts. If J17-040 crystallises clinopyroxenes which are in equilibrium the bulk composition, e.g. no mineral accumulation, it should be the blue bar shown on the Rhodes diagram (Fig. 6.15). In reality, there is no phenocrysts in J17-040 and other samples of the Las Cascadas Formation 2. If J17-040 picks up

neglectable amount of clinopyroxene spectrum 506, it should be the red bar with 0 % clinopyroxene (Fig. 6.15). Clinopyroxene is an early phase during crystallisation so spectrum 506 should be in equilibrium with the bulk composition of the whole rock in which the clinopyroxene crystallises. On the contrary, it should be in disequilibrium with the interstitial melt, which is formed in the very late stage. That is why it is above the equilibrium line when small amount of clinopyroxenes are entrained by the melt. The red bar will move to the right if J17-040 keeps picking up clinopyroxenes. Samples with 0-15% clinopyroxenes will be above the equilibrium line. Whole rock composition will show equilibrium with this clinopyroxene if ~20% clinopyroxenes added to this melt. It is below the equilibrium zone if more than ~20% clinopyroxenes added to the melt. For rocks in the Las Cascadas Formation 1, they can be formed by an evolving melt such as J17-040 trapping less than 20% spectrum506-like clinopyroxene.

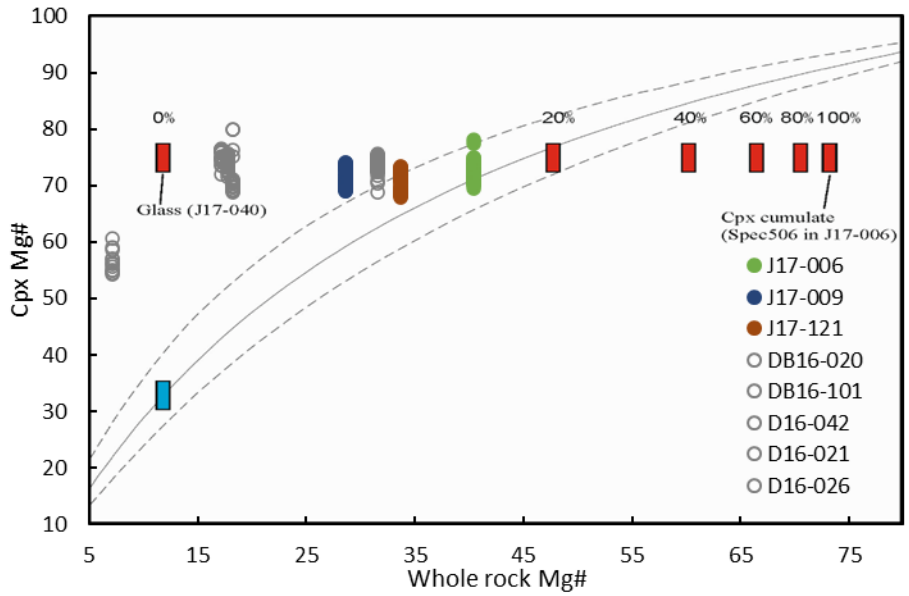

Fig. 6.15 Rhodes diagram for the Las Cascadas Formation (samples with grey circle are the Las Cascadas Formation along Panama canal from Buchs et al., 2019a). The Las Cascadas Formation 1(porphyritic samples such as all except for J17-040 in this diagram) is shown to be formed by adding clinopyroxenes to Las Cascadas Formation 2 (aphyric samples such as J17-040) through crystal entrainment.

The relationship between different components such as bulk rock, interstitial melts, and phenocryst can also be visually illustrated by Fig. 6.16. The bulk rock of the Las Cascadas 2 is the interstitial melt extracted from magma mush and it corresponds to the matrix glass of the Las Cascadas 1. This interstitial melt can also be trapped in glomerocrysts of the Panama and Las Cascadas 1 formation. Clinopyroxenes in glomerocrysts or phenocrysts from the Las Cascadas 1 have similar (CPX2) or slightly evolved (CPX3) composition with the less primary clinopyroxenes (CPX2) in glomerocrysts or phenocrysts from the Panama Formation (Fig. 6.16).

All these evidences indicate the felsic rocks of the Las Cascadas Formation are the interstitial melts extracted from a magma mush. Glomerocrysts and clinopyroxene/plagioclase phenocrysts in the Las Cascadas 1 are antecrysts derived from the mush framework which are entrained during melt extracting or erupting. This antecryst entrainment could be caused by mush disaggregation which might be triggered by magma mixing and replenishment (Costa et al., 2009; Moore et al., 2014). This is also supported by the magma mixing revealed in clinopyroxene and plagioclase composition of the Panama Formation in section 6.1.1.4.

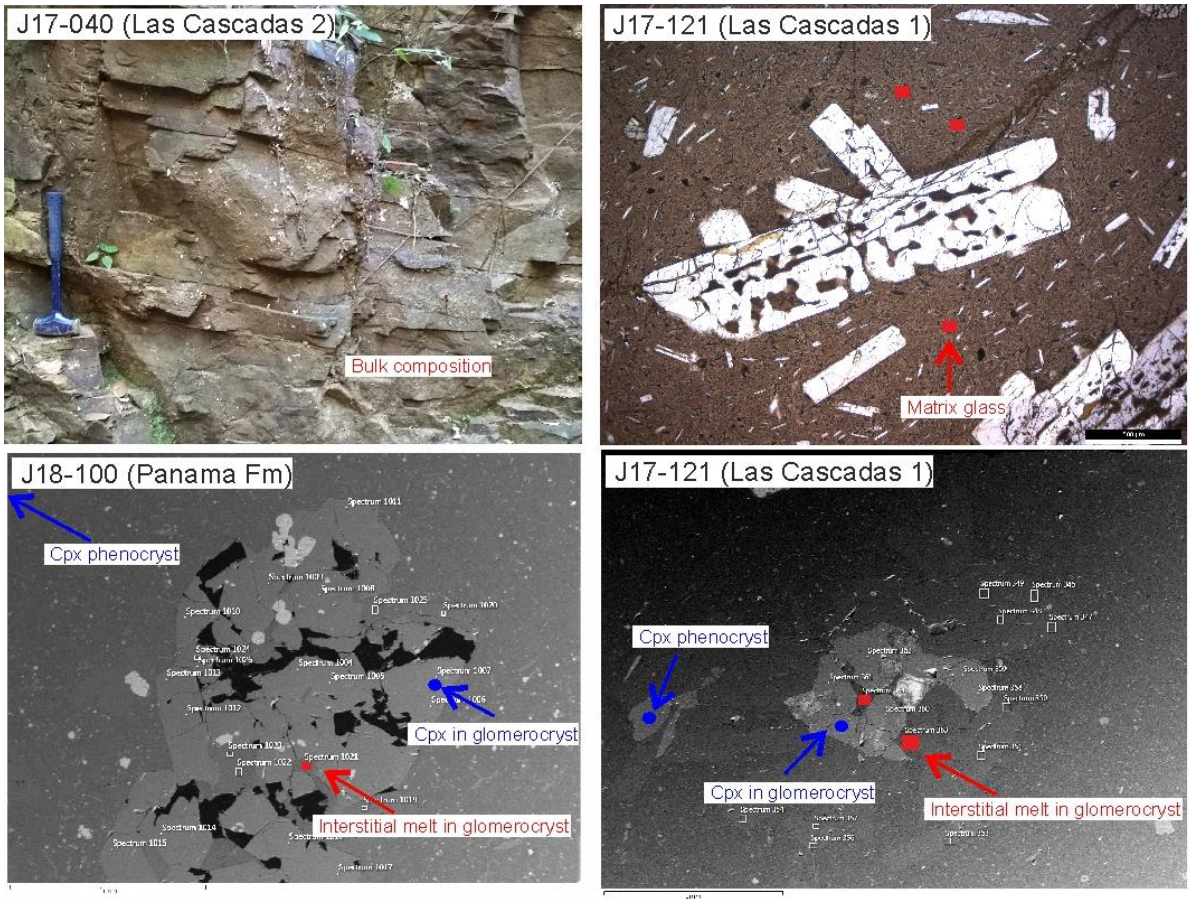

Fig. 6.16 Photos showing the relationship between the interstitial melts in glomerocrysts of the Las Cascadas 1 and Panama Formation, matrix glass in the Las Cascadas 1, and bulk composition of the Las Cascadas 2.

What is worth to mention is, even though the Las Cascadas Formation formed in a magma mush by crystallisation of a parent magma similar to the one for the Panama Formation, it is not necessary that the magma mush for the Las Cascadas Formation is exactly the same to the one for the Panama Formation. The earliest magmatism for the Las Cascadas Formation is ~ 21 Ma (Buchs et al., 2019a). Although the age for the Panama Formation is not known, the mixing relation between it and Caraba Formation (Chapter 3) and similar chemical composition suggests a similar or younger age than the Caraba Formation (~ 25 Ma; Rooney et al., 2011). Besides, the low water content model, e.g. 1 wt.%

+ 4100 bars works better in the TiO_2 vs SiO_2 diagram (Fig. 6.4) than the high water content models such as 2 wt.% and 4 wt.% water models (Fig. 6.5, Fig. 6.6). The best way to test if the Las Cascadas and Panama Formation came from the same magmatic plumbing system is to determine the age of the Panama Formation.

6.1.1.6 Synthesis

Whole rock, clinopyroxene, and glass composition presented here can be utilised to reconstruct the magmatic processes within the plumbing system of the Panama and Las Cascadas Formation. After the primary melt formed from the asthenosphere, it intruded into arc crust. During the time when the melt ponded in the magma chamber within crust, the melt crystallised and formed a crystal-rich magma mush in the plumbing system (*Fig. 6.17*). Meanwhile, mafic magma kept recharging into the magma chamber which caused substantial magma mixing, as revealed in the zoned phenocrysts, especially oscillatory zonation of clinopyroxenes and compositional disequilibrium of clinopyroxenes. The magma recharge might be the force to trigger magma mush disaggregation and eruption which formed the Panama Formation. There are locally some regions that magma mush locked up due to high crystallinity. Magma is difficult to erupt in these regions. However, interstitial melts can flow and extract from the magma mush and probably formed a melt-rich and crystal-poor region. Magma in these areas erupted and formed the Las Cascadas Formation. When the interstitial melt extracted or erupted, magma mush disaggregated and the framework of mush was entrained in the melt. The framework can be seen in the porphyritic Las Cascadas Formation samples as glomerocrysts and clinopyroxene/plagioclase phenocrysts. When the melts ascended without picking up framework crystals, it erupted and formed the aphyric samples of the Las Cascadas Formation (Fig. 6.17).

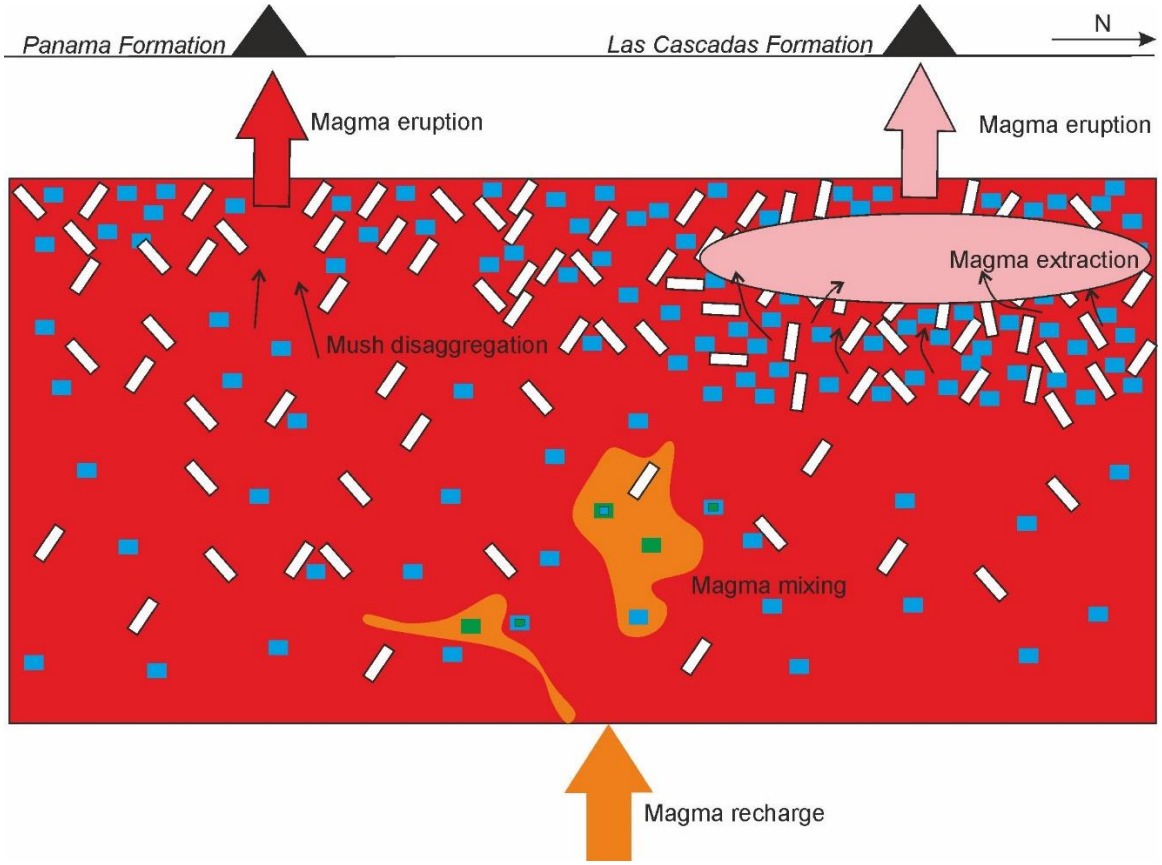

Fig. 6.17 Sketch to show crystallisation and magma mixing for the Panama Formation and Las Cascadas Formation

6.1.2 Cabra Formation

The Cabra Formation range from basalt to rhyolite and can be divided into a mafic member and a felsic member. Both members show evidence that plagioclase crystallise before clinopyroxene which is in contrast to the Panama and Las Cascadas Formation. The crystallisation process for the Cabra Formation is different from the Panama and Las Cascadas Formation.

6.1.2.1 Crystallisation

Major elements are modelled by rhyolite-MELTS with J17-034 as the starting composition which has relatively low SiO2 (53.8 wt.%), high MgO (5.0 wt.%), and the lowest HREE.

Due to the crystallising sequence in this formation, e.g. plagioclase crystallising before pyroxene, the pressure should be lower, or the water content should be lower in the magma chamber than the Panama and Las Cascadas Formations. Therefore, the pressure is set as 500 bar, 2500 bar, and 5000 bar. The water content is set as 1 wt.% and 3 wt.% for 2500 bars and 5000 bars. 3 wt.% water for 500 bar yields a non-supportive liquidus result so 1 wt.% and 2 wt.% water contents are set for 500 bars. Therefore, there are 6 fractional crystallisation schemes in the rhyolite-MELTS modelling. Model 1:

500 bars of pressure and 1 wt.% water; Model 2: 500 bars of pressure and 2 wt.% water; Model 3: 2500 bars of pressure and 1 wt.% water; Model 4: 2500 bars of pressure and 3 wt.% water; Model 5: 5000 bars of pressure and 1 wt.% water; Model 6: 5000 bars of pressure and 3 wt.% water.

1 or 2 wt.% water models work better than 3 wt.% water model in Al_2O_3, and especially Fe_2O_3, TiO_2 vs SiO_2 diagrams, under the same pressure (Fig. 6.18). High water content (3 wt.%) work slightly better than low water content (1 wt.% and 2 wt.%) schemes in CaO vs SiO_2 diagram. In the rest of diagrams, water content only makes a small difference in the dacite section (SiO_2 >63 wt.%). For low water models, the 5000 bars model is off the crystallisation trend in TiO_2 vs SiO_2 and MgO vs SiO_2 diagrams while the 500 bars model is below the evolving trend in Al_2O_3 vs SiO_2 diagram. Models of 500 bars+1 wt.% water, 500 bars+2 wt.% water, and 2500 bars+1 wt.% water show quite similar trends and overall overlap with the samples in Al_2O_3, CaO, Fe_2O_3, TiO_2, K_2O, and Na_2O vs SiO_2 diagrams. However, 2500 bars+1 wt.% works better in MgO vs SiO_2 diagram (Fig. 6.18). Therefore, 2500 bars+1 wt.% was chosen as the best fit.

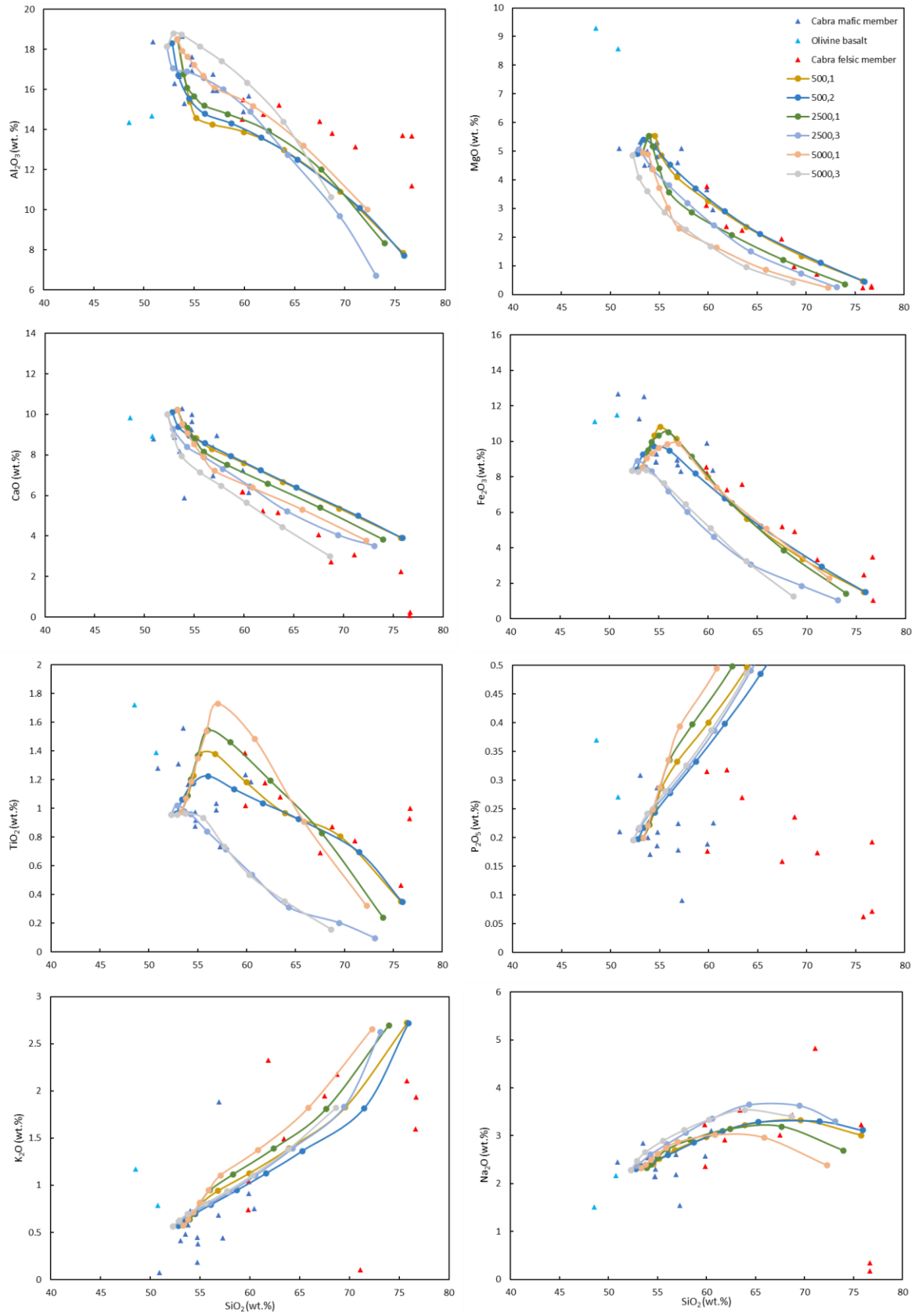

Fig. 6.18 Rhyolite-MELTS modelling with the starting composition of J17-034 at a interval of 20% crystallisaiton from 100% to 20%.

In the 2500 bar+1 wt.% model, crystallisation begins at 1188°C with plagioclase before being joined by small amount of orthopyroxene at 1148°C (~10% crystallisation) (Fig. 6.7). Clinopyroxene then joins the crystallising assemblage at 1133°C after 20% fractionation. Then Fe-Ti oxide crystallises at 1118°C after clinopyroxene. The lowest MgO in the Cabra Formation is 0.24 wt.% (J18-047) which corresponds to ~85% crystallisation.

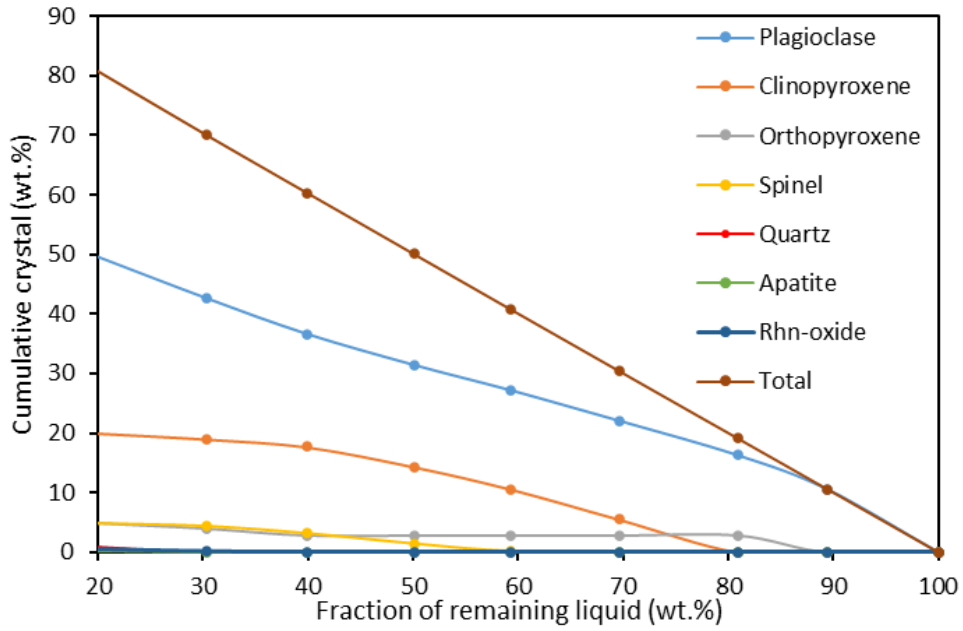

Fig. 6.19 Proportion of minerals formed during fractional crystallisation of J17-034 at 2500 bars+1 wt.% water at 10% intervals of crystallisation by rhyolite-MELTS.

Sr/Sr* decreases with decreasing MgO (Fig. 6.20) which is consistent with early stage plagioclase crystallisation. Eu/Eu* also decreases as MgO decreases which indicate Eu is the Eu^{2+} and magmas of the Cabra Formation are reduced. Ti/Ti* decreases with decreasing MgO is consistent with Fe-Ti oxide crystallisation. P/P* decreases with decreasing MgO which suggests apatite crystallisation (Fig. 6.20).

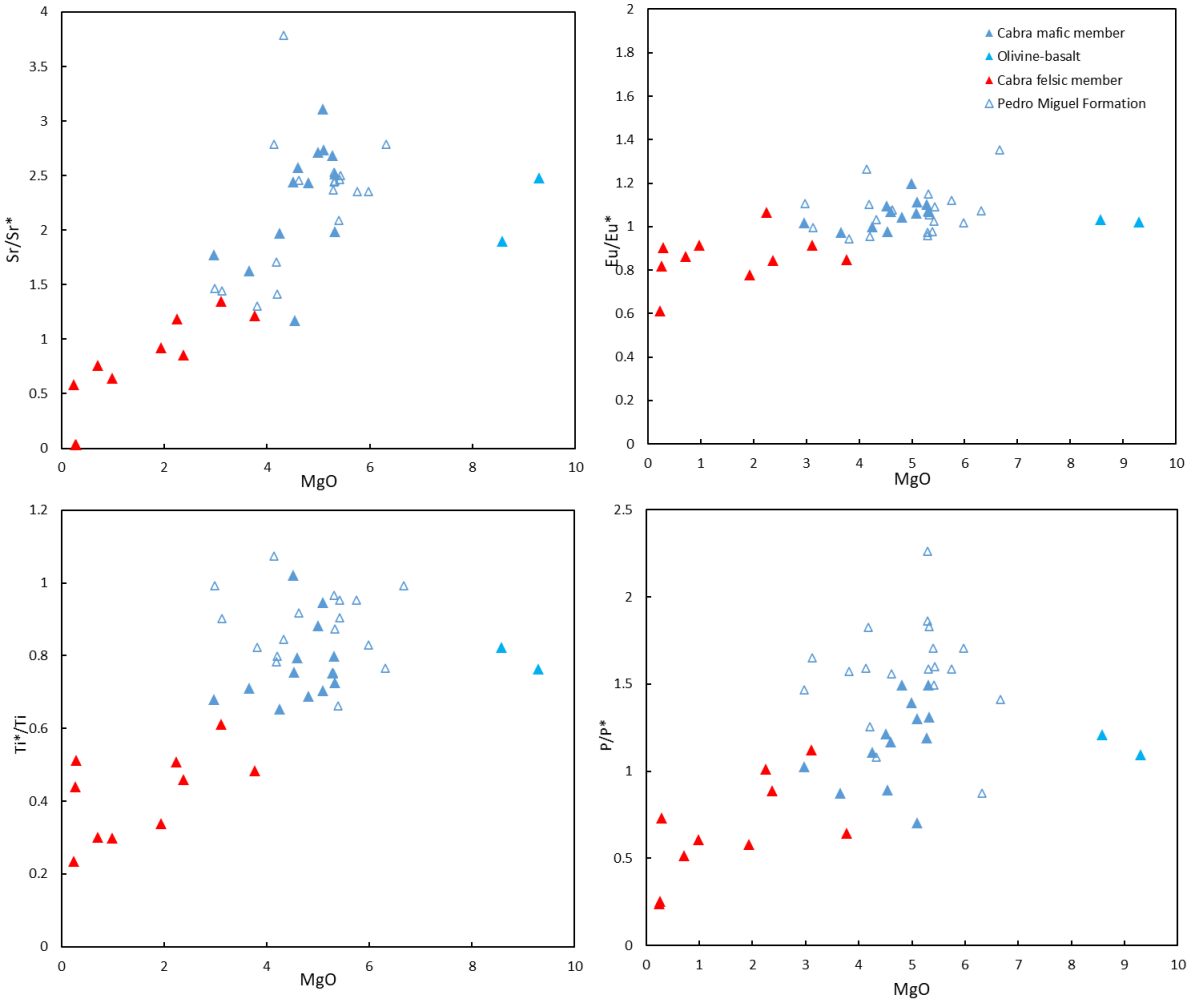

Fig. 6.20 Trace element anomaly vs MgO

Trace element modelling is also conducted using the same fractional crystallisation described in Equation 6.1. The mineral proportions at each 10% crystallisation intervals obtained in rhyolite-MELTS modelling are shown in Table 6.4. Therefore, the bulk partition coefficient is slightly different at each interval. The partition coefficients of each mineral is the same as those used in the Las Cascadas Formation and Panama Formation (Table 6.3) except Eu. The value of Eu in this model is higher (0.34 from Rollinson, 1993) due to less oxidized state of the Cabra magma. The sample with the highest trace element content require ~70% crystallisation in the first model and 70-80% crystallisation in the second model which is slightly lower than the crystallisation degree derived from the major element modelling.

Table 6.4 Mineral proportions at each 10% crystallisation interval derived from rhyolite-MELTS for trace element modelling of fractional crystallisation.

Mineral	% at 10%	% at 20%	% at 30%	% at 40%	% at 50%	% at 60%	% at 70%	% at 80%
Pla	100	85	73	67	63	61	61	61
Cpx	0	0	18	26	29	29	27	25
Opx	0	15	9	7	6	5	6	6
Mag	0	0	0	0	3	5	6	6

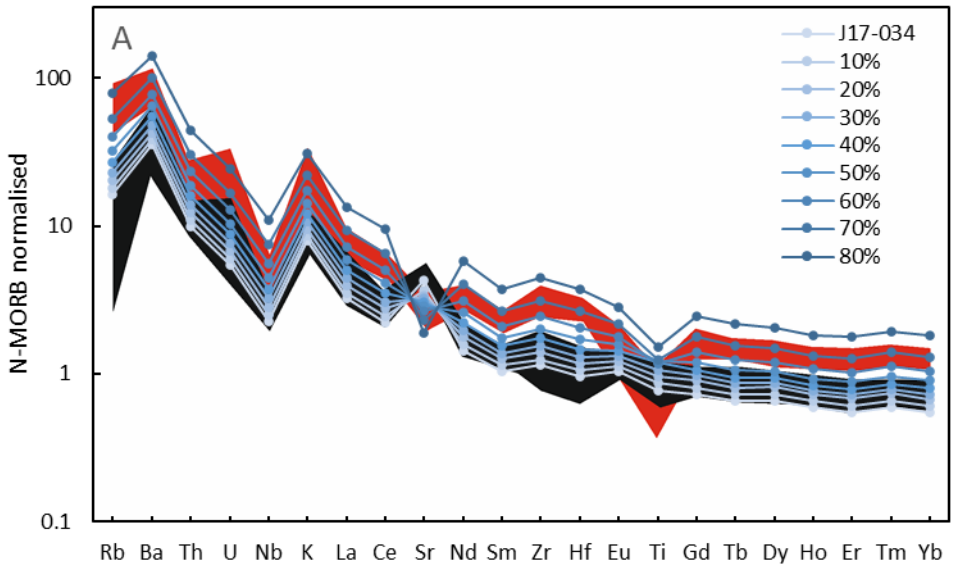

Fig. 6.21 Trace element modelling with changing bulk partition coefficient based on rhyolite-MELTS modelling (The red range is Cabra felsic member except J17-104 and the black is Cabra mafic member).

6.1.2.2 Magma Mixing

Magma mingling between the mafic member and the felsic member is obvious in the field in the hill of Cerro Cabra. Rocks in the felsic member have high trace element contents but they also have high MgO and low SiO_2, which can be explained by magma mixing, or crystal entrainment similar to the porphyritic rocks of the Las Cascadas Formation. As can be seen from Fig. 6.22, these rocks are on the mixing trend between the mafic rock and felsic rock.

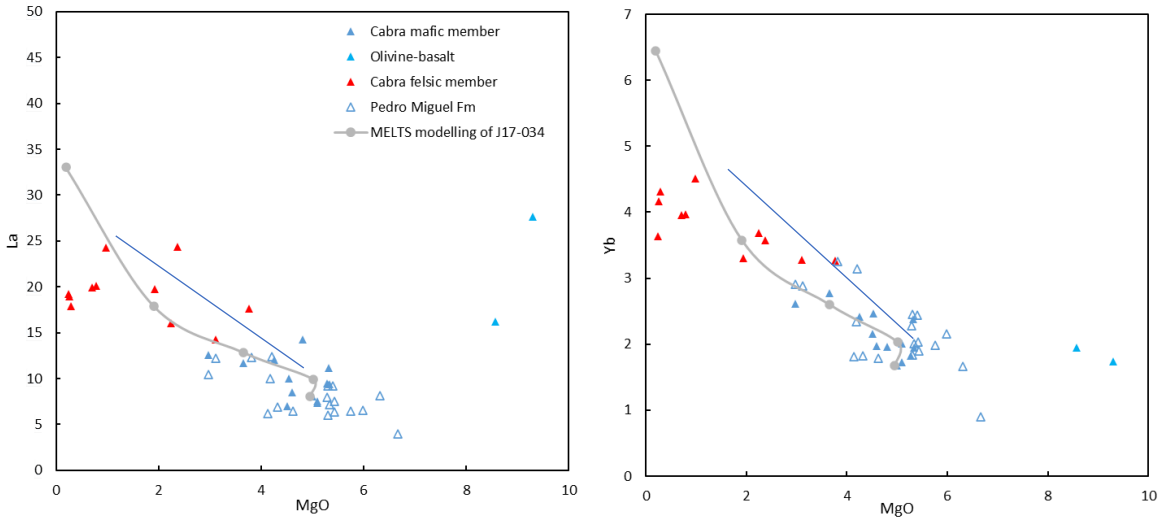

Fig. 6.22 Crystallisation and magma mixing revealed by trace element-MgO (grey dot line is based on 500 bar + 1% H2O from rhyolite-MELTS modelling of J17-034 at 20% crystallisation interval from 100% to 20%).

Reversed zonation in J17-034 is common. Extremely high An-number in this sample is not consistent with the rhyolite-MELTS modelling (the highest is 82 at 2500 bar and 1% water content). This suggests magma mixing occurred between J17-034 and more primitive magma.

Olivine xenocrysts, xenoliths, and glass patches in J18-034-4 indicate magma mingling between felsic rocks and olivine basalt. Clinopyroxene phenocrysts are found in J18-034-4 even though clinopyroxene phenocrysts are not common in this formation. They are similar to the ones in the Panama Formation or the Las Cascadas Formation. Besides, in the discrimination diagrams (Fig. 4.58), most of the clinopyroxene are plotted in the same area to those in J17-036-1 which suggests this rock belongs to the Panama Formation or Las Cascadas Formation. Due to the high trace element content, this rock should be from the Las Cascadas Formation and it mixed with olivine bearing magmas of the Cabra Formation.

6.1.3 Crystallisation of the Caraba Formation

Andesite in the Caraba Formation was dated as ~25 Ma (Rooney et al., 2011). Dacite in this formation was dated as ~24 Ma in this study. Besides, petrographic, major elements, and trace element characteristics also indicate dacite is the crystallising product of the andesite. Since rhyolite-MELTS can only do modelling for rocks without amphibole, only trace element modelling was conducted in this section.

Partition coefficients between minerals and dacitic melt are listed in Table 6.5. Amphibole and plagioclase are phenocrysts while magnetite and zircon are accessory minerals in rocks of this

formation. The proportion of these minerals used for trace element modelling is based on petrographic observation under microscope which is shown in Table 6.6.

Table 6.5 Partition coefficients used for trace element modelling.

	Damph/melt	Dplag/melt	Dmgt/melt	Dzircon/melt
Ba	0.395	0.307		
Th	0.088	0.0001		
U	0.101	0.0002		
Nb	4	0.0014	0.82	236
Ta	4	0.0003	1.12	
K	0.19	0.18		
La	0.279	0.143	0.0029	1.14
Ce	0.656	0.134	0.0038	1.17
Pb	0.354	0.1085		
Sr	0.397	1.9447		
Nd	1.827	0.104	0.0055	1.4
Sm	3.312	0.0743	0.0072	2.03
Zr	0.719	0.0039	0.88	977.5
Hf	1.214	0.0015		977.5
Eu	3.345	0.622	0.0064	0.9
Ti	5.89	0.0441	7.11	3.150
Gd	4.792	0.0507	0.0055	6.01
Dy	5.212	0.0321	0.0071	44.90
Ho	5.481	0.0254	0.0079	
Er	5.396	0.0202	0.0117	107.00
Yb	4.685	0.0132	0.0192	516.0
Y	5.012	0.0275	0.0039	71.4

**Partition coefficient between dacitic melt and minerals plagioclase, magnetite, ilmenite, and apatite are from Wanke et al., 2019. Partition coefficients between dacitic melt and amphibole are derived from sample RN12V2-2 from Nandedkar et al., 2016 except for Nb and Ta which are from Arth (1976). Partition coefficients between dacitic melt and zircon are from different sources: Nb and Ti are from Thomas et al., 2002; the rest are from GERM website.*

Table 6.6 Mineral proportion used in trace element modelling.

	% under microscope	% in modelling
Amphibole	35	53
Plagioclase	30	45.4
Magnetite	1	1.5
Zircon	0.1	0.2
Groundmass	33.9	

Fractional crystallisation is used for crystallisation modelling with the same equation to Equation 6.1. As can be seen from the diagram (Fig. 6.23), Caraba dacite can be formed by ~22 % crystallisation of andesite.

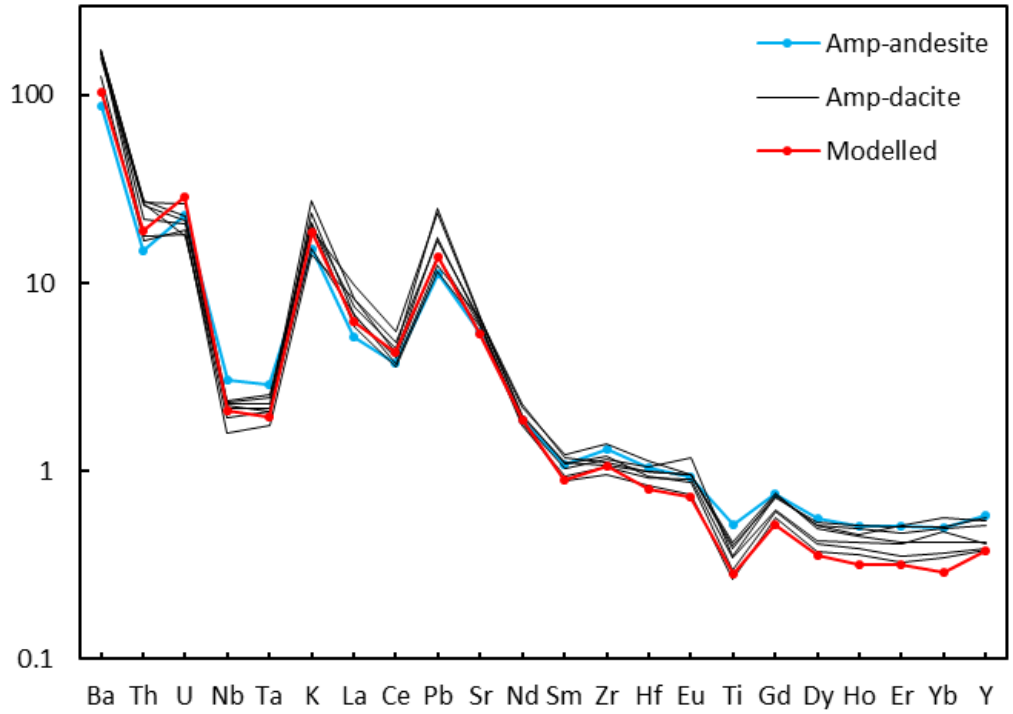

Fig. 6.23 Trace element modelling for the Caraba Formation with sample 4001 (Rooney et al., 2011) as the starting composition.

6.1.4 Summary

Detailed analyses of whole rock geochemistry, mineral chemistry, interstitial glass chemistry, and matrix glass chemistry indicate the Las Cascadas Formation derived from the interstitial melt of the magma mush which is similar to the magma mush for the Panama Formation. The Panama Formation and Las Cascadas Formation formed at ~4100 bars of pressure with ~2 wt. % water content. Take the most mafic sample J18-059-1 as the starting composition, the most evolved sample in the Panama Formation can be formed by ~50% fractional crystallisation while the Las Cascadas Formation can be

formed by 60-70% fractional crystallisation. When the magma mush reached its locking up point (>50% crystallinity), magma cannot erupt but the interstitial melt can be extracted to form the aphyric Las Cascadas 2. This is also the reason why there are gaps in major and trace elements between the Panama and Las Cascadas 2 Formation. During melt extracting or volcanic erupting, the framework can be entrained in the melt and this melt-crystal mixture formed the Las Cascadas 1. In the Panama Formation, magma mixing is common as revealed by clinopyroxene.

The Cabra Formation rocks have a large range in terms of chemical composition. Rocks in this formation can be achieved by fractional crystallisation of a mafic sample, e.g. J17-034. This crystallisation occurred at ~2500 bars of pressure with ~1 wt.% water content which are lower than the Panama and Las Cascadas Formation. The most evolved magma can be achieved by ~75% fractional crystallisation of the starting composition. Magma mixing is common as revealed by clinopyroxene and magma mingling is also common which can be observed in the field (Chapter 3). The Cabra Formation formed at a lower pressure (more extensional tectonic setting) and have slightly drier magma than the Panama and Las Cascadas Formation.

The Caraba Formation range from andesite to dacite and the dacite can be achieved by amphibole and plagioclase crystallisation.

6.2 Nature of the Mantle Source and Degrees of Partial Melting

Previous studies (e.g., Gill 1981; Pearce 1982; Tatsumi et al. 1986; Pearce and Parkinson 1993; Keppler, 1996; Hawkesworth et al. 1997; Elburg et al. 2002; Zheng, 2019) have demonstrated that subduction related magmas are characterized by significant enrichment in LILE (Cs, Rb, Ba, Sr), Pb and LREE relative to the HFSE (Nb, Ta, Zr, Hf) and HREE, with strongly negative Nb– Ta–Ti anomalies and positive Pb anomalies in primitive mantle normalised or N-MORB normalised incompatible trace element diagrams. These characteristics are also shown by rocks in this study (see Chapter 4).

For the magmatism in subduction zones, the ambient mantle, which is defined by Turner and Langmuir (2015) as the mantle prior to metasomatism of slab input, is normally metasomatized by material released from the slab. Enrichment of the ambient mantle above a subducted slab of oceanic lithosphere can be attributed to migration of (1) aqueous fluids derived from dehydration of subducted sediments or altered oceanic crust (AOC), (2) melts derived from partial melting of the subducted sediments and/or (3) melts derived from partial melts of the AOC. Large ion lithophile elements and Pb are added to the mantle sources of island arc magmatism via aqueous fluids as these elements are soluble in aqueous fluids during dehydration reactions (e.g., Hawkesworth et al., 1991; Pearce and Peate, 1995; Bebout et al., 1999; Elliott, 2003; Spandler and Pirard, 2013). These elements are also

termed as water-soluble elements. Light rare earth elements (LREE) and Th are not water-soluble but are soluble in hydrous melts which may come from sediment melting or/and AOC melting. However, Th are extremely enriched in sediment and therefore comes mainly from sediment melt (Johnson and Plank, 1999).

6.2.1 End-member Components in the Mantle Source

For the ambient mantle in the PVA, some studies consider it as N-MORB like mantle, e.g. DMM (Carr et al., 1990; Gazel et al., 2009; Gazel et al., 2011) while others suggest it is CLIP mantle (Feigenson et al., 2004) or Galapagos plume mantle (Abratis and Worner, 2001; Gazel et al., 2011). Therefore, average DMM (Workman and Hart, 2005 but originally from Su and Langmuir, 2003) and CNS (Cocos-Nazca spreading ridge from Werner et al., 2003) were compiled to represent the isotope characteristic of DMM. Data of the Galapagos hotspot and hotspot track (Werner et al., 2003; Hoernle et al., 2000) were compiled to represent the Galapagos plume end-member. Values of CLIP (Caribbean Large Igneous Province) from Kerr et al. (1997a) and Hauff et al. (2000a, 2000b) were also compiled to compare with the Galapagos plume. No data are available for sediment subducted during subduction in PVA. Therefore, slab sediments on the Cocos Plate which was drilled from DSDP 495 (Plank and Languir, 1998; Feigenson et al., 2004) and ODP 1256 (Sadofsky et al., 2009) were compiled to represent the sediment end-member. For the subducting AOC, I take the oceanic crust formed in the East Pacific Rise spreading centre or Galapagos related aseismic ridge. The isotope of the former can be represented by the DMM or CNS while the later can be represented by Galapagos plume or CLIP.

From the $^{207}Pb/^{204}Pb$ vs $^{206}Pb/^{204}Pb$ diagram (Fig. 6.24 A), Panama Formation/Las Cascadas Formation/Bas Obispo Formation/Caraba Formation trend from a high radiogenic Pb endmember to a sediment endmember. This suggests these formations have a high radiogenic Pb endmember mixed or metasomatized by sediment melt or fluid. The Chagres Complex are roughly on this trend and presents the highest sediment component. Besides, it might also have higher volume of AOC or DMM component as they trend toward CNS/DMM end-member. This is consistent with ƐNd vs $^{87}Sr/^{86}Sr$ (*Fig. 6.24* B, C) as Chagres Complex samples trend toward CNS/DMM to show higher ƐNd than the rest. If the ambient mantle is DMM, high ƐNd of the Chagres Complex in the ƐNd vs $^{87}Sr/^{86}Sr$ diagram would indicate less sediment component for this group. However, this is not consistent with $^{207}Pb/^{204}Pb$ vs $^{206}Pb/^{204}Pb$ diagram in which Chagres Complex show the highest sediment input. Besides, if this DMM mantle is metasomatized by sediment melts or mixture of sediment melts and Galapagos related AOC melt, the mixing line between them in ƐNd vs $^{87}Sr/^{86}Sr$ diagram is convex which cannot go across the samples. Therefore, the high radiogenic Pb should come from the ambient mantle and the high ƐNd end-member, e.g. CNS or DMM, should be AOC melts (as the AOC fluid

does not change the εNd value). This is consistent with the geological setting that in central America, oceanic crust subducted beneath CLIP which is considered to form above the Galapagos hotspot (Duncan and Hargraves, 1984; Sinton et al., 1998; Hauff et al., 2000a; Whattam and Stern, 2015) and can possess high radiogenic Pb isotope. This is also consistent with the studies that the mantle beneath PVA is a plume related mantle (Abratis and Worner, 2001; Feigenson et al., 2004; Gazel et al., 2011). In terms of sediment component, aqueous fluids carry very little REE, Th and HFSE (e.g., Nb, Ta, Zr and Hf), introduce significant amounts of large ion lithophile elements (e.g., K, Rb, Ba and Sr) and other fluid-mobile trace elements (e.g. Pb) into the mantle wedge (Kogiso et al., 1997; Kessel et al., 2005; Scambelluri et al., 2006; Zheng et al., 2011). Although Be and Th are relatively insoluble in aqueous solutions, they are highly soluble in sediment melts (Morris et al., 1990; Brenan et al., 1995a, 1995b; Elliott et al., 1997; Johnson and Plank, 1999). Since rocks in this study show not only LILE enrichment but also Th, LREE enrichment, the slab input must include sediment melt.

For the Cabra and Pedro Miguel Formation in Fig. 6.24 A, samples trend from a mixture of high radiogenic Pb and sediment endmember to N-MORB or DMM. This suggests, apart from high radiogenic Pb mantle and sediment, an extra N-MORB melt or aqueous fluid is required for these two formations. In $^{207}Pb/^{204}Pb$ vs εNd or $^{87}Sr/^{86}Sr$ vs εNd diagram (Fig. 6.24 B, C), radiogenic Nd increases toward N-MORB endmember which indicates this N-MORB component is AOC melt rather than aqueous fluid.

As shown in Fig. 6.24 A, the Chagres Complex presents the highest sediment component in the mantle source. Besides, it might also have certain degrees of AOC component, e.g. AOC aqueous fluid or/and AOC melt as they trend toward N-MORB end-member. Samples with AOC signature also have high εNd which suggest this AOC component is AOC melt (*Fig. 6.24*). The Bas Obispo Formation shows relatively low content of sediment input.

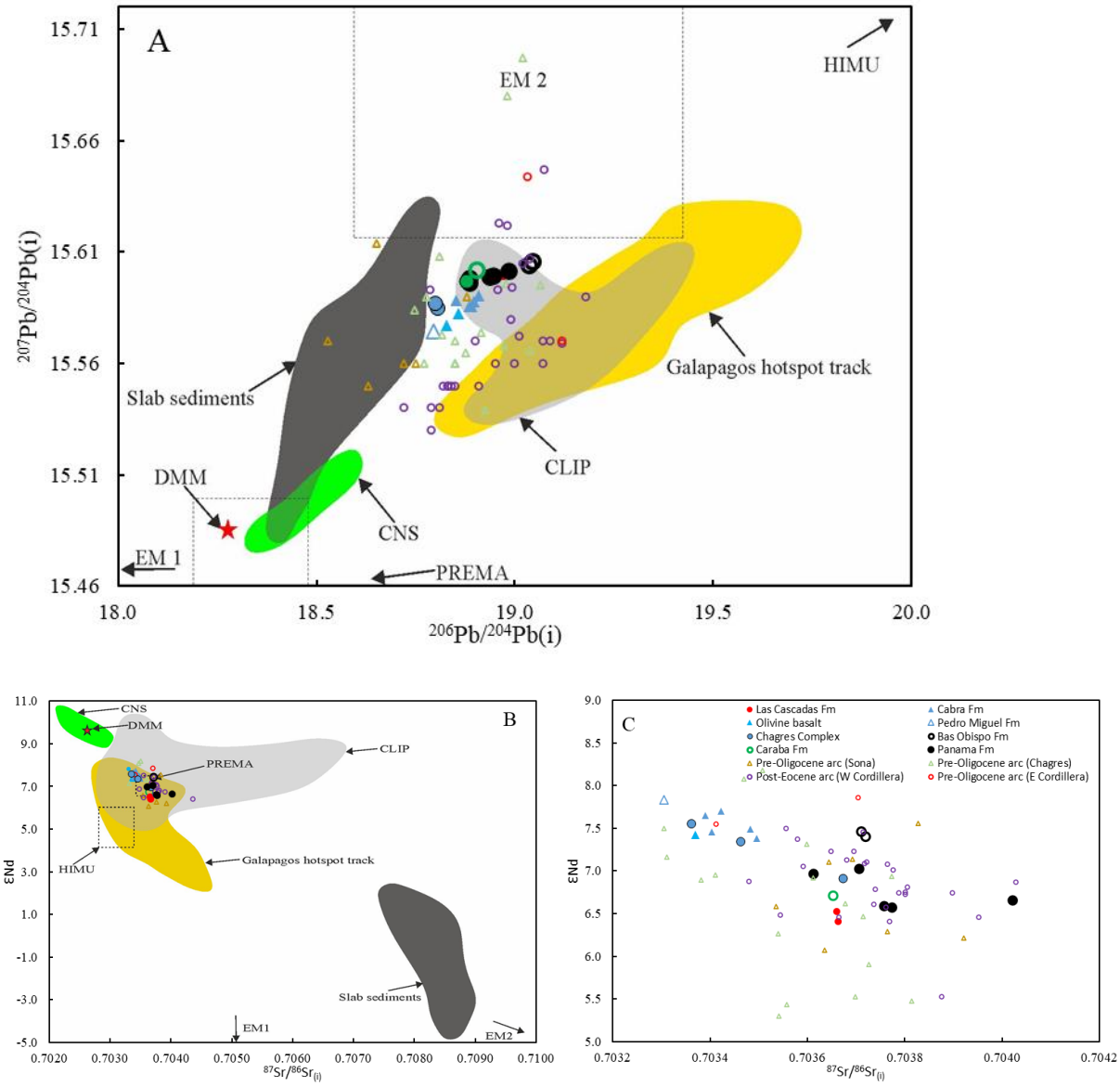

Fig. 6.24 (A) $^{207}Pb/^{204}Pb$ vs $^{206}Pb/^{204}Pb$ for rocks in central Panama. (B) εNd vs $^{87}Sr/^{86}Sr$. (C) Zoom in for the inset in B. Also plotted are average DMM (depleted MORB mantle, from Workman and Hart (2005) but originally from Sun an Langmuir (2003)); CNS (Cocos-Nazca spreading ridge from Werner et al. (2003)); Galapagos hotspot track from Werner et al., 2003 and Hoernle et al., 2000; slab sediments on the Cocos Plate from Sadofsky et al. (2009), Feigenson et al.(2004), and Plank and Languir (1998); CLIP (Caribbean Large Igneous Province) from Kerr et al. (1997a) and Hauff et al. (2000a, 2000b). Chagres arc and Cordillera arc* are from Lissinna (2005) and Wegner et al. (2011).*

With regard to trace element ratios as shown in Fig. 6.25, the post-Eocene rocks have small values of Th/Nb and Ba/La while the Chagres Complex overall have high values of Th/Nb and Ba/La. Th are enriched in sediment (Johnson and Plank, 1999) therefore Th/Nb value can indicate sediment melt. High Th/Nb suggests the Chagres Complex possesses high volume of sediment melt. Barium is also

enriched in sediment subducting beneath PVA (Plank and Langmuir, 1998; Patino et al., 2000; Gazel et al., 2009). Therefore, Ba/La also indicates sediment component including sediment melt and aqueous sediment fluid. High Ba/La is consistent with Th/Nb suggesting highest sediment component for the Chagres Complex.

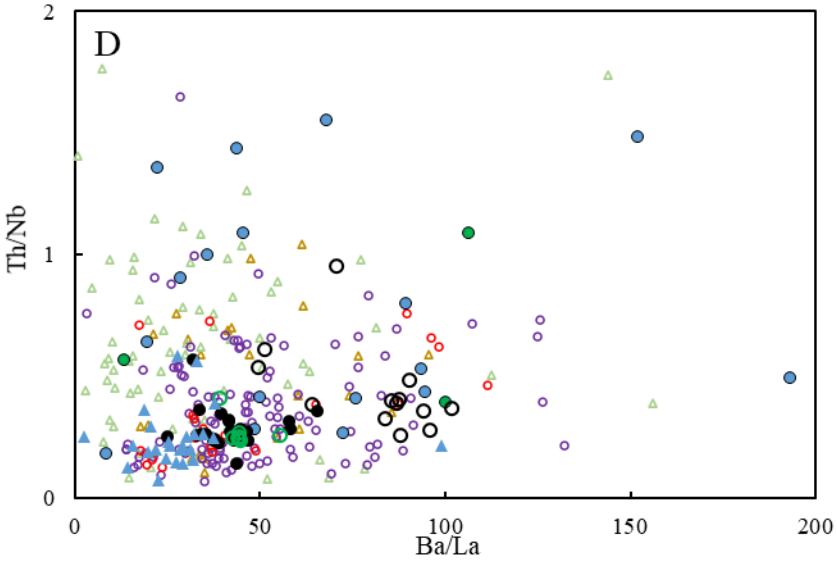

Fig. 6.25 Th/Nb vs Ba/La for rocks in central Panama and eastern Panama (Symbols are the same to the ones in Fig. 6.24*).*

Therefore, a 3-component source is revealed for rocks in central Panama: high radiogenic Pb ambient mantle, sediment melt, and AOC melt. Since the aqueous fluid is not revealed by isotopes or trace elements and it only affect fluid mobile elements such as Rb, Ba, U, and Pb, only high radiogenic Pb mantle, sediment melt, and AOC melt are considered to make modelling simple.

6.2.2 CLIP Mantle as the Ambient Mantle wedge

The volcanic fronts in south Central America between Nicaragua and Panama are characterised by temporally and spatially restricted high radiogenic Pb isotopes, with $^{208}Pb/^{204}Pb$ and $^{206}Pb/^{204}Pb$ values pointing towards, or overlapping with, those associated with the modern Galapagos hotspot, Cenozoic paleo-Gapalagos hotspot seamounts/oceanic islands, and some of the Upper Cretaceous oceanic plateau basalts of the CLIP (Feigenson et al. 2004; Lissinna, 2005; Hoernle et al., 2008; Gazel et al., 2009; Gazel et al., 2011; Wegner et al., 2011). For the ambient mantle in central America, there are two different points of view. One considers it as N-MORB like mantle, e.g. DMM (Gazel et al., 2009; Gazel et al., 2011). They suggest the high radiogenic Pb isotopes derive from slab component that come from Cocos/Coiba Ridge component or/and the highly enriched Seamount Province (Lissnna, 2005; Hoernle et al., 2008; Gazel et al., 2009; Gazel et al., 2011). On the other hand, studies on post-Miocene rocks in PVA suggest the ambient mantle beneath the arc is CLIP mantle or Galapagos

plume related mantle. High Pb isotopic ratios in eastern Nicaragua and Costa Rican back-arc lavas led Feigenson et al. (2004) to propose that the Galapagos-OIB signature is inherited from CLIP mantle. Similarly, based on trace elements and especially isotopes of small volumes of adakitic and alkalic back-arc lavas, Abratis and Worner (2001) propose the mantle for these rocks should be Galapagos hotspot related mantle. This hot Galapagos mantle rose into the mantle wedge below southern Costa Rica through a slab window proposed by Johnston and Thorkelson (1997).

As mentioned above in section 6.2.1, our data from central Panama suggest the high radiogenic Pb signature comes from the ambient mantle. To further figure out the ambient mantle and across-arc isotopic variation (through time) and also to avoid along-arc mantle heterogeneity, a cross-section from Sona-Azuero to central Cordillera was selected.As can be seen from Fig. 6.26 A, $^{206}Pb/^{204}Pb$ increases through time, as arc front moved away from trench. If the high radiogenic Pb is triggered by the Galapagos related slab input, e.g. the first possibility, the slab input should increases through time. Besides, the ƐNd should decreases through time as the radiogenic Nd of the CLIP crust is lower than DMM (Fig. 6.24 B). However, ƐNd increases through time according to the cross-section (Fig. 6.26 B). This inconsistency can be solved by assuming the ambient mantle is the CLIP mantle enriched in radiogenic Pb. Sediment component from slab has low radiogenic $^{206}Pb/^{204}Pb$ (Fig. 6.24 A) and low ƐNd (Fig. 6.24 B) and as sediment component decreases through time, $^{206}Pb/^{204}Pb$ along with ƐNd increase. Therefore, the ambient mantle beneath PVA is CLIP mantle which is enriched in radiogenic Pb. This rules out the possibility that high radiogenic Pb is caused by Galapagos related oceanic crust and similarly, by input of CLIP crust through subduction erosion.

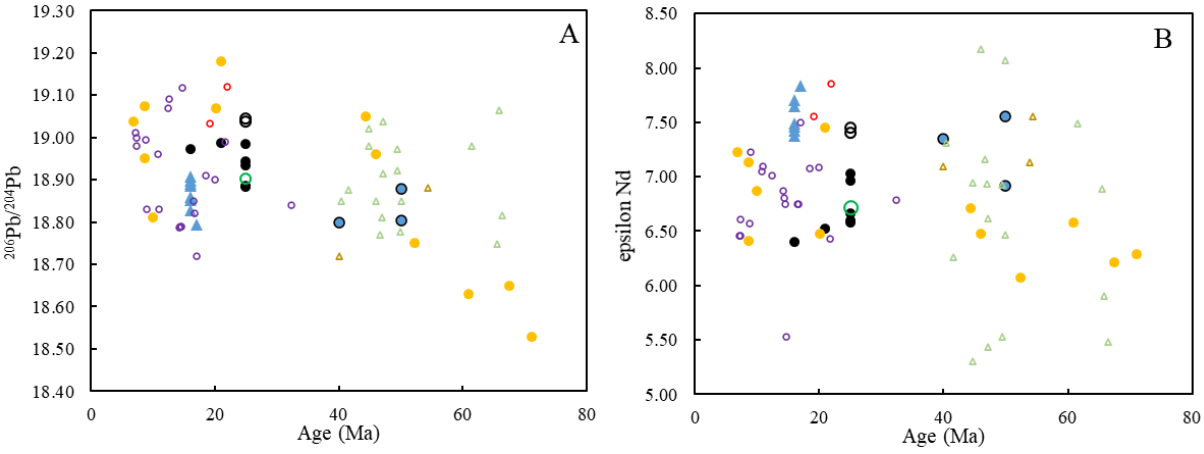

Fig. 6.26 Isotopes vs time for PVA. (A) $^{206}Pb/^{204}Pb$ vs age (B) ƐNd vs age. Yellow filled circles are samples from cross-section from Sona-Azuero arc to central Cordillera arc.

This idea is supported by research on early arc rocks in Panama. Buchs et al. (2007) found proto-arc rocks on the Azuero peninsula displaying REE compositions similar to the composition of the CLIP. They concluded that these proto-arc magmas were derived from the sub-plateau lithospheric mantle. Similarly, Study on the pre-Oligocene arc in Sona-Azuero by Wegner et al. (2011) suggest this first phase of arc magmatism displays trace element characteristics that resemble the CLIP basement so the

ambient mantle for the Sona-Azuero arc should be the CLIP mantle. The CLIP and earliest overlying arc units overlap in time, space, trace elements, and isotopes which suggests both derived from a similar mantle source associated with the Galapagos Plume which became increasingly modified by slab input through time (Whattam and Stern, 2015).

Hauff et al. (2000) and Kerr et al. (2002) recognize a HIMU-like component within the plume responsible for the Colombian/Caribbean oceanic plateau. The HIMU component within the Caribbean plateau mantle is also confirmed by Hastie et al. (2008) which demonstrate the Caribbean plateau lavas in Jamaica are composed of a larger HIMU component than the other Caribbean plateau lavas. Therefore, CLIP mantle source comprises a HIMU component which should exist in the ambient mantle beneath PVA.

6.2.3 Proportions of End-member Components and Degrees of Partial Melting

The metasomatism processes of the ambient mantle wedge can be divided into three cases, as addressed by Kuritani et al, (2008): (1) the ambient mantle is metasomatized firstly by sediment component and then metasomatized by AOC component, as preferred for this study; (2) the ambient mantle is metasomatized firstly by AOC component and then metasomatized by sediment component; (3) sediment component and AOC component mix to form slab input probably as supercritical fluid (Kuritani et al., 2008) and the ambient mantle get metasomatized by this slab input. For the second case, the HIMU ambient mantle get mixed by AOC melt to form a mixed source in between HIMU and N-MORB. When this mixture gets metasomatized by sediment melts, the sediment melt accounts for higher proportion in the Panama/Caraba Formation than in the Chagres Complex in ƐNd vs $^{87}Sr/^{86}Sr$, which is not consistent with the fact that the Chagres Complex have higher sediment melt. Pelagic sediments are easier to melt than AOC during subducting since they have the direct contact with the hot mantle wedge plus their melting point is lower than AOC (Schmidt and Poli, 2014). Therefore, the first case is adopted in this study.

To calculate the relative proportion of mantle peridotite, sediment melt, and AOC melt along with the partial melting degree, endmembers should be selected first. The detailed description can be seen below. A potential problem for modelling is the endmembers can be rather causal sometimes. The choices for mantle mineralogy and melting mechanisms (e.g. batch melting vs accumulated fractional melting) can also yield different results. To limit this uncertainty, both trace element and isotope modelling are conducted and their consistency shows the robustness of the result.

6.2.3.1 Trace Element Consideration

For slab input, sediment composition varies largely from place to place (Plank and Langmuir, 1998). There is no record for ancient subducting sediment in Central America. Therefore, I use modern

sediment composition obtained from drilling in Cocos Plate as sediment input for volcanic arc rocks in this study. Site 495 in DSDP drilling in the Cocos Plate off the Guatemala coast shows the sediment is 425 m thick composed of ~250 m pelagic carbonates in the lower column and ~175 m hemipelagic, diatom-rich mud in the upper part (Plank and Langmuir, 1998). Drilling in the fore-arc, however, failed to recover pelagic sediment derived from the down-going plate. These results suggest that thousands of kilometres of oceanic crust have been subducted, with no accretion of sediment to the continental margin (Aubouin et al., 1982), which indicates the entire 425 m of sediment at Site 495 is subducted. In synthetic systems it is well known that carbonates are very stable at subsolidus conditions: between 5 GPa and 9 GPa dolomite breaks down along a curved reaction line (Luth, 2001) to magnesite and $CaCO_3$ polymorphs, which are stable down to lower mantle pressures (Biellmann et al., 1993). In the subducting slab, carbonate minerals may remain stable in the presence of a siliceous melt and with increasing temperature decompose to form an immiscible carbonatite melt coexisting with a silicate melt (Schmidt and Poli, 2003). There is no occurrence of carbonatite and no evidence of carbonatite melt metasomatizing mantle in Central America, so only partial melt of 90% hemipelagic sediment + 10% carbonate is considered in this study (*Table 6.7*). This sediment composition is similar to the one used in Gazel et al. (2009) in which the sediment is composed of 70% mean hemipelagic + 30% mean carbonate. Both the partial melting degree and bulk partition coefficient between melt and resitite (Table 6.8) are derived from the experiment at 900 ℃ and 2 GPa from Johnson and Plank (1999). The result of the sediment melt can be found in *Table 6.7*. The simple batch melting model as shown below in Equation 6.2 and Equation 6.3 are used.

Table 6.7 End-member components used in trace element and isotope modelling

	Mantle	**Bulk sediment**	**Sediment melt**	**AOC**	**AOC melt**
Trace element	*DMM*[1]	*90% pelagic+10% carbonate*[2]	*12% melting of sediment*[3]	*37DR-1*[4]	*10% melting of 37DR-1*[5]
Rb	0.05	37.49	64.91	0.39	3.48
Ba	0.56	3761.40	6227.48	5.98	55.12
Th	0.01	2.73	3.58	0.12	0.66
U	0.00	4.43	6.02	0.03	0.23
Nb	0.15	4.61	3.50	1.67	12.53
Ta	0.01	0.32	0.25	0.12	0.70
La	0.19	20.02	11.81	1.59	10.50
Ce	0.55	25.97	14.93	5.06	25.29
Pb	0.02	9.31	7.42	0.17	1.26
Sr	7.66	452.80	1127.49	45.8	286.68

Nd	0.58	18.11	7.13	5.5	17.10
Sm	0.24	3.96	1.31	2.21	3.66
Zr	5.08	95.18	28.12	49	177.63
Hf	0.16	2.72	0.80	1.47	4.10
Eu	0.10	1.01	0.26	0.78	1.21
Ti	0.07	0.32	0.20		0.60
Gd	0.36	4.21	1.19	3.26	3.05
Dy	0.51	4.72	1.21	4.27	2.41
Y	3.33	31.18	7.92	26.7	13.18
Er	0.35	2.80	0.71	2.88	1.17
Yb	0.37	2.57	0.66	2.79	0.99
Lu	0.06	0.38	0.09	0.43	0.15
Isotope	*HIMU*[6]	*90% pelagic+10% carbonate*[7]	*90% pelagic+10% carbonate*[7]	*2DR-17*[8]	*2DR-17*[8]
$^{87}Sr/^{86}Sr$	0.703	0.70773	0.70773	0.70242	0.70242
$^{143}Nd/^{144}Nd$	0.5129	0.512471	0.512471	0.51315	0.51315
$^{206}Pb/^{204}Pb$	21.5	18.74	18.74	18.347	18.347
$^{207}Pb/^{204}Pb$	15.86	15.61	15.61	15.484	15.484
$^{208}Pb/^{204}Pb$		38.6	38.6	37.901	37.901

[1]*Trace elements of depleted MORB mantle (DMM) is the average DMM from Workman and Hart (2005).*

[2]*Trace elements of bulk sediment are 90% pelagic sediment +10% carbonate off Guatemala shore from DSDP 495 (Plank and Langmuir, 1998).*

[3]*12% melt is assumed to be equilibrated with sediment using the sediment/melt partition coefficients at 900 °C and 2 GPa from Johnson and Plank (1999).*

[4]*AOC composition is the MORB 37DR-1 formed in the Cocos-Nazca spreading centre (Werner et al., 2003)*

[5]*AOC melt is 10% partial melting of 37DR-1 in amphibolite facies in which quartz+plagioclase+amphibole=melt+clinopyroxene+garnet (Sen and Dunn, 1994). The melt is in equilibrium with the AOC composed of 10% amphibole+79% clinopyroxene+10% garnet+1% rutile. Partition coefficient between melt and minerals are from Bedard (2006).*

[6] *Isotopes of HIMU are the barycentre of the value range from Zindler and Hart (1986).*

[7]*Isotopes of bulk sediment and sediment melt are 90% pelagic sediment +10% carbonate off Guatemala shore from DSDP 495 (Plank and Langmuir, 1998).*

[8]*Isotopes of AOC and AOC melt are from sample 2DR-1 from Werner et al. (2004).*

In the pre-Miocene, the subducting oceanic crust was Farallon plate which was formed in the Pacific spreading centre. As the Cabra Formation show significant AOC melt signature, an AOC endmember (AOC melt) needs to be chosen for modelling. Therefore, the sample 37DR-1 from Cocos-Nazca spreading centre (Werner et al., 2003) was chosen as the subducting oceanic crust (*Table 6.7*). AOC melting is usually considered to be dehydration melting of amphibolite at 1.5-2.0 GPa (Sen and Dunn, 1994). The 2.0 GPa data in their study define two melting stages with the first stage involving nearly modal melting of the original amphibolite minerals (qtz, pl, amp) to produce melt + cpx + grt and the second stage involving the eclogite restite melts non-modally (0.86 cpx + 0.14 grt = 1 melt). Only high degree of partial melting of amphibolite can yield an eclogitic restite and partial melting of hot slab requires 10-15% melting degree to form adakite (Sen and Dunn, 1994). Partial melting of AOC here is the model in which the melt is in equilibrium with restite of amphibole: clinopyroxene: garnet: rutile = 0.1: 0.79: 0.1: 0.01. And the equation used here for modelling is the simple batch melting:

$$\text{Equation 6.2} \quad C_L = \frac{C_O}{D_{RS}+F(1-D_{RS})}$$

Where C_L is the concentration of a trace element in the melt; C_0 is the concentration of a trace element in the solid source; F is the weight fraction of the melt produced; D_{RS} is the bulk partition coefficient between melt and restite. D_{RS} is calculated from

$$\text{Equation 6.3} \quad D_{RS} = D1*Kd1+D2*Kd2+D3*Kd3+\ldots$$

Where D1 etc. is the normative weight fraction of mineral 1 in the restite and Kd1 is the mineral-melt distribution coefficient for a given trace element for mineral 1.

Partition coefficients of each minerals are from Bedard (2006) which can be found in Table 6.8. 10% partial melt of this sample was used and the result of this AOC melt can be found in Table 6.7.

Table 6.8 Partition coefficients used in sediment melting (Johnson and Plank, 1999) and AOC melting (Bedard, 2006).

	Sediment melting	AOC melting			
	Bulk Kd	Amp-melt	Cpx-melt	Grt-melt	Rt-melt
Rb	0.52	0.055	0.01	0.0007	0.0076
Ba	0.55	0.046	0.006	0.0004	0.0043
Th	0.73	0.055	0.104	0.0075	0.2
U	0.7	0.05	0.032	0.024	0.2
Nb	1.36	0.274	0.007	0.04	42.8

Ta	1.35	0.477	0.028	0.08	68
La	1.79	0.319	0.028	0.028	0.0057
Ce	1.84	0.56	0.059	0.08	0.0065
Pb	1.29	0.175	0.022	0.032	0.0154
Sr	0.32	0.389	0.032	0.019	0.036
Nd	2.75	1.32	0.115	0.222	0.0082
Sm	3.3	2.09	0.259	1.43	0.0954
Zr	3.71	0.417	0.125	0.537	3.7
Hf	3.71	0.781	0.208	0.431	4.97
Eu	4.22	1.79	0.341	1.54	0.00037
Ti	1.69	4.03	0.473	2.63	45
Gd	3.89	2.53	0.422	4.84	0.0106
Dy	4.29	2.55	0.57	11.5	0.0116
Y	4.34	2.47	0.603	14.1	0.0118
Er	4.33	2.22	0.64	18.8	0.0122
Yb	4.28	1.79	0.635	23.2	0.0126
Lu	4.79	1.59	0.617	24.1	0.0127

For the mantle peridotite, the mantle should be the CLIP mantle which shows HIMU-like component revealed by isotopes. For the trace element content, the mantle is the residue of plume mantle which has gone through partial melting to form CLIP. This plume mantle is heterogeneous with the forming basalt or picrite ranging from LREE-enriched to LREE-depleted (Kerr et al., 1997b; Kerr et al., 2002). PVA is the product of magmatism of oceanic lithosphere subducting beneath CLIP. The mantle beneath CLIP should be the mantle wedge of PVA. Previous geochemical studies on primary magmas of the Caribbean oceanic plateau show that the lavas are formed by 20–30% partial melting of a depleted and/or enriched spinel/garnet peridotite source (e.g. Kerr et al., 1996, 2002; Hauff et al., 1997; Révillon et al., 2000; Hastie and Kerr, 2010). As a result, the mantle plume residue is highly depleted and refractory (e.g. Fitton and Godard, 2004). Therefore, depleted MORB mantle - DMM (Workman and Hart, 2005) is assumed for the modelling (Table 6.7). N-MORB normalised multi-element diagrams for DMM, sediment melt, and AOC melt are shown in Fig. 6.27.

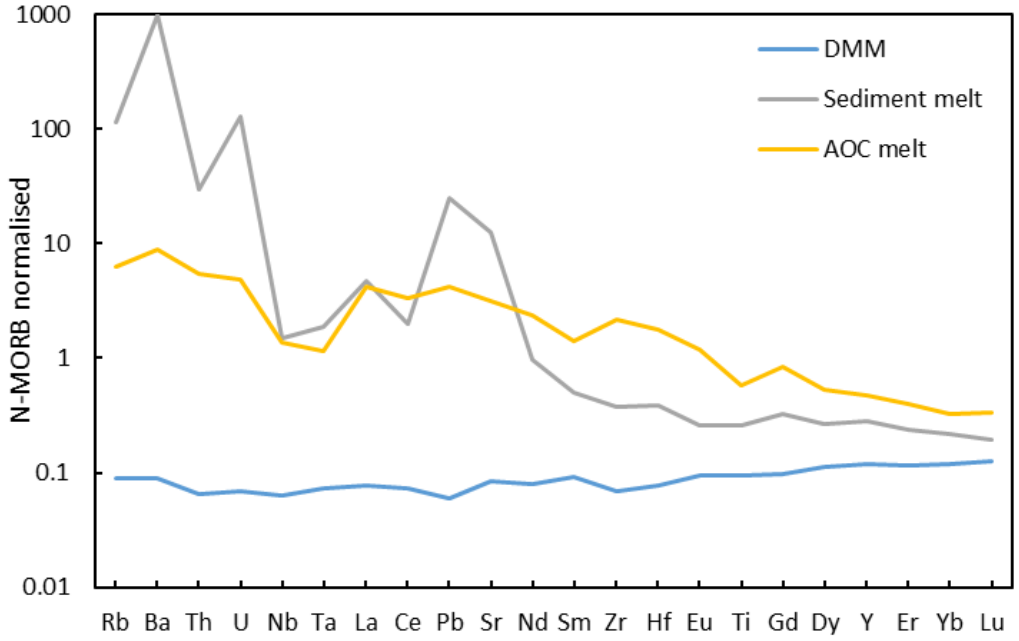

Fig. 6.27 N-MORB (Sun and McDonough, 1989) normalised multi-element diagrams for DMM, sediment melt, and AOC melt.

This DMM ambient mantle is metasomatized by sediment melt or/and AOC melt to be a metasomatized mantle before going through partial melting. The non-modal batch melting method is adopted to model partial melting of this metasomatized mantle using the equation below.

$$\text{Equation 6.4} \quad C_L = \frac{C_O}{D+F(1-P)}$$

Where C_L is the concentration of a trace element in the melt; C_0 is the concentration of a trace element in the solid source; F is the weight fraction of the melt produced; D is the bulk partition coefficient at the onset of melting; P is the bulk partition coefficient of the minerals which make contribution to the melt. P is calculated from

$$\text{Equation 6.5} \quad P = p_1*Kd_1+p_2*Kd_2+p_3*Kd_3+\ldots$$

Where p_1 etc. is the normative weight fraction of mineral 1 that contributes to the melt and Kd_1 is the mineral-melt distribution coefficient for a given trace element for mineral 1.

The mineral modes for spinel lherzolite and melt mode are taken from Johnson et al. (1990) and are shown in Table 6.9.

Table 6.9 Mineral modes for spinel lherzolite and partial melts. Taken from Johnson et al. (1998).

	Clinopyroxene	Olivine	Orthopyroxene	Spinel
Mineral mode	0.170	0.530	0.270	0.030

Melt mode	0.670	-0.060	0.280	0.110

The range of partition coefficients reported for individual elements from different studies is quite large, typically a factor of 2-10 (Hart and Dunn, 1993). To consistently relate a large group of partition coefficients to each other (REE, HFSE) as precisely as possible, Hart and Dunn (1993) set up experiemnts of clinopyroxene/melt partition coefficient in one single experiment at a P-T condition relevant to deep mantle melting, e.g. 3 GPa and 1380℃. The paritition coefficients from this study are widely used for mantle partial melting (such as Kelemen et al, 2003 and studies that cited the partition coefficients from this paper). However, this study only tried to create an internally consistent set of partition coefficients without considering factors of pressure, temperature, and composition. Besides, the samples they used is an alkali basalt in anhydrous condition (Hart and Dunn, 1993). Under hydrous conditions, most trace elements are more incompatible than those under anhydrous conditions and partition coefficients between minerals, e.g. clinopyroxene and anhydrous silicate melt cannot be used to model melt generation under hydrous conditions without taking into account the affect of water on trace element partitioning (Gaetani et al., 2003). For example, HREE are compatible (Blundy et al., 1998) or less incompatible (McDade et al., 2003a) in clinopyroxene on the anhydrous spinel-lherzolite solidus than on the hydrous spinel-lherolite solidus (Gaetani et al., 2003; McDade et al., 2003b). Therefore, partition coefficients of most trace elements between minerals, e.g. clinopyroxene and orthopyroxene, and hydrous MgO-rich melt are from McDade et al. (2003b) in which the experiment condition is similar to mantle wedge melting (1.3GPa and 1245℃). Partition coefficients which are not achieved in the study are taken from Bedard (2006). All the partition coefficients can be found in Table 6.10.

Table 6.10 Partition coefficients between minerals and mafic melt during partial melting of mantle wedge.

	Cpx	Ol	Opx	Spl	Grt
Rb	0.0021[4]	0.0013[4]	0.0108	0.0002[4]	
Ba	0.0007[4]	0.0013[4]	0.0146	0.0005[4]	
Th	0.0062[4]	0.0009[4]	0.0015	0.001[4]	
U	0.0047[4]	0.0006[4]	0.0058	0.001[4]	
Nb	0.008[1]	0.0008[4]	0.0028[1]	0.01[4]	0.05[3]
Ta	0.022[1]	0.0084[4]	0.0041[1]	0.01[4]	**0.05[3]**
La	0.043[1]	0.0002[4]	0.003[1]	0.0006[4]	0.0016[5]
Ce	0.089[1]	0.0004[4]	0.005[1]	0.0006[4]	0.01[3]
Pb	0.0164[4]	0.0013[4]	0.005	0.0006[4]	
Sr	0.077[1]	0.0013[4]	0.0044[1]	0.0006[4]	0.006[3]

Nd	0.211[1]	0.0012[4]	0.009[1]	0.0006[4]	0.071[3]
Sm	0.363[1]	0.0026[4]	0.021[1]	0.0006[4]	0.34[3]
Zr	0.103[1] (0.26)	0.0065[4] (0.02)	0.027[1] (0.021)	0.015[4] (0.015)	0.47[3]
Hf	0.206[1] (0.33)	0.006[4] (0.02)	0.062[1] (0.021)	0.015[4] (0.015)	0.24[5]
Eu	0.449[1]	0.0051[4]	0.031[1]	0.0006[4]	0.44[3]
Ti	0.296[1]	0.0132[4]	0.141[1]	0.125[4]	0.28[3]
Gd	0.4665[2]	0.005[4]	0.0215	0.0006[4]	1.77[2]
Dy	0.57	0.0089[4]	0.0371	0.0015[4]	3.2
Y	0.561[1]	0.0106[4]	0.101[1]	0.002[4]	3.1[3]
Er	0.578[1]	0.0143[4]	0.121[1]	0.003[4]	5[3]
Yb	0.543[1]	0.0203[4]	0.164[1]	0.0045[4]	7.4[3]
Lu	0.52[1]	0.0233[4]	0.186[1]	0.0045[4]	7.1[5]

**[1]Black numbers are form McDade et al. (2003b); [2]Green value of Gd=(Sm+Dy)/2; [3]Blue values are from Gaetani et al., 2003 and Ta is assumed to be equal to Nb in garnet; [4]Orange values are from Bedard (2006); [5]purple values are from Johnson (1998). The element Zr and Hf in bracket are from Bedard (2001).*

Firstly, trace element modelling is conducted. To reduce the effect of crystallisation, incompatible trace element ratios are used. Besides, only rocks with MgO > 4 wt.% are plotted by which the effect of crystallisation is minimised. Thorium is high in sediment or sediment melt. Hawkesworth et al. (1997) argue that most of the Th in arc volcanic rocks derives from subducted sediment. This can also be seen in Fig. 6.27. Therefore, Th/Yb can reflect sediment input and partial melting degree. MREE and HREE are relatively high in AOC melt comparing with sediment melt. Here, MREE, e.g. Sm is chosen to represent AOC melt and partial melting degree. Samarium should also be affected by sediment melt. However, the sediment component is relatively small comparing with AOC melt (discussed below) so Sm/Yb mainly represents AOC melt and partial melting degree. Since the trace element ratios used here are controlled by more than two factors, a large number of different combinations of these factors can form trends go through the data set. To obtain the reasonable result, only combination showing partial melting degree F < 0.25 are considered.

Data of the Chagres Complex are scattered which suggest a heterogeneous mantle source (the ambient mantle or/and slab materials). Overall, it requires high sediment melt (1-1.5%) and variable degree of AOC melt (0-4%) with high partial melting degree F (5-25%) (Fig. 6.28). Similarly, Bas Obispo Formation require high sediment melt (1-1.5%), AOC melt (0-2%), and high F (5-15%).

Panama Formation are well located along 0.2 - 0.6% sediment melt + 2 - 4% AOC melt. Partial melting degree ranges from 3-10%.

The Cabra and Pedro Miguel Formation trend from low Sm/Yb (low AOC melt) toward high Sm/Yb (high AOC melt). ~15% partial melting of ambient mantle metasomatized by ~0.2% sediment melt and ~6% AOC melt can explain the high Sm/Yb endmember while ~3% partial melting of ambient mantle metasomatized by ~0.6% sediment melt and ~2% AOC melt can explain the low Sm/Yb endmember. This is consistent with the trend going toward N-MORB as shown in Fig. 6.24 A. Therefore, Cabra and Pedro Miguel Formation can be formed by 3-15% partial melting of mantle peridotite which was metasomatized by 0.2-0.6% sediment melt and 2-6% AOC melt. One of the olivine basalts can be formed by < 5% partial melting of DMM metasomatized by 0.2% sediment melt and 6% AOC melt while the other requires higher (~10%) AOC melt with small partial melting degree (<5%). However, there two olivine basalt might possess garnet in the source which will be discussed in section 6.2.4.2.

The Cordillera arc rocks (Lissinna, 2005; Wegner et al., 2011) span a large range which cover both of the Panama Formation and Cabra/Pedro Miguel Formation. They can be formed by 3 - 15% partial melting of DMM metasomatized by 0.2-1% sediment melt and 2-6% AOC melt (Fig. 6.28).

Trace element modelling is consistent with Sr-Nd-Pb isotope discussed above, e.g. Chagres Complex require the highest sediment melt input while the highest AOC melt is found in the Cabra Formation. Besides, Chagres Complex went through higher partial melting degree (5-25%) than Panama and Cabra Formation (3-15%).

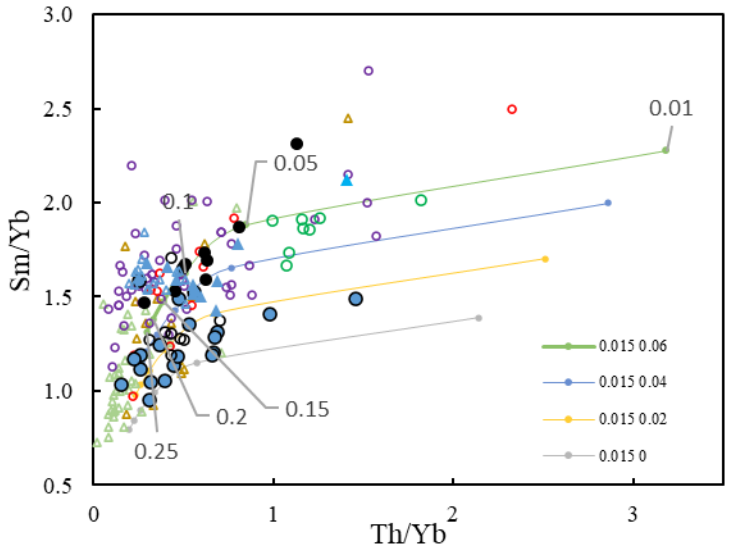

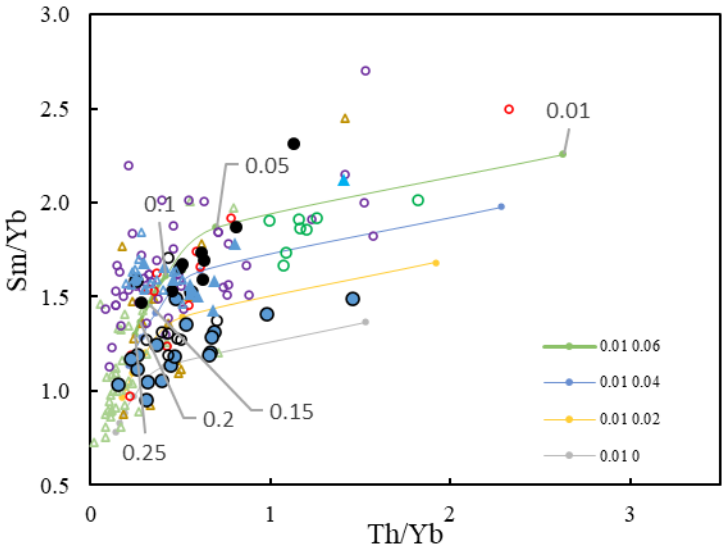
Sm/Yb
Th/Yb
0.01
0.05
0.1
0.2
0.15
0.25
0.01 0.06
0.01 0.04
0.01 0.02
0.01 0

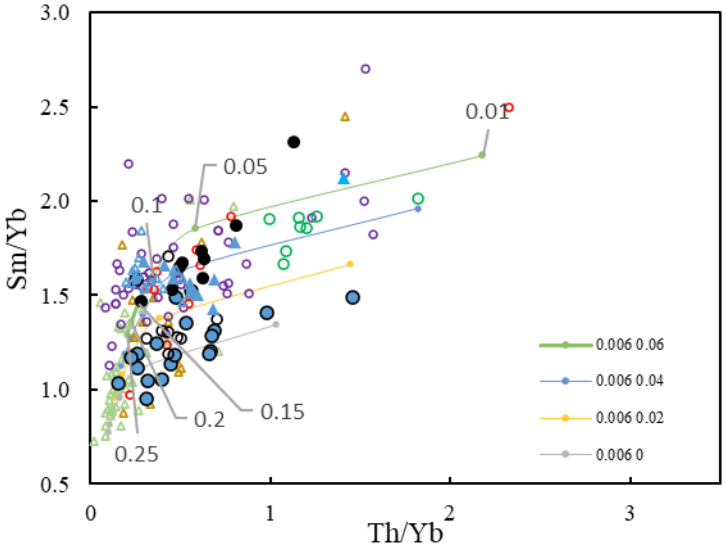
Sm/Yb
Th/Yb
0.01
0.05
0.1
0.2
0.15
0.25
0.006 0.06
0.006 0.04
0.006 0.02
0.006 0

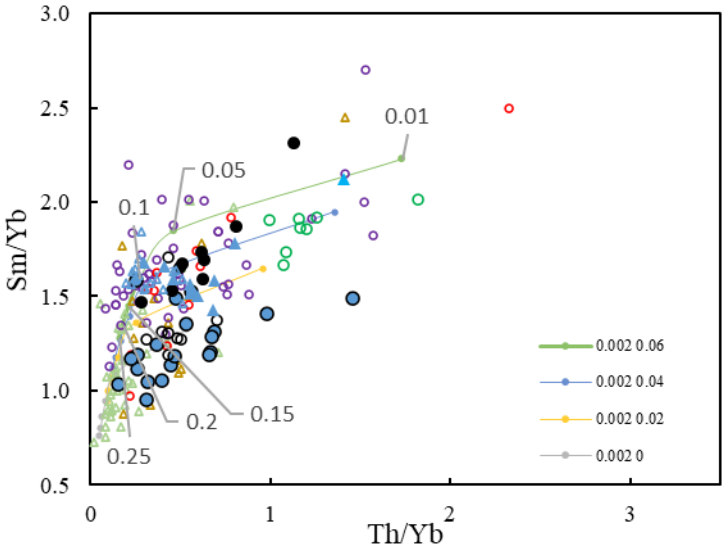
Sm/Yb
Th/Yb
0.01
0.05
0.1
0.2
0.15
0.25
0.002 0.06
0.002 0.04
0.002 0.02
0.002 0

Fig. 6.28 Sm/Yb vs Th/Yb diagram showing the proportions of sediment melt and AOC melt, along with partial melting degrees. The numbers in the partial melting labels are the proportions of sediment melt and AOC melt respectively (%/100). Numbers on the trend are degrees of partial melting. Only samples with MgO > 4 wt.% to avoid the effect of crystallisation. Samples symbols can be seen from Fig. 6.24.

6.2.3.2 Zr/Hf: Source Components and Degrees of Partial Melting

Zr/Hf values in different rock groups are different, especially Cabra Formation which have the highest values among all rocks in the study area. Rocks from Cabra and Pedro Miguel Formations plot in the OIB field while the rest are in the MORB field (Fig. 6.29).

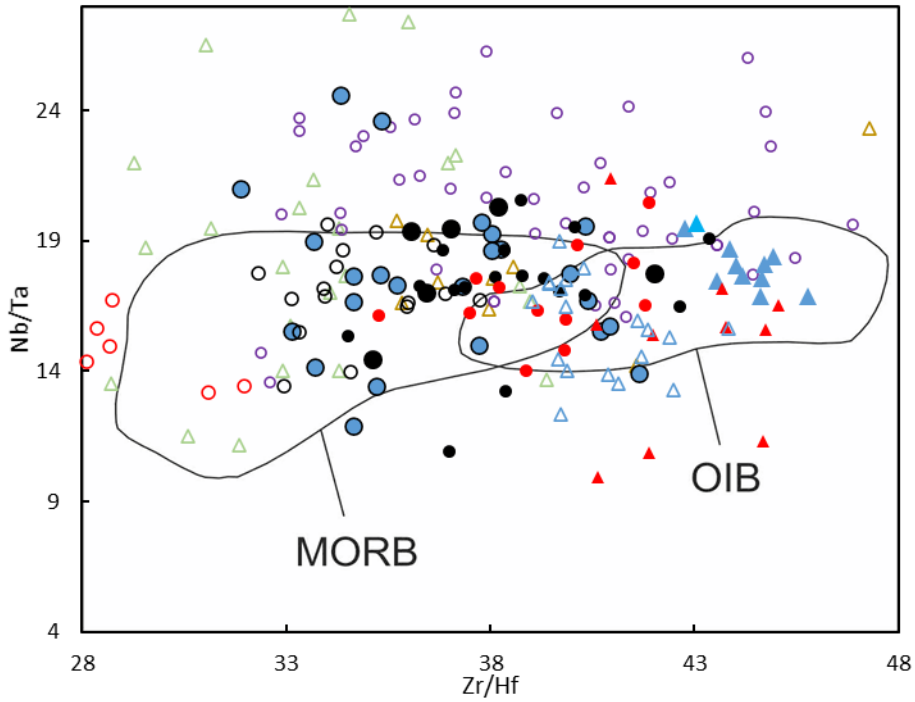

Fig. 6.29 Nb/Ta vs Zr/Hf diagram (MORB and OIB fields are from Guo et al., 2013; Symbols can be seen in Fig. 6.24. *Sona-Azuero arc, Chagres arc, and Cordillera arc samples are from Lissinna (2005) and Wegner et al. (2011); Bas Obispo Fm and Pedro Miguel Fm are from Farris et al. (2017) and Buchs et al. (2019b)).*

If two elements have similar partition coefficients, the slope of the linear trend of their log values should be ~ 1 (Sims and DePaolo, 1997). As can be seen from Fig. 6.30, the slope in Zr vs Hf is ~ 0.78 for samples in the study area and it is ~ 0.98 for Nb vs Ta. Nb and Ta do not fractionate during magmatic processes while Zr and Hf fractionate significantly.

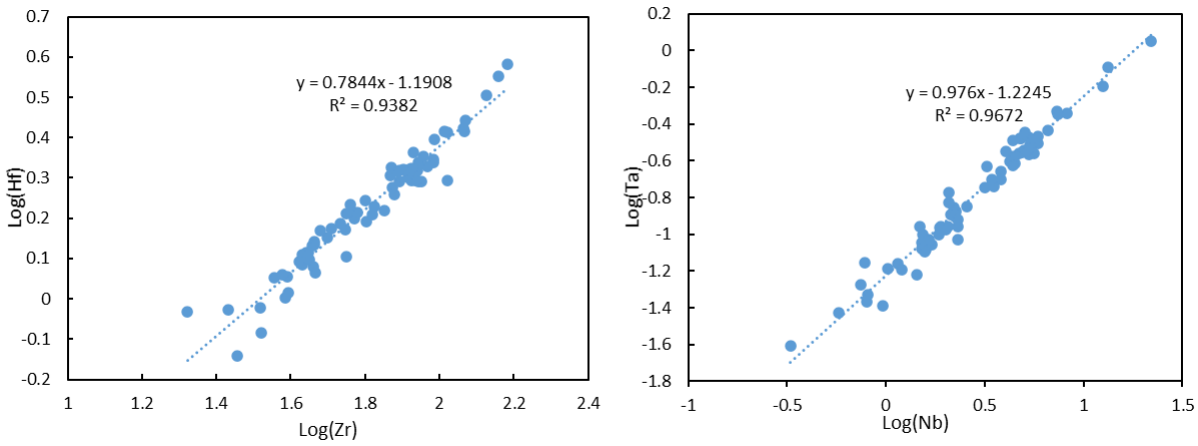

Fig. 6.30 log values of Zr - Hf and Nb - Ta for samples in the study area.

The Zr/Hf ratio is frequently higher in continental and oceanic intraplate basaltic rocks than the chondritic value and varies over a large range of 38-87 (Dupuy et al., 1992). The high values of Zr/Hf are normally explained by two theories: partial melting (Dupuy et al., 1992; Pfänder et al., 2007) and carbonate fluid metasomatism (Dupuy et al., 1992). The partition coefficient of Zr is lower than that of Hf and the ratio ($D_{Zr/Hf}$) for clinopyroxene is ~ 0.5 and it is ~0.6 for pyrope-rich garnet (Pfänder et al., 2007). Therefore, a high value of Zr/Hf (40-48) can be caused by partial melting of a spinel or garnet facies mantle peridotite. However, lavas with the extremely high Zr/Hf ratios (>70) are frequently associated with carbonatites which suggests an influence of carbonate fluids on Zr/Hf fractionation (Dupuy et al., 1992). Increasing metasomatism and increasing Zr/Hf ratio are correlated with increasing degree of silica undersaturation in the basalts. However, all rocks in the study area are silica oversaturated (except for two olivine-bearing basalts) and are plotted as subalkaline rocks in the TAS diagram, which suggest Zr/Hf variation and high values of the Cabra/Pedro Miguel Formation cannot be explained by carbonate metasomatism.

To see the relationship between Zr/Hf fractionation and partial melting, Zr/Hf versus Gd/Yb is plotted. HREE is immobile in aqueous fluids (Zheng, 2019) so Gd/Yb is only affected by partial melting and slab melts. Zr/Hf increases with increasing Gd/Yb from Chagres Complex/Bas Obispo to Panama Formation with some exceptions from the Chagres Complex. This indicates the higher Zr/Hf value in the Panama Formation is caused by lower partial melting degree than that of the Chagres Complex which is consistent with previous discussions in 6.2.2.1. On the contrary, Zr/Hf of the Cabra Formation and Pedro Miguel Formation increases from ~40 to ~45 with constant Gd/Yb. The high Zr/Hf in the Cabra and Pedro Miguel Formation cannot be explained by decreasing partial melting degrees.

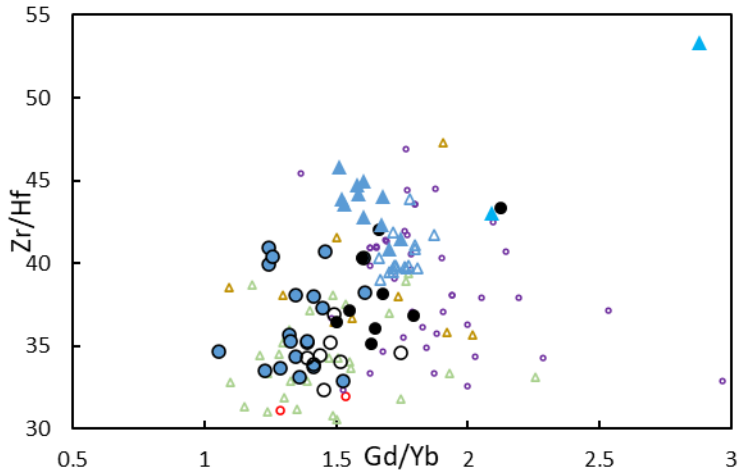

Fig. 6.31 Zr/Hf vs Gd/Yb (only samples with MgO > 4 wt.% are considered here. Sona-Azuero arc, Chagres arc, and Cordillera arc samples are from Lissinna (2005) and Wegner et al. (2011); Bas Obispo Fm and Pedro Miguel Fm are from Farris et al. (2017) and Buchs et al. (2019b)).

Sr-Nd isotopes correlate with Zr/Hf in abyssal basalt with high Zr/Hf associated with high $^{87}Sr/^{86}Sr$ and low $^{143}Nd/^{144}Nd$ (Niu et al, 2002; Huang et al. 2011). This is explained by magma mixing between two different mantle melts with high Zr/Hf from enriched mantle while low Zr/Hf from depleted mantle source (Huang et al., 2011). However, from the Panama Formation to the Cabra Formation, Zr/Hf increases with decreasing $^{87}Sr/^{86}Sr$ and increasing $^{143}Nd/^{144}Nd$ (Fig. 6.32). Rocks in this study should be explained in the opposite way: mantle mixed with depleted endmember which has high Zr/Hf value and low radiogenic Sr and Pb, and high radiogenic Nd. This depleted endmember can be well explained by N-MORB melt.

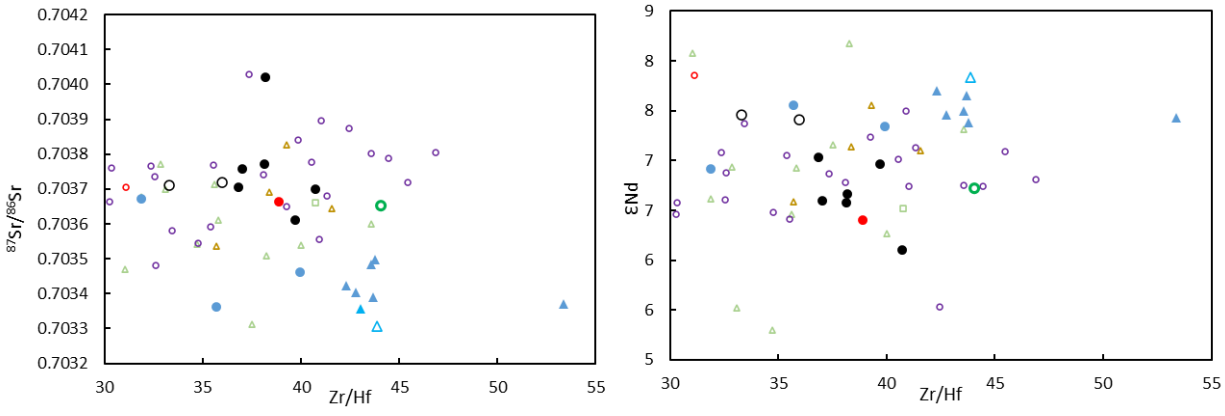

Fig. 6.32 Sr-Nd isotope vs Zr/Hf (samples are the same to Fig. 6.31).

To confirm the ideas that high Zr/Hf can be caused by partial melting degree (Panama Formation) and AOC melt (Cabra and Pedro Miguel Formation), the trace element modelling is conducted in Zr/Hf vs Gd/Yb diagram. All the parameters in this modelling, include the AOC melt, sediment melt, mantle minerology, and partition coefficients are the same to those in 6.2.3.1. As can be seen from Fig. 6.33

A, Zr/Hf increases significantly with decreasing degree of partial melting. This is in contrast with reality since volcanic arc rocks do not show significant change due to partial melting degree. This can be attributed to the partition coefficients which is significantly smaller for Zr that Hf in clinopyroxene and orthopyroxene. Therefore, another set of partition coefficients for Zr and Hf are adopted from Bedard (2001) (values in bracket in Table 6.10). Overall, Zr/Hf increases with increasing Gd/Yb from Chagres Complex/Bas Obispo Formation to Panama Formation (Fig. 6.33 B). Partial melting of DMM metasomatized by low volume of AOC melt (0% in Fig. 6.33) can explain the Zr/Hf in the Chagres Complex/Bas Obispo Formation/Panama Formation: the higher values of the Panama Formation were caused by lower degree of partial melting (1 - 5%) while lower values of the Chagres Complex/Bas Obispo Formation were caused by higher degree of partial melting (5 – 15%). For the Cabra and Pedro Miguel Formation, they show higher Zr/Hf than that of the Panama Formation at similar Gd/Yb values. This can be explained by partial melting of DMM which was metasomatized by relatively high volume of AOC melt. The high Zr/Hf of the Cabra and Pedro Miguel Formation can be well achieved by 5-15% partial melting of DMM metasomatized by 4% AOC melt. This is consistent with trace element modelling in 6.2.3.1. Sediment melts play a neglectable role in this diagram.

Zr/Hf values confirm that the Panama Formation went through lower degree of partial melting than Chagres Complex and Bas Obispo Formation. Besides, the mantle source for the Panama Formation only contain small volume of AOC melts. Overall, the Chagres Complex have gone through high degree of partial melting. Large range of Zr/Hf suggests the mantle source for this group possesses variable AOC melt which is consistent with trace element modelling in section 6.2.2.1. The Cabra and Pedro Miguel Formation have the highest percent of AOC melt in the source during mantle melting. This suggests special tectonic events occurred to give rise to high degrees of AOC melting for the final magmatism in central Panama.

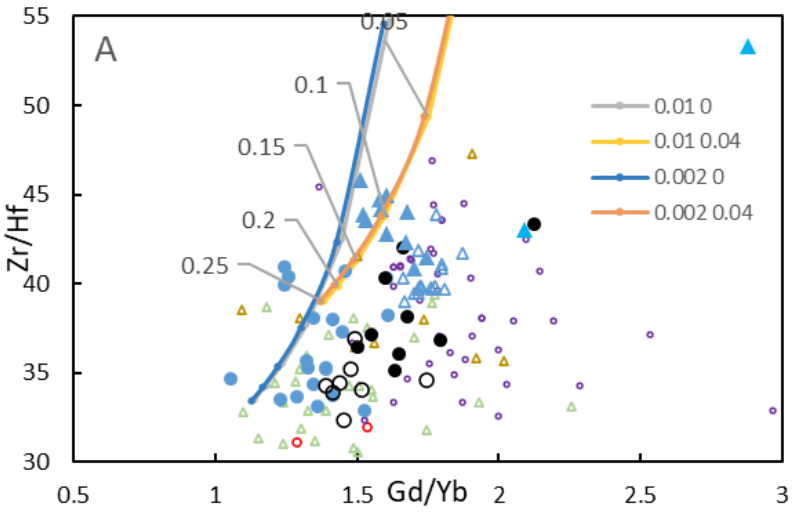

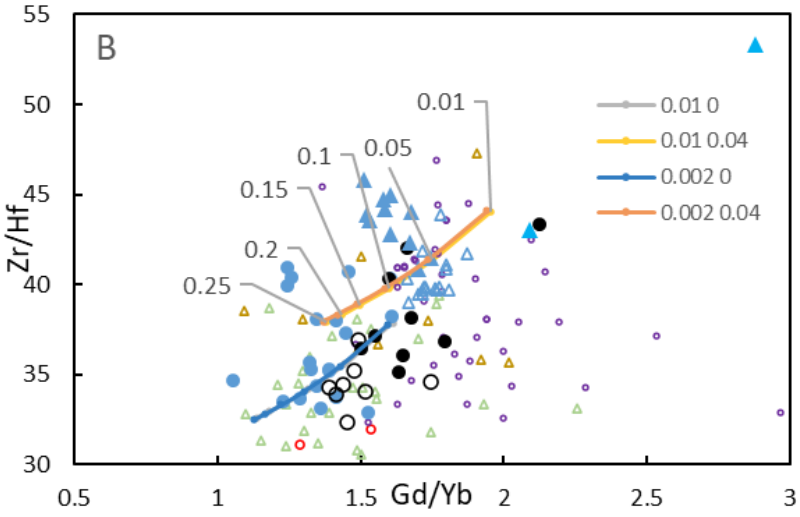

Fig. 6.33 Trace element modelling in Zr/Hf vs Gd. (A) Partition coefficients of Zr and Hf are from McDade et al. (2003b) and Bedard (2006) (B) Partition coefficients of Zr and Hf are from Bedard (2001). The first number in legend is the proportion of sediment melt and the second is AOC melt, e.g. '0.002 0.04' represents the ambient mantle is metasomatized by 0.2% sediment melt and 4% AOC melt. Numbers on the trend in the diagram are partial melting degrees. Compiled data are the same to Fig. 6.31.

6.2.3.3 Isotope Consideration

Isotope modelling for these three endmembers is also conducted to see if it is consistent with trace element modelling.

Sediment subducting beneath central America is considered to be comprised of 90% hemipelagic sediment + 10% carbonate which is the same to the one used in the trace element modelling (*Table 6.7*). In the pre-Miocene, the subducting oceanic crust was Farallon plate which was formed in the east Pacific spreading centre. Therefore, isotopes of sample 2 DR-1 formed in the Cocos-Nazca spreading centre was chosen to represent the isotopic composition of the AOC melt (*Table 6.7*). For the ambient mantle, the Sr-Nd-Pb values are the barycentre of the HIMU from Zindler and Hart (1986) (*Table 6.7*).

As can be seen from Fig. 6.34 A, Panama/Las Cascadas/Caraba/Bas Obispo Formation require 0.6-1.5% sediment melt. Chagres Complex requires 1.5-2% sediment input and 3-6% AOC melt. Cabra/Pedro Miguel Formation requires 1% sediment melt and up to 6% AOC melt. This is consistent with $^{144}Nd/^{143}Nd$ vs $^{207}Pb/^{204}Pb$ (Fig. 6.34 B) in which the Cabra Formation can be formed by a mantle metasomatized by 4-6% AOC melt with 1% sediment input. The Panama/Las Cascadas/Caraba Formation need 1-2% sediment melt with 2-4% AOC melt. The element Nd is fluid immobile elements while Pb is soluble in aqueous fluid. Comparing with the Panama/Las Cascadas/Caraba Formation, the high εNd in the Chagres Complex is caused by AOC melts (2-6%), with ~2% sediment melts metasomatizing the ambient mantle. This is also consistent with εNd vs Ba/La diagram (Fig. 6.34 C) in which high Ba/La is caused by high volume of sediment melt (0.6-1%) and high εNd is caused by high volume of AOC melt (2-6%). In Fig. 6.34 C, 0.1-0.3 % sediment melt plus

up to 1-2% AOC melt can meet the requirement for Panama/Las Cascadas/Caraba Formation while Cabra Formation needs AOC melt up to ~ 6% in this diagram. Data compiled for the Chagres arc and Cordillera arc (Lissinna, 2005; Wegner et al., 2011) have a large range which might indicate various volume of slab materials or heterogeneous ambient mantle. Despite the heterogeneous source, the diagrams display that sediment melt, AOC melt, and ambient mantle can still be considered as the end-members for the Chagres arc and Cordillera arc.

Nd and Pb isotopes vs Sr isotope (Fig. 6.34 D, E, F) show a consistent result that rocks in this study possess 0.2-1% sediment melt in the mantle source. In these diagrams, higher sediment melt in the Chagres Complex than the other formations is not revealed. However, they also show that the Cabra Formation possess the highest AOC melt with up to ~6%. The Chagres Complex have higher AOC component (3-6%) that the Panama/Las Cascadas/Caraba Formation (2-4%), which is consistent with the isotopes shown in Fig. 6.34 A, B, C. This can also be seen in Fig. 6.34 G.

The proportion obtained in isotope modelling is in consistent with the trace element modelling. Both models show that the Chagres Complex has the highest sediment melt while Cabra Formation has the highest AOC melt component.

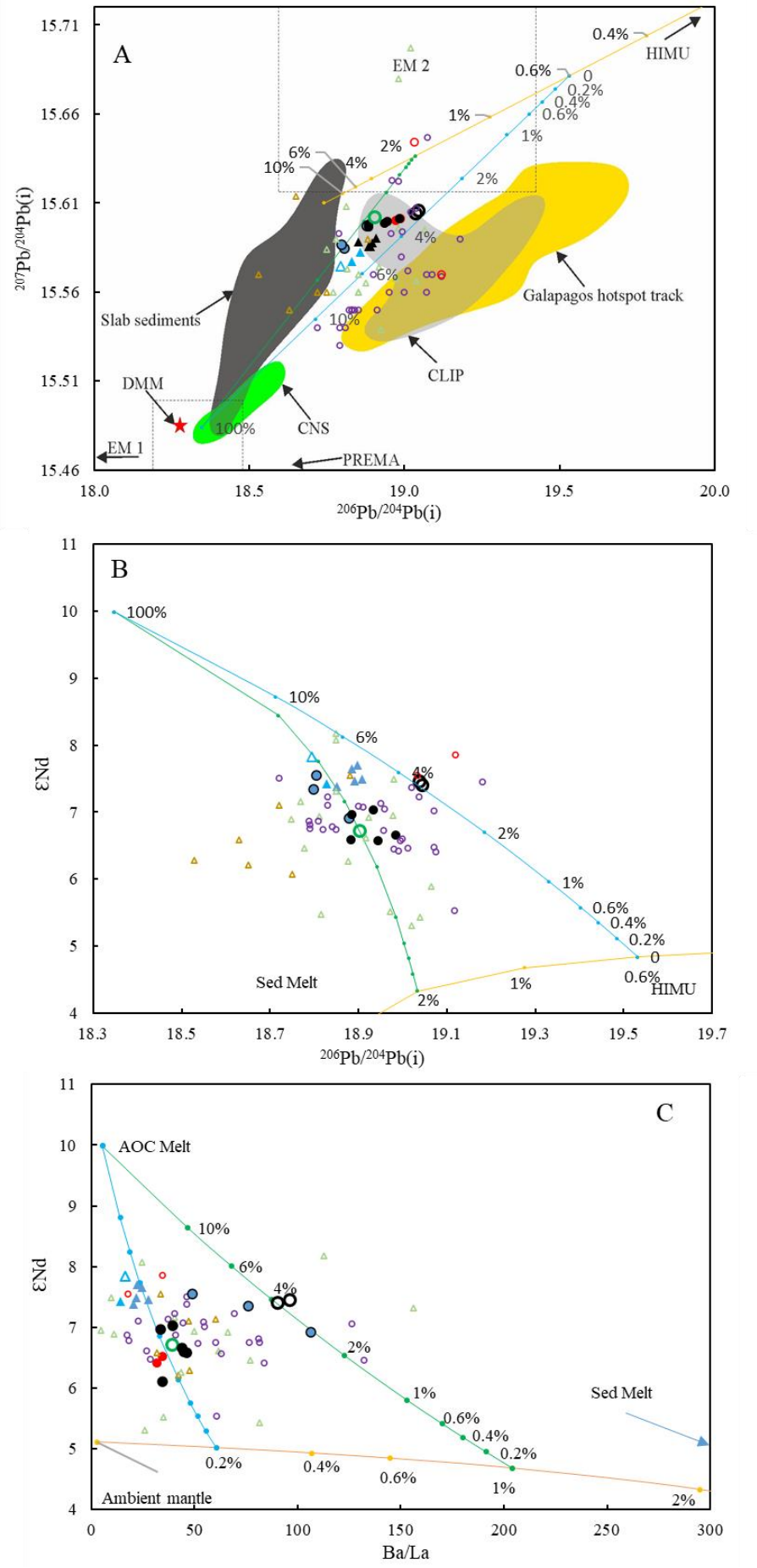
A
EM 2
HIMU
0.4%
0.6%
0
0.2%
0.4%
0.6%
1%
1%
2%
2%
6%
10%
4%
4%
6%
10%
Galapagos hotspot track
Slab sediments
CLIP
DMM
CNS
100%
EM 1
PREMA
15.71
15.66
15.61
15.56
15.51
15.46
18.0
18.5
19.0
19.5
20.0
207Pb/204Pb(i)
206Pb/204Pb(i)
B
100%
10%
6%
4%
2%
1%
0.6%
0.4%
0.2%
0
0.6%
HIMU
Sed Melt
1%
2%
εNd
18.3
18.5
18.7
18.9
19.1
19.3
19.5
19.7
206Pb/204Pb(i)
C
AOC Melt
10%
6%
4%
2%
1%
0.6%
0.4%
0.2%
Sed Melt
0.2%
0.4%
0.6%
1%
2%
Ambient mantle
εNd
0
50
100
150
200
250
300
Ba/La

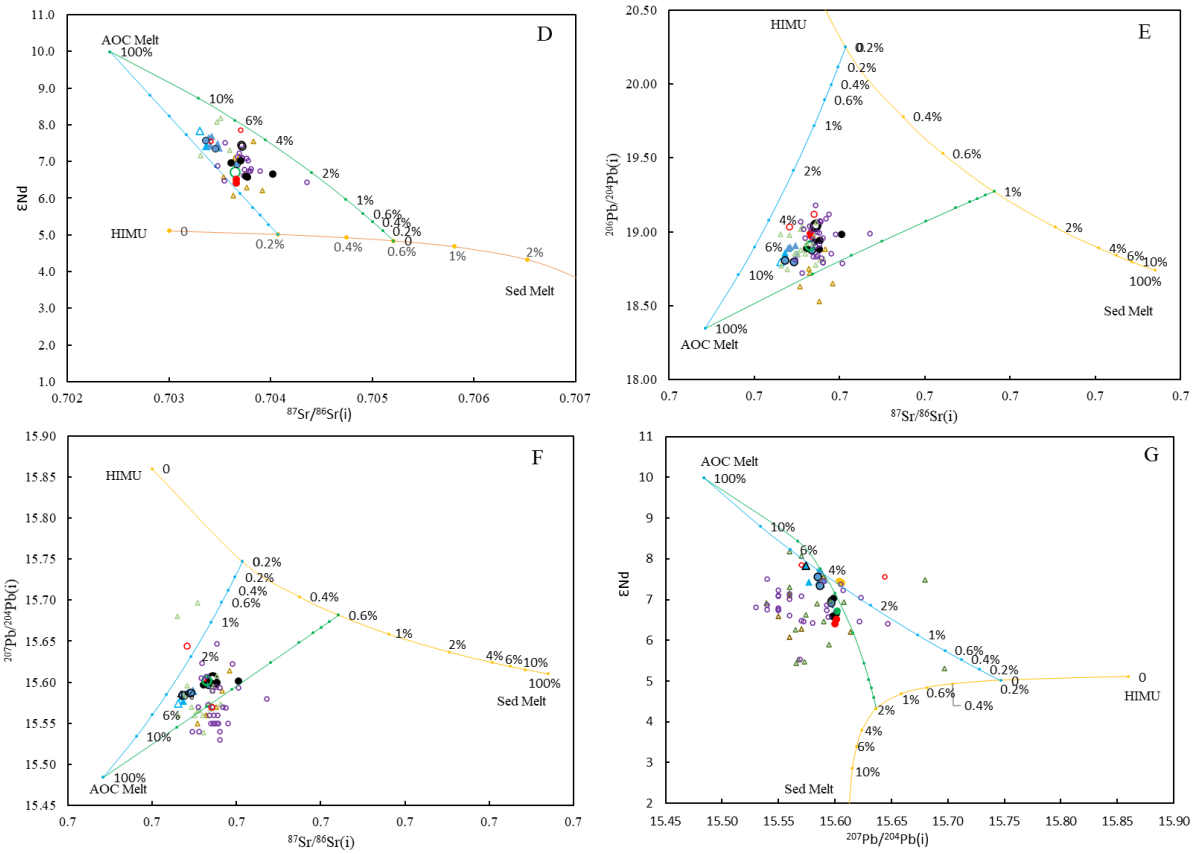

Fig. 6.34 Isotope and trace element ratio showing proportions of the three endmembers. Background fields and compiled data are the same to Fig. 6.24. *A, B, C, D can well tell these three end-members apart.*

6.2.4 Primary Melts and Trace Element Modelling

Rocks in this study are all evolved and rocks representing primary magma were not found and collected in the field. In the previous modelling in section 6.2.3.1, certain trace element ratios of rocks with MgO >4 wt.% were used to limit the effect of fractionation. In this section, more trace elements are considered to constrain mantle components and partial melting degrees. At first, primary melts are calculated by program PRIMACALC (Kimura and Ariskin, 2014) for rocks with MgO >4 wt.%. Then trace element modelling of partial melting of mantle source is conducted for these primary melts.

6.2.4.1 Primary Melt Derived from PRIMACACL2

All the rocks in this study are evolved and do not represent primitive melts. That is the reason why trace element ratios of rocks with MgO > 4% were utilised to rule out the effect of crystallisation for trace element modelling. In this section, primitive melts are reversely calculated for the Chagres Complex, Panama Formation, and Cabra mafic member so more trace elements can be utilised to work out the contribution of different mantle components and partial melting degree.

PRIMACALC2 is a program run in Excel macro to estimate the composition of water-bearing primary arc basalt and its source mantle conditions. It uses the thermodynamic fractional crystallisation model COMAGMAT3.72 to examine the mantle equilibrium and trace element calculations of a primary basalt. After inputting the analysed rock composition (STEP 1 in Fig. 6.35), PRIMACALC2 calculates the provisional composition of a primary basalt from the input data with PRIMACALC1 (STEP 2). To achieve this, a typical LLD template for an arc basalt are used. They choose a basaltic andesite composition from the averaged arc magma proposed by Tatsumi and Suzuki (2009). The basaltic andesite has an olivine, pyroxene, and plagioclase multiple saturated condition in a shallow magma chamber. They added 10 wt. % equilibrated olivine stepwise, thereby forcing the basaltic andesite to be equilibrated with a depleted mantle. The resultant primary basalt composition contained MgO= 14 wt. %, Mg# ($Mg/(Mg+Fe^2)$) = 0.68. The condition of the magma chamber for backward calculation is P= 0.3 GPa, fO_2= QFM+2, and various H_2O= 0–2.5 wt. % which is believed to represent the typical condition of an arc magma chamber (Tatsumi and Suzuki, 2009). Large errors can be caused by the difference between real condition and the estimated condition as a variable cotectic is basically related to P, T, fO_2, and H_2O in a magma chamber. To reduce this error, P, T, fO_2, and H_2O are considered as fitting parameters and need to be input into COMAGMAT3.72 for forward calculation.

After setting the parameters such as pressure, oxygen fugacity buffer, and water content for crystallisation (STEP 3), the provisional primary basalt is then forward calculated by COMAGMAT3.72 (STEP 4).The closest match result for the analysed rock composition will be found and the composition differences between them (DCx, STEP 5) will be used for iteration to calculate the best-fit rock composition and the primary magma. The iteration will finish when the calculated rock composition converges with the analysed rock composition and then yield a primary melt composition (column at STEP 6). The crystallisation sequence of the last iteration is also shown (panel at STEP 6). Once the fit is satisfied, back calculations of trace elements are made using stepwise addition of fractionated minerals (STEP 8).

Mantle equilibrium of the primary basalt is tested using the Fo-NiO relationship of olivine in equilibrium with the primary basalt, and thus with the source mantle. H_2O and P are the key variables in the COMAGMAT3.72 forward calculations. By adjusting the P and H_2O variables, a reasonable equilibrium of the primary basalt with the source mantle in terms of the Fo-NiO contents of olivine can be established.

Source mantle pressure, temperature, and degree of melting are estimated with PRIMELT2 using petrogenetic grids based on experimental data obtained in anhydrous systems. P and F are both estimated by the Ol-An-Qz (projected from Di) CMAS projection whereas T is estimated using the T-MgO (‘‘primary basalt’’) relationship (Herzberg et al., 2007). Mantle melting temperature in a

hydrous system is computed by adjusting T with a parameterisation for a water-bearing system. Fractional and batch melting are two extreme cases of mantle melting, but fractional melting is more plausible mechanism. It is, however, hard to introduce this into the model, as CMAS petrogenetic grids are formed based on the experimental results, which represent batch melting. Therefore, PRIMACALC2 uses the batch model of CMAS. However, partial melting degree and other parameters such as mantle melting pressure and temperature are all based on anhydrous experiment of KR-4003, which is reasonable to be considered as the source of OIB or MORB but not arc basalt. Therefore, PRIMICALC 2 is only used to calculate the trace element content of the primary melt in this study. This trace element pattern in the multi-element diagram can be used for trace element modelling.

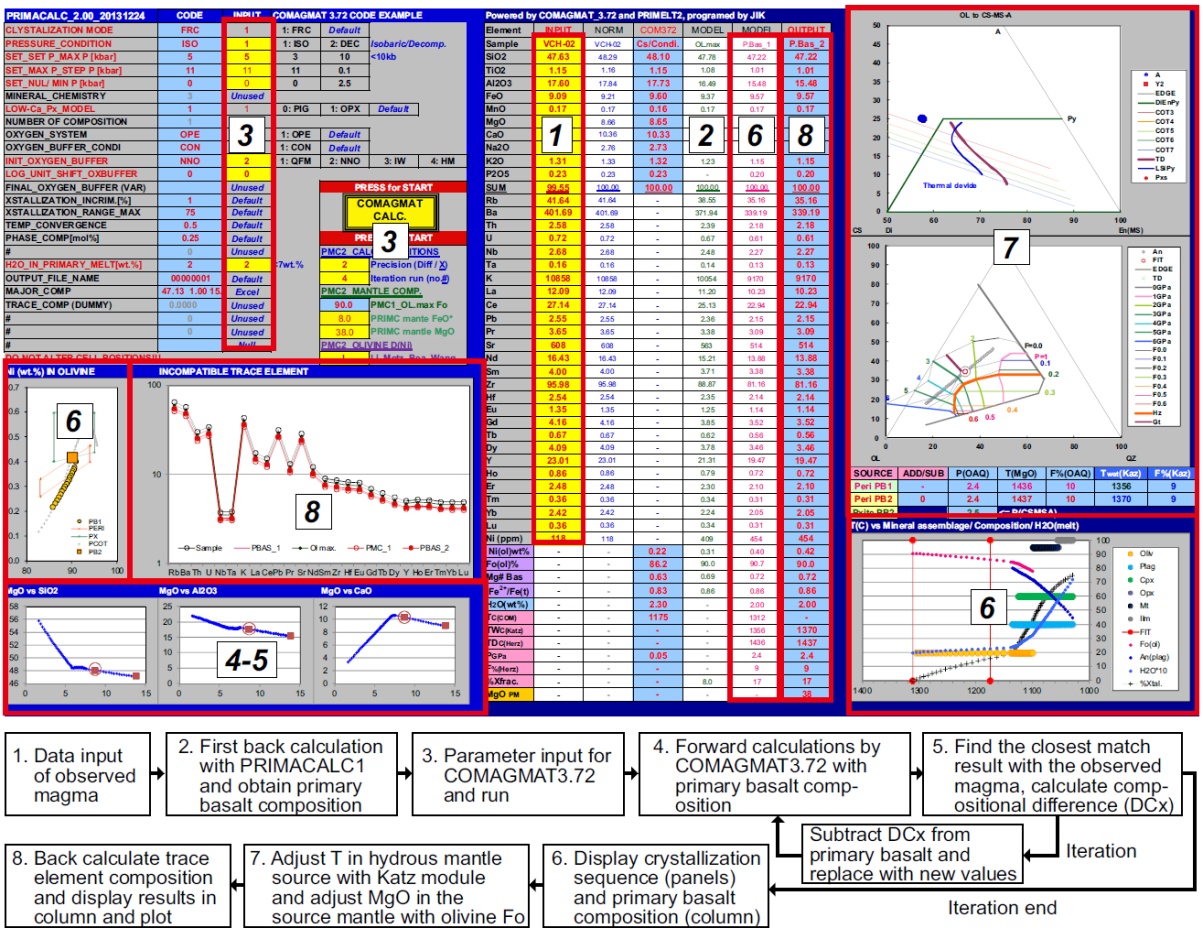

Fig. 6.35 Schematic calculation flow and screenshot of PRIMACACL2 (Kimura and Ariskin, 2014). (Major elements in wt.% and trace elements in ppm).

Take the Panama Formation for example, the maximum pressure is set as 5.4 kbar which is from the clinopyroxene-orthopyroxene barometer in 6.1.1.1. As ~2 wt.% water content works best for crystallisation in the rhyolite-MELTS modelling, 1 wt.% water content was set for the primary melts. Same parameter is set for the Cabra Formation. A higher water content, e.g. 2 wt.% is applied to the Chagres Complex. Since PRIMACALC 2 only works for rocks which went through olivine-

clinopyroxene-plagioclase crystallisation, the primary melts of amphibole bearing rocks in the Chagres Complex and Caraba Formation are not calculated with this program. Trace elements of the primary melts from PRIMACALC2 are listed in Table 6.11. Comparison of trace elements between analysed values and the primary magma calculated by PRIMACALC2 are shown in Fig. 6.36 .

Table 6.11 Primary melts calculated by PRIMACALC2 for the Chagres Complex, Panama Formation, and Cabra Formation.

	Chagres Complex										Panama Formation									Cabra Formation											
	J18-003	J18-004	J18-048	J18-049	J18-095	J18-088	J18-089	J18-090	J18-097	J17-133	J18-059-1	J18-016	J18-102	J17-059-2	J17-102	J17-091	J17-096	J17-053	J17-101	J18-043	J18-045	J18-052	J17-032	J18-031-2	J18-032	J18-033-1	J18-033-4	J18-034-2	J18-094-6	J17-024	J17-031	J17-034
Rb	7.9	1.7	3.2	3.2	2.4	0.5	9.0	24.6	3.1	0.1	7.1	11.2	4.5	6.3	15.6	16.7	10.7	10.1	5.1	3.0	16.5	9.0	8.7	2.0	6.2	25.5	3.1	6.7	0.7	1.3	2.4	4.7
Ba	339.2	36.9	109.2	150.2	74.2	119.6	477.7	713.5	267.4	5.0	174.8	223.4	171.5	221.5	211.3	241.1	189.5	206.7	163.7	100.6	327.6	211.2	141.0	165.0	189.1	567.5	151.7	177.2	72.0	109.1	138.8	119.7
Th	0.7	0.5	1.0	0.5	0.5	0.4	0.9	0.7	0.6	0.5	0.6	0.9	0.8	0.8	1.3	0.7	0.6	0.7	0.3	0.3	2.3	2.3	0.7	1.5	0.9	0.8	0.8	1.0	0.5	0.5	0.5	1.6
U	0.1	0.1	0.1	0.1	0.1	0.1	0.4	0.3	0.2	0.1	0.2	0.3	0.2	0.2	0.4	0.3	0.3	0.2	0.1	0.1	0.7	0.4	0.2	0.2	0.3	0.3	0.3	0.3	0.1	0.2	0.2	0.1
Nb	0.5	2.8	1.0	1.3	0.8	1.4	1.7	1.4	1.5	0.2	2.2	2.7	3.2	3.3	2.4	2.7	2.2	2.1	2.4	2.3	18.5	10.6	2.6	2.7	3.4	3.6	4.3	4.1	1.3	2.6	7.3	2.7
Ta	0.0	0.2	0.1	0.1	0.0	0.1	0.1	0.1	0.1	0.0	0.1	0.1	0.2	0.2	0.1	0.2	0.1	0.1	0.1	0.1	1.0	0.5	0.2	0.1	0.2	0.2	0.2	0.2	0.1	0.1	0.4	0.1
K	4617.9	1058.1	1867.3	2330.5	2123.8	662.6	6265.6	12298.2	3465.3	109.4	4263.5	4877.8	2981.8	1403.6	3950.4	5049.9	2320.7	5089.1	1699.1	2075.8	8225.5	5529.9	2150.7	1678.5	2921.2	10493.1	1977.3	4234.6	318.8	806.7	1884.1	2526.4
La	2.2	4.6	2.6	3.1	4.0	2.5	5.3	3.8	3.7	2.2	4.4	6.1	5.5	5.5	7.0	7.4	5.7	5.4	4.0	4.0	23.3	13.7	4.8	5.5	7.0	6.0	8.3	7.2	4.0	5.5	6.7	4.6
Ce	5.8	13.1	5.8	6.8	10.3	6.3	10.8	7.5	8.1	5.5	10.4	13.8	12.9	13.0	15.9	15.8	12.6	11.8	9.4	10.2	45.7	27.5	10.2	12.0	15.5	13.0	16.3	15.6	9.2	11.4	14.7	9.8
Pb	1.1	0.1	0.2	1.2	0.3	0.8	1.7	1.9	1.6	2.6	0.7	1.5	0.7	1.7	1.0	1.5	20.5	4.9	0.9	0.8	1.2	0.6	0.6	0.9	1.0	1.2	1.4	0.7	1.7	3.5	3.7	1.6
Pr	1.0	2.2	0.9	1.0	1.6	1.0	1.5	1.1	1.2	1.0	1.6	2.1	1.9	1.9	2.4	2.3	1.8	1.8	1.5	1.6	5.5	3.4	1.4	1.7	2.3	1.8	2.2	2.2	1.4	1.6	2.1	1.4

Sr	116.1	96.6	375.4	300.1	461.9	225.0	433.6	339.8	337.2	170.7	235.0	264.0	267.9	298.7	302.4	318.5	282.6	374.1	374.2	381.9	803.1	384.4	275.1	363.8	345.2	281.1	466.3	159.2	471.8	378.2	335.1	392.5
Nd	5.4	11.7	4.5	5.0	7.3	5.4	6.9	5.1	5.9	5.7	8.1	10.1	9.4	9.4	12.0	11.2	9.1	9.1	7.6	8.6	22.2	14.0	6.8	8.0	10.8	8.2	9.7	10.2	7.0	8.0	10.4	6.9
Sm	1.9	4.3	1.5	1.6	1.9	1.8	1.8	1.4	1.9	2.2	2.5	2.9	2.7	3.0	3.5	2.9	2.4	2.8	2.4	2.9	4.9	3.5	2.0	2.4	3.4	2.3	2.7	2.9	2.1	2.2	3.1	2.0
Zr	35.4	102.3	22.9	25.6	24.4	34.2	29.6	32.8	33.5	28.7	43.8	56.9	60.8	54.4	65.9	61.8	53.5	44.0	42.5	46.2	88.8	60.1	60.1	53.9	74.0	69.0	38.5	84.9	30.8	56.7	74.0	49.2
Hf	1.1	2.9	0.7	0.7	0.8	1.0	0.9	1.0	0.9	1.1	1.4	1.8	1.6	1.7	1.7	1.7	1.6	1.5	1.3	1.4	1.7	1.4	1.5	1.5	2.1	1.7	1.1	2.0	0.8	1.6	2.1	1.4
Eu	0.7	1.6	0.7	0.6	0.7	0.7	0.7	0.5	0.7	0.9	0.8	0.9	1.0	1.0	1.1	1.0	0.9	1.0	0.9	1.1	1.6	1.2	0.8	0.9	1.2	0.9	0.9	1.0	0.8	0.9	1.2	0.8
Gd	2.5	5.6	1.8	1.7	2.1	2.2	2.1	1.6	2.2	2.9	2.6	3.0	3.0	3.2	3.3	2.9	2.6	2.9	2.6	3.4	4.2	3.4	2.3	2.7	3.8	2.5	2.8	3.0	2.4	2.4	3.4	2.1
Tb	0.5	1.1	0.3	0.3	0.4	0.4	0.4	0.3	0.4	0.5	0.5	0.5	0.5	0.6	0.5	0.5	0.4	0.5	0.5	0.6	0.6	0.6	0.4	0.5	0.7	0.4	0.5	0.5	0.4	0.4	0.5	0.3
Dy	3.0	7.0	2.0	1.9	2.8	2.6	2.2	1.8	2.6	3.4	2.8	2.9	3.0	3.4	3.0	3.1	2.8	3.1	3.2	3.7	3.5	3.3	2.6	2.8	4.1	2.7	2.9	3.3	2.6	2.9	3.8	2.4
Y	19.9	44.7	11.6	10.8	17.3	15.8	13.6	10.9	15.1	21.3	15.7	18.6	17.2	19.8	16.7	19.6	18.3	19.2	19.6	23.7	17.6	17.7	14.8	17.7	26.7	16.4	17.8	22.3	14.8	18.6	24.1	15.7
Ho	0.7	1.5	0.4	0.4	0.7	0.6	0.5	0.4	0.6	0.8	0.6	0.6	0.6	0.7	0.6	0.6	0.6	0.6	0.6	0.8	0.7	0.7	0.6	0.6	0.9	0.6	0.6	0.7	0.6	0.5	0.7	0.5
Er	1.8	4.4	1.2	1.1	1.9	1.6	1.4	1.2	1.7	2.1	1.6	1.7	1.8	2.0	1.7	1.7	1.7	1.8	1.8	2.1	1.7	1.8	1.5	1.7	2.5	1.6	1.7	2.0	1.5	1.6	2.1	1.3
Tm	0.3	0.7	0.2	0.2	0.3	0.3	0.2	0.2	0.3	0.3	0.3	0.3	0.3	0.3	0.3	0.3	0.3	0.3	0.3	0.3	0.3	0.3	0.2	0.3	0.4	0.2	0.3	0.3	0.2	0.2	0.3	0.2
Yb	1.8	4.4	1.1	1.1	2.0	1.7	1.5	1.2	1.7	2.0	1.6	1.6	1.8	1.9	1.5	1.8	1.6	1.7	1.7	1.9	1.5	1.6	1.5	1.6	2.4	1.6	1.6	2.0	1.4	1.6	2.0	1.3
Lu	0.3	0.6	0.2	0.2	0.3	0.3	0.2	0.2	0.3	0.3	0.2	0.2	0.3	0.3	0.2	0.3	0.2	0.2	0.3	0.3	0.2	0.2	0.2	0.2	0.3	0.2	0.2	0.3	0.2	0.3	0.3	0.2

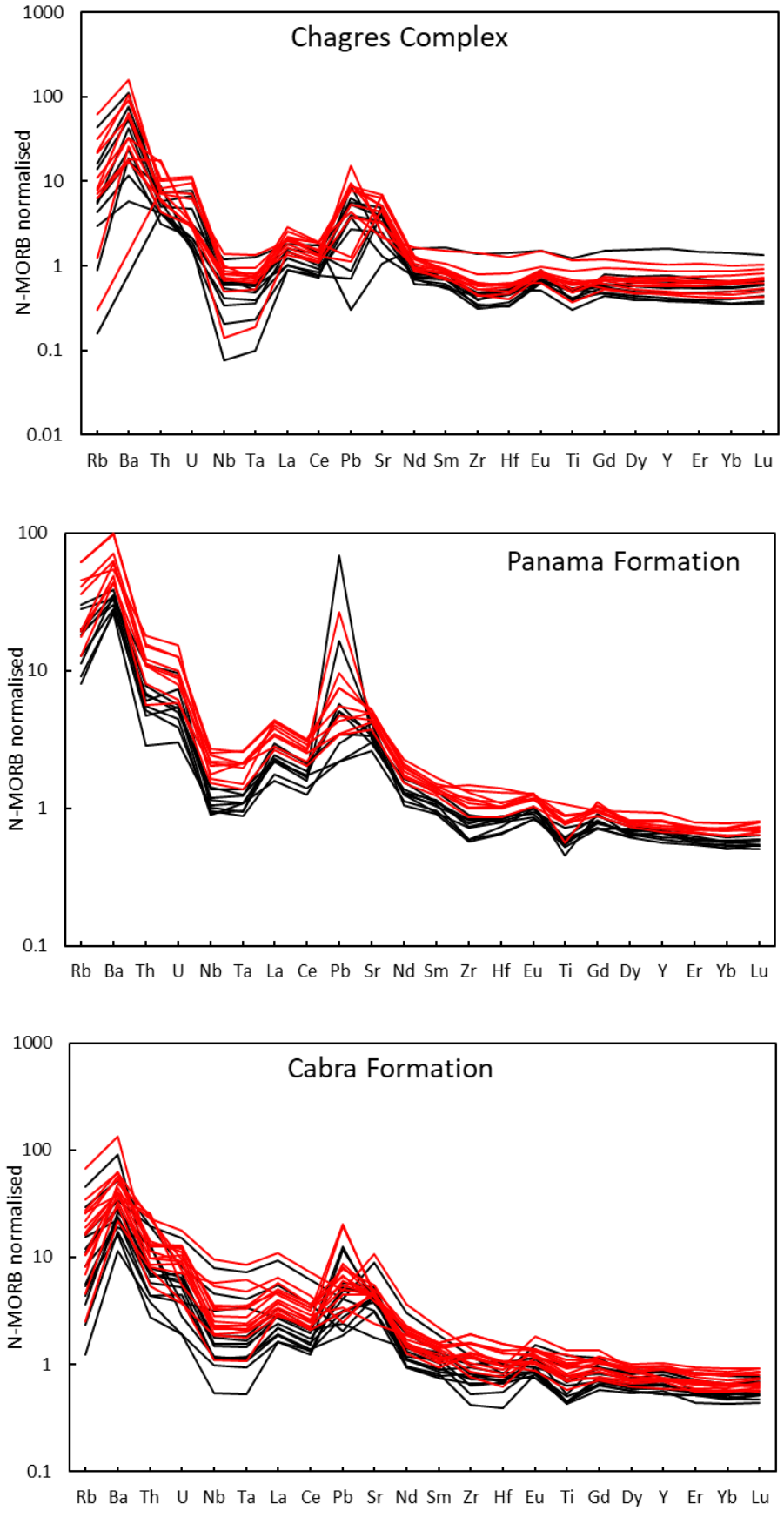

Fig. 6.36 Comparison of trace elements between analysed values and the primary magma calculated by PRIMACALC2 (red patterns are the analysed composition and the black patterns are calculated results).

6.2.4.2 Trace Element Modelling

For rocks in this study except for the olivine bearing basalt in the Cabra Formation, parameters such as compositions of the ambient mantle, the sediment melt, and the AOC melt along with the non-modal batch melting equation and mantle minerology are the same to the modelling in section 6.2.3.1.

As can be seen from the diagram below (Fig. 6.37), ~ 15% partial melting of DMM metasomatized by ~ 1% sediment melt with ~ 1% AOC melt can well represent the primary melt of the Chagres Complex. Some samples have extremely low Nb-Ta values which cannot be achieved by the modelling. High Pb and Sr in the primary magma might be caused by aqueous fluids.

The primary melt of the Panama Formation can be well achieved by ~ 7% partial melting of DMM which is metasomatized by ~ 0.2% sediment melt and ~ 2% AOC melt (Fig. 6.37). The high Pb and Sr of the primary magma are also attributed to the aqueous fluids released into ambient mantle from slab, which is a similar explanation to high Pb and Sr of the Chagres Complex.

As revealed by isotopes, a higher proportion of AOC melt was appointed to the Cabra Formation. It can be achieved by ~ 10% partial melting of DMM which is metasomatized by ~ 0.2% sediment melt and ~ 3% AOC melt. The high Pb and Sr of the primary magma are also attributed to the aqueous fluids. Two olivine bearing basalts do show display significant Nb-Ta-Ti depletion which suggest the AOC melt derived from rutile-free partial melting. To test this hypothesis, new mineral proportions, e.g. amphibole: clinopyroxene: garnet = 0.1: 0.8: 0.1 were adopted for AOC melting. In addition, high La/Yb and Sm/Yb suggest garnet as the residue in the mantle. Therefore, 1% garnet is adopted in the initial mineral phases and also in mineral phases contributing to the melt. As can be seen from Fig. 6.37, J18-052 can be achieved by ~ 5% partial melting of DMM which is metasomatized by ~ 0.1% sediment melt and ~ 5% AOC melt. J18-045 can be achieved by lower partial melting degree, e.g. ~ 3%. The DMM is metasomatized by ~ 0.05% sediment melt and ~ 6% AOC melt. Therefore, at least some samples in the Cabra Formation have slab melt which went through rutile-free AOC melting and garnet is a residue mineral during mantle melting.

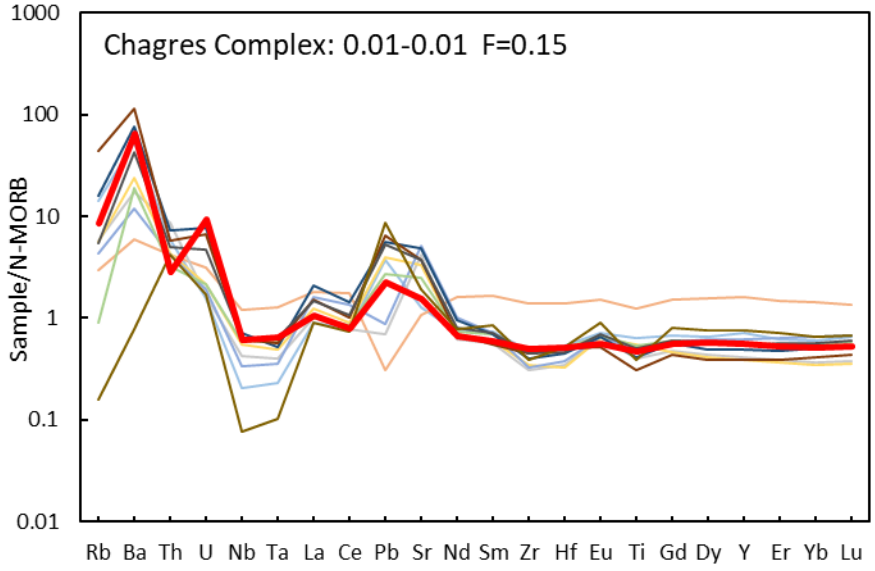
Chagres Complex: 0.01-0.01 F=0.15
Sample/N-MORB
1000
100
10
1
0.1
0.01
Rb Ba Th U Nb Ta La Ce Pb Sr Nd Sm Zr Hf Eu Ti Gd Dy Y Er Yb Lu

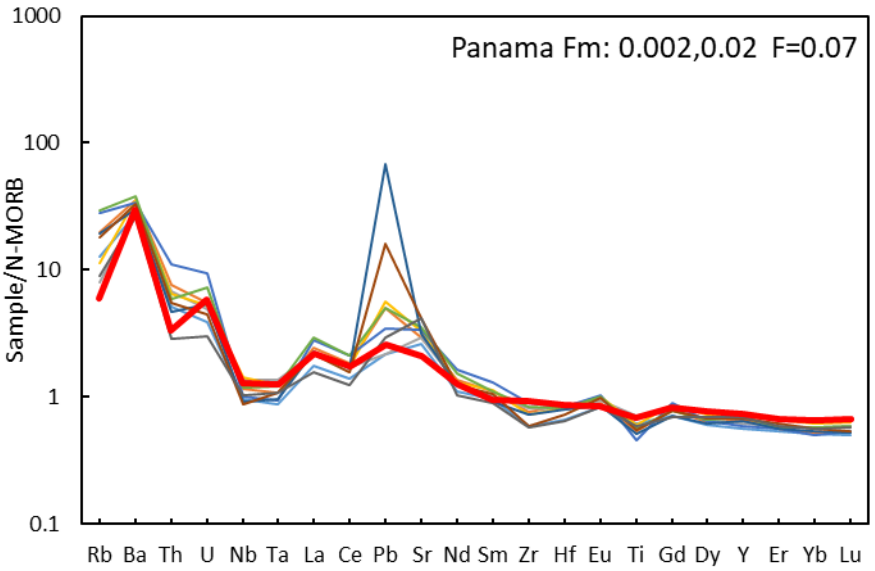
Panama Fm: 0.002,0.02 F=0.07
Sample/N-MORB
1000
100
10
1
0.1
Rb Ba Th U Nb Ta La Ce Pb Sr Nd Sm Zr Hf Eu Ti Gd Dy Y Er Yb Lu

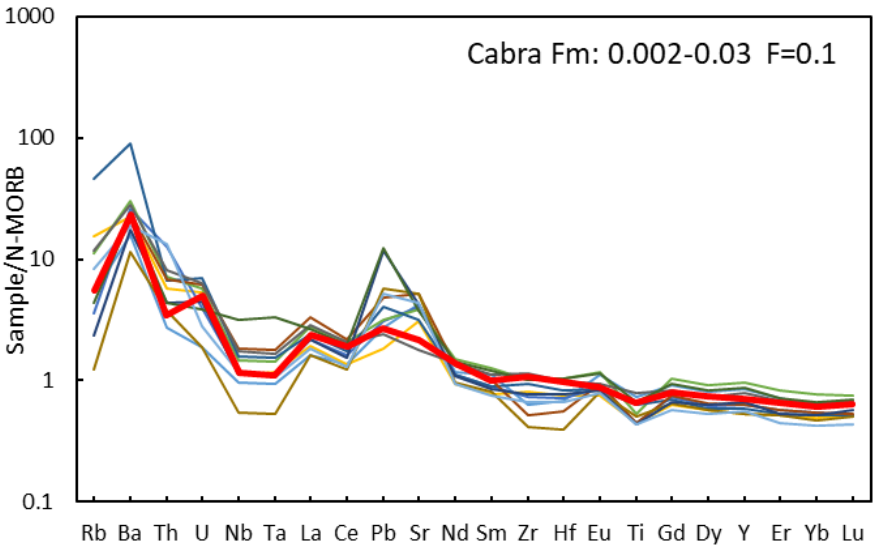
Cabra Fm: 0.002-0.03 F=0.1
Sample/N-MORB
1000
100
10
1
0.1
Rb Ba Th U Nb Ta La Ce Pb Sr Nd Sm Zr Hf Eu Ti Gd Dy Y Er Yb Lu

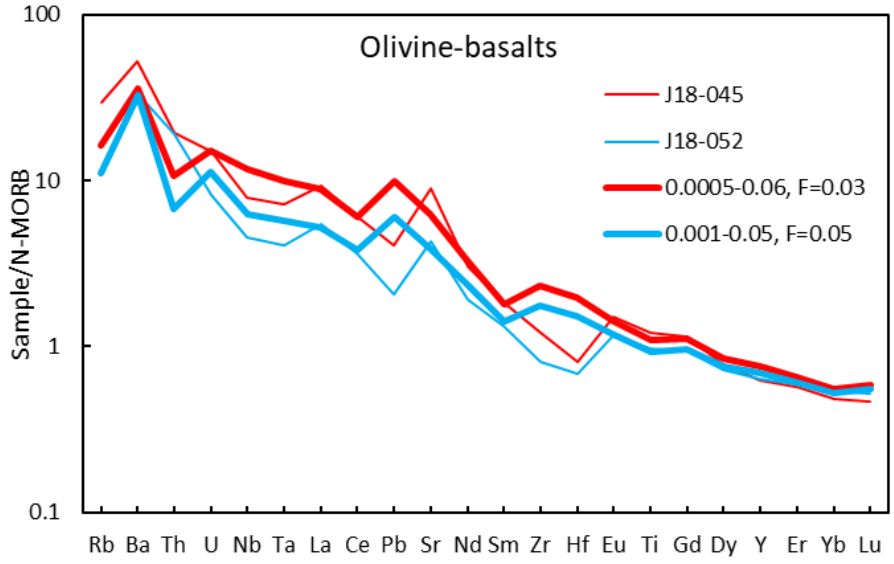

Fig. 6.37 N-MORB (Sun and McDonough, 1989) normalised multi-element diagram for trace element modelling (numbers in the labels mean sediment melt, AOC melt, and partial melting degree F. For example, '0.01-0.01 F=0.15' is 1% sediment melt and 1% AOC melt in the source which go through 15% partial melting).

6.2.5 Summary (including the description of the limitation of modelling)

The mantle source for rocks in this study is CLIP mantle which has been metasomatized by sediment melt and AOC melt released from the subducting slab. Based on different trace element modelling and isotope modelling, the proportion of different components and partial melting degree can be summarized below. Data of the Chagres Complex are scattered which suggest a heterogeneous mantle source. Overall, it requires high sediment melt (up to 1-1.5%) and variable AOC melt (0-4%) with high partial melting degree F (5-25%). Similarly, Bas Obispo Formation require high sediment melt (up to 1-1.5%), low AOC melt (0-2%), and high F (5-15%). Panama Formation can be formed by 3-10% partial melting of ambient mantle metasomatized by 0.2-0.6 % sediment melt and 2 - 4 % AOC melt. The Cabra and Pedro Miguel Formation require 3 -15% partial melting of ambient mantle metasomatized by 0.2 - 0.6% sediment melt and 2 - 6% AOC melt.

Trace element modelling mainly constitute two parts: composition of the ambient mantle and composition of the slab material. The ambient mantle is the CLIP mantle which is the residue after the plume underwent high degrees of melting. This residual mantle is considered to be depleted and that is why a DMM value is adopted here for modelling. However, the plume mantle is heterogeneous (Kerr et al., 1996, 2002; Hauff et al., 1997) and there is no information about the composition of the the ambient beneath central Panama. The situation is more complex for the slab materials. Here the sediment melt and AOC melt are adopted. The melt compositions are controlled by their original composition (sediment and AOC), partition coefficients, and melting degrees. All these are actually not 100% sure and their values are just estimates. For example, the partition coefficient for sediment melting is from an experiment (Johnson and Plank, 1999) in which the partition coefficients should be affected significantly by the composition of the starting material, pressure, and temperature. The same uncertainty occurs for the AOC melting. The isotope modelling is slightly better as it is not controlled by so many uncertain factors. The endmembers for mixing not quite accurate. However, the combination of the interpretation of trace elements, trace element modelling, and isotope modelling can still provide useful information about the magmatic evolution of the PVA.

6.3 Magmatic and Tectonic Evolution of Central Panama

6.3.1 Arc Migration and Associated Magmatic Evolution in Central Panama

Arc migration is a significant feature for PVA. Subduction-related volcanic and plutonic rocks from southern Azuero, Sona and Coiba Islands range in age from 61 to 50 Ma (Lissinna, 2005). Further north between the Sona-Azuero arc and the Cordillera arc, the age ranges from 47 to 34 Ma. In the Cordillera arc, subduction-related magmatism ranges in age from 32 to 7 Ma. The distance between the middle line of the old frontal arc, e.g. Sona-Azuero arc and the middle line of the new frontal arc, e.g. Cordillera arc is ~ 120 km. There is a large distance of norward migration of the arc in western

Panama. This northward arc migration is a regional geological event which should be found in central and eastern Panama. In central Panama, the Chagres arc forms the old frontal arc which is continuous with the Sona-Azuero arc in western Panama due to the similar age and geochemistry (Fig. 6.28; Wegner et al. 2011). The post-Eocene arc magmatism in the canal area such as the Panama Formation, shows similar geochemical characteristics with the Cordillera arc, e.g. more enriched in the most incompatible elements than the pre-Oligocene arc (Fig. 6.28). In eastern Panama, the post-Eocene magmatism in the Maje Range (ca. 20Ma; Whattam et al., 2012) and the Pearl Islands and Sapo Range (ca. 22 to 18 Ma; Lissinna, 2005) is similar to the Panama Formation in central Panama and Cordillera arc in eastern Panama in terms of geochemistry. These post-Eocene magmatism forms the new frontal arc across the western, central, and eastern Panama. Unlike the Cordilleran arc which is further away from the trench than the Sona-Azuero arc, the new frontal arc in central and the eastern Panama, is closer to the trench comparing to the Chagres arc. This has been explained by arc displacement between Sona-Azuero arc and Chagres arc (Buchs et al., 2019a; Lissinna, 2005) which will be discussed below.

Continental arc systems often show evidence of large-scale migration both toward and away from the incoming plate. In oceanic arc systems, both of arc migration toward the incoming plate and away from the incoming plate can be observed while the former case is more common (Allen et al., 2019). Two main hypotheses have been proposed to explain arc migration away from the incoming plate: (1) slab flattening (decreasing slab dip) which includes the subduction of buoyant oceanic features such as oceanic plateaus and seamounts (e.g., van Hunen et al., 2002; Liu et al., 2010; Marshall et al., 2003; Germa et al., 2011) and high convergence rate of the overriding plate (van Hunen et al., 2000); (2) subduction erosion, which leads to removal of the outer forearc through time (Kay et al., 2005; Goss et al., 2013; Jicha and Kay, 2018).

According to the isotopes in this study, no Galapagos hotspot track signature from the AOC aqueous fluid or melt are observed, which suggests arc migration is not caused by buoyant seamounts or plateaus subduction. Besides, previous studies show no evidence for such seamount/ plateau subduction in Panama during the time of arc migration (40-32 Ma in western Panama and 39-25 Ma in Central Panama) (Gazel et al., 2015) which also rules out the first hypothesis.

Fore-arc erosion is not significant in central Panama, as explained in section 6.2.2. Besides, if this arc migration is caused by fore-arc erosion, the thermal structure of the mantle and slab should remain the same. The slab input should be released in the similar location of the slab, comparing to the earlier frontal arc, and the proportions of sediment melt should remain the same. However, sediment melt in this study decreased from the old frontal arc to the new frontal arc. Fore-arc erosion is not likely to account for the volume of slab input so cannot explain the decreasing sediment melt. This indicates

the slab components for the young frontal arc might be released in a deeper location in which the slab has gone through higher degree of dehydration and melting (Schmidt and Poli, 2003).

Evidence from trace element characteristics and crust thickness data show the post-Eocene frontal arc has thicker crust than the pre-Oligocene frontal arc. The post-Eocene frontal arc magmatism in central Panama have the similar pattern in the N-MORB normalised multi-element diagram with the average continental arc basalt for which the incompatible elements are more enriched than the less incompatible elements (e.g. high La/Yb; Fig. 3.20). The pre-Oligocene frontal arc magmatism is less enriched in the most incompatible elements (e.g. low La/Yb) which make them similar to the average oceanic arc basalt (Fig. 3.14). This suggests the post-Eocene frontal arc formed in a tectonic setting similar to the continental arc while the pre-Oligocene frontal arc formed in a tectonic setting similar to the oceanic arc. The most apparent difference between continental arc and oceanic arc is the former has thicker crust or lithosphere than the latter. This is supported by studies on global arc magmatism which shows that trace element ratios such as La/Yb and Sr/Y of mafic rocks correlate with crust thickness as trace element ratios increase with increasing crust thickness (Mantle and Collins, 2008; Profeta et al., 2015). Studies on single areas such as Southern Volcanic Zone in South America also show the ratio of the more incompatible element to less incompatible element increases with increasing crust thickness (Kay et al., 2005). Therefore, the post-Eocene frontal arc has a thicker crust than the pre-Oligocene frontal arc according to their trace element characteristics. According to seismic studies, the crust of CLIP is 15 – 20 km thick (Mauffret and Leroy, 1997) which can be considered as the crust thickness of the early arc after subduction initiation. The thickness of the modern central America arc crust ranges from 25 km to 44 km (MacKenzie et al., 2008). CLIP is thicker than the average oceanic crust (~7.1 km; White et al., 1992) but thinner than the modern central America arc crust. This shows that crust thickens as the central America arc matures with time.

How does crust thickening affect the composition of arc rocks and arc migration? Even though the phenomenon that chemical composition of arc rocks correlate with crust thickness has been proposed by several studies (e.g. Mantle and Collins, 2008; Profeta et al., 2015), the exact controlling factors are not clear. Recently, two models on arc magmatism have been come up by Turner and Langmuir (2015): the Wedge Thermal Structure (WTS) model and Slab Thermal Structure (STS) Model. In the WTS model, the flux of slab aqueous fluids/melts to the mantle wedge is constant, while wedge thermal structure varies as a function of the overriding plate thickness. If sub-arc lithospheric thickness increases with crustal thickness, then the mantle wedge beneath the arc with thick crust resides at higher pressure and lower temperature, leading to lower F, which further give rise to higher incompatible element concentrations in melts. In the STS model, the wedge thermal structure is constant, while the slab flux varies as a function of the slab thermal structure. Hotter slabs provide a larger flux to the mantle wedge (Hermann and Rubatto, 2009), which leads to higher concentrations of

slab-derived elements in mantle-wedge melts. A more recent study by their team suggests arc magmatism is mainly directly controlled by wedge thermal structure rather than slab thermal structure (Turner et al., 2016). In this study, the combining effect of the changing condition of the mantle wedge thermal structure and the associated changing condition of dehydration and melting of the slab can explain arc rock composition and arc migration from the pre-Oligocene to the post-Eocene. In PVA, from subduction initiation to late Oligocene (e.g. ~25 Ma), the subducting plate was Farallon plate by which the slab thermal structure can be assumed to play a neglectable role in magmatic evolution and arc migration. Besides, according to the discussion 6.2, element transfer by aqueous fluids and sediment melts themselves play a small role in changing the content of HFSE of arc magma and they cannot give rise to the compositional change from oceanic arc basalt to the continental arc basalt. As crust thickens, the isotherms are displaced away from the trench and so is the melting field (Fig. 6.38). As the melting field of the mantle wedge deepens and migrates away from the trench, the location of the slab which provides aqueous fluids or/and melts deepens (Fig. 6.38). Dehydration of slab is a process that combines continuous and discontinuous reactions and production of an aqueous fluid or melt decreases with depth due to continuous reactions (Schmidt and Poli, 2003). Slab at deeper depth must has gone through higher degree of dehydration, which give rise to less amount of aqueous fluid and hydrous sediment melt into ambient mantle. This is the reason why the Chagres Complex has higher content of hydrous sediment melt while the Panama Formation have lower and the Cabra Formation have the lowest. The decreasing slab input triggers lower degree of partial melting which gives rise to higher content of incompatible elements in the Panama/Caraba Formation than the Chagres Complex. Meanwhile, the arc migrates away from the trench as the melting field moves away from the trench.

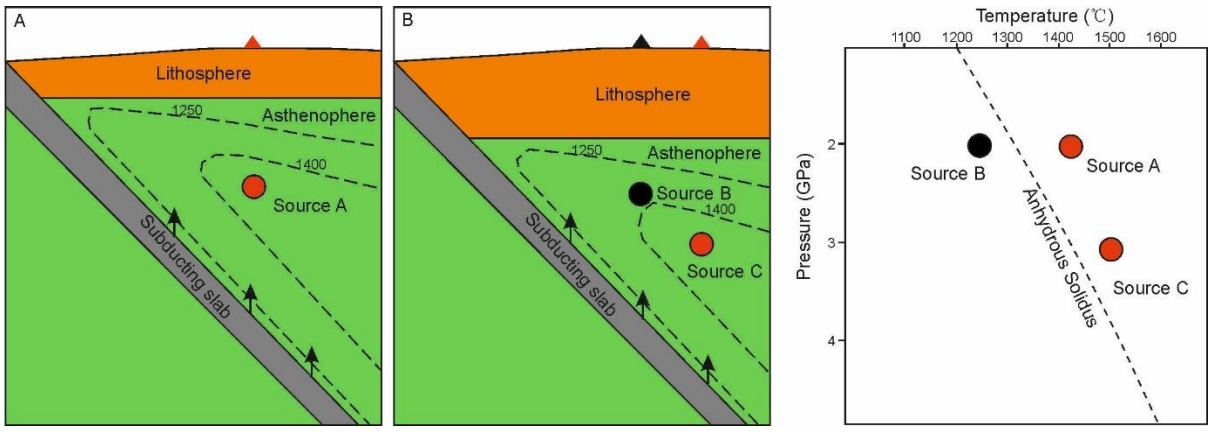

Fig. 6.38 A cartoon illustrating the relationship between lithosphere thickening and slab input decreasing, partial melting decreasing, and arc migration away from trench (revised from WTS model in Turner and Langmuir, 2015).

However, Earth sciences are controlled by many uncertainties or unknown factors. Mantle melting and also geochemical characteristics of arc rocks are also controlled by many poorly studied factors. We should be open to any possibilities. Arc migration might be the best example to demonstrate how important to be open to other different ideas. Why the arc front sits where it sits and how the mantle wedge undergo partial melting is a hot topic in Earth sciences. Some studies suggest arc location is controlled by mantle thermal structure and the location above where the mantle reaches the dry solidus (England and Katz, 2010; Perrin, et al., 2018). Some believe the volcanic front is controlled by the location of slab dehydration (Cooper et al., 2012; Wilson et al., 2014). Davies and Stevenson (1992) suggests mantle melting is controlled by amphibole-buffered solidus and the melt focusing (corresponding to volcanic front) is dictated by the least compressive stress in the wedge corner. Therefore, wedge melting is a complex and not well studied topic. Where the volcanic front sits and how it changes its location is not sure yet. Therefore, if the arc front does not migrate in central and eastern Panama and it stays stationary, as suggested by Buchs et al. (2019a), the story of the tectonic evolution will go to another interesting direction. If the arc front stays stationary, the melting location should stay the same assuming no change for other factors such as slab dip. As the mantle wedge cools down through time (Hall, 2012), the melting degree should decrease through time, which can also explain why the most incompatible elements in the younger arc is more enriched than the older arc. No matter what, the slab material, e.g. sediment melts decrease from the pre-Oligocene arc to the post-Eocene arc based on the isotope and trace element ratios. These decreasing slab materials should decrease the mantle melting degree as the PVA evolves.

6.3.2 A Slab Window for the Final Stage Magmatism in Central Panama and Volcanic Shutdown in Central/Eastern Panama

The final magmatism in central Panama is the Cabra Formation/Pedro Miguel Formation. Unlike the previous magmatism, this formation possesses up to ~6% AOC melt component according to isotopes and trace element modelling.

In a subduction zone, AOC melting requires special geological environments which are concluded here: (1) a young, hot oceanic crust: (2) a slab window. A young oceanic crust is hot enough to melt during subducting. This AOC melt is usually considered as adakite if it can penetrate through mantle wedge and erupt (Defant and Drummond, 1990; Hastie et al., 2011). If this AOC melt only accounts for a small amount, it will be exhausted during reaction with mantle peridotite. Partial melting of this metasomatized mantle wedge can form some special rock types such as high Nb basalts (Hastie et al., 2011) and adakitic rocks (Kepezhinskas et al., 1997; Rapp et al., 1999). Although the concept of that young oceanic crust can melt is generally accepted, how young and hot of the crust is controversial. Drummond and Defant (1990) and Maury et al. (1996) summarise known adakite occurrences and suggest that anatexis occurs in slabs as old as 20 Ma. The thermal structure of subduction zones as modelled by Peacock et al. (1994) and Peacock (1996) predicts melting in only very young crust (<5

Ma). Such a young age comes after the assumption that shear stress is negligible for modelling of P-T conditions (Peacock, 1996). However, if shear stress values as high as 66 MPa is applied in modelling, it results in higher model temperatures in the subducted crust, and thereby predicts melting in slabs as old as 40 Ma (Green and Harry, 1999). AOC melting in the Cabra Formation is not likely caused by a young oceanic crust. Magma erupted continuously from ~25 Ma and ~16 Ma for the Panama/Caraba Formation to the Cabra Formation, due to subduction of the Farallon plate. The age of the subducting Farallon plate is most likely to remain the same or only change slightly. A young oceanic crust was not likely formed and subducted all of a sudden. Besides, if we make an estimate from the modern tectonic settings that the Eastern Pacific Ridge, which formed the Farallon plate is ~ 2000 km away from the central America trench and the subducting rate of the Farallon plate is ~ 70 mm/y, the plate at the trench is ~ 30 Ma. This subducting plate might be too cold to melt. Therefore, the subducting slab cannot turn to be a much younger and hot plate which suggests the AOC melting cannot result from this mechanism.

A slab window is a slab-free region beneath the convergent margin of an overriding plate (Hole, 1991; Thorkelson and Taylor, 1989; Thorkelson, 1996). The window develops during “ridge subduction”, in which two oceanic plates are diverging, and the trailing edge of one or both plates is concurrently subducting. Once engulfed by the upwelling asthenosphere, a trailing edge becomes too hot for magma solidification, so growth of the slab ceases. Divergence without growth produces a slab window. A slab window is preferred to explain the petrogenesis of the Cabra Formation/Pedro Miguel Formation. The Farallon plate started to break up from the East Pacific Ridge ca. 23 Ma (Fig. 6.39 A; Lonsdale, 2005; Barckhausen et al., 2008). This breakup propagated to the Central America trench ca. 19.5 Ma (Fig. 6.39 B) when the Farallon plate break apart completely into the Cocos Plate and Nazca Plate (Barckhausen et al., 2008). Subduction of the Cocos-Nazca spreading centre formed a slab window beneath central Panama ca. 18 Ma, as revealed by the oldest age of the Pedro Miguel Formation from Buchs et al. (2019a). This slab window started earlier than 6-10 Ma in previous study (e.g. Johnston and Thorkelson, 1997).

The presence of a slab window is also consistent with the formation of OIB-like olivine-bearing basalts in the Caraba Formation. OIB-like or alkaline rocks commonly forms above a slab window. However, the exact mechanism for its formation is highly debated. Some suggest it can come from an ocean-island type mantle source, such as an enriched plume-head (Johnston and Thorkelson, 1997; Abratis and Worner et al., 2001). Some suggests small degrees of decompression melting of enriched asthenospheric mantle is one possible mechanism (Hole et al., 1991; Gazel et al., 2011). Based on our modelling for the olivine-bearing basalts in the Cabra Formation, an AOC-melt metasomatized mantle could be the source. The ambient mantle should be the same to the previous volcanism such as the Panama Formation rather than a new enriched mantle, as the ambient mantle cannot change significantly in a very short time span (<3 Ma). When the AOC undergo partial melting with no rutile

in the residue, Nb-Ta will be enriched or not depleted in the AOC melts. The mantle source will not show or only show minor depletion after being metasomatized by this AOC melts. Low degrees of partial melting of this mantle source will yield and OIB-like rocks, with no or minor Nb-Ta depletion and high ratios of not only LREE/HREE but also Gd/Yb (Fig. 6.37). This is supported by the most recent review work of Zheng (2019) and Zheng et al. (2020) in which they suggest the composition of the metasomatic agents (e.g. aqueous fluids vs melts) exert a first-order control on subduction zone magmas and the mantle metasomatized by rutile-consumed AOC melts is the source for OIB-like rocks.

The magmatism above this slab window in central Panama lasted till ca. 16 Ma and no younger magmatic rocks have been found from central to eastern Panama (Buchs et al.,2019a). The volcanic shutdown has been explained by oblique subduction of the Nazca Plate beneath the Caribbean Plate by Buchs et al. (2019a). The new data in this thesis support this mechanism for volcanic shutdown. After the breakup of the Farallon Plate into the Nazca and Cocos Plate at ca. 23Ma, the Nazca Plate subducted beneath the Caribbean Plate obliquely or more obliquely comparing to that prior to Farallon Plate breakup (Lonsdale, 2005). When the slab window formed at ca.18 Ma beneath central Panama, the orthogonal component of the Nazca convergence rate was minor or diminished. Without the supplement of ‘wet’ subducting oceanic lithosphere, no fluids can be released to trigger mantle melting (this study; Buchs et al., 2019a).

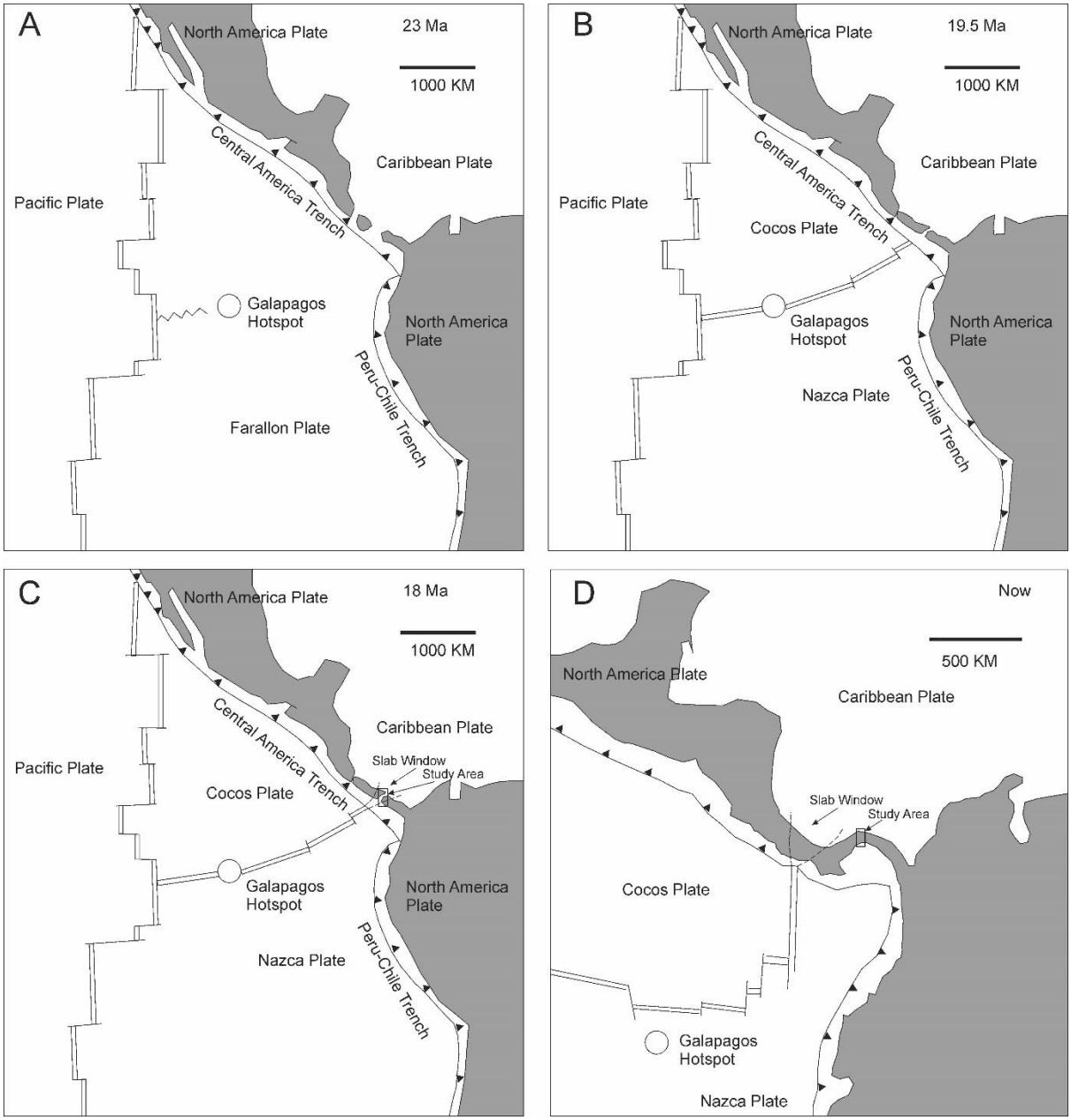

Fig. 6.39 Slab window under central Panama due to breakup of the Farallon plate (modified after Lonsdale et al., 2005; the age 19.5 Ma of the complete breakup is from Barckhausen et al., 2008 and the age 18 Ma of the formation of the slab window is the oldest age of Pedro Miguel Formation from Buchs et al., 2019a).

6.3.3 A try to Explain Arc Displacement

As discussed in 6.3.1, the frontal arc migrated further away from trench to form a new frontal arc (Cordillera arc) ca. 32 Ma (Baker et al., 2016) in western Panama. This new frontal arc shows enriched LREE relative to HREE and shows higher La/Sm and La/Yb than those in the pre-Oligocene arc. In Central Panama and Eastern Panama, a similar new frontal arc formed starting ca. 25 Ma (Rooney et al., 2011) south to the Chagres arc, before the old frontal arc. The frontal arc migrated

before the old frontal arc is caused by northward migration of the old frontal arc due to anticlockwise displacement, as shown by Buchs et al. (2019a). In other words, the new frontal arc migrated further away from the trench, like the Cordillera arc, but located before the Chagres arc due to the arc offset. However, the timing of this offset is poorly constrained and highly debated.

Paleomagnetic data collected by Montes et al. (2012b) indicated that the volcanic arc in central Panama was ~100 km offset by left- lateral strike-slip motion between 38 Ma and 28 Ma. The age is constrained by the radiometric ages in western and eastern Panama which shows continuous magmatism in western Panama but a 'magmatic lull' between 38 Ma and 28 Ma in eastern Panama. This 'magmatic lull' is believed to be caused by volcanic arc displacement. However, as shown in Chapter 2, there is no 'magmatic lull' between 38 Ma and 28 Ma in central and eastern Panama, as revealed by detrital zircons (Montes et al., 2012b; Ramirez et al., 2014).

Barat et al. (2014) propose that activation of a left-lateral deep fault zone (PCFZ), with an accumulated ~150 km of transtensive displacement occurred since the Late-Middle Eocene. The motion along the PCFZ resulted in the separation from each other of the Paleogene volcanic arc in the Azuero Peninsula and the San Blas–Darien Massif. However, the proposal for the offset is mainly based on the formation of Canal Basin, which is suggested to be formed during the displacement. The age of the Canal Basin, e.g. Late-Middle Eocene is revealed by the old sedimentation of the Gutuncillo Formation. However, there is no evidence to show any causal relationship between the displacement and formation of the the Canal Basin.

According to 6.3.1, magmatism only happens in specific mantle conditions (e.g., P-T-fluids condition) which indicates frontal arc only occurs in specific location. As mantle/slab conditions change through time, the old frontal arc magmatism becomes extinct when the conditions are not suitable for mantle partial melting. Therefore, the youngest magmatism in the Chagres arc and the oldest magmatism in the new frontal arc in central Panama can be considered as the oldest and youngest time constrains respectively for the arc offset. The earliest magmatism of the new frontal arc in central and eastern Panama is the Caraba Formation, e.g. Cerro Patacon andesite which was dated ~25 Ma (Rooney et al., 2011). This age suggests the offset occurred older than ~25 Ma. The oldest time constraint should come from the youngest magmatism in the Chagres arc. There are two possible scenarios for this age.

1. Bas Obispo Formation, with age of ca. 25-26 Ma display whole rock composition similar to the pre-Oligocene arc (Buchs et al., 2019b). This formation is considered as proximal alluvial deposit and the age dated for this formation came from basaltic andesite clasts (Buchs et al., 2019b). Since rocks in this formation show similar geochemical characteristics with Chagres arc, it is quite likely that clasts in this formation formed in volcanic eruption in Chagres arc and travelled from the highland Chagres arc in rivers down to the lowland forearc basin. 25-

26 Ma should be the oldest time when arc offset occurred, which also suggests the offset between Chagres arc and Sona-Azuero arc occurred during a short time, e.g. 25-26 Ma.

2. The youngest magmatism in Chagres arc is ~39 Ma for in situ lavas or intrusions (Wegner et al., 2011). However, the youngest detrital zircon in the Middle to Upper Eocene Gatuncillo Formation in central Panama is 36.73 ± 0.84 Ma (Ramirez et al., 2016) which suggest the youngest intrusions exhumed in this section of Chagres arc is ~36 Ma. The detrital zircons in the sand from Mamoni River in eastern Panama is no younger than 40.04 ± 0.57 Ma (Ramirez et al., 2016) which suggests the youngest intrusions exhumed in this section of Chagres arc is ~ 40 Ma. In the Upper Miocene Cucaracha and Culebra Formation along the Panama Canal, the detrital zircons range from 65.1 to 17.6 Ma with a gap of 28.1 ± 1.5 and 24.1 ± 1.3 Ma (Montes et al., 2012a). Together with the youngest detrital zircons in the Gatuncillo Formation and Mamoni River in the Chagres arc, it is reasonable to suggest that the arc offset occurred 28-25 Ma. This period of time also coincides with the event that the western part of the San Blas-Darien Massif (e.g. Chagres arc) suddenly rotated by up to ~ 25 ° (Montes et al., 2012b).

No matter if it is the first scenario or the second scenario, the offset between Chagres arc and Sona-Azuero arc occurred at a fast velocity between 28 Ma and 25 Ma. The reason for this arc offset is unclear. It might be caused by collision between South America Plate and PVA during this period of time, which is pointed by Farris et al. (2011) who attribute magmatic evolution in central Panama to arc-continent collision.

6.3.4 Tectono-magmatic Evolution of Central Panama

Based on the discussion above, tectono-magmatic evolution in central Panama can be described below. After subduction initiation ca. 75 Ma, Farallon plate subducted beneath CLIP. When the slab contacted the hot mantle wedge, slab dehydrated and partially melted and these aqueous fluids and sediment melts triggered large degree of partial melting of the mantle wedge. The old frontal arc development started in Chagres arc ca. 68 Ma (Lissinna, 2005; Worner et al., 2009; Wegner et al., 2011; Maury et al., 1995; Montes et al., 2012a), which is slightly later than ca. 71 Ma in another pre-Oligocene frontal arc, e.g. Sona-Azuero arc (Lissinna, 2005; Wegner et al., 2011) (Fig. 6.40). As the arc became mature with crust thickening, arc front migrated away from trench. This new frontal arc started first in western Panama ca. 32 Ma (Baker et al, 2016). During 28-25 Ma, collision between PVA and South America triggered arc displacement between western Panama and central/eastern Panama. The new frontal arc started ca. 25 Ma in central Panama after this arc displacement. This new frontal arc magmatism possesses a smaller volume of aqueous fluid and sediment melt and smaller degree of partial melting, comparing to the old frontal arc. Farallon plate started to break up at ca. 23 Ma (Lonsdale, 2005; Barckhausen et al., 2008) and ended up into Cocos Plate and Nazca Plate

ca.19.5 Ma. The breakup formed a slab window in central Panama at ca. 18 Ma and the Cabra Formation/Pedro Miguel Formation were formed above this slab window. AOC at the edge of the slab above the slab window was heated up by the upwelling asthenosphere mantle below to form AOC melt. This AOC melt went upward to metasomatize mantle wedge and the Cabra Formation/Pedro Miguel Formation formed by partial melting of this metasomatized mantle wedge. Magmatism ceased ca. 16 Ma in central Panama and probably also eastern Panama due to the oblique subduction or no subduction of the Nazca plate.

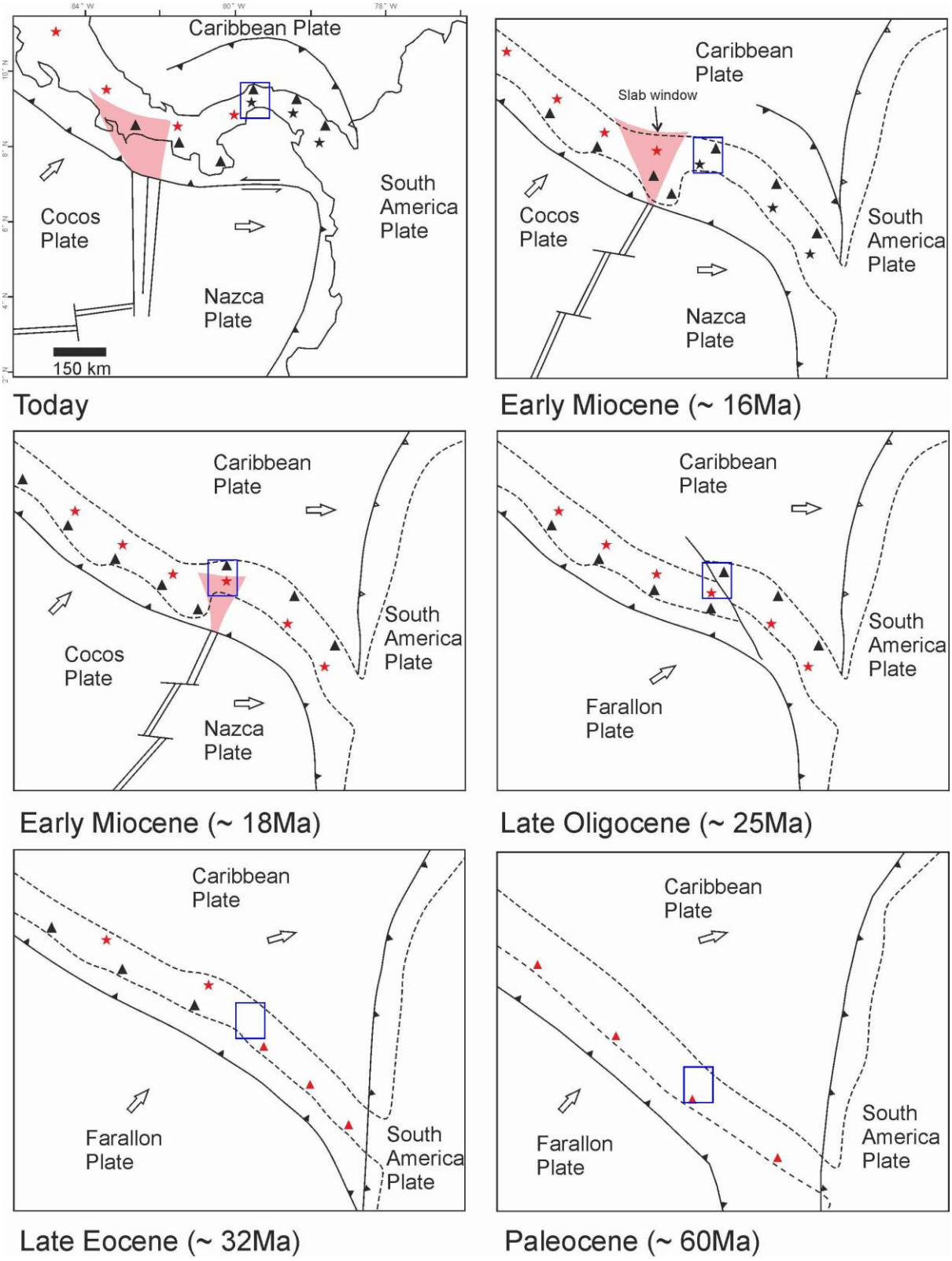

Fig. 6.40 Cartoon illustrating tectono-magmatic evolution of PVA

6.4 Future Work

This study helps to better understand the magmatic and tectonic evolution of central Panama and PVA, with several different methods such as field observation, petrographic observation, whole rock geochemistry, whole rock Sr-Nd-Pb isotopes, and mineral chemistry. However, Ar-Ar results for rocks of the Chagres Complex, Panama Formation, and one olivine bearing rock of the Cabra Formation have not yet come out due to lab facility problems and COVID-19. The Ar-Ar ages will better constrain different formations in the study area and will provide better magmatic and tectonic evolution model for the study area. Especially the dating for the Chagres Complex might help to reveal if there is a magmatic gap in central Panama. The Panama Formation and Las Cascadas Formation have a similar parental source based on Sr-Nd-Pb isotopes, major elements, and trace elements. Whether they are from the same plumbing system is not certain. The Ar-Ar ages of the Panama Formation will provide a strong evidence for this question.

Trace element content of clinopyroxene can provide more detailed information about magmatic evolution than the major elements. If clinopyroxenes in the Panama and Las Cascadas Formation can be analysed for trace elements, it will provide more information that the Las Cascadas Formation is the more evolved magma than the Panama Formation, even though they have similar parental magma. Trace element of clinopyroxene will tell information about magma mush dynamics such as melt extraction and porous reaction.

If slab window formed in central Panama at ca. 18 Ma and then migrated westward to the present position, we should expect to discover the slab window related magmatism such as the high-Nb basalts in western Panama. Besides, this magmatism should become younger westward. It is worth to conduct a field trip in the future to test this hypothesis.

7 CONCLUSIONS

Igneous rocks in central Panama are dominated by lava flows but also include volcanic tuffs (especially in silicic rocks such as the Las Cascadas Formation and Cabra mafic member) and hypabyssal intrusions (Caraba Formation). Rocks in the Chagres Complex are normally porphyritic with clinopyroxene and plagioclase as phenocrysts but amphibole bearing rocks can also be found in this complex. The crystallising sequence in the complex is clinopyroxene/amphibole, plagioclase, and magnetite. Zonation of clinopyroxenes in this complex suggests magma mixing. The Caraba Formation are amphibole bearing rocks with amphibole crystallising before plagioclase and magnetite. Amphibole and plagioclase are substantially zoned which indicates magma mixing. The Panama Formation are clinopyroxene bearing rocks with clinopyroxene crystallising before plagioclase and magnetite. Two groups can be divided: one have big, zoned clinopyroxenes which suggests magma mixing while the other is relatively small and homogeneous. The Las Cascadas Formation can be seen as aphyric but some samples are porphyritic with glomerocrysts as phenocryst. The Cabra Formation do not have clinopyroxenes as phenocrysts and plagioclases formed before clinopyroxenes. In this formation, there are two olivine bearing rocks with olivine absent in other formations.

Rocks in this study are relatively fresh. The oldest group, e.g. the Chagres Complex have the highest degree of alteration. The silicic rocks of the Cabra Formation collected along shore also went through high degree of alteration. All rocks in this study are subalkaline in TAS diagram and all rocks except for the Caraba Formation plot between the tholeiitic and calc-alkaline trend in the AFM diagram while the Caraba Formation rocks show calc-alkaline trend.

All rocks in this study show arc signatures in the N-MORB normalised multi-element diagram, e.g. Nb-Ta-Ti depletion. The post-Eocene rocks, e.g. the Panama, Las Cascadas, Caraba, and Cabra Formation are more enriched in the most incompatible elements than the pre-Oligocene rocks, e.g. the Chagres Complex. The Panama Formation and Las Cascadas Formation have similar shape in the multi-element diagram with the Las Cascadas Formation have overall higher element content. Major and trace element modelling shows the Las Cascadas Formation can be produced by fractional crystallisation of the Panama Formation, which suggest they might share similar parental magma. This can also be revealed by clinopyroxene composition. Clinopyroxenes also show rocks of the Panama Formation, especially the ones with big, zoned clinopyroxenes went through magma mixing. The Cabra Formation range from basalt to rhyolite and the silicic rocks can be achieved by fractional crystallisation of mafic rocks.

Sr-Nd-Pb isotopes display CLIP mantle with high radiogenic Pb isotope is the ambient mantle in central Panama. The Chagres Complex have the highest sediment component while the highest AOC component is found in the Cabra Formation. All these are consistent with trace element characteristics

such as Th/Yb. Furthermore, the Chagres Complex overall have higher partial melting degree than the rest of rocks which can be attributed to the high hydrous sediment melts in mantle source and thin arc crust at that time. The decreasing sediment melt and increasing incompatible elements from the Chagrex Complex to the Panama/Caraba Formation is associated with arc thickening and also arc migration away from the trench in central Panama. As arc matures and crust thickens, the melting field in the mantle wedge moves downward and away from trench which causes arc migration away from the trench. The corresponding location that slab releases hydrous sediment melt and perhaps also aqueous fluid also moves deeper, which gives rise to lower slab release, as shown in the smaller volume of sediment melt in the Panama Formation. Smaller volume of slab input along with the effect of crust thickening trigger lower degree of partial melting but forms rocks with high content of the most incompatible elements.

The high volume of AOC melt in the Cabra/Pedro Miguel Formation results from the formation of a slab window. The Farallon plate started to break up at ca. 23 Ma and the breakup into the Cocos and Nazca Plate finished thoroughly at ca. 19.5 Ma. Therefore, as the Cocos-Nazca spreading centre subducted, it formed a slab window at ca.18 Ma. The subsequent oblique subduction or no subduction beneath central Panama gave rise to the cessation of magmatism in the area.

REFERENCES

Abratis, M., & Wörner, G. (2001). Ridge collision, slab-window formation, and the flux of Pacific asthenosphere into the Caribbean realm. Geology, 29(2), 127-130.

Adamek, S., Frohlich, C., & Pennington, W. D. (1988). Seismicity of the Caribbean-Nazca boundary: Constraints on microplate tectonics of the Panama region. Journal of Geophysical Research: Solid Earth, 93(B3), 2053-2075.

Arculus, R. J. (2003). Use and abuse of the terms calcalkaline and calcalkalic. Journal of Petrology, 44(5), 929-935.

Arth, J. G. (1976). Behavior of trace elements during magmatic processes—a summary of theoretical models and their applications. J. Res. US Geol. Surv, 4(1), 41-47.

Asimow, P. D., & Ghiorso, M. S. (1998). Algorithmic modifications extending MELTS to calculate subsolidus phase relations. American Mineralogist, 83(9-10), 1127-1132.

Aubouin, J., Von Huene, R., Baltuck, M., Arnott, R., Bourgois, J., Filewicz, M., ... & Ogawa, Y. (1982). Leg 84 of the Deep Sea Drilling Project. Nature, 297(5866), 458-460.

Bachmann, O., & Bergantz, G. W. (2004). On the origin of crystal-poor rhyolites: extracted from batholithic crystal mushes. Journal of Petrology, 45(8), 1565-1582.

Bachmann, O., & Bergantz, G. W. (2008). Rhyolites and their source mushes across tectonic settings. Journal of Petrology, 49(12), 2277-2285.

Barker, S. J., Wilson, C. J. N., Baker, J. A., Millet, M. A., Rotella, M. D., Wright, I. C., & Wysoczanski, R. J. (2013). Geochemistry and petrogenesis of silicic magmas in the intra-oceanic Kermadec arc. Journal of Petrology, 54(2), 351-391.

Baker, M. J., Hollings, P., Thompson, J. A., Thompson, J. M., & Burge, C. (2016). Age and geochemistry of host rocks of the Cobre Panama porphyry Cu–Au deposit, central Panama: Implications for the Paleogene evolution of the Panamanian magmatic arc. Lithos, 248, 40-54.

Barat, F., de Lépinay, B. M., Sosson, M., Müller, C., Baumgartner, P. O., & Baumgartner-Mora, C. (2014). Transition from the Farallon Plate subduction to the collision between South and Central America: Geological evolution of the Panama Isthmus. Tectonophysics, 622, 145-167.

Barckhausen, U., Ranero, C. R., Cande, S. C., Engels, M., & Weinrebe, W. (2008). Birth of an intraoceanic spreading center. Geology, 36(10), 767-770.

Baumgartner, P. O., Flores, K., Bandini, A. N., Girault, F., & Cruz, D. (2008). Upper Triassic to Cretaceous radiolaria from Nicaragua and northern Costa Rica-The Mesquito composite oceanic terrane. Ofioliti, 33(1), 1-19.

Bebout, G. E., Ryan, J. G., Leeman, W. P., & Bebout, A. E. (1999). Fractionation of trace elements by subduction-zone metamorphism—effect of convergent-margin thermal evolution. Earth and Planetary Science Letters, 171(1), 63-81.

Bebout, G. E. (2013). Chemical and isotopic cycling in subduction zones. In Treatise on Geochemistry: Second Edition (pp. 703-747). Elsevier Inc..

Bédard, J. H. (2001). Parental magmas of the Nain Plutonic Suite anorthosites and mafic cumulates: a trace element modelling approach. Contributions to Mineralogy and Petrology, 141(6), 747-771.

Bédard, J. H. (2006). A catalytic delamination-driven model for coupled genesis of Archaean crust and sub-continental lithospheric mantle. *Geochimica et Cosmochimica Acta*, *70*(5), 1188-1214.

Bennett, E. N., Lissenberg, C. J., & Cashman, K. V. (2019). The significance of plagioclase textures in mid-ocean ridge basalt (Gakkel Ridge, Arctic Ocean). Contributions to Mineralogy and Petrology, 174(6), 49.

Biellmann, C., Gillet, P., Peyronneau, J., & Reynard, B. (1993). Experimental evidence for carbonate stability in the Earth's lower mantle. Earth and Planetary Science Letters, 118(1-4), 31-41.

Bold, W. V. D. (1973). Ostracoda of the La Boca formation, Panama canal zone. Micropaleontology, 18(4), 410-442.

Borg, L. E., & Clynne, M. A. (1998). The petrogenesis of felsic calc-alkaline magmas from the southernmost Cascades, California: origin by partial melting of basaltic lower crust. Journal of Petrology, 39(6), 1197-1222.

Bostock, M. G., Hyndman, R. D., Rondenay, S., & Peacock, S. M. (2002). An inverted continental Moho and serpentinization of the forearc mantle. Nature, 417(6888), 536-538.

Brenan, J. M., Shaw, H. F., & Ryerson, F. J. (1995a). Experimental evidence for the origin of lead enrichment in convergent-margin magmas. Nature, 378(6552), 54-56.

Brenan, J. M., Shaw, H. F., Ryerson, F. J., & Phinney, D. L. (1995b). Mineral-aqueous fluid partitioning of trace elements at 900 C and 2.0 GPa: Constraints on the trace element chemistry of mantle and deep crustal fluids. Geochimica et Cosmochimica Acta, 59(16), 3331-3350.

Brophy, J. G. (2008). A study of rare earth element (REE)–SiO 2 variations in felsic liquids generated by basalt fractionation and amphibolite melting: a potential test for discriminating between the two different processes. Contributions to Mineralogy and Petrology, 156(3), 337-357.

Buchs, D. M., Baumgartner, P. O., & Arculus, R. (2007). Late Cretaceous arc initiation on the edge of an oceanic plateau (southern Central America). AGUFM, 2007, T13C-1468.

Buchs, D. M., Coombs, H., Irving, D., Wang, J., Koppers, A., Miranda, R., ... & Pitchford, S. (2019a). Volcanic shutdown of the Panama Canal area following breakup of the Farallon plate. Lithos, 334, 190-204.

Buchs, D. M., Irving, D., Coombs, H., Miranda, R., Wang, J., Coronado, M., ... & Portugal, E. (2019b). Volcanic contribution to emergence of Central Panama in the Early Miocene. Scientific reports, 9(1), 1-16.

Buchs, N. C., Chilcott, M., Poletti, P. A., Buhler, L. H., & Morel, P. (2010). Vascular invasion in pancreatic cancer: Imaging modalities, preoperative diagnosis and surgical management. World journal of gastroenterology: WJG, 16(7), 818.

Camacho, E., Hutton, W., & Pacheco, J. F. (2010). A new look at evidence for a Wadati–Benioff zone and active convergence at the north Panama deformed belt. Bulletin of the Seismological Society of America, 100(1), 343-348.

Cann, J. R. (1970). Rb, Sr, Y, Zr and Nb in some ocean floor basaltic rocks. Earth and Planetary Science Letters, 10(1), 7-11.

Carr, M. J., Feigenson, M. D., & Bennett, E. A. (1990). Incompatible element and isotopic evidence for tectonic control of source mixing and melt extraction along the Central American arc. Contributions to Mineralogy and Petrology, 105(4), 369-380.

Cas, R., & Wright, J. (2012). Volcanic successions modern and ancient: A geological approach to processes, products and successions. Springer Science & Business Media.

Case, J. E. (1974). Oceanic crust forms basement of eastern Panama. Geological Society of America Bulletin, 85(4), 645-652.

Cashman, K. V., Sparks, R. S. J., & Blundy, J. D. (2017). Vertically extensive and unstable magmatic systems: a unified view of igneous processes. Science, 355(6331).

Caulfield, J. T., Turner, S. P., Dosseto, A., Pearson, N. J., & Beier, C. (2008). Source depletion and extent of melting in the Tongan sub-arc mantle. Earth and Planetary Science Letters, 273(3-4), 279-288.

Churikova, T., Dorendorf, F., & Wörner, G. (2001). Sources and fluids in the mantle wedge below Kamchatka, evidence from across-arc geochemical variation. Journal of Petrology, 42(8), 1567-1593.

Coates, A. G., Collins, L. S., Aubry, M. P., & Berggren, W. A. (2004). The geology of the Darien, Panama, and the late Miocene-Pliocene collision of the Panama arc with northwestern South America. GSA Bulletin, 116(11-12), 1327-1344.

Cobbing, E. J., & Pitcher, W. S. (1983). Andean plutonism in Peru and its relationship to volcanism and metallogenesis at a segmented plate edge. Geological Society of America Memoir, 159, 277-291.

Collins, L. S., Coates, A. G., Jackson, J. B., & Obando, J. A. (1995). Timing and rates of emergence of the Limon and Bocas del Toro basins: Caribbean effects of Cocos Ridge subduction?. SPECIAL PAPERS-GEOLOGICAL SOCIETY OF AMERICA, 263-263.

Cooper, L. B., Ruscitto, D. M., Plank, T., Wallace, P. J., Syracuse, E. M., & Manning, C. E. (2012). Global variations in H2O/Ce: 1. Slab surface temperatures beneath volcanic arcs. Geochemistry, Geophysics, Geosystems, 13(3).

Cooper, K. M. (2017). What does a magma reservoir look like? The “crystal's-eye” view. Elements, 13(1), 23-28.

Cooper, G. F., Macpherson, C. G., Blundy, J. D., Maunder, B., Allen, R. W., Goes, S., ... & Davidson, J. P. (2020). Variable water input controls evolution of the Lesser Antilles volcanic arc. Nature, 582(7813), 525-529.

Corral, I., Griera, A., Gómez-Gras, D., Corbella, M., i Sabaté, À. C., Falconett, M. P., & Cardellach, E. (2011). Geology of the Cerro Quema Au-Cu deposit (Azuero Peninsula, Panama). Geologica Acta.

Corral, I., Gómez-Gras, D., Griera, A., Corbella, M., & Cardellach, E. (2013). Sedimentation and volcanism in the Panamanian Cretaceous intra-oceanic arc and fore-arc: New insights from the Azuero peninsula (SW Panama). Bulletin de la Société Géologique de France, 184(1-2), 35-45.

Costa, F., Coogan, L. A., & Chakraborty, S. (2010). The time scales of magma mixing and mingling involving primitive melts and melt–mush interaction at mid-ocean ridges. Contributions to Mineralogy and Petrology, 159(3), 371-387.

Gutscher, M. A., Maury, R., Eissen, J. P., & Bourdon, E. (2000a). Can slab melting be caused by flat subduction?. Geology, 28(6), 535-538.

Gutscher, M. A., Spakman, W., Bijwaard, H., & Engdahl, E. R. (2000b). Geodynamics of flat subduction: Seismicity and tomographic constraints from the Andean margin. Tectonics, 19(5), 814-833.

Davidson, J., Turner, S., & Plank, T. (2013). Dy/Dy*: variations arising from mantle sources and petrogenetic processes. Journal of Petrology, 54(3), 525-537.

de Boer, J. Z., Defant, M. J., Stewart, R. H., & Bellon, H. (1991). Evidence for active subduction below western Panama. Geology, 19(6), 649-652.

Debari, S. M., & Sleep, N. H. (1991). High-Mg, low-Al bulk composition of the Talkeetna island arc, Alaska: Implications for primary magmas and the nature of arc crust. Geological Society of America Bulletin, 103(1), 37-47.

Defant, M. J., & Drummond, M. S. (1990). Derivation of some modern arc magmas by melting of young subducted lithosphere. nature, 347(6294), 662-665.

Defant, M. J., Clark, L. F., Stewart, R. H., Drummond, M. S., de Boer, J. Z., Maury, R. C., ... & Restrepo, J. F. (1991). Andesite and dacite genesis via contrasting processes: the geology and geochemistry of El Valle Volcano, Panama. Contributions to Mineralogy and Petrology, 106(3), 309-324.

Defant, M. J., Jackson, T. E., Drummond, M. S., De Boer, J. Z., Bellon, H., Feigenson, M. D., ... & Stewart, R. H. (1992). The geochemistry of young volcanism throughout western Panama and southeastern Costa Rica: an overview. Journal of the Geological Society, 149(4), 569-579.

DePaolo, D. J., & Wasserburg, G. J. (1976). Nd isotopic variations and petrogenetic models. *Geophysical Research Letters*, *3*(5), 249-252.

DePaolo, D. J. (1981). Trace element and isotopic effects of combined wallrock assimilation and fractional crystallization. Earth and planetary science letters, 53(2), 189-202.

Drake, M. J., & Weill, D. F. (1975). Partition of Sr, Ba, Ca, Y, Eu2+, Eu3+, and other REE between plagioclase feldspar and magmatic liquid: an experimental study. Geochimica et Cosmochimica Acta, 39(5), 689-712.

Drummond, M. S., & Defant, M. J. (1990). A model for trondhjemite-tonalite-dacite genesis and crustal growth via slab melting: Archean to modern comparisons. Journal of Geophysical Research: Solid Earth, 95(B13), 21503-21521.

Duncan, R.A. & Hargraves, R. B. (1984). Plate tectonic evolution of the Caribbean region in the mantle reference frame. The Caribbean-South American plate boundary and regional tectonics, 162, 81.

Dupuy, C., Liotard, J. M., & Dostal, J. (1992). Zr/Hf fractionation in intraplate basaltic rocks: carbonate metasomatism in the mantle source. Geochimica et Cosmochimica Acta, 56(6), 2417-2423.

Duque-Caro, H. (1990). Neogene stratigraphy, paleoceanography and paleobiogeography in northwest South America and the evolution of the Panama Seaway. Palaeogeography, Palaeoclimatology, Palaeoecology, 77(3-4), 203-234.

England, P. C., & Katz, R. F. (2010). Melting above the anhydrous solidus controls the location of volcanic arcs. Nature, 467(7316), 700-703.

Elardo, S. M., & Shearer Jr, C. K. (2014). Magma chamber dynamics recorded by oscillatory zoning in pyroxene and olivine phenocrysts in basaltic lunar meteorite Northwest Africa 032. American Mineralogist, 99(2-3), 355-368.

Elburg, M. A., Van Bergen, M., Hoogewerff, J., Foden, J., Vroon, P., Zulkarnain, I., & Nasution, A. (2002). Geochemical trends across an arc-continent collision zone: magma sources and slab-wedge transfer processes below the Pantar Strait volcanoes, Indonesia. Geochimica et Cosmochimica Acta, 66(15), 2771-2789.

Elliott, T. (2003). Tracers of the slab. Geophysical Monograph-American Geophysical Union, 138, 23-46.

Elliott, T., Plank, T., Zindler, A., White, W., & Bourdon, B. (1997). Element transport from slab to volcanic front at the Mariana arc. Journal of Geophysical Research: Solid Earth, 102(B7), 14991-15019.

Ewart, A., & Hawkesworth, C. J. (1987). The Pleistocene-Recent Tonga-Kermadec arc lavas: interpretation of new isotopic and rare earth data in terms of a depleted mantle source model. Journal of petrology, 28(3), 495-530.

Farris, D. W., Jaramillo, C., Bayona, G., Restrepo-Moreno, S. A., Montes, C., Cardona, A., ... & Valencia, V. (2011). Fracturing of the Panamanian Isthmus during initial collision with South America. Geology, 39(11), 1007-1010.

Farris, D. W., Cardona, A., Montes, C., Foster, D., & Jaramillo, C. (2017). Magmatic evolution of Panama Canal volcanic rocks: A record of arc processes and tectonic change. PloS one, 12(5), e0176010.

Feigenson, M. D., Carr, M. J., Maharaj, S. V., Juliano, S., & Bolge, L. L. (2004). Lead isotope composition of Central American volcanoes: Influence of the Galapagos plume. Geochemistry, Geophysics, Geosystems, 5(6).

Fitton, J. G., & Godard, M. (2004). Origin and evolution of magmas on the Ontong Java Plateau. Geological Society, London, Special Publications, 229(1), 151-178.

Fryer, P., Wheat, C. G., & Mottl, M. J. (1999). Mariana blueschist mud volcanism: Implications for conditions within the subduction zone. Geology, 27(2), 103-106.

Gaetani, G. A., & Grove, T. L. (1998). The influence of water on melting of mantle peridotite. Contributions to Mineralogy and Petrology, 131(4), 323-346.

Gaetani, G. A., Kent, A. J., Grove, T. L., Hutcheon, I. D., & Stolper, E. M. (2003). Mineral/melt partitioning of trace elements during hydrous peridotite partial melting. Contributions to Mineralogy and Petrology, 145(4), 391-405.

Gans, P. B., Alvarado-Induni, G., Perez, W., MacMillan, I., & Calvert, A. (2003, April). Neogene evolution of the Costa Rican arc and development of the Cordillera Central. In Geol. Soc. Am. Abstr. Programs (Vol. 35, No. 4, p. 74).

Garel, F., Goes, S., Davies, D. R., Davies, J. H., Kramer, S. C., & Wilson, C. R. (2014). Interaction of subducted slabs with the mantle transition‐zone: A regime diagram from 2‐D thermo‐mechanical models with a mobile trench and an overriding plate. Geochemistry, Geophysics, Geosystems, 15(5), 1739-1765.

Gardner, T. W., Fisher, D. M., Morell, K. D., & Cupper, M. L. (2013). Upper-plate deformation in response to flat slab subduction inboard of the aseismic Cocos Ridge, Osa Peninsula, Costa Rica. Lithosphere, 5(3), 247-264.

Gazel, E., Carr, M. J., Hoernle, K., Feigenson, M. D., Szymanski, D., Hauff, F., & Van Den Bogaard, P. (2009). Galapagos-OIB signature in southern Central America: Mantle refertilization by arc–hot spot interaction. Geochemistry, Geophysics, Geosystems, 10(2).

Gazel, E., Hoernle, K., Carr, M. J., Herzberg, C., Saginor, I., Van den Bogaard, P., ... & Swisher III, C. (2011). Plume–subduction interaction in southern Central America: Mantle upwelling and slab melting. Lithos, 121(1-4), 117-134.

Gazel, E., Hayes, J. L., Hoernle, K., Kelemen, P., Everson, E., Holbrook, W. S., ... & Calvert, A. J. (2015). Continental crust generated in oceanic arcs. Nature Geoscience, 8(4), 321-327.

Germa, A., Quidelleur, X., Labanieh, S., Chauvel, C., & Lahitte, P. (2011). The volcanic evolution of Martinique Island: Insights from K–Ar dating into the Lesser Antilles arc migration since the Oligocene. Journal of Volcanology and Geothermal Research, 208(3-4), 122-135.

Ghiorso, M. S., & Sack, R. O. (1995). Chemical mass transfer in magmatic processes IV. A revised and internally consistent thermodynamic model for the interpolation and extrapolation of liquid-solid equilibria in magmatic systems at elevated temperatures and pressures. Contributions to Mineralogy and Petrology, 119(2-3), 197-212.

Ghiorso, M. S. (1997). Thermodynamic models of igneous processes. Annual Review of Earth and Planetary Sciences, 25(1), 221-241.

Ghiorso, M. S., & Gualda, G. A. (2015). An H 2 O–CO 2 mixed fluid saturation model compatible with rhyolite-MELTS. Contributions to Mineralogy and Petrology, 169(6), 1-30.

Gill, J. B. (1981). Orogenic andesites and plate tectonics (Vol. 16). Springer Science & Business Media.

Goss, A. R., Kay, S. M., & Mpodozis, C. (2013). Andean adakite-like high-Mg andesites on the northern margin of the Chilean–Pampean flat-slab (27–28· 5° S) associated with frontal arc migration and fore-arc subduction erosion. Journal of Petrology, 54(11), 2193-2234.

Gräfe, K., Frisch, W., Villa, I. M., & Meschede, M. (2002). Geodynamic evolution of southern Costa Rica related to low-angle subduction of the Cocos Ridge: constraints from thermochronology. Tectonophysics, 348(4), 187-204.

Green, N. L., & Harry, D. L. (1999). On the relationship between subducted slab age and arc basalt petrogenesis, Cascadia subduction system, North America. Earth and Planetary Science Letters, 171(3), 367-381.

Greene, A. R., DeBARI, S. M., Kelemen, P. B., Blusztajn, J., & Clift, P. D. (2006). A detailed geochemical study of island arc crust: the Talkeetna arc section, south–central Alaska. Journal of Petrology, 47(6), 1051-1093.

Grove, T. L., Chatterjee, N., Parman, S. W., & Médard, E. (2006). The influence of H2O on mantle wedge melting. Earth and Planetary Science Letters, 249(1-2), 74-89.

Gualda, G. A., Ghiorso, M. S., Lemons, R. V., & Carley, T. L. (2012). Rhyolite-MELTS: a modified calibration of MELTS optimized for silica-rich, fluid-bearing magmatic systems. Journal of Petrology, 53(5), 875-890.

Hall, P. S. (2012). On the thermal evolution of the mantle wedge at subduction zones. Physics of the Earth and Planetary Interiors, 198, 9-27.

Hargraves, R. B. (1984). Plate tectonic evolution of the Caribbean region in the mantle reference frame. The Caribbean-South American plate boundary and regional tectonics, 162, 81.

Hastie, A. R., Kerr, A. C., Pearce, J. A., & Mitchell, S. F. (2007). Classification of altered volcanic island arc rocks using immobile trace elements: development of the Th–Co discrimination diagram. Journal of petrology, 48(12), 2341-2357.

Hastie, A. R., & Kerr, A. C. (2010). Mantle plume or slab window?: Physical and geochemical constraints on the origin of the Caribbean oceanic plateau. Earth-Science Reviews, 98(3-4), 283-293.

Hastie, A. R., Mitchell, S. F., Kerr, A. C., Minifie, M. J., & Millar, I. L. (2011). Geochemistry of rare high-Nb basalt lavas: Are they derived from a mantle wedge metasomatised by slab melts?. Geochimica et Cosmochimica Acta, 75(17), 5049-5072.

Hauff, F., Hoernle, K., Schmincke, H. U., & Werner, R. (1997). A Mid Cretaceous origin for the Galapagos hotspot: Volcanological, petrological and geochemical evidence from Costa Rican oceanic crustal segments. Geologische Rundschau, 86(1), 141-155.

Hauff, F., Hoernle, K., Tilton, G., Graham, D. W., & Kerr, A. C. (2000a). Large volume recycling of oceanic lithosphere over short time scales: geochemical constraints from the Caribbean Large Igneous Province. Earth and Planetary Science Letters, 174(3-4), 247-263.

Hauff, F., Hoernle, K., van den Bogaard, P., Alvarado, G., & Garbe-Schönberg, D. (2000b). Age and geochemistry of basaltic complexes in western Costa Rica: Contributions to the geotectonic evolution of Central America. Geochemistry, Geophysics, Geosystems, 1(5).

Hawkesworth, C. J., Hergt, J. M., Ellam, R. M., & McDermott, F. (1991). Element fluxes associated with subduction related magmatism. Philosophical Transactions of the Royal Society of London. Series A: Physical and Engineering Sciences, 335(1638), 393-405.

Hawkesworth, C. J., Turner, S. P., McDermott, F., Peate, D. W., & Van Calsteren, P. (1997). U-Th isotopes in arc magmas: Implications for element transfer from the subducted crust. Science, 276(5312), 551-555.

Hermann, J. (1997). Experimental constraints on phase relations in subducted continental crust. Contributions to Mineralogy and Petrology, 143(2), 219-235.

Hermann, J., & Rubatto, D. (2009). Accessory phase control on the trace element signature of sediment melts in subduction zones. Chemical Geology, 265(3-4), 512-526.

Hermann, J., & Spandler, C. J. (2008). Sediment melts at sub-arc depths: an experimental study. Journal of Petrology, 49(4), 717-740.

Herzberg, C., Asimow, P. D., Arndt, N., Niu, Y., Lesher, C. M., Fitton, J. G., ... & Saunders, A. D. (2007). Temperatures in ambient mantle and plumes: Constraints from basalts, picrites, and komatiites. Geochemistry, Geophysics, Geosystems, 8(2).

Hidalgo, P. J., Vogel, T. A., Rooney, T. O., Currier, R. M., & Layer, P. W. (2011). Origin of silicic volcanism in the Panamanian arc: evidence for a two-stage fractionation process at El Valle volcano. Contributions to Mineralogy and Petrology, 162(6), 1115-1138.

Hidalgo, P. J., & Rooney, T. O. (2014). Petrogenesis of a voluminous Quaternary adakitic volcano: the case of Baru volcano. Contributions to Mineralogy and Petrology, 168(3), 1011.

Hildreth, W., & Moorbath, S. (1988). Crustal contributions to arc magmatism in the Andes of central Chile. Contributions to mineralogy and petrology, 98(4), 455-489.

Hildreth, W. (2004). Volcanological perspectives on Long Valley, Mammoth Mountain, and Mono Craters: several contiguous but discrete systems. Journal of Volcanology and Geothermal Research, 136(3-4), 169-198.

Hoang, N., & Uto, K. (2006). Upper mantle isotopic components beneath the Ryukyu arc system: Evidence for 'back-arc'entrapment of Pacific MORB mantle. Earth and Planetary Science Letters, 249(3-4), 229-240.

Hochstaedter, A. G., Gill, J. B., Taylor, B., Ishizuka, O., Yuasa, M., & Monta, S. (2000). Across-arc geochemical trends in the Izu-Bonin arc: Constraints on source composition and mantle melting. Journal of Geophysical Research: Solid Earth, 105(B1), 495-512.

Hochstaedter, A., Gill, J., Peters, R., Broughton, P., Holden, P., & Taylor, B. (2001). Across-arc geochemical trends in the Izu-Bonin arc: Contributions from the subducting slab. Geochemistry, Geophysics, Geosystems, 2(7).

Hoernle, K., Werner, R., Morgan, J. P., Garbe-Schönberg, D., Bryce, J., & Mrazek, J. (2000). Existence of complex spatial zonation in the Galápagos plume. Geology, 28(5), 435-438.

Hoernle, K., van den Bogaard, P., Werner, R., Lissinna, B., Hauff, F., Alvarado, G., & Garbe-Schönberg, D. (2002). Missing history (16–71 Ma) of the Galápagos hotspot: Implications for the tectonic and biological evolution of the Americas. Geology, 30(9), 795-798.

Hoernle, K., Hauff, F., & van den Bogaard, P. (2004). 70 my history (139–69 Ma) for the Caribbean large igneous province. Geology, 32(8), 697-700.

Hoernle, K., Abt, D. L., Fischer, K. M., Nichols, H., Hauff, F., Abers, G. A., ... & Strauch, W. (2008). Arc-parallel flow in the mantle wedge beneath Costa Rica and Nicaragua. Nature, 451(7182), 1094-1097.

Hole, M. J., Rogers, G., Saunders, A. D., & Storey, M. (1991). Relation between alkalic volcanism and slab-window formation. Geology, 19(6), 657-660.

Huang, H., Niu, Y., Zhao, Z., Hei, H., & Zhu, D. (2011). On the enigma of Nb-Ta and Zr-Hf fractionation—a critical review. Journal of Earth Science, 22(1), 52-66.

Davies, J. H., & Stevenson, D. J. (1992). Physical model of source region of subduction zone volcanics. Journal of Geophysical Research: Solid Earth, 97(B2), 2037-2070.

Hyndman, R. D., & Peacock, S. M. (2003). Serpentinization of the forearc mantle. Earth and Planetary Science Letters, 212(3-4), 417-432.

Jacques, G., Hoernle, K., Gill, J., Wehrmann, H., Bindeman, I., & Lara, L. E. (2014). Geochemical variations in the Central Southern Volcanic Zone, Chile (38–43 S): the role of fluids in generating arc magmas. Chemical Geology, 371, 27-45.

Jicha, B. R., & Kay, S. M. (2018). Quantifying arc migration and the role of forearc subduction erosion in the central Aleutians. Journal of Volcanology and Geothermal Research, 360, 84-99.

Jischke, M. C. (1975). On the dynamics of descending lithospheric plates and slip zones. Journal of Geophysical Research, 80(35), 4809-4813.

Johnson, K. T., Dick, H. J., & Shimizu, N. (1990). Melting in the oceanic upper mantle: an ion microprobe study of diopsides in abyssal peridotites. Journal of Geophysical Research: Solid Earth, 95(B3), 2661-2678.

Johnson, K. T. (1998). Experimental determination of partition coefficients for rare earth and high-field-strength elements between clinopyroxene, garnet, and basaltic melt at high pressures. Contributions to Mineralogy and Petrology, 133(1-2), 60-68.

Johnson, M. C., & Plank, T. (1999). Dehydration and melting experiments constrain the fate of subducted sediments. Geochemistry, Geophysics, Geosystems, 1(12).

Johnston, S. T., & Thorkelson, D. J. (1997). Cocos-Nazca slab window beneath central America. Earth and Planetary Science Letters, 146(3), 465-474.

Kay, S. M., & Abbruzzi, J. M. (1996). Magmatic evidence for Neogene lithospheric evolution of the central Andean “flat-slab” between 30 S and 32 S. Tectonophysics, 259(1-3), 15-28.

Kay, S. M., Godoy, E., & Kurtz, A. (2005). Episodic arc migration, crustal thickening, subduction erosion, and magmatism in the south-central Andes. Geological Society of America Bulletin, 117(1-2), 67-88.

Kelemen, P. B., Hanghøj, K., & Greene, A. R. (2013). One view of the geochemistry of subduction-related magmatic arcs, with an emphasis on primitive andesite and lower crust. TrGeo, 3, 659.

Kellogg, J. N., Vega, V., Stallings, T. C., & Aiken, C. L. (1995). Tectonic development of Panama, Costa Rica, and the Colombian Andes: constraints from global positioning system geodetic studies and gravity. Special Papers-Geological Society of America, 75-75.

Kennan, L., & Pindell, J. L. (2009). Dextral shear, terrane accretion and basin formation in the Northern Andes: best explained by interaction with a Pacific-derived Caribbean Plate?. Geological Society, London, Special Publications, 328(1), 487-531.

Kepezhinskas, P., McDermott, F., Defant, M. J., Hochstaedter, A., Drummond, M. S., Hawkesworth, C. J., ... & Bellon, H. (1997). Trace element and Sr□ Nd□ Pb isotopic constraints on a three-component model of Kamchatka Arc petrogenesis. Geochimica et cosmochimica acta, 61(3), 577-600.

Keppler, H. (1996). Constraints from partitioning experiments on the composition of subduction-zone fluids. Nature, 380(6571), 237-240.

Kerr, A. C., Tarney, J., Marriner, G. F., Nivia, A., Klaver, G. T., & Saunders, A. D. (1996). The geochemistry and tectonic setting of late Cretaceous Caribbean and Colombian volcanism. Journal of South American Earth Sciences, 9(1-2), 111-120.

Kerr, A. C., Marriner, G. F., Tarney, J., Nivia, A., Saunders, A. D., Thirlwall, M. F., & Sinton, C. W. (1997a). Cretaceous Basaltic Terranes in western Columbia: elemental, chronological and Sr–Nd isotopic constraints on petrogenesis. Journal of petrology, 38(6), 677-702.

Kerr, A. C., Tarney, J., Marriner, G. F., Nivia, A., & Saunders, A. D. (1997b). The Caribbean-Colombian Cretaceous igneous province: The internal anatomy of an oceanic plateau. Geophysical monograph-American Geophysical Union, 100, 123-144.

Kerr, A. C., Tarney, J., Kempton, P. D., Spadea, P., Nivia, A., Marriner, G. F., & Duncan, R. A. (2002). Pervasive mantle plume head heterogeneity: Evidence from the late Cretaceous Caribbean-Colombian oceanic plateau. Journal of Geophysical Research: Solid Earth, 107(B7), ECV-2.

Kessel, R., Schmidt, M. W., Ulmer, P., & Pettke, T. (2005). Trace element signature of subduction-zone fluids, melts and supercritical liquids at 120–180 km depth. Nature, 437(7059), 724-727.

Kimura, J. I., & Yoshida, T. (2006). Contributions of slab fluid, mantle wedge and crust to the origin of Quaternary lavas in the NE Japan arc. Journal of Petrology, 47(11), 2185-2232.

Kimura, J. I., & Ariskin, A. A. (2014). Calculation of water-bearing primary basalt and estimation of source mantle conditions beneath arcs: PRIMACALC2 model for WINDOWS. Geochemistry, Geophysics, Geosystems, 15(4), 1494-1514.

Kincaid, C., & Griffiths, R. W. (2003). Laboratory models of the thermal evolution of the mantle during rollback subduction. Nature, 425(6953), 58-62.

Kirby, M. X., Jones, D. S., & MacFadden, B. J. (2008). Lower Miocene stratigraphy along the Panama Canal and its bearing on the Central American Peninsula. PLoS One, 3(7), e2791.

Kirby, S. H., Durham, W. B., & Stern, L. A. (1991). Mantle phase changes and deep-earthquake faulting in subducting lithosphere. Science, 252(5003), 216-225.

Klimm, K., Blundy, J. D., & Green, T. H. (2008). Trace element partitioning and accessory phase saturation during H2O-saturated melting of basalt with implications for subduction zone chemical fluxes. Journal of Petrology, 49(3), 523-553.

Kogiso, T., Tatsumi, Y., & Nakano, S. (1997). Trace element transport during dehydration processes in the subducted oceanic crust: 1. Experiments and implications for the origin of ocean island basalts. Earth and Planetary Science Letters, 148(1-2), 193-205.

Kolarsky, R. A., Mann, P., Monechi, S., Meyerhoff-Hull, D., & Pessagno, E. A. (1995). Stratigraphic development of southwestern Panama as determined from integration of marine seismic data and onshore geology. SPECIAL PAPERS-GEOLOGICAL SOCIETY OF AMERICA, 159-159.

Kushiro, I. (1960). Si-Al relation in clinopyroxenes from igneous rocks. American journal of science, 258(8), 548-554.

Kuritani, T., Yokoyama, T., & Nakamura, E. (2008). Generation of rear-arc magmas induced by influx of slab-derived supercritical liquids: Implications from alkali basalt lavas from Rishiri Volcano, Kurile arc. Journal of Petrology, 49(7), 1319-1342.

Langmuir, C. H. (1989). Geochemical consequences of in situ crystallization. Nature, 340(6230), 199-205.

Langmuir, C. H., Bezos, A., Escrig, S., & Parman, S. W. (2006). Chemical systematics and hydrous melting of the mantle in back-arc basins. Geophysical Monograph-American Geophysical Union, 166, 87.

Lambert, I. B., & Wyllie, P. J. (1972). Melting of gabbro (quartz eclogite) with excess water to 35 kilobars, with geological applications. The Journal of Geology, 80(6), 693-708.

Lapierre, H., Bosch, D., Dupuis, V., Polvé, M., Maury, R. C., Hernandez, J., ... & de Lépinay, B. M. (2000). Multiple plume events in the genesis of the peri-Caribbean Cretaceous oceanic plateau province. Journal of Geophysical Research: Solid Earth, 105(B4), 8403-8421.

Le Bas, M. J. (1962). The role of aluminum in igneous clinopyroxenes with relation to their parentage. American Journal of Science, 260(4), 267-288.

Leat, P. T., Smellie, J. L., Millar, I. L., & Larter, R. D. (2003). Magmatism in the South Sandwich arc. Geological Society, London, Special Publications, 219(1), 285-313.

Leeman, W. P., Carr, M. J., & Morris, J. D. (1994). Boron geochemistry of the Central American volcanic arc: constraints on the genesis of subduction-related magmas. Geochimica et Cosmochimica Acta, 58(1), 149-168.

Leterrier, J., Maury, R. C., Thonon, P., Girard, D., & Marchal, M. (1982). Clinopyroxene composition as a method of identification of the magmatic affinities of paleo-volcanic series. Earth and planetary science letters, 59(1), 139-154.

Liang, Y., Deng, J., Liu, X., Wang, Q., Qin, C., Li, Y., ... & Jiang, J. (2018). Major and trace element, and Sr isotope compositions of clinopyroxene phenocrysts in mafic dykes on Jiaodong Peninsula, southeastern North China Craton: Insights into magma mixing and source metasomatism. Lithos, 302, 480-495.

Lissenberg, C. J., MacLeod, C. J., & Bennett, E. N. (2019). Consequences of a crystal mush-dominated magma plumbing system: a mid-ocean ridge perspective. Philosophical Transactions of the Royal Society A, 377(2139), 20180014.

Lissinna, B., Hoernle, K., & Van Den Bogaard, P. (2002). Northern migration of arc volcanism in western Panama: evidence for subduction erosion?. AGUFM, 2002, V11A-1368.

Lissinna, B. (2005). A profile through the Central American Landbridge in western Panama: 115 Ma interplay between the Galápagos hotspot and the Central American subduction zone (Doctoral dissertation, Christian-Albrechts-Universität).

Liu, L., Gurnis, M., Seton, M., Saleeby, J., Müller, R. D., & Jackson, J. M. (2010). The role of oceanic plateau subduction in the Laramide orogeny. Nature Geoscience, 3(5), 353-357.

Lonsdale, P., & Klitgord, K. D. (1978). Structure and tectonic history of the eastern Panama Basin. Geological Society of America Bulletin, 89(7), 981-999.

Lonsdale, P. (2005). Creation of the Cocos and Nazca plates by fission of the Farallon plate. Tectonophysics, 404(3-4), 237-264.

Loucks, R. R. (1990). Discrimination of ophiolitic from nonophiolitic ultramafic-mafic allochthons in orogenic belts by the Al/Ti ratio in clinopyroxene. Geology, 18(4), 346-349.

Lowrie, A., Stewart, J., Stewart, R. H., Van Andel, T. J., & McRaney, L. (1982). Location of the eastern boundary of the Cocos plate during the Miocene. Marine Geology, 45(3-4), 261-279.

Luth, R. W. (2001). Experimental determination of the reaction aragonite+ magnesite= dolomite at 5 to 9 GPa. Contributions to Mineralogy and Petrology, 141(2), 222-232.

MacDonald, D. F. (1915). Some engineering problems of the Panama Canal in their relation to geology and topography (Vol. 86). US Government Printing Office.

MacKenzie, L., Abers, G. A., Fischer, K. M., Syracuse, E. M., Protti, J. M., Gonzalez, V., & Strauch, W. (2008). Crustal structure along the southern Central American volcanic front. Geochemistry, Geophysics, Geosystems, 9(8).

MacMillan, I., Gans, P. B., & Alvarado, G. (2004). Middle Miocene to present plate tectonic history of the southern Central American Volcanic Arc. Tectonophysics, 392(1-4), 325-348.

Maitre, L. E. (1989). A classification of igneous rocks and glossary of terms. Recommendations of the international union of geological sciences subcommission on the systematics of igneous rocks, 193.

Mann, P., & Corrigan, J. (1990). Model for late Neogene deformation in Panama. Geology, 18(6), 558-562.

Mann, P., & Kolarsky, R. A. (1995). East Panama deformed belt: Structure, age, and neotectonic significance. SPECIAL PAPERS-GEOLOGICAL SOCIETY OF AMERICA, 111-111.

Manning, C. E. (2004). The chemistry of subduction-zone fluids. Earth and Planetary Science Letters, 223(1-2), 1-16.

Mantle, G. W., & Collins, W. J. (2008). Quantifying crustal thickness variations in evolving orogens: Correlation between arc basalt composition and Moho depth. Geology, 36(1), 87-90.

Marshall, J. S., Idleman, B. D., Gardner, T. W., & Fisher, D. M. (2003). Landscape evolution within a retreating volcanic arc, Costa Rica, Central America. Geology, 31(5), 419-422.

Marschall, H. R., Altherr, R., & Rüpke, L. (2007). Squeezing out the slab—modelling the release of Li, Be and B during progressive high-pressure metamorphism. Chemical Geology, 239(3-4), 323-335.

Martin, H., Smithies, R. H., Rapp, R., Moyen, J. F., & Champion, D. (2005). An overview of adakite, tonalite–trondhjemite–granodiorite (TTG), and sanukitoid: relationships and some implications for crustal evolution. Lithos, 79(1-2), 1-24.

Mauffret, A., & Leroy, S. (1997). Seismic stratigraphy and structure of the Caribbean igneous province. Tectonophysics, 283(1-4), 61-104.

Maury, R.C., Defant, M.J., Bellon, H., de Boer, J.Z., Stewart , R.H., & Cotton, J. (1995). Early Tertiary arc volcanics from eastern Panama. Geologic and Tectonic Development of the Caribbean Plate Boundary in Southern Central America, 295, 29.

Maury, R. C., Sajona, F. G., Pubellier, M., Bellon, H., & Defant, M. J. (1996). Fusion de la croûte océanique dans les zones de subduction/collision récentes; l'exemple de Mindanao (Philippines). Bulletin de la Société géologique de France, 167(5), 579-595.

McDade, P., Blundy, J. D., & Wood, B. J. (2003a). Trace element partitioning on the Tinaquillo Lherzolite solidus at 1.5 GPa. Physics of the Earth and Planetary Interiors, 139(1-2), 129-147.

McDade, P., Blundy, J. D., & Wood, B. J. (2003b). Trace element partitioning between mantle wedge peridotite and hydrous MgO-rich melt. American Mineralogist, 88(11-12), 1825-1831.

McGeary, S., Nur, A., & Ben-Avraham, Z. (1985). Spatial gaps in arc volcanism: The effect of collision or subduction of oceanic plateaus. Tectonophysics, 119(1-4), 195-221.

McKenzie, D. A. N. (1984). The generation and compaction of partially molten rock. Journal of petrology, 25(3), 713-765.

Miyashiro, A. (1974). Volcanic rock series in island arcs and active continental margins. American journal of science, 274(4), 321-355.

Mollo, S., Forni, F., Bachmann, O., Blundy, J. D., De Astis, G., & Scarlato, P. (2016). Trace element partitioning between clinopyroxene and trachy-phonolitic melts: A case study from the Campanian Ignimbrite (Campi Flegrei, Italy). Lithos, 252, 160-172.

Montes, C., Cardona, A., McFadden, R., Morón, S. E., Silva, C. A., Restrepo-Moreno, S., ... & Bayona, G. A. (2012a). Evidence for middle Eocene and younger land emergence in central Panama: Implications for Isthmus closure. Bulletin, 124(5-6), 780-799.

Montes, C., Bayona, G., Cardona, A., Buchs, D. M., Silva, C. A., Morón, S., ... & Valencia, V. (2012b). Arc-continent collision and orocline formation: Closing of the Central American seaway. Journal of Geophysical Research: Solid Earth, 117(B4).

Moore, A., Coogan, L. A., Costa, F., & Perfit, M. R. (2014). Primitive melt replenishment and crystal-mush disaggregation in the weeks preceding the 2005–2006 eruption 9 50′ N, EPR. Earth and Planetary Science Letters, 403, 15-26.

Moore, J. C., & Vrolijk, P. (1992). Fluids in accretionary prisms. Reviews of Geophysics, 30(2), 113-135.

Morell, K. D., Kirby, E., Fisher, D. M., & Van Soest, M. (2012). Geomorphic and exhumational response of the Central American Volcanic Arc to Cocos Ridge subduction. Journal of Geophysical Research: Solid Earth, 117(B4).

Morell, K. D. (2015). Late M iocene to recent plate tectonic history of the southern C entral A merica convergent margin. Geochemistry, Geophysics, Geosystems, 16(10), 3362-3382.

Morimoto, N. (1988). Nomenclature of pyroxenes. Mineralogy and Petrology, 39(1), 55-76.

Morris, J. D., Leeman, W. P., & Tera, F. (1990). The subducted component in island arc lavas: constraints from Be isotopes and B–Be systematics. Nature, 344(6261), 31-36.

Nakagawa, M., Shimotori, H., & Yoshida, T. (1988). Across-arc compositional variation of the Quaternary basaltic rocks from the Northeast Japan arc. Journal of Mineralogy, Petrology and Economic Geology, 83(1), 9-25.

Nakagawa, M., Wada, K., Thordarson, T., Wood, C. P., & Gamble, J. A. (1999). Petrologic investigations of the 1995 and 1996 eruptions of Ruapehu volcano, New Zealand: formation of discrete and small magma pockets and their intermittent discharge. Bulletin of Volcanology, 61(1-2), 15-31.

Nandedkar, R. H., Hürlimann, N., Ulmer, P., & Müntener, O. (2016). Amphibole–melt trace element partitioning of fractionating calc-alkaline magmas in the lower crust: an experimental study. Contributions to Mineralogy and Petrology, 171(8-9), 71.

Nimis, P. (1995). A clinopyroxene geobarometer for basaltic systems based on crystal-structure modeling. Contributions to Mineralogy and Petrology, 121(2), 115-125.

Nisbet, E. G., & Pearce, J. A. (1977). Clinopyroxene composition in mafic lavas from different tectonic settings. Contributions to mineralogy and petrology, 63(2), 149-160.

Niu, Y., Regelous, M., Wendt, I. J., Batiza, R., & O'Hara, M. J. (2002). Geochemistry of near-EPR seamounts: importance of source vs. process and the origin of enriched mantle component. Earth and Planetary Science Letters, 199(3-4), 327-345.

Othman, D. B., White, W. M., & Patchett, J. (1989). The geochemistry of marine sediments, island arc magma genesis, and crust-mantle recycling. Earth and Planetary Science Letters, 94(1-2), 1-21.

O'Driscoll, L. J., Humphreys, E. D., & Saucier, F. (2009). Subduction adjacent to deep continental roots: Enhanced negative pressure in the mantle wedge, mountain building and continental motion. Earth and Planetary Science Letters, 280(1-4), 61-70.

O'Driscoll, L. J., Richards, M. A., & Humphreys, E. D. (2012). Nazca–South America interactions and the late Eocene–late Oligocene flat-slab episode in the central Andes. Tectonics, 31(2).

Peacock, S. M., Rushmer, T., & Thompson, A. B. (1994). Partial melting of subducting oceanic crust. Earth and planetary science letters, 121(1-2), 227-244.

Peacock, S. M. (1996). Thermal and petrologic structure of subduction zones. Subduction: top to bottom, 96, 119-133.

Pearce, J. A., & Norry, M. J. (1979). Petrogenetic implications of Ti, Zr, Y, and Nb variations in volcanic rocks. Contributions to mineralogy and petrology, 69(1), 33-47.

Pearce, J. A. (1982). Trace element characteristics of lavas from destructive plate boundaries. Andesites, 8, 525-548.

Pearce, J. A. (1983). Role of the sub-continental lithosphere in magma genesis at active continental margins.

Pearce, J. A., & Parkinson, I. J. (1993). Trace element models for mantle melting: application to volcanic arc petrogenesis. Geological Society, London, Special Publications, 76(1), 373-403.

Pearce, J. A., & Peate, D. W. (1995). Tectonic implications of the composition of volcanic arc magmas. Annual review of Earth and planetary sciences, 23, 251-286.

Pearce, J. A. (1996). A user's guide to basalt discrimination diagrams. Trace element geochemistry of volcanic rocks: applications for massive sulphide exploration. Geological Association of Canada, Short Course Notes, 12(79), 113.

Pearce, J. A., Stern, R. J., Bloomer, S. H., & Fryer, P. (2005). Geochemical mapping of the Mariana arc-basin system: Implications for the nature and distribution of subduction components. Geochemistry, geophysics, geosystems, 6(7).

Pearce, J. A., Kempton, P. D., & Gill, J. B. (2007). Hf–Nd evidence for the origin and distribution of mantle domains in the SW Pacific. Earth and Planetary Science Letters, 260(1-2), 98-114.

Perrin, A., Goes, S., Prytulak, J., Rondenay, S., & Davies, D. R. (2018). Mantle wedge temperatures and their potential relation to volcanic arc location. Earth and Planetary Science Letters, 501, 67-77.

Pfänder, J. A., Münker, C., Stracke, A., & Mezger, K. (2007). Nb/Ta and Zr/Hf in ocean island basalts—implications for crust–mantle differentiation and the fate of Niobium. Earth and Planetary Science Letters, 254(1-2), 158-172.

Rohrbach, A., Schuth, S., Ballhaus, C., Münker, C., Matveev, S., & Qopoto, C. (2005). Petrological constraints on the origin of arc picrites, New Georgia Group, Solomon Islands. Contributions to Mineralogy and Petrology, 149(6), 685-698.

Pindell, J. L., & Kennan, L. (2009). Tectonic evolution of the Gulf of Mexico, Caribbean and northern South America in the mantle reference frame: an update. Geological Society, London, Special Publications, 328(1), 1-55.

Plank, T., & Langmuir, C. H. (1998). The chemical composition of subducting sediment and its consequences for the crust and mantle. Chemical geology, 145(3-4), 325-394.

Plank, T. (2014). The chemical composition of subducting sediments. Elsevier.

Poli, S., & Schmidt, M. W. (2002). Petrology of subducted slabs. Annual Review of Earth and Planetary Sciences, 30(1), 207-235.

Pradhan, G. K., Fiquet, G., Siebert, J., Auzende, A. L., Morard, G., Antonangeli, D., & Garbarino, G. (2015). Melting of MORB at core–mantle boundary. Earth and Planetary Science Letters, 431, 247-255.

Profeta, L., Ducea, M. N., Chapman, J. B., Paterson, S. R., Gonzales, S. M. H., Kirsch, M., ... & DeCelles, P. G. (2015). Quantifying crustal thickness over time in magmatic arcs. Scientific reports, 5, 17786.

Putirka, K. D. (2008). Thermometers and barometers for volcanic systems. Reviews in mineralogy and geochemistry, 69(1), 61-120.

Ramírez, D. A., Foster, D. A., Min, K., Montes, C., Cardona, A., & Sadove, G. (2016). Exhumation of the Panama basement complex and basins: Implications for the closure of the Central American seaway. Geochemistry, Geophysics, Geosystems, 17(5), 1758-1777.

Rapp, R. P., Watson, E. B., & Miller, C. F. (1991). Partial melting of amphibolite/eclogite and the origin of Archean trondhjemites and tonalites. Precambrian Research, 51(1-4), 1-25.

Rapp, R. P., Shimizu, N., Norman, M. D., & Applegate, G. S. (1999). Reaction between slab-derived melts and peridotite in the mantle wedge: experimental constraints at 3.8 GPa. Chemical Geology, 160(4), 335-356.

Révillon, S., Hallot, E., Arndt, N. T., Chauvel, C., & Duncan, R. A. (2000). A complex history for the Caribbean Plateau: petrology, geochemistry, and geochronology of the Beata Ridge, South Hispaniola. The Journal of Geology, 108(6), 641-661.

Rollinson, H. R. (1993). Using geochemical data: evaluation, presentation, interpretation. Routledge.

Rogers, G., & Hawkesworth, C. J. (1989). A geochemical traverse across the North Chilean Andes: evidence for crust generation from the mantle wedge. Earth and Planetary Science Letters, 91(3-4), 271-285.

Rooney, T. O., Franceschi, P., & Hall, C. M. (2011). Water-saturated magmas in the Panama Canal region: a precursor to adakite-like magma generation?. Contributions to Mineralogy and Petrology, 161(3), 373-388.

Rooney, T. O., Morell, K. D., Hidalgo, P., & Fraceschi, P. (2015). Magmatic consequences of the transition from orthogonal to oblique subduction in P anama. Geochemistry, Geophysics, Geosystems, 16(12), 4178-4208.

Rustioni, G., Audetat, A., & Keppler, H. (2021). The composition of subduction zone fluids and the origin of the trace element enrichment in arc magmas. Contributions to Mineralogy and Petrology, 176(7), 1-19.

Sadofsky, S., Hoernle, K., Duggen, S., Hauff, F., Werner, R., & Garbe-Schönberg, D. (2009). Geochemical variations in the Cocos Plate subducting beneath Central America: implications for the composition of arc volcanism and the extent of the Galápagos Hotspot influence on the Cocos oceanic crust. International Journal of Earth Sciences, 98(4), 901-913.

Sak, P. B., Fisher, D. M., Gardner, T. W., Marshall, J. S., & LaFemina, P. C. (2009). Rough crust subduction, forearc kinematics, and Quaternary uplift rates, Costa Rican segment of the Middle American Trench. Geological Society of America Bulletin, 121(7-8), 992-1012.

Sakuyama, M., & Nesbitt, R. W. (1986). Geochemistry of the Quaternary volcanic rocks of the northeast Japan arc. Journal of Volcanology and Geothermal Research, 29(1-4), 413-450.

Scambelluri, M., Hermann, J., Morten, L., & Rampone, E. (2006). Melt-versus fluid-induced metasomatism in spinel to garnet wedge peridotites (Ulten Zone, Eastern Italian Alps): clues from trace element and Li abundances. Contributions to Mineralogy and Petrology, 151(4), 372.

Schiano, P., Clocchiatti, R., Shimizu, N., Maury, R. C., Jochum, K. P., & Hofmann, A. W. (1995). Hydrous, silica-rich melts in the sub-arc mantle and their relationship with erupted arc lavas. Nature, 377(6550), 595-600.

Schmidt, M. W., & Poli, S. (2003). Generation of mobile components during subduction of oceanic crust. TrGeo, 3, 659.

Schmidt, M. W., Vielzeuf, D., & Auzanneau, E. (2004). Melting and dissolution of subducting crust at high pressures: the key role of white mica. Earth and Planetary Science Letters, 228(1-2), 65-84.

Schmidt, M., & Poli, S. (2014). Devolatilization during subduction.

Schuth, S., Rohrbach, A., Münker, C., Ballhaus, C., Garbe-Schönberg, D., & Qopoto, C. (2004). Geochemical constraints on the petrogenesis of arc picrites and basalts, New Georgia Group, Solomon Islands. Contributions to Mineralogy and Petrology, 148(3), 288-304.

Sen, C., & Dunn, T. (1994). Dehydration melting of a basaltic composition amphibolite at 1.5 and 2.0 GPa: implications for the origin of adakites. Contributions to Mineralogy and Petrology, 117(4), 394-409.

Shervais, J. W. (1982). Ti-V plots and the petrogenesis of modern and ophiolitic lavas. Earth and planetary science letters, 59(1), 101-118.

Shore, M., & Fowler, A. D. (1996). Oscillatory zoning in minerals; a common phenomenon. The Canadian Mineralogist, 34(6), 1111-1126.

Shukuno, H., Tamura, Y., Tani, K., Chang, Q., Suzuki, T., & Fiske, R. S. (2006). Origin of silicic magmas and the compositional gap at Sumisu submarine caldera, Izu–Bonin arc, Japan. Journal of Volcanology and Geothermal Research, 156(3-4), 187-216.

Shuto, K., Nohara-Imanaka, R., Sato, M., Takahashi, T., Takazawa, E., Kawabata, H., ... & Fujibayashi, N. (2015). Across-arc variations in geochemistry of Oligocene to Quaternary basalts from the NE Japan arc: Constraints on source composition, mantle melting and slab input composition. Journal of Petrology, 56(11), 2257-2297.

Silver, E. A., Reed, D. L., Tagudin, J. E., & Heil, D. J. (1990). Implications of the north and south Panama thrust belts for the origin of the Panama orocline. Tectonics, 9(2), 261-281.

Silver, E. A., Galewsky, J., McIntosh, K. D., & Mann, P. (1995). Variation in structure, style, and driving mechanism of adjoining segments of the North Panama deformed belt. SPECIAL PAPERS-GEOLOGICAL SOCIETY OF AMERICA, 225-225.

Simonetti, A., Shore, M., & Bell, K. (1996). Diopside phenocrysts from nephelinite lavas, Napak Volcano, eastern Uganda; evidence for magma mixing. The Canadian Mineralogist, 34(2), 411-421.

Sims, K. W., & DePaolo, D. J. (1997). Inferences about mantle magma sources from incompatible element concentration ratios in oceanic basalts. Geochimica et Cosmochimica Acta, 61(4), 765-784.

Sinton, C. W., Duncan, R. A., & Denyer, P. (1997). Nicoya Peninsula, Costa Rica: A single suite of Caribbean oceanic plateau magmas. Journal of Geophysical Research: Solid Earth, 102(B7), 15507-15520.

Sinton, C. W., Duncan, R. A., Storey, M., Lewis, J., & Estrada, J. J. (1998). An oceanic flood basalt province within the Caribbean plate. Earth and Planetary Science Letters, 155(3-4), 221-235.

Sinton, J. M., & Detrick, R. S. (1992). Mid-ocean ridge magma chambers. Journal of Geophysical Research: Solid Earth, 97(B1), 197-216.

Skora, S., & Blundy, J. (2010). High-pressure hydrous phase relations of radiolarian clay and implications for the involvement of subducted sediment in arc magmatism. Journal of Petrology, 51(11), 2211-2243.

Smith, J. V., & Brown, W. L. (1988). Feldspars minerals, 2nd end, Vol. 1.

Smith, I. E., Worthington, T. J., Stewart, R. B., Price, R. C., & Gamble, J. A. (2003a). Felsic volcanism in the Kermadec arc, SW Pacific: crustal recycling in an oceanic setting. Geological Society, London, Special Publications, 219(1), 99-118.

Smith, I. E., Stewart, R. B., & Price, R. C. (2003). The petrology of a large intra-oceanic silicic eruption: the Sandy Bay Tephra, Kermadec Arc, Southwest Pacific. Journal of Volcanology and Geothermal Research, 124(3-4), 173-194.

Snow, J. E., & Dick, H. J. (1995). Pervasive magnesium loss by marine weathering of peridotite. Geochimica et Cosmochimica Acta, 59(20), 4219-4235.

Sobolev, A. V., Hofmann, A. W., Sobolev, S. V., & Nikogosian, I. K. (2005). An olivine-free mantle source of Hawaiian shield basalts. Nature, 434(7033), 590-597.

Sorensen, S. S. (1986). Petrologic and geochemical comparison of the blueschist and greenschist units of the Catalina Schist terrane, southern California. Geological Society of America Memoir, 164, 59-75.

Spandler, C., Mavrogenes, J., & Hermann, J. (2007). Experimental constraints on element mobility from subducted sediments using high-P synthetic fluid/melt inclusions. Chemical Geology, 239(3-4), 228-249.

Spandler, C., Yaxley, G., Green, D. H., & Rosenthal, A. (2008). Phase relations and melting of anhydrous K-bearing eclogite from 1200 to 1600 C and 3 to 5 GPa. Journal of Petrology, 49(4), 771-795.

Spandler, C., & Pirard, C. (2013). Element recycling from subducting slabs to arc crust: A review. Lithos, 170, 208-223.

Spera, F. J., & Bohrson, W. A. (2018). Rejuvenation of crustal magma mush: a tale of multiply nested processes and timescales. American Journal of Science, 318(1), 90-140.

Stern, C. R., & De Wit, M. J. (2003). Rocas Verdes ophiolites, southernmost South America: Remnants of progressive stages of development of oceanic-type crust in a continental margin back-arc basin. Geological Society, London, Special Publications, 218(1), 665-683.

Stern, R. J., & Gerya, T. (2018). Subduction initiation in nature and models: A review. Tectonophysics, 746, 173-198.

Stewart, R. H., & Stewart, J. L. (1980). Geologic map of the Panama Canal and vicinity, Republic of Panama (No. 1232).

Streck, M. J. (2008). Mineral textures and zoning as evidence for open system processes. Reviews in Mineralogy and Geochemistry, 69(1), 595-622.

Su, Y. (2003). Global MORB chemistry compilation at the segment scale. Ph. D. Thesis, Department of Earth and Environmental Sciences, Columbia University.

Sun, S. S., & McDonough, W. F. (1989). Chemical and isotopic systematics of oceanic basalts: implications for mantle composition and processes. Geological Society, London, Special Publications, 42(1), 313-345.

Tamura, Y., & Tatsumi, Y. (2002). Remelting of an andesitic crust as a possible origin for rhyolitic magma in oceanic arcs: an example from the Izu–Bonin arc. Journal of Petrology, 43(6), 1029-1047.

Tatsumi, Y. (1986). Formation of the volcanic front in subduction zones. Geophysical Research Letters, 13(8), 717-720.

Tatsumi, Y., & Suzuki, T. (2009). Tholeiitic vs calc-alkalic differentiation and evolution of arc crust: constraints from melting experiments on a basalt from the Izu–Bonin–Mariana Arc. Journal of Petrology, 50(8), 1575-1603.

Tera, F., Brown, L., Morris, J., Sacks, I. S., Klein, J., & Middleton, R. (1986). Sediment incorporation in island-arc magmas: Inferences from 10Be. Geochimica et Cosmochimica Acta, 50(4), 535-550.

Thomas, J. B., Bodnar, R. J., Shimizu, N., & Sinha, A. K. (2002). Determination of zircon/melt trace element partition coefficients from SIMS analysis of melt inclusions in zircon. Geochimica et Cosmochimica Acta, 66(16), 2887-2901.

Thorkelson, D. J., & Taylor, R. P. (1989). Cordilleran slab windows. Geology, 17(9), 833-836.

Thorkelson, D. J. (1996). Subduction of diverging plates and the principles of slab window formation. Tectonophysics, 255(1-2), 47-63.

Tollstrup, D., Gill, J., Kent, A., Prinkey, D., Williams, R., Tamura, Y., & Ishizuka, O. (2010). Across‐arc geochemical trends in the Izu‐Bonin arc: Contributions from the subducting slab, revisited. Geochemistry, Geophysics, Geosystems, 11(1).

Tomiya, A., & Takahashi, E. (2005). Evolution of the magma chamber beneath Usu Volcano since 1663: a natural laboratory for observing changing phenocryst compositions and textures. Journal of Petrology, 46(12), 2395-2426.

Trencamp, R., Kellogg, J. N., Freymuller, J. T., & Mora, H. P. (2002). Wider plate margin deformations, southern Central America and northwestern South America. CASA GPS observations: Journal of South American Earth Sciences, 15(2), 157-171.

Turner, F. J., & Verhoogen, J. (1960). Igneous and metamorphic rocks. New York.

Turner, S. P., Peate, D. W., Hawkesworth, C. J., Eggins, S. M., & Crawford, A. J. (1999). Two mantle domains and the time scales of fluid transfer beneath the Vanuatu arc. Geology, 27(11), 963-966.

Turner, S. J., & Langmuir, C. H. (2015). What processes control the chemical compositions of arc front stratovolcanoes?. Geochemistry, Geophysics, Geosystems, 16(6), 1865-1893.

Turner, S. J., Langmuir, C. H., Katz, R. F., Dungan, M. A., & Escrig, S. (2016). Parental arc magma compositions dominantly controlled by mantle-wedge thermal structure. Nature Geoscience, 9(10), 772-776.

Turner, S. J., Langmuir, C. H., Dungan, M. A., & Escrig, S. (2017). The importance of mantle wedge heterogeneity to subduction zone magmatism and the origin of EM1. Earth and Planetary Science Letters, 472, 216-228.

van Hunen, J., van den Berg, A. P., & Vlaar, N. J. (2000). A thermo-mechanical model of horizontal subduction below an overriding plate. Earth and Planetary Science Letters, 182(2), 157-169.

van Hunen, J., Van Den BERG, A. P., & Vlaar, N. J. (2002). On the role of subducting oceanic plateaus in the development of shallow flat subduction. Tectonophysics, 352(3-4), 317-333.

van Keken, P. E., Hacker, B. R., Syracuse, E. M., & Abers, G. A. (2011). Subduction factory: 4. Depth-dependent flux of H2O from subducting slabs worldwide. Journal of Geophysical Research: Solid Earth, 116(B1).

Vannucchi, P., Sak, P. B., Morgan, J. P., Ohkushi, K. I., Ujiie, K., & IODP Expedition 334 Shipboard Scientists. (2013). Rapid pulses of uplift, subsidence, and subduction erosion offshore Central America: Implications for building the rock record of convergent margins. Geology, 41(9), 995-998.

Vielzeuf, D., & Holloway, J. R. (1988). Experimental determination of the fluid-absent melting relations in the pelitic system. Contributions to Mineralogy and Petrology, 98(3), 257-276.

Vogel, T. A., Flood, T. P., Patino, L. C., Wilmot, M. S., Maximo, R. P. R., Arpa, C. B., ... & Stimac, J. A. (2006). Geochemistry of silicic magmas in the Macolod Corridor, SW Luzon, Philippines: evidence of distinct, mantle-derived, crustal sources for silicic magmas. Contributions to Mineralogy and Petrology, 151(3), 267-281.

Wadge, G., & Burke, K. (1983). Neogene Caribbean plate rotation and associated Central American tectonic evolution. Tectonics, 2(6), 633-643.

Wanke, M., Karakas, O., & Bachmann, O. (2019). The genesis of arc dacites: the case of Mount St. Helens, WA. Contributions to Mineralogy and Petrology, 174(1), 7.

Wegner, W., Wörner, G., Harmon, R. S., & Jicha, B. R. (2011). Magmatic history and evolution of the Central American Land Bridge in Panama since Cretaceous times. Bulletin, 123(3-4), 703-724.

Werner, R., Hoernle, K., Barckhausen, U., & Hauff, F. (2003). Geodynamic evolution of the Galápagos hot spot system (Central East Pacific) over the past 20 my: Constraints from morphology, geochemistry, and magnetic anomalies. Geochemistry, Geophysics, Geosystems, 4(12).

Whattam, S. A., Montes, C., McFadden, R. R., Cardona, A., Ramirez, D., & Valencia, V. (2012). Age and origin of earliest adakitic-like magmatism in Panama: Implications for the tectonic evolution of the Panamanian magmatic arc system. Lithos, 142, 226-244.

Whattam, S. A., & Stern, R. J. (2015). Late Cretaceous plume-induced subduction initiation along the southern margin of the Caribbean and NW South America: The first documented example with implications for the onset of plate tectonics. Gondwana Research, 27(1), 38-63.

Whattam, S. A., Montes, C., & Stern, R. J. (2020). Early central American forearc follows the subduction initiation rule. Gondwana Research, 79, 283-300.

White, A. J. R., & Chappell, B. W. (1983). Granitoid types and their distribution in the Lachlan Fold Belt, southeastern Australia. Geological Society of America Memoir, 159(12), 21-34.

White, R. S., McKenzie, D., & O'Nions, R. K. (1992). Oceanic crustal thickness from seismic measurements and rare earth element inversions. Journal of Geophysical Research: Solid Earth, 97(B13), 19683-19715.

Wilson, C. R., Spiegelman, M., van Keken, P. E., & Hacker, B. R. (2014). Fluid flow in subduction zones: The role of solid rheology and compaction pressure. Earth and Planetary Science Letters, 401, 261-274.

Woodhead, J. D. (1989). Geochemistry of the Mariana arc (western Pacific): source composition and processes. Chemical Geology, 76(1-2), 1-24.

Woodhead, J. D., & Johnson, R. W. (1993). Isotopic and trace-element profiles across the New Britain island arc, Papua New Guinea. Contributions to Mineralogy and Petrology, 113(4), 479-491.

Woodring, W. P. Woodring 1957–1982. Geology and paleontology of Canal Zone and adjoining parts of Panama. US Geological Survey Professional Paper, 306.

Workman, R. K., & Hart, S. R. (2005). Major and trace element composition of the depleted MORB mantle (DMM). Earth and Planetary Science Letters, 231(1-2), 53-72.

Wörner, G., Harmon, R. S., Hartmann, G., & Simon, K. (2005). Igneous geology and geochemistry of the Upper Río Chagres Basin. In The Río Chagres, Panama (pp. 65-81). Springer, Dordrecht.

Wörner, G., Harmon, R. S., & Wegner, W. (2009). Geochemical evolution of igneous rocks and changing magma sources during the formation and closure of the Central American land bridge of Panama. Backbone of the Americas: Shallow Subduction, Plateau Uplift, and Ridge and Terrane Collision: Geological Society of America Memoir, 204, 183-196.

Zhao, D., Tian, Y., Lei, J., Liu, L., & Zheng, S. (2009). Seismic image and origin of the Changbai intraplate volcano in East Asia: role of big mantle wedge above the stagnant Pacific slab. Physics of the Earth and Planetary Interiors, 173(3-4), 197-206.

Zheng, Y. F., Xia, Q. X., Chen, R. X., & Gao, X. Y. (2011). Partial melting, fluid supercriticality and element mobility in ultrahigh-pressure metamorphic rocks during continental collision. Earth-Science Reviews, 107(3-4), 342-374.

Zheng, Y. F. (2019). Subduction zone geochemistry. Geoscience Frontiers, 10(4), 1223-1254.

SUMMARY OF APPENDIXES

Appendix A – Whole Rock Geochemistry Laboratory Methods

Appendix B – SEM Laboratory Methods

Appendix C – Whole Rock Sr-Nd-Pb isotope Laboratory Methods

Appendix E1 – Sample Description

Appendix E2 – Whole Rock Geochemistry Data

Appendix E3 – Mineral Chemistry Data

Appendix E4 – Whole Rock Sr-Nd-Pb Isotope Data